Technische Universität München

Dissertation

Exotic Particles at the LHC: Production via the Higgs Portal and FIMP Dark Matter Searches

André Georg Hessler

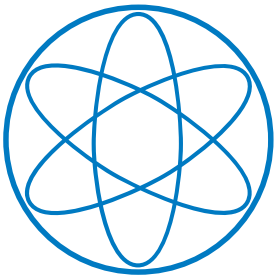

Physik-Department

Lehrstuhl T30d

Technische Universität München

Physik-Department

Dissertation

Exotic Particles at the LHC: Production via the Higgs Portal and FIMP Dark Matter Searches

---

André Georg Hessler

Vollständiger Abdruck der von der Fakultät für Physik der Technischen Universität München zur Erlangung des akademischen Grades eines

Doktors der Naturwissenschaften

genehmigten Dissertation.

Vorsitzende:	Univ.-Prof. Dr. Laura Fabbietti
Prüfer der Dissertation:	1. Univ.-Prof. Dr. Alejandro Ibarra
	2. Univ.-Prof. Dr. Wolfgang Hollik

Die Dissertation wurde am 03.08.2016 bei der Technischen Universität München eingereicht und durch die Fakultät für Physik am 05.09.2016 angenommen.

I am grateful for the funding by

FCT Fundação para a Ciência e a Tecnologia
MINISTÉRIO DA CIÊNCIA, TECNOLOGIA E ENSINO SUPERIOR

through the grant SFRH/BD/76052/2011, financed by the European Social Fund (ESF) through POPH under the QREN framework.

To my parents, Rudolf and Fátima

Abstract

Historically, the theoretical development of the Standard Model of Elementary Particle Physics is characterized by numerous pioneering contributions credited to many brilliant minds over the last century, going hand in hand with ingenious experimental endeavour. It impressively succeeds at explaining a vast number of experimental observations. The recent discovery of a Higgs boson by the ATLAS and CMS experiments at the Large Hadron Collider (LHC) marks a further milestone in cementing the model's validity, although it is clear that it needs to be extended in order to describe more observed phenomena. Since the Higgs boson mass has been very accurately measured, it is timely to assess the impact of this new interaction on the production of heavy particles predicted by some of these extensions. As a first part, this thesis presents results expected for the production cross sections of new scalar and fermionic particles at the LHC with masses at the electroweak scale and quantifies the Higgs portal contribution in a systematic way. It is found that the Higgs boson can have a sizeable effect and should definitely not be neglected in some cases. In the second part, we acknowledge that two of the Standard Model's shortcomings are its lack of an origin for the bulk dark matter content of the Universe and the fact that it does not provide a source for the oscillations of active neutrino flavours during propagation. Many models intending to cure these and other downsides have been developed over the last few decades. Ernest Ma's popular "scotogenic" model addresses these two issues in the most minimal way through an additional dark sector with a scalar electroweak doublet and at least two right-handed neutrino singlets. In case the lightest right-handed neutrino is the lightest dark particle and only undergoes feeble interactions, that is, if it is a FIMP, and furthermore if the next-to-lightest dark particle is the charged scalar, then the predicted collider signatures can be spectacular. In a second study, we present an analysis of the cases in which these particles contribute to the LHC signatures of stable charged tracks and of randomly-timed decays after being stopped due to their interactions with the detector material. The first analysis significantly weakens the existing limits on the production of singly-charged scalars when incorporating their instability, whereas the second analysis finds the LHC search for decaying stopped particles to be insensitive to the model due to low production cross sections and a low experimental timing efficiency. Nevertheless, the main outcome is the interesting result that the already accumulated LHC data allows to better understand the properties of the dark matter particle and its connection to the mechanism of neutrino mass generation in the framework of the scotogenic model, although our results can also be applied to a larger class of FIMP scenarios.

Zusammenfassung

Geschichtlich ist die theoretische Entwicklung des Standardmodells der Elementarteilchenphysik geprägt durch zahlreiche bahnbrechende Beiträge von brillanten Physikern im vergangenen Jahrhundert, welche Hand in Hand mit großem experimentellem Fortschritt einhergingen. Dem Modell gelingt es in eindrucksvoller Weise, eine große Anzahl experimenteller Beobachtungen zu erklären. Das kürzlich von den Experimenten ATLAS und CMS am Large Hadron Collider (LHC) entdeckte Higgs-Boson stellt einen weiteren Meilenstein darin dar, die Gültigkeit des Standardmodells zu festigen, allerdings ist es bekannt, dass es eine Erweiterung benötigt, um mehr beobachtete Phänomene zu beschreiben. Da die Higgs-Masse sehr genau bestimmt ist, ist jetzt ein angebrachter Zeitpunkt, die Auswirkung dieser neuen Wechselwirkung auf die Produktion schwerer Teilchen zu bemessen, welche in einigen dieser Erweiterungen vorhergesagt werden. Im ersten Teil dieser Dissertation werden erwartete Wirkungsquerschnitte für neue skalare und fermionische Teilchen am LHC präsentiert und der Beitrag des Higgs-Portals systematisch diskutiert. Sein Effekt wird in manchen Fällen als nicht vernachlässigbar befunden. Der zweite Teil stützt sich auf zwei der Mängel des Standardmodells, nämlich das Fehlen einer Erklärung für den Hauptanteil dunkler Materie im Universum und einer Deutung der Flavour-Oszillationen propagierender aktiver Neutrinos. Die letzten Jahrzehnte sahen die Entwicklung vieler Modelle, die versuchten, diese und weitere Defizite zu beheben. Das bekannte "skotogenische" Modell von Ernest Ma nimmt sich dieser Punkte in der minimalsten Weise an, indem es einen zusätzlichen dunklen Sektor mit einem skalaren Dublett und mindestens zwei rechtshändigen Neutrino-Singuletts der Eichgruppe einführt. Im Falle in welchem das leichteste rechtshändige Neutrino äußerst schwach wechselwirkt, d.h. wenn es sich um ein FIMP handelt, und wenn es gleichzeitig das leichteste und das geladene Skalar das nächstleichtere dunkle Teichen darstellt, sind die Signaturen in Teilchenbeschleunigern möglicherweise spektakulär. In einer zweiten Studie wird in der hiesigen Arbeit eine Analyse von zwei Fällen vorgestellt, in welchen die neuen Teilchen am LHC zu Signaturen mit geladenen Spuren und mit zufällig zeitlich stattfindenden Zerfällen nach vollständiger Abbremsung im Detektormaterial beitragen. Im ersten Fall werden existierende Beschränkungen an die Produktion dieser Teilchen signifikant geschwächt durch die Berücksichtigung ihrer Instabilität, während im zweiten Fall die Sensitivität der LHC-Suche aufgrund von niedrigen Produktionsraten und experimenteller Effizienzen nicht ausreicht, um das Modell zu beschränken. Nichtsdestotrotz erlangen wir das interessante Ergebnis, dass die bereits vorhandenen Daten des LHC einem besseren Verständnis der Eigenschaften des Teilchens dunkler Materie und seiner Rolle in der Generation von Neutrinomassen im skotogenischen Modell genügen. Darüberhinaus sind die präsentierten Ergebnisse auf eine größere Klasse von FIMP-Szenarien anwendbar.

Contents

CHAPTER 1

Introduction

The status quo of the Standard Model of Particle Physics (SM) [3, 4] can be described as a situation of two extremes. On the one hand, the SM is capable of predicting the overwhelming majority of observed elementary particle properties and interactions over a vast range of available energies; moreover, its validity is supported by the recent discovery of a Higgs boson at the ATLAS and CMS experiments [5, 6], an ingredient required to exist if particles do gain their masses through the Higgs mechanism [7] when the Higgs field acquires its vacuum expectation value (VEV). On the other hand, it is blatantly visible that the model represents an incomplete description of Nature. For instance, it does not incorporate the gravitational interaction, believed to be important at energies of the order of the Planck scale, $\Lambda_{\mathrm{P}} \sim 10^{19}$ GeV. However, much more pressing issues arise already at low energies. Common present understanding of cosmology sheds no doubt on the fact that the Universe consists of more forms of energy than merely visible matter. Very precise measurements of the anisotropies in the cosmic microwave background [8] indicate that the cosmos consists up to about 5% of baryonic matter, 26% of dark matter and 69% of dark energy. Putting the even more mysterious dark energy aside, dark matter is a factor of five times more abundant than the familiar population of ordinary atoms. The term 'dark matter' is utilized to denote the as yet unknown origin of what drives the observed intragalactic, galactic and intergalactic dynamics, as well as the explanation for the large scale structure and cosmic microwave background measurements. On another note, ever since the Homestake experiment revealed that there are less solar electron neutrinos reaching the Earth than expected [9], a large number of very ingenious experiments have shown that active neutrinos alter their quantum flavour during propagation, revealing that at least two of them are massive and that their masses are required to be tiny. Flavour oscillations and the neutrino mass scale lack any explanation in the SM, as it treats neutrinos as strictly massless and thus as purely left-chiral. Common lore is that neutrino masses require additional scalar or right-chiral fields with parameter configurations explaining their smallness; extra-dimensional scenarios introduce further methods to suppress sizeable neutrino masses [10–12]. The canonical frameworks providing tree-level neutrino masses in this manner are the seesaw mechanisms of type I [13], type II [14] and type III [15, 16].

Physics thrives on crisis, to put it in the words of Weinberg. Extending the SM particle spectrum to explain dark matter and neutrino masses therefore suggests itself. It is natural to presume that dark matter consists of a new particle or a new family of particles, as is the case in a myriad of models. An equal line of thinking applies to the origin of neutrino masses and to other serious problems inherent to the SM. For instance, the most popular solution to the *hierarchy problem* of the discrepancy between the electroweak and gravitational scales [17] is a supersymmetric (SUSY) extension of the SM [18], where the sensitivity of the Higgs mass to the ultraviolet scale becomes naturally suppressed due to a boson-fermion symmetry between the SM particles and newly introduced supersymmetric partners (see [19] and references therein). Supersymmetric theories are so versatile that they can be shaped, extended and constrained such as to solve the majority of theoretical difficulties. For instance, the stability of the proton is conventionally instated by an imposed discrete symmetry called R-parity, which inhibits gauge invariant operators violating baryon and lepton numbers and thus allowing proton decay through intermediate squarks. A dark matter candidate is also naturally provided in the form of the lightest sparticle, if it is electrically neutral. Alternatively, 'Little Higgs' theories treat the Higgs boson as a pseudo-Goldstone boson of a broken global symmetry, where the Higgs mass appears radiatively and is stable under quantum corrections and where new heavy particles at the TeV scale are introduced [20]. Another solution to the hierarchy problem is achieved by relating the two scales geometrically in theories with extra compactified dimensions with such small sizes

that they only play a role at microscopic scales [21–23]. Due to the compactification, the fields manifest in four-dimensional spacetime as an infinite tower of Kaluza-Klein modes [24] whose excitations are seen as heavy partners of the existing particles in the SM. Depending on the underlying metric and further symmetries, such theories may lead to dark matter candidates [25], gauge coupling unification [26] and explain the observed mass hierarchies and flavour structure in the quark and lepton sectors [27]. As a last example, the most well-known proposed solution to the *strong CP problem* is Peccei-Quinn theory, where a new scalar field, the axion, is introduced (among other new fields) [28]. If the Peccei-Quinn symmetry is not gauged, the QCD vacuum contains the axion as a pseudo-Nambu-Goldstone boson [29], which can serve as an attractive dark matter candidate [30]. Some of the new degrees of freedom predicted within these models can be produced in particle colliders under certain circumstances, though thus far there has been no direct hint of any as yet unknown elementary particle. Nevertheless, the searches are ongoing and the hope is to ultimately reach the point of a discovery.

From a more general point of view, the symmetry structure of the SM allows for the addition of new representations of the gauge and Lorentz groups that may furnish particle candidates contributing to the solution of some of the mentioned gaps. It is then necessary to study their implications for collider phenomenology. This thesis covers two studies dealing with exotic particle production at the Large Hadron Collider (LHC) [31], the particle accelerator at the CERN research facility near Geneva, in Switzerland and France. In the following, each of them is motivated and summarized.

As stated above, a new boson has recently been discovered, with properties strongly resembling those of the boson predicted by the dynamics of electroweak symmetry breaking through the Higgs mechanism. ATLAS and CMS have found its mass to be 125.09 GeV [32]. This value lies in the range expected from measurements of electroweak precision observables [33, 34] and is in accordance with unitarity requirements of longitudinal gauge boson scattering amplitudes [35]. Moreover, its decays correspond to what is expected in the SM [36, 37] and angular distributions of decay products strongly prefer the $J^{PC} = 0^{++}$ hypothesis regarding its spin and CP assignments [38, 39]. The Higgs mediates a new interaction in the production of the particles it couples to. By knowing the value of the mass, one is enabled to analyze this interaction in a quantitative way and assess its impact on the production of heavy particles predicted by some extensions of the SM. As a first part, we compute expected cross sections for the production of new uncoloured scalar and fermionic particles in simple benchmark scenarios at the LHC with masses at the electroweak scale and systematically quantify the Higgs portal contribution. It is found that it can be significant when compared to the leading-order electroweak mechanism for the production of the same final state, even of the order of QCD corrections, and should therefore not be neglected. Expectations for a hypothetical proton-proton collider operating at a center-of-mass energy of 100 TeV are also presented.

In a second study, we turn to a popular and well-motivated model extending the SM in a minimal way such as to explain neutrino masses and oscillations, while also providing a dark matter candidate, namely the "scotogenic" model by Ernest Ma [40], a variation of a previously proposed model [41] with different symmetry assignments. The model only introduces an additional scalar doublet and a set of at least two right-handed neutrinos (RHN) that are odd under a $\mathbb{Z}_2$ symmetry, while the regular SM fields transform evenly. The $\mathbb{Z}_2$ precludes the neutral component from acquiring a VEV. A further consequence of this exact symmetry is the total stability of the lightest odd particle (LOP), as is the case in supersymmetry due to R-parity. If the LOP is the lightest RHN N_1 or the lightest neutral scalar, then it may function as a viable dark matter candidate. Here we consider the former case, with the charged scalar $H^\pm$ being the next-to-lightest odd particle (NLOP). Following [42], the NLOP interaction with N_1 is taken to be so weak that N_1 decouples from thermal processes in the early Universe. Therefore N_1 classifies as a feebly interacting massive particle (FIMP) and, in the absence of late NLOP decays, the DM relic abundance is fully obtained via the freeze-in mechanism [43]. In that case, the decay lengths of the $H^\pm$ are macroscopic if its mass lies below the TeV scale and if the dark matter mass is $\gtrsim$ few keV, which is the warm dark matter regime. The expected signatures at the LHC are very exotic compared to what is looked for in standard SM tests or SUSY searches. ATLAS and CMS performed searches for tracks left in the tracker and muon systems by massive (meta-)stable charged particles [44, 45] and for long-lived particles decaying out-of-time with respect to the event trigger rate after being stopped by the dense material of the calorimeters [46, 47],

all using Run I data. Despite very low background rates, no excesses over the expected SM event numbers have been observed. We interpret the results of the collaborations in terms of the FIMP realization of the scotogenic model to compute constraints on its parameter space. It is found that accounting for the instability of the $H^{\pm}$ leads to significantly weaker bounds than when the charged scalar is presumed to be stable and the limits from the search on singly-charged particle production cross sections are directly adopted. Furthermore, through the interpretation of the stopped particles signal to stem from $H^{\pm}$ decays to τ leptons, it is found that the search is not sufficiently sensitive to this version of the model due to low production cross sections and the poor timing efficiency, even with little expected non-collision background.

In summary, two analyses are presented, the second being divided into two sub-analyses. To facilitate referring to one of the three, we label and name them according to:

Analysis I:	Impact of the Higgs boson on the production of exotic particles at the LHC
Analysis IIA:	Testing the FIMP realization of the scotogenic model at the LHC: Long-lived $H^{\pm}$ particles producing stable charged tracks in the CMS detector
Analysis IIB:	Testing the FIMP realization of the scotogenic model at the LHC: Long-lived stopped $H^{\pm}$ particles decaying out-of-time in the ATLAS detector

The thesis is organized as follows. Chapter 2 presents all necessary theoretical matters forming the base for the considered SM extensions. Section 2.1 discusses the SM, Section 2.2 is dedicated to cosmology, Section 2.3 to neutrino physics and Section 2.4 presents the scotogenic model and particularizes on the FIMP setting. In Chapter 3, we include all basic aspects related to the physics of hadron colliders deemed necessary for our analyses. The chapter ends with a detailed description of the ATLAS and CMS detectors for the end of creating a simplified detector simulation for Analyses IIA and IIB using toy detectors; these are presented in Section 3.2.3. Chapter 4 treats all concepts related to the detection of long-lived particles through the herein considered signatures, such as energy loss and decay and survival probabilities. Analysis I is then presented in Chapter 5, while Chapter 6 is dedicated to Analyses IIA and IIB. We finally conclude in Chapter 7.

The results of this work are presented in the articles

[1] A. G. Hessler, A. Ibarra, E. Molinaro, and S. Vogl, *Impact of the Higgs Boson on the Production of Exotic Particles at the LHC*, Phys. Rev. **D91**, 115004 (2015), arXiv 1408.0983 [hep-ph]

[2] A. G. Hessler, A. Ibarra, E. Molinaro, and S. Vogl, TUM-HEP-1058/16, (2016) [article in completion]

CHAPTER 2

Theoretical background

2.1 The Standard Model, its present status and going beyond

We commence the thesis[1] with a synopsis of the current state of the physics involving elementary particles, described by the Standard Model of Particle Physics (SM). Following that, before delving into its formal construction in Section 2.1.3, we deepen previously mentioned thoughts on why the SM cannot be considered a complete theory of Nature in Section 2.1.2.

2.1.1 The present status of the Standard Model

The SM represents our current understanding of how elementary particles interact. It is experimentally extremely well established and in itself theoretically consistent. The SM simultaneously describes electromagnetic [48], weak [49] and strong [4] processes, connecting the unbroken symmetry high-energy and the broken symmetry low-energy phases via the Higgs–Brout–Englert–Guralnik–Hagen–Kibble mechanism, or in short, Higgs mechanism [7]. In the very early Universe, the unbroken phase unifies electromagnetism and weak forces to a single electroweak theory (EW), also denoted quantum flavourdynamics (QFD) or Glashow-Weinberg-Salam (GWS) theory [3]. The Higgs mechanism lies at the heart of the phase transition reducing the GWS symmetry $\mathrm{SU}(2)_L \times \mathrm{U}(1)_Y$ down to electromagnetism $\mathrm{U}(1)_{\mathrm{EM}}$, which is quantum theoretically described by quantum electrodynamics (QED) [48]. While the SM surely does not account for all phenomena observed in or attributable to elementary particle processes, the astonishing accuracy of many of its verified predictions render it the most successful outcome in theoretical physics so far.

Indeed, consider the measurement of the value of the magnetic moment μ_e of the electron. No other property of any other particle has been experimentally determined with a comparable precision. In terms of the Landé factor g and the Bohr magneton μ_{B}, the magnetic moment of the electron is given by $\mu_e = -g/2 \times \mu_{\mathrm{B}}$. The Dirac equation dictates $g = 2$, but the SM predicts radiative corrections to this value, *i.e.* corrections due to interactions of the electron with the quantum vacuum, leading to an 'anomalous' contribution given by the following perturbative expansion in terms of the fine structure constant α:

$$a_e \equiv \frac{g-2}{2} = C_1 \left(\frac{\alpha}{\pi}\right) + C_2 \left(\frac{\alpha}{\pi}\right)^2 + C_3 \left(\frac{\alpha}{\pi}\right)^3 + \ldots + a_{\mu,\tau} + a_{\mathrm{had}} + a_{\mathrm{weak}} \,. \tag{2.1}$$

The series in α and the quantity $a_{\mu,\tau}$ are contributions from QED, where $a_{\mu,\tau}$ are terms depending on the ratio of the electron mass and the mass of the μ and τ leptons. All the numbers a_i and C_i are finite due to the renormalizability of the theory. a_{had} are hadronic processes involving bound states of quarks, coloured fermionic particles undergoing strong interactions described by quantum chromodynamics (QCD) involving gluons, and finally a_{weak} represents the weak force contributions mediated by the heavy W and Z bosons. Up to now, the most precise a_e-independent measurement of α was realized in 2010 by Biraben et al. (2010) in a determination of the recoil velocity v_{r} of a rubidium (Rb) atom after absorbing a photon, finding the value to be $\alpha^{-1}_{\mathrm{exp}} = 137.035\,999\,037(91)$. Use was made of a direct connection between α, v_{r} and $\hbar/m_{\mathrm{Rb}}$. The most recent measurement of a_e is by Gabrielse et al. (2008), yielding $a_e^{\mathrm{exp}} = 0.001\,159\,652\,180\,73\,(28)$. In the experiment, a_e is obtained via $\mu_e/\mu_{\mathrm{B}} = -\omega_s/\omega_{\mathrm{c}}$, where $\hbar\omega_s$ is the energy released by the electron in a spin flip while held in a Penning trap and ω_{c} is its cyclotron frequency. This requires an a priori input of α, for which they took the then most precise theoretical value obtained by Aoyama et al. (2007) from

[1] Throughout the thesis, natural units ($c = \hbar = k_{\mathrm{B}} = 1$) are employed, with the exception of some isolated instances.

a calculation of a_e, containing a corrected value of C_4. Until five years later, the QED calculation was updated by Aoyama et al. (2012). Using as input the value of α_{exp} by Biraben from 2010, the inclusion of C_5 resulted in $a_e^{\text{th}} = 0.001\,159\,652\,181\,78(77)$. From this, an even more precise value of α can be computed. Notice that the uncertainty is about 2.8 times higher than in the measurement, due to the uncertainty in α_{exp}. But now both uncertainties are in the ten parts per trillion, indeed a remarkable achievement. The values agree to $(1.06 \pm 0.82) \times 10^{-12}$, a tiny difference rendering QED the best tested of all theories and a_e a very useful quantity to constrain models altering the electron-photon coupling at the loop-level. A collection of the references forming the base of this discussion can be found in [50].

Other successes of the SM shall not remain unmentioned. Focus, for instance, on the recent discovery of a spin-0 boson with a mass of around 125 GeV in the year 2012 by the ATLAS and CMS collaborations [5, 6]. In the simplest formulation of spontaneous electroweak symmetry breaking (EWSB), one predicts the existence of a low-energy residuary degree of freedom (d.o.f.) in the form of a massive unstable CP-even spin-0 particle, the Higgs boson. Previous searches for the Higgs boson have been carried out at the Large Electron-Positron Collider (LEP) [51] and the Tevatron [52] experiments, where the LEP search hinted at the existence of a SM-like Higgs boson with a mass $\gtrsim 114$ GeV with a significance of 1.7σ and the Tevatron excluded the regions $m_h \in [100, 103]$ GeV and $m_h \in [147, 180]$ GeV at 95% confidence level (C.L.). The mass and the observed interactions and properties of the discovered particle strongly point to it being the scalar boson of the SM giving mass to gauge bosons and fermions. Should this be ultimately verified, then the SM consistently describes the true mechanism of electroweak symmetry breaking. The Higgs boson is the protagonist in our first study, Analysis I.

In the SM, the Higgs boson plays another crucial role. Without its existence, the SM would not predict any flavour structure in the fermion sector; in particular, the quarks would not exhibit mixing effects when probed through their gauge interactions. All quark mixing parameters have their origin in the misalignment between up- and down-type quark fields in the Yukawa interactions with the Higgs field. Since neutrinos are treated as massless, the SM does not predict mixing in the lepton sector, hence the leptons interact universally with the gauge bosons. For the quarks, mixing is described through the CKM matrix (*cf.* Section 2.1.3.2). Moreover, the SM does not predict flavour-changing neutral currents (FCNC) at tree-level by virtue of the GIM mechanism [53]. Whereas the lepton sector clearly requires an extension to account for neutrino mixing, the SM is quite successful in describing quark flavour effects, up to a few intriguing anomalies and tensions between some observables that either might hint at new physics or go away with better statistics [54].

2.1.2 Going beyond the Standard Model

Several reasons demanding an extension of the SM were given in the introduction. This section treats some of them with more qualitative detail, the choice being guided by the thesis content but also by personal bias. The reader is referred to [55] for a more thorough review of some of the SM's shortcomings.

□ **Absence of gravitation:** Gravitation is not an ingredient of the SM. The hypothesized graviton in a quantum gravity extension induces unrenormalizable interactions because the Einstein field equations [56] introduce the coupling parameter $1/m_{\text{P}}$, with a negative mass dimension, where $m_{\text{P}} = (8\pi G)^{-1/2} = 2.4 \times 10^{18}$ GeV is the reduced Planck mass. String theory and loop quantum gravity have been proposed to unify gravitation with the other three forces of Nature, though they still lack experimental verification.

□ **The hierarchy problem:** When extrapolating the SM to higher energies, one ultimately arrives at a point of extreme parameter tuning. The physical Higgs mass, *i.e.* the measured value obtained from the fundamental Lagrangian mass after renormalization, is highly sensitive to the radiative corrections, although it is found to be small [5, 6]. Hence GWS theory comes with an intrinsic *naturalness problem*, as was first pointed out by Susskind [17]. Loop momenta need to be evaluated up to energies Λ_{UV} at which the theory is valid; higher momenta imply a change in degrees of freedom and hence the validity of another theory. If the SM is valid until the Planck scale $\Lambda_{\text{UV}} \sim m_{\text{P}}$, the regime of quantum gravitation, every

particle coupling to the Higgs boson adds a gargantuan contribution to the corrected mass proportional to $\Lambda_{\mathrm{UV}}^2 \sim m_{\mathrm{P}}^2$. To put it in numbers, the squared mass parameter μ^2 (*cf.* Equation 2.5d) receives corrections about 30 orders of magnitude larger than required for a squared Higgs boson mass of $(125\ \mathrm{GeV})^2$ [19] if a regular loop integral cutoff is used. This sensitivity propagates into all fermion and gauge boson masses, since they all gain their mass through the Higgs mechanism. Moreover, should new mass scales Λ_m appear in the vast range between the electroweak scale Λ_{EW} and Λ_{UV}, the squared Higgs mass will receive further contributions which are proportional to Λ_m^2 if the new particles couple to the Higgs field. The *hierarchy problem*, in fact a synonym for the naturalness problem, consists of the difficulty in finding a theory valid somewhere between Λ_{EW} and Λ_{UV} with new physics content able to provide a means for eliminating the sensitivity to high energies and masses, as disturbingly precise cancellations are necessary. Nevertheless, the existence of far-apart though accessible transition scales, such as Λ_{QCD} and Λ_{EW}, suggests that such a new theory should be found to populate the 'gauge desert'. Some proposed solutions are supersymmetric extensions [18], Little Higgs models [20], models with extra dimensions [21–23] or a conformal high-energy formulation of the Higgs potential with a purely radiatively induced Higgs mass [57]. All these extensions predict new particles at the TeV scale to guarantee naturalness. The fact that no such particles have yet been found is termed the 'little hierarchy problem'.

□ **The cosmological constant problem:** Closely related to the hierarchy problem is the cosmological constant problem [58]. It is frequently formulated as the enormous discrepancy between the zero-point energy in the SM and the tiny measured value of the cosmological constant parametrizing the vacuum energy driving the present de Sitter phase of the Universe's dynamics. Since $\Omega_\Lambda = 0.69$ [8], one finds $\rho_\Lambda \approx (0.002\ \mathrm{eV})^4$. A theory valid up to energies of the order Λ contributes to the vacuum energy with terms of order Λ^4. For the SM, taking $\Lambda \sim 100$ GeV, one obtains a discrepancy of about $(100\ \mathrm{GeV}/1\ \mathrm{meV})^4 = 10^{56}$, indeed a gigantic mismatch. GUT theories valid to 10^{16} GeV raise the discrepancy until almost 120 orders of magnitude. The problem becomes even more severe when formulated properly, for it is more a matter of radiative instability, analogously to the hierarchy problem affecting scalar masses in GWS theory [59]. Upon renormalization, the quantity actually gravitating is the renormalized cosmological constant, $\bar{\Lambda} = \Lambda + V_{\mathrm{vac}}$, where Λ is the constant in the Lagrangian acting as a counterterm and V_{vac} is the energy of the vacuum calculated from quantum loop bubbles. If perturbation theory is applicable, one finds that the vacuum energy actually depends on an arbitrary energy scale, hence $\bar{\Lambda}$ cannot be calculated and needs to be measured, as is the case with couplings and masses in the SM. The actual cosmological constant problem resides in the fact that, if the needed huge cancellation is achieved at a given loop order, it will be destroyed by the next loop order, thus $\bar{\Lambda}$ is extremely sensitive to UV physics. This is widely regarded as the severest problem in all of theoretical physics.

□ **Dark matter (DM):** There exists compelling evidence for the existence of matter in the Universe with a gravitational effect on luminous matter that is incompatible with the predictions of Newtonian or general-relativistic dynamics applied solely to visible objects. This leads the large majority of the physicist community to believe that there exists a type of long-lived or stable, massive, weakly interacting and electrically neutral 'dark' particle responsible for these observations. It cannot consist of any field contained in the SM: On the one side, a baryonic DM particle would influence and possibly significantly alter the successful Big Bang nucleosynthesis predictions for the light element abundances and it would be incompatible with observations of the cosmic microwave background (CMB), *cf.* Section 2.2.1. Secondly, although the light neutrinos satisfy the main criteria for such a particle, they cannot constitute all of the DM in the Universe, as predictions for their role in the formation of large scale structure are not in accordance with observations, as we will discuss in Section 2.2.2.2. Therefore, if DM consists of particles, the SM particle content needs to be extended by the DM particle field(s). The scotogenic model [40] is one of countless SM extensions addressing this issue. We will study a particular setup of this model in Section 2.4.

□ **Neutrino masses and oscillations:** Neutrino masses and oscillations, besides the evidence for dark matter, are perhaps the most direct indication for new physics and are expected to be among the first phenomena to open an experimental window for directly looking beyond the Standard Model. They are integral background to the theme of the thesis and are treated in Section 2.3.

□ **Baryon asymmetry of the Universe:** Amongst the most pressing theoretical issues lies the question of the predominant abundance of baryons over antibaryons in the Universe. Assuming that matter and antimatter were created in equal initial abundances, one requires an explanation for why antimatter evanesced during the earliest phases. It is commonly accepted that the involved mechanism relies on the three conditions postulated by Sakharov [60]: baryon number violation, C and CP violation and thermal inequilibrium. The first condition is self-evident, so is the requirement for C violation, since otherwise C-conjugate reactions would counterbalance the baryon number-violating processes. CP violation is also needed because, if CP were a symmetry of Nature, the sum of a baryon number-violating process and its CP conjugate would again preserve baryon number. Lastly, the CPT theorem imposes equality of particle and antiparticle masses. Thermal equilibrium thus corresponds to equal amounts of matter and antimatter, as described by the Boltzmann equation (see Appendix B). Therefore a departure from equilibrium is also required. The SM can in principle account for generating a baryon asymmetry, though the amount of measured CP violation in the flavour sector is not sufficient to accomodate the observed imbalance [61]. Two proposed mechanisms are electroweak baryogenesis [62] and leptogenesis [63].

□ **The strong CP problem:** The u and d quarks are very light, $m_{u,d} \ll \Lambda_{\mathrm{QCD}}$. Hence, one would expect chiral symmetry to be an exact symmetry of the QCD vacuum in the limit $m_{u,d} \to 0$, with the massive theory being dynamically broken by the $\langle \bar{u}u \rangle$ and $\langle \bar{d}d \rangle$ condensates with four Nambu-Goldstone bosons. This would explain the non-observation of parity doublets. However, only three light mesons appropriate for the role exist, namely the pions, which Weinberg termed the $\mathrm{U}(1)_A$ problem [64]. Shortly thereafter, the solution followed through the introduction of instanton field configurations by 't Hooft [64]. With the introduction of the so-called θ-term, $\mathrm{U}(1)_A$ was not a symmetry of the QCD Lagrangian anymore, though this term violates CP, whereas CP violation is not observed in the strong interactions. The question of why this is the case is known as the *strong CP problem*, see *e.g.* [65]. The vacuum angle θ actually combines with radiative corrections to the quark masses. If an imaginary part is present, the quantity $\bar{\theta} = \theta + \arg\det M_q$ appears in the expression for the electric dipole moment (EDM) d_n of the neutron as a constant of proportionality. Since no neutron EDM has yet been measured, the upper bound of $d_n < 6.3 \times 10^{-36}\ e\,\mathrm{cm}$ [66] yields $\bar{\theta} < 10^{-9}$ [67]. Asking for the reason of the smallness (or the tuning) of $\bar{\theta}$ is another way to state the strong CP problem; $\bar{\theta}$ would be unobservable in the limit of one massless quark, though experiment shows that all known quarks are massive.

2.1.3 Field content and formulation of the Standard Model

The mathematical formulation of the SM uses the language of quantum field theory (QFT). A Lagrangian (density) $\mathcal{L}$ expresses how the particle fields, the main building blocks of the theory, interact as dictated by inherent symmetries described by transformation groups acting on the fields, such as the Lorentz and gauge groups. Through the application of the Euler-Lagrange equation, one derives the equations of motion. Conserved charges and symmetry currents are extracted from the Lagrangian using Noether's theorem [68]. In this section, we present separately the unbroken and broken phases, which are connected by the Higgs mechanism.

2.1.3.1 The Standard Model Lagrangian: Unbroken phase and EWSB

Formally, the SM is a Yang-Mills theory [69], thus containing gauge fields that transform under a non-Abelian gauge group. In both phases, the QCD group $\mathrm{SU}(3)_\mathrm{c}$ is trivially combined with either the GWS

Multiplet	**Particle field**	g_i	**Spin**	$\mathrm{SU(3)_c}\times\mathrm{SU(2)}_L\times\mathrm{U(1)}_Y$
$Q_i = \begin{pmatrix} u_i \\ d_i \end{pmatrix}_L$	LH quark doublet	36	1/2	(3, 2, 1/3)
u_{Ri}	RH up-type quark singlet	18	1/2	(3, 1, 4/3)
d_{Ri}	RH down-type quark singlet	18	1/2	(3, 1, -2/3)
$L_i = \begin{pmatrix} \nu_i \\ \ell_i \end{pmatrix}_L$	LH lepton doublet	12	1/2	(1, 2, -1)
ℓ_{Ri}	RH charged lepton singlet	6	1/2	(1, 1, -2)
B_μ	hypercharge gauge field	2	1	(1, 1, 0)
$A_\mu^{1,2,3}$	electroweak isospin gauge field	6	1	(1, 3, 0)
$G_\mu^{1,\dots,8}$	gluon field	16	1	(8, 1, 0)
H	Higgs doublet	4	0	(1, 2,1)

TABLE 2.1: Particle field content of the Standard Model

group or the electromagnetism group,

$$\mathcal{G}_{\mathrm{SM}} = \mathrm{SU(3)_c}\times\mathrm{SU(2)}_L\times\mathrm{U(1)}_Y \overset{\mathrm{EWSB}}{\longrightarrow} \mathcal{G}'_{\mathrm{SM}} = \mathrm{SU(3)_c}\times\mathrm{U(1)_{EM}}\,. \tag{2.2}$$

Here, 'c' stands for the QCD colour charge, 'L' indicates the presence of maximal parity violation through the exclusive action of the SU(2) factor on left-chiral fermions and $Y = 2(Q - T^3)$ is the weak hypercharge, calculated from the electric charge Q and the eigenvalue under the action of the third $\mathrm{SU(2)}_L$ generator T^3. Apart from the special Higgs boson, it contains two kinds of fields. On the one side, there are the spin-$\frac{1}{2}$ matter fields (quarks and leptons) and, on the other side, the spin-1 gauge fields, which mediate the interactions between the matter fields. The field content of the SM is presented in Table 2.1, along with their charges under $\mathcal{G}_{\mathrm{SM}}$ and the total number of relativistic degrees of freedom the field type contributes to thermodynamic quantities in cosmology, as required in Section 2.2. i is the generation/family index, running from 1 to 3 for lepton and quark fields. Given a quark's or lepton's weak isospin T^3 and its generation index, one can specify its *flavour* — there are six quark and six lepton flavours in the SM. Notice that the quantum numbers are attributed such that the electromagnetic and hypercharges sum to zero within each generation,

$$\sum_f Y_f = \sum_f Q_f = 0\,, \tag{2.3}$$

resulting in the cancellation of chiral anomalies [70–72] and thus rescuing the renormalizability of the model [73] (see also Appendix F).

The Lagrangian of the SM reads

$$\mathcal{L}_{\mathrm{SM}} = \mathcal{L}_{\mathrm{l}}^{\mathrm{kin}} + \mathcal{L}_{\mathrm{q}}^{\mathrm{kin}} + \mathcal{L}_{\mathrm{YM}} + \mathcal{L}_{\mathrm{H}} + \mathcal{L}_{\mathrm{Y}} + \mathcal{L}_\theta + \mathcal{L}_\xi + \mathcal{L}_\eta \tag{2.4}$$

$\mathcal{L}_{\mathrm{l,q}}^{\mathrm{kin}}$ are the kinetic terms of the leptons and quarks containing also the interactions with the gauge bosons in the form of gauge-covariant derivatives. $\mathcal{L}_{\mathrm{YM}}$ is the Yang-Mills Lagrangian, *i.e.* the kinetic energy and self-couplings of the gauge bosons. $\mathcal{L}_{\mathrm{H}}$ is the Higgs sector Lagrangian and $\mathcal{L}_{\mathrm{Y}}$ are the Yukawa interactions between the Higgs field and the fermions. $\mathcal{L}_\theta$ is the so-called θ-term, which solves the $U(1)_A$ problem but gives rise to the strong CP problem [64, 73, 74], *cf.* Section 2.2.2.2. Lastly, $\mathcal{L}_\xi$ fixes the Lagrangian to one of the covariant R_ξ gauges and $\mathcal{L}_\eta$ is the Faddeev-Popov Lagrangian containing the ghost fields η^a to cancel spurious degrees of freedom in processes with non-abelian gauge boson loops [75]. Explicitly, the terms are

$$\mathcal{L}_{\mathrm{q}}^{\mathrm{kin}} = \sum_{\substack{\text{colour}\\ \text{triplets}}} \left[\bar{Q}_i \, i\not{D}^{(L)} Q_i + \bar{u}_{Ri} \, i\not{D}^{(R)} u_{Ri} + \bar{d}_{Ri} \, i\not{D}^{(R)} d_{Ri}\right] + \mathrm{h.c.}\,, \tag{2.5a}$$

$$D_\mu^{(L)} = \partial_\mu - i g_{\mathrm{s}} \sum_{i=1}^{8} G_\mu^i \frac{\lambda_i}{2} - i g \sum_{i=1}^{3} A_\mu^i \tau_{\mathrm{C},i} - i g' B_\mu \frac{\hat{Y}}{2}$$

$$D_\mu^{(R)} = \partial_\mu - i g_{\mathrm{s}} \sum_{i=1}^{8} G_\mu^i \frac{\lambda_i}{2} - i g' B_\mu \frac{\hat{Y}}{2}$$

$$\mathcal{L}_{\mathrm{l}}^{\mathrm{kin}} = \bar{L}_i \, i\not{D}^{(L)} L_i + \bar{\ell}_{Ri} \, i\not{D}^{(R)} \ell_{Ri}\,, \tag{2.5b}$$

$$D_\mu^{(L)} = \partial_\mu - i g \sum_{i=1}^{3} A_\mu^i \tau_{\mathrm{C},i} - i g' B_\mu \frac{\hat{Y}}{2}\,, \qquad D_\mu^{(R)} = \partial_\mu - i g' B_\mu \frac{\hat{Y}}{2}$$

$$\mathcal{L}_{\mathrm{YM}} = -\frac{1}{4} G_{\mu\nu}^i G^{i\mu\nu} - \frac{1}{4} A_{\mu\nu}^i A^{i\mu\nu} - \frac{1}{4} B_{\mu\nu} B^{\mu\nu}\,, \tag{2.5c}$$

$$G_{\mu\nu}^i = \partial_\mu G_\nu^i - \partial_\nu G_\mu^i + g_{\mathrm{s}} f^{ijk} G_\mu^j G_\nu^k$$

$$A_{\mu\nu}^i = \partial_\mu A_\nu^i - \partial_\nu A_\mu^i + g \epsilon^{ijk} A_\mu^j A_\nu^k$$

$$B_{\mu\nu} = \partial_\mu B_\nu - \partial_\nu B_\mu$$

$$\mathcal{L}_{\mathrm{H}} = (D_\mu H)^\dagger (D^\mu H) - V(H)\,, \tag{2.5d}$$

$$V(H) = -\mu^2 H^\dagger H + \lambda (H^\dagger H)^2\,, \qquad D_\mu = \partial_\mu - i g \sum_{i=1}^{3} A_\mu^i \tau_{\mathrm{C},i} - i g' B_\mu \frac{\hat{Y}}{2}$$

$$\mathcal{L}_{\mathrm{Y}} = -\sum_{\substack{\text{colour}\\ \text{triplets}}} \left[Y_{ij}^u \bar{Q}_{Li} \tilde{H} \, u_{Rj} + Y_{ij}^d \bar{Q}_i H \, d_{Rj}\right] - Y_{ij}^\ell \bar{L}_i H \, \ell_{Rj} + \mathrm{h.c.}\,, \tag{2.5e}$$

$$H = \begin{bmatrix} \phi^+ \\ \phi^0 \end{bmatrix}\,, \qquad \tilde{H} = \epsilon H^* = \begin{bmatrix} \phi^0 \\ -\phi^- \end{bmatrix}$$

$$\mathcal{L}_\theta = \theta \frac{g_{\mathrm{s}}^2}{32\pi^2} G_{\mu\nu}^i \tilde{G}^{i\mu\nu}\,, \qquad \tilde{G}^{i\mu\nu} = \frac{1}{2} \epsilon^{\mu\nu\rho\sigma} G_{\rho\sigma}^i\,. \tag{2.5f}$$

$$\mathcal{L}_\xi = -\sum_V \frac{1}{2\xi} (\partial_\mu V^\mu)^2\,, \tag{2.5g}$$

$$\mathcal{L}_\eta = -\sum_\eta \bar{\eta}^a \partial^\mu D_\mu^{ac} \eta^c \tag{2.5h}$$

The gauge couplings associated to $\mathrm{SU}(3)_{\mathrm{c}}$, $\mathrm{SU}(2)_L$ and $\mathrm{U}(1)_{\mathrm{EM}}$ are, respecively, g_{s}, g and g'. $\tau_{\mathrm{C},i} = \tau_i/2$ are the three generators of $\mathrm{SU}(2)_L$ in the Cartesian basis defined through the Pauli matrices (*cf.* Section C.2), λ_i are the eight Gell-Mann matrices generating SU(3) and $\hat{Y}$ is the hypercharge operator. f^{ijk} and ϵ^{ijk} are the respective structure constants. The conjugate Higgs doublet $\tilde{H}$ with hypercharge -1 is constructed with the 2-dimensional antisymmetric tensor, *i.e.* $\epsilon \equiv i\tau_2$, thus it transforms like a doublet, $\tilde{H} \sim 2$. Finally, θ is the CP-violating QCD vacuum angle. Clearly, since the covariant derivatives transform like the fields, $\mathcal{L}_{\mathrm{SM}}$ is invariant under $\mathcal{G}_{\mathrm{SM}}$. However, mass terms for the fermions and the heavy gauge bosons mediating weak interactions, the $W^\pm$ and the Z, explicitly violate this symmetry. This is the point where the Higgs mechanism comes into play.

When the energy of interactions underruns a critical regime, the scalar degrees of freedom may be parametrized in terms of charge-neutral oscillations around a constant vacuum expectation value, leading to the appearance of a number of massless spin-0 bosons that is equal to the number of broken generators of the gauge group. This is the statement of the Goldstone theorem [76] and the gauge symmetry is said

to be *spontaneously broken*. In transforming to the unitary gauge,

$$H \longrightarrow \begin{bmatrix} 0 \\ \frac{1}{\sqrt{2}}(v+h) \end{bmatrix}, \tag{2.6}$$

these 'would-be' Nambu-Goldstone bosons disappear and an equal number of gauge bosons become massive by gaining longitudinal polarization states. In a non-gauge theory, the Nambu-Goldstone bosons would feature as physical particles, whereas in the SM, there are three such states and they are absorbed by the gauge field combinations forming the physical $W^{\pm}$ and Z bosons, while the photon A remains massless. When formulating the SM without eliminating the Goldstone bosons, one notes that they cancel the dependence of amplitudes on the gauge parameter ξ and the occurrence of unphysical polarizations of intermediate gauge bosons [77].

2.1.3.2 The Standard Model Lagrangian: Broken phase and mass eigenstates

Once $\mathrm{SU}(2)_L \times \mathrm{U}(1)_Y$ is spontaneously broken to $\mathrm{U}(1)_{\mathrm{EM}}$, $H \to \langle H \rangle_0 = v/\sqrt{2}$, the SM Lagrangian consists of the following terms:

$$\mathcal{L}'_{\mathrm{SM}} = \mathcal{L}^{\mathrm{kin}}_{\mathrm{f}} + \mathcal{L}^{\mathrm{kin}}_{\mathrm{g}} + \mathcal{L}^{\mathrm{kin}}_{\mathrm{H}} + \mathcal{L}^{\mathrm{m}}_{\mathrm{f}} + \mathcal{L}^{\mathrm{m}}_{\mathrm{g}} + \mathcal{L}^{\mathrm{m}}_{\mathrm{H}} + \mathcal{L}^{\mathrm{int}}_{\mathrm{g}} + \mathcal{L}^{\mathrm{int}}_{\mathrm{Y}} + \mathcal{L}^{\mathrm{int}}_{\mathrm{H}} + \mathcal{L}^{\mathrm{int}}_{\mathrm{Hg}} + \mathcal{L}^{\mathrm{int}}_{\mathrm{fg}} + \mathcal{L}_{\theta} + \mathcal{L}_{\xi} + \mathcal{L}_{\eta}\,. \tag{2.7}$$

$\mathcal{L}^{\mathrm{kin}}_{\mathrm{f,g,H}}$ are the purely kinetic terms of the fermions and the gauge and Higgs bosons, $\mathcal{L}^{\mathrm{m}}_{\mathrm{f,g,H}}$ are the respective mass terms, $\mathcal{L}^{\mathrm{int}}_{\mathrm{g}}$ ($\mathcal{L}^{\mathrm{int}}_{\mathrm{H}}$) are the gauge (Higgs) boson 3-point and 4-point interactions, $\mathcal{L}^{\mathrm{int}}_{\mathrm{Hg}}$ ($\mathcal{L}^{\mathrm{int}}_{\mathrm{fg}}$) are Higgs-gauge (fermion-gauge) interactions, $\mathcal{L}_{\xi}$ is the same as before, $\mathcal{L}_{\theta}$ features the angle $\theta \to \bar{\theta}$ and $\mathcal{L}_{\eta}$ now contains only the QCD ghost fields. We do not write these terms out explicitly here. The physical combinations diagonalizing the gauge boson mass matrix are

$$\begin{bmatrix} W^+_\mu \\ W^-_\mu \\ Z_\mu \\ A_\mu \end{bmatrix} = \begin{bmatrix} \frac{1}{\sqrt{2}} & -\frac{i}{\sqrt{2}} & 0 & 0 \\ \frac{1}{\sqrt{2}} & \frac{i}{\sqrt{2}} & 0 & 0 \\ 0 & 0 & \cos\theta_{\mathrm{w}} & -\sin\theta_{\mathrm{w}} \\ 0 & 0 & \sin\theta_{\mathrm{w}} & \cos\theta_{\mathrm{w}} \end{bmatrix} \begin{bmatrix} A^1_\mu \\ A^2_\mu \\ A^3_\mu \\ B_\mu \end{bmatrix}, \tag{2.8}$$

where θ_{w} is the weak interaction angle (or Weinberg angle) relating g, g' and the electric unit charge $e = |e|$ via $g'/g = \tan\theta_{\mathrm{w}}$ and $e = g \sin\theta_{\mathrm{w}}$. The residual degree of freedom is the Higgs boson h, with a tree-level mass equal to $\sqrt{2\lambda}v$.

We now focus on the fermion masses and touch upon the issue of fermion mixing in the quark sector as a preparation for the forthcoming treatment of neutrino oscillations in Section 2.3.2. Neutrinos pose an exception, as the absence of right-handed neutrino fields forbids Dirac-type mass terms. Moreover, a Majorana mass is interdicted as well due to the absence of a scalar SU(2) triplet.

Fermion masses are provided through the Higgs mechanism by coupling left- and right-chiral components via the Higgs VEV. With a bi-unitary diagonalization of the quark mass matrices

$$M_{u,d} = \frac{Y^{u,d} v}{\sqrt{2}}, \tag{2.9}$$

i.e. through the transformation to mass eigenstates $\hat{f}$,

$$u_{L,R} = U^u_{L,R}\, \hat{u}_{L,R}\,, \qquad d_{L,R} = U^d_{L,R}\, \hat{d}_{L,R}\,, \tag{2.10}$$

the charged current interactions of fermions with the $W^{\pm}$ boson become

$$\mathcal{L}^{\mathrm{cc}}_{\mathrm{q}} = -\frac{g}{\sqrt{2}} \bar{u}_{Li}\, i\not{W}^+ d_{Li} + \mathrm{h.c.} \longrightarrow -\frac{g}{\sqrt{2}} \bar{\hat{u}}_{Li}\, i\not{W}^+ [V_{\mathrm{CKM}}]_{ij}\, \hat{d}_{Lj} + \mathrm{h.c.}\,. \tag{2.11}$$

The 3×3-dimensional unitary matrix

$$V_{\mathrm{CKM}} \equiv U^{u\dagger}_L\, U^d_L = \begin{bmatrix} V_{ud} & V_{us} & V_{ub} \\ V_{cd} & V_{cs} & V_{cb} \\ V_{td} & V_{ts} & V_{tb} \end{bmatrix} \tag{2.12}$$

Parameter	Experimental value	Parameter	Experimental value
m_e	0.510998928(11) MeV	α_{em}^{-1}	137.035999074(44)
m_μ	105.658371(35) MeV	$\sin^2\theta_{\text{w}}$	0.23126
m_τ	1776.86(12) GeV	α_{s}	0.1193 ± 0.0016
m_u	$2.3^{+0.7}_{-0.5}$ MeV	v	$\simeq 246$ GeV
m_d	$4.8^{+0.5}_{-0.3}$ MeV	m_h	125.09 ± 0.3 GeV
m_s	95 ± 5 MeV	$\bar{\theta}$	$< 10^{-9}$
m_c	$1.274^{+0.030}_{-0.035}$ GeV		
m_b	4.199 ± 0.024 GeV		
m_t	173.24 ± 0.81 GeV		
θ_{12}	$13.04 \pm 0.05°$		
θ_{13}	$0.201 \pm 0.011°$		
θ_{23}	$2.38 \pm 0.06°$		
δ_{CP}	1.20 ± 0.08		

TABLE 2.2: The 19 parameters of the Standard Model, all experimental values are collected from PDG [78], except the limit on $\bar{\theta}$ [67] and the Higgs boson mass [32]. Lepton masses and the mass of the top quark are calculated in the on-shell scheme, the other five quark masses are specified in $\overline{\text{MS}}$ [79], where $m_{u,d,s}$ are evaluated at $\mu_{\overline{\text{MS}}} = 2$ GeV and $m_{c,b}$ at $\mu_{\overline{\text{MS}}} = m_{c,b}$. $\sin^\theta_{\text{w}}$ is also evaluated in the $\mu_{\overline{\text{MS}}}$ scheme, though at $\mu_{\overline{\text{MS}}} = m_Z$.

is the famous Cabibbo-Kobayashi-Maskawa (CKM) matrix [80] giving origin to the quantum superposition of flavour eigenstates in the quark sector and represents the only source of CP violation in the SM due to being complex [65]. Unitarity implies that V_{CKM} contains 9 real parameters for three quark generations, from which 5 can be extracted by rephasing the quark fields; remaining parameters are the Euler angles θ_{12}, θ_{13}, θ_{23} and the CP phase δ_{CP}. The arguments of V_{ij} are probed through CP-violating decays and mixing in the meson sector. As for the magnitudes, experiments mainly measure $|V_{ud}|$ through nuclear beta decay and neutron decay, $|V_{td}|$ and $|V_{ts}|$ through loop-mediated B-$\bar{B}$ mixing and rare K and B meson decays, $|V_{tb}|$ through top decays and all other entries via K, D and B decays, where applicable [78]. Demanding unitarity, PDG obtains the fit

$$|V_{\text{CKM}}| = \begin{bmatrix} 0.97427 \pm 0.00014 & 0.22536 \pm 0.00061 & 0.00355 \pm 0.00015 \\ 0.22522 \pm 0.00061 & 0.97343 \pm 0.00015 & 0.0414 \pm 0.0012 \\ 0.00886^{+0.00033}_{-0.00022} & 0.0405^{+0.0011}_{-0.0012} & 0.99914 \pm 0.00005 \end{bmatrix}, \tag{2.13}$$

and a Jarlskog invariant quantifying the amount of CP violation [81] of

$$J_{\text{CKM}} = \text{Im}[U_{us}U_{cs}^*U_{ub}^*U_{cb}] = \left(3.06^{+0.21}_{-0.20}\right) \times 10^{-5}\,. \tag{2.14}$$

Without the unitarity constraint, the magnitudes change a bit and the uncertainties slightly increase. Quarks could mix with new heavy coloured states such as vector-like quarks [82], though the low uncertainties regarding unitarity of the CKM matrix leave little room for such scenarios [78]. Note that V_{CKM} is quite close to the unit matrix, thus flavour violating weak processes involving quarks appear suppressed. Neutrino oscillation measurements point to the exact opposite behaviour in the lepton sector, *cf.* Section 2.3.2. Note that fermion mixing is directly related to the global baryon and lepton number symmetry of the SM,

$$\mathcal{G}_{\text{SM}}^{\text{global}} = \text{U(1)}_{\text{B}} \times \text{U(1)}_{\text{L}} = \text{U(1)}_{\text{B}} \times \text{U(1)}_{\text{L}_e} \times \text{U(1)}_{\text{L}_\mu} \times \text{U(1)}_{\text{L}_\tau}\,, \tag{2.15}$$

meaning that the SM Lagrangian conserves total baryon number, whereas gauge interactions of lepton flavours are universal, thus not only the total lepton number but also individual lepton flavours are symmetries of the SM. The evidence for neutrino oscillations indicates that neutrino mass and flavour eigenstates are largely misaligned, which can only be the case if the SM is properly extended. This is explored in Section 2.3.

2.2 Physics of cosmology and dark matter

In Section 2.1.2, we listed some of the phenomena the SM fails to describe, an important component being the absence of DM in the theory. Before discussing the observational evidence, particle DM candidates and search strategies in Section 2.2.2, it is inserted in a bigger picture in Section 2.2.1, where we explore how the cosmological standard model describes the evolution of the Universe from the hot Big Bang until the cold dark energy dominated state of the present. The evolution of dark matter among other species in this process is followed in Section 2.2.3. For this end, it is appropriate to treat the concept of thermal freeze-out in some detail, which is done in Section 2.2.3.2. A further motivation is our special interest in the variant of the scotogenic model incorporating the thermal freeze-in of dark matter (see Section 2.4.2). Both mechanisms, freeze-out and freeze-in, are intimately connected. Freeze-in is discussed in Section 2.2.3.3. Thermal DM freeze-in scenarios typically contain long-lived particles that can have an effect on Big Bang nucleosynthesis (BBN). BBN very successfully predicts the observed abundances through conventional and well-understood particle and nuclear physics. As the addition of long-lived particles to the SM can be dangerously affect these predictions, we opt to outline the main features of BBN and its sensitivity to such particles in Section 2.2.1.

2.2.1 Thermal history of the Universe

By measuring the redshift in the electromagnetic spectrum emitted by 46 extragalactic objects, E. Hubble discovered in 1929 that these objects are receding with a velocity apparently proportional to their distance [83]. It was found that this picture is independent of the direction of observation. In modern times, redshift surveys have been undertaken to map the entire large-scale structure of the observable Universe, see *e.g.* [84, 85]. The cosmological principle states that matter in the Universe should be homogeneously and isotropically distributed, which can be formulated to incorporate the Copernican principle, stating that no point in space is to be favoured. A necessary implication is the description of cosmic space with a metric expansion. A. Friedmann showed already in 1922 that Einstein's field equations when applied to the cosmos could admit an expanding solution [86], introducing the concept of a scale factor. In 1927, G. Lemaître went a step further and obtained an expression for the rate of the expansion [87]; this quantity would later become known as the Hubble rate. Lemaître first presented the distance-velocity relation, now called Hubble's law, and also proposed that the Universe could have begun at a single spacetime point. Together with contributions by H. Robertson [88] and A. Walker, this series of work culminated in the well-known Friedmann-Lemaître-Robertson-Walker (FLRW) line element, the basis for describing cosmic dynamics. FLRW cosmology is required in DM abundance computations, therefore some fundamentals are briefly supplied in Appendix A.

Spatial homogeneity and isotropy are now accepted to be an integral property of the Universe due to measurements of the cosmic microwave background (CMB) radiation by the COBE (1989-1993), WMAP (2001-2010) and Planck (2013-now) satellites.[2] It was accidentally discovered in 1964 by A. Penzias and R. Wilson [89]. R. Dicke measured the same radiation independently one year later [90], interpreting the radiation as thermal relic photons, as had already been predicted by G. Gamow in the context of big bang nucleosynthesis [91]. It is now known that the frequency distribution of this background radiation almost perfectly obeys a blackbody distribution law with a photon temperature of $T_0 = 2.7255$ K [92], the anisotropies being of the order of only 10^{-4} K. The near-perfect blackbody spectrum in combination with the predominant photon abundance is seen as justification for the application of equilibrium statistical mechanics combined with discretely happening out-of-equilibrium physics to describe the evolution of the early Universe and the decoupling of particle species from the thermal plasma. Measurements of the CMB anisotropies constitute one of the most important tools of experimental cosmology today, rendering it a

[2] Apart from satellite measurements, some balloon experiments measuring the CMB include QMAP (1996), BOOMERanG (1997,2003) and MAXIMA (1998, 1999) and some ground-based experiments are Saskatoon (1993,1995) and MAT/TOCO (1997,1998). Further recent ground-based experiments are BICEP1/BICEP2/Keck (2006-2008/2010-2012/2010-2011,2012,2013-today).

precision science. This is so because the anisotropies can be analytically modelled, with the modelling function depending on the parameters of the cosmological scenario one wishes to test by means of a likelihood analysis. We shall mention a few more details when discussing the evidence for DM at cosmological scales in Section 2.2.2.1.

CMB photons are regarded as evidence for the hot Big Bang model, in which the Universe started from a very dense and very hot initial state, underwent an inflationary phase and then cooled down while continuously expanding. Eventually, after electron-hydrogen recombination [93], the cosmic plasma ceased to be opaque to photons, whose mean free path lengths then exceeded the Hubble horizon and are today seen in the microwave spectrum as an image of the last-scattering density surface. While expanding, the Universe progressed from a radiation-dominated era to a matter-dominated era, ending with vacuum energy mainly driving the scale dynamics. Since in the radiation-dominated era the photons formed the heat bath for all other species, their temperature can be related to cosmic time and the history of the Universe can be recounted solely in terms of the decreasing photon temperature. Cosmic time, the scale factor and photon temperature are connected in FLRW cosmology through simple equilibrium thermodynamics, as shown in Appendix A and Section 2.2.3.

CMB anisotropies are attributed to two effects, the Sachs-Wolfe (SW) effect [94] on large scales and baryon acoustic oscillations (BAO) on small scales. Overdense regions in the baryon-photon plasma during early matter domination (the baryons are mostly H and ^{4}He nuclei coupled to the photons through electrons via Thomson and Coulomb scattering) are the seeds of the large scale structure (LSS), *i.e.* the pattern of galaxy clustering at the largest. The photons escaping from these regions at recombination are gravitationally redshifted and seen today as cold areas in the CMB spectrum, which is known as the non-integrated or immediate SW effect. The accumulated gravitational redshift of CMB photons between recombination and the photons reaching a critical underdensity is the so-called early-time integrated SW effect (ISW). From when vacuum energy starts to dominate until today, the effect is called late-time ISW. BAO arise when a portion of the photon-baryon fluid falls into the gravitational well of an overdense region. This initiates a cycle of compression producing heat, expansion due to increased pressure from radiated heat photons and recontraction due to gravitational pull. As a consequence, a spherical longitudinal pressure wave throughout the plasma is generated, like a sound wave. Dark matter stays in the center of this region because it only (or primarily) interacts gravitationally. At recombination, photons and baryons separate and the pressure gets fully released; propagation of the wave then halts at a radius called the sound horizon. Overlaps of such wave remnants are seen in the LSS as small regions of matter overdensity, plus, the sound horizon at recombination is a distinct anisotropy feature of the CMB, namely the famous acoustic peaks and troughs, shown in the right panel of Figure 2.4. See also [95] for a review and a discussion of the role of BAO in distance determination and dark energy studies and [96] for a review of CMB anisotropies.

Today's cosmological standard model is the so-called ΛCDM (Λ-Cold-Dark-Matter) model. It assumes spatial flatness, absence of tensor polarization modes, a cosmological constant Λ as dark energy and that DM is 'cold' (*cf.* Section 2.2.2). The cosmological constant is introduced to account for the observed acceleration in the expansion: By measuring intrinsic luminosities of high-redshift type-Ia supernovae, it was found that they are too faint to be described by the luminosity-redshift relation for a non-accelerating expansion, which can be explained through a positive (though tiny) cosmological constant in the FLRW metric [97].

It turns out that six independent parameters suffice to fit all other observables. For instance, the 'base ΛCDM model' used by the Planck collaboration relies on the baryon and cold DM density parameters $\Omega_{\rm B}$ and $\Omega_{\rm CDM}$, a parametrization of the sound horizon at last scattering denoted by $\theta_{\rm MC}$, the tilted scalar spectral index $n_{\rm s}$, the optical depth at reionization τ and the logarithm of the primordial curvature perturbations $\ln(10^{10}A_{\rm s})$ [98]. All of these parameters are inferred from CMB measurements by maximizing experimental likelihoods, assuming the ΛCDM model is true, fixing the total density to unity (*cf.* Equation A.7) and neglecting the light neutrino masses. Other quantities, like the Hubble rate, are derived from these parameters. Models incorporating more ingredients, such as tensor modes and non-zero neutrino masses, are also considered by Planck, but these are extensions of ΛCDM.

Table 2.3 summarizes the history of the Universe in terms of cosmic time and temperature. Additionally,

Event	t	z	T $[k_\mathrm{B}T]$
Inflation	10^{-34} (?)	(?)	(?)
Baryogenesis	(?)	(?)	(?)
EW phase transition	20 ps	10^{15}	100 GeV
QCD phase transition	20 μs	10^{12}	150 MeV
Dark matter FO/FI	(?)	(?)	(?)
Neutrino decoupling	1 s	6×10^9	1 MeV
$e^-\,e^+$ annihilation	6 s	2×10^9	500 keV
Big Bang nucleosynthesis	3 min	4×10^8	100 keV
Matter-radiation equality	60 kyr	3400	0.75 eV
Recombination	260-380 kyr	1100-1400	0.26-0.33 eV
Photon decoupling	380 kyr	1000-1200	0.23-0.28 eV
Reionization	100-400 Myr	11-30	2.6-7.0 meV
Dark energy-matter equality	9 Gyr	0.4	0.33 meV
Present	13.8 Gyr	0	0.24 meV

TABLE 2.3: Thermal history of the Universe. Table adapted from [99].

one could also specify the scale factor value for each event. In the following, we write a few words about a personally biased selection of three of these events.

□ **Inflation:** The idea of an exponential expansion phase in the very initial stage of the Universe was first found to be useful by A. Guth in 1981 [100]. Guth put forward the idea that cosmological inflation could solve the horizon and flatness problems, reasoning also that it could provide an explanation for the issue of missing magnetic monopoles. In 'new' inflation models, this is accomplished by assuming the existence of one or more scalar fields (inflatons). The main principle is that they slowly 'roll' down a very flat potential towards a global minimum, leading to an exponential expansion during the slow-roll phase [101]. We will quickly discuss these problems and how they are solved by inflation in a qualitative manner, following Chapter 4 of [102].

The horizon problem and the solution by inflation are formulated as follows. During the matter-dominated (MD) time of photon decoupling, the scale factor $a(t)$ is found to increase with cosmic time as $t^{2/3}$. In combination with the fact that in a radiation-dominated (RD) and MD Universe the causal horizon is of order t, it can be shown that the horizon today subtends an angle of about 1.6°. Surprisingly, up to tiny anisotropies, the CMB spectrum is found to be very highly homogeneous and isotropic, which is in accordance with the cosmological principle, but not with the observation that not all portions of the sky could have been in causal contact at some early stage. Gravitation alone could not have led to such a high degree of homogeneity and isotropy because regions with large separations receded from each other with speeds higher than the speed of light, therefore they could not have interacted. Inflation theory hypothesizes that the Universe started out tiny with every region causally connected, the horizon being at least of the order of the size of the Universe (or of the portion that would become our observable Universe). When inflation sets in, everything has had time to homogenize — this homogeneity is not only preserved during the (quasi-)exponential expansion during inflation, it is more than that increased due to the dilution of initial inhomogeneities caused by quantum fluctuations of the hypothetical inflaton field(s). At the end of this expansion period, the horizon would be much smaller than the observable Universe. By (quasi-)exponential expansion, it is meant that the scale factor grows as $a(t) = a(t_i)\exp(\int_{t_i}^{t} dt' H(t'))$, with $H(t) \simeq$ const. Thus the ratio $a(t_2)/a(t_1)$ evolves as $\sim \mathrm{e}^{\mathcal{N}}$, where $\mathcal{N}$ is the number of e-foldings which depends on the inflaton potential and is large if the field takes a value in a flat region.

The monopole problem is explained much in the same way. A rapid exponential expansion would cause an extreme dilution of any initial concentration of magnetic monopoles, explaining why today there seem to be no such objects.

Finally the apparent flatness of today's Universe can be used to infer that, at very early times, around

the moment of electron-positron annihilation, the curvature parameter Ω_k must have been no larger than about 10^{-16}. Inflation can originate such a number naturally without fine-tuning. During the inflationary phase, $\Omega_k \propto a(t)^{-2} \sim \exp(-2\mathcal{N}(t))$, a number that turns out to be very small at the end of the exponential expansion. In fact, a number of e-foldings that solves the horizon problem automatically solves the flatness and monopole problems.

The inflaton field is hypothesized to have a massive excitation, the inflaton particle. During inflation, the number densites of all matter and radiation fields except the inflaton are highly redshifted. At the end of inflation, the inflaton sits at the bottom of the potential oscillating very rapidly. This oscillation gradually decreases as energy gets transferred back to the matter fields in the form of inflaton particle decays to SM and DM particles. The energy is also transferred to the photons, setting the starting point of the radiation-dominated era. We name this process *reheating*, a term coming from early models requiring the Universe to start out in a very hot state already before inflation. More modern inflationary cosmology models from the early 90's do not have this requirement. All or almost all SM and DM particles are presumed to originate from this non-adiabatic process because initial abundances get diluted. After inflation, standard Big Bang cosmology can be applied. The inflaton energy density decreases with a rate equal to the decay rate of the inflaton particle to DM and SM particles, often assumed to be due to perturbative interactions. When this rate becomes less than the expansion rate, reheating is over. If one also assumes that the decay products rapidly thermalize after their production, then there is a temperature set by the radiation content. At the moment of the end of the reheating phase, this temperature is called the *reheating temperature* T_R. By Equation 2.32, the total energy density of the Universe is therefore initially proportional to $g_{*\rho}(T_\mathrm{R})T_\mathrm{R}^4$, where $g_{*\rho}(T)$ is the effective number of relativistic degrees of freedom contributing to ρ_r at temperature T. One can set an upper bound on the inflaton decay rate, leading to an upper bound on the reheat temperature,

$$T_\mathrm{R} < 10^9\,\mathrm{GeV}\,. \tag{2.16}$$

This is a very low temperature, in the sense that it indicates that particles were injected into the Universe with a temperature much below the GUT scale, $T_\mathrm{GUT} \sim 10^{16}$ GeV. The goal of making the energy transfer to matter more efficient by speeding up the reheating process led to the idea of *preheating* [103], in which the reheating phase is very short due to a parametric resonance. See *e.g.* [104] for details.

The most promising method to provide evidence for inflation is the detection of tensor B-mode perturbations in the CMB polarization [105]. B-modes and E-modes are both predicted by the presence of inflationary gravitational waves, though B-mode effects are less ambiguous than effects by E-modes [106]. Ambiguity in B-modes mainly stems from cosmic dust, as it can considerably contaminate the signal because it acquires a net polarization when aligning with the galactic magnetic field in certain circumstances. The BICEP2 experiment [107], located at the South Pole, gathered CMB data from a fixed patch in the CMB from 2010 to 2012 and claimed the detection of a highly significant B-mode component [108] resulting in a formidable wave of excitement in the scientific and world press. Unfortunately, the claim had to be withdrawn following a dedicated measurement by the Planck collaboration [109], which clearly attributed the signal to cosmic dust. Presently, there is no experimental evidence for the correctness of inflationary cosmology.

□ **Dark matter freeze-out/in:** Whether DM in the early Universe thermalizes or not depends on the strength of its interactions with the plasma. If DM is in thermal equilibrium with the cosmic plasma at some point, the time when it ceases to be is dubbed *freeze-out*; if, on the other hand, it is produced in a slow decay and/or annihilation process without thermalizing, the generation of its final abundance is called *freeze-in*. These two hypotheses for generating the observed abundance are discussed in detail in Sections 2.2.3.2 and 2.2.3.3, respectively. Mechanisms such as freeze-out and freeze-in are integral parts of so-called thermal DM scenarios, where the DM abundance is determined through the interactions with the plasma of the thermal bath in the early Universe, still before the onset of BBN (*cf.* next item).

The CPT theorem [110] requires the DM particle to possess an antiparticle or to be its own antiparticle, meaning it can annihilate to SM particles if the necessary interactions exist. If it has a large enough

thermal annihilation cross section $\langle\sigma v\rangle$ (*cf.* Equation B.14), it will thermalize in the primordial heat bath before the expansion rate outpaces the annihilation rate, leading the DM population to freeze-out at a given temperature. After freezing-out, the number density evolves independently with the expansion of space. In this mechanism, the final abundance does not depend on the initial density and the details of production [111]. The DM mass and the interaction rate determine whether it freezes-out while being non-relativistic, semi-relativistic or relativistic, in which cases the relics are respectively termed 'cold', 'warm' or 'hot'. As will be discussed in Section 2.2.3.2, the cold relic scenario is realized for annihilation cross sections in the electroweak range, that is, with couplings of the order of g, thus such particles are denoted 'Weakly Interacting Massive Particles' (WIMPs).

For small interaction rates, the DM particles are effectively decoupled from the rest and their production stems from decays and annihilations of bath particles. If these interactions are feeble enough, their final number densities are reached when their production rate is surpassed by the expansion rate. In that case, DM is labelled a 'Feebly Interacting Massive Particle' (FIMP) [43]. Note that one has to assume a negligible initial abundance, for otherwise there lurks the risk of overclosure ($\Omega > 1$) [111]. As for freeze-out, freeze-in models allow for cold, warm or hot relics.

Finally, if the interaction rates with the bath are negligibly small, DM will not thermalize and the relic abundance will coincide with the initial abundance. In inflationary cosmology, this initial abundance fully depends on the details of the reheating process, such as the reheating temperature.

□ **Big Bang nucleosynthesis (BBN):** BBN encompasses our current understanding of how today's abundances of light elements in the Universe can be understood. These elements are hyrdogen (H), deuterium (D or ^{2}H), helium-3 (^{3}He), helium-4 (^{4}He) and lithium-7 (^{7}Li). Standard BBN (SBBN) combines well-established Standard Model and nuclear physics with conventional FLRW cosmology and thermodynamics and has its root in the seminal '$\alpha\beta\gamma$' paper from 1948 [112]. Although it was only later found that the creation of heavier elements proceeds via stellar nucleosynthesis rather than through successive primordial neutron, proton and deuterium capture, the $\alpha\beta\gamma$ mechanism is commonly accepted to describe the origin of the before-mentioned light elements. However, despite all pleasant aspects, there is an issue with ^{7}Li, whose abundance cannot be accommodated with the other abundances, maybe hinting at as yet unknown processes or even new physics contributions. This is known as the 'lithium problem': Calculating the ^{7}Li abundance in SBBN models leads to a value up to three times above the abundance inferred from observations of low-metallicity stars (see *e.g.* [78]). The search for possible solutions has turned out to be highly difficult. For example, a systematic error in the determination of the cross section of the only significant process for primordial ^{7}Li production $^3\mathrm{He}(\alpha,\gamma)^7\mathrm{Be}$ is excluded to be responsible for the observed underabundance at 95% C.L. by means of the agreement of the standard solar model an solar neutrino data [113]. We shall not discuss this issue further. We will also not mention any forms of non-standard BBN, the literature on which being very rich [114]. However, since long-lived unstable particles are an integral part of this thesis, we are interested in whether one should worry if their decays can alter the predictions of SBBN in a drastic way.

BBN describes the evolution of thermonuclear reactions with time/temperature/redshift as the Universe cools from ~ 10 MeV (~ 0.01 seconds) to ~ 100 keV ($\gtrsim 3$ minutes). It is independent of the physics in the previous eras about which one can only speculate, therefore its attractiveness lies in the fact that no unknown or poorly understood mechanism plays a role. By starting with proton and neutron equilibrium densities in a proportion dictated by their masses, BBN correctly predicts the observed H $\sim 75\%$ and He $\sim 25\%$ mass fractions, along with the correct fractions of D and ^{3}He (the prediction for ^{7}Li being too high, as stated before). However, it is extremely sensitive to changes in fundamental parameters, like the number of active neutrino flavours N_ν, thus it places strong constraints on a large variety of BSM physics models. The success of BBN in predicting the measured abundances is widely regarded as solid proof for the correctness of the hot Big Bang hypothesis and for the non-baryonic nature of DM.

A key ingredient of BBN is the baryon number density $n_\mathrm{B} \equiv n_\mathrm{b} - n_{\bar{\mathrm{b}}}$. It is employed in the form of the matter-antimatter asymmetry parameter $\eta \equiv n_\mathrm{B}/n_\gamma$, with a conventional normalization to today's photon number density n_γ. It is directly related to the cosmological baryon density parameter Ω_B, thus

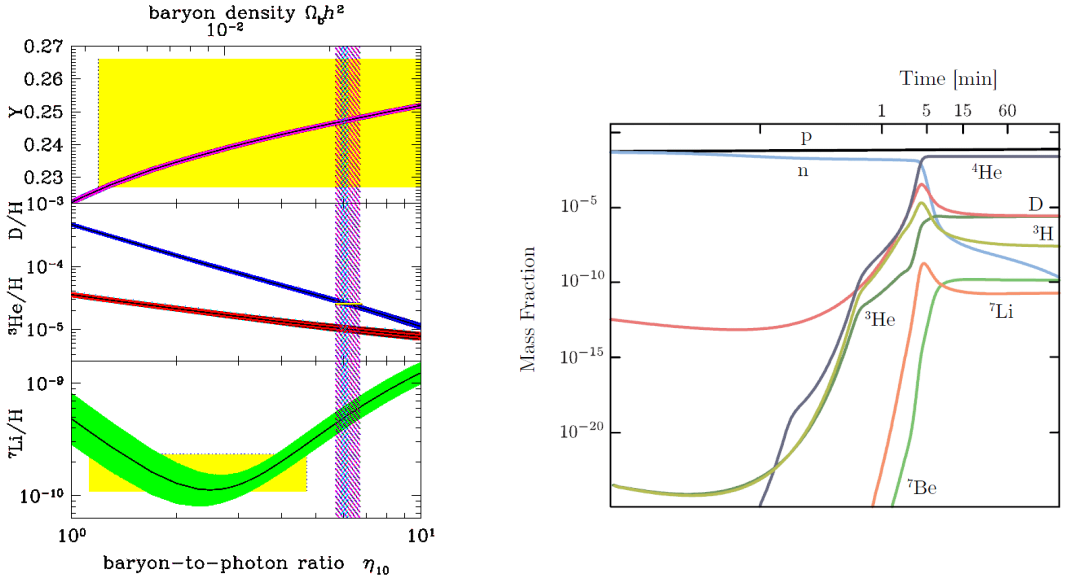

FIGURE 2.1: *Left panel:* Abundance of ^{4}He and, normalized to the abundance of hydrogen, the abundances of D, ^{3}He and ^{7}Li as a function of the baryon-to-photon ratio η. The plot is taken from [78], which is adapted from [115]. See these references for an explanation of the uncertainty bands. The boxes indicate the ranges of observations, from references recommended in [78]. Measurements of the primordial ^{3}He are difficult, for which there is no reliable experimental value. The wide and narrow vertical bands are, respectively, the concordance range of η as set by the range for D/H, namely $5.7 \leq \eta \times 10^{10} \leq 6.7$ [116], and the experimental value from CMB measurements by Planck using results presented in 2013 [98]. Notice the discrepantly low value of observed ^{7}Li, known as the lithium problem. *Right panel:* Example of a calculation of coupled abundances during the whole standard BBN process; plot taken from [99].

BBN can be tested through CMB measurements. BBN predicts the value of η from the observed element abundances, currently delimiting its range to [78]

$$5.1 \leq \eta \times 10^{10} \leq 6.5\,. \tag{2.17}$$

Remarkably, WMAP and Planck data finding the baryonic density to be $\Omega_{\rm B}h^2 \simeq 0.022$ [8, 117] leads to $\eta = (6.19 \pm 0.14) \times 10^{-10}$ [117], which is in excellent agreement with the value in Equation 2.17 and has a much higher accuracy than the theoretical prediction, see the left panel of Figure 2.1. According to BBN theory, the ratio of two abundances (most sensitively D/H) determines η, so any other abundance ratio provides a test for the value; hence it is in reality a theory without free parameters. The decrease of the D/H and increase of the ^{4}He abundance with η is explained by the fact that a higher baryon density leads to a more efficient fusion of deuterium to helium.

Here we loosely follow the sets of notes in [118] and [99] to sketch how to obtain the rough H and He abundances, giving only qualitative arguments. The full analysis is very involved and incorporates the use of a set of coupled of Boltzmann equations to describe the interplay of abundance evolutions with freeze-out temperatures (*cf.* Section 2.2.3.1). A simulation of the abundances of all involved light elements is exemplified in the right panel of Figure 2.1, taken from [99]. The goal is to end up with

$$Y \equiv \frac{4n_{\rm He}}{n_H} \simeq \frac{1}{4} \qquad \text{or} \qquad \frac{n_n}{n_p} \simeq \frac{1}{7}\,, \tag{2.18}$$

where the first fraction is the helium-to-hydrogen mass fraction. Basically all neutrons are used to form ^{4}He nuclei, up to some (calculable) traces of ^{3}H, D and ^{7}Li. More details may be found in *e.g.* [78, 102].

- *Starting conditions:* Beginning with an equal number of protons and neutrons at a temperature of about 10 MeV (~ 0.01s), the Universe consists of an equilibrium gas of protons, neutrons, electrons, photons and neutrinos, where the baryons (p and n) are non-relativistic. BBN takes place in the RD

era, so cosmic time evolves as $t \propto T^{-2}$. Before depleting part of the neutrons in favour of protons, the $pne\nu\gamma$-gas remains in thermal equilibrium through 2-body $p \leftrightarrow n$ interconversions involving $e^{\pm}$ and $\nu_e/\bar{\nu}_e$, neutron decay not taking place because the neutron's mean lifetime is ~ 15 minutes. The fact that the neutron is more massive eventually pushes the main reactions towards the energy-releasing $n \to p$ side, since $(n_n/n_p)^{(\mathrm{eq})} \propto \mathrm{e}^{-(m_n - m_p)/T}$. Deuterium is not formed yet because the temperature is not low enough to compensate the low baryon density and low deuterium binding energy.

- *Neutron decoupling:* At $T = 0.8$ MeV, the neutrinos decouple, which effectively stops the n-p equilibrium interactions and leads to neutron freeze-out.[3] Using the Boltzmann equation, one finds $(n_n/n_p)^{(\mathrm{eq})} \simeq 1/6$ at 0.8 MeV. Furthermore, the neutrons start decaying to protons.

- *Helium fusion:* Throughout the following 1-3 minutes, protons and neutrons start combining to form ^{4}He via a chain that includes D and ^{3}He. ^{4}He is favoured in the reactions because it has the largest binding energy of all light nuclei. The deuterium binding energy is low, so it starts forming late, at $\sim$ 100 keV ($\sim$ 3 min), and only then can heavier nuclei be created through fusion processes. This is called the 'deuterium bottleneck'. After that, practically every neutron is bound in a ^{4}He nucleus. Since over these three minutes the neutrons also underwent decays, the fraction $(n_n/n_p)^{(\mathrm{eq})}$ has decreased from $\sim 1/6$ to $\sim 1/7$.

New physics scenarios can heavily distort the nice but fragile interplay of all the elements involved in SBBN [119]. There are dependences on various parameters, like $g_{*\rho}$ and g_{*s} (*cf.* Section 2.2.3), η, the number of light neutrinos, etc. In particular, highly-energetic non-thermal cosmic rays in the form of electromagnetic or hadronic cascades from decays of long-lived particles not contained in the SM may significantly influence the evolution of abundances [119], as has been realized in the 1980s [120]. Moreover, bound states formed by negatively-charged massive particles may enable catalyzed BBN processes significantly altering abundances by adding new production mechanisms, especially those of ^{6}Li and ^{7}Li, provided their mean lifetimes are of the order $\sim 10^3$ s [121]. The cosmic rays stemming from the decays of such new particles rapidly thermalize for times before $T \sim 1$ eV, possibly changing SBBN rates along the way. For instance, as protons are more abundant than neutrons, hadronic interactions may increase Y by increasing n_n/n_p through processes such as $\pi^- + p \to \pi^0 + n$, although the dominant modifications to abundances stem from interactions with fast nucleons. Electromagnetic processes can include photodissociation of D and ^{4}He. Furthermore, such reactions may contribute considerably to the ^{6}Li and ^{7}Li abundances. Whereas hadronic interactions can be significant at times $t \gtrsim 0.1$ s ($T \lesssim 3$ MeV), non-thermal electromagnetic particles only affect BBN after $t \gtrsim 10^5$ s ($T \lesssim 3$ keV) (see [119] and references therein), which should be compared to the mean lifetimes of the long-lived particles contained in BSM scenarios and considered when calculating constraints.

2.2.2 Dark matter evidence, particle candidate categories and search strategies

This section is entirely devoted to DM, as it is an integral component of the last piece of work presented in this thesis. We will briefly sum up the main observational evidence, afterwards we present some of the paradigms under which DM can be treated and, finally, we discuss the three employed experimental methods to look for DM, namely direct detection, indirect detection and collider searches. For a review, see *e.g.* [122].

2.2.2.1 Evidence

The existence of DM as an 'unseen' component in a system of stellar bodies is often presented in analogy to the earliest discoveries due to gravitationally anomalous behaviours of visible objects: Neptune was

[3] As observed in [99], the fact that the neutrino freeze-out temperature and the neutron-proton mass differences are very similar seems coincidental. Were the weak interactions more efficient or the mass difference larger, the neutrons would have frozen out much later and there would be less helium, leading to a very different Universe from ours.

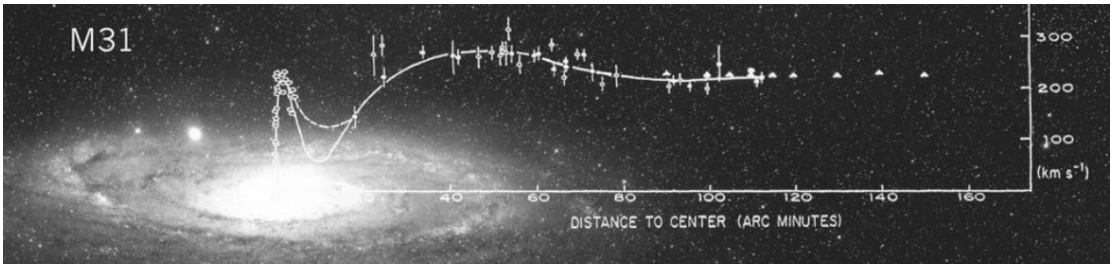

FIGURE 2.2: Rotation curve of the Andromeda galaxy. The curve fit to the open circles is from Rubin's original paper [124], the triangles are from measurements in the radio spectrum [125]. The superposition onto M31 is from reference [126].

discovered by J. Galle in 1846 after its existence was inferred from perturbations in the orbit of Uranus by A. Bouvard and its position was mathematically predicted by U. Le Verrier; secondly, the anomalous motion of the stars Sirius and Procyon led F. Bessel in 1844 to the conclusion that they were accompanied by fainter objects. These were later observed with telescopes and white dwarves were discovered. Rather than giving a chronological historical account of the relevant observations, we shall rather list the main evidence ordered by their spatial scales, in the spirit of the review [122].

□ **Galactic scales:** The clearest evidence for DM at the galactic scale is the rotational velocity distribution of stars and gas about the center of disk galaxies. It was as early as 1932 when J. H. Oort noticed that stars in the Milky Way had lower orbital speeds than expected [123]. This article is historically the first documented indication of a possibility for DM. Plotting these velocities versus the distance from the galactic nucleus, one produces a *rotation curve* or *velocity curve*. Since the velocity of an object in a system of gravitationally interacting bodies is dictated by the dynamical and not by the luminous mass of the system, these curves are a measure of the 'true' mass distribution inside galaxies, meaning the distribution of everything interacting gravitationally. According to Keplerian theory of orbital motion, the velocities v of stars and gas moving around the galactic center should decrease with their radial distance r like

$$v(r) = \sqrt{\frac{GM(r)}{r}}\,, \qquad M(r) = 4\pi \int_0^r dr' r'^2 \rho(r')\,. \tag{2.19}$$

Beyond the optical disk, the velocities should decrease like $1/\sqrt{r}$. In the late 1970's, V. Rubin and K. Ford began to measure the velocity curves of disk galaxies, starting with the Andromeda galaxy [124]; more studies followed, see *e.g.* [127]. The method was to measure the blueshift and redshift in the Hα 21.1 cm emission line of ionized hydrogen using a spectrograph built by Ford. They discovered that the rotation curve exhibited a flat shape (*cf.* Figure 2.2), until far beyond the presence of luminous constituents. Flatness in the velocity distributions implies

$$M(r) \sim r \quad \longrightarrow \quad \rho(r) \sim \frac{1}{r^2}\,. \tag{2.20}$$

There has to be an additional phenomenon responsible for the galaxy's stability and for the observed velocities, otherwise the galaxy would fall apart. This discovery was, until then, the strongest evidence for DM and is still seen as one of the most robust hints for its existence in the form of a galactic halo, with a density profile approximately behaving like $1/r^2$. For a historical account on the history of galaxy rotation curves, see [128]. Another galactic-scale indication for DM is the velocity dispersion of spiral galaxy satellites at very large distances from the nucleus, $\gtrsim 200$ kpc, hinting at the presence of a large spherical DM halo [129]. For more evidence at galactic scales, see [122].

□ **Galaxy cluster scales:** In 1933, F. Zwicky [130] observed that the Coma Cluster (Abell 1656) could not be held together by its visible galaxies, leading him to propose a dark form of matter ('dunkle Materie') to increase the cluster's mass-to-light ratio to the enormous observed value of about 400 solar masses per

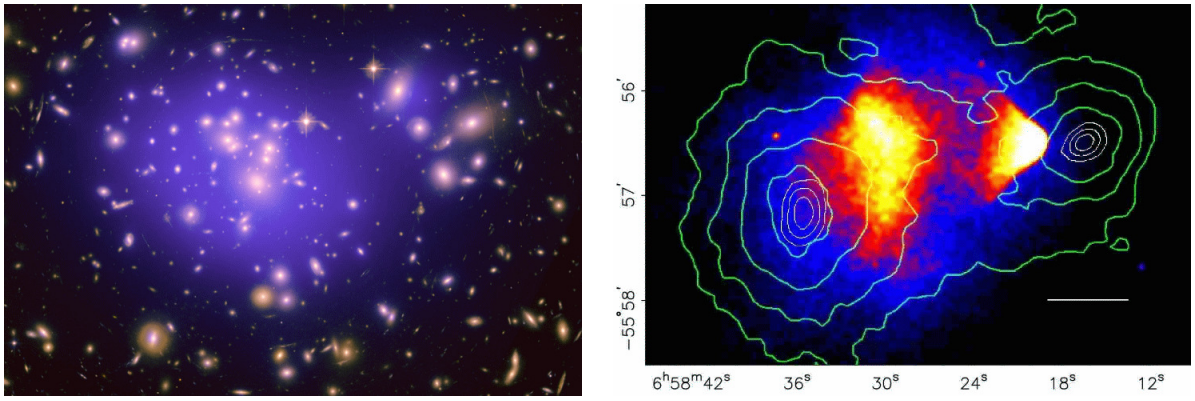

FIGURE 2.3: *Left panel:* The galaxy cluster Abell 1689 with the DM distribution overlaid in purple. The photo was taken with the ACS camera of the Hubble Space Telescope. Lensing effects on background galaxies are clearly visible. Image credit: NASA, ESA, E. Jullo (JPL/LAM), P. Natarajan (Yale) and J-P. Kneib (LAM). *Right panel:* The Bullet Cluster (1E0657-558), image taken from [135]. Shown are the κ-convergence lines delimiting contours of constant mass density obtained from weak lensing measurements and the coloured areas are x-ray measurements gained with Chandra, colour-coded according to the temperature. The white contours identify the mass peak region at 68.3, 95.5 and 99.7% C.L.; the white bar corresponds to 200 kpc.

solar luminosity, $M_\odot/L_\odot$. By today, studying galaxy clusters for DM research is a standard but complicated procedure. The virial mass of a cluster is inferred from the virial motion of its visible galaxies (using visible and IR spectrum data, *e.g.* from Hubble and Spitzer), from the temperature set by the collisions of the hot intracluster medium (with x-ray spectroscopy data, *e.g.* from Chandra) and from gravitational lensing effects seen in the visible. Since gravitation couples to all forms of matter, the geodesics of photons correspond to trajectories that bend when they pass by massive objects. This can either slightly alter the brightness of a lensed object (microlensing), cause magnification and distortion effects on images of multiple sources that are statistically analyzable (weak lensing), or heavily distort and magnify single-source images, creating multiple copies of the image or arcs (strong lensing). For strong lensing, the lensing object needs to be on or very close to the line of sight of the observer towards the lensed object, hence such images are not very numerous. Weak lensing is used to calculate the mass distribution within galaxy clusters, see the left panel of Figure 2.3 for the example of the Abell 1689 cluster, with a superposed DM distribution obtained from weak lensing. The right panel shows the most prominent example to date, the famous Bullet Cluster (1E0657-558 or 1E0657-56). It is a merger of two clusters at a redshift of $z = 0.296$ and its high temperature and high velocity dispersion seem to be indicative of a very large mass [131]. Inspiration for the name is due to the bullet-like shape of the gas of a small subcluster seeming to disrupt the gaseous component of a larger cluster. It has been claimed that theories of modified gravity like MOND (MOdified Newtonian Dynamics) [132] are excluded in favour of DM at 8σ, as the cluster exhibits a spatial offset of the two centers of the mass distribution from the peaks of bayronic mass with this significance[4] [135]. The original evidence for this can be seen in the right panel of Figure 2.3, where a so-called κ convergence map, *i.e.* mass density contours obtained through weak lensing measurements, is superposed onto a Chandra x-ray image showing the hot intracluster gas. It has also been argued that the merger dynamics can lead to an overestimation of the mass from temperature, as hydrostatic equilibrium is assumed, a serious source of theoretical error [136]. The nature of the bullet region as a cooling flow remnant delimited by a surface of high ram pressure is characterized in the same reference.

Galaxy clusters are also used to constrain models in which DM is self-interacting via forces other than gravity. The self-interaction cross section of DM within the Bullet Cluster, in particular, can be constrained

[4] A statement by the creator of MOND, who still defends his theory, can be found at [133]. In essence, the claim is that MOND only requires an additional 50% of the observed visible matter in the Bullet Cluster, as opposed to the DM paradigm, which requires about 10 times more. This missing mass could be baryonic, but telescopes are not able to observe it. See [134] for a discussion of the ΛCDM and MOND hypotheses in the light of galaxy dynamics and CMB measurements.

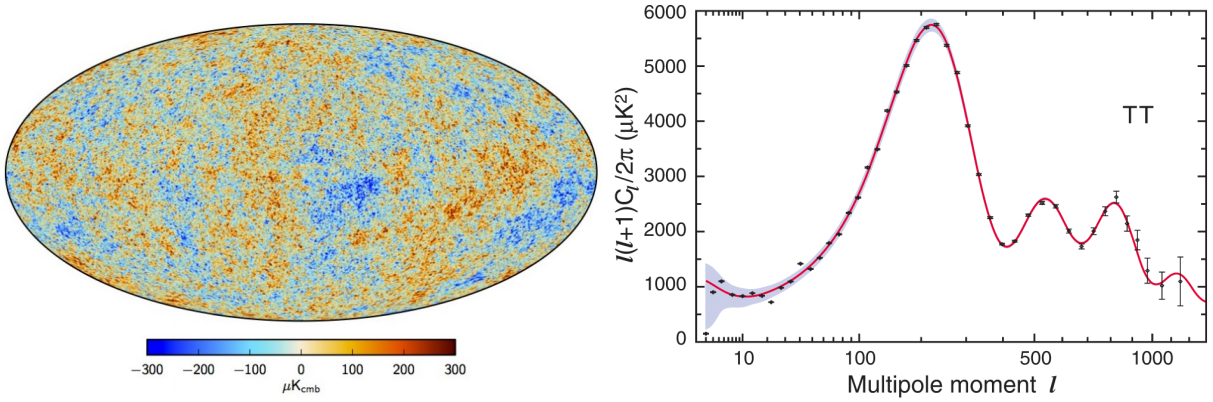

FIGURE 2.4: *Left panel:* Map of the CMB intensity difference w.r.t. the average temperature T_0 measured by Planck [142]. The dipole component is subtracted. *Right panel:* The CMB temperature power spectrum gained from 9-year WMAP data [117], including a fit to the ΛCDM model (red curve). 'TT' signifies that temperature is the only observable, *i.e.* this plot contains no information about photon polarizations. The location of the first acoustic peak can be shown to be roughly at $\ell \approx 220/\Omega_0$, strongly favouring $\Omega_0 = 1$, $\Omega_{k,0} = 0$ [140]. Planck is sensitive to multipoles up to $\ell = 2500$ [8].

to be $\sigma/m_{\rm DM} \lesssim 1$ cm^2/g [137];[5] the exact number does in fact depend on whether one describes the DM halo to be lost or dragged along during the merger, and if one considers a long-range or a short-range interaction. The outcome also depends on the implemented model to simulate the process. Recently, a galaxy was found in the cluster Abell 3827 whose DM halo is slightly offset from the stars [138]. From this observed offset, an upper bound on the self-interaction cross section $\sigma/m_{\rm DM}$ of 3 cm^2/g or 1.5 cm^2/g can be obtained, depending on whether the DM self-interaction results in a bulk drag force or if it is a contact interaction [139].

□ **Large scales:** The large scale structure (LSS) of the Universe is verified to consist of a foam-like pattern of matter filaments separated by huge voids at the very large. Filaments consist of galaxy superclusters glued together to chains or walls by DM; these conglomerates can span millions of light-years and represent the largest structures in the Universe. The hierarchy continues down to galaxy clusters and finally galaxies and gas clouds as the smallest building blocks [140]. There seems to be a correlation with the observed CMB power spectrum, an observation that can be explained through the Sachs-Wolfe effect (see Section 2.2.1). It is believed that the observed filaments consist of baryonic matter attracted by a cosmic DM web

□ **Cosmological scales:** In the beginning of Section 2.2.1, we introduced the history of the discovery of the CMB and roughly explained its physical origin and the meaning of the CMB anisotropies. To describe the anisotropies analytically, one projects the sky map CMB intensity data onto a sphere (see left panel of Figure 2.4) and expands the fluctuations around T_0 in spherical harmonics,[6]

$$\frac{\Delta T}{T}(\hat{\mathbf{n}}) \equiv \Theta(\hat{\mathbf{n}}) = \sum_{\ell=2}^{+\infty} \sum_{m=-\ell}^{+\ell} a_{\ell m} Y_{\ell m}(\hat{\mathbf{n}})\,, \tag{2.21}$$

where $\hat{\mathbf{n}}$ is the direction unit vector pointing to a location (θ, H) in the sky. The coefficients $a_{\ell m}$ of this

[5] $1\,\text{cm}^2/\text{g} = 10^{39}\,\text{fb/g} = 2.568 \times 10^{27}\,\text{GeV}^{-2}/5.618 \times 10^{23}\,\text{GeV} = 0.457\,\text{b/GeV}$

[6] Notice that the expansion starts at the quadrupole, $\ell = 2$. The monopole corresponds to the mean temperature $T_0 \simeq 2.7$ K, which is not contained in the anisotropy map, as anisotropies are temperature differences. The dipole originates from the Doppler shift in the CMB radiation resulting from the motion of the Earth relative to the 'local CMB rest frame', see [141]. This results in a temperature anisotropy of $\sim 10^{-3}$ K between one direction in the sky and the opposite direction. For the dipole, it is not possible to define an average, see [96] for an explanation.

multipole expansion are extracted from the temperature map. Simple single-field inflation models predict that the primordial density fluctuations, and hence the temperature anisotropies, are Gaussian, which means that n-point correlation functions in the ΔT map for $n > 2$ contain no additional information. Measurements are consistent with gaussianity [8]. Given that, the *angular power spectrum* of the temperature field's multipole moments in harmonic space

$$\Theta_{\ell m} = \int d\hat{\mathbf{n}}\, Y^*_{\ell m} \Theta(\hat{\mathbf{n}}) \tag{2.22}$$

then takes the simple form

$$\langle \Theta^*_{\ell m} \Theta_{\ell' m'} \rangle = \delta_{\ell\ell'} \delta_{mm'} C_\ell \,, \qquad C_\ell \equiv \langle |a_{\ell m}|^2 \rangle = \frac{1}{2\ell+1} \sum_{m=-\ell}^{+\ell} |a_{\ell m}|^2 \,. \tag{2.23}$$

The average C_ℓ is a measure for the variance of the coefficients $a_{\ell m}$ in the high-ℓ limit quantifying the amount of structure found within a subtended angle of $\Delta\theta \approx 180°/\ell$ [140]. Traditionally, one plots the power spectrum $C_\ell(\ell)$ with a normalization factor of $\ell(\ell+1)/2\pi$, see the right panel of Figure 2.4 for the power spectrum obtained by WMAP after nine years of data-taking [117]. The cosmological parameters are extracted by minimizing the χ^2 for a likelihood function built from the data $a^{(\mathrm{exp})}_{\ell m}$ and a theoretical set of coefficients $a^{(\mathrm{th})}_{\ell m}$ determined from input cosmological parameters Ω_B, Ω_c, etc. As cited in Appendix A, the best-fit value for the DM density in the ΛCDM model obtained by Planck is currently $\Omega_\mathrm{c} h^2 = 0.1188 \pm 0.0010$ [8], roughly 85% of the full matter content of the Universe.

2.2.2.2 Particle candidates

In this section we comment on some of the proposed particles that have been hypothesized to make up the DM content of the Universe. Non-Newtonian gravity theories such as MOND deserve their attention, but will not be considered in this discussion.

As mentioned in Section 2.1.2, no SM particle or conglomerate thereof is a suitable candidate for the bulk of the DM content. Baryonic astrophysical objects called MACHOS (MAssive Compact Halo Objects), including dense bodies like brown dwarfs, neutron stars and black holes, are commonly not accepted as principal constituents, since surveys for such objects looking for microlensing events in galactic halos found their abundances to be negligible [143]. Furthermore, BBN speaks against any type of baryonic particle. What speaks against active neutrinos, and all hot DM scenarios for that matter, is that galaxy formation started as early as $z > 7$ [144] or even $z > 8$ [145], a few Myr after the Big Bang. That is, the formation of large-scale structure, such as clusters and superclusters, occurred *after* the formation of structure at small scales, like galaxies, *i.e.* the evolution underwent bottom-up instead of top-down. SM neutrinos were highly relativistic at the age of matter-radiation equality [146], having comoving free streaming lengths much larger than the extent of overdense regions from primordial density perturbations, hence they could not have led these regions to clump together to form galaxies [147]. Therefore, SM neutrinos and any form of hot DM are ruled out as the only or the main constituent. Warm and cold DM, on the other hand, can account for LSS observations, due to the shorter free streaming lengths. Whether one or the other is more suited to explain structures at smaller scales (halos, numbers of satellites, etc.) is debated, see *e.g.* [148].

Now follows a selection of the plethora of possible candidates that have so far been proposed. A more complete exposition is presented in [122]. Some of the models adjoin a 'dark sector' to the SM Lagrangian, characterized by some symmetry that attributes a new conserved (or nearly conserved) quantum number to the dark sector particles. Due to this quantum number, assuming it is not violated by some suppressed mechanism, any interaction can only involve an even number of dark particles. This renders the lightest dark sector member stable or very long-lived.

□ **Weakly interacting massive particles (WIMPs):** WIMPs are the most studied type of DM particle, for they have masses in the electroweak range (few GeV to TeV) and annihilation cross sections are of the order of 1 pb, *i.e.* of electroweak interaction cross sections. Thermal WIMP production via freeze-out has

been conceptually introduced in Section 2.2.1. What mainly motivates the WIMP scenario is the fact that the measured DM relic density is naturally reproduced, what one may find 'miraculous'. Typical concrete candidates are the neutralino or the sneutrino in supersymmetric extensions of the SM. In Section 2.2.3, we show how to obtain the DM relic density as a function of the canonical annihilation cross section for s-wave WIMP scattering, *cf.* Equation 2.59.

□ **Feebly interacting massive particles (FIMPs):** The FIMP can be compared to the WIMP with the difference of interacting much more weakly (that is, *feebly*) with other particles. In consequence, its relic abundance is determined in out-of-equilibrium interactions rather than through freeze-out, as is the case of the WIMP. This mechanism is called freeze-in and is described in Section 2.2.3.3. Concrete examples of models with FIMPs are given in the original reference [43].

□ **Sterile neutrinos:** A neutrino not partaking in the gauge interactions could play the role of dark matter. Sterile (right-handed) neutrinos N with masses in the keV range as warm dark matter have first been considered by Dodelson and Widrow [149]. Their properties are summarized *e.g.* in [150]. If they mix with the active neutrinos present in the SM, they can be very long-lived if their decay is suppressed by a small mixing angle θ. The decay to a photon and a SM neutrino is loop-induced and should result in a detectable line feature in x-ray measurements with an energy of $M_N/2$. Classifying them as warm DM presupposes that their phase space distribution is proportional to the Fermi-Dirac function, but this is not a necessity because, if their production is suppressed by small θ, they never attain thermal equilibrium. If θ is large enough for equilibrium to be reached (with the primordial phase space distribution approximately set by the active neutrino temperature), the Universe overcloses unless the sterile neutrinos are diluted by late entropy production [151]. In fact, the parameter space (M_N, θ) is quite unconstrained when one does not demand thermal production. Otherwise, Lyman-α forest observations impose $M_N > 8$ keV [152].

□ **Axions:** A popular solution of the strong CP problem (*cf.* Section 2.1.2) due to R. D. Peccei and H. R. Quinn is the introduction of the global anomalous symmetry $\mathrm{U}(1)_{\mathrm{PQ}}$ [28], with the addition of new fields, among them the *axion field*. Upon spontaneous breaking of $\mathrm{U}(1)_{\mathrm{PQ}}$, the axion particle emerges as a pseudo-Nambu-Goldstone boson [29] and the VEV of the axion field effectively cancels $\bar{\theta}$. Axion masses of the order of Λ_{EW}, as originally proposed, are ruled out due to unobserved decays of mesons to axions [153]. However, a very light ($\lesssim 0.01$ eV) and feebly interacting axion is a viable and popular dark matter candidate, as there exist parameter space ranges where all astrophysical constraints are fulfilled [122, 154]. Such models are termed 'invisible axion' models. Searches for 'invisible' axions exploit their couplings to photons, which depend on the model details. Most well-known are the KSVZ [155] and DFSZ [156] models, see *e.g.* [74] for further details.

2.2.2.3 Search strategies

The hunt for the dark matter particle proceeds mainly in three types of experiments: direct detection (DD), indirect detection (ID) and in colliders. Most existing such experiments are optimized for WIMP searches. These are succinctly described next.

□ **Direct detection:** In direct detection, the DM particle is searched for in Earth-based experiments located underground to minimize the muon-induced neutron backgrounds. The setups consist of large volumes of high-Z materials to enhance the probability for scattering between the DM particle and a nucleon. Collisions cause the nucleus to recoil and emit scintillation radiation. By understanding the natural backgrounds, the DD experiments count the number of events over a live-time T compatible with signal, aiming to find an excess over the expected number by a number N_{s} due to the WIMP-induced scatterings. DD results are presented in terms of constraints on the DM-nucleon scattering cross section

as a function of the DM mass inferred from N_s. This number is calculated as [157]

$$N_\mathrm{s} = T \int_{E_\mathrm{low}}^{E_\mathrm{high}} dE_\mathrm{r}\, \epsilon(E_\mathrm{r}) \frac{dR}{dE_\mathrm{r}} \,. \tag{2.24}$$

This expression includes the following quantities. E_r is the nuclear recoil energy, $E_\mathrm{low,high}$ are the threshold energies characteristic to the detector material, $\epsilon(E_\mathrm{r})$ is the detection efficiency and dR/dE_r is the differential event rate. This rate steeply falls with E_r and is given by a convolution of the local WIMP velocity distribution $f(v)$ with the differential WIMP-nucleus cross section,

$$\frac{dR}{dE_\mathrm{r}} = \frac{\rho_0 M}{m_\mathrm{N} m_\chi} \int_{v_\mathrm{min}}^{v_\mathrm{max}} dv\, v f(v) \frac{d\sigma}{dE_\mathrm{r}} \,, \qquad \frac{d\sigma}{dE_\mathrm{r}} = \frac{m_\mathrm{N}}{2v^2\mu^2} \left(\sigma_\mathrm{SI} F_\mathrm{SI}^2(E_\mathrm{r}) + \sigma_\mathrm{SD} F_\mathrm{SD}^2(E_\mathrm{r})\right) \,, \tag{2.25}$$

where $m_\mathrm{N,\chi}$ are the masses of the nucleus and the WIMP, respectively, M is total detector mass, μ is the reduced mass of the WIMP-nucleus system and finally $\sigma_\mathrm{SI,SD}$ are the spin-independent (SI) and spin-dependent (SD) contributions, which appear multiplied by form factors F_i to account for coherence loss. In the limit of equal interaction strengths with protons and neutrinos, $\sigma_\mathrm{SI} = \sigma_n \frac{\mu^2}{\mu_n^2} A^2$, μ_n being the WIMP-nucleon reduced mass and A the atomic weight of the nucleus. In the limit of a large WIMP mass, the reduced masses tend to $\mu_n \to m_n$ and $\mu \to m_N$. The rate then becomes m_χ-dependent through the DM number density $n_0 \sim m_\chi^{-1}$, explaining the constant rise in the exclusion curves. Low WIMP masses imply small probabilities to transfer enough momentum above the E_low threshold, explaining the sensitivity loss with decreasing m_χ. Spin-dependent interactions exhibit no A^2 enhancement and depend exclusively on the nuclear spin wave function and the momentum transfer.

Current and planned future experiments are thoroughly discussed in [158], for instance. Presently the most sensitive results on the SI cross section have been published by the XENON100 [159] and LUX [160] noble gas detector experiments, see the left panel in Figure 2.5. They excluded cross sections of 2×10^{-45} and 1×10^{-45} cm^2 for WIMP masses of $m_\chi \sim 50$ GeV, respectively. LUX presently provides the most stringent constraints on SI scattering above $m_\chi \gtrsim 6$ GeV. There are two unresolved anomalies in the SI measurements. DAMA/LIBRA at LNGS (Italy) searches for an annual scintillation signal modulation in an apparatus containing NaI(Tl) crystals. Such a signal is indeed observed since the first-generation phase, DAMA/NaI, and by now amounts to a statistical significance of 9.3σ [161]. Depending on whether the interaction occurs with Na or with I nuclei, the signal is compatible with WIMP masses centered around 10 and 70 GeV, respectively. The other anomaly is the observation by CDMS-Si of 3 events in 2007/8 data with an expected background of 0.4, with the best likelihood obtained for a WIMP mass hypothesis of 8.6 GeV [162]. These results are incompatible with other experiments that are sensitive to low WIMP masses, among others SuperCDMS [163]. Null results for elastic WIMP-nucleon interactions imply that, if the WIMP is a member of an electroweak multiplet, its hypercharge needs to vanish (see *e.g.* [164]), as will be important in later discussions.

Spin-dependent scatterings can only take place if the nuclei have unpaired nucleon spins to which the WIMP may couple. Results for interactions with protons and neutrons are commonly given separately. The low-mass region ($\mathcal{O}(10$ GeV)) for spin-dependent proton-WIMP interactions has until recently been dominated by the COUPP [165], SIMPLE [166] and PICASSO [167] collaborations, employing a ^{19}F target. SIMPLE managed to establish an upper limit of $\sim 2 \times 10^{-38}$ cm^2 on the SD cross section for $m_\chi = 10$ GeV. Today's best limits are provided by the PICO-60 [168] and PICO-2L experiments [169], reaching below the 10^{-38} cm^2 mark. Far better limits for masses above ~ 200 GeV are set by IceCube [170] due to its sensitivity to neutrinos from possible WIMP annihilations in the Sun [171]. This is discussed below, since this measurement can be rather described as an ID experiment. Assuming specific effective interactions, collider data imposes the current most stringest constraints for masses below 100 GeV, as is also discussed below.

□ **Indirect detection:** Indirect searches for the DM particle work by detecting the products of its annihilation or its decay products to SM particles. This can be done by means of satellite probes or Earth-based telescope arrays. For a review, see [172].

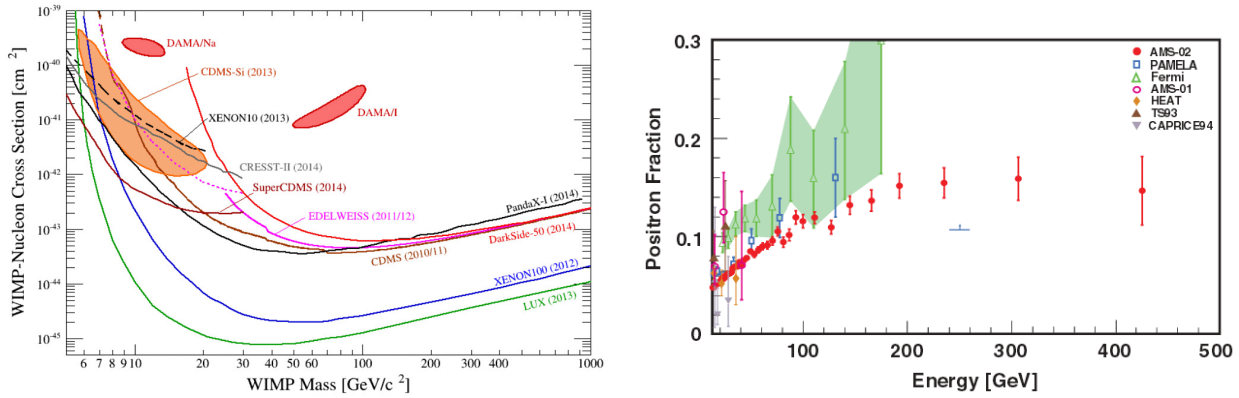

FIGURE 2.5: *Left panel:* Direct detection limits on the spin-independent WIMP-nucleon cross section as of 2014 [157]. *Right panel:* The positron fraction at high energies measured by AMS-02.

ID results are plagued by large uncertainties, mostly due to the lack of a good estimate of the DM density in the observed regions and the modelling of backgrounds. The experiments look for photon radiation in the γ and x-ray spectrum, neutrinos and charged antiparticles in cosmic rays. The latter searches suffer from a large uncertainty in the description of the propagation through the interstellar medium. The former two particle types propagate essentially unperturbed and their flux factorizes in terms of a particle physics part and an astrophysics part,

$$\frac{dN}{dt\,dA\,dE} = P \cdot J(\Delta\Omega)\,, \tag{2.26}$$

with

$$P = \frac{\langle\sigma_{\rm ann} v\rangle}{2m_\chi^2} \sum_i \mathcal{B}_i \frac{dN^i_{\gamma/\nu}}{dE_i}\,, \qquad J(\Delta\Omega) = \int_{\Delta\Omega} d\Omega \int_0^\infty dl\, d\Omega\, \rho^2_\chi(l)\,, \tag{2.27}$$

where $\langle\sigma_{\rm ann} v\rangle$ is the thermally averaged annihilation cross section of the WIMP χ (*cf.* Section 2.2.3.1 and Appendix B), ρ_χ is the WIMP density along the line of sight, $\Delta\Omega$ is the solid angle portion of the measurement, $\mathcal{B}_i$ is the branching ratio to a given final state i of the annihilation and $dN^i_{\gamma/\nu}$ is the differential number of photons or neutrinos resulting from this final state. Gamma ray searches focus on finding excesses and spectral features such as monochromatic lines and boxes salient against the power-law background from γ-rays produced by cosmic ray interactions, but also point sources of localized γ-ray emission. Satellites like the Fermi-LAT [173] are sensitive to radiation up to several 100 GeV, whereas Imaging Air Cherenkov Telescopes (IACT) such as H.E.S.S. [174] are better suited for higher energies. So far, no convincing signal has been observed in ID experiments. Notable claims, however, are the announcement of a tentative line feature in FERMI data at an energy of about 130 GeV a few years ago [175], an excess of γ-rays at about 2 GeV measured by FERMI coming from the galactic center (GC) [176] and an unidentified x-ray emission line incompatible with any known atomic transition at $E_\gamma = 3.55$ keV coming from galaxy clusters [177], detected by the Chandra and XMM-Newton satellites. As of today, there is no consensus that any of these findings is a clear deviation from known astrophysical processes. The global significance of the 130 GeV line feature is now of 1.5 standard deviations [178], pointing to a statistical fluctuation in the data. The 3.55 keV line is most readily interpreted as originating from a loop-induced decay of a sterile neutrino, though even though the claimed significance is $> 4\sigma$, the existence of the excess and its interpretation is highly disputed (see [179] and references therein). As for the GC excess, it has been argued that the radiation may rather stem from unresolved point sources, the best candidates being millisecond pulsars [180].

Charged cosmic rays are predicted to carry tiny fractions of positrons, anti-protons and anti-deuterons produced in secondary processes. In 2008, the PAMELA collaboration announced finding evidence for an excess of high-energy positrons relative to the sum of positrons and electrons compared to the expected flux

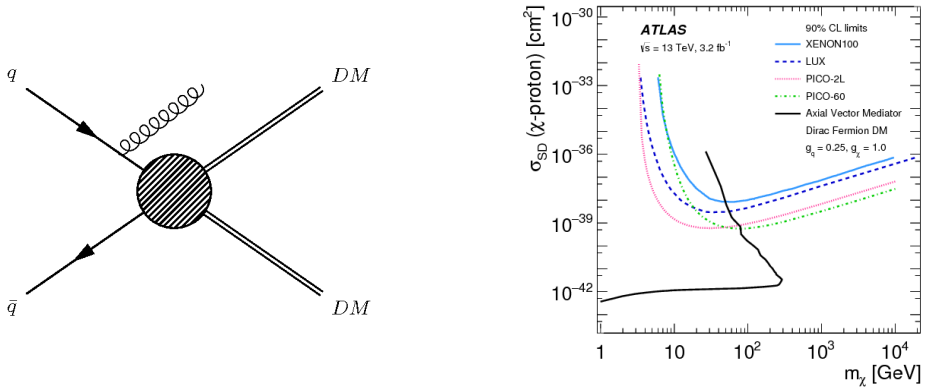

FIGURE 2.6: *Left panel:* DM pair production with ISR jet emission for the case of an effective contact interaction. Figure taken from [188]. *Right panel:* ATLAS limits at 90% C.L. compared to the constraints from direct detection experiments on the spin-dependent WIMP–proton scattering cross section in the context of a Z'-like simplified model with axial-vector couplings. For comparison, the SD limits from XENON100 [189], LUX [190] and the PICO experiments [163, 168] are also shown. Figure taken from [191].

from cosmic ray propagation models [181]. The excess was found to lie in the range $1.5 - 100$ GeV; later AMS-02 extended the measurement up to an energy of 500 GeV and found the flux to stop increasing at ~ 200 GeV [182], see Figure 2.5 (right panel). A pair of annihilating DM particles is expected to produce a particle and its antiparticle, so the interpretation of DM annihilation to e^+e^- suggests itself. Furthermore, AMS also found the antiproton flux to be in excess over the expected background [183], which could originate from DM annihilating hadronically. Alternative suggested sources are electron/positron pairs from pulsars or secondary positrons produced in supernova remnants, see [184] and references therein.

Neutrinos are an interesting object of study because they interact with WIMP dark matter in numerous models and their paths through the interstellar medium are undisturbed. As for γ-rays, they are looked for in the GC, in dwarf galaxies and in galaxy clusters with the ANTARES undersea telescope in the Mediterranean sea [185] and the IceCube telescope at the South Pole [186]. Both collaborations have also performed searches for neutrinos produced in annihilations of WIMPs captured in the gravitational well of the Sun [170, 187]. When traversing the Sun, they are predicted to lose their energies in spin-dependent scatterings with the contained hydrogen. Thus, such searches are very sensitive to the SD cross section; IceCube managed to set a limit on the SD WIMP-proton cross section almost as low as 10^{-40} cm^2 for $m_\chi \gtrsim 200$ GeV.

□ **Collider searches:** Collider experiments standardly look for events with pair-produced DM particles in the form of WIMPs causing a large imbalance in transverse momentum/energy by not depositing any energy. The assumption of pair production relies on the presumed discrete symmetry rendering the DM particle stable. For instance, the lightest supersymmetric particle is often taken to be the lightest neutralino, $\tilde{\chi}_1^0$, which necessarily acts as a DM particle [122]. Events are flagged through the SM particles recoiling against the unseen WIMP pair. One commonly considers the signature with the emission of a gauge boson or a quark by one of the colliding partons; this is known as *initial state radiation* (ISR), *cf.* Section 3.1.3. The signature is a hard jet or an energetic photon accompanied by large missing transverse energy and possibly soft side products, see Figure 2.6. ATLAS and CMS have performed searches during the first [188, 192] and second [191, 193] runs. The $\sqrt{s} = 13$ TeV results correspond to the most stringent limits on the spin-dependent WIMP-proton cross section if interpreted in terms of a particular effective operator, see Figure 2.6 (right panel). Thus, collider experiments are regarded as strong dark matter probes acting complementarily to DD and ID. However, there is increasing criticism to the EFT approach due to inaccurately describing the UV theory at high momentum transfers [194]. To remedy this, there is a strong trend to rather interpret collider searches for DM in terms of simplified benchmark models containing various specific types of mediators, see [195].

In contrast to WIMP searches, FIMP scenarios feature very different collider signatures characterized by the presence of particles with macroscopic decay lengths due to the FIMP condition. There are numerous possibilities to detect such particles, some of them are discussed in Section 4.1. The FIMP hypothesis is the basis for our collider studies in Analyses IIA and IIB.

2.2.3 Thermal dark matter production

2.2.3.1 Decoupling during radiation-driven expansion and relic abundances

This section explores how relic abundances of particle species are calculated and mentions the principal thermodynamic quantities playing a role. As a well-suited example, we present the result of the standard calculation of WIMP annihilation via freeze-out. Subsequently, it is shown how the alternative process of freeze-in can also lead to the observed DM relic abundance.

□ Basic thermodynamics

In FLRW cosmology, the energy-matter content drives and determines the nature of the expansion. This relation is most directly seen in the connection between the Hubble rate and the energy density. Recall that the Friedmann equation (see Appendix A) reads (with $k, \Lambda \to 0$)

$$H^2 = \frac{8\pi G}{3}\rho\,. \tag{2.28}$$

Mostly based on the standard references [196, 197], we start this discussion by characterizing the exact nature of this expansion. As the Universe augments its volume, the energy density, the temperature and the chemical potential of all particle species need to vary, according to the first law of thermodynamics. In the RD and later eras, this expansion is slow, in the sense that it can be regarded as an adiabatic process to a very good approximation and thus the total entropy remains constant. Thermal equilibrium[7] is maintained all throughout until photon decoupling and non-equilibrium processes will cause a negligible change in entropy. Such non-equilibrium processes delimit several phases in the early cosmic chronology, that is, the decoupling times of particular particle species. These are moments when a component of the thermal bath stops contributing to the bulk of equilibrium reactions. As all such energy-matter content transitions with an effect on the evolution happen in the RD era,[8] we require the radiation energy density ρ_r in order to compute the Hubble rate according to Equation 2.28. Photons are, and according to common understanding have always been, the most abundant type of particle in the Universe. Furthermore, they represent the only species contributing to the equilibrium interactions all throughout, therefore they constitute the heat reservoir determining the temperature of the cosmic plasma. Particles will be in thermal equilibrium with the photons until the interaction rate has dropped below the expansion rate, which for all massive particles except neutrinos happens around when the photon temperature decreases to a value below their mass, $T_\gamma \lesssim m$. After decoupling, particles can either end up being non-relativistic — then they are said to be 'frozen-out' and their number density becomes Boltzmann-suppressed — or they can end up relativistic, maintaining their relativistic phase space distribution until the present. The latter is the case for neutrinos, which decoupled at $T \approx 0.8$ MeV, continued lowering their temperature as predicted for ultrarelativistic particles and maybe became non-relativistic at some point in the Universe's history, depending on their mass. Of course, this doesn't need to apply to all three massive neutrino eigenstates, though experiments indicate that the scale of neutrino masses lies well above the present temperature, *cf.* Section 2.3.

[7] Thermal equilibrium corresponds to having kinetic a.k.a. statistical equilibrium, meaning that energy is efficiently exchanged and entropy is maximized, *and* chemical equilibrium, such that the chemical potentials of reacting particles and reaction products add up to the same value. The CMB background photons are not in thermal equilibrium for this reason, although having a Bose-Einstein spectrum: CMB photons have mean free paths of the order of the length of the observable Universe, hence they don't interact and therefore can't be considered to be in thermal equilibrium.

[8] An exception is when the photons themselves decouple due to electron-proton recombination to neutral hydrogen, which took place already in the MD era.

We first make a statement regarding chemical potentials. Recall that the chemical potential μ_i of a species i describes the response of a thermodynamical system to a change in the i-type particle number N_i through the relation

$$\mu_i = -T \left.\frac{\partial S}{\partial N_i}\right|_{U,V} , \tag{2.29}$$

where S, U and V are the total entropy, energy and volume, respectively. But since the entropy of the early Universe is practically not affected by decoupling particles,[9] this implies

$$\left.\frac{\partial S}{\partial N_i}\right|_{U,V} \approx 0 \implies \mu_i \approx 0 , \tag{2.30}$$

so chemical potentials can be neglected for all species when it comes to quantities that are relevant for describing the expansion of the Universe. For photons, this is even more true, because their number is far from conserved. For example, double Compton scattering $e^- + \gamma \leftrightarrow e^- + 2\gamma$ is a very frequent interaction leading to significant changes in N_γ. However, the chemical potential needs to be considered when treating the decoupling process of a particle type by means of the Boltzmann equation, as described in Appendix B.

Without chemical potentials henceforth, the energy density of an ultrarelativistic species i as a function of temperature is given by the Stefan-Boltzmann law,

$$\rho_i(T) = \frac{3}{\pi^2}\,\zeta(4)\,g_i\,T^4 \times \begin{cases} 1\,, & \text{bosons} \\ \frac{7}{8}\,, & \text{fermions} \end{cases} , \tag{2.31}$$

where $\zeta(4) = \pi^4/90$ is the Riemann zeta function $\zeta(s) = \sum_{n=1}^{\infty} \frac{1}{n^s}$ for $s = 4$ and g_i is the number of internal d.o.f. of the species. The different numerical prefactors for bosonic and fermionic particle gases have their origin in the Bose enhancement and Pauli blocking terms ± 1 in the distributions, *cf.* Equation B.7. Hence, the total radiation energy density is given by

$$\rho_{\rm r}(T) = \sum_{\text{rel. species } i} \rho_i(T_i) = \frac{3}{\pi^2}\,\zeta(4)\,g_{*\rho}(T)\,T^4 , \tag{2.32}$$

with $g_{*\rho}(T)$ being the effective number of relativistic d.o.f. in the energy density at temperature T, taken to be the photon temperature, $T = T_\gamma$. This number is given by the sum over d.o.f. of relativistic particles interacting with the photon bath (including the photons themselves) and the sum over decoupled relativistic species,

$$\begin{aligned} g_{*\rho}(T) &= g_{*\rho}^{\text{eq.}}(T) + g_{*\rho}^{\text{dec.}}(T) \\ &= \left[\sum_{i=\text{b}} g_i + \frac{7}{8}\sum_{i=\text{f}} g_i\right] + \left[\sum_{i=\text{b}} g_i \left(\frac{T_i}{T}\right)^4 + \frac{7}{8}\sum_{i=\text{f}} g_i \left(\frac{T_i}{T}\right)^4\right] . \end{aligned} \tag{2.33}$$

Relativistic particles that are in thermal equilibrium with the photons contribute to the first sum, decoupled relativistic particles having a lower temperature T_i contribute to the second. For the SM fields, the number of d.o.f. is given in Table 2.1 and the effective number of d.o.f. adds up to 106.75 if all particles are in equilibrium. Now use Equation 2.32 for the Hubble rate, with the result

$$H(T) = \sqrt{\frac{8\pi G}{3}\,\frac{3}{\pi^2}\,\zeta(4)\,g_{*\rho}(T)\,T^4} = \sqrt{\frac{4\pi^3}{45}}\,M_{\rm P}^{-1}\sqrt{g_{*\rho}(T)}\,T^2 \simeq 1.66\,M_{\rm P}^{-1}\sqrt{g_{*\rho}(T)}\,T^2 , \tag{2.34}$$

where the non-reduced Planck mass is given by $M_{\rm P} = 1/\sqrt{G} = 1.2209 \times 10^{19}$ GeV, so the expansion in the RD epoch decelerates.

Of fundamental importance is also the radiation entropy density, whose expression is ($\mu_i \ll T_i$)

$$s_{\rm r} = \sum_{\text{rel. species } i} s_i(T_i) = \sum_{\text{rel. species } i} \frac{\rho_i + P_i}{T_i} = \frac{4}{\pi^2}\,\zeta(4)\,g_{*s}(T)\,T^3 . \tag{2.35}$$

[9] This is obviously rooted in the huge overabundance of photons w.r.t. other particles, recall Equation 2.17 for baryons, for instance.

P_i is the pressure of species i and $g_{*s}(T)$ is the effective number of relativistic d.o.f. in entropy,

$$\begin{aligned} g_{*s}(T) &= g_{*s}^{\text{eq.}}(T) + g_{*s}^{\text{dec.}}(T) \\ &= \left[\sum_{i=\text{b}} g_i + \frac{7}{8}\sum_{i=\text{f}} g_i\right] + \left[\sum_{i=\text{b}} g_i \left(\frac{T_i}{T}\right)^3 + \frac{7}{8}\sum_{i=\text{f}} g_i \left(\frac{T_i}{T}\right)^3\right] . \end{aligned} \tag{2.36}$$

As mentioned before, photons are by far the most abundant species in the Universe, so they dominate the entropy density in the RD era and any group of particles falling out of equilibrium will transfer a negligible amount of entropy to the other particles contributing to $g_{*s}^{\text{th. eq.}}$ and $g_{*\rho}^{\text{th. eq.}}$. Due to the adiabaticity of the expansion, the total entropy of the Universe, $S \simeq s_{\text{r}}\, a^3$, stays constant during the RD era, which implies that the photon temperature evolves like $g_{*s}^{-1/3} a^{-1}$. The temperature of a decoupled particle, on the other hand, will evolve like a^{-1} if it is relativistic or like a^{-2} if it is non-relativistic, only being redshifted by the Hubble expansion. Whenever a particle decouples, $g_{*\rho}$ and g_{*s} decrease. The decrease of the latter will cause T_γ to drop a bit less slowly than a^{-1} during the decoupling phase, leading to a heating of the photon bath. This only happens when electrons and positrons stop to annihilate and to be created by photon pairs at $T \approx m_e$ (see *e.g.* [196]). Shortly before this phase, at $T \approx 1$ MeV, the neutrinos decouple from the bath, ceasing to interact with the electrons. The entropy of the electrons is then only transferred to the photons, but not to the neutrinos (or almost not, as we shall see). Since the neutrinos are the only species that decouples while being relativistic, they represent the only type of particles whose temperature continues dropping as $T_\nu \sim a^{-1}$ after decoupling. Due to the difference in g_{*s} before and after $T \approx m_e$, we have $T_\nu/T = (4/11)^{1/3}$ and therefore, for N_ν light neutrino flavours, we end up with

$$g_{*\rho} = 2 + \frac{7}{8} \times 2N_\nu \left(\frac{4}{11}\right)^{4/3} \tag{2.37}$$

$$g_{*s} = 2 + \frac{7}{8} \times 2N_\nu \left(\frac{4}{11}\right) . \tag{2.38}$$

Would the neutrinos have decoupled completely before $e^+\, e^-$ annihilation, one would have $N_\nu = 3$. However, neutrino decoupling took a bit longer, therefore three-neutrino flavour oscillation effects lead to an effective number $N_{\nu,\text{eff}} = 3.046$ [198], which is perfectly consistent with Planck results [8]. For the effective numbers of relativistic d.o.f., this implies

$$g_{*\rho} = 3.36\,, \qquad g_{*s} = 3.94\,. \tag{2.39}$$

Finally, we also require the equilibrium number densities for a vanishing chemical potential. Defining

$$đ^3 p_i \equiv \frac{d^3 p_i}{(2\pi)^3}\,, \tag{2.40}$$

these are given by

$$\bar{n}_i = g_i \int đ^3 p_i\, f_i(E_i, T) = \begin{cases} g_i \left(\frac{m_i T}{2\pi}\right)^{3/2} \mathrm{e}^{-m_i/T}\,, & m_i \gg T \\ \frac{1}{\pi^2}\, g_i\, \zeta(3)\, T^3 \times \begin{cases} 1\,, & \text{bosons} \\ \frac{3}{4}\,, & \text{fermions} \end{cases}, & m_i \ll T \end{cases} \tag{2.41}$$

For $m_i \gg T$, the distinction between bosons and fermions is lost and the density follows a Maxwell-Boltzmann (MB) distribution.

□ Thermal decoupling

We begin with an illustrative example [196]. For a collision process of a particle in the photon bath with a reaction rate Γ, one can derive a general result for the case when Γ scales as T^n with temperature, with a power $n > 2$. With $t = 1/2H$ and $H \propto T^2$, ignoring the T dependence of the $g_{*\rho}$ parameter,[10] it is then

[10] One may take $g_{*\rho} \simeq g_{*\rho}(m_X)$, where X is the particle that freezes-out. During the freeze-out process, the temperature of the photon bath will always be around the mass of the decoupling particle; in fact, it is proportional to $\mathcal{O}(10) \times m_X$.

not difficult to show that after some time t the number of such interactions will be

$$\int_t^\infty dt'\,\Gamma(t') = \frac{\Gamma(T)}{H(T)}\int_0^T dT'\,\frac{T^2}{T'^3}\left(\frac{T'}{T}\right)^n = \frac{\Gamma(T)}{H(T)}\,\frac{1}{n-2}\,. \tag{2.42}$$

Note that the integral is only finite for $n > 2$. Hence, when $H(T) \gtrsim \Gamma(T)$ and for $n > 2$, the particle interacts $\lesssim 1$ times during the rest of its existence and is said to be *frozen-out*: The interaction rate becomes lower than the expansion rate and the lack of further scatterings leads to a further decrease of Γ with respect to H, causing the particle to fall out of thermal equilibrium because the expansion renders the gas too dilute to sustain the elastic scattering processes.

More generally, an interaction rate does not need to be proportional to $T^{n>2}$. The collision rate is always calculated via

$$\Gamma_i\,(i + \text{bath particle}\, j \leftrightarrow \ldots) = n_j \sigma v \propto \sigma T^3\,, \tag{2.43}$$

where n_j is the number density of j-type particles, σ is the collision cross section of particles i and j and v is their relative velocity. For instance, an electroweak or QCD collision cross section is of order T^{-2}, giving $\Gamma \sim T$. Yet, one can still in general compare the collision rate to the Hubble rate and identify the decoupling temperature by imposing equality of the two rates,

$$\Gamma(T) \approx H(T) \implies T_{\rm sol} \approx T_{\rm dec}\,. \tag{2.44}$$

For cold relics, *i.e.* particles that decouple while they are non-relativistic, a more exact value of the temperature at which this happens is calculated by means of the Boltzmann equation. Equation 2.44 is still used for particles that decouple while they are relativistic (hot relics), as is the case for neutrinos. The Boltzmann equation is discussed in detail in Appendix B.

□ The Boltzmann equation for thermal freeze-out

Consider a $(1,2) \leftrightarrow (3,4)$ reaction, where the numbers stand for particle types, and focus on the density $n_1(t)$ of species 1. The Boltzmann equation for n_1 reads

$$\dot{n}_1 + 3Hn_1 = -\langle\sigma v\rangle\left[n_1 n_2 - \frac{\bar{n}_1\bar{n}_2}{\bar{n}_3\bar{n}_4}n_3 n_4\right]\,, \tag{2.45}$$

where $\bar{n}_i$ are the equilibrium number densities with a vanishing chemical potential, as defined in Equation B.12. Clearly, Equation 2.45 relates the temporal variation of particle species 1 to its creation and annihilation rates, which are proportional to the *thermally averaged annihilation cross section* $\langle\sigma v\rangle$, *cf.* Equation B.14. The r.h.s. is called the collision term — it is non-zero in the presence of out-of-equilibrium processes leading to an increase or decrease of 1-type particles (and of any other types of involved particles, for that matter). If it vanishes, all particles are found in their thermal equilibrium states, $\bar{n}_i$.

Let us write the Boltzmann equation in a more suggestive way to recover Equation 2.44. Recalling the expression for the total radiation energy density in Equation 2.35, the total number of particles of a species i in a comoving volume is given by the dimensionless quantity

$$Y_i \equiv \frac{n_i}{s}\,, \tag{2.46}$$

which we call the *yield*.[11] Like n_i, it only changes due to out-of-equilibrium processes, but it doesn't scale with a^{-3} and is instead constant during an equilibrium phase. It is customary to write the Boltzmann equation in the form

$$\dot{Y}_1 = -s\,\langle\sigma v\rangle\left[Y_1 Y_2 - \left(\frac{\bar{Y}_1\bar{Y}_2}{\bar{Y}_3\bar{Y}_4}\right)Y_3 Y_4\right]\,, \tag{2.47}$$

[11] Note that Y may be defined differently in other texts, as long as it goes like n_i/T^3; we use the Kolb & Turner [196] convention.

or, using $\Gamma_1 = n_2 \langle\sigma v\rangle$,

$$\frac{d\ln Y_1}{d\ln a} = -\frac{\Gamma_1}{H}\left[1 - \left(\frac{\bar{Y}_1\bar{Y}_2}{\bar{Y}_3\bar{Y}_4}\right)\left(\frac{Y_3Y_4}{Y_1Y_2}\right)\right] . \tag{2.48}$$

Γ/H is called the *annihilation effectiveness*. Of course, a similar equation holds for the other three particle species. Consider the case $\Gamma_1 > H$. If $Y_1 \gg \bar{Y}_1$ and $Y_{2,3,4} \sim \bar{Y}_{2,3,4}$, the r.h.s. is negative and Y_1 will decrease towards $\bar{Y}_1$. If, on the other hand, $Y_1 \ll \bar{Y}_1$, then the r.h.s. is positive and Y_1 will increase towards $\bar{Y}_1$. The same applies if more than one species are away from equilibrium. Therefore, a larger production rate than the expansion rate will drive the system towards thermal equilibrium, where it will stay as long as this condition is fulfilled. However, if $\Gamma_1 < H$, the r.h.s. becomes small and Y_1 approaches a final constant value, the *relic abundance* — the particle species 1 is then 'frozen-out'.

2.2.3.2 Thermal dark matter freeze-out: The WIMP miracle

We now consider the case of DM particles χ and antiparticles $\bar{\chi}$ being in thermal equilibrium with a bath particle species, $(1,2) \leftrightarrow (3,4) = (\chi\,\bar{\chi}) \leftrightarrow (\phi_\mathrm{b}\,\bar{\phi}_\mathrm{b})$. The conventional WIMP freeze-out scenario starts with equal amounts of χ and $\bar{\chi}$ and assumes that the particles χ interacts with are in thermal equilibrium with the primordial plasma all throughout, so $Y_{\phi_\mathrm{b},\bar{\phi}_\mathrm{b}} = \bar{Y}_{\phi_\mathrm{b},\bar{\phi}_\mathrm{b}}$. Defining the dimensionless variable

$$x \equiv \frac{m_\chi}{T} , \tag{2.49}$$

the Boltzmann equation (2.47) can then be written as

$$\frac{dY_\chi}{dx} = -\frac{\lambda(x)}{x^2}[Y_\chi^2 - \bar{Y}_\chi^2] , \tag{2.50}$$

where

$$\lambda(x) \equiv \frac{s(m_\chi)\,\langle\sigma v\rangle\,(x)}{H(m_\chi)} = \frac{4}{\pi^2}\,\zeta(4)\,g_{*s}(m_\chi)\,\frac{m_\chi^3\,\langle\sigma v\rangle\,(x)}{H(m_\chi)} . \tag{2.51}$$

Here we approximated $g_{*s}(T) \approx g_{*s}(m_\chi)$, since that is the relevant temperature region for freeze-out[12] and therefore

$$\frac{d}{dt} = \frac{dT}{dt}\frac{d}{dT} \approx -HT\frac{d}{dT} = Hx\frac{d}{dx} . \tag{2.52}$$

Equation 2.50 is a Riccati-type equation (quadratic in the function), so it can only be solved numerically.

If χ is non-relativistic, its velocity follows a Boltzmann distribution, which has an average given by $\langle v\rangle \sim \sqrt{T} \sim x^{-1/2}$, thus if we expand $\langle\sigma v\rangle$ in partial waves, $\langle\sigma v\rangle = a + bv^2 + \ldots$, we get

$$\langle\sigma v\rangle\,(x) = \langle\sigma v\rangle_0\; x^{-n} , \tag{2.53}$$

with $n = 0$ for an s-wave, $n = 1$ for a p-wave, etc. Note that we need $v \ll 1$ ($x \gg 1$) for this expansion to be adequate. We then rewrite the Boltzmann equation in the form

$$\frac{dY_\chi}{dx} = -\frac{\lambda_0}{x^{n+2}}[Y_\chi^2 - \bar{Y}_\chi^2] , \qquad \lambda_0 \equiv \frac{s(m_\chi)\,\langle\sigma v\rangle_0}{H(m_\chi)} . \tag{2.54}$$

Figure 2.7 shows the evolution of the yield for a DM Majorana fermion $\chi = \bar{\chi}$ ($g_\chi = 2$) in the case of s-wave scattering. We consider the case when it freezes-out as a cold relic. On the left, we compare the evolution for different masses and on the right for different annihilation cross sections. As χ already starts out non-relativistic, $\bar{Y}_\chi$ tracks its Boltzmann equilibrium distribution given in the upper line of Equation 2.41 until the temperature of freeze-out T_f is reached. Subsequently, χ ends up as a cold relic. We observe that, contrary to the relic abundance, x_f is not very sensitive to the DM mass, neither to the cross section; it is always a number in the vicinity of $x \sim 20$. Also note that larger cross sections lead to stronger Boltzmann suppression before freeze-out, as more annihilations occur in equilibrium and freeze-out happens later.

[12] Notice though that it is possible to also incorporate the temperature dependence of g_{*s}, as is done in [199]

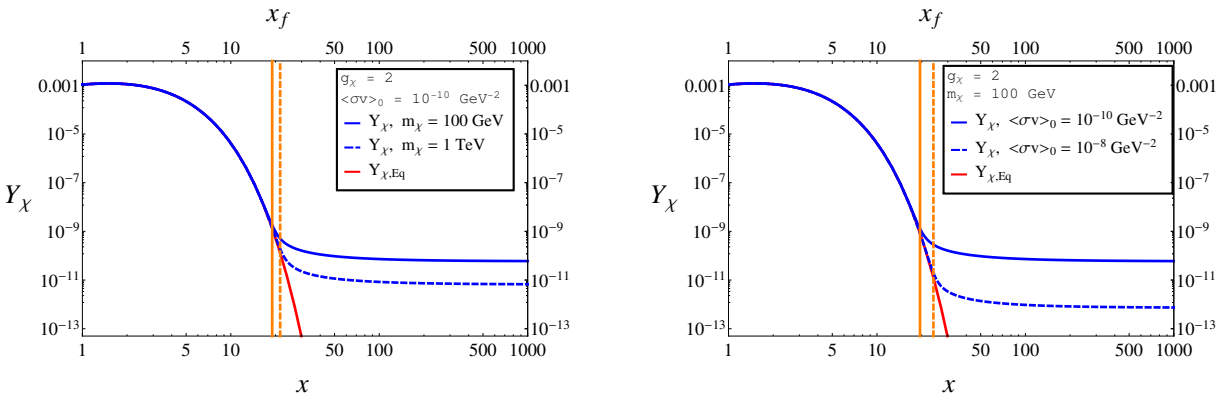

FIGURE 2.7: Yield of a Majorana fermion χ ending up as a cold relic as a function of $x = m_\chi/T_\gamma$. The plot starts at $x = 1$, where the particles start being non-relativistic. Therefore the curves start out proportional to the Boltzmann-type yield, $x^{3/2}\mathrm{e}^{-x}$. The red curve would be the evolution if freeze-out would never take place. *Left panel:* Comparison between the yield evolutions for different WIMP masses with a fixed annihilation cross section. The higher the mass, the later the time of freeze-out and the lower the relic density. *Right panel:* Comparison between the yield evolutions for different annihilation cross sections with a fixed WIMP mass. The higher the cross section, the later the time of freeze-out and the lower the relic density.

Continuing with the s-wave case, the final yield can be estimated by noting that $Y_\chi^\infty \gg Y_\chi^\mathrm{f}$, thus we can neglect the equilibrium term at high x values and obtain[13]

$$Y_\chi^\infty \simeq \frac{x_\mathrm{f}}{\lambda_0}\,. \tag{2.55}$$

The χ relic density is then easily calculated. With $Y_{\chi,0} = Y_\chi^\infty$, $\rho_{\chi,0} = m_\chi n_{\chi,0}$ and $g_{*\rho}(T_0)$ given in Equation 2.39, we get

$$\Omega_{\chi,0}h^2 = \frac{\rho_{\chi,0}}{\rho_\mathrm{c}}\,h^2 = \frac{8\pi G}{3H_0^2}\,m_\chi Y_\chi^\infty s_0 h^2 = (2.77\times10^8)\times Y_\chi^\infty \times \left(\frac{m_\chi}{1\,\mathrm{GeV}}\right)\,. \tag{2.56}$$

This result is usually expressed in the form

$$\Omega_{\chi,0}h^2 \simeq 0.1188\,\frac{x_\mathrm{f}}{\sqrt{g_*(m_\chi)}}\,\frac{7.264\times10^{-10}\,\mathrm{GeV}^{-2}}{\langle\sigma v\rangle_0}\,, \tag{2.57}$$

setting $g_{*s}(m_\chi) = g_{*\rho}(m_\chi) \equiv g_*(m_\chi)$ along the way. With $1\,\mathrm{cm}/s = 3.342\times10^{-11}$ in natural units, this gives

$$\Omega_{\chi,0}h^2 = 0.1188\,\frac{x_\mathrm{f}}{\sqrt{g_*(m_\chi)}}\,\frac{8.464\times10^{-27}\,\mathrm{cm}^3\,\mathrm{s}^{-1}}{\langle\sigma v\rangle_0}\,. \tag{2.58}$$

For $x_\mathrm{f} = 20$ and $g_*(m_\chi) \simeq 31$, we recover the *canonical s-wave annihilation cross section*,

$$\langle\sigma v\rangle_{0,\mathrm{can}} \equiv 3\times10^{-26}\,\mathrm{cm}^3\,\mathrm{s}^{-1} \simeq 2.575\times10^{-9}\,\mathrm{GeV}^{-2} \simeq 1\,\mathrm{pb}\times\frac{\mathrm{cm}}{\mathrm{s}}\,, \tag{2.59}$$

an often seen reference value in the literature. For this typical value of a weak interaction cross section, the observed DM relic abundance is reproduced, which is generally termed the 'WIMP miracle'. We remark that this treatment has been very superficial, for we ignored the T dependence of g_{*s} and merely read off the freeze-out temperature from the obtained curves. It is possible to find better analytical results, as shown in [199]. For s-wave annihilation, one obtains

$$\Omega_{\chi,0}h^2 = \frac{9.92\times10^{-28}\,\mathrm{cm}^3\,\mathrm{s}^{-1}}{\langle\sigma v\rangle_0}\,\frac{x_*}{\sqrt{g_{*\rho}}}\,\frac{(\Gamma_\chi/H)_*}{1+\alpha_*(\Gamma_\chi/H)_*}\,, \tag{2.60}$$

[13] The general solution is $Y_\chi^\infty = \frac{n+1}{\lambda_0}x_\mathrm{f}^{n+1}$.

where $\Gamma_\chi = n_\chi \langle \sigma v \rangle_0$ is the annihilation rate and the subscript $*$ stands for evaluation at a temperature $T = T_*$, to be obtained iteratively, at which the deviation of n_χ from thermal equilibrium starts to increase exponentially. $\alpha_* \sim 1$ is a number accounting for the temperature dependence of $g_{*\rho}$. The agreement of this expression with the exact numerical result is found to be better than 3%. It should be emphasized that the authors of reference [199] do not state that $x_* = x_\mathrm{f}$, instead they define the freeze-out temperature to be approximately $T_*/100$, such that it is regarded as frozen out when the yield has had time to stabilize at today's value. For an expression of Ω_χ in the presence of p-wave annihilations, we refer to [122].

The standard calculation just presented ignores the possibility of additional resonant WIMP annihilations with other hypothetical dark sector particles with a similar mass. If the dark sector consists of χ, $\bar{\chi}$ and other heavier particles ϕ_i it can interact with, then *all* the processes altering the number of any type of dark sector particle, like $\chi + \phi_i \to \mathrm{SM} + \mathrm{SM}$ or $\phi_i \to \chi + \mathrm{SM}$, have to be included in a coupled set of Boltzmann equations. Such processes are known as *coannihilations* [200] and these can very considerably alter the results of the standard calculation. Hence, depending on the model, coannihilations may contribute a significant fraction to the final yield. As all of the dark sector particles but χ have a lifetime that is shorter than the age of the Universe, one defines the dark sector particle yield

$$Y \equiv \sum_{\substack{\text{all dark sector} \\ \text{particles}}} Y_i \,, \tag{2.61}$$

which ultimately coincides with Y_χ because all ϕ_i eventually decay to χ due to the assumed underlying symmetry. One then rewrites the Boltzmann equation (Equation 2.47) in the form [201]

$$\dot{Y} = -s \langle \sigma_\mathrm{eff} v \rangle \left[Y^2 - \bar{Y}^2 \right] \,, \tag{2.62}$$

with the effective annihilation rate

$$\langle \sigma_\mathrm{eff}\, v \rangle = \sum_{i,j} \langle \sigma_{ij}\, v_{ij} \rangle \frac{\bar{Y}_i}{\bar{Y}} \frac{\bar{Y}_j}{\bar{Y}} \,. \tag{2.63}$$

The sum only runs over dark sector particles and the relative velocity between particles i and j is given by Equation B.15.

2.2.3.3 Thermal dark matter freeze-in

Attention should be immediately drawn to the fact that the FO scenario described above is unaffected by the initial conditions, *i.e.* the starting abundance of DM particles injected into the cosmic plasma at the beginning of the RD epoch. Whatever is the starting temperature, FO generally sets in at temperatures around 20-25 times the DM mass. We now discuss a recently proposed alternative mechanism that is also independent of the uncertain physics at high UV scales, provided only renormalizable interactions are involved, called *freeze-in* (FI) [43]. In this section, we closely follow the very complete and thorough main reference, resorting to the same notation.

FI can in several ways be regarded as the opposite process to FO, though it is also IR dominated. Whereas FO is based on the assumption that the initial DM population is in thermal equilibrium, frozen-in DM emanates from a negligibly small initial abundance, maybe due to the nature of inflation, that is too weakly coupled to the bath particles for thermal equilibrium to ever be attained. Perhaps the most significant aspect in opposite behaviour is the increase (decrease) of the final DM abundance with the DM-bath interaction strength in FI (FO) once the temperature drops below a fraction of 2-5 (20-25) of m_DM, *cf.* Figure 2.8. The reason lies in the nature of DM production: FO happens through the depletion of the DM population via annihilations to bath particles, while in FI, DM is produced in collisions, decays and inverse decays of bath particles, all suppressed by the very small involved couplings. This rules out FIMP DM candidates that are not singlets under the SM gauge group.

FO scenarios offer a rich phenomenology because DM interactions with the bath require a mediator carrying the (maybe approximately) conserved quantum number responsible for stability. Similarly, FI models necessarily introduce new particles beyond the DM candidate; this opens a vast pool of spectra

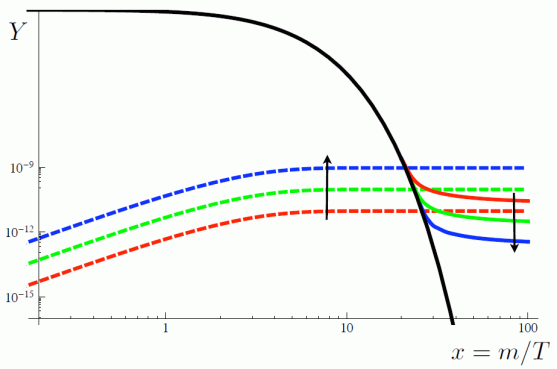

FIGURE 2.8: Comparison of the yield evolutions in the freeze-out (solid coloured) and freeze-in (dashed coloured) scenario as a function of $x = m_{\rm DM}/T$, figure taken from the original reference [43]. The solid black line is the prediction for sustained thermal equilibrium and the arrows indicate increasing coupling strengths of the DM particle with the bath.

Scenario 1	**FI of FIMP DM:** The dominant contribution to the DM (X) abundance is due to FI, during which the LOSP is in thermal equilibrium. After DM is frozen-in, the LOSP decays to DM adding a small contribution to the relic abundance.
Scenario 2	**LOSP FO and decay to FIMP DM:** The interactions of the DM particle (X) with the bath are too feeble to result in a significant population. The dominant contribution is provided by the decay of the LOSP after it has suffered a conventional FO.
Scenario 3	**FIMP FI and decay to LOSP DM:** The DM particle is the LOSP and its FO results in a subdominant part of the DM relic abundance. Late FIMP (X) decays provide the dominant part.
Scenario 4	**FO of LOSP DM:** The DM particle is the LOSP and its FO is the dominant mechanism producing the relic abundance. A subdominant component stems from FIMP (X) FI, which later decays to the LOSP. If the latter process is negligible, this corresponds to the conventional FO mechanism.

TABLE 2.4: The four freeze-in scenarios.

with fundamentally different phenomenologies. As opposed to the WIMP in FO, the fundamental particle type in FI is the *Feebly Interacting Massive Particle* or *Frozen-In Massive Particle* (FIMP) X, a particle species with extremely small interactions with the bath, such that its thermalization never occurs. Of equal importance is the so-called *Lightest Observable Sector Particle* (LOSP), *i.e.* the lightest particle carrying the stabilizing quantum number with sizeable interactions with the primordial plasma and therefore undergoing a conventional freeze-out. Phenomenology then depends on whether the DM candidate is the FIMP or the LOSP. As discussed in the main reference, both cases can be subdivided into two fundamentally different cases, depending on the impact of the LOSP freeze-out. Thus there are the four different scenarios listed in Table 2.4 and schematically depicted in Figure 2.9. Of course, one can also envisage models with similar importances of the contributions from FI/FO and LOSP/FIMP decay. In particular, a contribution to DM by late decays of frozen-out long-lived particles (WIMPs) like in scenarios 1 and 2 is termed the *superWIMP mechanism* (sW) [202]. In that case, the DM relic density is given by the sum of both contributions,

$$\Omega_{\rm DM} h^2 = \Omega^{\rm FI}_{\rm DM} h^2 + \Omega^{\rm sW}_{\rm DM} h^2 \,. \tag{2.64}$$

We shall be especially interested in scenario 1 with a Yukawa interaction responsible for X production, *i.e.* without a DM injection through the sW mechanism.

Denoting by m the mass of the heaviest particle participating in the interactions relevant to the FI

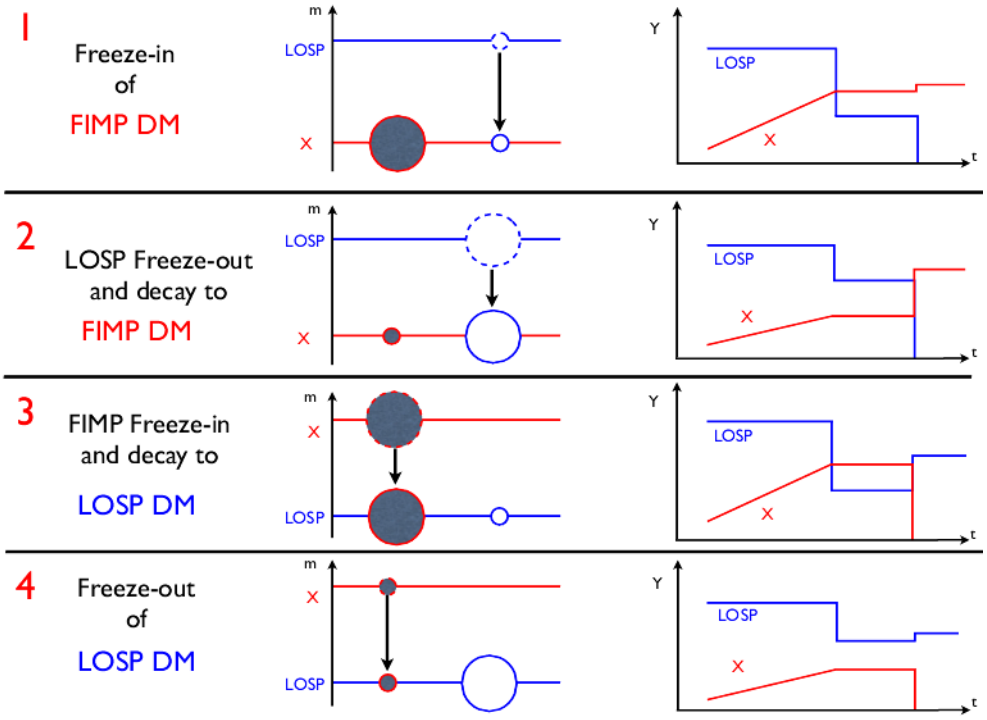

FIGURE 2.9: The four possible scenarios in a model containing a FIMP, taken from the original reference [43]. Large (small) circles represent the dominant (subdominant) contribution to the DM relic abundance, dashed (solid) circles indicate that the particle is unstable (stable) and filled (unfilled) circles designate production via FI (FO). On the right, the temporal evolutions of the FIMP and LOSP yields are depicted, assuming masses of the same order.

processes, it is easy to see that the FIMP will be frozen-in at temperatures around $T \sim m$, since at lower temperatures, there will be a Boltzmann suppression by a factor $\exp(-m/T)$. The freeze-in condition for the FIMP is therefore

$$\Gamma(\text{bath} \to \text{FIMP} + \ldots) \lesssim H(T \sim m)\,. \tag{2.65}$$

Thus, renormalizable interactions lead to the (UV-insensitive) yield evolution during a Hubble doubling time (by Equation 2.69)

$$Y(T) \sim \lambda^2 \frac{M_\mathrm{P}}{T}\left(1, \frac{m^2}{T^2}\right) \overset{T\to m}{\longrightarrow} Y_\mathrm{FI} \sim \lambda^2 \frac{M_\mathrm{P}}{m}\,, \tag{2.66}$$

where $\lambda \ll 1$ is dimensionless and it is indicated that it could either parametrize a quartic scalar interaction or a Yukawa interaction proportional to λm. FO, on the other hand, predicts (*cf.* Equation 2.55)

$$Y_\mathrm{FO} \sim \frac{1}{\sigma v M_\mathrm{P} m} \sim \frac{1}{\lambda^2}\frac{m}{M_\mathrm{P}}\,, \tag{2.67}$$

provided m is the only mass scale in the annihilation cross section. Indeed, Equations 2.66 and 2.67 clearly reveal the inverse effect of the size of the coupling strength.

Now consider the interaction of X with two bath particles B_1 and B_2, with $m_{B_1} > m_{B_2} + m_X$. B_1 is assumed to exclusively decay to the FIMP via

$$B_1 \to B_2 X\,, \tag{2.68}$$

the relevant Boltzmann equation for which is given in Appendix B in Equation B.9. Neglecting inverse decays and quantum statistical effects due to bosonic or fermionic particle natures, the Boltzmann equation

turns out to have a simple decay term,

$$\dot{n}_X + 3Hn_X = -sHT\frac{dY_X}{dT} = \frac{g_{B_1} m_{B_1}^2 \Gamma_{B_1}}{2\pi^2} TK_1(m_{B_1}/T)\,, \tag{2.69}$$

where K_1 is the modified Bessel function of the first kind, g_{B_1} is the number of spin degrees of freedom of particle species B_1, Γ_{B_1} is its decay rate and we applied Equation 2.52 in the first equality. With Equations 2.34 and 2.35, one can integrate over T to obtain the final yield of the FIMP,

$$Y_X \approx \frac{135 g_{B_1}}{8\pi^3 1.66 g_{*s}\sqrt{g_{*\rho}}} \frac{M_{\mathrm{P}}\Gamma_{B_1}}{m_{B_1}^2}\,, \tag{2.70}$$

leading to a relic X abundance from the decay in Equation 2.68 of

$$\Omega_X h^2 = \frac{1.09\times 10^{27} g_{B_1}}{g_{*s}\sqrt{g_{*\rho}}} \frac{m_X \Gamma_{B_1}}{m_{B_1}^2}\,. \tag{2.71}$$

Numerous concrete examples for models with potential FIMPs are provided in the original paper. For example, an additional term in the superpotential of the MSSM providing Dirac neutrino masses leads to the freeze-in of the $\tilde{\nu}_R$ through inverse decay processes involving leptons and higgsinos. We shall not discuss this further, as all cosmological aspects necessary for our studies of the scotogenic model with FIMP dark matter have now been treated.

2.3 Physics of neutrinos

Neutrinos are by far the most mysterious of the known particle species. Oscillations among the three active neutrino flavours indicate that at least two of them have a non-vanishing mass, but oscillation experiments with atmospheric, solar, reactor and accelerator neutrinos, along with measurements from cosmology and of neutrinoless double beta decay, point to an overall mass scale that is tiny when compared to the other known massive elementary particles. Indeed, direct neutrino mass measurements with tritium beta decay have led to a model-independent upper bound of $\lesssim 2.1$ eV for the effective electron antineutrino mass [203]; this value will be superseded by the KATRIN experiment [204], whose sensitivity is projected to reach 0.2 eV. Further constraints come from cosmology: Planck [98] has set the bound on the sum of neutrino masses to be in the range $0.23 - 1$ eV, though results depend on the data used and are model-dependent [205]. Neutrino oscillation measurements imply that at least one neutrino mass eigenstate has a mass of at least 0.05 eV, as we will see in Section 2.3.2.

Hence, with a mass scale constraint of $\lesssim 1$ eV, they are at least six orders of magnitude lighter than the electron. This fact has been the focus of countless attempts at extending the SM, as it does not provide an underlying reason for the observed mass hierarchies. One of these attempts is the model we consider in Section 2.4. Furthermore, even though neutrinos are produced abundantly in Nature and experimentally, their detection and study is plagued by a great difficulty due to their rare interactions with other matter. Since they have no electromagnetic or colour charge, neutrinos produce no electromagnetic or hadronic signals, leaving only the possibility to detect them via their interactions through charged and neutral weak currents. These currents are suppressed by the gauge boson masses, leading to extremely low interaction rates. Nevertheless, due to the hugely successful experimental progress in the last few decades and the promising prospects, the neutrino sector may ultimately be the first to open a window to BSM physics.

To start with some history, W. Pauli proposed in 1930 the neutrino particle in his famous 'Dear Radioactive Ladies and Gentlemen' letter as a nucleus constituent in an attempt to explain the observed continuous beta decay spectrum of ^{14}N and ^{6}Li nuclei. He originally termed the particle a 'neutron'. The electron and neutrino energies would add to the constant value of the nucleus mass difference and the additional spin-$\frac{1}{2}$ particles would reconcile the behaviour of the nuclei with the spin-statistics theorem. The latter problem was solved in 1932 when J. Chadwick discovered the particle we today know as the neutron [206]. Energy conservation in beta decay still needed to be addressed. This led E. Fermi to present a tentative theory in 1934 [49] that contained the neutrino as a hypothetical particle produced in nuclear

beta decay. The neutrino would carry away a varying amount of kinetic energy, explaining observations. Today the neutrino's existence is an experimentally well-established fact and we know Fermi's theory to be an accurate description of nuclear beta decay because it is a low-energetic process. However, Fermi's proposed four-fermion operator of mass dimension $d = 6$ involving a neutron, a proton, an electron and an electron anti-neutrino generates infinities that are not controllable through the renormalization procedure, for which the full theory is necessarily a gauge theory. Neutrinos participating in beta decay and other electroweak processes mediated by gauge bosons are termed *active* neutrinos; there is as well the possibility for the existence of so-called *sterile* neutrinos, so named because they do not participate in the gauge interactions, *cf.* Section 2.2.2.2.

Along with Fermi's electron neutrino, two more active neutrinos are known to exist, each being a flavour partner of a charged lepton.[14] As was discussed in Section 2.1.3, left-handed neutrinos and left-handed charged leptons are grouped in three families of $\mathrm{SU}(2)_L$, a fourth sequential family now being strongly ruled out [208]. A plethora of ingenious experiments unequivocally points to the non-conservation of lepton flavour due to the observation of neutrino oscillations, in a fashion that is perfectly consistent with the picture of three active neutrinos.[15] Therefore, lepton flavour is not a symmetry of Nature. An immediate consequence is the non-zero value of at least two of their masses. Lepton flavour models intend to explain the observed pattern of lepton and neutrino masses and neutrino flavour mixing. As for neutrino masses, experiments have thus far only been able to extract two squared-mass differences, leaving open the possibility for a democratic spectrum or two different hierarchical realizations.

The following sections summarize the basic elements of modern neutrino theory, with possibilities of mass generation (clearly happening beyond the SM sector) and occasionally mention relevant experiments. For this end, we follow the review [209] from 2007 to a somewhat large extent and refer to the more thorough listing of bibliography in that article.

2.3.1 Neutrino masses

To account for neutrino masses, the SM Lagrangian needs to be properly extended. In contrast to the charged leptons and quarks, no right-handed neutrinos exist in the SM, thus there is no gauge-invariant Yukawa term that can lead to Dirac-type masses. There are also no masses arising from loop corrections, since those would stem from a lepton number violating operator. Moreover, the $\mathrm{U}(1)_{\mathrm{B-L}}$ subgroup of $\mathcal{G}_{\mathrm{SM}}^{\mathrm{global}}$ (Equation 2.15) is not broken by non-perturbative effects because it is non-anomalous. Neutrino masses in the SM can consequently only be generated by violating one or more of its symmetries and/or abandoning renormalizability. Thus, they remain strictly massless in the Standard Model and it follows the requirement for the introduction of new fields. Operators involving these new fields may violate $\mathcal{G}_{\mathrm{SM}}^{\mathrm{global}}$; since it is accidental, nothing speaks against this possibility. The most popular way of extending the SM is to generate a Majorana mass term for the active neutrinos, violating lepton number by two units, $\Delta L = 2$. Lepton number is conserved in the case of Dirac neutrinos, but it can also remain a symmetry in specific models of gravity. For example, allowing fermions to propagate in the bulk of the Randall-Sundrum geometry [22] may result in a higher-dimensional scenario where neutrino masses are Planck scale-suppressed [11]. The following discussion disregards gravitation.

In the broken phase of the SM, chiral symmetry is broken as well, meaning that left- and right-chiral fermionic fields are coupled through the VEV of the neutral Higgs field component. The grand exception are the neutrino fields, which can still be freely chirally transformed, $\nu \to \exp(i\theta\gamma_5)\nu$. Thus, higher-order corrections are forbidden from generating effective neutrino masses, be it at tree or at loop-level. However, the gauge symmetry of the SM allows for the addition of new field content leading to a Dirac mass term or an effective Majorana mass term. As of today, there is no experimental evidence favouring one type over the other. We now touch upon these two fundamentally different scenarios.

[14] Formally, we are speaking about a charged lepton flavour eigenstate. However, charged lepton coherence properties imply the equivalence of charged lepton flavour and mass eigenstates [207].

[15] For a thorough review, see *e.g.* [209]. A more up-to-date but compact review with recent fits of neutrino mixing parameters is presented in [210].

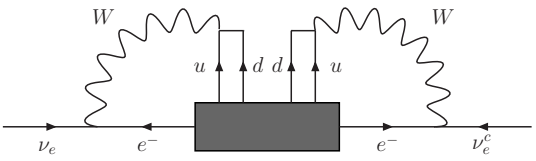

FIGURE 2.10: Schechter-Valle 'Black Box' operator contribution to the electron neutrino mass.

2.3.1.1 Dirac neutrinos

If neutrinos are Dirac particles, the SM is extended with a set of $n \geq 2$ right-handed singlets $N_k \neq N_k^c$ and the Yukawa interaction

$$\mathcal{L}_{Y^\nu} = -Y^\nu_{\ell k}\, \bar{L}_\ell\, \tilde{H}\, N_k + \text{h.c.}\,, \tag{2.72}$$

leading to Dirac neutrino masses $(m_\text{D})_{\ell k} = Y^\nu_{\ell k} \langle H^0 \rangle$ through the usual EWSB mechanism. On the one side, this simple extension is appealing because it restores the quark-lepton symmetry in the case $n = 3$ and contains a conserved lepton number $L = L_\nu + L_N$. Furthermore, neutrino oscillations are accounted for through the CKM-like rotation of weak eigenstates to mass eigenstates. On the other side, this scenario lacks a natural explanation for the extreme smallness of the entries of m_D, or equivalently for the question of why $|Y^\nu| \ll |Y^{\ell,u,d}|$. To generate Dirac neutrino masses of the order of 1 eV, we would require $Y^\nu \sim \mathcal{O}(10^{-11})$.

2.3.1.2 Majorana neutrinos

The other possibility is the generation of a Majorana mass for the light neutrinos, at tree- or loop-level. A Majorana mass mixes a field with its own charge-conjugate, which has opposite chirality. For the three light neutrinos, it has the form

$$\mathcal{L}_{m_\nu} = \frac{1}{2}(m_\nu)_{ij}\, \overline{\nu^c_{Li}}\, \nu_{Lj} + \text{h.c.}\,, \tag{2.73}$$

where $\nu^c_L = C\bar{\nu}^T_L$. In the LH lepton doublets L, a Majorana mass for the neutrinos is not permitted by the SM gauge group in the absence of triplet Higgs fields, hence the general need for new field content. For example, the addition of a Majorana mass term for a set of new fermionic self-conjugate singlets is a very attractive and popular option recurred to in neutrino mass model building, as it offers a natural explanation for why the active neutrinos are so light if the Majorana mass is sufficiently large and if there are no symmetries forbidding the mixing of doublet and singlet fields. This particular scenario of light neutrino mass generation at tree-level is the famous *seesaw mechanism* of type I [13]. Two other basic variants of tree-level seesaws exist: The type II seesaw [14] includes an additional scalar triplet and the type III [15, 16] features a fermionic triplet of $\text{SU}(2)_L$, all with masses large enough to push the light neutrino masses down to their tiny scale, conforming to the main idea of the seesaw mechanism. In addition to explaining neutrino masses, the seesaw models predict low-energy LFV processes such as the rare decays $\mu \to e\gamma$ or $\mu \to 3e$ and $\mu \to e$ flavour conversion in atomic nuclei [211]. A very natural scenario is achieved if the new physics mass scale lies far above the electroweak scale, $\Lambda_\text{EW} \sim v$. Typically, if the involved couplings are $\mathcal{O}(1)$, this scale turns out to be of the order of the GUT scale, $\Lambda_\text{GUT} \sim 10^{16}$ GeV. The lower the new physics scale, the closer it gets to a regime available at colliders and the easier it will be to observe LFV interactions. However, more parameter tuning is required to reproduce the low-energy parameters of the neutrino sector, unless some symmetry (*e.g.* lepton number) keeps the tuning reasonably small by controlling the renormalization group running [212]. In addition to the type-I, II and III seesaws, there also exist the inverse seesaw (ISS) [213] and the linear seesaw (LS) [214] mechanisms. All these tree-level neutrino mass realizations are described in Appendix C.

Proving the Majorana character of the active neutrinos experimentally is highly difficult. An ultimate smoking-gun signal indicating the Majorana character of the electron neutrino would be the observation of neutrinoless double beta decay ($0\nu\beta\beta$), as stated by the Schechter-Valle or the 'Black Box' theorem [215]. It states that whatever process mediates $0\nu\beta\beta$ also generates a Majorana mass for the electron neutrino at the four-loop-level through the diagram shown in Figure 2.10. Conversely, if neutrinos are not Majorana fermions, there cannot be neutrinoless double beta decay. The $0\nu\beta\beta$ decay amplitude is proportional to the 'effective Majorana neutrino mass' $m_{\beta\beta} = \sum_j (V_{\mathrm{PMNS}})_{ej} m_j$, where V_{PMNS} is the PMNS mixing matrix (*cf.* Section 2.3.2) and m_j is the mass of the jth neutrino mass eigenstate. $m_{\beta\beta}$ is equal to the electron-electron element of the neutrino mass matrix, m_{ee}, *i.e.* the only parameter violating electron flavour by two units. This provides a means of also probing the Majorana phases in V_{PMNS}, which neutrino oscillation experiments are not sensitive to, though thus far no excess over background events has been experimentally observed [216]. A recent review of $0\nu\beta\beta$ can be found in [217].

The type I seesaw mechanism is the prototype for a plethora of models where, through the presence of new heavy fields, small Majorana neutrino masses are generated. Like with the W boson in Fermi's theory, though maintaining gauge invariance and all other symmetries of the full theory (let us term the full symmetry group $\mathcal{G}$), the effects of such heavy fields can be described by $(d > 4)$-dimensional, *i.e.* so-called irrelevant operators added to the fundamental Lagrangian. This Lagrangian is most often renormalizable and thus contains only relevant ($d = 4$) and marginal ($d < 4$) operators. Irrelevant operators appear suppressed by powers $d - 4$ of the new physics scale Λ, usually of the order of the masses of the heavy particles. Amplitudes for higher-order processes happening at an energy scale E are thus suppressed by powers of E/Λ, hence the terminology: Irrelevant operators are negligible at energies that are very small compared to Λ, which however may change due to the breaking of some symmetry when the energy scale underruns some threshold. Following the general principle, all possible operators involving all fields from the fundamental theory allowed by $\mathcal{G}$ need to be added to the Lagrangian. In case the fundamental theory is renormalizable, all operators with dimension higher than 4 stem from the fundamental ($d \leq 4$)-dimensional interactions; the coefficients then need to be evaluated to all orders in perturbation theory and grouped with the corresponding counterterms, in order for the theory to remain unaltered when rewriting the Lagrangian in this non-renormalizable fashion. An infinite number of counterterms is needed because non-renormalizability stems from the impossibility to impose a finite number of renormalization conditions that are valid at all orders in perturbation theory, implying the need for an infinite number of experimental observables. The additional Lagrangian then has the form

$$\delta\mathcal{L} = \delta\mathcal{L}^{(d=5)} + \delta\mathcal{L}^{(d=6)} + \ldots = \sum_{d=5}^{\infty} \frac{\kappa^{(d)}}{\Lambda^{d-4}} \mathcal{O}_d + \sum_{d=5}^{\infty} \delta\mathcal{L}^{(d)}_{\mathrm{c.t.}} \,, \tag{2.74}$$

where $\mathcal{O}_d$ are products of field operators, $\kappa^{(d)} \sim \mathcal{O}(1)$ are effective couplings (Wilson coefficients) and $\delta\mathcal{L}^{(d)}_{\mathrm{c.t.}}$ are the counterterm Lagrangians. In practice, one often adds to a renormalizable Lagrangian containing light SM fields the irrelevant operators invariant under $\mathcal{G}$ suited for the higher-order interactions among SM particles mediated by the heavy particles that are to be studied until the desired order of suppression, such as multipole moments and higher-order scattering processes. When working with such a limited truncated Lagrangian, one lies within the regime of an effective field theory (EFT). Whereas a renormalizable Lagrangian that also includes the heavy degrees of freedom may 'know about' all these processes at any order in perturbation theory, the effective Lagrangian contains them in the form of irrelevant operators. The underlying microscopic interactions formed by strings of tree-level or by loop processes are encoded in the corresponding Wilson coefficients. When working consistently to a specific power in E/Λ, the number of counterterms and hence predictions for observables will be finite.

We now focus on the particular case in which effective Majorana mass terms for the active neutrinos are generated through the presence of new heavy fields when the electroweak symmetry is broken, $H^{(0)} \to \langle H^{(0)} \rangle = v/\sqrt{2}$. If the post-EWSB Lagrangian knows about neutrino masses, the pre-EWSB theory needs to have them encoded as well. It turns out that, at dimension $d = 5$, the SM field content does only allow for one operator leading to a Majorana neutrino mass, the so-called Weinberg operator [218]. Schematically,

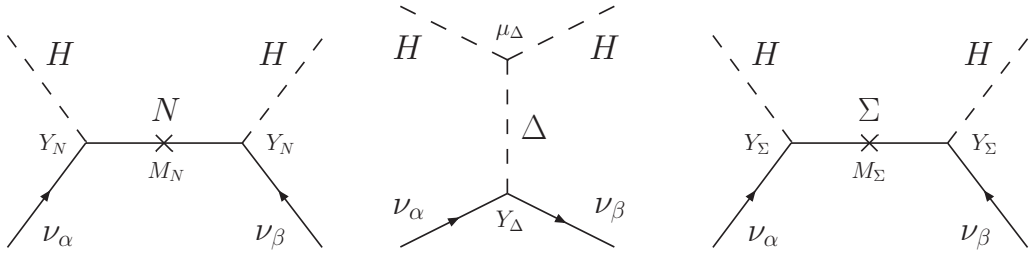

FIGURE 2.11: The three tree-level seesaw realizations. *Left panel:* Type I (RH singlet fermion N with $Y_N = 0$). *Middle panel:* Type II (scalar triplet Δ with $Y_\Delta = -2$). *Right panel:* Type III (RH triplet fermion Σ with $Y_\Sigma = 0$).

one writes it $LLHH$. Three possibilities to express it explicitly are[16]

$$\mathcal{O}_5^{(\mathrm{I})} = \kappa_{ij}(\bar{L}_i\,\tilde{H})(H^\dagger\,\tilde{L}_j) + \mathrm{h.c.}\,, \tag{2.75a}$$

$$\mathcal{O}_5^{(\mathrm{II})} = \frac{1}{2}\kappa_{ij}(\bar{L}_i\,\vec{\tau}_\mathrm{C}\,\tilde{L}_j)\cdot(H^\dagger\,\vec{\tau}_\mathrm{C}\,\tilde{H}) + \mathrm{h.c.}\,, \tag{2.75b}$$

$$\mathcal{O}_5^{(\mathrm{III})} = -\frac{1}{2}\kappa_{ij}(\bar{L}_i\,\vec{\tau}_\mathrm{C}\,\tilde{H}_j)\cdot(H^\dagger\,\vec{\tau}_\mathrm{C}\,\tilde{L}) + \mathrm{h.c.}\,. \tag{2.75c}$$

All three expressions are exactly the same. For example, the equality of $\mathcal{O}_5^{(\mathrm{I})}$ and $\mathcal{O}_5^{(\mathrm{II})}$ can be checked using the identity $(\psi^T\,\vec{\sigma}\,\epsilon\chi)\cdot(H^T\,\vec{\sigma}\,\epsilon H) = 2(\psi^T\,\epsilon H)(H^T\,\epsilon\chi)$ for arbitrary 2-vectors H, ψ, χ. Writing

$$\kappa(\bar{L}\,\tilde{H})(H^\dagger\,\tilde{L}) = \kappa\bar{L}\,(\tilde{H}\otimes H^\dagger)\,\tilde{L} = \kappa\bar{L}\begin{bmatrix} H^0H^- & H^{0\dagger}H^{0\dagger} \\ -H^-H^- & -H^-H^{0\dagger}\end{bmatrix}\tilde{L} \xrightarrow{\text{EWSB}} -\frac{\kappa v^2}{2}\bar{\nu}_L\nu_L^c + \ldots\,, \tag{2.76}$$

we see that the neutrino masses will be of the order of $\kappa v^2/\Lambda$. Notice that the operator in the mass term is of dimension 3, hence we have added a *relevant* effective operator to the broken SM sector. We mentioned above that such an occurrence is possible when symmetries get broken. However, the mass term can only appear in conjunction with the irrelevant operators describing higher-order scatterings implied in the ellipses in Equation 2.76, to ensure gauge invariance. We can thus build an effective renormalizable theory with Majorana neutrino masses added to the post-EWSB Lagrangian invariant under $\mathrm{U}(1)_\mathrm{EM}$, provided we add additional interactions at the order $1/\Lambda$ and equal-order counterterms, including $-\frac{1}{2}\delta_{m_\nu}\overline{\nu^c}\nu$.

Motivation exists for effective models where the Majorana mass is only generated by $d > 5$-dimensional operators, due to the high amount of possible realizations at high-energy. Lepton number violating interactions are highly suppressed in such models in a very natural way, by the presence of heavy mediators and/or the impossibility of such processes at tree-level. These operators are systematically categorized and discussed in Reference [219].

□ Effective Majorana mass generation at tree-level

At tree-level, there are only three UV-complete Lagrangians with one representation in addition to the SM fields able to generate $\mathcal{O}_5$, namely the three basic seesaw models [15]. The type I seesaw introduces $n \geq 2$ RH fermionic singlets N_k of hypercharge $Y(N) = 0$ and mass scale M_N. Type II is fundamentally different: It introduces a scalar triplet Δ of mass scale M_Δ with $Y(\Delta) = 2$ which acquires a VEV v_Δ, *i.e.* it is a particular extension of the Higgs triplet model [220] with a lepton number violating parameter μ_Δ present in the scalar potential. Finally, type III adds a RH fermionic triplet Σ of mass scale M_Σ with $Y(\Sigma) = 0$, where it so happens that the light neutrinos gain their masses like in the type I model. The respective diagrams of the high-energy processes realizing the effective Weinberg operator are shown in Figure 2.11, where we also indicate the involved model-specific couplings. Note the suggestive naming of the Weinberg operator in Equations 2.75a-2.75c: Each operator can be obtained by substituting the new

[16] Another possibility is $(\bar{L}L)(H^\dagger H)$, but this is not equivalent to expressions (2.75a)-(2.75c) and, in particular, does not result in a term containing a Majorana neutrino mass.

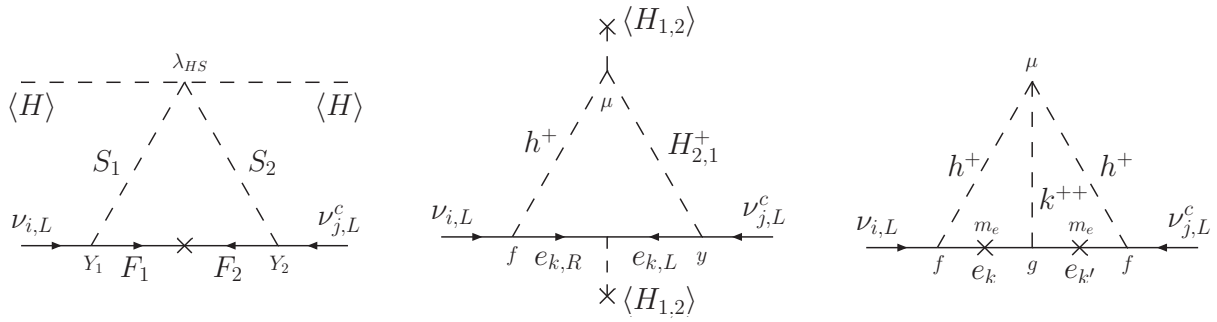

FIGURE 2.12: The three tree-level seesaw realizations. *Left panel:* Diagram T3, which appears, for example, in the scotogenic model [40]. We use the generic notation of [227] for the inserted fields. Note that F_1 is right-chiral and F_2 is left-chiral. *Middle panel:* Diagram contributing to neutrino mass in the Zee model [223] (T1-ii). *Right panel:* Diagram contributing to neutrino mass in the Zee-Babu model [228].

field representation in the renormalizable Lagrangian (*cf.* Appendix C) by an equivalent representation formed with L and/or H, with an additional mass dimension. The effective light Majorana neutrino mass matrices in each scenario are, respectively,

$$m_\nu^{(\mathrm{I})} \simeq -\frac{1}{2}\, Y_N\, M_N^{-1}\, Y_N^T\, v^2\,, \tag{2.77a}$$

$$m_\nu^{(\mathrm{II})} \simeq Y_\Delta\, \mu_\Delta\, v^2/M_\Delta^2\,, \tag{2.77b}$$

$$m_\nu^{(\mathrm{III})} \simeq -\frac{1}{2}\, Y_\Sigma\, M_\Sigma^{-1}\, Y_\Sigma^T\, v^2\,, \tag{2.77c}$$

as shown in Appendix C. These are the lowest-order expressions; for type I/III, it is possible to write m_ν up to an arbitrary order in the inverse seesaw scale, see [221]. While these models represent minimal SM extensions, one can work out a large number of combinations. For instance, in models with left-right gauge symmetry at some high energy scale with additional RH neutrino singlets, the parity breaking electroweak vacuum is obtained through the VEV of two scalar triplets $\Delta_{L,R}$ having Majorana Yukawa terms with the LH and RH neutrinos, respectively [222]. Breaking to the SM gauge group then results in a Majorana mass term for the active neutrinos formed by a sum of type I and type II contributions, Equations 2.77a and 2.77b.

□ Effective Majorana mass generation at loop-level

Progressing to loop order, plenty ways of generating $\mathcal{O}_5$ are available. Historically, the first radiative neutrino mass model is the Zee model from 1980 [223], a two-Higgs doublet model (2HDM) [224] with an additional charged scalar $\mathrm{SU}(2)_L$ singlet h^+. Lepton number is violated through a combination of an antisymmetric L-L-h^+ Yukawa coupling f, a L-e-$H_{1,2}$ Yukawa coupling y and a cubic H_1-H_2-h^+ scalar coupling μ, which provides Majorana neutrino masses generated at the one-loop-level, as depicted in the middle panel of Figure 2.12. Its motivation lies in the fact that it leads to neutrino mixing patterns that may explain solar and atmospheric neutrino data. In its minimal version [225], it is restricted to a type III 2HDM, in order to suppress Higgs-mediated FCNC, however it has been ruled out some time ago as it fails to reproduce observed mixing data in the atmospheric and solar neutrino sector by predicting maximal mixing [226].

Discussing radiative neutrino masses at two-loop order or higher is beyond our scope. The motivation to go to higher loop orders is to accommodate small neutrino masses with sizeable couplings and loop particle masses low enough to be tested in collider and low-energy experiments. We refer to the classification of two-loop models in [229] and to [230] for a summary of several models with one-, two- and three-loop Majorana neutrino mass generation, as well as one-loop scenarios with Dirac neutrino mass generation. Instead, we only mention the historically important case of the Zee-Babu model [228]. Like the original

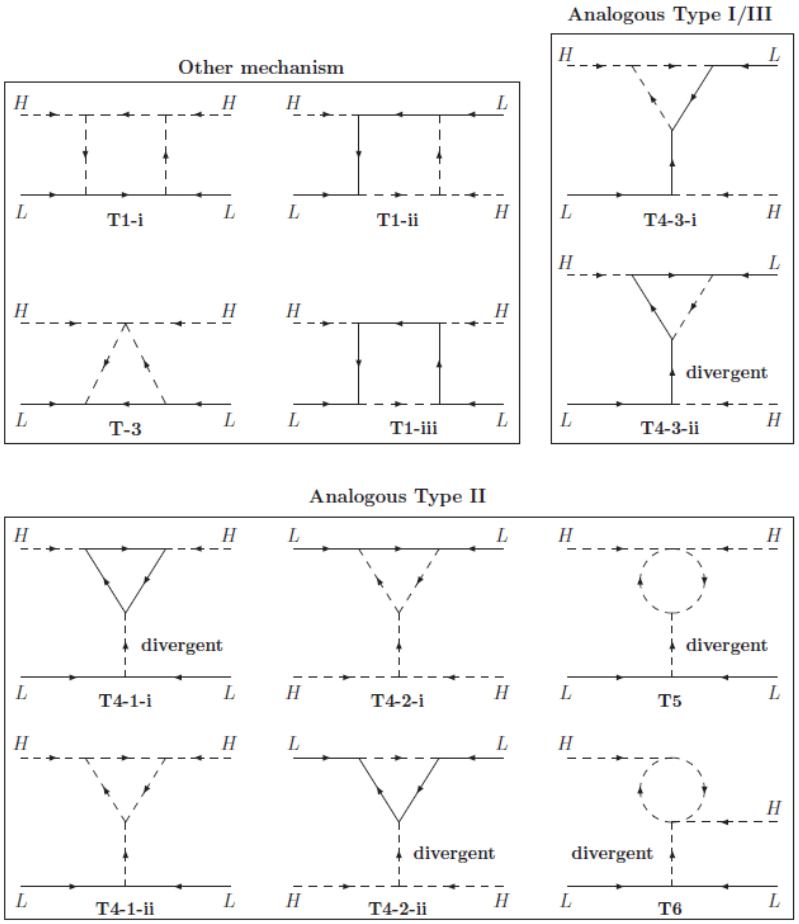

FIGURE 2.13: Lorentz structures for the one-loop topologies leading to an effective Majorana neutrino mass after EWSB through the Weinberg operator. The figure is taken from [232]. Diagram T1-ii is the Zee model [223], *cf.* Figure 2.12, middle panel. It is also indicated if a diagram is divergent, in which case a counterterm is required.

Zee model, it contains a singly-charged scalar h^+, but rather than another scalar doublet, it additionally comprises a doubly-charged singlet k^{++} of the electroweak gauge group. The Feynman diagram is shown in Figure 2.12 on the right. Updated constraints on the model have been worked out in [231], limiting the new scalars to be too heavy to be produced at the LHC with a high statistical significance.

A special role in this thesis is played by the scotogenic model [40], thus we are interested in placing it in the landscape of radiative one-loop neutrino mass scenarios that are genuine, *i.e.* without a tree-level contribution to m_ν. All one-loop realizations of $\mathcal{O}_5$ are systematically listed in [232], including all models comprising additional representations up until the adjoint of $\mathrm{SU}(2)_L$. The important subset of radiative neutrino mass models containing viable DM candidates is studied in [233] and a detailed study of all models where neutrino mass stems from a diagram with the same topology as in the scotogenic model (Figure 2.12, left panel) can be found in [227]. This topology is examined in detail below. We now intend to briefly summarize the results of [232].

First, the $LLHH$ diagrams are grouped into five one-loop $2 \to 2$ topologies without self-energies, T1, T3, T4, T5, T6, see Figure 2 in [232]. A sixth topology, T2, does not lead to neutrino masses, explaining its absence in the numbering. After the possible Lorentz structure insertions with quantum number assignments in accord with the electroweak gauge group,[17] the diagrams are grouped according to whether they can be regarded as loop realizations of the tree-level seesaws or whether radiative neutrino mass generation occurs differently, as sketched in Figure 2.13. Diagrams T4-3-i and T4-3-ii are cases

[17] Coloured fields are possible, but assignments are trivially fixed, since the external fields are colour singlets.

yielding one-loop realizations of the Yukawa couplings Y_N and Y_Σ of the type I/III seesaws, whereas the remaining T4 diagrams and T5 and T6 are realizations of or contributions to the couplings Y_Δ and μ_Δ of the type II. One observes that the topologies T3, T5 and T6 are unique, whereas T1 and T4 may accomodate various field type insertions. In several cases, the field content of the models contains representations mediating the tree-level realization of $\mathcal{O}_5$ in addition to the one-loop realization. For T1 and T3, these can always be forbidden by introducing a $\mathbb{Z}_2$ symmetry on the new fermions, a specific case being T3 with a fermionic singlet, *i.e.* the scotogenic scenario (in Reference [233], the scotogenic model is model T3-B). The authors further investigate two questions: (1) Under what conditions does one obtain a genuine one-loop seesaw from the finite seesaw-like diagrams, *i.e.* from T4-1-ii, T4-2-i and T4-3-i, without tree-level contributions? (2) Can loop corrections lead to an inverse and/or a linear seesaw scenario, in which LNV is naturally small, not due to a symmetry but due to the loop suppression, with the new physics scale being reachable at colliders? As for question (1), the focus is on the finite diagrams because it can be shown that the divergent cases are all corrections to the tree-level seesaws containing appropriate counterterms for divergence absorption. For example, diagram T4-1-i is a correction of the type II parameter μ_Δ. All finite diagrams are revealed to contain a generally dominant tree-level contribution that cannot be forbidden by only imposing an additional U(1) or $\mathbb{Z}_2$ symmetry. One rather needs to further require the possibility of lepton number assignments such that all new couplings be lepton number conserving and that fermions running in the loop be Majorana particles and therefore the only source of LNV for these lepton numbers (prohibiting this option for T4-1-ii, which thus necessarily contains a tree-level neutrino mass). An example is the model studied in [234]. The answer to question (2) is affirmative. For instance, diagram T4-3-i allows for a radiative linear seesaw model with the LS particle content, where the *S-H-L* coupling (*cf.* Equation C.80) is a loop vertex that can be suppressed not only by the loop factor, but also by the heavy particles within the loop, thus explaining the smallness of $Y_\nu \sim \epsilon$ (*cf.* Section C.4). In the same manner, a self-energy diagram with heavy particles in the loop can lead to a radiative inverse seesaw scenario.

Notice from the discussions of tree- and loop-level neutrino mass generation that the effective masses always vanish when any parameter of the lepton number violating sector is put to zero. This would increase the symmetry of the theory because a conserved additive lepton number could then be defined. Therefore, these parameters need to be self-renormalized and no neutrino masses could be generated radiatively if one of them was zero [212].

□ The T3 topology

We deem it important to pause and zoom in on the 1-loop topology for radiative neutrino masses inherent to the scotogenic model, *i.e.* T3 (shown in the left panel of Figure 2.12). It was thoroughly discussed by Ma in [15] and by Law and McDonald in [227]. Ma's treatment is generic and doesn't touch upon a possible connection between neutrino masses and DM, whereas the second reference dwells on particular T3 realizations containing new representations with neutral components rendered stable by a $\mathbb{Z}_2$ symmetry imposed on the new particle sector. Here we study realizations involving fermionic Majorana and Dirac multiplets and, as an exercise, derive the expression for the radiatively generated masses.

Main focus in [227] is put on representations no larger than the adjoint of the electroweak gauge group, though it is shown that higher-dimensional representations may also be suitable extensions. Majorana masses for the active neutrinos violate lepton number, hence the loop diagram either requires a Majorana mass insertion involving F_1 and F_2 or a Dirac mass insertion together with one lepton number violating vertex. This statement presupposes that one opts for assigning the same lepton number to the new fermions as to the charged leptons in the SM and a lepton number of zero to the new scalars.[18] The two possibilities

[18] Alternatively, one could assign a lepton number of zero to the fermion. Then lepton number is broken by λ_{HS} in the Majorana and Dirac case. Moreover, if F is a Dirac particle, $L(F) = -1$ or different lepton numbers for F_L and F_R are also a viable choices leading to $\Delta L = 2$. What matters is that lepton number in neutrino mass generation is always violated by the combination of several Lagrangian terms.

are implemented with the $\mathbb{Z}_2$-symmetric Lagrangian terms

$$\mathcal{L}_{\mathrm{M}} \supset -\frac{M_F}{2}\overline{F_R^c}F_R - Y\bar{L}\tilde{S}F_R - \lambda_{HS}(S^\dagger H)^2 + \text{h.c.}\,, \tag{2.78a}$$

$$\mathcal{L}_{\mathrm{D}} \supset -M_F\bar{F}F - Y_1\bar{L}F_R S_1 - Y_2\bar{L}F_L^c\tilde{S}_2 - \lambda_{HS}S_1\tilde{S}_2H^2 + \text{h.c.}\,. \tag{2.78b}$$

In the first scenario, $F_1 = F_R$ and $F_2 = F_R^c$, hence $Y(F) = 0$. The $\mathrm{SU}(2)_L$ quantum number of F must be odd, in order to exclude factionally charged stable fermions; this constraint also ensures the existence of a fermionic neutral particle. With the restriction to $R^{\max}_{F,S_1,S_2} = 3$, the minimal versions are for $S_1 = S_2 \equiv S$, which are Ma's original 'scotogenic' model with $F \sim (1,1,0)$ and $S \sim (1,2,1)$, and the dark triplet case $F \sim (1,3,0)$, proposed by Ma and Suematsu [235]. The quantum number assignments are such that the scalar and the fermionic multiplets in both models contain a neutral component. Dark matter candidates are furnished in the form of the lightest of these. As pointed out in [227], the scotogenic model has difficulty in providing thermal fermionic DM because interactions with the SM sector take place exclusively via the Yukawa coupling, though this coupling must be small in order to suppress LFV effects, whereas the triplet achieves equilibrium via gauge interactions. However, it was later suggested that the lightest RHN can reach the observed DM relic abundance through the freeze-in mechanism [42], *i.e.* the DM particle can be a FIMP. The second part of this thesis is based on this hypothesis.

If the new fermions are of Dirac type ($F_1 = F_R$, $F_2 = F_L \neq F_R^c$, $Y(F_{L,R}) \neq 0$), then LNV has its origin in the Yukawa coupling Y_2 according to our assignments. F must be a vectorlike fermion for chiral anomaly cancellation and the two scalars must be different representations, *i.e.* gauge invariance demands $Y(S_1) = -Y(F) - 1$ and $Y(S_2) = Y(S_1) + 2$. If one again restricts the $\mathrm{SU}(2)_L$ quantum number to $R^{\max}_{F,S_1,S_2} = 3$ and demands the existence of neutral particles, seven minimal models with a Dirac mass insertion surge as possibilities. We do not list them here, as they are thoroughly treated in the main reference. However, it is worth mentioning that none of the models containing neutral fermions has fermionic multiplets with non-vanishing hypercharge. Remaining at tree-level, this immediately leads to tension with direct detection experiments such as XENON100 (see Section 2.2.2.3), but at the one-loop-level, the neutral components of F_L and F_R are each split into quasi-degenerate pseudo-Dirac pairs by the tiny Majorana mass insertion m_ν when the electroweak symmetry is broken. Thus, the T3 topology is responsible for neutrino masses and the mass splitting of $F^{(0)}_{L,R}$ in this scenario. Would the splitting be larger than the average kinetic energy locally expected for DM particles, then interactions with nuclei in direct detection experiments would be strongly suppressed, however, for $M_F \sim \mathcal{O}(\mathrm{TeV})$, this is not the case. Hence, fermionic DM with a Dirac mass insertion in this minimal scenario is ruled out and one is left with inert scalar DM models where $M_F > m_{S_{1,2}}$. Most of these models with $R^{\max}_{S_1,S_2} = 3$ are very well known, most of them being constrained to contain too heavy scalar states to be observed at the LHC.

After EWSB, the theories described by the Lagrangians in Equations 2.78a and 2.78b predict self-energies for the left-handed neutrinos, which are massless at tree-level. Let us consider the example of two models with a Dirac mass insertion, models A and B in [227]. Both feature the scalar doublets $S_1 \sim (1,2,1)$, $S_2 \sim (1,2,3)$, while being distinguished by the $\mathrm{SU}(2)_L$ quantum numbers of the dark fermions, $F_A \sim (1,1,-2)$, $F_B \sim (1,3,-2)$. The relevant Lagrangians read

$$-\mathcal{L}_A \supset M_F\,\bar{F}_L F_R + Y_1\,\bar{L}F_R S_1 + Y_2\,\bar{L}F_L^c\tilde{S}_2 + \text{h.c.} + \mathcal{V}(H,S_1,S_2)\,, \tag{2.79a}$$

$$-\mathcal{L}_B \supset M_F\,\bar{F}_L F_R + Y_1\,\bar{L}(\vec{F}_R\cdot\vec{\tau})S_1 + Y_2\,\bar{L}(\vec{F}_L^c\cdot\vec{\tau})\tilde{S}_2 + \text{h.c.} + \mathcal{V}(H,S_1,S_2)\,, \tag{2.79b}$$

with the potential terms

$$\mathcal{V}(H,S_1,S_2) \supset \sum_{i=1,2}\left[\mu_i^2\,S_i^\dagger S_i + \lambda_{HS_i}(H^\dagger H)(S_i^\dagger S_i)\right] + \lambda_{HS}[(H\,\epsilon S_1)(H\,\epsilon\tilde{S}_2) + \text{h.c.}]\,. \tag{2.80}$$

Ignoring the summation over generations, the self-energy in each model at lowest order is given by the sum of two diagrams with singly-charged particles running in the loops, what might seem unexpected for model B. While both models feature two (non-degenerate) singly-charged scalar mass eigenstates and scalars of charge 0 and 2, model A has one singly-charged fermion and model B contains three fermions of charge 0, 1 and 2. However, it is straightforward to check that only the singly-charged fermion and

the singly-charged scalar mass eigenstates will be coupled through both Y_1 *and* Y_2, therefore there is no self-energy with neutral or doubly-charged particles within the loop. The renormalized self-energy[19] $\bar{\Sigma}(p)$ then provides effective light neutrino masses, also leading to the generation of a mass counterterm. To see how this comes about, consider the resummed Fourier-transformed interacting active neutrino propagator in the flavour basis,

$$\bar{S}_{ij}(p) = Z_{\nu_i}^{-1/2} Z_{\nu_j}^{-1/2} \mathcal{F} \langle\Omega| T\{\nu_i(x)\, \bar{\nu}_j(0)\} |\Omega\rangle = \frac{i}{\not{p}\, \delta_{ij} - \bar{\Sigma}(p)_{ij}} \,. \tag{2.81}$$

where $\bar{\Sigma}(p)$ is the renormalized self-energy. For the transition $f_i \to f_j$ between two Majorana fermions of flavours i and j, the most general unrenormalized transition amplitude $\Sigma(p)$ can be split into a scalar part and a component proportional to $\not{p}$ [236–239],

$$\Sigma_{ij}(p) = [A_{ij}^L(p) + B_{ij}^L(p)\not{p}]P_L + [A_{ij}^R(p) + B_{ij}^R(p)\not{p}]P_R \,, \tag{2.82}$$

due to Lorentz covariance. Hermiticity and the Majorana property enforce the following conditions on the functions A and B:

$$A^{L,R} = \left(A^{L,R}\right)^T \,, \qquad B^{L,R} = \left(B^{R,L}\right)^* \,. \tag{2.83}$$

Field strength renormalizations are found by imposing the on-shell renormalization conditions first proposed by Aoki et al. [236], meaning the convention that the renormalized propagator, with residue set to unity, becomes mass-diagonal and singular when asymptotic fields go on-shell, such that external leg corrections vanish. The poles in the two-point function follow from the LSZ theorem (see *e.g.* [77]). For the decomposition in Equation 2.82, these are given in [238] for Dirac and Majorana fermions existing in a theory of flavour. For models with radiative neutrino masses originating from the T3 topology, such as models A and B, only A^R is required, as the external neutrinos couple to the loop interactions with a P_R projector, see the left panel of Figure 2.12. It turns out that the absence of a bare neutrino mass term leads to

$$\bar{A}^R = A^R \,, \tag{2.84}$$

therefore A^R has to be finite. By inspecting the underlying high-energy diagram, this is readily evident through power counting. The mass matrix is taken to be the non-absorptive part of the self-energy at vanishing momentum, since the massive theory is effective and not valid at energies comparable to the particles propagating in the loops, *i.e.*

$$\mathcal{M}_\nu = U^* \mathrm{Re}\{\hat{A}^R(0)\}\, U^\dagger = U^* \mathrm{Re}\{P_R\, \hat{\Sigma}(0) P_R\}\, U^\dagger \,, \tag{2.85}$$

the hat meaning that the matrix is mass-diagonal and U is the unitary matrix rotating the neutrino flavour eigenstates to mass eigenstates, *cf.* Section 2.3.2. Now, the CP-even and CP-odd singly-charged mass eigenstates are obtained with the same transformation of the singly-charged flavour eigenstates,

$$\begin{bmatrix} S_{\mathrm{r}1}^+ \\ S_{\mathrm{r}2}^+ \end{bmatrix} = O(\theta) \begin{bmatrix} \mathrm{Re}S_1^+ \\ \mathrm{Re}S_2^+ \end{bmatrix} \,, \quad \begin{bmatrix} S_{\mathrm{i}1}^+ \\ S_{\mathrm{i}2}^+ \end{bmatrix} = O(\theta) \begin{bmatrix} \mathrm{Im}S_1^+ \\ \mathrm{Im}S_2^+ \end{bmatrix} \,. \tag{2.86}$$

$O(\theta)$ is the orthogonal matrix diagonalizing the mass matrix of $S_1^{(+)}$ and $S_2^{(+)}$, leading to an equal mass for $S_{\mathrm{r}1}^+$ and $S_{\mathrm{i}1}^+$ and for $S_{\mathrm{r}2}^+$ and $S_{\mathrm{i}2}^+$. We term them $m_{>,<}$, $>$ ($<$) denoting the larger (smaller) one. The masses are given by expressions that depend on $\mu_{1,2}^2$, λ_{HS_1,HS_2}, λ_{HS} and the Higgs VEV; it can be easily checked that the squared-mass difference amounts to

$$m_>^2 - m_<^2 = \frac{1}{4}\sqrt{[2(\mu_1^2 - \mu_2^2) + (\lambda_{HS_1} - \lambda_{HS_2})v^2]^2 + \lambda_{HS}^2 v^4} \,. \tag{2.87}$$

The relative factor of i between the real and imaginary parts of the CP-even and CP-odd fields is crucial, for it leads to a relative minus sign between the contributions of scalars with different masses to the neutrino self-energy, resulting in the cancellation of the occurring UV divergences. Working in a basis where M_F is

[19] Overlines indicate renormalized quantities, however in Equation 2.81, $\bar{\nu}$ is the Dirac adjoint of the bare ν field.

diagonal, we then have at one-loop-level

$$-i\Sigma^{[2]}(p)_{ij} = 2\,c\,\cos\theta\sin\theta\,(-iY_1)_{ik}(-iY_2)_{jk} \times \int \frac{d^4\ell}{(2\pi)^4}\frac{i(\not{\ell}+M_k)}{\ell^2-M_k^2}\left(\frac{i}{(p-\ell)^2-m_>^2+i\epsilon}-\frac{i}{(p-\ell)^2-m_<^2+i\epsilon}\right), \tag{2.88}$$

where M_k is the mass of the fermionic mass eigenstate F_k and the superscript [2] signifies that the evaluation is performed to second order in the Yukawa couplings. The constant c equals 1 in model A and 1/2 in model B due to the factors of $1/\sqrt{2}$ present in the Yukawa terms involving the singly-charged fermions in the spherical basis (*cf.* Appendix C). Therefore the resulting neutrino mass matrix is

$$(\mathcal{M}_\nu^{[2]})_{ij} = \Sigma_{ij}^{[2]}(0) = 2\,i\,c\,\cos\theta\sin\theta\,(Y_1)_{ik}(Y_2)_{jk}\,M_k\,I_k(m_>^2, m_<^2, M_k^2)\,. \tag{2.89}$$

It is practical to express the loop integrals contained in I_k in terms of the Passarino-Veltman 2-point function B_0 (see Appendix D),

$$\begin{aligned} I_k &\equiv \int \frac{d^4\ell}{(2\pi)^4}\frac{1}{\ell^2-M_k^2}\left(\frac{1}{\ell^2-m_>^2+i\epsilon}-\frac{1}{\ell^2-m_<^2+i\epsilon}\right) \\ &= \frac{i}{(4\pi)^2}\left[B_0(0,m_>^2,M_k^2)-B_0(0,m_<^2,M_k^2)\right] \\ &= \frac{i}{(4\pi)^2}\left[\frac{m_>^2}{M_k^2-m_>^2}\ln\frac{m_>^2}{M_k^2}-\frac{m_<^2}{M_k^2-m_<^2}\ln\frac{m_<^2}{M_k^2}\right], \end{aligned} \tag{2.90}$$

using Equation D.28. Notice how the subtraction of both contributions results in the cancellation of the infinite Δ_ϵ terms, thus $\mathcal{M}_\nu$ is finite, as expected. Moreover, neutrino masses vanish in the limit $\lambda_{HS}\to 0$, since $\theta\propto\lambda_{HS}$, as is necessary because this parameter contributes to LNV. Finally, consider the Majorana case with a single additional doublet of hypercharge $Y=+1$. The λ_{HS} term then changes to the λ_5 interaction of the scotogenic model and the effective neutrino masses one finds are, at LO,

$$(\mathcal{M}_\nu^{[2]})_{ij} = i\,(Y_1)_{ik}(Y_2)_{jk}\,M_k\,I_k(m_>^2, m_<^2, M_k^2)\,, \tag{2.91}$$

with the same function I_k. This mass term can be conveniently simplified in the small λ_5 limit [40], see also Section 2.4.1.

2.3.2 Neutrino oscillations

Neutrinos are known to oscillate, *i.e.* their flavours are interconverted during propagation due to quantum superposition of mass and flavour eigenstates. Hard evidence first came from the SuperKamiokande and SNO experiments in 1998 and 2001 [240, 241]. This phenomenon, in conjunction with the MSW effect describing the propagation of neutrinos through matter [242], finally sealed the solar neutrino problem: Since the Homestake experiment in 1968 [9], it was an open question why fluxes of solar electron neutrinos were significantly smaller than expected according to the standard solar model when one doesn't account for ν_e disappearance. This section treats, in a nutshell, the basics of neutrino oscillation theory and presents a recent fit of the relevant set of parameters. We shall use the usual plane wave picture, although a correct quantum mechanical formulation requires the language of wave packets [243].

We assume there are n sterile right-handed neutrinos ν_{Ri} in addition to the SM field content. Then, upon re-expressing the neutrino and charged lepton fields in terms of their mass eigenstates,[20]

$$\begin{bmatrix}\nu'_L\\ \nu_R\end{bmatrix} = U_{\nu N}\begin{bmatrix}\nu_L\\ N_R\end{bmatrix} = \begin{bmatrix}K & G\\ S & T\end{bmatrix}\begin{bmatrix}\nu_L\\ N_R\end{bmatrix}, \qquad \ell'_L = U_L^\ell\,\ell_L\,, \tag{2.92}$$

with the dimensions of K, G, S and T being, respectively, 3×3, $3\times n$, $n\times 3$ and $n\times n$ [244], the charged

[20] In this section, we opt for the same notation as in Section C.2, denoting charged lepton and active neutrino flavour eigenstates by a prime, ℓ', ν'_L.

current interaction in the lepton sector becomes

$$\mathcal{L}_\ell^{\rm cc} = -\frac{g}{\sqrt{2}}\overline{\ell'_L}\,\not{W}^-\nu'_{L\ell} + \text{h.c.} \quad\longrightarrow\quad -\frac{g}{\sqrt{2}}\bar{\ell}_L\,\not{W}^- V_{\rm cc}^{\rm mix}\begin{bmatrix}\nu_L\\ N_L\end{bmatrix} \tag{2.93}$$

$$= -\frac{g}{\sqrt{2}}\bar{\ell}_L\,\not{W}^-\left[(V_{\rm PMNS})_{\ell i}\nu_{Li} + (U_L^{\ell\dagger}G)_{\ell j}N_{Lj} + \text{h.c.}\right]. \tag{2.94}$$

Mixing in the leptonic charged current occurs through the $3\times(3+n)$-dimensional matrix

$$V_{\rm cc}^{\rm mix} = \left[U_L^{\ell\dagger}K \;\; U_L^{\ell\dagger}G\right], \qquad V_{\rm cc}^{\rm mix}V_{\rm cc}^{\rm mix\dagger} = \mathbf{1}_3\,, \quad V_{\rm cc}^{\rm mix\dagger}V_{\rm cc}^{\rm mix} \neq \mathbf{1}_{3+n}\,, \tag{2.95}$$

U_L^ℓ being the matrix that diagonalizes the charged lepton mass matrix by rotating the left-handed weak eigenstates ℓ' into the mass eigenstates ℓ, $U_L^{\ell\dagger}\,m_\ell\,m_\ell^\dagger\,U_L^\ell = \text{diag}(m_e^2, m_\mu^2, m_\tau^2)$. The matrix

$$V_{\rm PMNS} \equiv U_L^{\ell\dagger}K = \begin{bmatrix} V_{e1} & V_{e2} & V_{e3}\\ V_{\mu1} & V_{\mu2} & V_{\mu3}\\ V_{\tau1} & V_{\tau2} & V_{\tau3}\end{bmatrix} \tag{2.96}$$

is known as the Pontecorvo-Maki-Nakagawa-Sakata (PMNS) matrix and parametrizes the mixing in the ℓ-ν gauge interactions [245]. Since charged leptons are not seen to exhibit oscillations (and are very unlikely to due to coherence properties of flavour eigenstate superpositions [207]), it is common to set the natural basis to $U_L^\ell = \mathbf{1}$, $V_{\rm PMNS} = K$. $V_{\rm PMNS}$ is a (3×3)-dimensional submatrix acting within the ν-ℓ gauge interactions and is unitary in the case of Dirac neutrinos, since then $G = S = \mathbf{0}$; for Majorana neutrinos, K introduces a minor deviation from unitarity, as is explicitly shown for the type I and III seesaw models in Appendix C. However, unitarity in the $\nu-\ell$ interactions has been established at the percent level and therefore provides a strong constraint in neutrino model building [246, 247].

Working now in the limit of exact or acceptable unitarity, the PMNS matrix can be decomposed in terms of three Euler angles and three CP-violating phases. For both $V_{\rm CKM}$ and $V_{\rm PMNS}$ one commonly adopts the Chau-Keung parametrization [248],

$$V_{\rm PMNS} = K_{123}\,O_{23}\,K_3(\delta_{\rm CP})\,O_{13}\,K_3^*(\delta_{\rm CP})\,O_{12}\,K_{12}(\phi_1,\phi_2)\,. \tag{2.97}$$

O_{ij} are 3-dimensional orthogonal rotation matrices with Euler angles θ_{ij} and $K_{i\ldots}$ are unitary diagonal matrices with non-zero phases contained in the positions of the main diagonal specified in the indices. The leftmost phase matrix can be absorbed by redefining the charged lepton fields, whereas the rightmost one can only be absorbed by Dirac neutrino fields, analogously to the procedure with $V_{\rm CKM}$. In the Majorana case, these so-called *Majorana phases* $\phi_{1,2}$ are physical and contribute to CP violation in the leptonic sector. Keeping the Majorana phases, the PMNS matrix reads explicitly

$$V_{\rm PMNS} = \begin{bmatrix} c_{12}c_{13} & s_{12}c_{13} & s_{13}\mathrm{e}^{-i\delta_{\rm CP}}\\ -s_{12}c_{23} - c_{12}s_{23}s_{13}\mathrm{e}^{i\delta_{\rm CP}} & c_{12}c_{23} - s_{12}s_{23}s_{13}\mathrm{e}^{i\delta_{\rm CP}} & s_{23}c_{13}\\ s_{12}s_{23} - c_{12}c_{23}s_{13}\mathrm{e}^{i\delta_{\rm CP}} & -c_{12}s_{23} - s_{12}c_{23}s_{13}\mathrm{e}^{i\delta_{\rm CP}} & c_{23}c_{13}\end{bmatrix}\begin{bmatrix}\phi_1 & 0 & 0\\ 0 & \phi_2 & 0\\ 0 & 0 & 1\end{bmatrix}, \tag{2.98}$$

where c_{ij} and s_{ij} are abbreviations for $\cos\theta_{ij}$ and $\sin\theta_{ij}$. One can choose the ranges $\theta_{ij}\in[0,\pi/2]$ and $\delta_{\rm CP}\in[0,2\pi]$ without loss of generality. As for CP violation, we can compute the Jarlskog parameter as was done for the CKM matrix, *cf.* Equation 2.14,

$$J_{\rm PMNS} = \text{Im}[V_{e1}V_{\mu2}^*V_{e2}^*V_{\mu2}] = s_{12}\,s_{13}\,s_{23}\,c_{12}\,c_{23}\,c_{13}^2\sin\delta_{\rm CP}\,, \tag{2.99}$$

which accounts for the magnitude of CP violation due to the Dirac phase $\delta_{\rm CP}$ and is not sensitive to the Majorana phases $\phi_{1,2}$.

We now change notation and adopt the common practice of specifying light neutrino flavour (mass) eigenstates by Greek (Roman) indices. According to our assumption of acceptable unitarity, we also let the heavy neutrinos decouple, thus having effectively

$$V_{\rm cc}^{\rm mix} \sim [V_{\rm PMNS}\;\mathbf{0}]\,. \tag{2.100}$$

Experiment	L (m)		E (MeV)	Δm^2 (eV^2)
Solar		10^{10}	1	10^{-10}
Atmospheric		$10^4 - 10^7$	$10^2 - 10^5$	$10^{-1} - 10^{-4}$
Reactor	SBL	$10^2 - 10^3$	1	$10^{-2} - 10^{-3}$
	LBL	$10^4 - 10^5$		$10^{-4} - 10^{-5}$
Accelerator	SBL	10^2	$10^3 - 10^4$	> 0.1
	LBL	$10^5 - 10^6$	10^4	$10^{-2} - 10^{-3}$

TABLE 2.5: Characteristic baselines, energies and squared mass differences for the main types of neutrino oscillation experiments. 'SBL' ('LBL') stands for short (long) baseline. Table adopted from [209].

A quantum state with one flavour neutrino at an instant t is given by

$$|\nu_\alpha\rangle = \sum_{i=1}^{3} V_{\alpha i}^* \, |\nu_i\rangle \ . \tag{2.101}$$

Would we include the contribution by the heavy neutrinos, the sum would run to $3 + n$. With the approximation that the neutrinos are described by orthonormal plane wave states, all three mass eigenstates with the same momentum $p_i \equiv p \simeq E$, the energy of state i is [209]

$$E_i = \sqrt{p_i^2 + m_i^2} \simeq p + \frac{m_i^2}{2p} \simeq p + \frac{m_i^2}{2E} \, , \tag{2.102}$$

which includes the assumption that all active neutrinos are relativistic. Thus one may set t equal to L, the travelled distance or *baseline*. One can now easily compute the probability for an oscillation from flavour α to β,

$$P_{\alpha\beta} = \delta_{\alpha\beta} - 4 \sum_{i<j} \mathrm{Re}[V_{\alpha i} V_{\beta i}^* V_{\alpha j}^* V_{\beta j}] \sin^2 \frac{\phi_{ij}}{2} + 2 \sum_{i<j} \mathrm{Im}[V_{\alpha i} V_{\beta i}^* V_{\alpha j}^* V_{\beta j}] \sin \phi_{ij} \, , \tag{2.103}$$

with the oscillation phase[21]

$$\phi_{ij} = \frac{\Delta m_{ij}^2 L}{2E} \, , \qquad \Delta m_{ij}^2 \equiv m_i^2 - m_j^2 \, . \tag{2.104}$$

One concludes that the most likely cause for the effect of neutrino flavour oscillations is the presence of mixing ($V \neq \mathbf{1}$) and the non-vanishing of at least one mass difference. Notice that $P_{\alpha\beta}$ depends on elements of the products $VV^\dagger$ and is therefore independent of the Majorana phases. This can be understood from the fact that oscillations do not violate lepton number, thus the Majorana phases cannot be probed in oscillation experiments. Notice further that if neutrinos don't mix or if they are mass-degenerate, then there are no oscillations. Moreover, the last term of $P_{\alpha\beta}$ can be written in a form proportional to J (Equation 2.99). In particular,

$$A_{\mathrm{CP}}^{(\alpha\beta)} = P(\nu_\alpha \to \nu_\beta) - P(\bar{\nu}_\alpha \to \bar{\nu}_\beta) = -4 \sum_{i<j} \mathrm{Im}[V_{\alpha i} V_{\beta i}^* V_{\alpha j}^* V_{\beta j}] \sin \phi_{ij} \propto J \, , \tag{2.105}$$

so a non-zero CP asymmetry in the oscillation pattern involving two neutrinos and their corresponding antineutrino species would be a clear hint of CP violation due to δ_{CP}.

$P_{\alpha\beta}$ is characterized by an oscillation length [249]

$$L_{ij}^{\mathrm{osc}} = \frac{4\pi E}{\Delta m_{ij}^2} = 2.48\,\mathrm{m} \times \left(\frac{E}{1\,\mathrm{MeV}}\right) \left(\frac{\mathrm{eV}^2}{\Delta m^2}\right) \, , \tag{2.106}$$

meaning that an experiment measuring $|\nu_\alpha\rangle \to |\nu_\beta\rangle$ oscillations needs to be located at an appropriate distance ($L \sim E/\Delta m_{ij}^2$), otherwise oscillations are either inefficient (too small L) or average out (too

[21] In fact, experiments are sensitive to the averages $\left\langle \sin^2 \frac{\phi_{ij}}{2} \right\rangle$ and $\langle \sin \phi_{ij} \rangle$, taken over the energy spectrum $d\Phi/dE$, the efficiency $\epsilon(E)$ and the detection cross section $\sigma_{\mathrm{det}}(E)$, an electroweak cross section [209].

	Normal Ordering ($\Delta\chi^2 = 0.97$)		Inverted Ordering (best fit)		Any Ordering
	bfp $\pm 1\sigma$	3σ range	bfp $\pm 1\sigma$	3σ range	3σ range
$\sin^2\theta_{12}$	$0.304^{+0.013}_{-0.012}$	$0.270 \to 0.344$	$0.304^{+0.013}_{-0.012}$	$0.270 \to 0.344$	$0.270 \to 0.344$
$\theta_{12}/^\circ$	$33.48^{+0.78}_{-0.75}$	$31.29 \to 35.91$	$33.48^{+0.78}_{-0.75}$	$31.29 \to 35.91$	$31.29 \to 35.91$
$\sin^2\theta_{23}$	$0.452^{+0.052}_{-0.028}$	$0.382 \to 0.643$	$0.579^{+0.025}_{-0.037}$	$0.389 \to 0.644$	$0.385 \to 0.644$
$\theta_{23}/^\circ$	$42.3^{+3.0}_{-1.6}$	$38.2 \to 53.3$	$49.5^{+1.5}_{-2.2}$	$38.6 \to 53.3$	$38.3 \to 53.3$
$\sin^2\theta_{13}$	$0.0218^{+0.0010}_{-0.0010}$	$0.0186 \to 0.0250$	$0.0219^{+0.0011}_{-0.0010}$	$0.0188 \to 0.0251$	$0.0188 \to 0.0251$
$\theta_{13}/^\circ$	$8.50^{+0.20}_{-0.21}$	$7.85 \to 9.10$	$8.51^{+0.20}_{-0.21}$	$7.87 \to 9.11$	$7.87 \to 9.11$
$\delta_{\mathrm{CP}}/^\circ$	306^{+39}_{-70}	$0 \to 360$	254^{+63}_{-62}	$0 \to 360$	$0 \to 360$
$\frac{\Delta m^2_{21}}{10^{-5}\ \mathrm{eV}^2}$	$7.50^{+0.19}_{-0.17}$	$7.02 \to 8.09$	$7.50^{+0.19}_{-0.17}$	$7.02 \to 8.09$	$7.02 \to 8.09$
$\frac{\Delta m^2_{3\ell}}{10^{-3}\ \mathrm{eV}^2}$	$+2.457^{+0.047}_{-0.047}$	$+2.317 \to +2.607$	$-2.449^{+0.048}_{-0.047}$	$-2.590 \to -2.307$	$\begin{bmatrix}+2.325 \to +2.599\\ -2.590 \to -2.307\end{bmatrix}$

TABLE 2.6: Three-flavor oscillation parameters from a fit to global data by the NuFIT group after the NOW 2014 conference. Table taken from [250]. The numbers in the 1st (2nd) column are obtained assuming NO (IO). In the NuFIT convention, $\ell = 1$ for NO and $\ell = 2$ for IO.

large L). Table 2.5 lists the main types of neutrino oscillation experiments, specifying the characteristic baselines L, neutrino beam energies E and the squared mass differences Δm^2 that can be probed. As for the latter, one Δm^2 value is mainly measured in atmospheric neutrino experiments, $\Delta m^2_{\mathrm{atm}}$, and the other stems from solar ν_e oscillations, $\Delta m^2_\odot$. Most experiments are not sensitive to CP violation and therefore only the CP-conserving term in Equation 2.103 contributes significantly. Consequently, there is no sensitivity to the signs of Δm^2_{ij} and a convention needs to be established. One commonly defines $\Delta m^2_{12} > 0$ and associates it with $\Delta m^2_\odot$. As the baseline from the Sun to the Earth is very long and the energies are low, solar neutrino oscillation experiments are sensitive to very small Δm^2. We list a recent fit of neutrino oscillation parameters by the NuFIT group [250] in Table 2.6, who obtain a mass-squared difference of $\Delta m^2_\odot \approx 7.5 \times 10^{-5}\ \mathrm{eV}^2$. Atmospheric neutrinos, on the other hand, have characteristic baselines and energies such that the highest sensitivity is to larger Δm^2, which can be either positive or negative. Indeed, measurements find $|\Delta m^2_{\mathrm{atm}}|$ to be much larger than $\Delta m^2_\odot$. The sign of $\Delta m^2_{\mathrm{atm}}$ determines whether the neutrino mass hierarchy is *normal* (NH) or *inverted* (IH):

$$\begin{aligned} \text{NH}: \quad & m_1 < m_2 < m_3 \quad \Longrightarrow \quad \Delta m^2_{12} < \Delta m^2_{31} \approx \Delta m^2_{32}\,, \\ \text{IH}: \quad & m_3 < m_1 < m_2 \quad \Longrightarrow \quad \Delta m^2_{12} < -\Delta m^2_{31} \approx -\Delta m^2_{32}\,. \end{aligned}$$

Atmospheric neutrinos are similar in energy to long baseline accelerator neutrinos. From the angular distribution of fully contained ν_μ events in SK, one can reach an estimate of $\Delta m^2_{\mathrm{atm}} \sim 10^{-4} - 10^{-2}$ [209]; the MINOS accelerator experiment measured values of $2 - 3 \sim 10^{-3}\ \mathrm{eV}^2$ [251], the current fit by the NuFIT group being $2.46 \times 10^{-3}\ \mathrm{eV}^2$. This implies that at least one mass eigenstate has a mass of at least $\sqrt{\Delta m^2_{\mathrm{atm}}} \approx 0.05$ eV, hence being non-relativistic. It also turns out that solar and atmospheric neutrino oscillation probabilities are each most sensitive to one of the Euler angles. With the parametrizations in Equation 2.98, these are, respectively, $\theta_{12} \equiv \theta_\odot$ and $\theta_{23} \equiv \theta_{\mathrm{atm}}$. θ_{13} is commonly referred to as the reactor angle, due to reactor experiments having the best corresponding sensitivity.

For a long time, data were compatible with a maximal atmospheric mixing angle, $\theta_{\mathrm{atm}} \sim 45^\circ$, and a vanishing value of θ_{13}. This led theorists to work out simple mixing schemes for the structure of V_{PMNS}, following experimental trends. Very notably, the *tri-bimaximal* [252] mixing pattern

$$V_{\mathrm{TBM}} \sim \begin{bmatrix} \frac{2}{\sqrt{6}} & \frac{1}{\sqrt{3}} & 0 \\ -\frac{1}{\sqrt{6}} & \frac{1}{\sqrt{3}} & -\frac{1}{\sqrt{3}} \\ -\frac{1}{\sqrt{6}} & \frac{1}{\sqrt{3}} & \frac{1}{\sqrt{3}} \end{bmatrix}, \tag{2.107}$$

where ν_2 is tri-maximally mixed with all three flavour eigenstates and ν_3 is bi-maximally mixed with

ν_μ and ν_τ, comes close to the observed mixings [253]. It corresponds to the assignments $\theta_{12} \simeq 35.26°$, $\theta_{23} = 45°$ and $\theta_{13} = 0°$. TBM might be the manisfestation of an underlying symmetry in the second and third generation entries of the non-diagonal neutrino mass matrix (see [254] and references therein). Exact TBM is now excluded because the reactor angle θ_{13} has been measured by the Daya Bay and RENO collaborations to be small but non-vanishing [255, 256], *cf.* Table 2.6.

2.4 The scotogenic model and its FIMP realization: A minimal framework with thermal DM and neutrino masses

The *scotogenic model* by E. Ma [40], also known as the *radiative seesaw model*, *dark scalar doublet model* or simply *Ma model*, is perhaps the most elegant[22] way to explain the identity of dark matter and active neutrino masses and oscillations. It is furthermore capable to account for thermal leptogenesis [257]. Its virtue lies in its simplicity, for it minimally extends the SM Lagrangian with merely two new field representations and imposes a $\mathbb{Z}_2$ parity symmetry onto the new 'dark' sector, preventing it from mixing with SM fields. In the second study presented in this thesis, we focus on the collider phenomenology of a particular variant of this model.

2.4.1 New particles and interactions

Newly introduced are $n \geq 2$ right-handed singlet neutrinos N_k and an additional scalar doublet H_2 with hypercharge $Y(H_2) = +1$. It is therefore a combination of two of the simplest frameworks to explain dark matter and neutrino masses, namely the inert doublet model (IDM) [258] and the type I seesaw model [13]. Due to the $\mathbb{Z}_2$ symmetry, H_2 is precluded from acquiring a VEV, so the scalar doublets have the components

$$H_1 = \begin{bmatrix} G^+ \\ \frac{1}{\sqrt{2}}(v + h + iG^0) \end{bmatrix}, \qquad H_2 = \begin{bmatrix} H^+ \\ \frac{1}{\sqrt{2}}(H^0 + iA^0) \end{bmatrix}. \tag{2.108}$$

H^0 and A^0 are, respectively, CP-even and CP-odd neutral scalars presumed to have masses below the TeV scale, in order to allow for interesting collider phenomenology. Together with the lightest RHN, they constitute the set of dark matter candidates accommodated by the model. The actual DM particle is determined once one fixes a mass spectrum — its stability is then guaranteed by the $\mathbb{Z}_2$ symmetry. Another effect of the $\mathbb{Z}_2$ is that the new doublet is necessarily leptophilic, meaning there is only a Yukawa coupling between the SM leptons and the RHNs, but none involving the quark fields. This forbids the occurrence of flavour-changing neutral currents. The full Lagrangian reads

$$\mathcal{L} = \widetilde{\mathcal{L}}_{\mathrm{SM}} + \mathcal{L}_{\mathrm{mass}}(N_k) + \mathcal{L}_{\mathrm{kin}}(N_k, H_2) + \mathcal{L}_{\mathrm{Y}}(L_i, N_k, H_2) + \mathcal{L}_{\mathrm{V}}(H_1, H_2)\,, \tag{2.109}$$

with

$$\mathcal{L}_{\mathrm{kin}}(N_k, H_2) = \frac{i}{2}\,\bar{N}_k \partial\!\!\!/ N_k + (D_\mu H_2)^\dagger (D^\mu H_2)\,, \tag{2.110a}$$

$$-\mathcal{L}_{\mathrm{mass}}(N_k) = \frac{1}{2}\,M_k\,\overline{N_k^c}\,N_k\,, \tag{2.110b}$$

$$-\mathcal{L}_{\mathrm{Y}}(L_i, N_k, H_2) = Y_{ik}\,\bar{L}_i\,\tilde{H}_2\,N_k + \mathrm{h.c.}\,, \tag{2.110c}$$

$$\begin{aligned} -\mathcal{L}_{\mathrm{V}}(H_1, H_2) = &\sum_{i=1,2}\left[\mu_i^2 H_i^\dagger H_i + \frac{\lambda_i}{2}(H_i^\dagger H_i)^2\right] + \lambda_3 (H_1^\dagger H_1)(H_2^\dagger H_2) \\ &+ \lambda_4 (H_1^\dagger H_2)(H_2^\dagger H_1) + \frac{\lambda_5}{2}\left[(H_1^\dagger H_2)^2 + (H_2^\dagger H_1)^2\right], \end{aligned} \tag{2.110d}$$

[22] Elegance is a matter of taste in this context, since a discrete symmetry needs to be imposed by hand, which may be regarded as implying the necessity for an extension of the model at higher scales. This is surely no drawback though, since the model does not solve other pressing issues, such as the hierarchy problem.

and where $\widetilde{\mathcal{L}}_{\rm SM} = \mathcal{L}_{\rm SM} - \mathcal{L}_{\rm V,SM}$. H_1 is the usual SM Higgs doublet, thus $\mu_1^2 < 0$; μ_2^2 can in principle also be negative as long as $\langle H_2 \rangle = 0$, otherwise the $\mathbb{Z}_2$ symmetry would be spontaneously broken. Usually one works in the minimum

$$\langle H_1 \rangle = \frac{v}{\sqrt{2}} = \sqrt{-\frac{\mu_1^2}{\lambda_1}}\,, \qquad \langle H_2 \rangle = 0\,, \tag{2.111}$$

though whether it is global (or stable at time scales larger than the age of the Universe) has to be verified through the RGEs [259]. We shall only impose the positivity of the squared scalar masses (see below).

The model introduces a Majorana mass term for the RHNs, which in Equation 2.110b is expressed in a basis where the mass matrix M_k is diagonal, plus a L-N-H_2 Yukawa interaction and the familiar scalar potential of the IDM. In total, the model adds to the SM $n + 5$ parameters through *e.g.* the set $\{M_k, m_{H^\pm}, m_{H^0}, m_{A^0}, \lambda_2, \lambda_4\}$, plus 9 new Yukawa couplings Y^ν_{ij}. Active neutrino masses are radiatively generated through the lepton number violating set of parameters $\{M_k, Y^\nu, \lambda_5\}$, resulting in the effective mass term at one-loop given in Equation 2.91, *i.e.*

$$(\mathcal{M}_\nu)_{ij} = \frac{Y_{ik}Y_{jk}}{16\pi^2}\, M_k \left[\frac{m_{H^0}^2}{M_k^2 - m_{H^0}^2} \ln \frac{m_{H^0}^2}{M_k^2} - \frac{m_{A^0}^2}{M_k^2 - m_{A^0}^2} \ln \frac{m_{A^0}^2}{M_k^2} \right] = \left(Y \Lambda Y^T \right)_{ij}\,, \tag{2.112}$$

where we defined the diagonal matrix Λ with entries

$$\Lambda_k \equiv \frac{M_k}{16\pi^2} \left[\frac{m_{H^0}^2}{M_k^2 - m_{H^0}^2} \ln \frac{m_{H^0}^2}{M_k^2} - \frac{m_{A^0}^2}{M_k^2 - m_{A^0}^2} \ln \frac{m_{A^0}^2}{M_k^2} \right]\,, \tag{2.113}$$

in order to emphasize the formal similarity with the type I and type III seesaw models, *cf.* Equations 2.77a and 2.77c. Therefore, the new Yukawa matrix Y can be decomposed by means of the widely known Casas-Ibarra parametrization [260].

At the EW minimum (Equation 2.111), the dark scalars acquire the tree-level masses

$$m_{H^\pm}^2 = \mu_2^2 + \frac{\lambda_3}{2} v^2\,, \tag{2.114a}$$

$$m_{H^0}^2 = \mu_2^2 + \frac{\lambda_3 + \lambda_4 + \lambda_5}{2} v^2\,, \tag{2.114b}$$

$$m_{A^0}^2 = \mu_2^2 + \frac{\lambda_3 + \lambda_4 - \lambda_5}{2} v^2\,. \tag{2.114c}$$

Notice that, as in the seesaw models, the Higgs mechanism is necessary for neutrino mass generation through the splitting of m_{H^0} and m_{A^0} by the lepton number violating parameter λ_5. As discussed previously, λ_5 is a self-renormalized coupling (see *e.g.* [261]), it is therefore natural to assume that it is small, as is usually done [262]. In that case, H^0 and A^0 become quasi-degenerate and $\mathcal{M}_\nu$ in Equation 2.112 can be conveniently expressed in a form proportional to λ_5 [40]. In the case $m_{H^0}, m_{A^0} \ll M_k$, the lightest of H^0, A^0 represents the model's dark matter candidate, corresponding to the limit of the IDM [263, 264]. For a small value of λ_5, *i.e.* $|m_{H^0}^2 - m_{A^0}^2| \ll m_0^2$, where $m_0^2 \equiv (m_{H^0}^2 + m_{A^0}^2)/2$, Λ_k can be approximated as [40]

$$\Lambda_k \simeq \frac{\lambda_5 v^2}{8\pi^2} \frac{1}{M_k} \left[\ln \frac{M_k^2}{m_0^2} - 1 \right] \tag{2.115}$$

and a radiative seesaw mechanism is realized with the canonical seesaw scale reduced by a factor of $\lambda_5/8\pi^2$. On the other hand, if $m_0^2 \gg M_k$, one has

$$\Lambda_k \simeq \frac{\lambda_5 v^2}{8\pi^2} \frac{M_k}{m_0^2} \tag{2.116}$$

and neutrino masses are small due to light RHNs, a small λ_5 parameter and presumably very heavy neutral scalars. The provided DM candidate is provided through the lightest RHN [262, 265]. Without

the degeneracy requirement, the expression is approximated as [266]

$$\Lambda_k \simeq \frac{M_k}{16\pi^2} \ln \frac{m_{H^0}^2}{m_{A^0}^2} \,. \tag{2.117}$$

The size of λ_5 is not only important for the neutrino mass and oscillation sector, but also for collider phenomenology involving Higgs mediation, so we shall come back to this point at a later stage.

The parameter space of the scotogenic model is constrained by collider and low-energy observables, as well as direct and indirect dark matter searches. An exhaustive discussion is beyond our goals, since they highly depend on which mass spectrum is realized. Here we focus on fermionic dark matter provided through the lightest heavy neutrino N_1, thus we postpone a discussion of the constraints in this specific setup to Chapter 6.

2.4.2 Fermionic FIMP dark matter within the scotogenic model

Consider a version of the scotogenic model with three RHNs N_k, $k = 1, 2, 3$, with $M_1 < M_2 < M_3$ and the particular hierarchy of Yukawa couplings

$$|Y_{i1}| \ll |Y_{i2}|, |Y_{i3}| \,, \qquad i = e,\, \mu,\, \tau \,. \tag{2.118}$$

such that N_1 effectively decouples from the radiative mechanism responsible for active neutrino mass generation. Consequently, one active neutrino remains effectively massless, while the other two gain their masses through the contribution by N_2 and N_3. In order to successfully reproduce neutrino oscillation data, N_1 is the only neutrino allowed to decouple if $n = 3$. The authors of Reference [42] studied the case of having couplings Y_{i1} that are in fact so small that N_1 is unable to reach thermal equilibrium in the early Universe due to the absence of gauge interactions, thus freezing-in with a given final abundance. Therefore, N_1 is a FIMP and all considerations of Section 2.2.3.3 apply with the Yukawas $\{Y_{11}, Y_{21}, Y_{31}\}$ playing the role of the FIMP coupling λ. In what follows, we shall denote the *next-to-lightest odd particle* by NLOP rather than LOSP, to comply with the nomenclature in [42]. Depending on whether there is a sizeable superWIMP contribution, one has the following four possible fundamental configurations:

(i) $M_1 < m_S, M_{2,3}$, no sW: The DM particle is N_1 and the NLOP is the lightest scalar. The dominant contribution to DM is the freeze-in of N_1 via decays of heavier $\mathbb{Z}_2$-odd particles. This corresponds to scenario 1 in Table 2.4.

(ii) $M_1 < m_S, M_{2,3}$, with sW: Same as case (i), but a significant (maybe dominant) contribution to $\Omega_{\rm DM}$ of the superWIMP type stems from late decays of the frozen-out NLOP, so this corresponds to scenario 2 in Table 2.4. This can either be one of the scalars or N_2.

(iii) $m_{H^0/A^0} < M_1$, with sW: The DM particle is one of the neutral scalars, H^0/A^0. In principle, it could also be N_2, but in [42] it is shown that $\Omega_{N_2}^{\rm FO}$ is typically too large to be in correspondence with observations, therefore that case is unappealing. The H^0/A^0 is a WIMP in this case. A significant (maybe dominant) contribution to $\Omega_{\rm DM}$ of the superWIMP type stems from late decays of the frozen-in FIMP N_1. This setup corresponds to scenario 3 in Table 2.4.

(iv) $m_{H^0/A^0} < M_1$, no sW: Same as case (iii), but the dominant contribution is due to H^0/A^0 freeze-out. This option matches scenario 4 in Table 2.4.

In [42], it is shown that the superWIMP contribution is negligible as long as $m_S \lesssim 500$ GeV, imposing constraints on neutrino masses, $\mu \to e\gamma$ and the condition of the scalar decaying between its freeze-out and the onset of BBN,

$$10^{-13} \left(\frac{1\,\text{TeV}}{m_S}\right)^{1/2} \lesssim y_1 \lesssim 10^{-8} \left(\frac{m_S}{1\,\text{TeV}}\right)^{1/2} \,. \tag{2.119}$$

We shall come back to the point of BBN in Chapter 6. We now turn to the hypothesis that the odd scalars are heavier than N_1,

$$m_S > M_1 \,, \tag{2.120}$$

m_S standing for the generalized scalar mass scale, assuming there are not too high mass splittings. This assumption implies the relevance of the FI mechanism for generating a significant N_1 abundance, otherwise the N_1 population would be generated by scatterings and $N_{2,3}$ decays, which are heavily suppressed compared to simple 2-body decays of scalars to N_1 and SM leptons [42]. With such decays, the yield evolves with the temperature according to

$$\frac{dY_{N_1}}{dT} = -\frac{1}{sH}\sum_S \frac{g_S\, m_S^2}{2\pi^2}\, K_1\left(\frac{m_S}{T}\right)\, \Gamma(S \to N_1 + \ldots)\,, \tag{2.121}$$

by Equation 2.69, with $g_S = g_{H^\pm, H^0, A^0} = 1$. The decay rates are

$$\Gamma(H^\pm \to \ell_i\, N_1) = \frac{m_{H^\pm}\,|Y_{i1}|^2}{16\pi}\left(1 - \frac{M_1^2}{m_{H^\pm}^2}\right) \overset{M_1 \ll m_{H^\pm}}{\approx} \frac{m_{H^\pm}\,|Y_{i1}|^2}{16\pi}\,, \tag{2.122a}$$

$$\Gamma(H^0/A^0 \to \nu_i\, N_1) = \frac{m_{H^0/A^0}\,|Y_{i1}|^2}{32\pi}\left(1 - \frac{M_1^2}{m_{H^0/A^0}^2}\right) \overset{M_1 \ll m_{H^0/A^0}}{\approx} \frac{m_{H^0/A^0}\,|Y_{i1}|^2}{32\pi}\,, \tag{2.122b}$$

the approximations corresponding to the mass hierarchies we shall consider in our analyses. With these rates, the FIMP condition (Equation 2.65) in the scotogenic scenario reads

$$\Gamma(S \to \ell/\nu\, N_1) \lesssim H(T \sim m_S)\,. \tag{2.123}$$

Equation 2.123 implies values for the FIMP coupling y_1

$$y_1 \lesssim 10^{-8}\,, \tag{2.124}$$

where we let the modulus of a typical Yukawa coupling $|Y_{ik}|$ to N_k be denoted by y_k, like in the main reference. As for $y_{2,3}$, the couplings responsible for neutrino masses and mixing, having them reproduce the neutrino mass scale of $\gtrsim 10^{-2}$ eV while at the same time respecting the $\mu \to e\gamma$ bound, requires

$$0.1 \lesssim y_{2,3} \lesssim 10^{-6}\,. \tag{2.125}$$

We readily note from Equation 2.124 that the FIMP condition forces N_1 to decouple from low-energy lepton flavour phenomena, while $N_{2,3}$ definitely attain thermal equilibrium and could mediate such processes.

CHAPTER 3

Collider physics and the ATLAS and CMS experiments

As stated in the introduction, this thesis comprises two studies, Analyses I and II(A+B), concerned with exotic particle production at the LHC. It is therefore apposite to have the analyses preceded by a chapter covering the working principles of such machines. We shall accordingly discuss the technique of detecting particles that originate from collisions taking place in the detectors of particle accelerators, in particular in the general-purpose LHC detectors ATLAS and CMS. Moreover, the second analysis requires a good understanding of the physical properties of the detectors. These are also provided in this chapter.

We begin by introducing particle accelerators and reviewing some basic physics quantities related to collision events in Section 3.1 and briefly describe the LHC and the ATLAS and CMS experiments in Section 3.2, with mention of important aspects of their geometries and used materials. These sections suffice as a preparation for the minimal scenarios considered in the first study, presented in Chapter 5.

As for the second study, the focus will be on the full deceleration of long-lived scotogenic $H^{\pm}$ bosons on the one side and their escape on the other. To account for both signatures, we develop through the treatments of ATLAS and CMS in Section 3.2.2 a set of two simplified detectors ('toy detectors') to simulate deceleration effects and to determine the fraction of escaping $H^{\pm}$ particles by combining the toy detector geometry with Monte Carlo samples for various spectra of the scotogenic particle sector. These toy detectors are described in Section 3.2.3, with basis on the detector descriptions from Section 3.2.2 and especially on Appendix E. Topics specific to these types of signatures are postponed to Chapter 4.

3.1 Elements of collider physics

Particle accelerators have been an important cornerstone in experimental physics and technology alike, ever since their invention [267]. Their purpose is the creation of highly energetic narrowly focused beams of electrically charged particles by means of static or oscillating electromagnetic fields. Development has come a long way from the invention of the cathode ray tube in the end of the 19th century over the first proper higher-energy accelerators in the early 1930s up to the powerful modern-day accelerators such as the LHC, reaching several TeV for the individual protons contained in the beams. Their applicability is manifold. Usage includes medical treatments, isotope production, material studies and modification, and so forth. The utilization of particle accelerators to explore the subatomic world can undoubtedly be traced back to E. Rutherford who, after the discovery of the atomic nucleus in 1910 and the first creation of artificial nuclear reactions in 1919, advocated the development of devices capable of producing fast enough particles (many MeV) to break through the Coulomb barrier of nuclei, which ultimately gave birth to nuclear physics [268].

When beams are controlled to intersect at particular points such that the particles are smashed into each other, one speaks of a *colliding-beam experiment*. On the other hand, if there is only one beam that is brought to collide with a target particle at rest in the laboratory, one is performing a *fixed-target experiment*. As we shall see, the highest achievable transmutation of the total energy contained in the two-particle system into interaction products is realized when the system's frame coincides with its center-of-momentum (CM) frame; this forms the conceptual principle for the design of circular high-energy physics colliders such as the Large Electron-Positron Collider (LEP) and the LHC at CERN, the Hadron-Elektron-Ringanlage (HERA) at DESY, the Tevatron at Fermilab and linear colliders like the Stanford

Linear Collider (SLC) at the SLAC National Accelerator Laboratory [269].[1] Linear colliders follow the same principle, though to achieve the same energies, they are required to be extremely long. Moreover, accelerating high-voltage cavities cannot be reused for increasing the beam energy.

The mentioned circular colliders are examples for so-called *storage rings*. These are a kind of accelerators where particles are boosted up to a specified kinetic energy and then made to keep circulating at constant speed for several hours up to a day, forming either continuous beams or discrete particle *bunches*. Two beams directed to circulate oppositely are brought to collide at *interaction points* (IP) located inside particle detectors, which are used to register and identify the products from the collision events with their kinematical information. SLC and LEP are examples for e^+e^- colliders — these produce final states that can be reconstructed more easily when compared to hadron colliders, since there is no complication of them being in bound states and collision products are cleaner in terms of QCD background. However, even e^+e^- collisions are far from simple to analyze, in particular the CM is not necessarily at rest in the detector frame. $e^\pm p$ collisions were conducted at HERA and pure hadron colliders either collide $p\bar{p}$ pairs, as did the Tevatron and the SPS (Super Proton Synchrotron) at CERN, or pp pairs, as is the case of the LHC. Finally, beams of heavy ions have been brought to collide for high-energy nuclear physics research. In the past, this was achieved with accelerators like the SPS and the AGS (Alternating Gradient Synchrotron) at Brookhaven National Laboratory (BNL); the two contemporary accelerators carrying heavy ion beams are the LHC and the Relativistic Heavy Ion Collider (RHIC) at BNL, a linear accelerator.

All modern high-energy circular accelerators are types of *synchrotrons*. Synchrotrons accelerate particles by means of oscillating electric fields at radio frequency and the particles' trajectories are bent by magnetic fields whose intensity is synchronized w.r.t. their energy. As we shall discuss shortly, this leads to considerable energy loss due to bremsstrahlung (synchrotron radiation).

High-energy colliders have become the principal tool to conduct research of matter at the most fundamental level, *i.e.* at distance scales of 10^{-13} cm or smaller. Modern-day collider experiments aim to verify the correctness of the standard model and to find evidence for physics beyond its scope. The procedure consists of calculating the impact of particles and interactions within the theory under study on the statistics of the experiment in the form of observables such as the predicted cross sections and branching ratios (*cf.* Sections 3.1.2.2 and 3.1.2.3), with the outcome of either *a*) a discovery and possible confirmation, *b*) limits on the parameter space if there is no statistically significant signal or *c*) a dismissal of the theory. Before treating these observables in Section 3.1.2, we first discuss the main defining features of a particle collider, largely following the lectures [269–271].

3.1.1 Basic concepts

A centripetally accelerated charged particle will lose a certain amount of energy in the form of synchrotron radiation due to the magnetic field bending its trajectory. Virtual photons separate from the radiative cloud around the particle as it transversally accelerates and are seen as on-shell bremsstrahlung radiation. For electron accelerators such as LEP, this represents the main nuisance effect to be considered in the accelerator's technical design. If the particle has a given mass m and has been boosted up to an energy E, then the energy lost per revolution ΔE, in SI units, is calculated to be [272–274]

$$-\Delta E = \frac{4\pi\alpha}{3\epsilon_0}\hbar c^2 \frac{\beta^3\gamma^4}{\rho} \propto \frac{1}{\rho}\left(\frac{E}{m}\right)^4 \qquad (\beta \sim 1)\,. \tag{3.1}$$

ρ is the curvature radius depending on the magnetic field strength B and it is comparable to the actual radius of the accelerator. Therefore, a large radius and/or a large particle mass are desirable for reducing this effect. At LEP, the prior collider inside the LHC tunnel, the beams contained electrons and positrons with energies up to ~ 100 GeV throughout the second run and $-\Delta E$ was about 2.3 GeV, whereas protons at LHC with an energy of 7 TeV during the initial phase of the first run in 2011 only emitted about 7 keV

[1] Note that colliders aimed at studying CP violation in meson systems, such as PEP-II hosting BaBar and KEKB hosting Belle, usually control the CM to be in motion relative to the detector, in order to identify decays more clearly.

Name, Phase	Type	$\sqrt{s}$ (GeV)	L (pb^{-1})	Operational period	Detectors	Length (km)	Location
LEP (LEP-I)	e^+e^-	91.2	~ 200	1989-95	ALEPH, OPAL,	26.7	CERN
LEP (LEP-II)		130-209	~ 600	1996-2000	DELPHI, L3		
SLC	e^+e^-	91.2	20	1992-98	SLD	2.9	SLAC
HERA	$e^\pm p$	320	500	1992-2007	ZEUS, H1	6.34	DESY
Tevatron (Run I)	$p\bar{p}$	1800	160	1987-96	DØ, CDF	6.28	Fermilab
Tevatron (Run II)		1960	12000	2001-2011			
LHC (Run I 2011)	pp , PbPb,	7000	6000	2011	ALICE, ATLAS,	26.7	CERN
LHC (Run I 2012)	pPb	8000	23300	2012	CMS, LHCb		
LHC (Run II 2015-?)		13000	4200	2015			

TABLE 3.1: List of recent high-energy storage ring colliders. Luminosities correspond to delivered luminosities, which for the LHC are only specified for ATLAS and CMS. Heavy ion runs at LHC are not considered.

per revolution [274]. Hence, synchrotron radiation at the LHC has a negligible impact, though for LEP it was of uttermost significance.

One of the two most important quantities defining a collider is the energy in the CM frame of the scattering particles. It is a Lorentz-invariant quantity given by the square root of the Mandelstam variable

$$s \equiv (p_1 + p_2)^2 = \begin{cases} (E_1 + E_2)^2 & \text{in the CM frame where } \vec{p}_1 + \vec{p}_2 = 0\,, \\ m_1^2 + m_2^2 + 2(E_1E_2 - \vec{p}_1 \cdot \vec{p}_2) & \text{in general}\,, \end{cases} \tag{3.2}$$

where p_1 and p_2 are the two particles' 4-momenta. In the ultra-relativistic limit ($m_i \ll E_i$), the CM energy is approximated as

$$E_{\mathrm{CM}} = \sqrt{s} \approx \begin{cases} 2E_1 \approx 2E_2 & \text{in the CM frame}\,, \\ \sqrt{2E_1 m_2} & \text{in the fixed-target frame where } \vec{p}_2 = 0\,. \end{cases} \tag{3.3}$$

E_{CM} is the energy available for creating the collision products and the threshold for a given interaction to occur is the equality of E_{CM} and the sum of the rest masses of the product particles. Equation 3.3 shows that the projectile energy in a fixed-target experiment is always much higher than the sum of the energies of the colliding particles in the CM frame, since the net kinetic motion of the latter is zero. For example, to reach $\sqrt{s} = 10$ GeV in a pp collision, one requires two protons with energies of 5 GeV in the CM frame, while the moving proton in the fixed-target frame requires an energy of approximately 50 GeV.

The second defining quantity is the instantaneous luminosity, $\mathcal{L}(t)$, which corresponds to the ratio of the inelastic collision rate and the cross section for the collision of the inelastically scattering particles. It tells how many collisions are taking place per unit of cross-sectional area and per unit of time. If there are n_1 (n_2) particles in each bunch in beam 1 (2), then

$$\mathcal{L} = \frac{R_{\mathrm{inel}}}{\sigma_{\mathrm{inel}}} = \frac{f_{\mathrm{rev}}\, n_1 n_2 n_{\mathrm{b}}}{4\pi\sigma_x\sigma_y}\,, \tag{3.4}$$

where f_{rev} is the revolution frequency, n_{b} is the number of bunches per beam and $\sigma_{x,y}$ are the characteristic beam width dispersions in the two transverse directions at the interaction point. All these parameters are time-dependent and need to be monitored while the beams are circulating, hence the time dependence of $\mathcal{L}$. For instance, the beam intensity decreases during the time of a fill due to beam loss induced by collisions, beam-beam interactions and interactions with residual gas within the pipes [275]. Of course, the rate of events of a given type needs to be proportional to $\mathcal{L}$, so the rate of such a specific interaction at a given CM energy s is simply[2]

$$R(s,t) = \sigma(s)\mathcal{L}(t)\epsilon\,, \tag{3.5}$$

[2]In fact, since the beam energy is not perfectly constant, the luminosity will exhibit a spread around $\sqrt{s}$, meaning that σ will have to be convoluted with a spread function,

$$R(s) = \mathcal{L}\int d\tau \frac{d\mathcal{L}}{d\tau}\sigma(\tilde{s})\epsilon\,,$$

with $\int d\tau(d\mathcal{L}/d\tau) = 1$ and $\tilde{s} = \tau s$. In practice, it is a good simplification to take $d\mathcal{L}/d\tau \to \delta(1-\tau)$ [269], which we will always opt for.

$\epsilon < 1$ being the efficiency of the detector to identify the event and the proportionality factor σ is the *total scattering cross section*, a measure for the probability of the process to happen (*cf.* Section 3.1.2.2). Practically, one is interested in the number of certain events taking place over the lifetime of a collider or over the duration of a particular run at a certain value of $\sqrt{s}$. This number is calculated via

$$N_{\text{ev}} = \sigma L \varepsilon \,, \qquad L \equiv \int dt \mathcal{L}(t) \tag{3.6}$$

where L is the *integrated luminosity*, though one often simply calls it *luminosity*. Here we also assume that ϵ is temporally constant, though this is not necessarily true. Cross sections are usually given in units of barn ($1\text{ b} = 10^{-24}\text{ cm}^2$) and for luminosities one uses the inverse thereof. A list of the main recent storage ring colliders and some descriptive elements combined from tables in [269] and [271] with some actualizations is presented in Table 3.1. Note that the luminosities correspond to the luminosities *delivered* to the experiments by the colliders; these need to be distinguished from the actually usable recorded luminosities by each experiment, which are always somewhat lower.[3]

At this stage, we return to the point of how complicated the analysis of a scattering process can be and why the CM of the colliding particles does not have to be at rest in the detector frame, even in the case of e^+e^- scattering. In practice, hadron colliders accelerate protons and antiprotons (LHC only uses protons), or ionized nuclei. Hadrons are bound states of so-called *partons*, the nomenclature having its origin in Feynman's 'parton model' [277]. These are the quarks and gluons confined in the hadronic state by the strong force carrying part of the hadron's longitudinal momentum (transverse momenta perpendicular to the beam line are negligibly small). The carried momentum fractions are probabilistically distributed according to the hadron's *parton distribution function* (PDF), see Section 3.1.3. If photons or partons are emitted by the incoming (outgoing) particles before (after) the collision, one speaks of *inital (final) state radiation* (ISR/FSR). Processes such as $e^\pm \to e^\pm\gamma$ are called *splitting processes*. The resulting $e^\pm$ is then slightly off-shell. Soft and/or collinear ISR has the effect of placing the CM of the actual e^+e^- or parton-parton interaction in motion relative to the detector frame due to the recoil. The condition of being low-energetic or collinear with the colliding particles guarantees that the recoil is small enough for the main event (*i.e.* the *'hard process'*) to still take place, otherwise the particles would fly by each other. Hadronic collisions are even more affected by this problem because the gluon-gluon and gluon-quark coupling is significantly stronger than the electromagnetic coupling strength. FSR is the process of photons and/or partons being emitted by final state particles and also producing a recoil. Very soft and very collinear ISR and FSR is unobservable, yet they can significantly contribute to the cross section of the scattering process.

Further complication in the hadronic case is contributed through the PDF, which is only known phenomenologically, as shall be treated more deeply in Section 3.1.3. Proton and antiproton PDFs have, in part, been measured in deep inelastic $e^\pm p$ scatterings with the HERA collider at DESY. The absence of a first-principle understanding of these functions in combination with relatively high experimental uncertainties and the fact that for highly energetic collisions one has to rely on extrapolations is a major obstacle for precision physics, especially at higher energies. A similar situation arises in e^+e^- colliders: Electron and positron beams are, in fact, electron-positron-photon beams, as electrons radiate off photons and can split to states containing positrons at higher perturbative orders. Furthermore, photons can split to yield e^+e^- states, thus an electron at smallest distances appears as a composite with the electron carrying part of the momentum, plus a cloud of photons and $e^\pm$ pairs [77]. Therefore, kinematics of initial states in e^+e^- collisions need to be convoluted with the probabilities to find an electron and a positron within the beam, similar to the hadronic case, where one needs to convolute with the (anti-)proton PDF, *cf.* Equation 3.30. Finally, if the initial or final state is hadronic, one needs to account for the as yet poorly understood process of *hadronization*. Initial spectator partons, ISR partons and final partons eventually bind with quarks and gluons extracted from the QCD vacuum to form colour-neutral hadronic states. Hadronization occurs with many splittings in-between until the energies of the fragmentation processes reach the QCD scale, $\Lambda_{\text{QCD}} \approx 0.2$ GeV. Since the strong interaction becomes stronger with decreasing energy due to the

[3] Delivered and recorded ATLAS and CMS luminosities are available in the pages linked in [276].

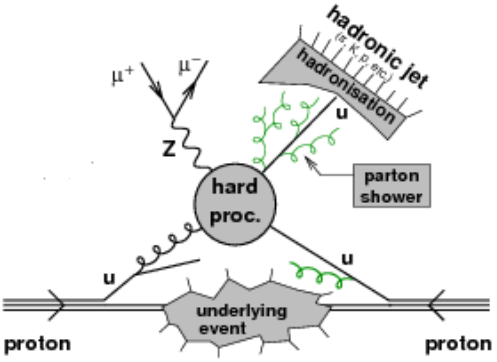

FIGURE 3.1: Schematic depiction of a proton-proton collision. The hard process is $qg \to Z^*q \to \mu^+\mu^- j$. Taken from [278].

property of asymptotic freedom, the outcome is a cascade of collimated hadronically confined particles (π, $p/\bar{p}$, K, $\Lambda, \ldots$). Most final hadrons will therefore be pions, since they are the lightest meson species, $m_\pi \sim \Lambda_{\mathrm{QCD}}$. The stage when partons propagate and split is called *parton showering*, the consecutive stage involving the confined hadrons is termed *hadron showering*. Hadron showers in detectors are seen as a conic spray of particles called *jets*, which in sum carry the initial parton's energy and momentum. Empirical models for parton and hadron showering are employed in Monte Carlo simulators like Pythia [279] and HERWIG [280]; such programs are required to generate realistic final states to be passed to detector simulation software. They also account for *underlying events*, a term encompassing all processes not related to the hard scattering event, including ISR/FSR, softer partonic collisions from the same pp event and proton remnants along the beam direction [281]. All these effects are schematically presented in an exemplary pp collision event in Figure 3.1. It is of uttermost importance to understand them well for the end of performing precision measurements. Note that showering also applies to electrons and photons in the form of *electromagnetic showers* [78]. At high energies, electrons and photons suffer splittings through pair creation and bremsstrahlung processes, while at lower energies, the photoelectric effect and Compton scattering dominate until they are absorbed.

3.1.2 Collider observables

If an event in a detector at LHC is recorded, each participating final state particle is registered. The recorded information consists of its type, deposited energy, measured momentum and path. From these basic observables, more informative quantities such as missing transverse energy ($\not{E}_{\mathrm{T}}$), cross sections and decay rates are derived. The path is defined by the polar and azimuthal angles (θ, ϕ) of the particle's trajectory relative to the beam axis, conventionally set to be the z-direction in a Cartesian (x, y, z) coordinate system. Scattering takes place at the origin, *i.e.* in the center of the cylindrical detector. Thus the polar angle corresponds to the actual (lab frame) scattering angle, whereas the cylindrical detector symmetry implies a uniform scattering probability in the ϕ range $[0, 2\pi]$ if the beams are unpolarized, as is the case of the LHC.

3.1.2.1 Rapidity and pseudorapidity

Since the CM of e^+e^- and parton-parton collisions is generally boosted along the beam line with respect to the laboratory frame, it is convenient to work with kinematical quantities that are invariant under these boosts. In particular, particle physics experiments opt for expressing the polar angle in the form of the (pseudo-)rapidity because of its convenient properties under Lorentz transformations. Since the rapidity $w = \tanh^{-1}\beta = \cosh^{-1}\gamma = \sinh^{-1}\beta\gamma$ is additive under consecutive boosts along the same direction, a difference $\Delta w = w_1 - w_2$ between the rapidities of two particles is invariant under boosts along the z axis.

The azimuthal direction is also unaffected by boosts along z, therefore one can define an invariant measure for particle separation by $\Delta R = \sqrt{\Delta w^2 + \Delta\phi^2}$, a useful quantity to impose particle isolation cuts. It is, however, difficult to measure a particle's full 3-momentum. Hence a slightly different definition of w is employed in collider physics, namely

$$w = \tanh^{-1}\beta = \frac{1}{2}\ln\left(\frac{E+|\vec{p}|}{E-|\vec{p}|}\right) \quad \longrightarrow \quad y = \frac{1}{2}\ln\left(\frac{E+p_z}{E-p_z}\right), \tag{3.7}$$

where p_z is the modulus of the particle's momentum along the z-direction. While also not being easily measurable though still being additive under boosts along the beam axis, y has a significant advantage over w in the case of highly relativistic particles ($p \gg m$). This is therefore viable for all SM particles except on-shell W, Z, H and t. To see the benefit, expand the numerator and the denominator in the argument of the logarithm as

$$y = \frac{1}{2}\ln\left(\frac{1+\frac{p_z}{p}+\frac{m^2}{2p^2}+\ldots}{1-\frac{p_z}{p}+\frac{m^2}{2p^2}+\ldots}\right) = \frac{1}{2}\ln\left(\frac{2\cos^2\frac{\theta}{2}+\mathcal{O}\left(\frac{m^2}{p^2}\right)}{2\sin^2\frac{\theta}{2}+\mathcal{O}\left(\frac{m^2}{p^2}\right)}\right) \simeq \eta\,, \tag{3.8}$$

defining the purely θ-dependent *pseudorapidity*

$$\eta \equiv y(m=0) = \frac{1}{2}\ln\left(\frac{|\vec{p}|+p_z}{|\vec{p}|-p_z}\right) = -\ln\tan\frac{\theta}{2}\,. \tag{3.9}$$

η is directly measurable because θ is the lab frame scattering angle, and for most produced SM particles in pp collisions, it well approximates y. Even if the mass or the momentum is unknown, η can still be measured to record part of the particle's kinematical information. Note that, if p_z vanishes, then $\eta \to 0$ and when $p_z \to \pm|\vec{p}|$, $\eta \to \pm\infty$, in contrast to the rapidity y of a massive particle, which is bounded by $\pm\ln(2E/m)$. With η rather than y, the separation measure ΔR becomes purely angular,

$$\Delta R = \sqrt{\Delta\eta^2 + \Delta\phi^2}\,. \tag{3.10}$$

Another advantage lies in the fact that the full lab frame 4-momentum can be expressed in terms of η, ϕ and the easily measurable *transverse momentum* $p_\mathrm{T} = \sqrt{p_x^2 + p_y^2}$ in the highly relativistic case,

$$p^\mu = (m_\mathrm{T}\cosh\eta,\, p_\mathrm{T}\cos\phi,\, p_\mathrm{T}\sin\phi,\, m_\mathrm{T}\sinh\eta) \overset{p\gg m}{\longrightarrow} p_\mathrm{T}\,(\cosh\eta,\,\cos\phi,\,\sin\phi,\,\sinh\eta)\,, \tag{3.11}$$

where the invariant $m_\mathrm{T} = \sqrt{p_\mathrm{T}^2 + m^2}$ is called the particle's *transverse mass* [78]. Furthermore, Lorentz invariance along the z axis implies that differential distributions in y or η are also invariant and can be compared between different experiments.

Rapidity (or pseudorapidity) come in especially handy in the case of a $2 \to 2$ process $(1,2) \leftrightarrow (3,4)$. Additivity of y implies $\hat{y}_3 = -\hat{y}_4 = \hat{y}$, the hat $\hat{}$ denoting partonic CM quantities. Additivity also implies that the measured rapidities are given by

$$y_3 = \hat{y} + y_\mathrm{CM}\,, \qquad y_4 = y_\mathrm{CM} - \hat{y}\,, \tag{3.12}$$

where y_CM is the rapidity of the partonic CM relative to the detector rest frame. We can therefore solve for $\hat{y}_{3,4}$ and y_CM via

$$\hat{y} = \frac{1}{2}(y_3 - y_4)\,, \qquad y_\mathrm{CM} = \frac{1}{2}(y_3 + y_4)\,, \tag{3.13}$$

so together with the measured p_T, we can find the parton-frame scattering angles $\hat{\theta}$ and the 4-momentum of the CM system [270, 282]. Of course, the reason for this is the fact that the final 4-momenta in $2 \to 2$ scattering are completely fixed by the initial 4-momenta.

A final technological point regarding the use of η can be made regarding the segmentation of readout channels in detectors in hadron colliders [283]. Parton-parton collisions generally yield final particle states with quite uniform pseudorapidity distributions. An immediate benefit is that readout modules can be arranged very evenly across the range of detector coverage.

3.1.2.2 Scattering cross section

Clearly, the major task in examining the collider phenomenology of a given model is the computation of the production probabilities of its constituting particles. This probability is given in terms of the *cross section*, as we have seen when discussing the event rate in the previous section. In relativistic quantum field theory, the total cross section for $2 \to n$ scattering in a frame where both particles are incident along the beam axis reads [77, 284]

$$\sigma = \frac{1}{J}\left(\int d\Pi_{i=1}^{n}\right)\left|\mathcal{M}(1,2\to n)\right|^2 (2\pi)^4 \delta^{(4)}\left(p_1+p_2-\sum p_f\right). \tag{3.14}$$

J is the factor describing the flux of incoming particles. It is invariant under boosts along the z direction and has the form [285]

$$J = |\vec{v}_1 - \vec{v}_2| 2E_1 2E_2 = 4\sqrt{(p_1\cdot p_2)^2 - m_1^2 m_2^2}\,. \tag{3.15}$$

If particle 2 is at rest in the lab frame, then $J = 4m_2|\vec{p}_{1,\mathrm{lab}}|$. In the CM frame, $J = 4|\vec{p}_{1,\mathrm{CM}}|\sqrt{s}$, simplifying to $2s$ in the case of negligible masses. The measure

$$d\Pi_i \equiv \frac{\bar{d}^3 p_i}{2E_i}\,, \tag{3.16}$$

with $\bar{d}^3 p$ defined in Equation 2.40, is the Lorentz-invariant phase space element of particle i one is integrating over. For $2 \to 2$ processes, the differential cross section is often expressed in terms of the CM scattering angle or the Mandelstam variable t. Choosing the former, it is given by

$$\frac{d\sigma}{d\cos\theta} = \frac{S}{32\pi s}\frac{|\vec{p}_{3,\mathrm{CM}}|}{|\vec{p}_{1,\mathrm{CM}}|}|\mathcal{M}|^2 = \frac{S}{16\pi}\frac{|\vec{p}_{3,\mathrm{CM}}|}{s^{3/2}}|\mathcal{M}|^2\,, \tag{3.17}$$

for the process $(1,2) \to (3,4)$, after integration over ϕ. For the case $m_3 = m_4 = m$, the expression simplifies to

$$\frac{d\sigma}{d\cos\theta} = \frac{S}{32\pi s}|\mathcal{M}|^2\beta\,, \tag{3.18}$$

where

$$\beta = \sqrt{1-\frac{4m^2}{s}} \tag{3.19}$$

is the speed of the two final state particles in the CM frame. S is the symmetry factor given by $1/n_{\mathrm{id}}!$, where n_{id} is the number of identical particles in the final state. $\mathcal{M}$ is the *invariant matrix element*, *i.e.* the S-matrix element connecting the asymptotic single-particle states $|\{p_{f1},\ldots,p_{fn}\}\rangle$ and $|\{p_{i1},p_{i2}\}\rangle$ at times $t=+\infty$ and $t=-\infty$, respectively, modulo the energy-momentum conserving delta function appearing in Equation 3.14. It is generally calculated in perturbation theory by means of Feynman diagrams according to

$$\begin{aligned} i\mathcal{M} = &\left(\textstyle\prod_{\text{ext. part.}}\sqrt{Z_i}\right)\times(\text{amputated connected diagrams}) \\ &\xrightarrow{\text{ren. PT}} (\text{amputated connected diagrams including counterterms}) \end{aligned} \tag{3.20}$$

The quantities Z_i are the field strengths of the $n+2$ external on-shell fields. In going from the first to second line, we are changing from bare to renormalized perturbation theory. Propagator residues Z_i are then set to 1, which needs to be guaranteed to remain so under radiative corrections by means of renormalization conditions (among further conditions for propagator poles and coupling strengths). Reorganizing the Lagrangian results in counterterm interactions that need to be accounted for if one performs calculations beyond tree-level [77].

3.1.2.3 Decay width, branching ratio and mean lifetime

On-shell particles can be totally stable due to several reasons. For example, a massive particle will not decay if the sum of the masses of the particles it could decay to, as allowed by the structure and symmetries of the Lagrangian, exceeds its own mass, which is clearly an argument based on energy conservation. Similarly, massless particles cannot decay to massive particles. The case of massless particles decaying to other massless particles is, in principle, kinematically allowed if the products are collinear with the initial particle. The question whether a quantum field theory based on a particular Lagrangian allows such a decay is an interesting and highly non-trivial one. In [286], it is proven through Ward identities that all decay amplitues for photons in QED, Yang-Mills bosons in Yang-Mills theories and gravitons in quantum gravity vanish perturbatively. By means of a more qualitative argument, it is shown that, even in the case of amplitudes that diverge when an introduced IR regulator approaches zero, the vanishing of phase space demanded by collinearity overpowers the divergence in the amplitude and the total decay width in these theories therefore vanishes. This is as well the case for a hypothetically unconfined gluon in QCD. Splitting processes mentioned in Section 3.1.1, on the other hand, allow massless particles to 'decay' if they are located in an external field acting as a catalyst and thus enabling conservation of energy and momentum. Consider a photon entering the electric field of a resting nucleus with an energy that is higher than twice the electron mass. Radiative interactions with the QED vacuum will then cause the photon to temporarily split into virtual e^+e^- pairs. It may then happen that these particles absorb photons from the electric field of the nucleus kicking them onto their mass shell, with the nucleus suffering a small recoil; this process is known as pair creation. Photons contained in the electron and positron beams in e^+e^- colliders can also create e^+e^- pairs, since they travel within the electric fields of the electrons and positrons. These processes contribute to the previously mentioned probability functions for encountering $e^\pm$ particles within the beam.

Let us now derive a formula for the *decay rate* Γ of a massive particle, provided it is kinematically allowed and no intrinsic symmetries render it stable. It is well-known that the matrix element $\mathcal{M}(s)$ of a Feynman diagram only develops an imaginary part when certain internal virtual particles go on-shell, namely those states whose propagators can be truncated with a single cut. This imaginary part corresponds to a discontinuity of $\mathcal{M}(s)$ across the branch cut $s > s_{\text{thr}}$, s_{thr} being the squared threshold energy for producing these multiparticle states on their mass shell. Having computed this imaginary part for the amplitude of a $n \to n$ process at a given order with m intermediate states (*i.e.* in loops) in the limit of forward scattering, the optical theorem guarantees that it is proportional to the integral over the m-particle phase space of $|\mathcal{M}(n \to m)|^2$, with the m particles on-shell. Up to an energy-momentum conserving delta function, this means that

$$\text{Im}\mathcal{M}(n \to n) = \frac{1}{2} \sum_f \int d\Pi_f |\mathcal{M}(n \to m_f)|^2 \,. \tag{3.21}$$

This relation can be used to find the decay rate (or *width*) Γ of an unstable particle with physical rest mass m, provided it is long-lived, *i.e.* $\Gamma \ll m$. For that, we use the example of a boson, following [77, 271]. A bosonic propagator $D(p^2)$ is proportional to $1/[p^2 - m_0^2 - \Pi(p^2)]$, where m_0 is the bare mass and $-i\Pi(p^2)$ is the expression for all 1PI insertions into the $1 \to 1$ amplitude,

$$\mathcal{M}(p \to p) = -Z\Pi(p^2) \,. \tag{3.22}$$

Z is the field strength renormalization — a use of renormalized perturbation theory would slightly alter the following arguments, with the main aspect of renormalization constants being absent. The propagator pole is at the physical mass $p^2 = m^2$, lower momenta result in a real value of Π. If p^2 is above this threshold, Π gains an imaginary part and the pole is complex-valued. m is then defined to be the solution of $p^2 - m_0^2 - \text{Re}\Pi(p^2) = 0$ and in the vicinity of the pole, the LSZ formula implies

$$D(p^2) \overset{p^2 \to m^2}{\propto} \frac{iZ}{p^2 - m^2 - iZ\text{Im}\Pi(p^2)} \,. \tag{3.23}$$

An s-channel process with a cross section proportional to the square of the propagator,

$$\sigma \propto \left| \frac{1}{s - m^2 - iZ\mathrm{Im}\Pi(s)} \right|^2 , \tag{3.24}$$

thus exhibits a resonance at $s = m^2$ (without the radiative 1PI insertions, it would blow up at the pole). For small $\mathrm{Im}\Pi(s)$, meaning a narrow width of the resonance, one approximates $\mathrm{Im}\Pi(s) \approx \mathrm{Im}\Pi(m^2)$ and ends up with the Breit-Wigner form of the cross section,

$$\sigma \propto \left| \frac{1}{s - m^2 - iZ\mathrm{Im}\Pi(m^2)} \right|^2 = \frac{1}{(s - m^2)^2 + m^2\Gamma^2} , \tag{3.25}$$

with Equations 3.21 and 3.22 yielding the final form for Γ,

$$\Gamma \equiv -\frac{Z}{m}\mathrm{Im}\Pi(m^2) = \frac{1}{2m}\sum_f \int d\Pi_f |\mathcal{M}(p \to \{p_f\})|^2 \delta^{(4)}\left(p - \sum p_f\right) , \qquad p = (m, \vec{0}) . \tag{3.26}$$

If the particle is not long-lived, this approach is invalid and one has to use the p^2-dependent quantity $\mathrm{Im}\Pi(p^2)$. Note that the matrix element $\mathcal{M}(p \to \{p_f\})$ is the Fourier transform of the amplitude in configuration space, with the temporal coordinate of the initial field taken to $-\infty$. Clearly, this is not appropriate for highly unstable particles, with widths Γ broader than m [77, 287].

In SI units, $\hbar\Gamma$ has units of s^{-1} and corresponds to a particle's decay rate in its rest frame. For instance, the probability for a particle at rest to decay within the time interval $[0, t]$ is given by $1 - \exp(-\Gamma t)$, where we absorbed the reduced Planck constant $\hbar$ in Γ, defining the latter as the decay rate. Under boosts, it transforms as $\Gamma \to \Gamma/\gamma$. The reciprocal of Γ is the particle's *mean lifetime*

$$\tau = \frac{1}{\Gamma} \tag{3.27}$$

and expresses the expectation value of t using an exponential distribution for the decay probability. These quantities are discussed in more detail in Section 4.3.

The statistical fraction of decays to a particular final state i out of all available decay products is called the *branching ratio* (BR),

$$\mathcal{B}_i = \frac{\Gamma_i}{\Gamma} = \frac{\Gamma_i}{\sum_j \Gamma_j} , \tag{3.28}$$

where Γ_i is the partial decay width for the decay to the state i. The BR is one of the most important observables in collider experiments, as it allows to verify the correctness of a model's prediction regarding the frequency of certain decays. It is especially useful in the case of highly-peaked narrow widths, *i.e.* long mean lifetimes. One usually checks for the conditions that Γ be much smaller than the decaying and resonant particle's masses, m and m^*, and that the scattering energy s be much larger than m^*. Furthermore, non-resonant processes shouldn't interfere considerably [288]. Then, cross sections involving a resonant intermediate particle ψ^* can be approximated as

$$\sigma(i \to \psi^* + \ldots, \psi^* \to k) \quad \longrightarrow \quad \sigma(i \to \psi + \ldots) \times \mathcal{B}(\psi \to k) , \tag{3.29}$$

so the resonance is treated as an on-shell particle subsequently decaying to a final state k a fraction $\mathcal{B}(\psi \to k)$ of times. This method is known as the *narrow width approximation* [289]. For a derivation and a discussion of potential problems regarding specific instances of its usage, see *e.g.* [288, 290].

3.1.3 Total hadronic scattering cross section and parton distribution functions

As mentioned in Section 3.1.1, inelastic hadronic collisions have the inherent complication that one does not a priori know which constituents of the hadrons are colliding and what is the speed of the CM relative to the lab frame, unless one completely reconstructs the final state. Similar to electron beams consisting of electrons, positrons and photons, hadrons consist of partons (quarks and gluons) and their interactions being reigned by QCD makes the theoretical analysis considerably more involved. The complications are

encoded in parton distribution functions (PDFs), which need to be taken from experiment [284].

Consider an inelastic pp collision to an inclusive final state $Y + X$, where Y is the final state of interest and X are the unimportant collision remnants. At a pp CM energy $\sqrt{s}$, the total cross section is calculated by summing over the cross sections of individual parton-parton collisions happening at CM energies $\sqrt{\hat{s}}$ weighted by the associated parton distribution functions [271],

$$\begin{aligned}\sigma(p(P_1) + p(P_2) \to Y + X;\ s) \\ = \int_0^1 dx_1 \int_0^1 dx_2 \sum_{i_1,i_2} f_{i_1}(x_1, \mu_\mathrm{F}) f_{i_2}(x_2, \mu_\mathrm{F})\, \hat{\sigma}\left(i_1(x_1 P_1) + i_2(x_2 P_2) \to Y;\ \hat{s} = \tau s\right) .\end{aligned} \tag{3.30}$$

Here, $P_{1,2}$ are the proton 4-momenta, $x_{1,2}$ are the momentum fractions carried by the partons $i_{1,2}$ (the *Bjorken-x*) and $\hat{\sigma}$ is the partonic cross section. For protons, i_k ($\bar{i}_k$) can be the quark (antiquark) flavours u, d, s, c, b ($\bar{u}$, $\bar{d}$, $\bar{s}$, $\bar{c}$, $\bar{b}$) or the gluon g. Top quarks are too mass-suppressed to appear as sea quarks. Most importantly, the parton distribution functions $f_{i_k}(x_k)$ give the probability of finding a parton of the type i_k with a fraction x_k of the proton's momentum P_k. μ_F is the *factorization scale*, an energy scale we introduce below.

In the protons' rest frame (or the detector frame, for that matter), the parton CM frame will move with a speed $\beta = (x_1 - x_2)/(x_1 + x_2)$ and

$$P_{1,2} = (P, 0, 0, \pm P)\,, \qquad s = 4P^2\,, \qquad \tau \equiv \frac{\hat{s}}{s} = x_1 x_2\,, \tag{3.31}$$

τ being the so-called *Drell-Yan variable*. Integration over one fraction simplifies Equation 3.30 to

$$\sigma(p(P_1) + p(P_2) \to Y + X;\ s) = \int_{\tau_\mathrm{thr}}^1 d\tau \sum_{i_1,i_2} \frac{d\mathcal{L}_{i_1 i_2}}{d\tau}\, \hat{\sigma}\left(i_1 + i_2 \to Y;\ \hat{s} = \tau s\right) , \tag{3.32}$$

where τ_thr is the lower threshold for τ (minimal fraction of s to produce the final state) and

$$\frac{d\mathcal{L}_{i_1 i_2}}{d\tau} = \int_0^1 \frac{dx}{x} f_{i_1}(x, \mu_\mathrm{F}) f_{i_2}(\tau/x, \mu_\mathrm{F}) \tag{3.33}$$

is the *luminosity function*[4] for the specified colliding parton types [291]. We shall revert to this notation in our analysis in Chapter 5.

We now briefly discuss the meaning of the factorization scale μ_F, following [271] and [284]. In short, it is a rather arbitrary energy scale quantifying where exactly to set the transition between a 'hard' process with transverse momenta $> \mu_\mathrm{F}$ contributing the calculable small-distance part of the cross section and 'soft' processes with very collinear partons, *i.e.* with transverse momenta $< \mu_\mathrm{F}$. If two particles interact via QCD and are very collinear, their interactions will be too strong to be calculated perturbatively and their effects need to be experimentally determined. Collinear (mass) divergences belong to the problematic IR behaviour in quantum field theories involving massless particles. The Kinoshita-Lee-Nauenberg (KLN) theorem [292], a generalization of the Bloch-Nordsieck theorem in QED [293], states that all observables in the SM are IR safe at any perturbative order in the massless particle limit, provided one adds up the S-matrix elements for all indistinguishable initial and final states, $\sum_{\mathrm{i,f}} |S_{\mathrm{i}\to\mathrm{f}}|^2$, and integrates over phase space.[5] That is, the more inclusive the calculation of an observable is, the less it will be driven to infinities by non-perturbative effects. In practice, the KLN theorem implies the cancellation of soft and collinear/mass divergences except for the case of mass divergences from ingoing lines in the calculation of physical cross sections with coloured particles in the initial state because one cannot prepare an initial state with an ingoing jet, for instance. These remaining (logarithmic) divergences, *e.g.* due to collinear gluon emission by an initial (massless) quark, are absorbed in the PDFs, with the factorization scale μ_F determining at what energy to separate perturbative from non-perturbative effects arising due to collinearity. This procedure resembles

[4] It is not to be confused with the beam spread function, mentioned earlier, denoted by the same symbol.

[5] The Bloch-Nordsieck theorem only refers to QED with massive electrons and only demands the addition over final states. This is not sufficient in QCD.

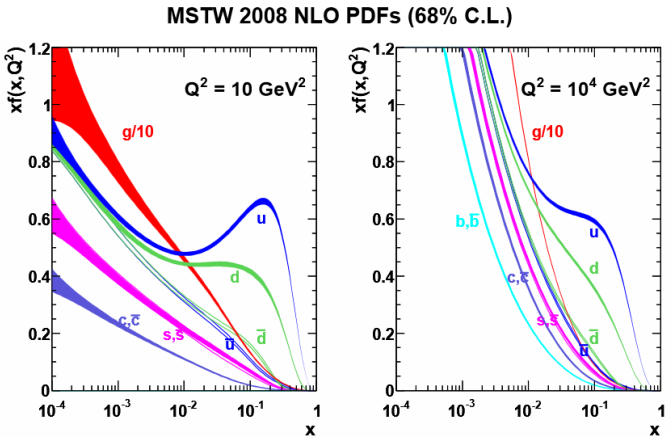

FIGURE 3.2: NLO MSTW-2008 parton distribution functions at energy scales $Q^2 = 10$ GeV^2 (left) and $Q^2 = 10^4$ GeV^2 (right) in the range $x \in [10^{-4}, 1]$, taken from [295]. Uncertainties are represented as varying thicknesses.

UV renormalization, where the renormalization scale μ_R is regarded as the characteristic scale for the high-energy behaviour of the theory, with comparatively light degrees of freedom being integrated out. In fact, one often sets $\mu_\mathrm{F} = \mu_\mathrm{R}$, both of the order of the transferred momentum [291] and uncertainty bands are usually given by varying μ_F in the range $[\frac{1}{2}\mu_\mathrm{R}, 2\mu_\mathrm{R}]$. Similarly to the RGEs describing the UV evolution of observables with μ_R, the evolution of observables with μ_F is translated to the variation of the PDFs, as described by the Dokshitzer–Gribov–Lipatov–Altarelli–Parisi (DGLAP) equations [294]. These replace μ_F by Q, the energy scale at which the proton is being probed. The four splitting processes ($q \to qg$, $q \to gq$, $g \to qg$, $g \to gg$), equivalent to the splitting processes in electron beams (*cf.* Section 3.1.1), then contribute much (little) to the running if Q is small (large), a direct consequence of asymptotic freedom. As an example, the gluon PDF evolves as

$$\frac{\partial f_g(x,Q)}{\partial \ln Q} = \frac{\alpha_\mathrm{s}(Q)}{\pi} \int_x^1 \frac{dz}{z} \left\{ P_{gq}(z) \sum_q \left[f_q(x/z,Q) + f_{\bar{q}}(x/z,Q) \right] + P_{gg}(z) f_g(x/z,Q) \right\} , \tag{3.34}$$

the leading-order splitting functions P_{ij} for splittings $j \to i$ are given in [77], for instance. Clearly, increasing scales Q lead to a slower evolution due to asymptotic freedom. Contrary to the corresponding $e^\pm$ and γ evolution equations in QED, the DGLAP equations cannot be solved by integration because the unknown nature of QCD at low energies precludes the imposition of appropriate initial conditions; one is therefore exclusively bound to experimental measurements.

PDFs are probed in various kinds of processes, such as deep inelastic scattering (DIS), neutrino-nucleon scattering, fixed-target experiments and inclusive jet production [271]. Each process is controlled to happen at a given energy scale Q and is sensitive to a specific set of PDFs in a particular x range. For instance, DIS experiments conducted at the HERA collider ($e^\pm p$) probed the gluon and quark PDFs up to the c quark by measuring the proton structure functions $F_1(x,Q)$ and $F_2(x,Q)$. From data, dedicated collaborations produce sets of PDFs by fitting their values for given x and Q, such as CTEQ [296], MSTW [295] and NNPDF [297], and evolving them to other values through the DGLAP equations at tree-level and higher orders. PDFs induce large uncertainties in the calculation of observables such as hadronic cross sections due to the uncertainties in their determination. These stem from systematic and statistical errors in measurements, theoretical errors and, mostly, the method to extract the PDFs from data [298]. We show in Figure 3.2 two exemplary sets of MSTW-2008 PDFs at different energy scales from Reference [295], also indicating the uncertainties as line widths. Parton evolutions are calculated at NLO. We notice that the gluon PDF is completely dominating over the quark content below the region mainly dominated by valence quarks, $x \gtrsim 0.1$. The lower x, the more gluons populate the proton and the more the valence quark flavours become purely sea quarks. Note that, with increasing Q, more partons are emitted by the original

partons, thus lowering the momentum fractions and leading to a concentration of the PDFs at lower x values.

3.2 The Large Hadron Collider, ATLAS and CMS

In this section, some general and some technical details about the LHC and the ATLAS and CMS experiments are reviewed. Whereas the description of the LHC is more directed towards inserting the two experiments into the larger picture, the discussions of the experiments are necessary in order to understand our procedure in analysing long-lived particle scenarios. Those sections are supplemented by Appendix E.

3.2.1 The Large Hadron Collider

3.2.1.1 Generalities and some specifications

The LHC [31, 299] is the world's largest storage ring particle collider, located at CERN near Geneva (Switzerland). Accelerated particles are protons and lead ions, which are grouped in the counter-rotating beams as bunches. Its tunnel previously harboured the LEP collider; LEP was operational during the 11-year period of 1989-2000, see Table 3.1. History of conception and development dates back to the early 1980s and its construction was officially approved in 1994 [300]. With the unprecedented nominal pp (Pb^+-Pb^+) beam energy of 7 TeV (2.76 TeV/nucleon) and a design luminosity of 10^{34} (10^{27}) $\mathrm{cm}^{-2}\,\mathrm{s}^{-1}$, it is designed to produce about $\sim 10^9$ (~ 8000) inelastic collisions per second, with a collision cross section at $\sqrt{s} = 14$ (574) TeV that amounts to roughly 100 mb (7.7 b) [301, 302]. With its two general-purpose detectors ATLAS and CMS providing independent measurements, the LHC aims to explore the mechanism of spontaneous symmetry breaking, believed to occur via the Higgs mechanism, and to search for BSM physics, such as sypersymmetry, extra dimensions, dark matter and new heavy gauge bosons, to name a few. As was discussed in the introduction, part of the Higgs mechanism is likely to have been unlocked with the discovery of a Higgs boson in 2012 [5, 6]. Apart from that, the LHC opens a large window into top quark physics, a task the Tevatron was not powerful enough for (while the Tevatron produced several thousands of tops, the LHC will produce tens per second due to the much higher cross section and luminosity [303, 304]). There are two more big LHC experiments for more specialized studies. LHCb (LHC beauty) [305] is a detector measuring parameters mainly related to CP violation and rare decays within the B meson system. ALICE (A Large Ion Collider Experiment) [306] records the products of collisions of Pb ions. It aims to explore strongly interacting matter at extreme energies and studies the possibility of the formation of quark gluon plasma (QGP), a phase believed to have occurred in the early Universe before the QCD phase transition to confined states, *cf.* Table 2.3. While ALICE is principally dedicated to heavy-ion physics, the other three large detectors are also capable to detect products of heavy ion collisions [307], whereas ALICE can also detect proton-proton events [308]. Three further smaller detectors for very specialized measurements are LHCf, TOTEM and MoEDAL, located at large distances in the very forward regions of ATLAS, CMS and LHCb, respectively.

For protection against radiation and to reduce the contamination of recorded events with cosmic muons, the LHC tunnel lies at about 50 to 175 meters below ground. It is not a perfect ring, but a sequence of eight arcs connected by straight sections, each containing an interaction point where the beams are acted upon. IP1, IP2, IP5, IP8 are the sites of ATLAS, ALICE, CMS and LHCb, respectively. At IP3 and IP7, the beams are collimated and IP6 is the beam dump point, where the beam is ejected from the ring. Finally, IP4 contains RF cavities for beam acceleration. 1232 (392) superconducting dipole (quadrupole) magnets are installed to steer the beams. Figure 3.3 shows a schematic of the full accelerator complex at CERN. As was the case with LEP, LHC makes use of older CERN accelerators for pre-acceleration. Most of these accelerators are also used for measurements at lower energies. We now describe the acceleration chain as it prevailed during the first period of data taking (Run I, 2010-2013) [31]. First, LINAC2 (LINAC3) accelerates protons (Pb ions) to an energy of 50 MeV (4.2 MeV/u). The protons (Pb ions) are then

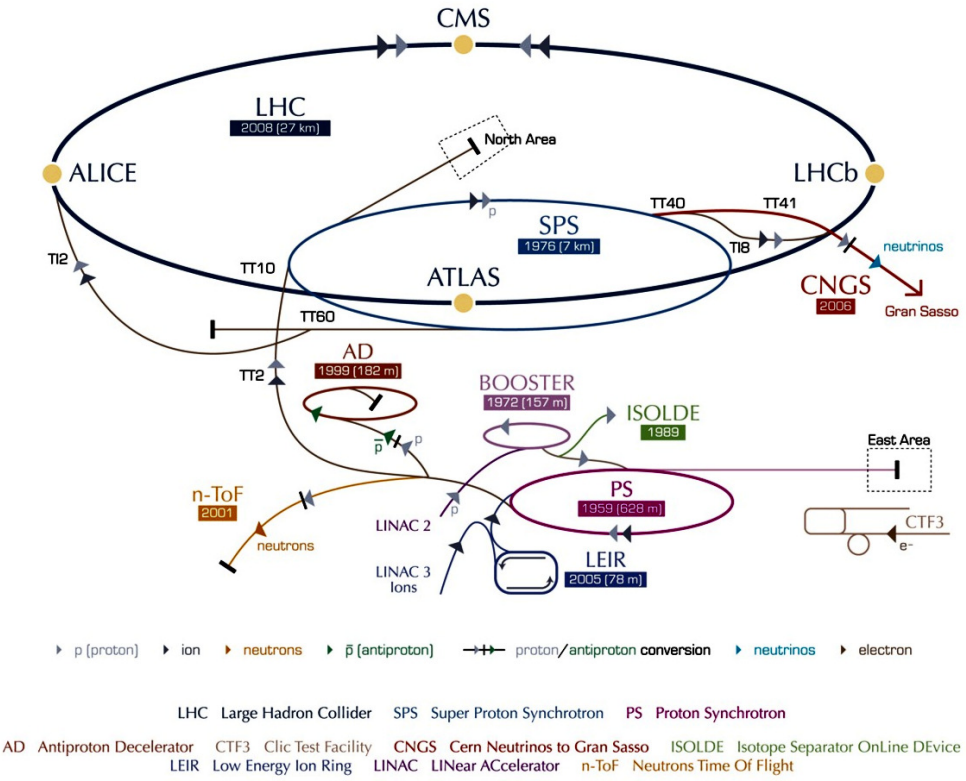

FIGURE 3.3: Schematic diagram of all accelerators and some experiments at CERN, showing also the LHC injector chain. Numbers below names are starting years of operation and accelerator dimensions. Image Credit: CERN.

accelerated to 1.4 GeV (72 MeV/u) in the PS booster (LEIR) and are then passed to the PS, providing further acceleration to 25 GeV (5.9 GeV/u). The particles are then injected into the SPS, which accelerates them to 450 GeV (177 GeV/u) until they are fed into the LHC, the final link in the chain. In 2010-2011, the LHC boosted proton energies to 3.5 TeV, meaning that the $^{208}Pb^{+}$ beams were accelerated to 1.38 TeV per nucleon during the two heavy ion runs in that period. This corresponds to 287 TeV per beam and a CM energy of 2.76 TeV per nucleon pair. In 2012, the year of the Higgs boson discovery, only protons circulated in the pipe in data-taking runs, with an energy of 4 TeV per beam. Finally, in the beginning of 2013, protons and Pb ions were collided for the ALICE detector at a CM energy of 5.02 TeV per nucleon pair. At the time of writing, the LHC is acquiring data for Run II and is accelerating protons at a CM energy of 13 TeV. A series of significant updates is in store and is discussed *e.g.* in [309].

3.2.1.2 Bunch structure and non-collision backgrounds

We shall require some information about the bunch structure of the injected proton beams for Analyses IIA and IIB. Detailed discussions can be found in References [310] and [311]. The RF system of proton bunch injection provides a certain number of bunch slots per beam with a given temporal separation that can be filled according to preset *filling schemes*. At nominal service, a filled bunch contains about 1.15×10^{11} protons and the LHC's RF frequency of 400.79 MHz allows for 35640 bunch slots that could be filled with protons. The LHC finds the optimal scheme to be the '3564' or '334334334333' scheme [311], featuring 3564 slots with a separation of 25 ns (40 MHz) and is depicted in Figure 3.4. Note that not all 3564 slots are filled due to time intervals necessary for injection and extraction happening from PS via SPS to LHC executed with kicker magnets. 72 filled bunches form a *batch* and groups of n batches are called *n-batches* or *bunch trains*. The 3564 scheme provides each beam with three 4-batches and nine 3-batches, amounting to 2808 filled bunches. However, in 2011 and 2012, the temporal separation between filled slots

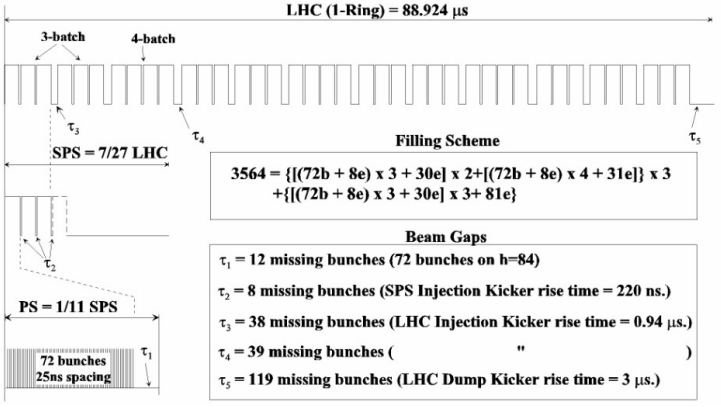

FIGURE 3.4: The nominal LHC proton bunch filling scheme [311]. During Run I, filled bunch slots in batches were separated by unfilled slots, leading to a time separation of 50 ns instead of the nominal 25 ns.

within a batch was 50 ns, a choice that leads 1380 filled bunches per beam and bunch crossings (BX) at every 50 ns in the detectors. Whereas filled bunches contain $\sim 10^{11}$ protons, unfilled bunches contain $< 10^8$ protons [46]. There are consequently the following types of BX: so-called *paired* crossings consist of two crossing filled bunch slots, *unpaired* crossings consist of a filled and an unfilled crossing slot and in *empty* crossings, two unfilled bunches cross. In standard searches, the collaborations use data from collisions happening in paired crossings. Events recorded during filled BX and empty BX periods each flow into separate data streams. Whether current bunches from beam 1 and beam 2 are filled or unfilled is determined by means of two beam position and timing monitors (BPTX) positioned close to the beam at either end of the detectors, which can detect the passage of a filled proton bunch.

A further significant point of concern of technical nature regarding Analysis IIB are the *non-collision backgrounds* (NCB). These leave hits in the detectors at random times and therefore need to be considered in combination with the temporal bunch structure [312]. NCBs consist of cosmic muons and *beam-induced backgrounds* (BIB). The latter contribute to the beam loss and are caused by interactions of the protons upstream from the IP, creating secondary particle cascades that evolve parallel to the beam line which can reach the detector and contaminate data samples used for physics analyses. They are subdivided by some authors into *beam-halo* and *beam-gas* backgrounds. The former has its origin in interactions with material outside the pipe forming a halo of products travelling along with the beam in its supposedly low-density regions, the latter stems from collisions with the protons from residual gas within the beam pipe [313]. While cosmic backgrounds happen at a constant rate on average, BIB rates increase in part proportionally with the luminosity. Moreover, they increase with the proton beam energy because particles in the cascades generally suffer a higher boost and therefore more easily overcome energy thresholds imposed by online and/or offline cuts: The squared CM energy $\sqrt{s}$ of a beam proton with energy E colliding with a proton at rest is approximately $\sqrt{2Em_p}$ (*cf.* Equation 3.3) — Thus, comparing for instance the pp CM energies at LHC of $\sqrt{s} = 8$ TeV and 14 TeV, the CM energy between the colliding protons in the BIB reaction is

$$\sqrt{\bar{s}}_{14} = 114.59 \text{ GeV} = \frac{\gamma_{\text{CM},14}}{\gamma_{\text{CM},8}} \times \sqrt{\bar{s}}_8 = \frac{61.08}{46.18} \times \sqrt{\bar{s}}_8 = 1.32 \times \sqrt{\bar{s}}_8 = 1.32 \times 86.63 \text{ GeV}\,, \tag{3.35}$$

with $\gamma_{\text{CM}} = \sqrt{\bar{s}}/(2m_p)$ being the Lorentz boost of the CM of the colliding protons. Therefore, boost factors E/m of cascade particles, such as muons, can be higher at nominal operation than during the 8 TeV LHC run by a maximum factor of

$$\frac{\gamma_{\text{CM}}\gamma_{\mu,\text{CM}}(1+\beta_{\text{CM}}\beta_{\mu,\text{CM}})|_{14}}{\gamma_{\text{CM}}\gamma_{\mu,\text{CM}}(1+\beta_{\text{CM}}\beta_{\mu,\text{CM}})|_{8}} = 1.32 \times \frac{\gamma_{\mu,\text{CM}}(1+\beta_{\text{CM}}\beta_{\mu,\text{CM}})|_{14}}{\gamma_{\mu,\text{CM}}(1+\beta_{\text{CM}}\beta_{\mu,\text{CM}})|_{8}}\,, \tag{3.36}$$

where $\gamma_{\mu,\text{CM}}$ is the boost of the produced muon in the pp CM frame with a momentum directed parallel

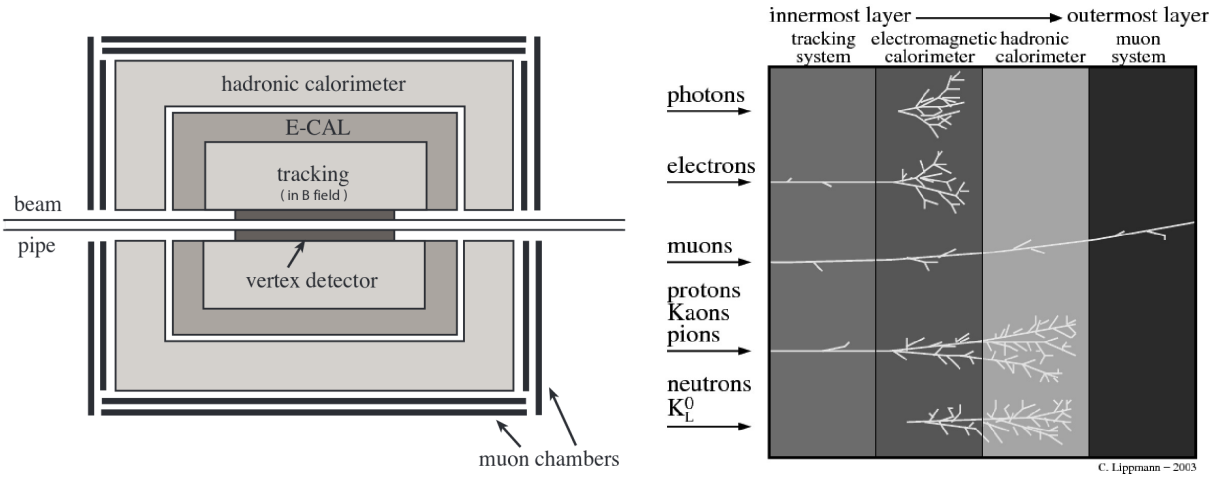

FIGURE 3.5: *Left panel:* Typical layout of a high-energy particle detector. Image taken from [269]. *Right panel:* Detector components used for absorption and particle identification. Image taken from [314].

to the beam line and β_{CM} ($\beta_{\mu,\mathrm{CM}}$) is the CM (muon) velocity in the laboratory (CM) frame. Here, $\beta_{\mathrm{CM}}|_{14}$ and $\beta_{\mathrm{CM}}|_{8}$ have a negligible difference of about 10^{-4}, but the higher CM energy allows for higher muon boosts $\gamma_{\mu,\mathrm{CM}}$. Higher collision energies therefore require a much better understanding of these types of backgrounds, as they can interfere considerably with measurements.

3.2.2 The ATLAS and CMS experiments

Before treating the features specific to the ATLAS and CMS detectors, we first discuss their common aspects and general characteristics of all same-type particle detectors, to avoid redundancy. The goal is not to merely understand the principles of particle detectors, but to also gather the necessary information for a computational implementation of simplified versions of ATLAS and CMS.

Both experiments intend to explore physics at the high-energy frontier and therefore require large dense structures to absorb the tremendous amounts of energy created in the pp collisions. Their geometry is described by a right-handed coordinate system centered in the nominal interaction point, where the proton beam defines the z axis and the $x-y$ plane is transverse to the beam, with the positive x-axis (y-axis) pointing towards the center of the LHC ring (upwards). More commonly, one uses a combination of cylindrical coordinates (z, $\phi = \sphericalangle(\vec{x}, \vec{y})$) with the pseudorapidity coordinate η to describe event kinematics and detector geometry specifications. These coordinates are especially adapted to the typical geometry of the detectors, whose onion-like stratified layers always consist of a cylindrical *barrel* part (low pseudorapidities) and a circular *endcap* part in the forward regions (high pseudorapidities). They are structured as schematically depicted in the left panel of Figure 3.5. An inner detector (ID) (or inner tracker) immersed in a strong magnetic field bending the trajectories of charged particles contains a vertexing and a tracking system. By measuring the track curvature radius ρ through the sagitta, one can measure the particle's transverse momentum p_{T} in GeV through $p_{\mathrm{T}} \approx 0.003 B\rho$, where ρ is to be given in cm and B in T [315]. Moreover, measuring the energy loss in the tracking modules and the particle's speed, one can infer the mass (*cf.* Section 4.2.2). Surrounding the ID, there is a dense module for electromagnetic and one for hadronic calorimetry (ECAL, HCAL). The former absorbs electron and photon radiation and the latter is intended to absorb hadrons (protons, neutrons, pions, etc.). These can occur in the form of single isolated particles or electromagnetic/hadronic showers (*cf.* Section 3.1.1). Characteristic interaction lengths of electrons and photons within the ECAL are considerably shorter than the interaction lengths of hadrons in the HCAL, therefore the HCAL is generally thicker than the ECAL and cannot be placed before it. As for materials, there are *sampling calorimeters* and *homogeneous calorimeters*, the former employing alternating layers of

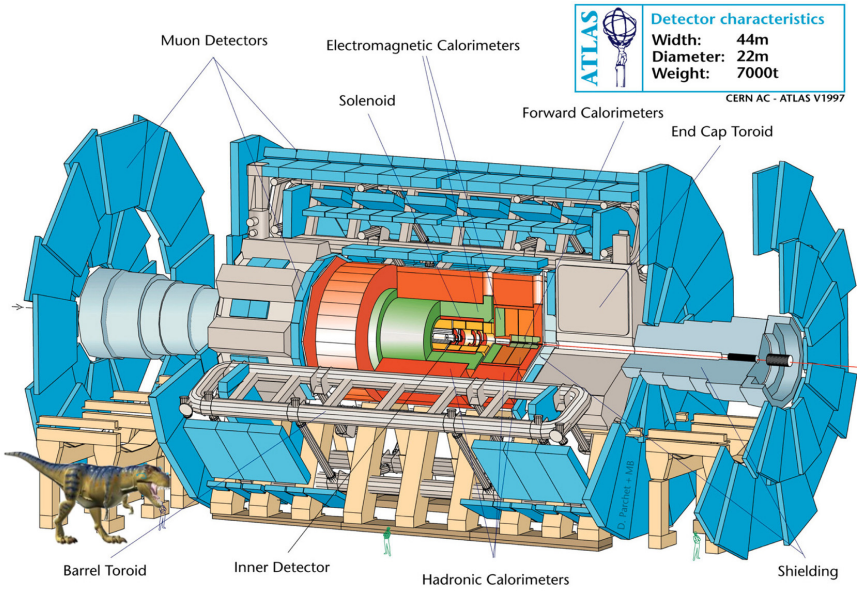

FIGURE 3.6: Cutaway view on the ATLAS detector with its main modules and muon spectrometer subsystems specified. The detector schematic has been found on the web [319]. For illustration of the scale, a Tyrannosaurus Rex has been added to the persons in front (length up to ~ 12.4 m [320]). Idea taken from Figure 3.1 in [321].

absorber and radiator materials and the latter consisting of a single material type. The outermost system is dedicated to muon spectroscopy. Since muons are minimally ionizing (*cf.* Section 4.2.2), they interact very weakly with the calorimeters and are therefore not absorbed. Hence, muon systems (MS) external to the calorimetry sectors are employed to track their trajectories. The four detection layers are shown in the right panel of Figure 3.5. Due to the high energies and huge fluxes of collision products, stringent technological requirements are imposed on the LHC detectors [303, 316]. For instance, all used materials for detection and front-end signal readout need to be highly radiation-resistant. Moreover, readout electronics have to be very fast: Both detectors employ hardware-level triggers constructed from custom-made electronics with a design accept rate of ~ 100 kHz and decisions need to be pipelined from the calorimeters and muon detectors to the front-end electronics of high-level triggering within 2.5 μs (3.2 μs) in ATLAS (CMS) after the associated bunch crossing. Each second, the triggers of both experiments select several hundred events tagged as potentially interesting out of the $\sim 10^9$ pp collisions. The two trigger systems are discussed and compared in [317]. They also have to be efficient at rejecting jets from QCD background over large energy ranges and p_{T} measurements of relatively low-energetic leptons need to be very precise, as required by Higgs searches involving leptonic channels [318]. This requires very fast tracking and vertexing algorithms, in particular good impact parameter resolutions are needed to distinguish primary and secondary interaction vertices and to tag for c- and b-flavoured objects, τ leptons and other long-lived particles. More physics-motivated requirements on the trigger systems are listed in [317]. The detectors also need feature a high acceptance range in readout channels with a fine granularity and a very good energy resolution in the calorimeters and muon systems. These conditions are in part also motivated through the goal of performing Higgs searches. For instance, a Higgs mass below $2m_Z$ (as has been experimentally verified), renders the decay $h \to \gamma\gamma$ a very important one and hence the energy resolution of the ECALs needs to be excellent.

We next describe the ATLAS and CMS detectors by mentioning their generic and main defining features. More detailed discussions required for the detector simulation are contained in Appendix E.

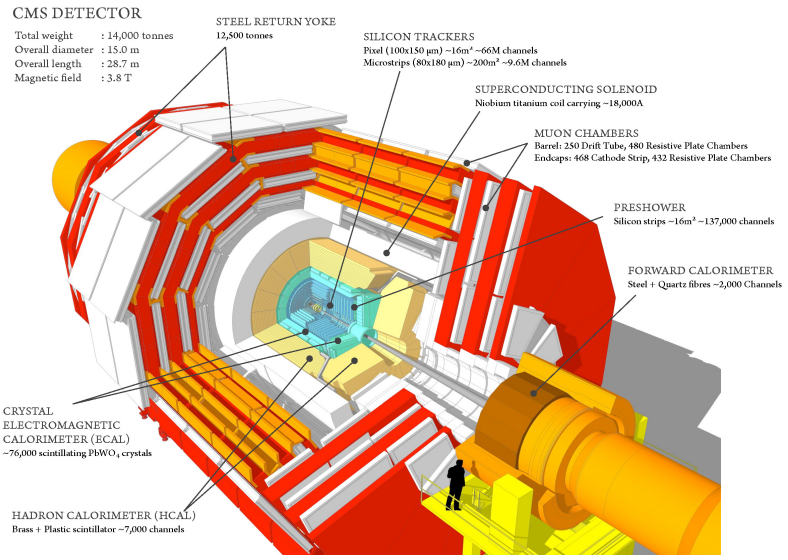

FIGURE 3.7: Cutaway view on the CMS detector with its main modules and several technical details specified. Image taken from [324].

3.2.2.1 ATLAS

ATLAS (A Toroidal LHC ApparatuS) [303, 322] is thus far the largest particle detector ever constructed. It is depicted in Figure 3.6, including information about its approximate overall dimensions and weight. The fundamental feature determining the design of ATLAS and CMS is the magnet structure. ATLAS uses a superconducting central solenoid located between the ID and calorimeters to create a magnetic field with a strength of 2 T at the center of the inner tracker to measure charged particles' momenta p and p_{T} and eight superconducting toroidal coils interspersed with the muon chambers with a strength of about 1 T for muon tracking, p_{T} measurement and triggering [323]. All calorimeters employed in the ATLAS detector are sampling calorimeters.

The triggering system of ATLAS comprises three levels [322]. Level-1 (L1) is hardware-based and uses reduced-granularity information from several detector parts to trigger for high-p_{T} muons, electromagnetic and hadronic clusters, τ-leptons, $\not{E}_{\mathrm{T}}$ and large transverse momentum, which occurs in every bunch crossing. During Run I, it operated at 75 kHz, but has been upgraded to a rate of 100 kHz during the long shutdown period preceding Run II due to the increased instantaneous luminosity [325]. L1 creates regions of interest (RoI) around the triggered objects and feeds them into the also hardware-based level-2 (L2) trigger, where the events are processed and reduced to an accept rate of about 3.5 kHz. Finally, the offline event filter (EF) further processes the events and reduces the number to a manageable amount corresponding to a rate of 200 Hz, followed by storage of the information to hard disk. Together with L2, the EF forms the high-level trigger (HLT). Some standard cuts imposed by the trigger system on charged tracks are $|\eta| < 2.5$, $p_{\mathrm{T}} > 1$ GeV, $d_0 < 2$ mm and $|z_0 - z_{\mathrm{pv}}| < 10$ mm, where d_0 is the transverse impact parameter and z_0 (z_{pv}) is the z coordinate of the vertex (primary vertex), see [326, 327] and Section 3 in [322]. The latter two cuts constrain the standard searches to promptly produced particles, *i.e.* particles whose tracks originate from within a small vicinity around the IP. Thus the bulk of searches is insensitive to scenarios containing long-lived particles with significantly displaced vertices. Such particles can in principle be looked for though, because using dedicated settings for the trigger systems could allow for impact parameters up to ~ 1 m [328].

3.2.2.2 CMS

CMS (Compact Muon Solenoid) [316], like ATLAS, is a general-purpose detector aiming to maximize acceptances through high coverages of measured kinematical quantities. A schematic view is shown in Figure 3.7. Its design is distinguished by the design of ATLAS in two aspects: First, it is only about two thirds in size, thus requiring the use of much denser materials for particle absorption. In fact, the densities are so high that, even though it is considerably smaller, CMS weighs about twice as much as ATLAS. Second, while it also features a central solenoid bending particle tracks in the ID, it does not opt for a toroid in the muon system but rather closes the solenoidal magnetic field by placing flux return yoke layers made from iron between the layers containing the muon chamber plates. Within the ID, the solenoid creates a magnetic flux density of 3.8 T, whereas in the barrel wheels (endcap disk), it varies from 0.6 T to 2.1 T (1.4 T to 2.1 T) [329]. Its calorimetric structure is identical to the structure in ATLAS, though the solenoid lies outside the ECAL and HCAL and the used materials are in part very different. Contrary to ATLAS, its ECAL is not a sampling but a homogeneous calorimeter made from lead tungsten ($PbWO_4$). As the name suggests, it is highly specialized in efficient muon detection and accurate muon event reconstruction. Combining muon tracks in the ID and the MS through a global fit, offline muon p_T resolutions are reduced to at most 1% (5%) for low (high) transverse momenta, which is superior to the p_T determination in ATLAS. Motivation for excellence in muon momentum and charge measurement was especially drawn from the 'golden' Higgs decay channel $h \to ZZ^{(*)} \to 4\mu$ for a Higgs mass in the region $m_h > 130$ GeV. The trigger structure is similar to that of ATLAS, though a 2-level instead of a 3-level system is used in the form of a hardware-based L1 trigger and a software-based HLT [330]. Like with ATLAS, the recorded event rate is 100 kHz. The maximally allowed impact parameter for a charged track in standard tracking algorithms is also in the 1 mm range, depending on the impact parameter computed at the various ID stations [331].

3.2.3 Simplified detectors for simulations

The preceding descriptions of the ATLAS and CMS detectors serve as the basis for the more thorough treatments in Appendix E. Analyses IIA and IIB both require geometrical input, while Analysis IIB also crucially depends on calorimeter material properties, since it is a study of the deceleration of heavy charged particles by these very dense modules. For this end, the Bethe-Bloch equation is the appropriate tool for our goals and its introduction is postponed to the next chapter. It is a differential equation describing the mean rate $\langle -dE/dx \rangle$ of the loss of total energy as a relativistic charged particle with a moderate velocity interacts with the electrons of the medium. To compute the stopping distances of slow particles emitted in a given direction with a given velocity, we solve the equation for simplified implementations of ATLAS and CMS with geometries and material constants described in the accompanying appendix. The material constants are the mean (sampling) densities $\langle \rho \rangle$, the mean electronic excitation energies $\langle I \rangle$ and the mean ratios of the atomic number and atomic weight of the medium, $\langle Z/A \rangle$. More realistic outcomes could be obtained with dedicated detector simulation software, such as Geant4 [332], though our level of ambition rather justifies the creation of a more simplified Mathematica [333] code which exclusively serves our purposes. While other theoretical analyses of scenarios featuring heavy long-lived particles also employ the Bethe-Bloch equation (see *e.g.* [334, 335]), we go a step further in realism by avoiding crude approximations such as ignoring radiator layers and implementing spherical detectors. Considering the cylindrical nature is important because a particle traversing the barrel part with a large pseudorapidity will penetrate significantly more calorimeter material than a particle with a low pseudorapidity, thus interacting with the detector along a longer path.

The relevant details of our toy detectors are summarized in Table 3.2 and the calorimeters are schematically drawn in Figures 3.8a and 3.8b. The CMS EB and EE thicknesses vary with z and y, respectively. Since the crystals all have approximately the same length and point towards the interaction point (with a tilt angle of 3° that we neglect), the particle will always travel through the same path length in the ECAL barrel or endcap. For simplicity, the short gap between the back faces of the crystals and the inner edge of

Layer	Δ [cm]	$[\lvert\eta\rvert_{\min}, \lvert\eta\rvert_{\max}]$	Material	$\langle\rho\rangle$ [g/cm^3]	$\langle I\rangle$ [eV]	$\langle Z/A\rangle$
ATLAS Barrel						
ID+Sol.	150.0	[0, 1.4]	Vacuum	-	-	-
EMB R1	47.5	[0, 0.8]	LAr+Pb	4.01	487	0.406
EMB R2	47.5	[0.8, 1.4]	LAr+Pb	3.67	447	0.408
HLB+HEB	197.0	[0, 1.4]	Fe+PS	6.40	286	0.466
MS+Tor.	∞/1000.0	[0, 1.05]	Vacuum	-	-	-
ATLAS Endcap						
ID+Sol.	370.4	[1.4, 3.2]	Vacuum	-	-	-
EMEC R3 (o. w.)	51.0	[1.4, 2.5]	LAr+Pb	5.01	601	0.399
EMEC R4 (i. w.)	51.0	[2.5, 3.2]	LAr+Pb	5.39	624	0.399
HEC	177.8	[1.4, 3.2]	LAr+Cu	7.48	322	0.456
MS+Tor.	∞/2150.0	[1.05, 2.7]	Vacuum	-	-	-
CMS Barrel						
ID	129.0	[0, 1.4]	Vacuum	-	-	-
EB	23.0	[0, 1.4]	$PbWO_4$	8.28	601	0.413
HB	96.0	[0, 1.4]	Brass+PS	7.22	324	0.457
MS+Sol.+Yoke	∞/738.0	[0, 1.2]	Vacuum	-	-	-
CMS Endcap						
ID	317.0	[1.4, 3.0]	Vacuum	-	-	-
EE	22.0	[1.4, 3.0]	$PbWO_4$	8.28	601	0.413
HE	168.4	[1.4, 3.0]	Brass+PS	6.99	324	0.457
MS+Sol.+Yoke	∞/975.0	[1.2, 2.4]	Vacuum	-	-	-

TABLE 3.2: Details of our two simplified LHC detectors. The length of CMS is considered until the third endcap disk of the muon system, appropriate for service during Run I (*cf.* Appendix E). 'Sol.' abbreviates the central solenoids. The dimensions specified for 'ID+Sol.' (ATLAS) and 'ID' (CMS) are to be understood as the distances from the interaction point to the inner faces of the ECALS.

the HB used for electronics are ignored in the implementation. In Figure 3.8b, this is indicated by the use of red colour. Instrumentation gaps between the ECAL and HCAL layers of ATLAS are also neglected.

We remark that the magnet systems could stop the particles as well. For example, the CMS magnet yoke consists of steel, which may cause a considerable deceleration. However, this will be ignored, because (i) a charged particle that managed to escape the hadronic calorimeter parts will most likely not contribute to the stopped particles signal, (ii) we intend to simplify the analysis and (iii) a dedicated search for isolated corresponding signals in the muon systems seems unlikely in the near future. Hence, the magnets and muon systems will be considered to consist of vacuum and the particles will either be taken to be located 'outside' the detector after they exit the HCAL barrel module (in Analysis IIB) or still 'inside' but invisible to existing long-lived particle searches if they decay before exiting the muon system (Analysis IIA). We equally ignore the ID materials, since their effect on the particles' energies is not that significant. For example, in ATLAS this introduces an error of 0.63 neglected radiation lengths in the solenoid and 1.7 radiation lengths in the tracker [336].

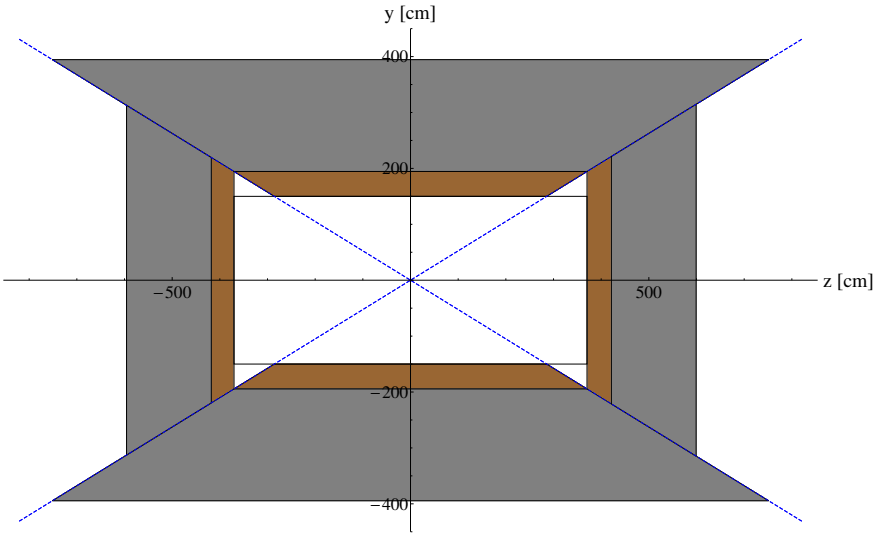

(A) Longitudinal view of the calorimeter structure of our ATLAS toy detector. Brown corresponds to the ECAL and gray corresponds to the HCAL.

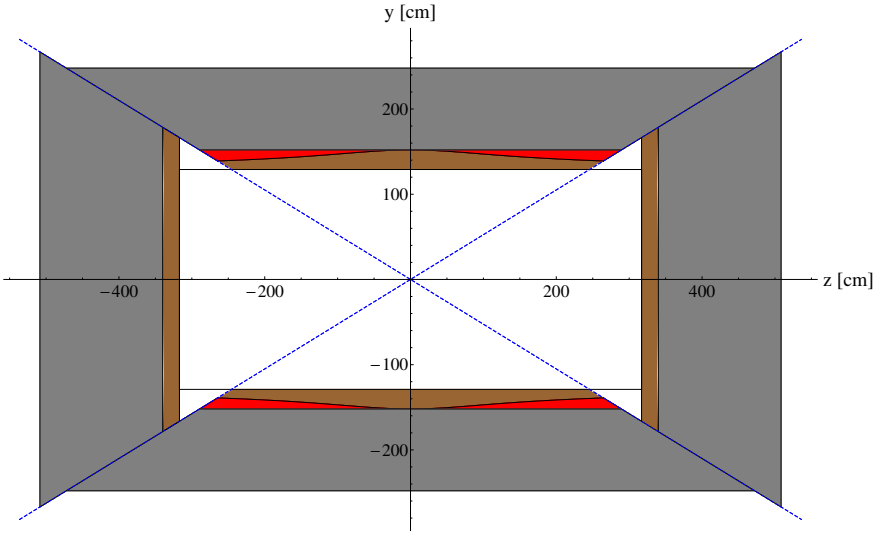

(B) Longitudinal view of the calorimeter structure of our CMS toy detector. Brown corresponds to the ECAL and gray corresponds to the HCAL. Red regions are computationally non-existent, meaning that the particle passes directly from the ECAL to the HCAL modules in our implementation.

FIGURE 3.8: Schematic longitudinal views of the ATLAS and CMS toy detectors implemented for Analysis IIA and Analysis IIB.

CHAPTER 4

Detecting heavy long-lived charged particles with the ATLAS and CMS experiments

The considerations and developments in this chapter are the foundation for the second study. A plethora of theoretical scenarios predict the existence of stable or metastable particles, where the latter may exhibit macroscopic decay lengths. In this thesis, special emphasis is placed on aspects related to electrically charged particles not decaying promptly but possibly far inside any of the modules of a particle detector or even outside. We treat in this chapter several aspects exclusively related to the experimental inference of the presence of such *Heavy Long-Lived Charged Particles*, from now on abbreviated as HLLCP.[1]

While Analysis I is exclusively focused on Higgs effects in prompt production, the more involved Analyses IIA and IIB require knowledge about the properties of the physical detectors and about unstable particle lifetimes, where the detectability of a specific realization of the scotogenic model [40] with a long-lived charged scalar particle $H^{\pm}$ is examined. This model predicts very distinct signatures that depend on properties of the particle detectors. Consequently, consideration of detection methods, detector characteristics and long-lived particle properties are essential elements to discuss. Although presented for the scotogenic $H^{\pm}$ boson, the treatment is in fact model-independent, as long as the particle does not interact strongly.

An introductory exposition concerning the expected signatures with some examples of theoretical frameworks containing HLLCPs is first given in Section 4.1. Subsequently, Section 4.2 discusses how energy loss is generally treated in particle detection and how it is quantified with the Bethe-Bloch equation in Section 4.2.1, followed by further deepening concepts in Section 4.2.2 and finally by a demonstration based on the ATLAS and CMS toy detectors in Section 4.2.3. In Section 4.3, we discuss decay and survival probabilities and investigate how the changes in these quantities are to be tied to energy variations, as predicted when there is deceleration. Section 4.4 provides a numerical comparison of stopping times and mean lifetimes of a HLLCP in ATLAS, as a preparation for the final study looking for stopped particles decaying at rest at random times with respect to the trigger rate. Finally, in Section 4.5, we introduce the fundamental statistical parameters needed for our two HLLCP analyses, namely the fractions of particles decaying in-flight (or accordingly surviving and escaping) and the fraction of particles being stopped before reaching their mean lifetime.

4.1 Introduction: HLLCP signatures and exemplary models

Many BSM physics models may manifest themselves in unusual forms due to particular realized parameter configurations or other special features. A primary example is furnished by supersymmetry. All thus far performed searches for supersymmetric partners of SM particles turned out to deliver null results and consequently led to strong constraints on a large variety of SUSY scenarios, mainly on the coloured sector due to larger squark and gluino production cross sections at hadron colliders. As yet, no excess over the SM background expected for any benchmark SUSY model has been observed, making one wonder whether naturalness can still be salvaged in a supersymmetric scenario [337]. Thus the current situation appears to indicate that low-scale SUSY, at least in a fairly unrestricted form, may not be realized in Nature. However,

[1] Other terminologies found in the literature are *e.g.* HSCP (Heavy Stable Charged Particle) or long-lived CHAMP (CHArged MAssive Particle).

it is well-known that the supersymmetric parameter space allows for numerous theories with exotic collider phenomenologies, which are therefore not targeted by most, if not any, existing searches. A disregard of deviations from looked-for signatures consequently implies the inference of too strong constraints on the theory under survey. In particular, the vast majority of SUSY collider searches are optimized for prompt sparticle decays ($c\tau \lesssim 100$ μm) with a large missing transverse momentum. The assumption of microscopic decay lengths implies that derived constraints may be too stringent if one allows the parameter space to extend to regions where decay lengths are macroscopic, such that the decay happens far inside the tracker, the calorimeters or the muon system (unstable particles), or even outside the detector (metastable particles).[2] Macroscopic decay lengths may occur due to small couplings or compressed spectra, such as in weak muon or neutron decay, or when an approximately conserved quantum number is involved. The possibility for in-detector decay of exotic charged particles is addressed in [327], in the context of supersymmetry, with the definition of the concept of 'untracked' events. These are events with tracks not matching standard selection criteria and are therefore rejected, *i.e.* the searches are blind to them. By accounting for the possibility of untracked signatures, existing bounds can be significantly weakened.

We remain for a while inside the exemplary supersymmetric setting. Several SUSY scenarios introduce particles with large decay lengths and hence with highly exotic signatures. A well-known example is gauge-mediated supersymmetry breaking (GMSB) [338], where the decay of the NLSP to the LSP, a very light gravitino $\tilde{G}$, is suppressed by the Planck scale because gravity induces the soft SUSY-breaking mass terms. Another possibility is the presence of R-parity violating (RPV) interactions [339]. These models provide the gravitino as an unstable but very long-lived dark matter candidate. The involved Yukawa couplings are constrained to be very small, mainly by diffuse γ-ray flux observations, the observed cosmological baryon asymmetry and BBN, see [340] and references therein. Theories with GMSB and R-parity violation usually contain long-lived sleptons as NLSPs. Minimal split SUSY ('mini-split') [341] predicts macroscopic gluino decay lengths if their masses are ~ 1 TeV and squark masses are several orders of magnitude larger [342]. Finally, the presence of long-lived sparticles enables the possibility for the formation of R-hadrons or R-glueballs, *i.e.* coloured sparticles that outlive their hadronization time exhibiting uncommon signatures which depend on the hadronization model [335]. From a collider point of view, one of the most interesting phenomenologies is expected when the long-lived particle is heavy and electrically charged, *i.e.* what we herein denote a HLLCP.

One can also envision numerous non-supersymmetric frameworks containing HLLCPs, for example the universal extra dimensions scenario [23]. For our goals, the most important possibility is having dark matter freezing-in due to the suppressed decay of another particle that is charged under a discrete symmetry responsible for the stability of the dark matter particle, in analogy to R-parity. Suppression stems mainly from the smallness of the involved coupling strength, leading to macroscopic decay lengths when this particle is produced in a collider. The scotogenic model in a specific fermionic FIMP realization, as discussed in Section 2.4, provides the displaced decay

$$H^{\pm} \to \ell^{\pm} N_1 \,, \tag{4.1}$$

given that the RHN N_1 is the lightest and the $H^{\pm}$ the next-to-lightest $\mathbb{Z}_2$-odd member of the spectrum. This process has a signature in principle similar to $\tilde{\ell}^{\pm} \to \ell^{\pm} \tilde{G}$ or $\tilde{\chi}^{\pm} \to \ell^{\pm} \nu \tilde{G}$ in GMSB.

Various further exotic signatures may be realized, as we will now discuss without the aim to exhaust the full list of possibilities. Collider phenomenology of models containing long-lived particles may incorporate:

□ **Stable charged tracks:** In a framework containing a HLLCP, the mass spectrum may be such that production in a collider is feasible and that its decay length may lie well outside the detector. It would leave behind a charged track in the tracking and muon systems, with a considerable amount of deposited energy in the tracker layers due to ionization of the material, thus it would look like a very slow muon.

[2]Note that some unstable particles present in the SM are also long-lived: The muon, depending on its energy, has a decay length of $c\tau \sim \mathcal{O}(1$ km) and D and B mesons can decay after several hundred μm to several mm due to CKM-suppressed quark generation crossing. These particles represent background to searches for signals originating from exotic long-lived particles predicted in BSM theories.

High-momentum muon backgrounds to such events can be efficiently reduced by demanding to veto velocities close to the speed of light and low ionizations. Both ATLAS [44] and CMS [45] have conducted searches for metastable charged particles, deriving production cross section limits mostly in the context of supersymmetry. Our Analysis IIA is an application of the CMS search to the scotogenic FIMP model.

□ **Kinked charged tracks:** In case a charged particle has a decay length of $c\tau \sim \mathcal{O}(10\,\mathrm{cm}) - \mathcal{O}(1\,\mathrm{m})$, the trace left in the tracking modules will be a track exhibiting an abruptly bent shape, provided its decay products are also long-lived or stable and contain exactly one charged member sufficiently energetic to be seen. For example, in supergravity one may have the kink-producing decay $\tilde{e}^{\pm} \to e^{\pm}\tilde{G}$, or similarly the before-mentioned process in the scotogenic model with FIMP sterile neutrino dark matter, probably with some kinematical differences. Kink signatures are in principle very simple and topologically easy to distinguish from SM-only events, provided the detectors are able to resolve the decay vertex, which involves reconstructing two connected tracks. Unfortunately, this is presently not possible because the track recognition algorithms enforce small impact parameters, *cf.* Section 3.2.2. This means that current recorded data does not contain events with kinked track topologies happening far inside the tracker. However, the algorithm employed in ATLAS can be tweaked to allow for considerably larger impact parameters suitable for long-lived particle searches [343, 344]. Moreover, there is an algorithm to identify charged particle decays inside the ATLAS muon spectrometer from standalone vertices [345], though it requires more than one charged track emerging from the decay. In summary, there is currently no possibility to look for kinked tracks in existing data, as there were no applied sets of appropriate track finding rules.

This is especially unfortunate, because the kinked track topology can shed a light on the most important bit of information about the model, namely the invisible particle's mass. For illustration, let us suppose it was possible to trigger for kinked tracks and a model containing a displaced decay $\psi_{\mathrm{mother}} \to \psi_{\mathrm{daughter}} + \psi_{\mathrm{inv}}$ is being tested. ψ_{mother} is heavy, long-lived and charged, ψ_{daughter} is an equally-charged decay product and ψ_{inv} is a metastable or stable invisible neutral particle, perhaps a dark matter constituent. Measuring the mother particle's mass with the tracking system (*cf.* Section 4.2.2) and the daughter's energy with the calorimeters or the muon system, the invisible particle's mass could in principle be (crudely) estimated from the event kinematics via the formula

$$\begin{aligned} m_{\mathrm{inv}}^2 &= m_{\mathrm{mother}}^2 + m_{\mathrm{daughter}}^2 - 2\,(E_{\mathrm{mother}}\,E_{\mathrm{daughter}} - \vec{p}_{\mathrm{mother}} \cdot \vec{p}_{\mathrm{daughter}}) \\ &\simeq m_{\mathrm{mother}}^2 + m_{\mathrm{daughter}}^2 - 2\,m_{\mathrm{mother}}\,E_{\mathrm{daughter}}\,, \end{aligned} \tag{4.2}$$

as m_{mother} is hypothesized to be large and therefore it will be slow in most events. The neglected term $\vec{p}_{\mathrm{mother}} \cdot \vec{p}_{\mathrm{daughter}} \propto \cos\theta_{\mathrm{kink}}$ is not necessarily small, as is discussed below. By measuring the decay length, the involved coupling can be extracted. For instance, in GMSB with a stau NLSP ($\tilde{\tau}_1$) and gravitino LSP ($\tilde{G}$), the decay width depends exclusively on $m_{\tilde{\tau}_1}$, $m_{\tilde{G}}$ and the Planck mass. Having estimated the masses through Equation 4.2, one can solve the expression of $\Gamma_{\tilde{\tau}_1}$ for the Planck mass and henceforth test the prediction of supergravity [346]. Similarly, the scotogenic model with N_1 constituting the FIMP dark matter particle involves a Yukawa coupling depending only on the mother and daughter masses to a good approximation if the scalar spectrum is sufficiently compressed, see Equation 6.3a, thus one might expect the same measurement to be possible for the decay in Equation 4.1 if the produced $H^{\pm}$ bosons are sufficiently slow. However, there is a devastating downside to the appliance of Equation 4.2 in that case, as there are only in-detector kinks for highly sub-GeV N_1 masses (*cf.* Chapter 6), but the uncertainties in the measurement of $m_{H^{\pm}}$ and the energy of the charged lepton are $\mathcal{O}(\mathrm{GeV})$, making it impossible to measure M_1 in this manner. An alternative approach would be to estimate $\Gamma_{H^{\pm}}$ through the decay length and the velocity of $H^{\pm}$ with the tracker and then solve Equation 6.3b or 6.3d for M_1.

Let us now examine the occurring values of the kink angle, $\theta_{\mathrm{kink}} \equiv \sphericalangle(\vec{p}_{\mathrm{mother}}, \vec{p}_{\mathrm{daughter}})$, in the scotogenic model, for the decay in Equation 4.1. Figure 4.1 shows a scatter plot containing the angles of the charged lepton and a light N_1 produced in the decay of $H^{\pm}$ w.r.t. the momentum vector of $H^{\pm}$ in the lab frame, so $\theta_{\mathrm{kink}} = \theta_{\mathrm{lab}}(\ell)$. The varied quantities are the CM angle of ℓ and the Lorentz boost γ of $H^{\pm}$ from its rest frame to the detector frame, with a uniform probability distribution in the scanned intervals. In the CM

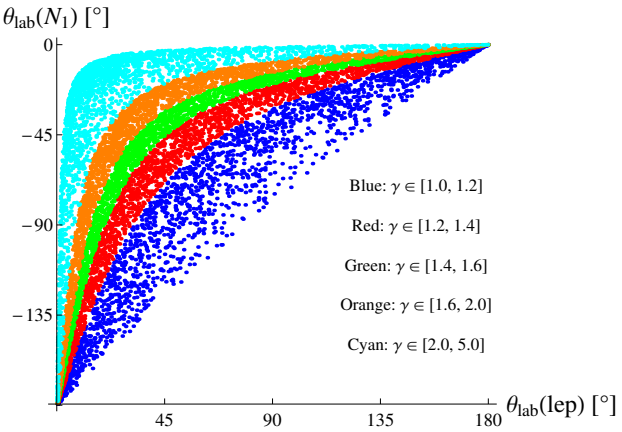

FIGURE 4.1: Angles of ℓ and N_1 in the lab frame for various boosts. We chose $m_{H^\pm} = 200$ GeV, $\ell = e^\pm$ and $M_1 = 1$ GeV. The lepton and RH neutrino masses can be neglected, therefore the scatter plot looks the same for all scalar masses in the $\mathcal{O}(100$ GeV) range.

frame, ℓ and N_1 are emitted back-to-back. Note that the plot looks the same for any charged scalar mass as long as the masses of the decay products are negligible. However, a given $H^\pm$ mass will correspond to a particular range of most probable boost factors, *cf.* Section 6.1.2. The CM angle of ℓ is taken to be intrinsically positive between 0° and +180°, so the CM and lab frame angle of N_1 is always negative due to momentum conservation. We see that all angles between 0° and 180° are possible for θ_{kink}, the distribution being symmetric in the modulus of both angles. Highly boosted $H^\pm$ preferentially decay with small angles between ℓ and N_1. The bulk of the angles is large enough ($\sim$ 45° - 90°) to unequivocally distinguish kinked tracks from unkinked tracks, though not sufficiently concentrated at 90° to justify neglecting the $\vec{p}_{H^\pm} \cdot \vec{p}_\ell$ term in Equation 4.2, so this corresponds to a rather bold approximation.

□ **Disappearing charged tracks:** One can work out models with massive charged particles whose decay products are unlikely to be detected, giving rise to disappearing tracks if the decay happens inside the detector. This signature arises when each member of the decay products is either too soft to overcome energy thresholds or when it is not electrically charged. For example, if a charged massive particle is quasi-degenerate with other particles in the spectrum it can decay to, then its lifetime is strongly enhanced because of the small available phase space. There is the possibility that the heavy particle emerging from the decay is neutral, thus the other decay products containing the electric charge, possibly SM leptons or pions, may be too soft to be reconstructed. A well-known case is again provided by supersymmetry, where some scenarios contain a lightest chargino decaying to the slightly lighter lightest neutralino [347] and a very soft unseen charged pion. In a search for such signatures, CMS places a lower bound of 260 GeV on the lightest chargino mass in the context of the anomaly-mediated SUSY breaking scenario [348]. Another example is the case of GMSB with a slepton decaying to a charged lepton and a gravitino. In the slepton NLSP scenario [349], the right-handed selectron and smuon are degenerate while the stau decouples. Selectron/smuon pair production may result in charged tracks disappearing at displaced vertices without any other associated tracks if the corresponding electron/muon is not reconstructed [349]. Unfortunately, the CMS search [348] is not sensitive to this process due to the requirement of an additional high-p_{T} jet from initial state radiation and the imposition of a lepton veto. In the scotogenic model with the N_1 as the FIMP, such a signature may arise if the NLOP is the H^0 or A^0 and the NNLOP is the $H^\pm$. In that case, if the charged and neutral scalar masses are compressed, the products of the 3-body decay $H^\pm \to H^0/A^0 + 2f$ would be invisible. Such a signature seems quite unnatural though, as one would rather expect a larger splitting [350].

□ **Displaced charged tracks:** Charged tracks can arise at vertices that are significantly displaced from the main collision point, as can occur when a long-lived neutral particle is produced and then decays to charged particles leaving behind visible trails in the tracker or muon system. To give another supersymmetric example, if the lightest neutralino is the LSP and if R-parity is violated, there is the decay $\tilde{\chi}^0 \to \ell jj$, which can have a large impact parameter. A search by ATLAS for this signature is found in [351]. Alternatively, the neutralino can have a displaced decay to $\ell^\pm \ell^\mp \nu$, a process searched for by the DØ collaboration [352]. Another typical example are 'hidden valley' models [353], where the SM gauge group is enlarged with a non-abelian group, $\mathcal{G}_{\text{SM}} \to \mathcal{G}_{\text{SM}} \times \mathcal{G}_v$, with new light particles charged under $\mathcal{G}_v$ but not under $\mathcal{G}_{\text{SM}}$. Such models have a rich phenomenology, such as late decays of these new 'v-pions' π_v. Their production can occur via a new gauge boson Z' or through the decay of a v-charged scalar h_v that mixes with the SM Higgs boson [354]. They preferentially decay to $b\bar{b}$ pairs, which can happen as far as inside the muon system, therefore triggering in these models is very difficult [355]. ATLAS used this scenario as a benchmark model to test the before-mentioned new algorithm for finding standalone vertices iniside the muon spectrometer [345]. Finally, a search for displaced dileptons from decays $\pi_v \to e^+e^-$ and $\pi_v \to \mu^+\mu^-$ has been performed by the CMS collaboration [356], setting stringent limits on the h_v mass for decay lengths up to 100 cm. Through the contained dimuon analysis, we were able to put constraints on the FIMP realization of the scotogenic model with another spectrum [2].

□ **Decays of stopped HLLCPs:** Definitely one of the most interesting and spectacular collider signatures is the decay of a HLLCP after it has been slowed down sufficiently by the calorimeter material until it stopped completely. Such decays happen randomly w.r.t. the trigger rate and have no associated tracks pointing to the area of the hadronic or electromagnetic shower. Standard searches are not sensitive to these kinds of events and appropriate trigger rules need to be defined. This signature is only possible for particles produced with a very low kinetic energy: If the energy is low but still too large for the particle to stop, it would exhibit the signature of a stable charged track (see above). If it is slow enough to stop, on the other hand, it is possible to specifically trigger for random ('out-of-time') calorimetric energy depositions; these have very distinguishable non-collision backgrounds, though they are very difficult to understand (*cf.* Section 3.2.1.2). If one has a particle that is heavy, one may hope that it is frequently produced with a low momentum placing it in the kinematical region where the energy loss is appreciable. ATLAS [46] and CMS [47] have published such analyses with limits on R-hadron production cross sections. We use the ATLAS search in the context of the scotogenic FIMP scenario in Analysis IIB and reinterpret the signal in terms of stopped $H^\pm$ decays.

4.2 Energy loss in the detectors

As already mentioned, Analysis IIA only relies on detector geometries and Analysis IIB additionally requires the quantification of the energy decrease $\langle -dE/dx \rangle$ of the $H^\pm$ particles as they traverse the detector. PDG offers a thorough discussion of the contributing effects [78]. In essence, charged particles mainly lose energy to the medium through ionization processes, multiple scatterings off nuclei (Rutherford scattering), bremsstrahlung, Cherenkov radiation and possibly transition radiation. Photons suffer energy losses through the photoelectric effect, Compton scattering and pair production. At high energies, charged particles mainly lose their energies through bremsstrahlung and Rutherford scattering with an average distance between interactions characteristic to the material given by the *radiation length*

$$X_0 \approx \frac{4Z(Z+1)\alpha^3}{m_e^2} \frac{\rho}{A} \ln \frac{Z^{1/3}}{183} , \tag{4.3}$$

where Z, A and ρ are the medium's atomic number, atomic weight and density. Energy losses are proportional to the energy, consequently

$$-\frac{dE}{dx} = \frac{E}{X_0} \implies E(x) = E_0 \mathrm{e}^{-x/X_0} \,. \tag{4.4}$$

Similarly, the intensity of a hadron shower traversing the HCAL is decreased according to

$$I(x) = I_0 \mathrm{e}^{-x/\lambda_h} \,, \tag{4.5}$$

where λ_h is the *hadronic interaction length* within the absorber material. It is always larger than X_0 (about a factor 10-30 for high-Z absorbers), therefore the HCAL is always thicker and denser than the ECAL by construction and cannot be placed before it. A calorimeter is always composed of an absorber material and an active material producing an energy-proportional output signal, *e.g.* through scintillation. These materials can be the same (homogeneous case), but are usually different and layered, with the absorber layers having the thickness of about one radiation/interaction length. Guidelines in material and thickness choices are the cost, the ability to absorb the largest possible amount of energy with the best possible energy linearity, energy resolution and radiation hardness.

4.2.1 Bethe-Bloch equation for mean energy loss

The history of the theory of moving particle interactions with the traversed matter is a long one [357] and dates back to pioneering work by J. J. Thomson and N. Bohr. In the 1930s, H. Bethe [358] and F. Bloch [359] reformulated the theory incorporating quantum mechanics and derived the fundamental form for $\langle -dE/dx \rangle$, which over the following decades became subject to numerous adjustments and corrections to account for more effects. Formally, it is an expansion in powers of the projectile atomic number z,

$$\left\langle -\frac{dE}{dx} \right\rangle = \kappa \left\langle \frac{Z}{A} \right\rangle \frac{1}{\beta^2} z^2 L(\beta) \,, \qquad L(\beta) \equiv L_0(\beta) + z L_1(\beta) + z^2 L_2(\beta) + \dots \,, \tag{4.6}$$

where $L(\beta)$ is termed the *stopping number* containing all main contributions in the *primary stopping number* L_0 and all subleading contributions (bremsstrahlung, screening, etc.) in $L_{k>0}$ [357]. These corrections are reviewed in [360], for instance. Here, we shall only consider the L_0 term, accounting merely for ionizations and atomic excitations. That is, we do not correct for the shell corrections and disregard corrections for the density effect occurring at the same order, since these are subleading at the energies relevant to our goals [78, 361]. Including shell corrections and the density effect (accounting for the fact that the projectiles polarize the absorber medium) for completeness, the Bethe-Bloch equation with the primary term in SI units reads

$$\left\langle -\frac{dE}{dx} \right\rangle = \kappa \left\langle \frac{Z}{A} \right\rangle \frac{1}{\beta^2} z^2 L_0(\beta) = \kappa \left\langle \frac{Z}{A} \right\rangle \frac{1}{\beta^2} z^2 \left[\frac{1}{2} \ln \frac{2 m_e c^2 \beta^2 \gamma^2 E_{\max}}{I^2} - \beta^2 - \frac{C}{Z} - \frac{\delta}{2} \right] . \tag{4.7}$$

The quantities are:

κ	$\kappa = 4\pi N_A r_e^2 m_e c^2 = 0.307075$ [MeV g^{-1} cm^2] or [MeV mol^{-1} cm^2]
z	Atomic number/charge of the projectile
Z, A	Atomic number and atomic weight (average nucleon number) of the absorber
$E_{\max}$	Maximum energy transfer possible in a single collision
I	Mean excitation energy of the medium (approximately (10 eV)$\times Z$)
C/Z	Shell corrections accounting for relative velocity of projectile and electrons
$\delta/2$	Density effect; for very high energies, $\delta/2 \to \ln(\hbar\omega_\mathrm{p}/I) + \ln\beta\gamma - 1/2$

The units of κ depend on whether the material density ρ is given in g/cm^3 or mol/cm^3. In the latter case, the definition of κ needs a further division by the molar mass constant, $M_u \equiv 1$ g/mol. We will work with the g/cm^3 definition. ω_p in the δ term is the plasma frequency of the electrons of the medium.

For the following treatment, we mostly follow the review by PDG [78]. $\langle -dE/dx \rangle$ is the *specific* energy

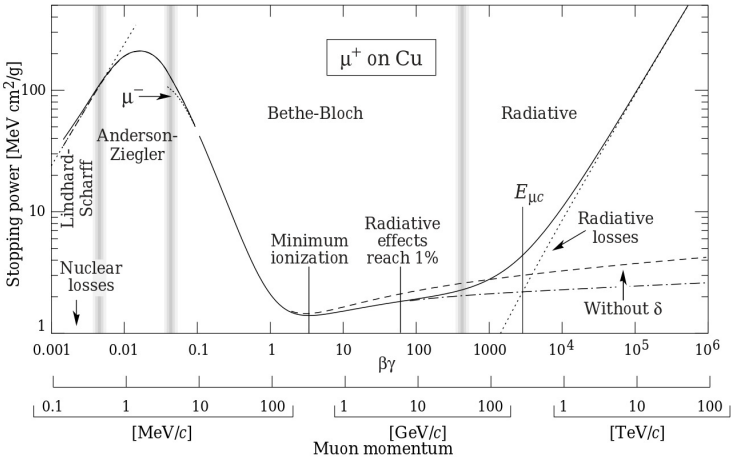

FIGURE 4.2: $\langle -dE/dx \rangle$ for an antimuon going through Cu, taken from PDG [78]. The plot depicts various kinematical regions over nine orders of magnitude of $\beta\gamma$ and several effects not discussed here are indicated. For example, 'μ^-' denotes the Barkas effect, accounting for the charge dependence at low projectile momenta.

loss (sometimes also denoted by S, for *stopping power*), the units are usually given in $\mathrm{MeV\,g^{-1}\,cm^2}$, consequently it needs to be multiplied by the material density ρ to obtain the actual energy loss per unit path length. In this unit system, some refer to dx as the unit of *specific thickness* or *mass thickness* traversed within the detector, which has units of $\mathrm{g\,cm^{-2}}$ and is obtained by multiplying the actual unit path by ρ. $E_{\max}$ corresponds to the largest possible energy loss in a single interaction, resulting in a free electron. In natural units, it is given by

$$E_{\max} = \frac{2m_e\beta^2\gamma^2}{1 + 2\gamma m_e/M + (m_e/M)^2}\,, \tag{4.8}$$

where M is the mass of the incident particle. Highly energetic electronic interactions with energy transfers actually as high as $E_{\max}$ are very rare and most processes occur with energies of the order of the mean excitation energy I. For low energies, $E_{\max} \to 2m_e\beta^2\gamma^2$ (valid for $2\gamma m_e \ll M$), and for high energies, $E_{\max} \to M\beta^2\gamma$ (valid for $2\gamma m_e \gg M$). $W_{\max}$ introduces a minor M dependence, but for all practical purposes, $\langle -dE/dx \rangle$ is a function only of β, as long as $\beta\gamma$ lies in the so-called *Bethe region* $0.1 \lesssim \beta\gamma \lesssim 1000$, where the upper value would *e.g.* correspond to a proton with an energy of about 1 TeV. For such moderately relativistic velocities, one commonly only considers the primary term. In the high-energy regime of the Bethe region, there is a relativistic rise in the energy loss, which is at some point weakened by the $\ln\beta\gamma$ term from the density effect. For even higher energies, outside this region, $\langle -dE/dx \rangle$ increases more steeply due to radiative effects, such as bremsstrahlung. In the low-$\beta\gamma$ region, $\langle -dE/dx \rangle$ is significantly larger due to the $\beta^{-2}\ln\beta\gamma$ dependence on the velocity. The singularity for very low β is then lifted by other effects, as described by Fermi-Teller-Lindhard-Scharff theory [362]. $\langle -dE/dx \rangle$ peaks, usually around $\beta\gamma \sim 0.01 - 0.05$, and then decreases again for $\beta\gamma \to 0$. In practical cases, for incident particles with $\beta\gamma$ higher than this and traversing a very thick absorber, it is legitimate to assume that, as β decreases, $\langle -dE/dx \rangle$ will rise to a peak and then the particle stops and gets trapped, as the final distance travelled will be negligible when the speed approaches zero [335]. Figure 4.2 shows the various kinematical regimes for the example of an antimuon travelling through copper.

The Bethe-Bloch equation can also be applied to mixed materials by using the Bragg additivity rule [363] to effectively combine the material constants. We shall use this rule to find the effective material properties for the simplified ATLAS and CMS detectors, as described in Section E.2.1.

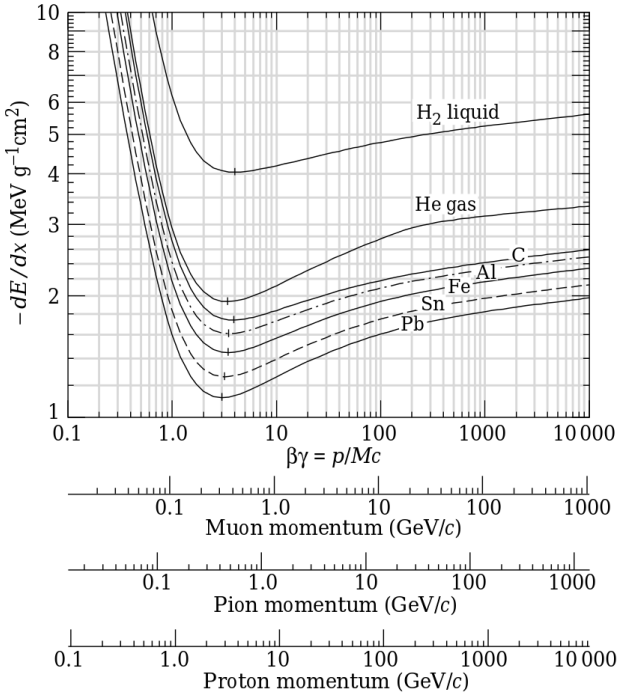

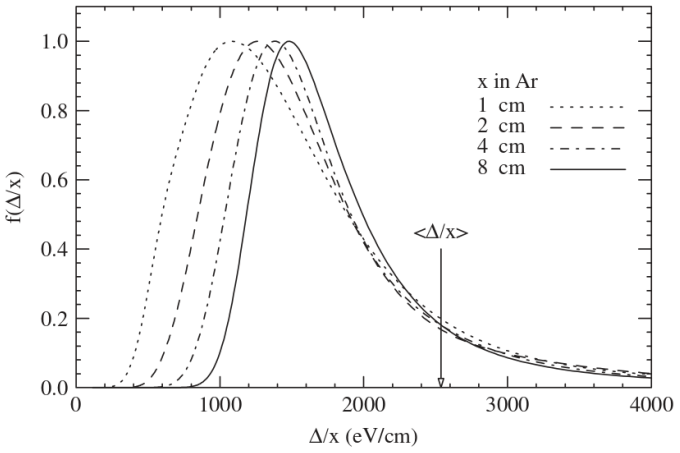

FIGURE 4.3: *Left panel:* $\langle -dE/dx \rangle$ for a muon, a pion and a proton for various absorber materials. Note the similar locations of the minima of $\beta\gamma$ corresponding to the MIP regions. Figure taken from PDG [78]. *Right panel:* Straggling functions for various argon absorber thicknesses x. Δ/x corresponds to dE/dx in our notation. The indicated mean $\langle \Delta/x \rangle$ is the value obtained with the Bethe-Bloch equation, while the MPV Δ_p/x is located at the peak of the Landau-Vavilov distribution. As x increases, the peak approaches the Bethe-Bloch value and the weight of the Landau tail decreases. Figure taken from [364].

4.2.2 Concepts and applications of energy loss in particle detection

□ **Minimum ionizing particles (MIP):** For many materials, the energy loss function has a broad minimum for momenta in the range $1 \lesssim \beta\gamma \lesssim 10$ (*cf.* Figure 4.3, left panel). Generally the minima are located at similar values of $\beta\gamma$ for most absorbers. In fact, $\beta\gamma|_{\text{min}}$ drops from 3.5 to 3.0 as Z increases from 7 to 100, so there is little variation in $\langle -dE/dx \rangle$ [78]. A relativistic particle with $\beta\gamma$ in this range is called a *minimum ionizing particle*. In most practical cases, $\langle -dE/dx \rangle$ of a particle will lie close to the minimum with values of 1-2 MeV g^{-1} cm^2, so detectors measuring the energy loss are usually calibrated using the MIP reference values. MIPs deposit their energy solely via ionization processes.

□ **Most probable value of energy loss (MPV):** The *most probable value* of energy loss is an important quantity in particle detection because it is needed for particle identification with the tracking modules. Moreover, detector thickness and particle velocities will determine whether it is de facto legitimate to use the Bethe-Bloch formula. If a particle traverses a thin absorber layer, like a silicon cell in the tracking modules, processes with energy transfers up to E_{max} are unlikely to happen and rather correspond to rare fluctuations in dE/dx. A more meaningful estimate for the quantification of the energy loss is needed in that case, with a sensible weighting of the amount of transferred energy per event. Therefore, one requires a probability density function for dE/dx, called the 'straggling function', containing information about the detector thickness x, its density and the variance corresponding to the high-energy fluctuations. Such an estimate, lying considerably below the Bethe-Bloch $\langle -dE/dx \rangle$ for all materials, is the MPV. When a particle traverses a portion of small specific thickness (*i.e.* thin absorbers and/or absorbers with a small density ρ), its energy loss probability follows a Landau-Vavilov distribution, with a characteristic narrow peak and a long tail to the right of the peak. This so-called 'Landau tail' accounts for the small number of high-energy collisions corresponding to the before-mentioned fluctuations. The MPV then corresponds to the energy deposit at which the Landau-Vavilov distribution reaches its maximum. The larger the

travelled path length, the less significant become the fluctuations. Then the more the Landau-Vavilov distribution approaches a Gaussian with the peak becoming narrower and being pushed upwards towards the Bethe-Bloch mean $\langle -dE/dx \rangle$. Hence, $\langle -dE/dx \rangle$ is a good measure as long as the particles get stopped or deposit much of their energy in the material. A criterion for gaussianity is [361, 365]

$$K(x) \equiv \frac{\xi(x)}{T} > 10\,, \qquad \text{where} \qquad \xi(x) \equiv \frac{\kappa}{2}\frac{Z}{A}\frac{\rho x}{\beta^2}\,, \qquad T \equiv E_{\max}\sqrt{1+\frac{2\gamma m_e}{M}+\frac{m_e^2}{M^2}}\,. \tag{4.9}$$

This is not fulfilled for the silicon cells in the ATLAS and CMS inner detectors, as these have thicknesses $x \sim \mathcal{O}(100\ \mu\text{m})$, but it is definitely fulfilled for a slow projectile passing through the electromagnetic and hadronic calorimeters of large detectors such as ATLAS and CMS.[3]

Denoting the energy the most likely to be deposited by Δ_p (the location of the peak of the Landau-Vavilov distribution), the most probable energy loss, in natural units, is given by

$$\text{MPV}_{\frac{dE}{dx}}(\beta\gamma, x) = \frac{1}{x}\xi(x)\left[\ln\frac{2m_e(\beta\gamma)^2}{I} + \ln\frac{\xi(x)}{I} + j - \beta^2 - \delta(\beta\gamma)\right] \equiv \frac{1}{x}\Delta_\text{p} \tag{4.10}$$

with $\xi(x)$ defined in Equation 4.9 and $j = 0.2$. The location of Δ_p has the same β dependence as the Bethe $\langle -dE/dx \rangle$, but while $\langle -dE/dx \rangle$ is independent of the thickness, the MPV scales as $a \ln x + b$. An example is depicted in the right panel of Figure 4.3, showing the energy loss distribution for a projectile going through a layer of argon of various thicknesses. At the peak lies the MPV Δ_p, which approaches the Bethe-Bloch value $\langle \Delta \rangle$ as the thickness increases. The FWHM corresponds to about 4ξ.

□ **Mass measurement using dE/dx and TOF:** It is interesting how the specific energy loss comes in handy in the identification of particles by providing a means for measurement of their mass. By measuring the deposited energy in the silicon cells of the tracker, the experiments can determine the $\beta\gamma$ factor of the particle by numerically inverting the formula for the MPV (or the Bethe-Bloch formula, as it is equivalent for large thicknesses and densities). For the tracker layers, this dependence is determined through a numerical fit of MC and real data containing known particles (for ATLAS, this is thoroughly discussed in [366]). ATLAS and CMS find the best fits to be

$$\text{MPV}_{\frac{dE}{dx}}(\beta\gamma) = \frac{p_1}{\beta^{p_3}}\ln(1 + (|p_2|\beta\gamma)^{p_5}) - p_4\,, \qquad I_\text{h}(\beta\gamma) \equiv K\beta\gamma + C\,, \tag{4.11}$$

respectively, with the fitted parameters p_{1-5}, K, and C given in [366] and [45]. In combination with the measured momentum p, one then calculates the mass via the relation

$$m_{\beta\gamma} \equiv p/\beta\gamma\,. \tag{4.12}$$

As reported by ATLAS, since the MPV fit is obtained from data with light particles such as pions and protons, the extrapolated fit will result in a biased mass measurement if the particle is heavy and needs to be corrected. The particle's speed β can be determined by measuring the *time-of-flight* (TOF) to the calorimeter cells and/or the muon system parts responsible for timing and triggering, depending on the analysis. Through measuring the time difference δ_t of a hit relative to the expected timing of a particle with the speed of light c, the TOF yields the reciprocal speed,

$$\frac{1}{\beta} = 1 + \frac{c\delta_t}{L}\,, \tag{4.13}$$

where L is the distance to the interaction point [45]. In the stable charged track searches, ATLAS measures the TOF to the calorimeters and to the DT chambers and RPC layers in the muon system [44], while CMS only uses timing signals from the DTs and CSCs [45]. These measurements can again be combined with the momentum p to calculate the mass via Equation 4.12, denoted by

$$m_\beta \equiv p/\beta\gamma(\beta)\,. \tag{4.14}$$

[3] For example, using our ATLAS toy detector, one finds that K becomes smaller than 10 for $\beta\gamma \gtrsim 1.25$ (1.5) if the particle enters the electromagnetic barrel (endcap) perpendicularly, for any heavy $H^\pm$ mass. This is by far faster than the energies we find that lead to stopping, so a use of the Bethe-Bloch equation is appropriate.

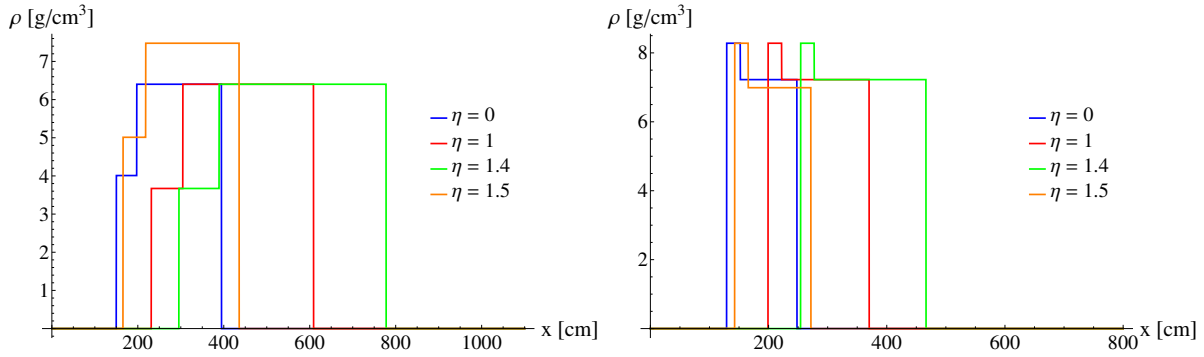

FIGURE 4.4: Distance- and pseudorapidity-dependent density in the toy detectors for four different pseudorapidities. Note the increase in travelled path length in the barrel with increasing pseudorapidity. In the endcap, on the other hand, it decreases with $|\eta|$. *Left panel:* ATLAS. *Right panel:* CMS.

The two experimental masses $m_{\beta\gamma}$ and m_β can be used to define consistency requirements on events containing charged tracks. By knowing the specific energy loss in silicon, searches for stable charged tracks left by heavy particles trigger for amounts of deposited energy above the MIP region and low $\beta\gamma$ values.

4.2.3 Simulating the energy loss in ATLAS and CMS

To account for the geometry and material constants of the implemented simplified detectors as the particle loses energy, we write the Bethe-Bloch equation in terms of position-dependent material constants defined through box functions,

$$\left\langle -\frac{dE}{dx} \right\rangle [E,x,\eta] = \kappa z^2 \langle Z/A \rangle (x,\eta)\rho(x,\eta) \times \frac{1}{\beta^2[E]} \left[\ln\left(\frac{2m_e}{I(x,\eta)} \frac{E^2 - M^2}{M\sqrt{M^2 + 2m_e E + m_e^2}} \right) - \beta^2[E] \right] , \tag{4.15}$$

with $\beta[E] = \sqrt{1 - \frac{M^2}{E^2}}$. η is assumed to remain constant as $H^\pm$ traverses the magnetic field. Notice that $\langle -dE/dx \rangle$ in Equation 4.15 is not the specific but the proper energy loss, in order to showcase the explicit position dependence of the density ρ. The cylindrical detector geometry allows one to focus only on positive pseudorapidities. ρ, $\langle Z/A \rangle$ and I are plotted in Figure 4.4 for fixed η.

Now consider the particle travelling through the ATLAS and CMS toy detectors, in which we are counting the ID and the central solenoid (CS) as one layer without energy loss and everything beyond the HCAL as 'outside'. In Figures 4.5-4.7, we plot the $\beta\gamma$ value of a $H^\pm$ particle ($z = z_{H^\pm} = 1$) with a mass of 300 GeV for initial energies of 340 ($\gamma = 1.13$), 315 ($\gamma = 1.05$) and 305 GeV ($\gamma = 1.02$) and a fixed pseudorapidity of $\eta = 0$, as it travels through the ATLAS (left) and CMS (right) calorimeter systems, obtained by numerically solving the Bethe-Bloch equation. We see that an energy of 340 GeV is by far too much energy for the particle to stop; for 315 GeV, however, the ATLAS calorimeters are dense and thick enough to bring it to rest, while in CMS it escapes the calorimeter system. Figures 4.8 and 4.9 compare the $\beta\gamma$ evolution in ATLAS and CMS for two different pseudorapidities, for energies of 340 GeV and 315 GeV, respectively, to show the effect of the varying distances travelled through the barrel in the case of different scattering angles. We notice that ATLAS clearly has the superior stopping power. The last two plots in Figure 4.10 directly compare the $\beta\gamma$ evolution in both detectors for the same energies, at a common pseudorapidity of $\eta = 0$; the curves are also featured in the preceding two figures.

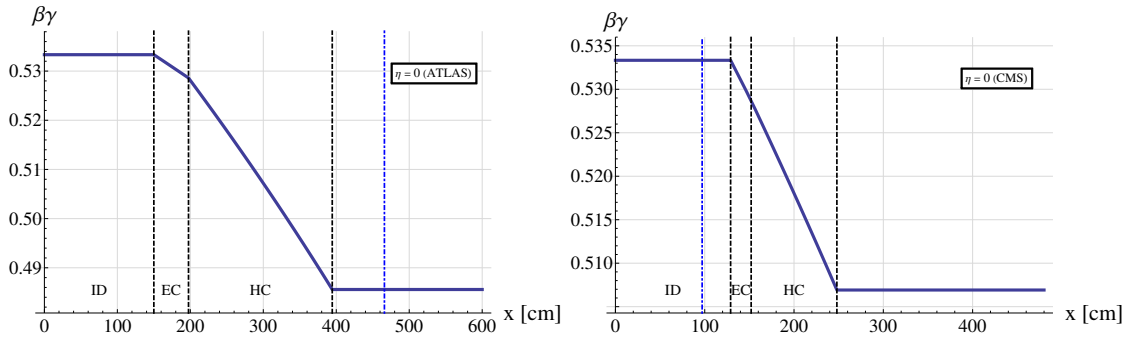

FIGURE 4.5: $\beta\gamma$ evolution of a $H^{\pm}$ particle in the ATLAS (left panel) and CMS (right panel) toy detector with a mass of 300 GeV and an initial energy of 340 GeV ($\gamma(0) = 1.13$, $\beta\gamma(0) = 0.53$). It is too energetic to stop and exits the calorimeter system with a final energy of 333 GeV (ATLAS, $\beta\gamma_{\text{final}} = 1.11$) and 336 GeV (CMS, $\beta\gamma_{\text{final}} = 1.12$). It is assumed that the particle continues to propagate freely after exiting the HCAL. The orange dot-dashed vertical line is at the particle's decay length for an example N_1 mass of 100 keV.

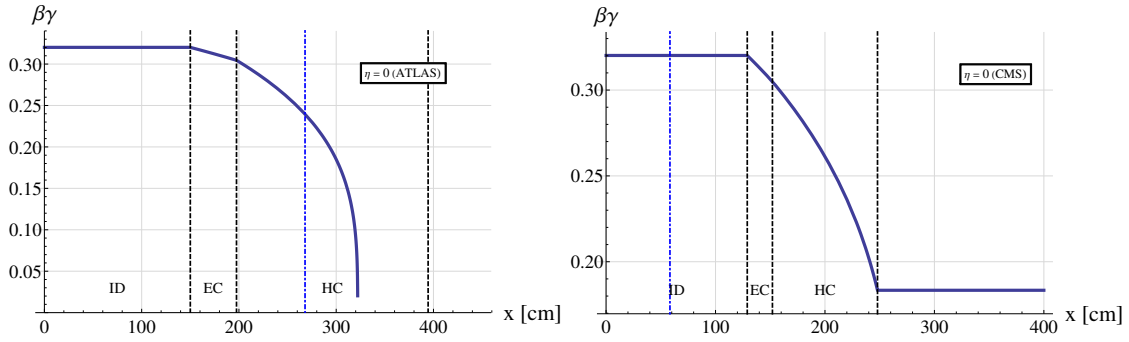

FIGURE 4.6: Initial energy of 315 GeV ($\gamma = 1.05$, $\beta\gamma = 0.32$).

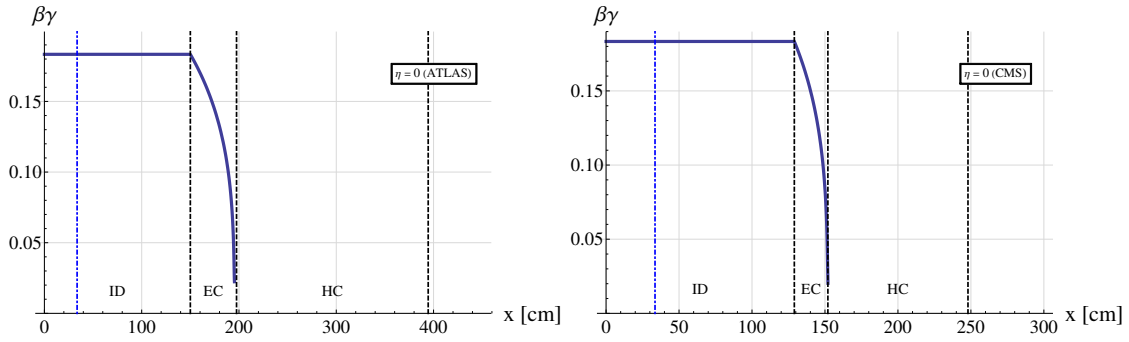

FIGURE 4.7: Initial energy of 305 GeV ($\gamma = 1.02$, $\beta\gamma = 0.18$).

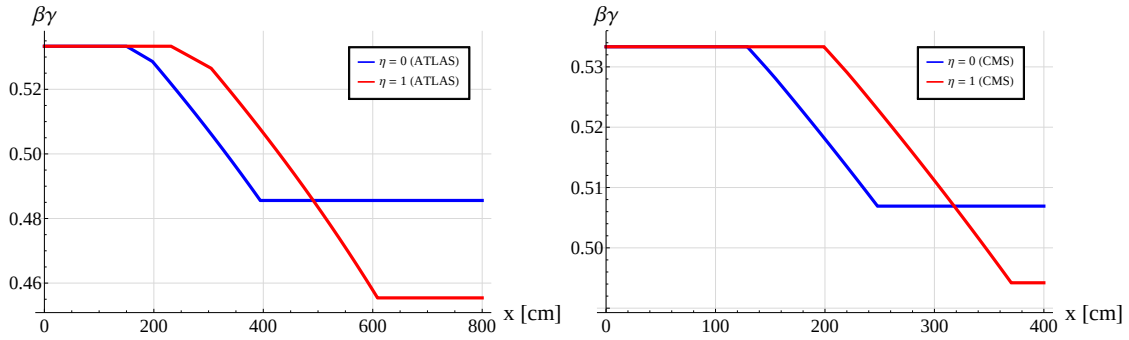

FIGURE 4.8: $\beta\gamma$ evolution of a $H^{\pm}$ particle with a mass of 300 GeV in ATLAS (left panel) and CMS (right panel) produced with an energy of 340 GeV at different pseudorapidities.

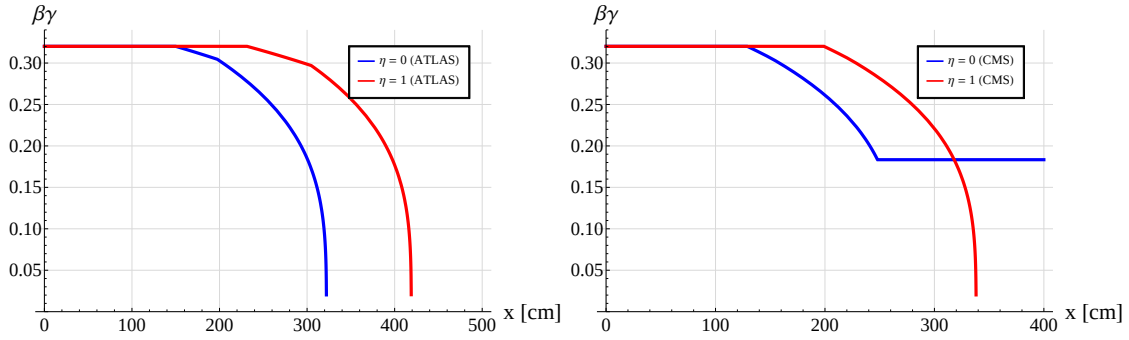

FIGURE 4.9: Initial energy of 315 GeV ($\gamma = 1.05$, $\beta\gamma = 0.32$).

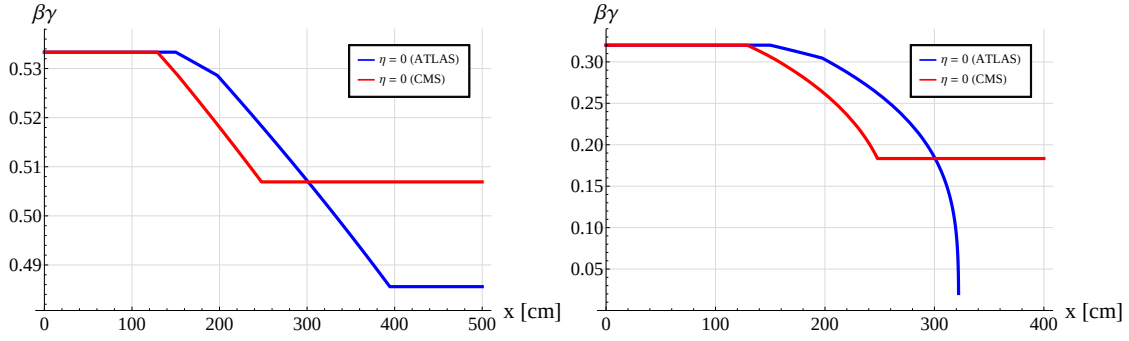

FIGURE 4.10: *Left panel:* Comparison of the $\beta\gamma$ evolution of a $H^{\pm}$ particle with a mass of 300 GeV produced in ATLAS and CMS with an initial energy of 340 GeV at $\eta = 0$. *Right panel:* Initial energy of 315 GeV.

4.3 Decay/survival probability and mean lifetime

This section deepens considerations on unstable particle decay, which was already touched upon in Section 3.1.2.3. The probability of decaying after a given time is given by the well-known exponential decay formula. When passing through a medium in a boosted frame, the formula is modified to account for variations of the momentum, or the boost factor, caused by the deceleration as described by the Bethe-Bloch equation. In this section, the interplay of energy loss and particle instability is worked out in detail, since there seems to be no comparable treatment in the literature. We will separately consider constant and varying boosts. An especially important quantity is the *survival probability*, as it will be fundamental for Analysis IIA and IIB. For the case of varying boosts, we shall see that the low energies relevant for significant decelerations don't necessitate the heavy developed machinery. Here we employ SI units ($c \neq 1$).

4.3.1 In the rest frame

We begin with some notation and define the basic quantities in the rest frame (RF). If a particle has in its RF a rate of decay $\Gamma_{\mathrm{RF}} \equiv \Gamma$, then we write the probability for decaying in the time interval $[t_{\mathrm{RF}}, t_{\mathrm{RF}} + dt_{\mathrm{RF}}]$ in the form

$$\Gamma \exp(-\Gamma\, t_{\mathrm{RF}})\, dt_{\mathrm{RF}} \equiv f_{t_{\mathrm{RF}}}(t_{\mathrm{RF}})\, dt_{\mathrm{RF}}\,. \tag{4.16}$$

That is, we specify in this section the functional form of probability densities and cumulative probabilities by indices with the respective variables, *i.e.* $f_{t_{\mathrm{RF}}}(\xi) = \Gamma \exp(-\Gamma\,\xi)$. The expression for the $H^{\pm}$ width Γ in the scotogenic model for a pair of $(m_{H^{\pm}}, M_1)$ values is given in Equation 6.3b; the decay rate is obtained through multiplication by $1.51927 \times 10^{24}\ \mathrm{s}^{-1}\mathrm{GeV}^{-1}$. The probability for decaying within the time interval $[0, t_{\mathrm{RF}}]$ corresponds to the cumulative probability

$$P^{\mathrm{dec}}_{t_{\mathrm{RF}}}(t_{\mathrm{RF}}) = \int_0^{t_{\mathrm{RF}}} dt'_{\mathrm{RF}}\, f_{t_{\mathrm{RF}}}(t'_{\mathrm{RF}}) = 1 - \exp(-\Gamma t_{\mathrm{RF}})\,, \qquad P^{\mathrm{dec}}_{t_{\mathrm{RF}}}(0) = 0\,, \qquad P^{\mathrm{dec}}_{t_{\mathrm{RF}}}(\infty) = 1\,, \tag{4.17}$$

hence the probability for a particle to survive until t_{RF} is calculated as

$$P^{\mathrm{sur}}_{t_{\mathrm{RF}}}(t_{\mathrm{RF}}) = 1 - P^{\mathrm{dec}}_{t_{\mathrm{RF}}}(t_{\mathrm{RF}}) = \exp(-\Gamma t_{\mathrm{RF}})\,, \qquad P^{\mathrm{sur}}_{t_{\mathrm{RF}}}(0) = 1\,, \qquad P^{\mathrm{sur}}_{t_{\mathrm{RF}}}(\infty) = 0\,. \tag{4.18}$$

The mean lifetime of a particle is given by the expectation value of t_{RF}, that is, $\tau_{\mathrm{RF}} \equiv \tau = E[t_{\mathrm{RF}}] = 1/\Gamma$. At that time, $P^{\mathrm{sur}}_{t_{\mathrm{RF}}}$ has dropped from 1 to $1/e$.

4.3.2 Constant γ

If the particle moves in the laboratory frame at a constant speed $v_{\mathrm{lab}} = \beta c$, then the probability can be expressed in terms of $t_{\mathrm{lab}} = \gamma t_{\mathrm{RF}}$,

$$\begin{aligned} f_{t_{\mathrm{RF}}}(t_{\mathrm{RF}}) dt_{\mathrm{RF}} &= f_{t_{\mathrm{RF}}}\left(\frac{t_{\mathrm{lab}}}{\gamma}\right) \frac{dt_{\mathrm{RF}}}{dt_{\mathrm{lab}}}\, dt_{\mathrm{lab}} = f_{t_{\mathrm{RF}}}\left(\frac{t_{\mathrm{lab}}}{\gamma}\right) \frac{dt_{\mathrm{lab}}}{\gamma} = \frac{\Gamma}{\gamma} \exp\left(-\frac{\Gamma}{\gamma}\, t_{\mathrm{lab}}\right) dt_{\mathrm{lab}} \\ &= f_{t_{\mathrm{lab}}}(t_{\mathrm{lab}})\, dt_{\mathrm{lab}}\,, \end{aligned} \tag{4.19}$$

with

$$f_{t_{\mathrm{lab}}}(t_{\mathrm{lab}}) = f_{t_{\mathrm{RF}}}\left(\frac{t_{\mathrm{lab}}}{\gamma}\right) \frac{dt_{\mathrm{RF}}}{dt_{\mathrm{lab}}} = \frac{\Gamma}{\gamma} \exp\left(-\frac{\Gamma}{\gamma}\, t_{\mathrm{lab}}\right) \tag{4.20}$$

and

$$P^{\mathrm{dec}}_{t_{\mathrm{lab}}}(t_{\mathrm{lab}}) = 1 - \exp\left(-\frac{\Gamma}{\gamma}\, t_{\mathrm{lab}}\right)\,, \qquad P^{\mathrm{sur}}_{t_{\mathrm{lab}}}(t_{\mathrm{lab}}) = \exp\left(-\frac{\Gamma}{\gamma}\, t_{\mathrm{lab}}\right)\,. \tag{4.21}$$

In the laboratory, the mean lifetime is the expectation value

$$\tau_{\mathrm{lab}} = E[t_{\mathrm{lab}}] = \gamma/\Gamma = 1/\Gamma_{\mathrm{lab}}\,, \tag{4.22}$$

so therefore $\Gamma_{\rm lab} = \Gamma/\gamma$ is decay rate in the laboratory. One can then compute the *laboratory decay length* L from the *proper decay length* $c\tau$ via

$$L = \beta c \tau_{\rm lab} = \frac{\beta c}{\Gamma_{\rm lab}} = \beta c \frac{\gamma}{\Gamma} = \beta\gamma c\tau\,. \tag{4.23}$$

In the literature, it is common use to simply specify $c\tau$.

4.3.3 Varying γ

Now consider the case of interest, $\beta = \beta(t_{\rm lab})$ and $\gamma = \gamma(t_{\rm lab})$. We intend to calculate the same quantities that were previously presented for constant velocities.

One may pose the question whether a treatment only in terms of the travelled distance x rather than $t_{\rm lab}$ would suffice. After all, $\beta\gamma$ is obtained as an x-dependent function and an avoidance of the complication in going to a time-dependent description would be desirable. Unfortunately, it cannot be avoided. First note that it is possible to express the decay probability in terms of the travelled distance through

$$t_{\rm lab} = \frac{x}{v_{\rm lab}} = x\,\frac{dt_{\rm lab}}{dx} = \frac{x}{\beta c}\,, \tag{4.24}$$

so one gets

$$f_x(x)\,dx = f_{t_{\rm lab}}(t_{\rm lab})\,dt_{\rm lab} = f_{t_{\rm lab}}\left(\frac{x}{\beta c}\right)\frac{dt_{\rm lab}}{dx}\,dx = \frac{\Gamma}{\beta\gamma c}\exp\left(-\frac{\Gamma}{\beta\gamma c}\,x\right)dx\,,$$

Γ being the rest frame decay rate. Therefore,

$$f_x(x) = f_{t_{\rm lab}}\left(\frac{x}{\beta c}\right)\frac{dt_{\rm lab}}{dx} = \frac{\Gamma}{\beta\gamma c}\exp\left(-\frac{\Gamma}{\beta\gamma c}\,x\right)\,. \tag{4.25}$$

Since we are interested in the case in which particles stop and decay any given time afterwards, this expression will vanish as $\beta\gamma \to 0$. However, the particle can be trapped at an instant $t_{\rm lab} = t_{\rm stop}$ and then continue to exist for a while before it decays at $t_{\rm decay} > t_{\rm stop}$, so the probability density in Equation 4.25 is not appropriate. We are thus bound to work in the time picture and shall work out a function $t_{\rm lab}(x)$ by imposing that the laboratory time $t_{\rm lab}$ evolves linearly with $t_{\rm RF}$ after the particle stopped. This has the additional advantage that particle lifetimes can be directly compared to detector trigger rates.

Having settled this issue, the starting point of our numerical computation is the determination of $\beta\gamma(x,\eta)$ for a fixed value of η and a given initial momentum $\beta\gamma_0$ by numerically solving the Bethe-Bloch equation.[4] If the particle stops, the Mathematica code registers the position, $x_{\rm stop}$. During movement, with or without deceleration, the Bethe-Bloch solution for some $\beta\gamma_0$ and η is then coupled to an equation yielding the function $t_{\rm lab}(x,\eta)$, *i.e.* the elapsed laboratory time as a function of travelled distance,

$$t_{\rm lab}(x,\eta) = \frac{1}{c}\int_0^x \frac{dx'}{\beta(x',\eta)}) = \frac{1}{c}\int_0^x dx'\,\frac{\sqrt{1+(\beta\gamma)^2(x',\eta)}}{\beta\gamma(x',\eta)}\,, \qquad t_{\rm lab} < t_{\rm stop}\ (t_{\rm exit})\,. \tag{4.26}$$

This function is employed for obtaining time-dependend β and γ factors, as the Bethe-Bloch solution can also be used to compute $\beta(x)$ and $\gamma(x)$. The distance as a function of time can be determined by inverting the above function. We define $x(t_{\rm lab},\eta) = t_{\rm lab}^{-1}(t_{\rm lab},\eta)$, which branches into three cases, depending on whether the particle is decelerating, whether it stopped or whether it was energetic enough for exiting the HCAL without getting trapped:

$$x(t_{\rm lab},\eta) = \begin{cases} t_{\rm lab}^{-1}(t_{\rm lab},\eta)\,, & t_{\rm lab}^{-1}(t_{\rm lab},\eta) < x_{\rm stop}/x_{\rm exit}(\eta)\,, \\ x_{\rm stop}(\eta)\,, & t_{\rm lab}^{-1}(t_{\rm lab},\eta) > x_{\rm stop}(\eta)\,, \\ \beta(x_{\rm exit}(\eta))c\,(t_{\rm lab} - t_{\rm lab}(x_{\rm exit},\eta)) + x_{\rm exit}(\eta)\,, & t_{\rm lab}^{-1}(t_{\rm lab},\eta) > x_{\rm exit}(\eta) \end{cases} \tag{4.27}$$

[4] Due to the momentum of a relativistic particle being given by the product of $\beta\gamma$ and its mass, at times the term 'momentum' will be used for $\beta\gamma$, by an abuse of language. Sometimes, we shall also say 'energy' for γ.

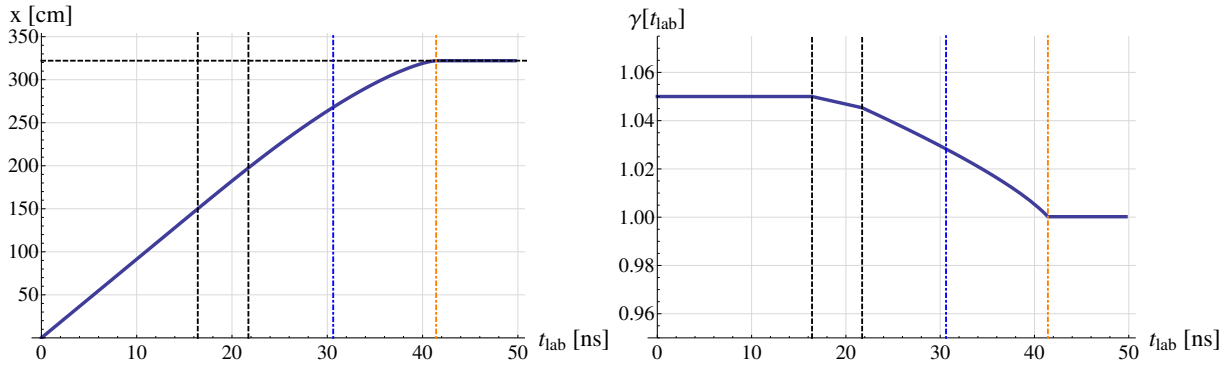

FIGURE 4.11: *Left panel:* Travelled distance as a function of laboratory time (*cf.* Equation 4.27) of a particle with mass 300 GeV, an initial energy of 315 GeV and a pseudorapidity of $\eta = 0$, stopping in the ATLAS HCAL at $x \sim 322$ cm. The mean lifetime is for the example of $M_1 = 100$ keV. The vertical lines mark the following times: Passage ID-ECAL at 16.4 ns and ECAL-HCAL at 21.7 ns (black dashed), $\tau_{\rm lab} = 30.6$ ns (blue dot-dashed) and stopping at 41.4 ns (orange dot-dashed). The initial slope is $\beta_0 c$. *Right panel:* Corresponding time evolution of the particle's gamma factor, as given by Equation 4.28.

i.e. the final position evolution is constant if the particle stops or it is linear with time if the particle exits the HCAL at $x_{\rm exit}(\eta) = \Delta x_{\rm ID}(\eta) + \Delta x_{\rm ECAL}(\eta) + \Delta x_{\rm HCAL}(\eta)$ with a final velocity $\beta = \beta(x_{\rm exit})$, in accordance with the approximation of the muon and magnet system consisting of vacuum. Here, the Δx are the distances travelled in the various detector parts for the given pseudorapidity, *cf.* Table 3.2. The code constructs the function $x(t_{\rm lab}, \eta)$ through an interpolation of $(t_{\rm lab}, (x, \eta))$ value pairs connected by the integral in Equation 4.26. An example is shown in the left panel of Figure 4.11. Now we can immediately construct the varying Lorentz boost,

$$\gamma(t_{\rm lab}, \eta) = \sqrt{1 + (\beta\gamma)^2[x(t_{\rm lab}, \eta)]}\,, \tag{4.28}$$

as shown in the right panel of Figure 4.11, where the particle in the example of the left panel is traced. The decay probability density in the laboratory frame is obtained as before. Analogously to Equation 4.20, we have

$$f_{t_{\rm lab}}(t_{\rm lab}, \eta) = f_{t_{\rm RF}}(t_{\rm RF}(t_{\rm lab}), \eta)\, \frac{dt_{\rm RF}}{dt_{\rm lab}} = \frac{\Gamma}{\gamma(t)} \exp\left(-\frac{\Gamma}{\gamma(t)}\, t_{\rm lab}\right) \tag{4.29}$$

which is normalized to unity.[5] Integrating over $t_{\rm lab}$ yields the lab frame decay and survival probability

[5]The verification is as follows. We first need to use

$$t_{\rm RF}(t_{\rm lab}, \eta) = \frac{1}{c}\int_0^{x(t_{\rm lab},\eta)} \frac{dx}{\beta\gamma(x,\eta)}\,, \qquad \gamma^{-1}(t_{\rm lab}, \eta) = \frac{dt_{\rm RF}}{dt_{\rm lab}} = \frac{1}{\beta\gamma(x(t_{\rm lab},\eta),\eta)c}\,\frac{dx(t_{\rm lab},\eta)}{dt_{\rm lab}}$$

to rewrite the probability density. If the particle stops, it reads

$$f_{t_{\rm lab}}(t_{\rm lab}, \eta) = \begin{cases} \dfrac{\Gamma}{\beta\gamma(x(t_{\rm lab}),\eta)c} \exp\left(-\Gamma \displaystyle\int_0^{x(t_{\rm lab},\eta)} \frac{dx}{\beta\gamma(x,\eta)c}\right) \frac{dx(t_{\rm lab},\eta)}{dt_{\rm lab}}\,, & t_{\rm lab} < t_{\rm stop}\,, \\ \Gamma \exp\left(-\Gamma\left[t_{\rm lab} - \left\{t_{\rm stop} - \displaystyle\int_0^{x(t_{\rm stop},\eta)} \frac{dx}{\beta\gamma(x,\eta)c}\right\}\right]\right)\,, & t_{\rm lab} \geq t_{\rm stop}\,, \end{cases}$$

if it exits, it is always given by the upper formula. The integral in the lower formula corresponds to the RF stopping time, $t_{\rm stop,RF}$. In the case of stopping, integration to infinity results in

$$\begin{aligned} P^{\rm dec}_{t_{\rm lab}}(\infty, \eta) &= P^{\rm dec}_{t_{\rm lab}}([0, t_{\rm stop}], \eta) + P^{\rm dec}_{t_{\rm lab}}([t_{\rm stop}, \infty], \eta) \\ &= \left[-\exp\left(-\Gamma t_{\rm stop,RF}\right) + 1\right] + \left[-\exp\left(-\infty\right) + \exp\left(-\Gamma t_{\rm stop,RF}\right)\right] = 1\,. \end{aligned}$$

If it doesn't stop, then

$$P^{\rm dec}_{t_{\rm lab}}(\infty, \eta) = -\exp\left(-\Gamma \int_0^{x(\infty,\eta)} \frac{dx}{\beta\gamma(x),\eta)c}\right) + \exp\left(-\Gamma \int_0^{x(0,\eta)=0} \frac{dx}{\beta\gamma(x),\eta)c}\right)\,.$$

As time progresses to infinity, $1/\beta\gamma(x),\eta)c \to$ const and $x(\infty, \eta) \to \infty$, so the first term vanishes. The second term equals 1.

and the mean lifetime is found by computing the expectation value of t_{lab},

$$P^{\mathrm{dec}}_{t_{\mathrm{lab}}}(t_{\mathrm{lab}},\eta) = \int_0^{t_{\mathrm{lab}}} d\bar{t}_{\mathrm{lab}}\, f_{t_{\mathrm{lab}}}(\bar{t}_{\mathrm{lab}},\eta)\,, \tag{4.30}$$

$$P^{\mathrm{sur}}_{t_{\mathrm{lab}}}(t_{\mathrm{lab}},\eta) = 1 - \int_0^{t_{\mathrm{lab}}} d\bar{t}_{\mathrm{lab}}\, f_{t_{\mathrm{lab}}}(\bar{t}_{\mathrm{lab}},\eta)\,, \tag{4.31}$$

$$\tau_{\mathrm{lab}}(\eta) = \int_0^{\infty} dt_{\mathrm{lab}}\, \bar{t}_{\mathrm{lab}}\, f_{t_{\mathrm{lab}}}(\bar{t}_{\mathrm{lab}},\eta)\,. \tag{4.32}$$

The decay length cannot be expressed analytically in terms of τ_{lab} for non-constant speeds. But with a numerical evaluation of $x(t_{\mathrm{lab}},\eta)$, L is easily computed via

$$L(\eta) = x(\tau_{\mathrm{lab}}(\eta),\eta)\,. \tag{4.33}$$

We constructed the framework of equations to exactly deal with energy loss of unstable particles in detectors. Whether an initial boost is significant or not depends on the detector geometry and therefore on the path of the particle. It might *in principle* be the case that for a low pseudorapidity, the amount of crossed material in the barrel is not enough to lead to a large deviation of t_{stop} from $t_{\mathrm{stop,RF}}$ (or τ_{lab} from τ_{RF}), while for a higher pseudorapidity, the energy loss is considerable due to the enhanced effective barrel thickness. Now it will be verified that the RF and constant-γ equations do, in fact, suffice for our purposes, as is desirable due to a lower requirement of computational resources.

We focus on the case of slow stopping particles. Consider the survival probability calculated in the particle's rest frame,

$$P^{\mathrm{sur}}_{t_{\mathrm{RF}}}(t_{\mathrm{RF}}) = \exp(-\Gamma t_{\mathrm{RF}})\,. \tag{4.34}$$

Using this expression with the substitution $t_{\mathrm{RF}} \to t_{\mathrm{lab}}$ rather than $P^{\mathrm{sur}}_{t_{\mathrm{lab}}}$ in Equation 4.31 yields a hybrid survival probability at the instant t_{lab} in the lab frame. The committed error is

$$\begin{aligned} E_{P_{\mathrm{sur}}} &= P^{\mathrm{sur}}_{t_{\mathrm{lab}}}(t_{\mathrm{lab}}) - P^{\mathrm{sur}}_{t_{\mathrm{RF}}}(t_{\mathrm{lab}}) \simeq P^{\mathrm{sur}}_{t_{\mathrm{lab}},\mathrm{const}}(t_{\mathrm{lab}}) - P^{\mathrm{sur}}_{t_{\mathrm{RF}}}(t_{\mathrm{lab}}) = \exp\left(-\frac{\Gamma}{\gamma_0}t_{\mathrm{lab}}\right) - \exp(-\Gamma t_{\mathrm{lab}}) \\ &= P^{\mathrm{sur}}_{t_{\mathrm{lab}},\mathrm{const}}(t_{\mathrm{lab}}) \times [\Gamma t_{\mathrm{lab}}\delta_\gamma] + \mathcal{O}(\delta_\gamma^2)\,, \qquad \delta_\gamma = \gamma_0 - 1\,, \qquad \gamma_0 = \gamma(t=0)\,. \end{aligned} \tag{4.35}$$

One finds numerically that approximating the exact expression $P^{\mathrm{sur}}_{t_{\mathrm{lab}}}(t_{\mathrm{lab}})$ by $P^{\mathrm{sur}}_{t_{\mathrm{lab}},\mathrm{const}}(t_{\mathrm{lab}})$ in the first step is only justified for sufficiently small widths Γ, otherwise $P^{\mathrm{sur}}_{t_{\mathrm{lab}}}(t_{\mathrm{lab}})$ turns out to be significantly larger. Large widths are not of interest though, because the bosons would be too short-lived to leave a positive signal and dark matter could become marginally hot. Equation 4.35 needs to be evaluated at stopping times with the maximal boosts for which the particles still stop. We choose the example of a $H^\pm$ with a mass of 100 and 300 GeV and compare the error for production with $|\eta| \sim 0$, minimizing the traversed barrel portion, and $\eta = 1.4$, maximizing it. Using the ATLAS toy detector, the particle with $m_{H^\pm} = 100$ (300) GeV produced with $|\eta| = 0$ and 1.4 is found to stop if its boost differs from 1 by at most $\delta_\gamma \simeq 0.12$ and 0.18 (0.06 and 0.09), stopping after about 35 and 60 (45 and 80) ns, respectively. From Table 6.1, we note that detector-scale decay lengths are realized for widths of about $\sim 10^{-17}$ GeV, corresponding to $M_1 = 10$ (100) keV and a decay rate of ~ 0.4 ns^{-1}. An exact computation gives

$$\left.\frac{E_{P_{\mathrm{sur}}}}{P^{\mathrm{sur}}_{t_{\mathrm{lab}},\mathrm{const}}(t_{\mathrm{lab}} \sim t_{\mathrm{stop}})}\right|_{m_{H^\pm}=100\,\mathrm{GeV}} \simeq 12\%\ (\eta = 0)\,, \quad 30\%\ (|\eta| = 1.4) \tag{4.36}$$

and

$$\left.\frac{E_{P_{\mathrm{sur}}}}{P^{\mathrm{sur}}_{t_{\mathrm{lab}},\mathrm{const}}(t_{\mathrm{lab}} \sim t_{\mathrm{stop}})}\right|_{m_{H^\pm}=300\,\mathrm{GeV}} \simeq 8\%\ (\eta = 0)\,, \quad 21\%\ (|\eta| = 1.4)\,. \tag{4.37}$$

This result implies that the thorough treatment of energy loss can have an effect as high as 30% at high pseudorapidities, while being fairly small at smaller scattering angles. However, this is of no concern due to two reasons. First, slow particles are never produced at large $|\eta|$, as will be checked in Section 6.1.2;

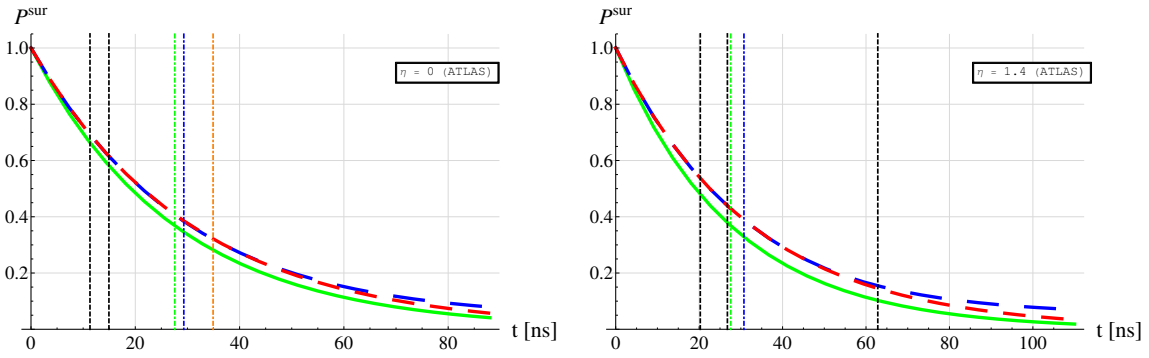

(A) Survival probability of a particle with mass 100 GeV traversing the barrel at pseudorapidity $\eta = 0$ (left panel) and $|\eta| = 1.4$ (right panel) for initial energies chosen close to the maximal energies for which they stop ($\gamma = 1.115$, $\gamma = 1.18$). The decay width is $\Gamma = 2.39 \times 10^{-17}$ GeV ($M_1 = 10$ keV). Among the shown curves are the lab frame probability with a varying γ factor (blue dashed curve) and with constant $\gamma = \gamma_0$ (red dashed curve). For these two curves, the t axis is t_{lab}. The green continuous curve is the RF survival probability, for which the t axis means t_{RF}. The vertical dashed lines represent the passages ID $\rightarrow$ ECAL, ECAL $\rightarrow$ HCAL, HCAL $\rightarrow$ outside (black), τ_{lab} (blue), τ_{RF} (green) and t_{stop} (orange).

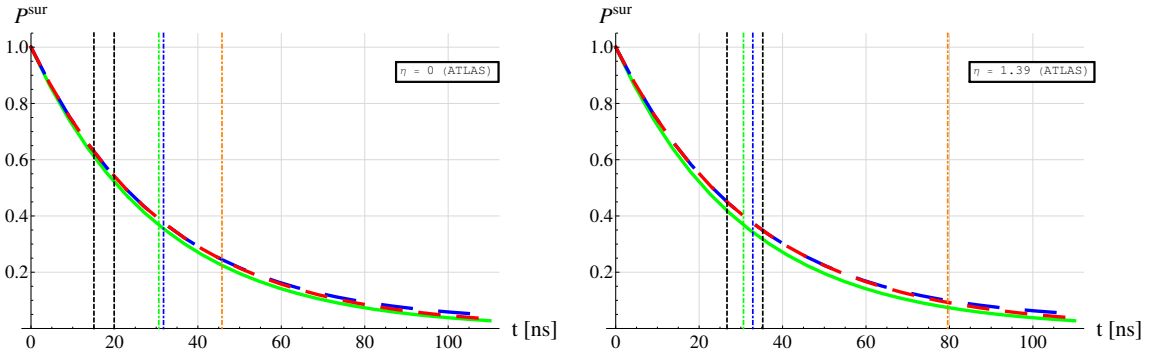

(B) The case of $m_{H^\pm} = 300$ GeV, for pseudorapidities $\eta = 0$ (left panel) and $|\eta| = 1.39$ (right panel). Initial boosts are $\gamma = 1.06$ and $\gamma = 1.09$ and the decay width is $\Gamma = 2.15 \times 10^{-17}$ GeV ($M_1 = 100$ keV). Choosing $|\eta| = 1.4$ in the right plot led to numerical instabilities because the angle corresponds to the barrel-endcap transition point.

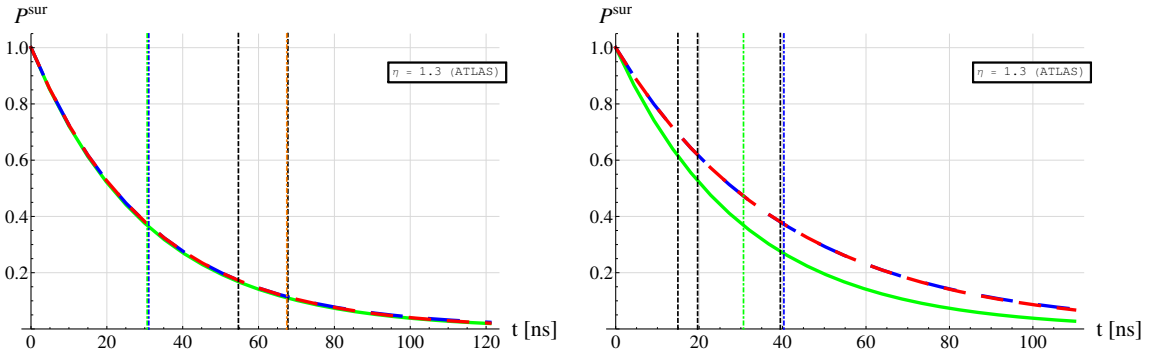

(C) Survival probability of a particle with mass 300 GeV traversing the barrel at pseudorapidity $\eta = 1.3$ with an initial energy of 305 GeV (left panel) and 400 GeV (right panel). The decay width is $\Gamma = 2.15 \times 10^{-17}$ GeV ($M_1 = 100$ keV). One sees that the energy is either too small or too high for the energy loss to have a noticeable impact.

FIGURE 4.12: Survival probabilities for various cases. See captions and text for details and discussion.

second, only very small widths turn out to be of interest in both analyses, IIA and IIB, thus the error due to neglecting energy loss will always be negligibly small.

One can verify in the same way that a use of $P^{\text{sur}}_{t_{\text{lab}},\text{const}}$ is justified if the energy loss is small, *i.e.* when γ never deviates much from γ_0, as shall be the case in Analysis IIA. For the mean lifetimes, these considerations imply $\tau_{\text{lab}} \simeq \tau_{\text{RF}}$ ($\tau_{\text{RF}}/\gamma_0$) for low (large) Lorentz boosts.

For illustration, we depict the survival probabilities of the discussed examples in Figures 4.12a and 4.12b. The blue dashed curve is the exact lab frame probability calculated with Equation 4.31, with a γ factor evolving as in Fig. 4.11. For the red dashed curve, we took $\gamma = \gamma_0$ all throughout the trajectory to see the effect of its variation. This effect clearly results in an increase of P^{sur}, even more so for the larger pseudorapidity. For these two curves, the t axis is t_{lab}. The green curve is the RF survival probability, calculated with Equation 4.18, for which the t axis stands for t_{RF}. It is quite similar to the lab frame curve overall because the boost is small, as we are arguing. τ_{lab} (τ_{RF}) corresponds to the blue (green) vertical dot-dashed line, where τ_{lab} is computed from Equation 4.32. Figure 4.12c compares two extreme cases. On the left, the particle is very low-energetic ($\gamma_0 \simeq 1.017$), whereas on the right, its boost is very significant ($\gamma_0 \simeq 1.33$). As expected, for the slow particle, $P^{\text{sur}}_{t_{\text{lab}}}$ and $P^{\text{sur}}_{\text{lab,const}}$ are indistinguishable from $P^{\text{sur}}_{t_{\text{RF}}}$, while for the energetic case, $P^{\text{sur}}_{t_{\text{lab}}} \approx P^{\text{sur}}_{\text{lab,const}} > P^{\text{sur}}_{t_{\text{RF}}}$. And indeed, one finds $\tau_{\text{lab}} \simeq \tau_{\text{RF}}$ in the first case and $\tau_{\text{lab}} \simeq \tau_{\text{RF}}/\gamma_0$ in the second.

4.4 Comparing stopping times and mean lifetimes

We are now equipped with the tools to calculate the stopping times t_{stop} and mean lifetimes τ_{lab} in ATLAS for mass configurations that are relevant to Analysis IIB. This comparison will give an idea of the sensitivity of the search, because if mean lifetimes are too small, most $H^\pm$ particles will not survive until they become trapped and there will be no signal. As it turns out, the signal is extremely suppressed by small $H^\pm$ production cross sections in the scotogenic model, even with sizeable contributions from gluon fusion, therefore it is very difficult to discover charged scalars with this signature if they are heavy. Our analysis will exclusively treat the cases $m_{H^\pm} = 120$ GeV and $m_{H^\pm} = 150$ GeV, since lower masses result in signals vetoed by a jet energy cut and larger masses suppress phase space too heavily, as we hereby anticipate. In this section, however, we work with the masses

$$m_{H^\pm} \in \{100,\, 120,\, 150\}\ \text{GeV} \tag{4.38}$$

i.e. the case $m_{H^\pm} = 100$ GeV will be included, so that the evolution in behaviour with increasing $m_{H^\pm}$ can be better traced. Furthermore, we consider the 18 RHN masses

$$\begin{aligned} M_1 \in\ & \{1,\, 5,\, 10,\, 20,\, 50,\, 100,\, 200,\, 500\}\ \text{keV}\,, \\ & \{1,\, 2,\, 5,\, 10,\, 20,\, 50,\, 100,\, 200,\, 500\}\ \text{MeV}\,, \\ & 1\ \text{GeV}\,, \end{aligned} \tag{4.39}$$

covering the interesting range more than enough. As we have seen before, both t_{stop} and τ_{lab} depend on the initial energy γ_0 and on the pseudorapidity η. The sterile neutrino masses are only relevant for τ_{lab}. Fixing the pseudorapidy at $\eta = 0$, *i.e.* particle emission perpendicularly to the beam axis, we find that only very low boosts lead to stopped particles, as we have seen in the preceding section. For the three $H^\pm$ masses, the maximum boost factors for which the particles are still stopped by the ATLAS calorimeters are

$$\gamma_{0,\text{lim}}(\eta = 0) = 1.11,\, 1.10,\, 1.09\,. \tag{4.40}$$

Hence, as discussed above, it is justified to use $\tau_{\text{lab}} \simeq \tau_{\text{RF}}$. For larger η, one finds that the maximum limiting boosts are still low enough such that this approximation may be used.

In Figure 4.13, we compare t_{stop} and τ in the left panels, for a given charged scalar mass, while the right panels depict the stopping time as a function of γ_0 from $\gamma_0 = 1.01$ to $\gamma_{0,\text{lim}}$ in steps of $\Delta\gamma_0 = 0.01$. The right plots are independent of M_1. It is easy to identify the points on the right with the lines on

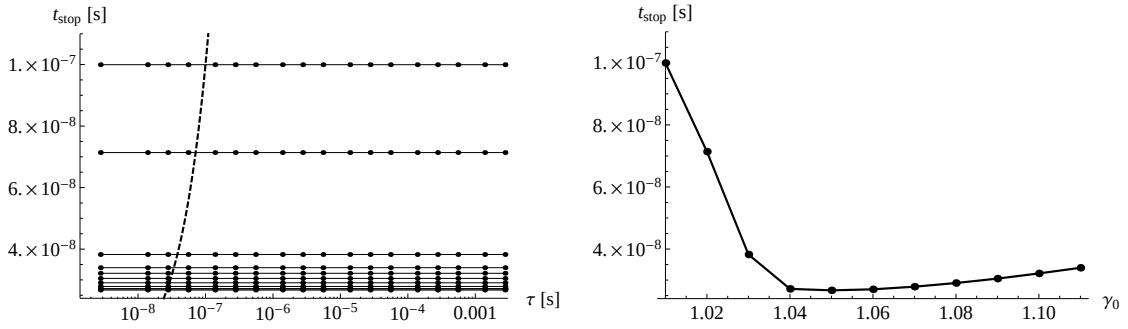

(A) Case of $m_{H^\pm} = 100$ GeV.

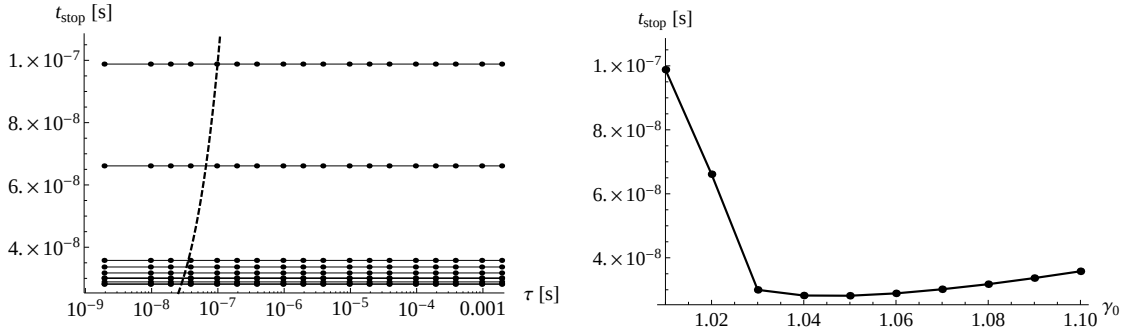

(B) Case of $m_{H^\pm} = 120$ GeV.

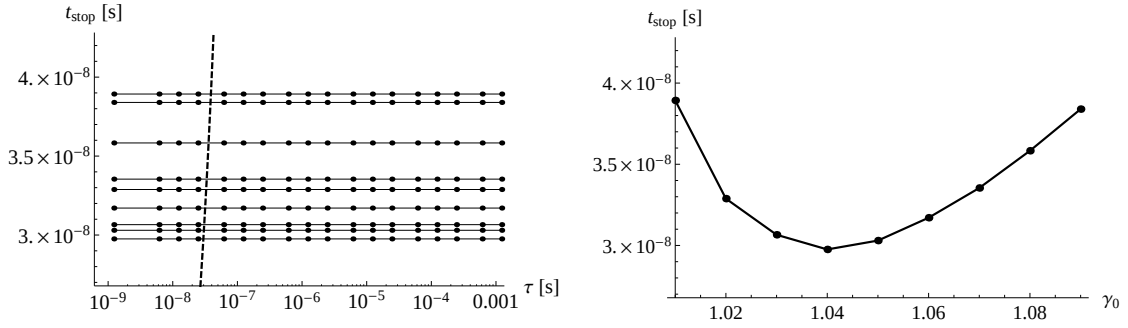

(C) Case of $m_{H^\pm} = 150$ GeV.

FIGURE 4.13: *Left panels:* Mean lifetimes and stopping times in the ATLAS toy detector of $H^\pm$ particles with different masses, for pseudorapidity $\eta = 0$ and initial boosts of $\gamma_0 = 1.01$ to $\gamma_{0,\text{lim}}$ in steps of 0.01 for the N_1 masses given in Equation 4.39. On the black dashed line, both times are equal, $t_{\text{stop}} = \tau$. To its right, the particles get stopped before existing up to their mean lifetime; to its left, the mean lifetime is shorter than the stopping time. *Right panels:* Stopping time as a function of γ_0; this plot looks the same for any M_1 value. Since the t_{stop} axes are up to scale, the points can be easily matched to the lines in the left plot.

the left, because the plots are drawn with the same vertical scale. Each of the horizontal lines in the left plots corresponds to an initial boost γ_0 and the black dashed curve marks the transition from $t_{\text{stop}} > \tau$ to $t_{\text{stop}} < \tau$. τ increases with M_1, so the leftmost point on each of the lines in the left plots corresponds to $M_1 = 1$ keV, the rightmost to $M_1 = 1$ GeV. We note that, as $m_{H^\pm}$ increases, the more N_1 masses end up in the region in which the $H^\pm$ decay before they stop.

From these plots, we can infer the mass configurations for which a search for decaying particles at rest might be sensitive and how the analysis could complement other searches for HLLCPs. From the

expression for the width, Equation 6.3b, one notes that the charged scalar becomes more short-lived with increasing $m_{H^\pm}$. Thus, given a $H^\pm$ mass, the observation of such events would point towards higher dark matter masses, the higher the value of $m_{H^\pm}$. For $m_{H^\pm} = 100$-150 GeV, the lower sensitivity limit on M_1 lies around 10 to 20 keV and, in principle, there is no upper limit. However, an upper sensitivity limit on M_1 stems from the *timing acceptance* originating from the detector trigger and bunch structure, to be discussed in conjunction with the actual analysis.

4.5 Observable decay/survival fraction and stopping efficiency from the kinematical distribution

Having produced a sample of long-lived $H^\pm$ particles, we will be interested in the fraction of particles that decay before (survive until) they reach the end of the detector and are registered, *i.e.* the *observable decay (survival) fraction* (ODF/OSF), and in the observable fraction that is slow enough to stop in the calorimeter material before they decay, the *stopping efficiency*, also called *stopping acceptance*. The first quantity is central to Analysis IIA, the second to Analysis IIB. For the latter, the stopping times have been compared to the mean lifetimes in the previous section, in order to gain an estimate of the parameter space to which a search of this kind could be sensitive. We now get more concrete.

4.5.1 Kinematical distribution

Both the observable decay/survival and the stopping fractions depend on the energies and pseudorapidities the particles originate with from the pp collisions in the LHC detectors, thus we need to work out the probability distributions $f(\eta, \gamma_0)$ of these kinematic variables at the point of production. f is obtained from a Monte Carlo sample of some large number of pp collision events, N_{events}. By dividing the sample into bins with a certain granularity $(\Delta\eta, \Delta\gamma_0,)$, the distributions are created numerically by isolating the $H^\pm$ particles from the decay products and creating respective histograms. In Analysis IIB, this happens by taking

$$f(\Delta\eta, \Delta\gamma_0) \longrightarrow \frac{N_{\text{counts}}(\Delta\eta, \Delta\gamma_0)}{2N_{\text{events}}}\,, \tag{4.41}$$

where the division by 2 is necessary due to the fact that the $H^\pm$ are always pair-produced and both particles are consequently contained in the generated histogram. The distribution is thus to be seen as a one-particle distribution, with information regarding the 2-per-event nature being ignored. Integrals over this distribution are then discretized by summing over counts contained in bins. In Analysis IIA, our approach will be to treat the distribution in a per-event manner, due to a slightly different approach to compute the signal efficiencies. The difference merely lies in the entangling of survival probabilities and detection efficiencies, but a treatment in terms of $f(\Delta\eta, \Delta\gamma_0)$ is completely equivalent.

Finally note that $f(\eta, \gamma_0)$ is a marginal distribution, as we have integrated over the azimuthal angle,

$$f(\eta, \gamma_0) = \int_0^{2\pi} d\phi\, f(\eta, \gamma_0, \phi) = 2\pi\, f(\eta, \gamma_0, \phi_{\text{ref}})\,, \tag{4.42}$$

ϕ_{ref} being some reference angle. We are taking into account the fact that the beams are well enough collimated such that the distribution of produced particles is uniform in the azimuthal direction. The distributions are examined in detail in Section 6.1.2. We next introduce the two fundamental quantities needed for the two studies, however the explanation of their exact application is postponed to the actual analysis sections.

4.5.2 Observable decay/survival fraction (Analysis IIA)

In this section, an expression for the fraction of particles decaying in-flight and passing trigger cuts is derived. Similarly, one works out the fraction of observable particles surviving until they escape the muon system, thus contributing to the charged track signal. The treatment will be in terms of the kinematical distribution f introduced in the previous section and is to be regarded as purely formal. Indeed, CMS provide an official efficiency table to be combined with particle kinematics on a per-event basis, for which the distribution f is unsuited. However, the final computation follows the same principle as the herein presented developments.

First recall the path-dependent decay probability $f_x(x)$ for a RF decay rate Γ, as written in Equation 4.25, with the interaction point placed at the origin, $x = 0$. From previous sections, we know that this expression would be more complicated if one accounted for the effect of the detector material on the particle's energy, though this will be ignored because the search by CMS is only sensitive to relatively highly energetic particles. Hence, the mean lifetime is well approximated by $\gamma_0 \tau_{\mathrm{RF}}$ and one may safely set

$$\gamma_0 \equiv \gamma \,. \tag{4.43}$$

With this definition, the probability to have a decay of a particle with energy in $[\gamma, \gamma + d\gamma]$ in the differential distance and pseudorapidity intervals $[x, x + dx]$ and $[\eta, \eta + d\eta]$ is given by

$$f(x, \eta, \gamma)\, dx\, d\gamma\, d\eta = f(\eta, \gamma)\, f_x(x, \gamma)\, dx\, d\gamma\, d\eta \,. \tag{4.44}$$

$f(\eta, \gamma)$ corresponds to the distribution of $H^{\pm}$ pairs discussed above, treated as a one-particle distribution. With a sample of N_0 produced unstable particles, the differential number of decays along the direction η from the origin until a distance D from the interaction point can be computed as

$$\frac{dN_{\mathrm{dec}}}{d\gamma\, d\eta} = N_0\, f_{\mathrm{dec}}(D, \eta, \gamma) \,, \tag{4.45}$$

where we defined the distribution of one-particle decays within the interval $[0, D]$, for particles emitted with the kinematical configuration (η, γ),

$$f_{\mathrm{dec}}(D, \eta, \gamma) \equiv \int_0^D dx\, f(x, \eta, \gamma) = f(\eta, \gamma) \int_0^D dx\, f_x(x, \gamma) = f(\eta, \gamma)\, P_{\mathrm{dec}}(D, \gamma) \,. \tag{4.46}$$

$P_{\mathrm{dec}}(x, \gamma)$ is the path-equivalent quantity to the decay probability expressed in terms of time in Equation 4.21,

$$P_{\mathrm{dec}}(x, \gamma) = 1 - \exp\left(-\frac{\Gamma}{\beta\gamma c}\, x\right) , \qquad \beta\gamma \equiv \beta\gamma_0 \,. \tag{4.47}$$

It decreases with increasing energy γ, for a fixed position x. Now let R denote the outer radius of the outermost detector barrel layer a HLLCP can leave a signal in. For CMS, this is the last drift tube layer of the muon system at $\gtrsim 7$ m from the beam line (*cf.* Table 3.2). Then the final position of a particle with pseudorapidity η travelling through the barrel until escaping the detector is

$$x_{\mathrm{barrel,max}} = \frac{R}{\sin\theta(\eta)} \,, \tag{4.48}$$

where we can express the polar angle in terms of the pseudorapidity by inverting Equation 3.9,

$$\theta(\eta) = 2 \arctan \mathrm{e}^{-\eta} \,. \tag{4.49}$$

The number of decays in the barrel η range is therefore

$$N_{\mathrm{barrel}} = 2N_0 \int_0^{|\eta|_{\mathrm{barrel}\to\mathrm{EC}}} d\eta \int_1^{\infty} d\gamma\, f_{\mathrm{dec}}(R/\sin\theta(\eta), \eta, \gamma) \,. \tag{4.50}$$

$|\eta|_{\mathrm{barrel}\to\mathrm{EC}}$ is the pseudorapidity separating the barrel from the endcap (*i.e.* marking the detector edge).

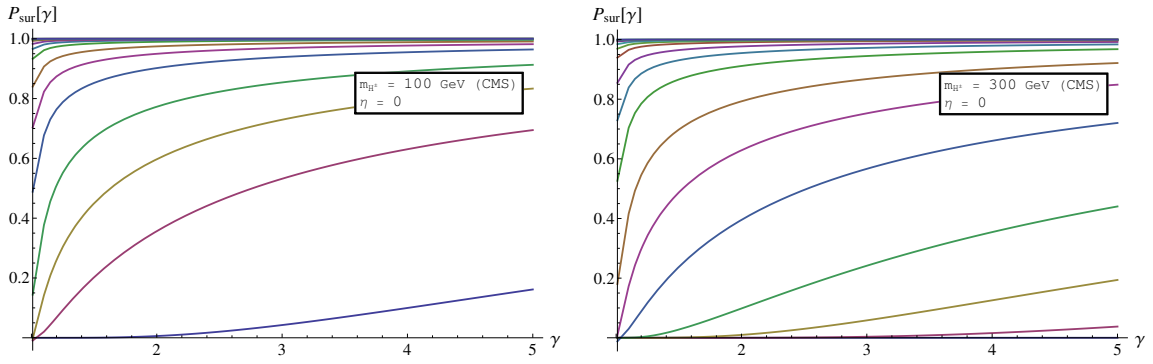

FIGURE 4.14: $P_{\rm sur}(\eta = 0, \gamma)$ for charged scalar masses of 100 GeV (left panel) and 300 GeV (right panel). N_1 masses are those in Equation 4.39. The higher the value of M_1, the higher the curve.

Similarly, the number of decays in the pseudorapidity range of the endcaps is

$$N_{\rm EC} = 2N_0 \int_{|\eta|_{\rm barrel}\to{\rm EC}}^{\infty} d\eta \int_1^{\infty} d\gamma\, f_{\rm dec}(L_z/\cos\theta(\eta), \eta, \gamma)\,, \tag{4.51}$$

where L_z is the distance from the interaction point to the center of the last muon system endcap module (the last endcap CSC active during Run I in CMS was located at a distance of $\lesssim 10$ m). To obtain the fraction of in-flight decays within the detector, simply add the barrel and endcap contributions and divide by N_0,

$$\epsilon_{\rm dec} = \sum_{i={\rm B,E}} \int_{[\eta]_i} d\eta \int_1^{\infty} d\gamma\, f(\eta, \gamma)\, P_{\rm dec}(D_i(\eta), \gamma)\,, \tag{4.52}$$

where $[\eta]_{\rm B,E}$ are the pseudorapidity ranges of the barrel and the endcap and

$$D_{\rm B}(\eta) = \frac{R}{\sin\theta(\eta)}\,, \qquad D_{\rm E}(\eta) = \frac{L_z}{\cos\theta(\eta)}\,. \tag{4.53}$$

In an experimental analysis, one has to account for signal efficiencies reducing the overall acceptance, such as fiducial cuts, quality requirements and detector deficiencies of various kinds. We express these losses in acceptance formally through an efficiency function $\epsilon_{\rm eff}(\eta, \gamma)$ and the final form, the ODF, becomes

$$\boxed{\epsilon_{\rm dec} = \sum_{i={\rm B,E}} \int_{[\eta]_i} d\eta \int_1^{\infty} d\gamma\, f(\eta, \gamma)\, P_{\rm dec}(D_i(\eta), \gamma)\, \epsilon_{\rm eff}(\eta, \gamma)\,.} \tag{4.54}$$

More important for our goals is the OSF,

$$\boxed{\epsilon_{\rm sur} = \sum_{i={\rm B,E}} \int_{[\eta]_i} d\eta \int_1^{\infty} d\gamma\, f(\eta, \gamma)\, P_{\rm sur}(D_i(\eta), \gamma)\, \epsilon_{\rm eff}(\eta, \gamma)\,,} \tag{4.55}$$

with the survival probability in vacuum

$$P_{\rm sur}(\eta, \gamma) = \exp\left(-\frac{\Gamma}{\beta\gamma c}\, D(\eta)\right)\,. \tag{4.56}$$

The number of particles surviving until they exit the detector and therefore potentially contributing to the signal sample in Analysis IIA is then proportional to $\epsilon_{\rm sur}$, which is equal to the experimental acceptance,

$$\boxed{\mathcal{A} = \epsilon_{\rm sur}\,.} \tag{4.57}$$

To finalize this discussion, we plot $P_{\rm sur}(D(\eta), \gamma)$, as a function of the initial boosts γ, for the masses $m_{H^\pm} = 100$ and 300 GeV and for $\eta = 0$, in Figure 4.14. Each curve corresponds to one of the 18 N_1

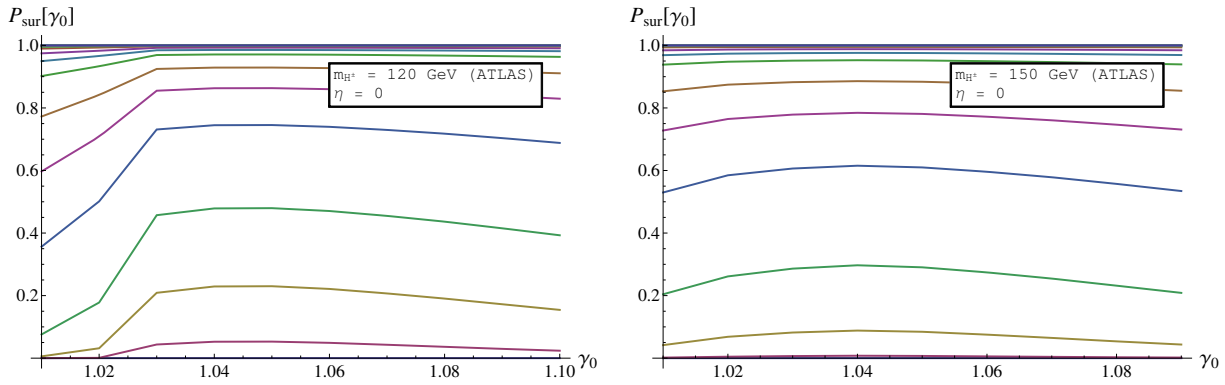

FIGURE 4.15: $P_{\text{sur}}(\eta = 0, \gamma_0, t = t_{\text{stop}})$ for a charged scalar mass of 100 GeV (left panel) and 300 GeV (right panel). N_1 masses are those in Equation 4.39. The higher the value of M_1, the higher the curve.

masses listed in Equation 4.39. We observe that the survival probabilities decrease with increasing $m_{H^\pm}$. This means that more particles will decay before they contribute to the signal, negatively affecting the sensitivity. In addition to the lower survival probabilities, higher masses also imply lower production cross sections. This is counteracted by more $H^\pm$ particles being slow and hence passing cuts on the minimal p_{T}, thus acting favourably on the acceptance $\mathcal{A}$; moreover, the effect on P_{sur} is only appreciable for very small M_1. This tendency of increasing $\mathcal{A}$ with $m_{H^\pm}$ will be explicitly observed in the analysis (Section 6.2). In combination with the absence of a signal excess, this allows to weaken existing bounds on charged heavy particle production (interpreted as $H^\pm$), especially in the low-mass regime due to the much larger cross sections.

4.5.3 Stopping efficiency

In Section 4.4, we have worked out the stopping times t_{stop} for all low initial boosts γ_0 at which the $H^\pm$ particles become trapped in the ATLAS calorimeters when produced with a pseudorapidity $\eta = 0$, for a set of three $H^\pm$ masses. In accordance with the study in Section 4.3.3, the decay probability evolution has been treated as if the particle was at rest relatively to the lab frame. We can thus take the expression for the RF survival probability, Equation 4.18, and define the probability of a $H^\pm$ surviving until the stopping time t_{stop} is reached for a given initial boost, pseudorapidity and decay width Γ,

$$P_{\text{sur}}(\eta, \gamma_0) \equiv \exp\left(-\Gamma\, t_{\text{stop}}(\eta, \gamma_0)\right) . \tag{4.58}$$

$P_{\text{sur}}(\eta, \gamma_0)$ corresponds to the average fraction of particles produced with a boost γ_0 in the direction η not decaying until they are stopped. Its values for $m_{H^\pm} = 120$ and 150 GeV, again for $\eta = 0$, are shown in Figure 4.15, for all 18 N_1 masses. From here, together with the $t_{\text{stop}}(\gamma_0)$ plots in Figure 4.13, the behaviour of P_{sur} with γ_0 can be easily understood. For low boosts, t_{stop} decreases to a minimum from some high initial value, leading to a maximum of $P_{\text{sur}}(t_{\text{stop}})$. As t_{stop} then slowly increases, the probability function, Equation 4.18, starts to slowly decrease. It should be borne in mind that the error using Equation 4.58 can be of the order of 100% in the range $M_1 <$ 1-10 keV due to the neglect of energy losses, as concluded in Section 4.3.3. However, the exact and the approximated survival probabilities are both so small that stopping efficiencies turn out to be tiny and therefore completely negligible. Nevertheless, we include this range in all discussions and in final results in order to gain an idea of the general behaviour of probabilities and efficiencies.

We define the *stopping efficiency*, *i.e.* the fraction of $H^\pm$ particles surviving until they come to rest in

the body of the detector without decaying beforehand, as

$$\boxed{\epsilon_{\text{stop}} = \sum_{i=\text{B,E}} \int_{[\eta_i]} d\eta \int_1^{\gamma_{0,\text{lim}}(\eta)} d\gamma_0 \, f(\eta, \gamma_0) \, P_{\text{sur},i}(\eta, \gamma_0) \, .} \tag{4.59}$$

The *total* stopping efficiency corresponds to the case in which the limits of the η range are the limiting angles marking the inner radii of the calorimeter endcap modules, otherwise we call it the *fiducial* stopping efficiency. In fact, the ATLAS search [46] only considers signals in the barrel region, so we will work with the fiducial stopping efficiency.

CHAPTER 5

Analysis I: On the impact of the Higgs boson on the production of exotic particles at the LHC

5.1 Introduction

As accounted in Section 2.1.1, the announcement by ATLAS and CMS of the discovery of a new bosonic particle [5, 6] with a mass of 125.09 GeV [32] proved the existence of a new interaction in Nature and the striking compliance with properties expected of the SM Higgs boson leads us to believe that we have experimentally started to probe the mechanism of electroweak symmetry breaking. It is well-known that this new interaction is crucial for gurantanteeing the perturbative unitarity at high energies and the renormalizability of the electroweak theory [367]. Moreover, a Higgs boson affects SM phenomenology, such as electroweak precision observables (EWPO) [33, 34] and particle production at colliders [291].

Various alternative mechanisms have been proposed which provide elements mimicking the action of the Higgs field in giving the property of mass to the other particles as described in the SM, like the dynamical symmetry breaking case of composite Higgs models [368] or Higgs-less extra dimension models [369], where the gauge boson and fermion masses emerge from the boundary conditions imposed on the wave functions. However, although it isn't yet established whether the newly found particle is elementary or not, its existence is an indication that the simplest of all mechanisms or some variation thereof might indeed be at work and focus can to some extent be withdrawn from numerous models that were specifically developed for circumventing this approach. In addition, the exact same principle is already found to be realized in Nature by means of the Meißner effect [370], the original inspiration for the Higgs mechanism in high-energy physics. Furthermore, even though the SM doesn't predict the value of its mass, the small measured value lies in a range where it was anticipated to be, due to two principal reasons. First, enabling only the fermionic and vector particle content, a scalar particle is found to be needed to guarantee for the unitarity of longitudinal gauge boson scattering amplitudes, however these violate unitarity again if $m_h \gtrsim 1$ TeV [35] (a simple partial wave expansion yields the more exact upper bound of 780 GeV). Second, already before the discovery by the two LHC experiments, fits of EWPO led to fitted values of m_h around 120 GeV and 90 GeV in the absence of new physics, when and when not including direct Higgs searches, respectively [34].

Of course, other mechanisms might be in effect as well. Indeed, the origin of symmetry breaking is one of the biggest open questions in particle physics and identifying a scalar boson as the resulting particle degree of freedom in the breaking of GWS symmetry is completely dependent on the assessment of the properties of the new particle. One of the key measurements is to what final states it decays. The reason why this is so important is that, now since its mass is known, one can exactly calculate its branching ratios to any kinematically allowed decay product predicted by the Lagrangian. If it turns out to couple to gauge bosons and fermions in proportions compatible with the SM, then one can be assured that its originating $\mathrm{SU}(2)_L$ doublet is to a large extent responsible for the mechanism of EWSB. Nevertheless, the measurements are already very visibly in favour of the SM. While the new boson has been discovered in the high-sensitivity $H \to \gamma\gamma$, $H \to ZZ^* \to 4\ell$ and $H \to WW^* \to \ell\ell\nu\nu$ ($\ell = e, \mu$) channels, the ATLAS and CMS collaborations have already started to determine the decay strengths to the final states comprising third generation fermion pairs $b\bar{b}$ and $\tau^+\tau^-$, improve the measurements of $\gamma\gamma$, ZZ^* and WW^*, obtain upper limits on the BRs to $\mu^+\mu^-$ and $Z\gamma$ and tag for production via ttH. Both experiments do not find significant deviations from the SM values, except for the ttH channels, which are difficult to tag [36, 37] (see Figure 5.1). The fact that decays to the heavy third generation quarks and leptons are

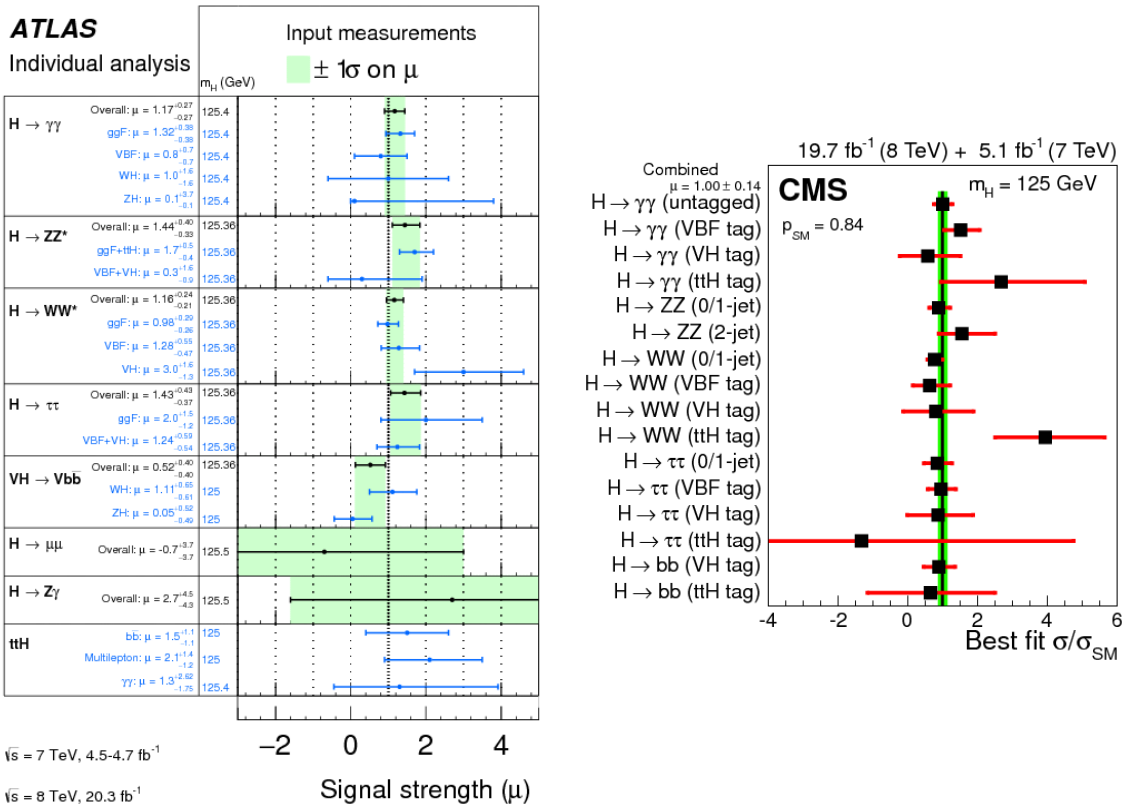

FIGURE 5.1: Measured Higgs signal strengths, kinematically tagged for the production mechanism. A negative signal strength can appear when the number of events lies below the expected background-only hypothesis yield. *Left panel:* Signal strengths measured by ATLAS [36]. The overall signal strength is the combination of all production modes assuming SM cross section ratios. For the subprocesses, the 1σ uncertainties are represented by error bars and for the overall signal strength it is represented by the green shaded areas. The m_H column shows the Higgs mass value at which the result of each analysis is given. The global signal strength result is $\mu = 1.18^{+0.15}_{-0.14}$. *Right panel:* Signal strengths measured by CMS [37]. Results for the overall combinations are shown in a different plot in the cited reference. The error bars indicate the individual 1σ uncertainties, while the green band indicates the overall 1σ uncertainty for $\sigma/\sigma_{\mathrm{SM}}$. The global signal strength result is $\mu = 1.00^{+0.14}_{-0.13}$.

observed but not yet to second generation muons, is already an indication that it might indeed couple to the fermions via a Yukawa interaction that is proportional to the fermion mass, as foreseen within the SM (*cf.* Equation 2.9). As for the spin of the newly found particle, the presence of the VV channels forbids a half-integer spin and according to the Landau-Yang theorem [371], its spin cannot be unity because it decays to two photons. In fact, studies of Higgs diboson decays already strongly favour the $J^{PC} = 0^{++}$ quantum number assignments [38, 39], in consistency with the standard theory. Hence, data seemingly suggests that the discovered boson is truly a Higgs particle.

Despite these facts, there is still plenty of room for new particles beyond the SM to couple to the Higgs field. In particular, renormalizability and the Lorentz and gauge symmetries allow the Higgs doublet H to couple to new scalars S through terms such as H^2S^2, or to fermions Ψ_1, Ψ_2, with Yukawa interactions of the form $\bar{\Psi}_1\Psi_2 H$. In this study, we consider for simplicity a minimal number of new degrees of freedom in addition to the SM fields by adding a single uncoloured representation of $\mathrm{SU}(2)_L$, *i.e.* one extra $\mathrm{SU}(2)_L$ multiplet that is either a Lorentz scalar or a new chiral fermion. We do not consider the case of coloured particles because the production will be largely dominated by the strong interaction. The scalar Higgs portal term is present for any gauge quantum number assignment, whereas the interaction with fermions can only be realized if either Ψ_1 or Ψ_2 is a SM lepton and the new chiral fermion has gauge quantum numbers under $\mathcal{G}_{\mathrm{SM}}$ equal to $(1,1,0)$ or $(1,3,0)$. Clearly, the latter two scenarios correspond to the type I

and type III seesaw models, while the seesaw model of type II provides an example for the former case, with the scalar being an adjoint triplet (*cf.* Sections 2.3.1.2 and Appendix C). In all such scenarios, the new particles can be produced at colliders through their gauge interactions (see *e.g.* [372–374]). A point we want to stress here is that the discovered boson can mediate the production of exotic scalars or fermions as well, since it is a/the Higgs particle. Given the fairly good determination of its mass [32], one can now undertake a systematic study of its quantitative effect on exotic particle production rates at the LHC and other colliders, much in the same spirit radiative corrections have started to be quantified already several decades ago. This task has not been performed by other authors prior to this analysis and posterior to the discovery of the new boson by the ATLAS and CMS collaborations. In the considered case of new uncoloured representations, it is found that the impact can be significant, even of the order of radiative corrections to production via gauge bosons. For instance, there is an ATLAS search for doubly-charged particles [375] containing an interpretation in terms of the doubly-charged scalars featured in Zee-Babu models [228]. Only gauge-mediated production is taken into account. K-factors at the 14 TeV LHC run amount to about 1.2 at NLO over a wide range of scalar masses [376] — this is comparable to what we find for the Higgs-mediated contribution to new particle production in scenarios with additional scalar representations, depending on the electroweak quantum number assignments. Thus our aim in this analysis is to quantify the rates of Higgs-mediated production, including the off-shell regime, in the face of the well-studied electroweak (Drell-Yan) channels yielding the same final states. In some cases, these can be channels which are comparatively subleading with respect to the main channels for the discovery of a model, though any model must ultimately be tested through all experimentally available processes. We additionally remark that the analysis is restricted to a contribution to the total production cross section. In Analysis IIB (Section 6.3.1), we shall see an example not only benefitting from an increase due to the Higgs portal, but also (especially) due to the kinematics characteristic of the channel.

This chapter is organized as follows. Section 5.2 opens by listing the main processes of Higgs production in a pp collider and arguing that the mechanism to be quantified in new heavy particle production is the gluon fusion process. In Section 5.3, we extend the SM by adding a new scalar representation of the gauge group. After discussing the constraints, we work out analytical expressions for the cross sections of the various subprocesses for scalar pair production and present the results in Section 5.3.4. The fermionic case follows with Section 5.4 and is treated completely analogously. Following the common trend of the discussion in the high-energy physics community, we conclude the chapter in Section 5.5 with a brief estimation of the possibilities regarding exotic particle production at a $\sqrt{s} = 100$ proton-proton TeV collider. The contents of this chapter are based on the publication [1].

5.2 Exotic particle production at the LHC and the role of Higgs-mediated gluon fusion

We start by discussing the main subprocesses partaking in the pp collisions at the LHC featured in the production of the new particles. The additional fields interact with the Higgs and electroweak gauge bosons and it is necessary to identify the processes contributing at an appreciable level. The largest LO cross section for the production of new heavy uncoloured particles is that of Drell-Yan-like processes mediated by gauge bosons created in quark-antiquark collisions [377], see Section 5.2.2. Higgs mediation at the LHC, the contribution we intend to quantify, is dominated by the channel also dominating on-shell Higgs production. For a given pp CM energy $\sqrt{s}$, this depends on the mass of the Higgs boson. Figure 5.2, taken from [378], shows the cross section for the Higgs production subprocesses in the SM as a function of the Higgs mass at $\sqrt{s} = 14$ TeV on the left and for $m_h = 125$ GeV as a function of $\sqrt{s}$ on the right. Not drawn are the values for associated tH production, which provides the weakest contribution [378]. The gluon-gluon fusion (ggF) process $gg \to h$ (ggH) [379] is very visibly dominant over the full shown mass range, as was also the case for the Tevatron operating at $\sqrt{s} = 1.96$ TeV [291]. The reason, as has been known for a long time [380], is the enhancement due to the gluon distribution function in the protons,

cf. Section 3.1.3. For Higgs masses $\gtrsim$ 1 TeV, ggH gets superseded by the vector boson fusion (VBF) process [381]. We now quickly summarize the main contributions, along with representative diagrams and cross sections for on-shell Higgs production at the LHC from [378]. The orders are specified in Figure 5.2 and information on SM K-factors can be found in [291].

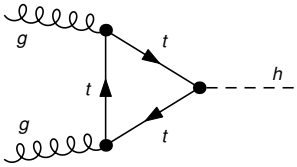

Gluon-gluon fusion [379]:
The ggH channel provides the dominant contribution to Higgs production at hadron colliders over the entire interesting mass and energy range. For $m_h = 125$ GeV, the cross section at LHC amounts to about 19.5 (49.7) pb at $\sqrt{s} = 8$ (14) TeV, the uncertainties being up to 20% [78]. The 14 TeV cross section is almost two orders of magnitude larger than at the Tevatron during the 1.96 TeV run [291]. At a hypothetical 100 TeV collider, it rises to 740 pb [382]. Its (finite) amplitude consists of a triangle loop with heavy quarks coupling to the Higgs with a strength proportional to their mass. The K-factor is pretty large, already about 1.6 at NLO at the LHC (and even above 2 at the Tevatron). At NNLL, the LHC K-factor is increased to about 2, with an uncertainty of about 5% from the gluon PDF. For being by far the strongest, we utilize the ggH channel for computing the impact of Higgs mediation.

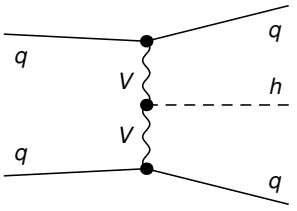

Vector boson fusion [381]:
VBF follows ggH, with a cross section of 1.6 (4.3) pb at $\sqrt{s} = 8$ (14) TeV. It is thoroughly discussed in [291]. In both the LHC and the Tevatron, it is an order of magnitude smaller than ggH. This remains so at a 100 TeV collider, where the cross section amounts to 82 pb [382]. The events can be tagged by knowing that the Higgs decay products will be quite central, whereas the two quarks are emitted at high pseudorapidities of $1 \lesssim |\eta| \lesssim 5$. The QCD NLO K-factor lies somewhere between 1.02 and 1.08, depending on the used factorization scheme.

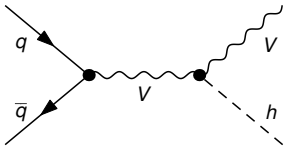

Higgsstrahlung [383]:
This is the emission of a Higgs boson off an on- or off-shell W or Z produced in the s-channel (the 'Bjorken process'). For $m_h = 125$ GeV, only the off-shell case is viable. At $\sqrt{s} = 8$ TeV, the W (Z) channel contributes with 0.7 (0.4) pb and at $\sqrt{s} = 14$ TeV, the cross sections are increased to about 1.5 (1) pb. While at LO, the gauge bosons are produced by colliding quarks, radiative corrections additionally provide the loop-induced process $gg \to Z^{(*)} \to Z\,h$ at NLO, the sum of a fermion triangle and a box. Due to the large gluon PDF, these corrections can be significant. At NNLO including QCD and EW corrections, the K-factor at the 14 TeV LHC amounts to about 1.2 for both final states.

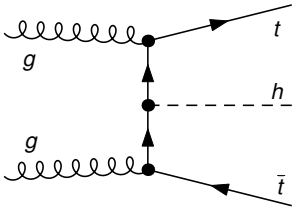

Associated production with two top quarks [384]:
The ttH process is very involved to compute already at LO due to the three massive particles in the final state. At LO, the cross section varies rapidly with m_h and becomes stabilized when including the even more cumbersome NLO corrections. At the LHC with $\sqrt{s} = 8$ (14) TeV, the NLO cross section has a value of 0.13 (0.61) pb. The K-factor varies between 1.2 and 1.4, depending on the factorization scale. For $\sqrt{s} \sim 12$ TeV and lower, the final state $b\bar{b}h$ actually yields somewhat larger cross sections due to the wider phase space, though it is more difficult to tag due to the large QCD background to the dominant $b\bar{b}b\bar{b}$ final state [291].

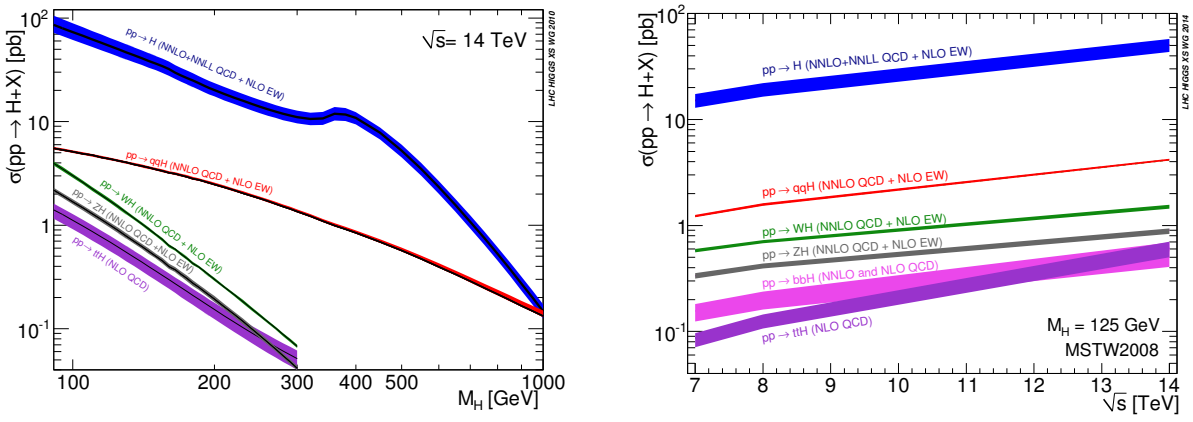

FIGURE 5.2: SM Higgs production cross sections for pp collision subprocesses. Orders in QCD range from NLO (ttH) to NNLL (ggF). *Left panel:* Cross sections as a function of m_h for $\sqrt{s} = 14$ TeV, the nominal LHC pp CM energy. *Right panel:* Cross sections for m_h fixed at 125 GeV and $\sqrt{s}$ varying from 7 to 14 TeV. Figure from [378].

Other subleading processes are associated th production and the Yukawa process $q\bar{q} \to h$, the latter being totally insignificant due to the tiny masses of the first and second generation quarks and the negligible virtual b-quark content within the proton.

Given the enormous enhancement of the ggH cross section at the high LHC energies, we consider this channel exclusively for analyzing Higgs mediation in BSM scenarios. Another electroweak process of equal significance is ggF with Z mediation [380], to be discussed in Section 5.2.1.2. The computation of its contribution is very interesting in itself theoretically. Its amplitude is closely related to the well-known chiral anomaly [70–72] and we dedicate Appendix F to a discussion of the connection. The relative importance of the production mechanisms depends on the details of the new physics model. In the following, we discuss separately the cases of scalar and of fermionic particle production. Since we are not aiming to give precise predictions, we shall work with the LO contributions to the partonic cross sections, though the eventually large K-factors in ggF should be borne in mind. For consistency, LO parton PDFs will be chosen for total numerical pp cross section computations. More concretely, we mostly opt for the CTEQ5L PDF set [296], except where it is explicitly stated otherwise.

5.2.1 Production via ggF

At hadron colliders, ggF incorporates the ggH and the ggZ processes. Before outlining these specific production channels, we focus on the generic aspect of how to compute the total pp cross section of two colliding gluons. At the LHC, the production cross section of the final state X_1X_2, where X_1 and X_2 are not necessarily different particles, is given by the convolution of the partonic cross section $\hat{\sigma}$ with the corresponding PDF, as discussed in Section 3.1.3. Concretely for the case of gluon-gluon fusion in a pp collision at a given CM energy $\sqrt{s}$, Equation 3.32 provides the expression

$$\sigma\left(pp \to X_1X_2;\, s\right) = \int_{\tau_{\text{thr}}}^{1} d\tau \, \frac{d\mathcal{L}_{gg}}{d\tau} \, \hat{\sigma}\left(gg \to X_1X_2;\, \hat{s} = \tau s\right) , \tag{5.1}$$

where $\tau_{\text{thr}} \equiv (m_{X_1} + m_{X_2})^2/s$ and $\mathcal{L}_{gg}$ is the gluon luminosity function (*cf.* Equation 3.33), defined as

$$\frac{d\mathcal{L}_{gg}}{d\tau} = \int_{\tau}^{1} \frac{dx}{x} \, g\left(x, \mu_{\text{F}}\right) g\left(\frac{\tau}{x}, \mu_{\text{F}}\right) . \tag{5.2}$$

The gluon PDF, $g(x, \mu_F)$, depends on the fraction x of the proton momentum carried by the gluon and on the factorization scale μ_{F}.

5.2.1.1 The ggH process

At leading order, the contribution to the ggH vertex consists of a triangular diagram with effectively only the top quark in the loop with subleading corrections due to the bottom quark, while lighter flavours are essentially negligible. The diagrams for scalar and fermionic particle production are

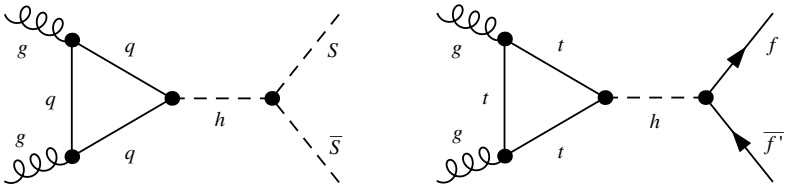

It is common procedure in the literature [385] to take the ggH process into account by introducing an effective Lagrangian for the Higgs interaction with gluons

$$\mathcal{L}_{h,\text{eff}} = \frac{1}{4} G_h G^a_{\mu\nu} G^{a\mu\nu} \frac{h}{v}, \tag{5.3}$$

where G_h is an effective coupling and $v \simeq 246$ GeV is the Higgs VEV, while $G^a_{\mu\nu}$ and h correspond to the gluon field strength tensor and the Higgs field operator, respectively. To find G_h, one computes the spin-averaged $gg \to h$ s-channel triangle matrix element and matches the coefficient to the known cross section for on-shell Higgs production [385]. The computation is easily done with FeynCalc [386], which takes care of the arising subtleties regarding the dimensional regularization procedure. One obtains

$$\begin{aligned} \overline{\mathcal{M}} &\propto \sum_q m_q^2 \left[2 + (4m_q^2 - \hat{s}) C_0(0,0,\hat{s},m_q^2,m_q^2,m_q^2)\right] \\ &\propto \sum_q \left[2\tau_q + \hat{s}(\tau_q - 1) C_0(0,0,\hat{s},m_q^2,m_q^2,m_q^2)\right] , \end{aligned} \tag{5.4}$$

where m_q is the mass of the quark in the loop, $\hat{s}$ is the CM energy of the colliding gluons and $C_0(0,0,\hat{s},m_q^2, m_q^2,m_q^2)$ is the scalar 3-point Passarino-Veltman function, *cf.* Section D.3. Moreover, we are using the Drell-Yan variable from Equation 3.31, *i.e.*

$$\tau_q = \frac{4m_q^2}{\hat{s}} . \tag{5.5}$$

The analytical form of this particular C_0 integral is [387]

$$C_0(0,0,\hat{s},m_q^2,m_q^2,m_q^2) = -\frac{2}{\hat{s}} f(\tau) , \tag{5.6}$$

$f(\tau)$ being the well-known function

$$f(\tau) = \begin{cases} \arcsin^2 \dfrac{1}{\sqrt{\tau}} & \text{if } \tau \geq 1 , \\ -\dfrac{1}{4}\left[\ln\left(\dfrac{1+\sqrt{1-\tau}}{1-\sqrt{1-\tau}}\right) - i\pi\right]^2 & \text{if } 0 \leq \tau < 1 . \end{cases} \tag{5.7}$$

Matching to the on-shell Higgs production cross section [387] with the substitution $m_h^2 \to \hat{s}$ yields

$$G_h(\hat{s}) = \frac{\alpha_s}{4\pi} \left| \sum_q A_{1/2}(\tau_q) \right| , \tag{5.8}$$

employing the commonly used notation [291, 385]

$$A_{1/2}(\tau) = 2\tau \left[1 - (1-\tau) f(\tau)\right] . \tag{5.9}$$

Since the loop function $A_{1/2}$ is proportional to the loop quark mass due to the involved Yukawa interaction, light quarks do not contribute significantly, even with a smaller propagator suppression in the fermion

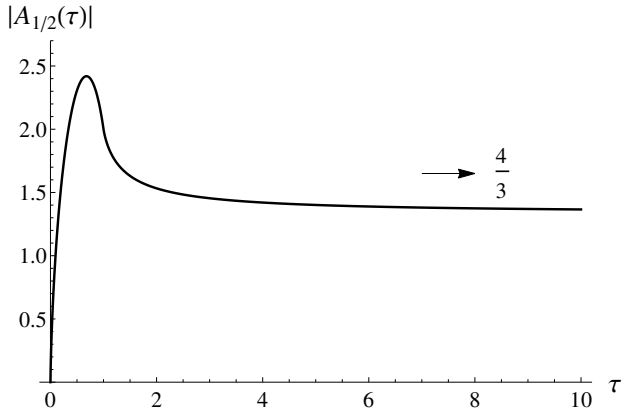

FIGURE 5.3: The loop factor $A_{1/2}(\tau)$ appearing in the ggH amplitude, as contributed by a quark with mass $m = 2\sqrt{\hat{s}}$. See text for some details.

triangle. Hence, only the third generation quarks are usually considered and in our computations, we only include the top quark. The behaviour of the loop form factor is depicted in Figure 5.3. As the quark mass decreases from a large value compared to $\hat{s}$, $|A_{1/2}|$ slowly increases from $sim4/3$ to start quickly rising at $\tau \sim 1.6$ up to a peak of about 2.42 at $\tau \approx 0.68$ and then decreases to zero, with an evolution that is linear modulo logarithmic coefficients, *i.e.* $A_{1/2} \sim \tau \ln(4\tau)$ [385]. At the threshold of real quark pair production, $\tau = 1$, $A_{1/2}$ becomes complex and its modulus equals exactly 2.

5.2.1.2 The ggZ process

In addition to ggH, another contribution can arise from the gluon-gluon-Z triangle diagram. Furry's theorem [388] forbids VVV triangles, therefore the analogous process with an intermediate photon is not allowed and the Z acts as a pure pseudovector, coupling to the triangle exclusively axially. This relates the amplitude to the chiral anomaly. Furthermore, it turns out that the LO amplitude vanishes for a degenerate final scalar pair [389]. Here we only consider multiplets in which neutral components remain complex fields after EWSB, thus we only need to consider fermionic states:

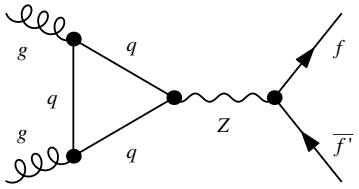

As we are only interested in the production from real on-shell gluons in the initial state, the general form of the ggZ vertex originally derived by J. S. Bell and R. Jackiw in [72] can be simplified by means of transversality relations of the gluon polarization vectors. The gauge invariant form appropriate for this process was first used by D. A. Dicus and S. S. D. Willenbrock in [380] and the first explicit appearance of the vertex (Equation F.60) is to be attributed to Dicus and P. Roy [390]. Through the vertex, one can write down the effective Lagrangian

$$\mathcal{L}_{Z,\text{eff}} = \frac{1}{4} G_Z \partial_\alpha Z^\alpha G^a_{\mu\nu} \tilde{G}^{a\mu\nu} \,, \tag{5.10}$$

where $\tilde{G}^{a\mu\nu}$ is the dual gluon field strength tensor, and the effective coupling G_Z is given by [380, 390]

$$G_Z = \frac{\alpha_\mathrm{s}}{2\pi}\frac{e}{\mathrm{s_w}\,\mathrm{c_w}}\left|\sum_Q (-1)_Q\, F_Z(\hat{s}, m_Q^2)\right|, \tag{5.11}$$

where $\mathrm{s_w}$ and $\mathrm{s_w}$ correspond to the sine and the cosine of the weak mixing angle angle, with the form factor

$$F_Z(\hat{s}, m_Q^2) = \frac{1}{\hat{s}}\left\{1 + \frac{2m_Q^2}{\hat{s}}\int_0^1 \frac{dx}{x}\ln\left[1 - \frac{\hat{s}}{m_Q^2}\,x\,(1-x)\right]\right\}. \tag{5.12}$$

The sum runs over all quark flavours Q present in the triangle loop and $(-1)_Q$ equals $+1$ for up-type quarks and -1 for down-type quarks. The first term in the from factor is flavour-independent and therefore drops out in the sum over quark generations. As the second term is proportional to the square of the quark mass, the top contribution will again be dominant and one can confidently neglect lighter quark flavours. F_Z can also be expressed in terms of Passarino-Veltman functions, see *e.g.* [391]. Due to the pseudoscalar nature of the intermediate Z boson, couplings to final vectorial currents are suppressed compared to the interaction with axial currents,

$$\begin{aligned}\hat{\sigma}_{\mathrm{ggZ}}(f_1, f_2) = {} & \frac{\alpha_\mathrm{em}\,\alpha_\mathrm{s}^2\sqrt{(\hat{s}-(m_1-m_2)^2)\,(\hat{s}-(m_1+m_2)^2)}}{2048\,\pi^2\,\mathrm{s_w^2\,c_w^2}\,m_Z^4}\left|\sum_Q (-1)_Q\, F_Z(Q)\right|^2 \\ & \times\left[g_\mathrm{v}^2\,(m_1-m_2)^2\,(\hat{s}-(m_1+m_2)^2)\right. \\ & +\left.\ g_\mathrm{a}^2\,(m_1+m_2)^2\,(\hat{s}-(m_1-m_2)^2)\right].\end{aligned} \tag{5.13}$$

Though not our main focus, this process contributes with a strength comparable to ggH [391] and understanding the form of the vertex is an interesting exercise due to its connection to the chiral anomaly. This issue is explored in Appendix F.

As a final remark, the Lorentz structures of the ggH [387] and ggZ [380] amplitudes are[1]

$$\mathcal{M}_h^{\mu\nu} \sim A P^{\mu\nu} + B p_1^\mu p_2^\nu, \qquad \text{with} \quad P^{\mu\nu} = g^{\mu\nu} - \frac{2p_1^\mu p_2^\nu}{\hat{s}} \tag{5.14}$$

and

$$\mathcal{M}_Z^{\alpha\mu\nu} \sim \epsilon^{\mu\nu\lambda\tau}\, p_{1\lambda}\, p_{2\tau}\,(p_1+p_2)^\alpha, \tag{5.15}$$

respectively. With the relation

$$\sum_{\text{all pol.}} \epsilon^\mu \epsilon^{*\nu} = -g^{\mu\nu}, \tag{5.16}$$

it is straightforward to verify that interference terms in spin-averaged cross sections $\bar{\sigma} \sim \sum_{\text{pol.}} |\mathcal{M}_h + \mathcal{M}_Z|^2$ cancel, such that both processes sum incoherently.

5.2.2 Production via Drell-Yan

In proton-proton collisions, the Drell-Yan (DY) process [377] comes in at lowest-order in perturbation theory for new particle production. Originally, the name stood for dilepton production in hadron collisions mediated by virtual photons, possibly including contributions by the Z boson. In modern terms, one often speaks of pair production mediated by any gauge boson in the s-channel, a nomenclature we herein adopt, excluding ggZ. At LO, the collision happens between a valence quark and a $\bar{u}$, $\bar{d}$ or $\bar{c}$ sea quark, resulting in W or Z boson mediation, depending on the sum of the initial charges. This process is a standard candle in determining nucleon quark PDFs, which differ from the PDFs in free protons [392]. The LO process is represented by the diagrams

[1] In fact, gauge invariance requires the gluon fields to be transversal with respect to their momenta, hence the $p_{1,2}$ portions of $\mathcal{M}_h$ don't contribute to the averaged cross section.

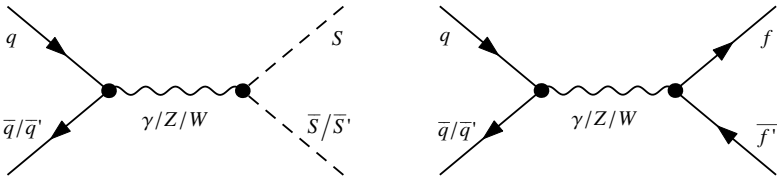

Correspondingly, the total cross section reads

$$\sigma\left(p\,p \to X_1 X_2;\, s\right) = \sum_{q=u,d} \int_{\tau_{\rm thr}}^{1} d\tau\, \frac{d\mathcal{L}_{q\bar{q}}}{d\tau}\, \hat{\sigma}\left(q\bar{q} \to X_1 X_2; \hat{s} = \tau s\right)\,, \tag{5.17}$$

with the quark luminosity function

$$\frac{d\mathcal{L}_{q\bar{q}}}{d\tau} = \int_{\tau}^{1} \frac{dx}{x} \left[q\left(x, \mu_{\rm F}\right) \bar{q}\left(\frac{\tau}{x}, \mu_{\rm F}\right) + q\left(\frac{\tau}{x}, \mu_{\rm F}\right) \bar{q}\left(x, \mu_{\rm F}\right)\,. \right]\,, \tag{5.18}$$

$q(x, \mu_{\rm F})$ and $\bar{q}(x, \mu_{\rm F})$ being the quark and antiquark PDFs, respectively.

5.3 Adding a scalar multiplet

5.3.1 The benchmark model

We consider the addition of a complex scalar field S to the SM particle spectrum, assumed to be uncoloured, and taken to be a generic multiplet of $\mathrm{SU}(2)_L$with weak isospin T and hypercharge Y. S has the $n = 2T+1$ components

$$S = \left(S_1, \ldots, S_n\right)^T\,. \tag{5.19}$$

Then, all the interactions of S with the SM electroweak gauge bosons and the Higgs doublet H are given by the Lagrangian

$$\mathcal{L}_S = \left(D_\mu\, S\right)^\dagger \left(D^\mu\, S\right) - \mathcal{V}(S, H)\,. \tag{5.20}$$

In the spherical/charge basis of weak isospin (*cf.* Section C.2), the covariant derivative D_μ of S includes the usual terms involving the Z and photon fields,

$$D_\mu \supset -i\frac{1}{\sqrt{g^2 + g'^2}}\, Z_\mu \left(g^2 T^3 - g'^2 \frac{Y}{2}\right) - i\frac{g g'}{\sqrt{g^2 + g'^2}}\, A_\mu\, Q\,, \tag{5.21}$$

where we define the electric charge $Q = T^3 + Y/2$.

As benchmark scenario, we consider the most generic renormalizable scalar potential $\mathcal{V}(S, H)$ invariant under a global $U(1)$ symmetry [393]:[2]

$$\begin{aligned}\mathcal{V}(S, H) = {} & \mu^2\, H^\dagger H + f_1 \left(H^\dagger H\right)^2 + \mu_S^2\, S^\dagger S + f_2 \left(S^\dagger S\right)^2 + f_3 \left(H^\dagger H\right) \left(S^\dagger S\right) \\ & + f_4 \left(H^\dagger \tau^a H\right) \left(S^\dagger T^a S\right) + f_5 \left(S^\dagger T^a S\right) \left(S^\dagger T^a S\right)\,.\end{aligned} \tag{5.22}$$

Here, T^a (τ^a), $a = 1, 2, 3$, are the generators of $\mathrm{SU}(2)_L$ in a generic (the fundamental) representation. To be more precise, τ^a in the $H\tau H$ term are the Cartesian generators given by the Pauli matrices σ_i divided by 2 and T^a span the Cartesian SU(2) algebra in an arbitrary dimension while acting on multiplets defined in the spherical basis in which T^3 is diagonal (see the discussion in Section C.2). Since the third generator is diagonal in such a representation, this implies $T^3 S_1 = T S_1$ and $T^3 S_n = -T S_n$.

[2] In the case of a real multiplet, the operator $S^\dagger T^a S$ in $\mathcal{V}$ is identically zero, so that the components of a real multiplet are degenerate in mass, at tree-level.

Due to the U(1) symmetry, the Lagrangian in Equation 5.20 contains all terms involving S. Depending on the attributed quantum numbers, one of the components of S can be electrically neutral. In the following, we assume that neutral components do not acquire a VEV or, if they do, a negligibly small one compared to the SM Higgs VEV, *i.e.* $\langle S^{(0)} \rangle \ll v$. Various well-motivated such models exist. For instance, one member of the pool of E. Ma's models for neutrino mass generation is a 2HDM adding to the SM spectrum a set of RHNs and a Higgs doublet η with lepton number $L = -1$ [41]. Allowing only for soft lepton number breaking then forbids Yukawa terms of the RHNs with the SM Higgs doublet H and introduces the scalar interaction $\mu_{H\eta}^2(H^\dagger\eta)$, in addition to $\mu_\eta^2(\eta^\dagger\eta)$. $\mu_{H\eta}$ softly breaks lepton number, hence it is natural to assume that it remains naturally small when renormalized and phenomenology involving the scalars will be hardly affected by $\mathrm{U(1)_L}$ violation. If $\mu_\eta \sim 1$ TeV, then $\langle \eta^{(0)} \rangle \sim \mu_{H\eta} v/\mu_\eta \ll v$. This is similar to the canonical type II seesaw mechanism [14], which only relies on a Higgs triplet naturally acquiring a small VEV and where $\mathrm{U(1)_L}$ is softly broken by a term in the scalar potential (see Appendix C.2). Moreover, the triplet VEV is required to be small compared to v in order to comply with fits of the ρ parameter [394]. Another example is provided by minimal dark matter models, where dark matter is provided through the neutral component of one additional scalar representation only interacting with SM fields via the Higgs portal. Under the condition that its hypercharge vanishes, as required by direct detection constraints, and that it corresponds to the lightest member of the multiplet, stability is guaranteed by a global U(1) or $\mathbb{Z}_2$ symmetry. In the case $n \geq 7$, no such symmetry is necessary due to the absence of renormalizable or dimension-5 operators that could allow decays to SM particles [395].

At tree-level, the mass splitting within the multiplet S is controlled by the coupling f_4 in the potential.[3] In the following, we will classify the multiplet components by the electric charge, where we refer to the component with charge equal to Q by $S^{(Q)}$. The tree-level squared mass of each eigenstate after EWSB is then given by

$$m_{S^{(Q)}}^2 = \mu_S^2 - \frac{1}{4}\Lambda_Q v^2 \,, \tag{5.23}$$

where the coupling Λ_Q is defined as

$$\Lambda_Q = -2f_3 + f_4 T^3 = -2f_3 + f_4\left(Q - \frac{Y}{2}\right) \,, \tag{5.24}$$

and sets the strength of the interaction of the Higgs boson with two scalars, that is

$$\mathcal{L}_{\mathrm{int}} = \frac{1}{2}\Lambda_Q v h S^{(Q)}\bar{S}^{(Q)} + \frac{1}{4}\Lambda_Q h^2 S^{(Q)}\bar{S}^{(Q)} \,. \tag{5.25}$$

Note that the mass difference between two consecutive multiplet members can be either positive or negative, depending on the sign of f_4. Moreover, there is a mass splitting induced by gauge boson loops that is independent of the quartic couplings [395]. However, it only amounts to a contribution of $\Delta m_{\mathrm{loop}} \sim \mathcal{O}(100\ \mathrm{MeV})$. Compared to our considered splittings of several GeV, this represents an insignificant correction and shall henceforth remain neglected.

We sufficiently specified the basics of our model. Before presenting numerical results, it is necessary to consider the constraints on the parameters of the Lagrangian.

5.3.2 Constraints

The parameter space of the model at high-energy is spanned by the couplings and mass parameters in the potential, which are constrained theoretically. Additionally, one must consider the parameters at low energies, *i.e.* the masses and low-energy couplings. These are especially constrained phenomenologically.

[3] If the global U(1) is explicitly broken to an accidental $\mathbb{Z}_2$ symmetry, then for n even and $Y = 1$, the operator $(H^\dagger\tau^a\tilde{H})(S^\dagger T^a\tilde{S})$ is allowed, where $\tilde{H} = \epsilon_2 H^*$ and $\tilde{S} = \epsilon_n S^*$ are the conjugate scalar multiplets, with $\epsilon_n = \exp(iT_2^{(n)})$. This operator provides an independent contribution to the relative mass splittings.

Under the requirement of vacuum stability, the couplings must fulfil the tree-level conditions [393]

$$f_{1,2} > 0\,, \tag{5.26}$$

$$\Lambda_Q < 4\sqrt{f_1 f_2} = 2\,\frac{m_h}{v}\,\sqrt{2 f_2} \simeq 5\,, \tag{5.27}$$

where the numerical bound in the last equation comes from taking the perturbativity limit $f_2 = 4\pi$. Furthermore, we choose masses $m_{S^{(Q)}} \geq 100$ GeV, in order not to fall into conflict with gauge boson invisible width measurements at LEP [78, 396].

Constraints on the mass splitting between two states are set by unitarity bounds of scalar-scalar and scalar-gauge boson scattering amplitudes and EWPO. The latter are commonly formulated in terms of the so-called oblique parameters S, T and U [397]. Expressions for these in the case of an additional VEV-less scalar multiplet of arbitrary size have been calculated in [398]. The authors obtain

$$S = -\frac{Y}{3\pi}\sum_{j=-J}^{J} j\,\ln\frac{m_j^2}{\mu^2} - \frac{2}{\pi}\sum_{j=-J}^{J}\left(j\,\mathrm{c_w^2} - Y\,\mathrm{s_w^2}\right)^2 \xi\left(\frac{m_j^2}{m_Z^2}, \frac{m_j^2}{m_Z^2}\right)\,, \tag{5.28}$$

$$T = \frac{1}{16\pi\,\mathrm{s_w^2}\,\mathrm{c_w^2}\,m_Z^2}\sum_{j=-J}^{J}\left(J^2 - j^2 + J + j\right)\theta_+(m_j^2, m_{j-1}^2)\,, \tag{5.29}$$

$$\begin{aligned} U = {} & \frac{1}{6\pi}\sum_{j=-J}^{J}\left(J^2 + J - 3j^2\right)\ln\frac{m_j^2}{\mu} \\ & + \frac{1}{\pi}\sum_{j=-J}^{J} 2\left(j\,\mathrm{c_w^2} - Y\,\mathrm{s_w^2}\right)^2 \xi\left(\frac{m_j^2}{m_Z^2}, \frac{m_j^2}{m_Z^2}\right) - \left(J^2 - j^2 + J + j\right)\xi\left(\frac{m_j^2}{m_W^2}, \frac{m_{j-1}^2}{m_W^2}\right)\,. \end{aligned} \tag{5.30}$$

Here, we relabelled $T \to J$, $T^3 \to j$ due to the naming of the T parameter. μ is the renormalization scale and it cancels in the sums over j. For the loop factors ξ and θ_+, we point the reader to the cited reference. The fitted values we shall use are [399]

$$S = 0.05 \pm 0.11\,, \qquad T = 0.09 \pm 0.13\,, \qquad U = 0.01 \pm 0.11\,. \tag{5.31}$$

We find that, out of these three parameters, the model is the most constrained by T through the mass splittings within the multiplet S.

Unitarity constraints on the couplings cannot be specified in all generality, since for each multiplet dimension and quantum number assignment, one has to work out the bounds from the contributing process amplitudes involving the respective couplings. They are therefore completely model-dependent. For a scalar with weak isospin $Y = 2T$ (*i.e.* with a neutral lightest component acting as DM) and $n = 5, 6, 7, 8$, the authors of [400] have computed limits on the parameter space $(m_{S^{(0)}}, \Delta m_{(1,0)})$, *i.e.* the mass of the neutral component and the mass difference between singly-charged and the neutral member, by demanding unitarity of the zeroth partial wave amplitudes of scalar-scalar annihilation into scalar and gauge boson pairs. Their results show that the highest allowed mass splitting decreases as n increases. For instance, $n = 5$ requires $|f_3| < 7.64$ and $|f_4| < 11.1$, whereas $n = 6$ requires $|f_3| < 6.49$ and $|f_4| < 8.17$, leading to smaller maximal mass differences within the multiplet. Gauge interactions restrict the sizes of complex (real) multiplets to $n \leq 8$ ($n \leq 9$) [401]. We expect the bounds to be significantly weaker for lower-dimensional representations and shall not consider unitarity further because we will compute cross sections for multiplets up to $n = 4$ only. We shall test for the agreement with unitarity constraints in Section 6.1.1 for the particular case of the doublet with $Y = 1$ in the context of the scotogenic model. It will indeed be found that other bounds are by far more constraining.

Lastly, additional electrically charged particles $S^{(Q)}$ coupling to the SM Higgs boson contribute to the rate of diphoton decay, $h \to \gamma\gamma$. This happens through a top triangle, like in ggH production, a W triangle and a sum of triangles involving all charged members of S. The bound is accounted for in the form of the signal strength $\mu_{\gamma\gamma}$ of the $h \to \gamma\gamma$ process, which is to be compared to the combined ATLAS and CMS result [402]. The only deviation from unity stems from the contribution by the charged scalar bosons

coupling to the photons because the h production cross section coincides with that in the SM. Hence, using the narrow width approximation (*cf.* Section 3.1.2.3), we have

$$\mu_{\gamma\gamma} \equiv \frac{\sigma(pp \to h \to \gamma\gamma)_{\rm BSM}}{\sigma(pp \to h \to \gamma\gamma)_{\rm SM}} \approx \frac{\mathcal{B}(h \to \gamma\gamma)_{\rm BSM}}{\mathcal{B}(h \to \gamma\gamma_{\rm SM}} = \frac{\Gamma(h \to \gamma\gamma)_{\rm BSM}}{\Gamma(h \to \gamma\gamma)_{\rm SM}} \frac{\Gamma(h)_{\rm SM}}{\Gamma(h)_{\rm BSM}}\,, \tag{5.32}$$

with the total BSM Higgs width

$$\Gamma(h)_{\rm BSM} = \Gamma(h)_{\rm SM} - \Gamma(h \to \gamma\gamma)_{\rm SM} + \Gamma(h \to \gamma\gamma)_{\rm BSM}\,. \tag{5.33}$$

The partial widths in the SM and our BSM model are [403]

$$\Gamma(h \to \gamma\gamma)_{\rm SM} = \frac{G_{\rm F}\alpha_{\rm em}^2 m_h^3}{128\sqrt{2}\pi^3} \left|N_{\rm c} Q_t^2 A_{1/2}(\tau_t) + A_1(\tau_W)\right|^2\,, \tag{5.34a}$$

$$\Gamma(h \to \gamma\gamma)_{\rm BSM} = \frac{G_{\rm F}\alpha_{\rm em}^2 m_h^3}{128\sqrt{2}\pi^3} \left|N_{\rm c} Q_t^2 A_{1/2}(\tau_t) + A_1(\tau_W) + Q^2 g_{hS^{(Q)}\bar{S}^{(Q)}} A_0(\tau_{H^\pm})\right|^2\,, \tag{5.34b}$$

where the contributions from all but the top are neglected, $N_{\rm c} = 3$ is the number of quark colours, $Q_t = \frac{2}{3}$ is the top charge and

$$g_{hS^{(Q)}\bar{S}^{(Q)}} = \frac{\Lambda_Q v^2}{4m^2_{S^{(Q)}}}\,. \tag{5.35}$$

with Λ_Q given in Equation 5.24. The loop function $A_{1/2}$ was given in Equation 5.9 and the other two are

$$A_0(\tau) = -\tau[1 - \tau f(\tau)]\,, \tag{5.36a}$$

$$A_1(\tau) = -[2 + 3\tau + 3(2\tau - \tau^2) f(\tau)]\,. \tag{5.36b}$$

Note that now $\tau_i = 4m_i^2/m_h^2$.

5.3.3 Cross sections

Recall that only Higgs mediation is relevant for the production of degenerate scalar pairs. The differential partonic cross section away from the resonance with CM energy $\hat{s}$ is given by the expression

$$\frac{d\hat{\sigma}_{\rm ggH}}{d\cos\theta}\left(g\,g \to S^{(Q)}\bar{S}^{(Q)};\,\hat{s}\right) = \frac{\Lambda_Q^2 G_h^2 \hat{s}\beta}{2048\pi\left(m_h^2 - \hat{s}\right)^2}\,, \tag{5.37}$$

the ggH effective coupling G_h being defined in Equation 5.8, θ is the CM scattering angle and β is the speed of each $S^{(Q)}$ particle produced in the CM frame, as given in Equation 3.19. For the total partonic cross section, multiply by 2. On the other hand, the LO Drell-Yan production cross section of a scalar pair for a generic multiplet of weak isospin T and hypercharge Y reads, including the Z and photon contributions,

$$\begin{aligned}\frac{d\hat{\sigma}_{\rm DY}}{d\cos\theta}&\left(q\,\bar{q} \to S^{(Q)}\bar{S}^{(Q)};\,\hat{s}\right) = \\ &\frac{\pi\alpha_{\rm em}^2\hat{s}\beta^3\sin^2\theta}{216 c_{\rm w}^4 s_{\rm w}^4\left(m_Z^2 - \hat{s}\right)^2}\left[4Q^2 c_{\rm w}^4\left(\frac{(2a_q)^2 m_Z^4 s_{\rm w}^4}{9\hat{s}^2} - 1\right) + 4\left(Q c_{\rm w}^2 - \frac{a_q Y s_{\rm w}^2}{3}\right)^2\right. \\ &\left. + \left(2Q c_{\rm w}^2\left(1 - \frac{2a_q m_Z^2 s_{\rm w}^2}{3\hat{s}}\right) - Y\left(1 - \frac{4a_q s_{\rm w}^2}{3}\right)\right)^2 + \frac{4a_q}{3}Y^2 s_{\rm w}^2\left(c_{\rm w}^2 + (1 - a_q)s_{\rm w}^2\right)\right]\,,\end{aligned} \tag{5.38}$$

where quark masses have been neglected as the proton PDFs suppress contributions by quarks heavier than the valence quarks and we defined

$$a_q = \begin{cases} 2\,, & T^3(q) = +\frac{1}{2}\,, \\ 1\,, & T^3(q) = -\frac{1}{2}\,. \end{cases} \tag{5.39}$$

The expression for the full cross section is obtained by removing $\sin^2\theta$ and multiplying by 4/3. The neutral component within a real multiplet ($Y = 0$) cannot be pair-produced in this way, as can be readily inferred

from the expression.

Notice that $\hat{\sigma}_{\mathrm{DY}} \propto \beta^3$ due to the p-wave suppression ($|\mathcal{M}| \sim \beta$) and due to phase space ($\int d^4p \sim \beta$, *cf.* Section 3.1.2.2). Higgs mediation is purely s-wave and the proportionality of $\hat{\sigma}_{\mathrm{ggH}}$ in Equation 5.37 stems exclusively from phase space. Thus the obtained angular dependences of $d\hat{\sigma}$ are expected. Let us therefore explore the origin of the form of the corresponding cross sections at a more formal level. We note that, for DY, $\frac{d\hat{\sigma}}{d\theta} \propto \sin^3\theta$, so there is a preference for scattering angles around $\pm\pi/2$ ($\eta \sim 0$). For a $2 \to 2$ DY process, the angular dependence of the matrix element is

$$|\mathcal{M}|^2 \sim \frac{d\hat{\sigma}}{d\hat{t}} \sim \frac{d\hat{\sigma}}{d\cos\theta} \sim \frac{1}{\sin\theta}\frac{d\hat{\sigma}}{d\theta}\,, \tag{5.40}$$

where $\hat{t} \sim (1 - \cos\theta)$ is the usual spacelike Mandelstam variable. For the Drell-Yan process, the incoming fermions contribute the factor $\bar{u}\,\Gamma^\mu\,u$, with $\Gamma^\mu = \gamma^\mu$, $\gamma^\mu\gamma^5$. As

$$\bar{\psi}_{L,R}\,\gamma^\mu\,\psi_{R,L} = \bar{\psi}_{L,R}\,\gamma^\mu\,\gamma^5\psi_{R,L} = 0\,, \tag{5.41}$$

chirality is conserved if the vector field coupling vectorially or axially propagates in the t-channel and so is helicity in the limit $E \gg m$. If it is in the s-channel, *i.e.* in case of the Drell-Yan process, Equation 5.41 forces the incoming quarks to have opposite chirality and hence they either couple to the state $|j\,m\rangle = |1\,1\rangle$ or $|j\,m\rangle = |1\,-1\rangle$ in the high-energy limit. The final $S^{(Q)}\bar{S}^{(Q)}$ state has total angular momentum 1 along the axis that is rotated relative to the beam axis by the scattering angle θ, so the amplitude in the CM frame is proportional to the projection of the initial state $|1\,\pm1\rangle$ onto a combination of $R_y(\theta)\,|1\,0\rangle$ and $R_y(\theta)\,|1\,\pm1\rangle$, where $R_y(\theta)$ is the operator for rotations around the y-axis. This amplitude is given by the Wigner d-function, which in the z-y-z convention is defined as

$$d^j_{m'm}(\theta) = \langle j\,m'|\,\mathrm{e}^{-i\theta J_y}\,|j\,m\rangle\ . \tag{5.42}$$

Its values are tabulated in most standard textbooks on angular momentum. In general, for the decay of a virtual spin-1 boson V with spin projection $m = \pm1$ along the beam line to a pair of particles X_1, X_2 with spin S and helicities λ_1 and λ_2, the amplitude reads schematically

$$\langle X^{(S)}_{1,\lambda_1}\,X^{(S)}_{2,\lambda_2};\,\theta|V_m\rangle \propto d^1_{\lambda m}(\theta)\,\mathcal{T}_{\lambda_1\lambda_2}\,, \qquad \lambda = \lambda_1 - \lambda_2\,. \tag{5.43}$$

The reduced helicity amplitude $\mathcal{T}_{\lambda_1\lambda_2}$ is independent of m. In this case, it vanishes for $\lambda \neq 0$ because the final scalars cannot have non-zero helicities, hence the final state $R_y(\theta)\,|1\,\pm1\rangle$ is not produced and the scalar pair only couples to $R_y(\theta)\,|1\,0\rangle$. Therefore, the Drell-Yan matrix element is proportional to the sum of the projections $|1\,\pm1\rangle \to |1\,0\rangle$, where the final state is rotated with respect to the initial state by an angle θ. The required d-functions read

$$d^1_{01} = -d^1_{0\,-1} = \frac{1}{\sqrt{2}}\sin\theta\,, \tag{5.44}$$

so $|\mathcal{M}|^2 \sim \sin^2\theta$ and hence $\frac{d\hat{\sigma}}{d\theta} \sim \sin^3\theta$, by Equation 5.40. As for ggF, the dependence on the scattering angle is $\frac{d\hat{\sigma}}{d\cos\theta} \sim |\mathcal{M}|^2 = \text{const}$, which could also have been directly inferred from the Wigner d-function $d^1_{00} = 1$. Clearly, the final state can only be a state of vanishing angular momentum because the triple scalar coupling has no angular dependence. See *e.g.* [404] for more details about the helicity formalism.

5.3.4 Results

As both photon and Z boson exchange contribute, DY partonic cross sections can be relatively enhanced or suppressed depending on the quantum numbers of the multiplet components to be produced. Figure 5.4 depicts the ratio between the ggF cross section σ_{ggF} normalized to the effective squared low-energy coupling Λ_Q and the DY production cross section σ_{DY} for proton-proton CM energies of 8 TeV (left panel) and 14 TeV (right panel). For a fixed mass $m_{S^{(Q)}}$, this ratio is independent of the quartic couplings f_i in the scalar potential; it is rather exclusively determined through the electroweak quantum numbers of the multiplet S, *cf.* Equations 5.37 and 5.38. The numbers on each line represent the electric charge of the scalar mass

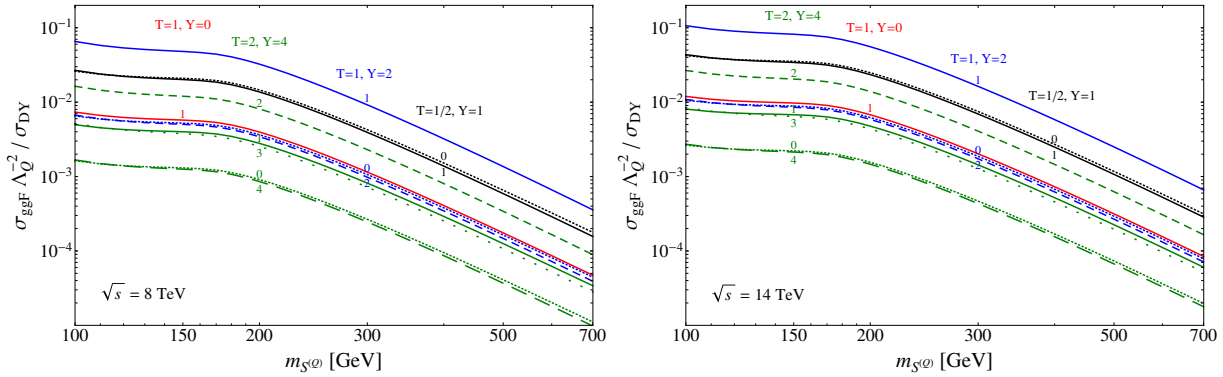

FIGURE 5.4: Relative contribution of the Higgs-mediated ggF cross section normalized to the effective squared low-energy coupling Λ_Q and the Drell-Yan production cross sections as a function of the scalar mass for 4 different $SU(2)_L$ multiplets, with $\sqrt{s} = 8$ TeV (left panel) and 14 TeV (right panel). The number on each line identifies the particle by the electric charge.

eigenstate. The cross sections are obtained numerically by convoluting the partonic cross sections with the CTEQ5L Mathematica package provided by the CTEQ group [405], fixing both the factorization scale μ_F and the renormalization scale μ_R of the strong coupling constant $\alpha_s^{LO}(\mu_R)$ at the invariant mass of the final state.[4] Notice the different behaviour of the cross section before and after $m_{S^{(Q)}} \sim m_t$, caused by a change in the behaviour of the function $f(\tau)$ in the loop factor when beyond threshold, see Equation 5.7. Moreover, we find that for the electrically neutral component of the multiplet, the ratio $\sigma_{ggF}\Lambda_Q^{-2}/\sigma_{DY}$ decreases as the weak isospin increases. Nevertheless, due to the complicated dependence of the Drell-Yan cross section on the electric charge and the hypercharge, it is not possible to ascertain a clear pattern within the members of the same multiplet.

To provide a concrete example, we plot in Figure 5.5 the scalar production cross sections associated with the ggF (blue lines) and DY (red lines) subprocesses for fixed values of the quartic couplings f_3 and f_4, for the case of a doublet with $Y = 1$ (upper panels) and a triplet with $Y = 2$ (lower panels). The first case corresponds to the inert doublet model [258] and the latter is a U(1)-conserving Higgs triplet model [220]. The couplings have been verified to be in agreement with the constraints discussed in the previous section. In the shown mass range, the $h \to \gamma\gamma$ signal strength has been verified to be consistent with early CMS limits [407] at the 2σ level, though the most recent combined fit by ATLAS and CMS [402] challenges the results for the triplet. This can be cured by slightly lowering f_3 and/or f_4 (which in turn would somewhat lower $|\Lambda_Q|$). The T parameter never deviates from the best fit value by more than 1σ. The dashed, solid and dotted lines correspond to the production of scalars with electric charge equal to +2, +1 and 0, respectively. Notice that Equation 5.23 sets a lower bound on the mass of each component of the multiplet; therefore, since we let the lowest-T^3 component start with a mass of 100 GeV, higher-T^3 curves commence at a distance corresponding to the mass splitting fixed by f_3 and f_4. We find, in particular, that the ggH production cross section of the two doublet components is approximately a factor 5 (2) smaller than the corresponding DY cross section for $m_{S^{(Q)}} \simeq 140$ GeV and a pp CM energy of 8 (14) TeV. For the triplet, the ggH and DY production cross sections of the singly-charged component differ by a factor smaller than 4 (2) for $m_{S^{(+1)}} \lesssim 180$ GeV at 8 (14) TeV, while electroweak interactions by far the dominate the production of the neutral and doubly-charged scalars within all the mass range.

[4] The results have been cross-checked through a fully numerical computation with the Monte Carlo generator CalcHEP [406] with the CTEQ6L PDF set and have been found to agree very well with our semi-numerical computation.

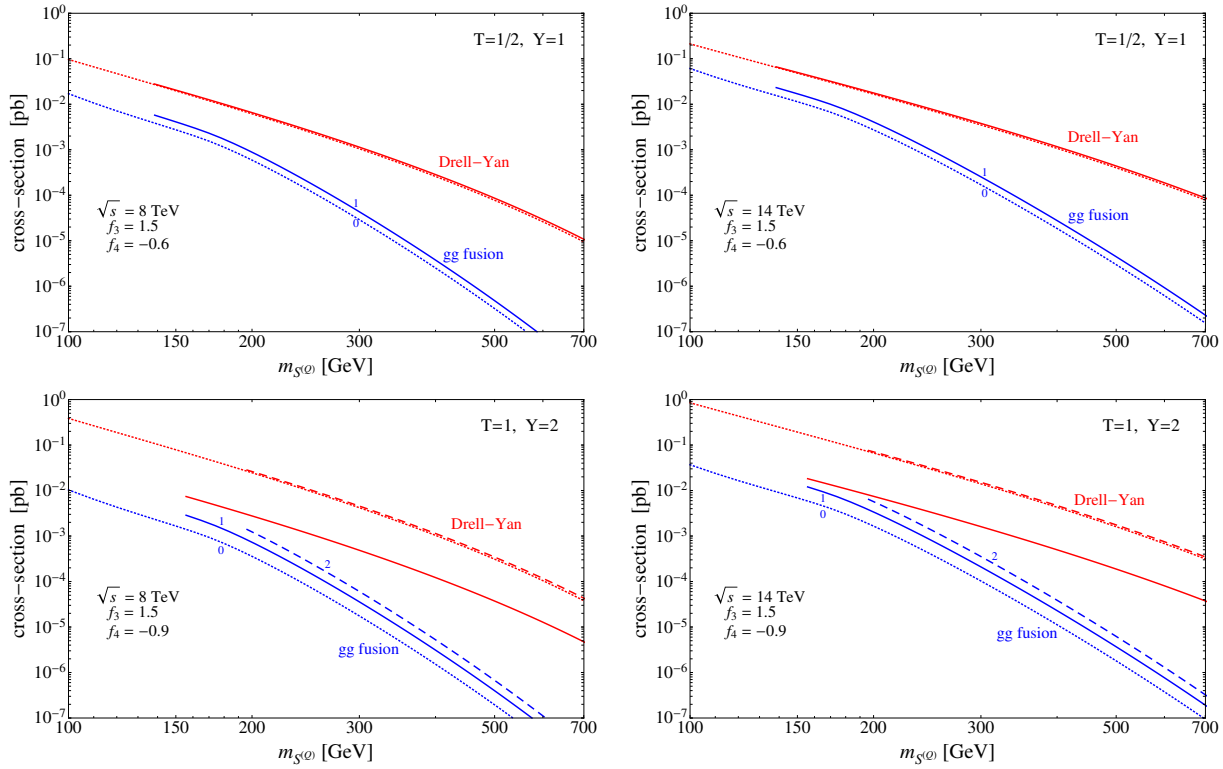

FIGURE 5.5: ggH and Drell-Yan production cross sections for two different representations of $SU(2)_L$. The dashed, solid and dotted lines correspond to the production of scalars with electric charge equal to +2, +1 and 0, respectively. For the doublet, the effective couplings are $\Lambda_{+1} = -3.3$, $\Lambda_0 = -2.7$ and, for the triplet, $\Lambda_{+2} = -3.9$, $\Lambda_{+1} = -3$ and $\Lambda_0 = -2.1$.

5.4 Adding a fermionic multiplet

In this section, we turn to investigate the effect of the gluon-gluon fusion mechanism on the production of new fermionic representations at the LHC.

5.4.1 The benchmark model

In what follows, we consider a simplified scenario with just one extra uncoloured fermionic multiplet ψ, with renormalizable Yukawa-type interactions involving the Higgs doublet and the SM leptons L, ℓ_R,[5]

$$\mathcal{L}_\psi \;=\; c\bar{\psi}\left(i\not{D} - m_\psi\right)\psi + \mathcal{L}_Y\left(H, \psi, L, \ell_R\right) \,. \tag{5.45}$$

The constant c equals 1 (1/2) if ψ is a Dirac (Majorana) fermion. Depending on the quantum number assignments, such an interaction may or may not exist at the renormalizable level. The spontaneous breaking of the electroweak symmetry results in an interaction between the Higgs boson and the new fermionic mass eigenstate(s), as well as a mixing between SM lepton flavours and the new fermion(s). These mixings can be sizeable, depending on the details of the model. The requirement of renormalizability of the Lagrangian and the fact that we are limiting ourselves to only one additional representation, restricts the analysis to the cases $\psi \sim (1,1,0)$ and $\psi \sim (1,3,0)$, as in the well-known type I [13] and type III [15, 16] seesaw extensions of the SM, see Appendix C. Both frameworks contain additional heavy right-handed Majorana neutrinos mixing with the left-handed neutrinos already contained in the SM; this mixing can be encoded in a matrix $\Theta_{\alpha k}$ (*cf.* Equations C.18 and C.76) entering the expression of the light neutrino

[5] A simple interesting yet somewhat less minimal alternative are models with vector-like fermions, see e.g. [408]. For an analysis of the impact of gluon-gluon fusion in these models, see [391].

mass matrix, $(m_\nu)_{\alpha\beta} = \Theta^*_{\alpha k}\, M_k\, \Theta^\dagger_{k\beta}$, M_k being the kth heavy RHN mass. In the type III seesaw, the SM Lagrangian is extended with new fermionic representations in the adjoint of the weak gauge group. As a consequence, each Majorana neutrino N_k is partnered by one Dirac fermion E_k with electric charge -1 and degenerate in mass with N_k at leading order in the mixing parameter Θ, Θ here being of the same order as in the ν-N mixing, but generally not the same matrix.

The procedure now is analogous to the work of the previous section treating the scalar case, but the constraints of the fermionic scenario do not require an equally extended discussion, since we are not interested in the details of the flavour structure and the quasi-degeneracy of the components within the triplet in type III implies a negligible contribution to the oblique parameters.

The elements of Θ are constrained by lepton flavour violating processes, most notably $\mu \to e\,\gamma$ and μ-e flavour conversion in nuclei. Typical constraints on the effective couplings are $|\Theta_{\alpha k}| \lesssim 10^{-2}$ in the type I seesaw for a heavy neutrino mass in the range $M \sim 100$ GeV÷1 TeV, though this possibility depends on the parameter configuration. More specifically, two RHNs N_1 and N_2 either need to be quasi-degenerate and form a pseudo-Dirac pair as it occurs in the inverse seesaw mechanism (*cf.* Section C.4) or one opts for a highly tuned Dirac mass contribution to m_ν, as can be done by means of the Casas-Ibarra parametrization [260]; for the type III, generally smaller values are required [409]. In our computations, we shall consider the optimistic hypothesis $|\Theta_{\alpha k}| = 10^{-2}$. Cross sections can then be rescaled for other assumptions regarding the mixing.

We compare in this low-scale seesaw framework the ggF and DY production of heavy Majorana fermions, N_k ($k = 1, 2, \ldots$), and charged Dirac fermions, E_k, with a mass M_k varying in the electroweak range. The gluon-gluon fusion mechanism involves a Higgs and a Z, as discussed in Section 5.2.1. For a collider signal analysis of the far stronger channels $q\bar{q}' \to W^* \to N\ell^\pm$ for type I and $q\bar{q} \to Z^* \to E^+E^-$, $q\bar{q}' \to W^* \to E^\pm N$ for type III, see *e.g.* [372, 373]. These channels are not considered here because either the final state cannot be obtained via a Higgs-mediated process, or it is suppressed by a higher power of the mixing parameter.

As derived in Appendix C, in both the type I and III seesaw mechanism, the relevant couplings to the Z and the Higgs boson after EWSB can be parametrized by the effective Lagrangian terms

$$\mathcal{L}_{\rm nc} = -\frac{g}{2\mathrm{c_w}}\,\bar{\nu}_{L\alpha}\,\not{Z}\,\Theta_{\alpha k}\,N_{Lk} + \text{h.c.}\,, \tag{5.46}$$

$$\mathcal{L}_h = -\frac{g M_k}{2 m_W}\,\bar{\nu}_{L\alpha}\,\Theta_{\alpha k}\,N_{Rk}\,h + \text{h.c.}\,. \tag{5.47}$$

where M_k is the mass of the kth heavy Majorana neutrino, g is the $\mathrm{SU}(2)_L$ coupling, $\mathrm{s_w}$ is the sine of the weak mixing angle and m_W denotes the W boson mass. The E_k present in type III couple to electroweak gauge bosons and the SM leptons through the mixing matrix as determined by the interaction terms

$$\mathcal{L}^{\ell E}_{\rm nc} = -\frac{g}{\sqrt{2}\mathrm{c_w}}\bar{\ell}'_{L\alpha}\,\not{Z}\,\Theta_{\alpha k}\,E_{Lk} + \text{h.c.}\,, \tag{5.48}$$

$$\mathcal{L}^{\ell E}_{h} = -\frac{g M_k}{\sqrt{2} m_W}\bar{\ell}_{L\alpha}\,\Theta_{\alpha k}\,E_{Rk}\,h + \text{h.c.}\,. \tag{5.49}$$

5.4.2 Cross sections

Neglecting the mass of the SM leptons, the partonic ggH cross section for ν-N production is

$$\hat{\sigma}_{\rm ggH}\left(g\,g \to N_k\,\nu_\alpha;\,\hat{s}\right) = \hat{\sigma}_{\rm ggH}\left(g\,g \to E_k\,\bar{\ell}_\alpha;\,\hat{s}\right) = \frac{\pi\,\alpha^2_{\rm em}\,|\Theta_{\alpha k}|^2\,G_h^2 M_k^2\left(\hat{s}-M_k^2\right)^2}{512\mathrm{s_w^4 c_w^4}\,m_Z^4\left[\left(\hat{s}-m_h^2\right)^2 + m_h^2\Gamma_h^2\right]}\,, \tag{5.50}$$

where the possibility for resonant production has been accounted for through the Higgs width. Z-mediated gluon fusion, on the other hand, is characterized by the never resonant cross section

$$\hat{\sigma}_{\rm ggZ}\left(g\,g \to N_k\,\nu_\alpha;\,\hat{s}\right) = \hat{\sigma}_{\rm ggZ}\left(g\,g \to E_k\,\bar{\ell}_\alpha;\,\hat{s}\right) = \frac{\alpha_{\rm em}\,|\Theta_{\alpha k}|^2\,G_Z^2 M_k^2\,\hat{s}^2\left(1-\frac{M_k^2}{\hat{s}}\right)^2}{2048\mathrm{s_w^2 c_w^2}\,m_Z^4}\,, \tag{5.51}$$

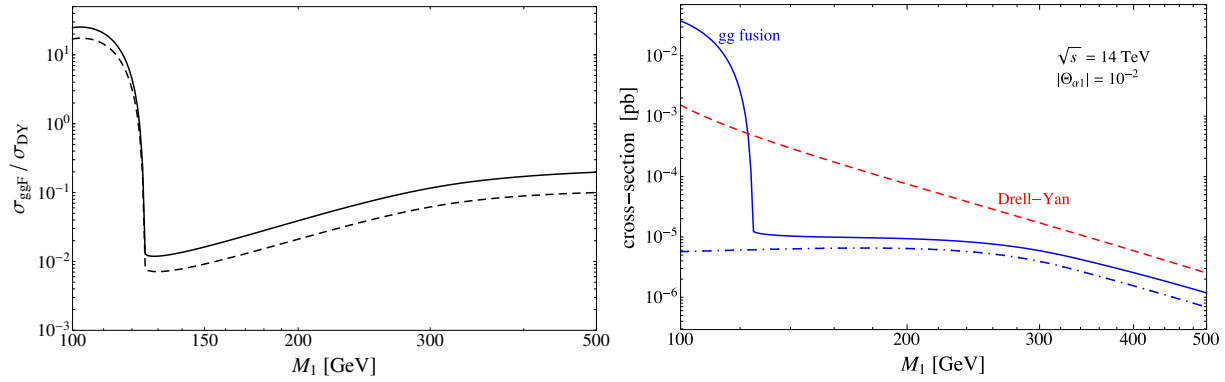

FIGURE 5.6: *Left panel:* Ratio of the gluon-gluon fusion and Drell-Yan production cross sections of heavy fermions in the type I/III seesaw scenarios at $\sqrt{s} = 8$ (14) TeV, corresponding to the dashed (continuous) line. *Right panel:* Fermion production cross sections for $\sqrt{s} = 14$ TeV and $|\Theta_{\alpha 1}| = 10^{-2}$. The solid blue line represents the full ggF contribution, while the dot-dashed blue line represents the contribution of only the ggZ process.

G_Z being given in Equation 5.11. There is no resonance at $\hat{s} = m_Z^2$ due to the Landau-Yang theorem [371], which forbids the production of an on-shell Z boson in the collision of two massless spin-1 vector bosons. Lastly, the expressions for the production cross section in a quark-antiquark collision read

$$\begin{aligned}\hat{\sigma}_{\rm DY}\left(u\,\overline{u} \to N_k\,\nu_\alpha;\,\hat{s}\right) &= \hat{\sigma}_{\rm DY}\left(u\,\overline{u} \to E_k\,\bar{\ell}_\alpha;\,\hat{s}\right) \\ &= \frac{\pi\,\alpha_{\rm em}^2\,|\Theta_{\alpha k}|^2\left(\hat{s}-M_k^2\right)^2\left(M_k^2+2\hat{s}\right)}{1296\,{\rm c}_{\rm w}^4\,{\rm s}_{\rm w}^4\left(\hat{s}-m_Z^2\right)^2\hat{s}^2}\left(9{\rm c}_{\rm w}^4 - 6{\rm c}_{\rm w}^2{\rm s}_{\rm w}^2 + 17{\rm s}_{\rm w}^4\right)\,, \end{aligned} \tag{5.52}$$

$$\begin{aligned}\hat{\sigma}_{\rm DY}\left(d\,\overline{d} \to N_k\,\nu_\alpha;\,\hat{s}\right) &= \hat{\sigma}_{\rm DY}\left(d\,\overline{d} \to E_k\,\bar{\ell}_\alpha;\,\hat{s}\right) \\ &= \frac{\pi\,\alpha_{\rm em}^2\,|\Theta_{\alpha k}|^2\left(\hat{s}-M_k^2\right)^2\left(M_k^2+2\hat{s}\right)}{1296\,{\rm c}_{\rm w}^4\,{\rm s}_{\rm w}^4\left(\hat{s}-m_Z^2\right)^2\hat{s}^2}\left(9{\rm c}_{\rm w}^4 + 6{\rm c}_{\rm w}^2{\rm s}_{\rm w}^2 + 5{\rm s}_{\rm w}^4\right)\,. \end{aligned} \tag{5.53}$$

The total fermion production cross section at the LHC, for a given CM energy $\sqrt{s}$, is given by the convolution of the partonic cross section with the corresponding parton luminosity functions, taking $\tau_{\rm thr} \equiv M_k^2/s$ in the limit of massless charged leptons.

5.4.3 Results

Figure 5.6 shows the resulting cross sections for heavy fermion production. In the left panel, we plot the ratio of the gluon-gluon fusion and the Drell-Yan production cross sections of a Majorana neutrino N_k or a heavy charged Dirac fermion E_k as a function of the heavy mass M_k (taking $k = 1$). As for the scalars, we consider the pp CM energies of 8 TeV (dashed line) and 14 TeV (continuous line). At lowest order in the mixing of heavy fermions and SM leptons, the ratio $\sigma_{\rm ggF}/\sigma_{\rm DY}$ is independent of Θ. The right panel shows the individual cross sections for $\sqrt{s} = 14$ TeV with the mixing parameter fixed at $|\Theta_{\alpha 1}| = 10^{-2}$. We note that the Higgs-mediated gluon fusion process dominates the production at heavy fermion masses below the on-shell Higgs threshold, $M_k \lesssim m_h$. When resonant, this channel offers the possibility to test the low-scale type I seesaw mechanism through the decay $h \to \nu_{L\alpha}\,N_k$, with $N_k \to \ell_\beta W^{(*)}, \nu Z^{(*)}$, with the gauge bosons subsequently decaying producing jets or leptons [410]. Above the resonance, ggF is clearly the subdominant process. However, for this pp CM energy, gluon fusion can represent up to 40%-50% of the total production cross section for Majorana neutrino masses $M_k \gtrsim 300$ GeV and should therefore be included in analyses of low-scale type I/III seesaw LHC phenomenology, especially since the heavy fermion masses in type III have already been constrained to lie above this value. To be more specific, ATLAS [411] and CMS [412] have performed searches for expected type III signatures using pp collisions at $\sqrt{s} = 8$ TeV. The collaborations looked for multiple charged lepton events from heavy fermion pair production through

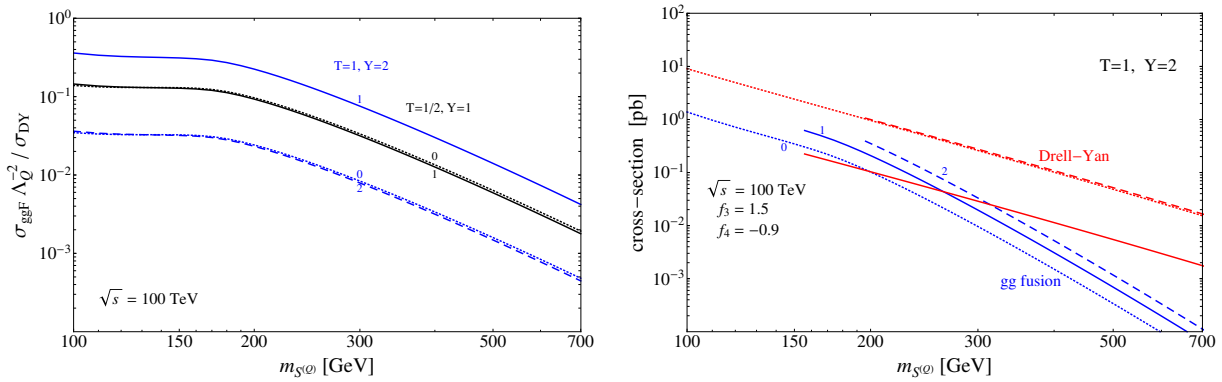

FIGURE 5.7: *Left panel:* Ratio between the Higgs-mediated and Drell-Yan production cross sections of a scalar triplet at $\sqrt{s} = 100$ TeV. *Right panel:* Scalar triplet production cross sections with parameters as in Figure 5.5 for $\sqrt{s} = 100$ TeV.

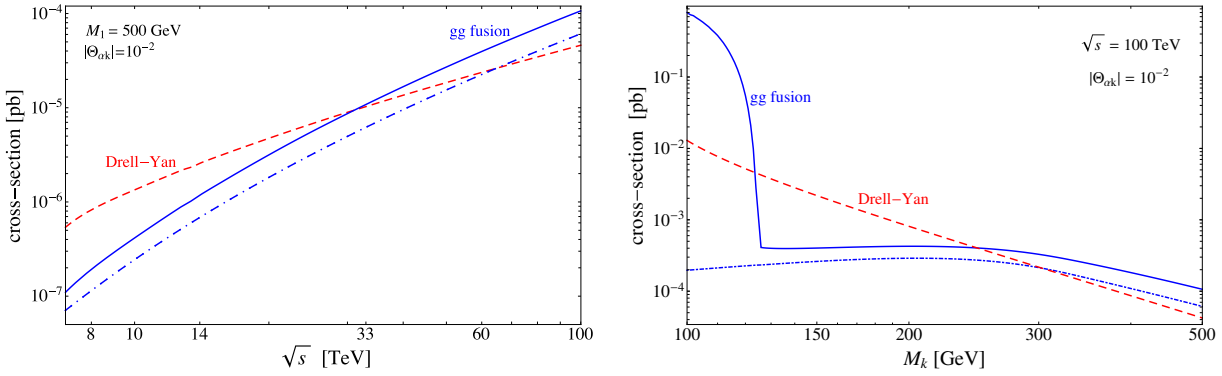

FIGURE 5.8: *Left panel*: pp cross section for the production of an $E_k\,\ell_\alpha$ or $N_k\,\nu_\alpha$ pair with $|\Theta_{\alpha k}| = 10^{-2}$ both from Drell-Yan and gluon-gluon fusion for varying $\sqrt{s}$. *Right panel*: Fermion production cross sections for $\sqrt{s}$ =100 TeV and $|\Theta_{\alpha 1}| = 10^{-2}$ as a function of M_k.

the Drell-Yan process, including signatures with missing transverse energy due to neutrinos. Depending on the assumed mixings taken as benchmark, *i.e.* for various mixing patterns determining whether the heavy fermions prefer to couple to Ws or Zs and varying the branching ratios to the various SM lepton flavours, the search by ATLAS was able to set the strongest constraints on the model, finding lower limits for M_k varying from 325 to 540 GeV.

5.5 Perspectives for a $\sqrt{s} = 100$ TeV proton-proton collider

With the physics programme of the LHC steadily ongoing and with mass bounds on BSM particles in many scenarios like supersymmetry moving upwards and in part even beyond the electroweak scale, the trend within the particle physics community to discuss the first steps towards the post-LHC era has been visibly growing during the last few years. An early assessment of the technical challenges and physics opportunities is surely necessary, since the construction of high-energy facilities represents a long-time and costly effort. It is therefore timely to ascertain the contribution of the gluon fusion process to the production rate of heavy BSM particles at hypothetical future proton-proton colliders, in the same manner as in the preceding sections. Such a machine could be an upgrade of the LHC to reach the 33 TeV mark [413] or a new 100 TeV proton-proton collider [414]. We herein focus on the latter possibility.

The impact of ggF on scalar production is a sizeable increase with respect to the DY process and an

increase of the gluon-gluon fusion cross section $\sigma_{\rm ggF}(100\text{ TeV})$ by two orders of magnitude compared to $\sigma_{\rm ggF}(14\text{ TeV})$ for $\Lambda_Q \sim 1$. The origin lies in two effects. First, a larger pp CM energy implies a larger cross section for both Drell-Yan and the gluon-gluon fusion mechanism because all parton luminosities increase and a larger phase space for final states becomes available. Second, as discussed in Section 3.1.3, the relative importance of different partons changes and the contributions to Drell-Yan processes become more equally distributed in quark flavour. As can be seen in the right panel of Figure 5.7, the larger gluon luminosity can render the gluon-gluon fusion mechanism dominant for the singly-charged component of a scalar triplet, with couplings equal to the values chosen for the 8 and 14 TeV cases, *cf.* Figure 5.5, up to masses of 260 GeV. With such large cross sections, one can expect exotic scalars to be copiously produced at a 100 TeV collider with a proposed luminosity of up to $L = 10\text{ ab}^{-1}$. More specifically, we estimate that at least 10^7 to 10^4 pairs of singly-charged scalars can be produced for masses in the range $100 \div 700$ GeV, even if Λ_Q should happen not to be very large.

To finalize the study, we consider the production rate of a fermionic triplet E_k with mass $M_k = 500$ GeV and a mixing parameter $|\Theta_{\alpha k}| = 10^{-2}$, in association with a charged lepton ℓ_α. In the left panel of Figure 5.8, we plot the DY and ggF cross sections as a function of the pp CM energy $\sqrt{s}$. The relative importance of ggF increases by one order of magnitude and hence becomes as important as the Drell-Yan contribution $\sigma_{\rm DY}$ at $\sqrt{s} = 30$ TeV and is completely dominant at $\sqrt{s} = 100$ TeV. As can be seen in the right panel, at $\sqrt{s} = 100$ TeV, the ggF contribution becomes the dominant production channel for the range of masses currently allowed by the ATLAS search for heavy lepton partners as predicted in the type III seesaw model [411]. For $L = 10\text{ ab}^{-1}$, hundreds of events can be expected, provided $M_k \lesssim 500$ GeV.

CHAPTER 6

Analyses IIA & IIB: Testing the FIMP realization of the scotogenic model at the LHC

In this chapter we present the two studies, Analysis IIA and IIB, addressing different LHC phenomenologies of the scotogenic model in the realization with a fermionic FIMP dark matter particle represented by the lightest right-handed neutrino N_1, as discussed in Section 2.4.2. Our present interest is in the simple case devoid of sizeable DM injections via superWIMP-like decays, *i.e.* we regard case (i) of the four scenarios described in Section 2.4.2 with suitably light scalar masses to justify the assumption that the FI mechanism dominates DM production. Independently of the hierarchies in the mass structure, only $\mathbb{Z}_2$-odd scalars can in principle be directly produced in colliders at appreciable rates. The production is followed by a decay chain down to a pair of LOSPs, provided these have not already been created directly, which ultimately each decay to a N_1. The LOSP may or may not be stable at collider scales. In [2], we analyze the LHC phenomenology of the following three concrete spectra:

- spectrum A: $M_1 < m_{H^\pm} < m_{H^0,\,A^0} < M_{2,3}$
- spectrum B: $M_1 < M_2 < m_{H^0,\,A^0,\,H^\pm} < M_3$
- spectrum C: $M_1 < M_2 < M_3 < m_{H^0,\,A^0,\,H^\pm}$

All these spectra contain long-lived $\mathbb{Z}_2$-odd particles, so their signatures are either quite exotic, in case there is enough sensitivity, or comparable to SUSY-like signatures involving a significant transverse momentum imbalance. This chapter is devoted to the presentation of the results concerning **spectrum A**. Section 6.1 discusses the relevant production modes, kinematical distributions and parameter space constraints. The two subsequent Sections, 6.2 and 6.3, present Analyses IIA and IIB, respectively.

In this spectrum, the NLOP potentially causing the interesting LHC signals is the $H^\pm$. Since its decay amplitude is $\mathcal{O}(y_1)$, it is long-lived and the decay vertex in colliders will be displaced, unless M_1 is very small and/or $m_{H^\pm}$ is very large. One estimates

$$\Omega_{N_1} h^2 \approx 0.2744 \left(\frac{M_1}{10\text{ MeV}}\right)\left(\frac{100\text{ GeV}}{m_{H^\pm}}\right)\left(\frac{y_1}{10^{-10}}\right)^2 , \tag{6.1}$$

where it is assumed that all three scalars have similar masses. This is found to be a very acceptable approximation. The authors of [42] show that the final N_1 yield obtained for one scalar mass of 400 GeV and the others in a range of ±200 GeV around this mass exhibits very little variation. Hence, with $\Omega_{N_1} h^2 \approx 0.12$ [8],

$$y_1^2 \approx \frac{\Omega_{N_1} h^2}{0.2744} \times 10^{-20} \left(\frac{10\text{ MeV}}{M_1}\right)\left(\frac{m_{H^\pm}}{100\text{ GeV}}\right) \approx 4 \times 10^{-20} \left(\frac{1\text{ MeV}}{M_1}\right)\left(\frac{m_{H^\pm}}{100\text{ GeV}}\right) . \tag{6.2}$$

Therefore the freeze-in condition allows for the calculation of the coupling y_1, the $H^\pm$ width $\Gamma_{H^\pm}$ and the proper lifetime and decay length $c\tau$ solely from the mass of $H^\pm$ and of N_1,

	100 GeV				200 GeV			
	y_1	$\Gamma_{H^\pm}$ [GeV]	τ_{RF} [s]	$c\tau/\beta\gamma$ [m]	Y_1	$\Gamma_{H^\pm}$ [GeV]	τ_{RF} [s]	$c\tau/\beta\gamma$ [m]
1 keV	6.32×10^{-9}	2.39×10^{-16}	2.76×10^{-9}	0.83	8.94×10^{-9}	9.55×10^{-16}	6.89×10^{-10}	0.21
10 keV	2.00×10^{-9}	2.39×10^{-17}	2.76×10^{-8}	8.25	2.83×10^{-9}	9.55×10^{-17}	6.89×10^{-9}	2.06
100 keV	6.32×10^{-10}	2.39×10^{-18}	2.76×10^{-7}	82.5	8.94×10^{-10}	9.55×10^{-18}	6.89×10^{-8}	21
1 MeV	2.00×10^{-10}	2.39×10^{-19}	2.76×10^{-6}	825	2.83×10^{-10}	9.55×10^{-19}	6.89×10^{-7}	206
10 MeV	6.32×10^{-11}	2.39×10^{-20}	2.76×10^{-5}	8250	8.94×10^{-11}	9.55×10^{-20}	6.89×10^{-6}	2063
100 MeV	2.00×10^{-11}	2.39×10^{-21}	2.76×10^{-4}	82500	2.83×10^{-11}	9.55×10^{-21}	6.89×10^{-5}	20625
1 GeV	6.32×10^{-12}	2.39×10^{-22}	2.76×10^{-3}	825000	8.94×10^{-12}	9.55×10^{-22}	6.89×10^{-4}	206250
	300 GeV				400 GeV			
	y_1	$\Gamma_{H^\pm}$ [GeV]	τ_{RF} [s]	$c\tau/\beta\gamma$ [m]	Y_1	$\Gamma_{H^\pm}$ [GeV]	τ_{RF} [s]	$c\tau/\beta\gamma$ [m]
1 keV	1.10×10^{-8}	2.15×10^{-15}	3.06×10^{-10}	0.09	1.26×10^{-8}	3.82×10^{-15}	1.72×10^{-10}	0.05
10 keV	3.46×10^{-9}	2.15×10^{-16}	3.06×10^{-9}	0.92	4.00×10^{-9}	3.82×10^{-16}	1.72×10^{-9}	0.52
100 keV	1.10×10^{-9}	2.15×10^{-17}	3.06×10^{-8}	9.17	1.26×10^{-9}	3.82×10^{-17}	1.72×10^{-8}	5.16
1 MeV	3.46×10^{-10}	2.15×10^{-18}	3.06×10^{-7}	92	4.00×10^{-10}	3.82×10^{-18}	1.72×10^{-7}	52
10 MeV	1.10×10^{-10}	2.15×10^{-19}	3.06×10^{-6}	916	1.26×10^{-10}	3.82×10^{-19}	1.72×10^{-6}	516
100 MeV	3.46×10^{-11}	2.15×10^{-20}	3.06×10^{-5}	9167	4.00×10^{-11}	3.82×10^{-20}	1.72×10^{-5}	5156
1 GeV	1.10×10^{-11}	2.15×10^{-21}	3.06×10^{-4}	91667	1.26×10^{-11}	3.82×10^{-21}	1.72×10^{-4}	51563
	500 GeV				600 GeV			
	y_1	$\Gamma_{H^\pm}$ [GeV]	τ_{RF} [s]	$c\tau/\beta\gamma$ [m]	Y_1	$\Gamma_{H^\pm}$ [GeV]	τ_{RF} [s]	$c\tau/\beta\gamma$ [m]
1 keV	1.41×10^{-8}	5.97×10^{-15}	1.10×10^{-10}	0.03	1.55×10^{-8}	8.59×10^{-15}	7.66×10^{-11}	0.02
10 keV	4.47×10^{-9}	5.97×10^{-16}	1.10×10^{-9}	0.33	4.90×10^{-9}	8.59×10^{-16}	7.66×10^{-10}	0.23
100 keV	1.41×10^{-9}	5.97×10^{-17}	1.10×10^{-8}	3.30	1.55×10^{-9}	8.59×10^{-17}	7.66×10^{-9}	2.29
1 MeV	4.47×10^{-10}	5.97×10^{-18}	1.10×10^{-7}	33	4.90×10^{-9}	8.59×10^{-18}	7.66×10^{-8}	23
10 MeV	1.41×10^{-10}	5.97×10^{-19}	1.10×10^{-6}	330	1.55×10^{-10}	8.59×10^{-19}	7.66×10^{-7}	229
100 MeV	4.47×10^{-11}	5.97×10^{-20}	1.10×10^{-5}	3300	4.90×10^{-10}	8.59×10^{-20}	7.66×10^{-6}	2292
1 GeV	1.41×10^{-11}	5.97×10^{-21}	1.10×10^{-4}	33000	1.55×10^{-11}	8.59×10^{-21}	7.66×10^{-5}	22917

TABLE 6.1: Yukawa couplings, decay widths, mean lifetimes and proper decay lengths for several N_1 masses, for $m_{H^\pm} = 100$ to 600 GeV.

$$y_1 \approx 2\times10^{-10}\left[\left(\frac{1\,\mathrm{MeV}}{M_1}\right)\left(\frac{m_{H^\pm}}{100\,\mathrm{GeV}}\right)\right]^{1/2}, \tag{6.3a}$$

$$\Gamma_{H^\pm} \approx \frac{3}{4\pi}\times10^{-18}\,\mathrm{GeV}\times\left(\frac{1\,\mathrm{MeV}}{M_1}\right)\left(\frac{m_{H^\pm}}{100\,\mathrm{GeV}}\right)^2, \tag{6.3b}$$

$$\tau \approx 2.8\times10^{-4}\,\mathrm{s}\left(\frac{M_1}{100\,\mathrm{MeV}}\right)\left(\frac{100\,\mathrm{GeV}}{m_{H^\pm}}\right)^2, \tag{6.3c}$$

$$c\tau \approx 8.25\,\mathrm{m}\left(\frac{M_1}{10\,\mathrm{keV}}\right)\left(\frac{100\,\mathrm{GeV}}{m_{H^\pm}}\right)^2. \tag{6.3d}$$

We approximate $\Gamma_{H^\pm}$ by the expression in Equation 2.122a with the typical Yukawa coupling y_1 times a factor of 3, to account for the number of lepton families. Values for these quantities are listed in Table 6.1, considering N_1 masses in the range from 1 keV up to 1 GeV, the transition region from warm to cold dark matter. For these values, y_1 is found to always be of order 10^{-12} to 10^{-8} and $\Gamma_{H^\pm}$ varies between 10^{-22} and 10^{-15} GeV — as this width is very narrow, lifetimes are very long and decay lengths are macroscopic. It is clearly noticeable that N_1 is required to be very light for $H^\pm$ to decay inside the detector.

Since the $H^\pm$ lifetime increases linearly with M_1, it only reaches the second or minute scale if the mass of N_1 amounts to several orders of a GeV. We shall not consider such long lifetimes, therefore there is no danger of BBN perturbations due to electromagnetic energy injection in the early Universe (*cf.* Section 2.2.1). Yet, the $H^\pm$ can decay to a τ lepton, which itself decays hadronically with a branching fraction of 64.9% [415]. This leads to cascades containing fast mesons (τ decays don't yield nucleons [78]) and, since hadronic interactions may have an impact on BBN predictions while already happening early, one should verify whether these originate significant disturbances of the predictions for the BBN phase with respect to observations. This is presumably not the case because the effect of mesons is not as large as the effect of fast nucleons [119, 416], however a study of these matters is far beyond our scope and shall not be considered further.

6.1 Parameter space constraints and kinematics

Before presenting the actual analyses, some preparatory work is in order. As has been done in the previous study, we start by discussing the dominant mechanisms for producing the new particles ($H^{\pm}$) at the LHC. These are outlined in Section 6.1.1, together with discussions of the relevant parameter space constraints. Recall further from Section 4.5 that the computation of observable survival fractions (OSF) and stopping efficiencies requires knowledge of the kinematical distributions upon production. The distributions are analyzed in Section 6.1.2. Practically all computations refer to proton collisions at a CM energy of $\sqrt{s} = 8$ TeV, since we make use of ATLAS and CMS analyses of Run I data.

6.1.1 Charged scalar production

At the LHC, charged scalar pairs in the scotogenic model are produced in pp collisions via the Drell-Yan (*cf.* Section 5.2.2) and the gluon-gluon fusion (*cf.* Section 5.2.2) mechanisms, the latter involving the SM Higgs particle h and the Z boson, as we discussed in the preceding chapter. Quark-antiquark-Higgs reactions are not significant due to the small Yukawa couplings involved in such processes. In the following, we discuss the DY and ggF contributions to scotogenic scalar production.

Although we shall investigate the effect of a non-negligible quartic coupling λ_5 in the discussion of gluon fusion, we anticipate here that the most beneficial mass configuration is to have degenerate neutral scalar bosons H^0 and A^0, hence we shall always work in the approximation

$$\lambda_5 \approx 0\,. \tag{6.4}$$

While a very compressed neutral scalar sector might not seem natural, this constitutes a natural set of masses in terms of the lightness of the active neutrinos in the scotogenic FIMP scenario, in the sense that $M_{2,3}$ are not required to lie far above the electroweak scale. Moreover, lepton number is expected to inhibit λ_5 from running strongly. One immediate simplification of a collider study of $H^{\pm}$ production is the suppression of the ggZ process, since the matrix element is proportional to the difference of the squared masses of the two produced particles [389]. The other major simplification is the phase space suppression of the cascade process shown in the following figure:

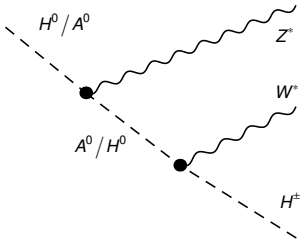

FIGURE 6.1: $H^{\pm}$ production through the cascade decay $H^0/A^0 \to A^0/H^0 + Z^* \to H^{\pm} + W^*$.

If the mass of H^0/A^0 is very close to the mass of A^0/H^0, then this process is highly suppressed and needn't be taken into account. As we shall see, DY and ggF are then each dominated by only three processes.

Clearly, mass splittings within the scalar sector of the scotogenic model will be of major concern. As the model provides three new scalars ($H^{\pm}$, H^0, A^0), three mass splittings contribute to the space of physical parameters. The squared scalar masses are given in Equations 2.114a - 2.114c; from these, one directly derives expressions for the mass splitting between H^0/A^0 and $H^{\pm}$ in terms of $m_{H^{\pm}}$ and the two (real) couplings λ_4 and λ_5,

$$\Delta m_{H^0/A^0\,H^{\pm}} \equiv m_{H^0/A^0} - m_{H^{\pm}} = \sqrt{m_{H^{\pm}}^2 + \frac{\lambda_4 \pm \lambda_5}{2} v^2} - m_{H^{\pm}}\,, \tag{6.5}$$

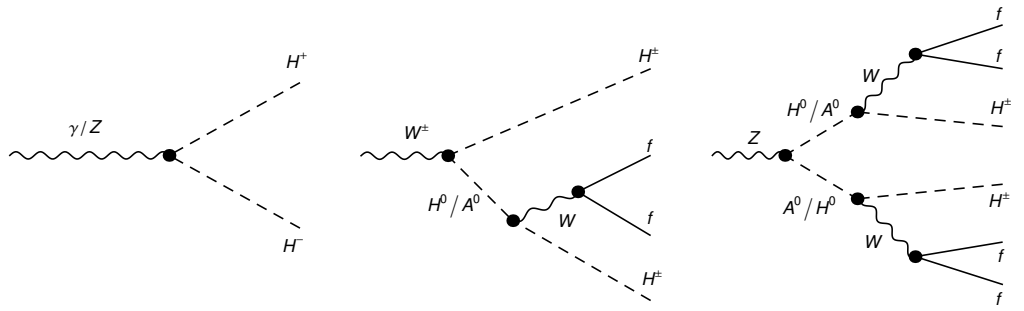

FIGURE 6.2: Main DY production processes for $H^\pm$. *Left panel:* Subprocess 1 - Direct pair production via γ/Z. *Middle panel:* Subprocess 2 - $H^\pm + H^0/A^0$ production via W. *Right panel:* Subprocess 3 - $H^0 + A^0$ production via Z. In the last two processes, H^0/A^0 decays to $H^\pm$ and two fermions ($\ell\nu$ or jj).

with + (−) for H^0 (A^0), and furthermore

$$\Delta m_{\rm nn} \equiv m_{H^0} - m_{A^0} = \sqrt{m_{A^0}^2 + \lambda_5 v^2} - m_{A^0}\,. \tag{6.6}$$

For convenience, we add to the definitions of $\Delta m_{H^0/A^0\,H^\pm}$ and $\Delta m_{\rm nn}$ the splitting

$$\Delta m_{\rm nc} \equiv m_{H^0} - m_{H^\pm} = m_{A^0} - m_{H^\pm} \qquad (\lambda_5 = 0)\,. \tag{6.7}$$

Both analyses consider two benchmark scenarios with a compressed neutral scalar sector, to wit

$$\Delta m_{\rm nc} = 10\ {\rm GeV}\,, \qquad \Delta m_{\rm nc} = 70\ {\rm GeV}\,, \tag{6.8}$$

in order to examine the effect of small to moderately large mass splittings, though still not allowing for 2-body decays of H^0/A^0 to $H^\pm$ and a physical Z.

6.1.1.1 Production via Drell-Yan

The three leading Drell-Yan subprocesses are shown in Figure 6.2. The first, *subprocess 1* (SP1), corresponds to direct production of the H^+H^- pair, whereas in *subprocess 2* (SP2), the $q\bar{q}$ collision first produces an on-shell charged and an on-shell neutral scalar. In *subprocess 3* (SP3), two on-shell neutral scalars are first created. The H^0/A^0 subsequently decay to $H^\pm$ and two fermions via a virtual W. RHN-mediated channels are suppressed due to the smallness of the Yukawa couplings and the heaviness of $N_{2,3}$. Moreover, the heavier of the neutral scalars will not decay to the lighter, in accordance with the small λ_5 assumption. They are always produced on their mass shell because small phase space factors extremely suppress the 4- and 6-body final states when compared to chain decays.

Neglecting the masses of the highly energetic quarks, we obtain from Equation 5.38 the following expressions for the partonic cross sections:

$$\begin{aligned}\hat{\sigma}_1(u\,\bar{u} \to H^+\,H^-;\,\hat{s}) = &\frac{\alpha_{\rm em}^2\,\pi\,\beta_{H^\pm}^3}{2592\,{\rm s}_{\rm w}^4\,{\rm c}_{\rm w}^4(\hat{s}-m_Z^2)^2\,\hat{s}} \\ &\times\left[(9-12\,{\rm s}_{\rm w}^2+20\,{\rm s}_{\rm w}^4)\,\hat{s}^2 - 16\,{\rm s}_{\rm w}^2(3-{\rm s}_{\rm w}^2-2\,{\rm s}_{\rm w}^4)\,\hat{s}\,m_Z^2 + 128\,{\rm s}_{\rm w}^4\,{\rm c}_{\rm w}^4\,m_Z^4\right]\,,\end{aligned} \tag{6.9}$$

$$\begin{aligned}\hat{\sigma}_1(d\,\bar{d} \to H^+\,H^-;\,\hat{s}) = &\frac{\alpha_{\rm em}^2\,\pi\,\beta_{H^\pm}^3}{2592\,{\rm s}_{\rm w}^4\,{\rm c}_{\rm w}^4(\hat{s}-m_Z^2)^2\,\hat{s}} \\ &\times\left[(9-24\,{\rm s}_{\rm w}^2+20\,{\rm s}_{\rm w}^4)\,\hat{s}^2 - 8\,{\rm s}_{\rm w}^2\,(3-5\,{\rm s}_{\rm w}^2+2\,{\rm s}_{\rm w}^4)\,\hat{s}\,m_Z^2 + 32\,{\rm s}_{\rm w}^4\,{\rm c}_{\rm w}^4\,m_Z^4\right]\,,\end{aligned} \tag{6.10}$$

$$\begin{aligned}&\hat{\sigma}_2(u\,\bar{d}/\bar{u}\,d \to H^\pm + H^0/A^0;\,\hat{s}) = \\ &\qquad\frac{\alpha_{\rm em}^2\,\pi\,\hat{s}\big(1-\frac{(m_{H^\pm}+m_{H^0/A^0})^2}{\hat{s}}\big)^{3/2}\big(1-\frac{(m_{H^\pm}-m_{H^0/A^0})^2}{\hat{s}}\big)^{3/2}}{144\,{\rm s}_{\rm w}^4\,(\hat{s}-m_W^2)^2}\,,\end{aligned} \tag{6.11}$$

	100 GeV	120 GeV	150 GeV	200 GeV	300 GeV	400 GeV	500 GeV	600 GeV
SP1: $H^+ + H^-$	97.79	49.23	20.93	6.631	1.142	0.2839	0.08588	0.02921
$\Delta m_{\rm nc} = 10$ GeV								
SP2: $H^\pm + H^0/A^0$	293.9	150.4	65.08	21.14	3.78	0.9652	0.2961	0.1012
SP3: $H^0 + A^0$	69.38	35.83	15.67	5.109	0.9068	0.2275	0.06894	0.0234
$\sigma_{\rm T}$	461.0	235.4	101.7	32.88	5.829	1.477	0.4509	0.1538
$\Delta m_{\rm nc} = 70$ GeV								
SP2: $H^\pm + H^0/A^0$	106.8	62.9	31.35	11.75	2.427	0.6639	0.2118	0.07421
SP3: $H^0 + A^0$	12.23	7.748	4.187	1.706	0.3842	0.1094	0.03564	0.0127
$\sigma_{\rm T}$	216.8	119.9	56.47	20.08	3.953	1.057	0.3333	0.1161

TABLE 6.2: Cross sections of the three Drell-Yan subprocesses of spectrum A1 in fb for $\sqrt{s} = 8$ TeV, eight different $H^\pm$ masses and $\Delta m_{\rm nc} = 10$ and 70 GeV. The cases $m_{H^\pm} = 120$ GeV and 150 GeV are included, as they are relevant for Analysis IIB. The values have been obtained with CalcHep using CTEQ6L and agree well with the analytical results calculated in Mathematica with CTEQ5L.

$$\hat{\sigma}_3(u\,\bar{u} \to H^0 + A^0;\, \hat{s}) = \frac{\alpha_{\rm em}^2\,\pi\,\hat{s}\,\big(1 - \frac{(m_{H^0}+m_{A^0})^2}{\hat{s}}\big)^{3/2}\big(1 - \frac{(m_{H^0}-m_{A^0})^2}{\hat{s}}\big)^{3/2}}{2592\,{\rm s}_{\rm w}^4\,{\rm c}_{\rm w}^4\,(\hat{s}-m_Z^2)^2}\,\big[17\,{\rm s}_{\rm w}^4 + 9\,{\rm c}_{\rm w}^4 - 6\,{\rm s}_{\rm w}^2\,{\rm c}_{\rm w}^2\big]\,, \tag{6.12}$$

$$\hat{\sigma}_3(d\,\bar{d} \to H^0 + A^0;\, \hat{s}) = \frac{\alpha_{\rm em}^2\,\pi\,\hat{s}\,\big(1 - \frac{(m_{H^0}+m_{A^0})^2}{\hat{s}}\big)^{3/2}\big(1 - \frac{(m_{H^0}-m_{A^0})^2}{\hat{s}}\big)^{3/2}}{2592\,{\rm s}_{\rm w}^4\,{\rm c}_{\rm w}^4\,(\hat{s}-m_Z^2)^2}\,\big[5\,{\rm s}_{\rm w}^4 + 9\,{\rm c}_{\rm w}^4 + 6\,{\rm s}_{\rm w}^2\,{\rm c}_{\rm w}^2\big]\,, \tag{6.13}$$

where

$$\beta_{H^\pm} = \sqrt{1 - \frac{4m_{H^\pm}^2}{\hat{s}}} \tag{6.14}$$

is the velocity of the $H^\pm$ particles in the CM frame of the collision. The velocity of the non-degenerate pairs produced in SP2 and SP3 have more complicated expressions, but they tend to velocities given by the formula in Equation 6.14 in the limit of degeneracy. We list numerical values for the total pp cross sections mediated by the three DY subprocesses at $\sqrt{s} = 8$ TeV in Table 6.2. The mass difference between the neutral and charged scalars is chosen according to our benchmark, $\Delta m_{\rm nc} = 10$ GeV and 70 GeV.

6.1.1.2 Production via gluon fusion

Motivated by the results of Analysis I, we investigate in two parts the circumstances for the ggF process to play a role in Analysis IIB. Gluon fusion is unimportant in Analysis IIA, which unlike in IIB has no sensitivity to the low-energy region and could only benefit from a comparatively large *total* ggH cross section. Unfortunately, the total ggF contribution is highly subdominant in the case of the doublet, as we saw in Analysis I (see Figure 5.4). Like before, the possibilities are ggH and ggZ production, whereas ggγ is disallowed by Furry's theorem. As a start, we carefully go over the various existing theoretical and experimental constraints on the model's low-energy parameters. Our intentions with this parameter space study are twofold.

First, we aim to study the full range of allowed low-energy parameters that are relevant for the production of charged scalar bosons in the scotogenic FIMP scenario, with $m_{H^0,A^0} > m_{H^\pm}$. We examine whether there exists an allowed configuration with a light $H^\pm$ and with a large combination $|\lambda_3 + \lambda_4 \pm \lambda_5|$, in order to maximize the $H^\pm$ ggF production cross section. The cross section also benefits from small mass differences $\Delta m_{\rm nn}$ and $\Delta m_{H^0/A^0 H^\pm}$, which are controlled by λ_4 and λ_5. If one of them is large, it is more desirable to have a large value of $\Delta m_{\rm nn}$ than of $\Delta m_{H^0/A^0 H^\pm}$, such that only one neutral scalar is unlikely to participate significantly in the production. Due to the higher phase space suppression than in Drell-Yan, the best configuration is provided by a spectrum that is as compressed as possible, *i.e.* a total

mass scale set by the size of the quartic coupling λ_3, with comparably small values of λ_4 and λ_5. We shall thus conclude in the first part that it is justified to neglect λ_5 and therefore we will only require the process of gluon fusion with an intermediate Higgs boson, as the ggZ amplitude for H^+H^- production vanishes and for $H^0 + A^0$ production it is suppressed by small λ_5 values.

Second, since λ_3 plays the crucial role for $H^\pm$ production via ggH, it is important to quantify its impact on other directly measurable effects, in particular the $h \to \gamma\gamma$ rate.[1] After all, the scotogenic model provides an additional contribution to the two-photon decay of the SM-like Higgs given by a $H^\pm$ triangle loop. We shall see that, in the low-$m_{H^\pm}$ regime, $h \to \gamma\gamma$ constraints imposed by LHC data countervail sizeable production rates through ggH.

□ Constraints on scalar couplings I: Theoretical constraints

The scalar potential of this model has been given in Equation 2.110d, with the two scalar doublets

$$H_1 = \begin{bmatrix} 0 \\ \frac{1}{\sqrt{2}}(v+h) \end{bmatrix}, \qquad H_2 = \begin{bmatrix} H^+ \\ \frac{1}{\sqrt{2}}(H^0 + iA^0) \end{bmatrix}. \tag{6.15}$$

Only $H_1^{(0)}$ acquires a vacuum expectation value v. Our chosen parameters for computations are

$$m_{H^\pm}\,, \quad \Delta m_{H^0 H^\pm}\,(>0)\,, \quad \lambda_3\,, \quad \lambda_5\,, \tag{6.16}$$

the latter being equivalent to specifying $\Delta m_{\rm nn}$ instead. This choice makes it necessary to work out a formula for λ_4, which can be done via Equation 6.5,

$$\lambda_4 v^2 = 2\Delta m_{H^0/A^0 H^\pm}(\Delta m_{H^0/A^0 H^\pm} + 2m_{H^\pm}) \mp \lambda_5 v^2\,, \tag{6.17}$$

where $-$ $(+)$ is for $\Delta m_{H^0\,H^\pm}$ $(\Delta m_{A^0\,H^\pm})$. That is, λ_4 represents a *dependent* parameter in our study. A lower bound on λ_4 is established by Equations 2.114a - 2.114c for a given $m_{H^\pm}$ and λ_5, since the mass splittings must not have an imaginary part,

$$\lambda_4 \geq -\frac{2m_{H^\pm}^2}{v^2} + |\lambda_5|\,. \tag{6.18}$$

The evident meaning of this condition is that H^0 and A^0 must not become tachyonic — demanding $m_{H^0}^2 \geq 0$ is a fundamental requirement for the tree-level electroweak vacuum to maintain the $\mathbb{Z}_2$ symmetry after EWSB.[2] It can also be written as [259]

$$\mu_2^2 \geq \frac{\lambda_3 + \lambda_4 + \lambda_5}{\lambda_1}\,\mu_1^2\,, \tag{6.19}$$

because at the electroweak vacuum conserving the $\mathbb{Z}_2$ (Equation 2.111), the Hessian of $\mathcal{V}$ reads

$$\partial^2 V_{\rm EW} = \begin{bmatrix} -2\mu_1^2 & 0 \\ 0 & \mu_2^2 - \frac{\lambda_3+\lambda_4+\lambda_5}{\lambda_1}\,\mu_1^2 \end{bmatrix} = \begin{bmatrix} m_h^2 & 0 \\ 0 & m_{H^0}^2 \end{bmatrix}, \tag{6.20}$$

so Equation 6.19 follows. Notice that the r.h.s. of Equation 6.19 can clearly be negative, and so can μ_2^2, without H_2 acquiring a VEV. It is a weaker condition than requiring $\mu_2^2 > 0$, since it can be checked that, for the parameter space we are considering, Equation 6.19 is fulfilled even if $\mu_2^2 < 0$. In fact, for $\lambda_5 \sim 0$, the case of equality is never satisfied because that would lead to a condition equivalent to $m_{H^\pm}^2 < 0$ (this would break electric charge).

We actually need to be more restrictive than in Equation 6.19 due to the imposition of $m_{H^0/A^0} > m_{H^\pm}$. As $\Delta m_{H^0 H^\pm}$ functions as a fundamental parameter, it can be chosen positive a priori and the only needed

[1] In the scotogenic model, as in all 2HDMs with a $\mathbb{Z}_2$ symmetry, only the SM-like Higgs boson may decay to two photons.

[2] If one allows for a relative phase between v_1 and v_2, an additional condition for the $\mathbb{Z}_2$ symmetry is the positivity of $m_{A^0}^2$.

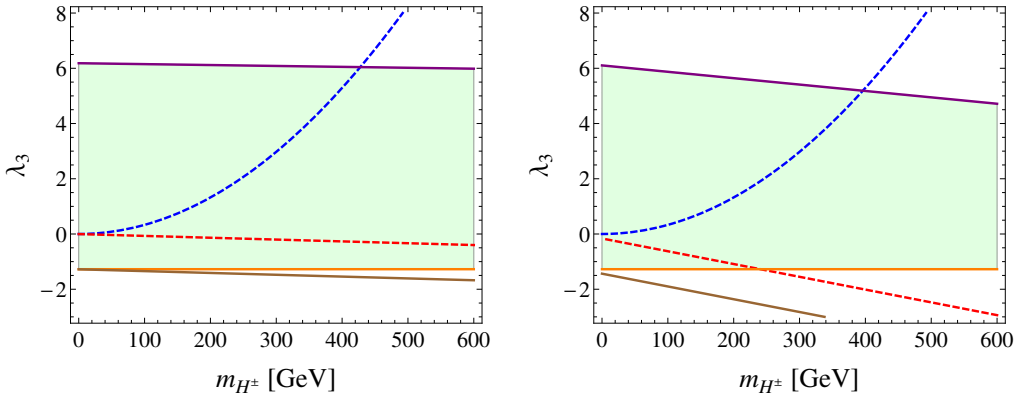

FIGURE 6.3: Region in $(m_{H^\pm}, \lambda_3)$-space allowed by all constraints, excluding $h \to \gamma\gamma$, for $\Delta m_{H^0 H^\pm} = 10$ GeV (left panel) and 70 GeV (right panel), with $\lambda_5 = 0$ in both plots. The curves representing actual bounds correspond to the following continuous contours: $\lambda_3 = -\sqrt{\lambda_1 \lambda_2}$ (orange), $\lambda_3 + \lambda_4 = -\sqrt{\lambda_1 \lambda_2}$ (brown) and the unitarity bound C_+ (purple). For λ_2, we took the value 2π. Additional illustrating dashed contours not corresponding to actual bounds are $\mu_2^2 = 0$ (blue; μ_2^2 is positive (negative) below (above) the curve) and $\frac{\lambda_3+\lambda_4+\lambda_5}{\lambda_1}\,\mu_1^2 = 0$ (red; this quantity is also positive (negative) below (above) the curve). The continuous brown and the dashed red lines are parallel because both are contours of an equation of the form $\lambda_3 + \lambda_4 = \text{const}$.

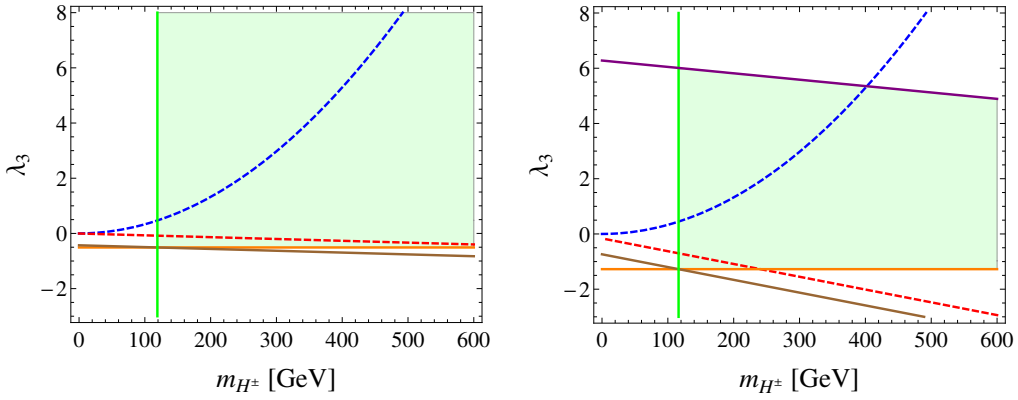

FIGURE 6.4: Region in $(m_{H^\pm}, \lambda_3)$-space allowed by all constraints, excluding $h \to \gamma\gamma$, for $\Delta m_{H^0 H^\pm} = 10$ GeV, $\lambda_5 = 0.041$ (left panel) and 70 GeV, $\lambda_5 = 0.36$ (right panel). We plot the same contours as in Fig. 6.3, with the addition of the condition $m_{A^0} > m_{H^\pm}$, Equation 6.21 (green). For $\lambda_5 = 0$ (or negative), this bound is always satisfied, hence this line is absent in the plots in Fig. 6.3.

condition is $m_{A^0} > m_{H^\pm}$, *i.e.*

$$\lambda_4 > \lambda_5 \quad \Longrightarrow \quad m_{H^\pm} > \frac{1}{2}\left(\frac{\lambda_5 v^2}{\Delta m_{H^0 H^\pm}} - \Delta m_{H^0 H^\pm}\right). \tag{6.21}$$

Next, requiring the potential to be bounded from below, leads to the tree-level relations [224]

$$\lambda_1 > 0\,, \qquad \lambda_2 > 0\,, \qquad \lambda_3 > -\sqrt{\lambda_1 \lambda_2}\,, \qquad \lambda_3 + \lambda_4 - |\lambda_5| > -\sqrt{\lambda_1 \lambda_2}\,. \tag{6.22}$$

Unitarity of tree-level scalar-scalar to scalar-scalar scattering amplitudes yields several further constraints after diagonalizing the scattering matrices and demanding that the eigenvalues do not exceed 8π. One

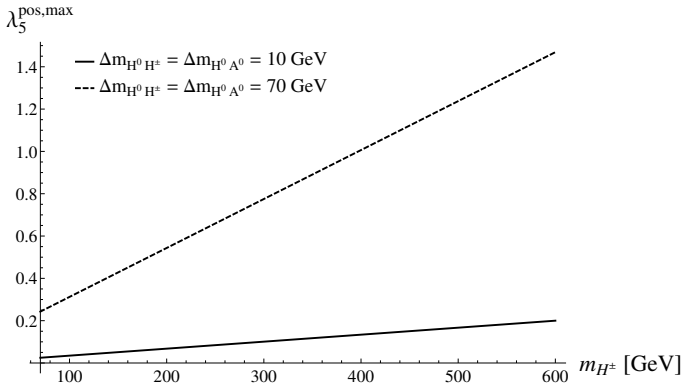

FIGURE 6.5: Upper bound on positive λ_5 as obtained from Equation 6.25. On these curves, $\Delta m_{\rm nn}$ coincides with $\Delta m_{H^0 H^\pm}$.

obtains [417]

$$A_\pm : \quad \frac{1}{2}\left|\lambda_1+\lambda_2 \pm \sqrt{(\lambda_1-\lambda_2)^2+4\lambda_4^2}\right| < 8\pi\,, \tag{6.23a}$$

$$B_\pm : \quad \frac{1}{2}\left|\lambda_1+\lambda_2 \pm \sqrt{(\lambda_1-\lambda_2)^2+4\lambda_5^2}\right| < 8\pi\,, \tag{6.23b}$$

$$C_\pm : \quad \frac{1}{2}\left|3(\lambda_1+\lambda_2) \pm \sqrt{9(\lambda_1-\lambda_2)^2+4(2\lambda_3+\lambda_4)^2}\right| < 8\pi \tag{6.23c}$$

from scattering processes involving $\mathbb{Z}_2$-even scalar pair states and

$$D_\pm : \quad |\lambda_3 \pm \lambda_4| < 8\pi\,, \tag{6.24a}$$

$$E_\pm : \quad |\lambda_3 \pm |\lambda_5|| < 8\pi\,, \tag{6.24b}$$

$$F_\pm : \quad |\lambda_3 + 2\lambda_4 \pm 3|\lambda_5|| < 8\pi \tag{6.24c}$$

for scattering of $\mathbb{Z}_2$-odd states. C_+ represents the strongest bound concerning allowed values for $|\lambda_3|$. This bound becomes more stringent as λ_2 increases and kills all parameter space from the positive and negative λ_3 direction when λ_2 reaches ~ 8.4, independently of the value of λ_5. In fact, λ_5 is found to have no effect on the viable λ_3 region, but only on the lower bound on $m_{H^\pm}$ through Equation 6.21. The effect of C_+ on λ_3 in the negative region is counteracted by an increase of the allowed range of negative values by the last two potential boundedness conditions in Equation 6.22 for increasing λ_2 values, which becomes overpowered by C_+ at $\lambda_2 \sim 8.24$. From the third potential constraint, we note that the largest possible negative λ_3 is ~ -1.8, if we exhaust perturbativity of λ_2 and set it equal to 4π. This might be relaxed if radiative corrections to the potential are taken into account, however this possibility is ignored in the present discussion.

We show the region in $(m_{H^\pm}, \lambda_3)$-space allowed by the constraints thus far discussed in Figure 6.3 for $\Delta m_{H^0 H^\pm} = 10$ GeV (left panel) and 70 GeV (right panel), with $\lambda_5 = 0$. Figure 6.4 depicts the situation for positive λ_5 by showing the allowed region corresponding to two different values for this coupling. λ_2 has been set to 2π in all plots. For each point, λ_4 is calculated with the formula in Equation 6.17. The constraint 6.19 is fulfilled in all of the parameter space, since $m^2_{H^0}$ is always positive. All unitarity constraints are satisfied, with the exception of a violation of C_+ above the purple continuous line. The orange (brown) line corresponds to the third (fourth) potential boundedness condition in Equation 6.22. Since λ_1 and λ_2 are fixed, the orange line marks the global lower limit for λ_3, this limit being at most ~ -1.8 for $\lambda_2 = 4\pi$, as already stated. $m_{H^\pm}$ is bounded from below through the condition in Equation 6.21, resulting in a parameter space exclusion only for the case $\lambda_5 > 0$. In that case, if we insist on having charged scalar masses equal to ~ 120 GeV, as selected in Analysis IIB, then λ_5 must not be larger than ~ 0.041 (~ 0.36) when $\Delta m_{H^0 H^\pm} = 10$ (70) GeV, otherwise the relation $m_{H^\pm} < m_{H^0/A^0}$ is broken; this is delimited in the two plots in Figure 6.4 by the green vertical lines. This upper bound is found by solving $m_{A^0} = m_{H^\pm}$ (or

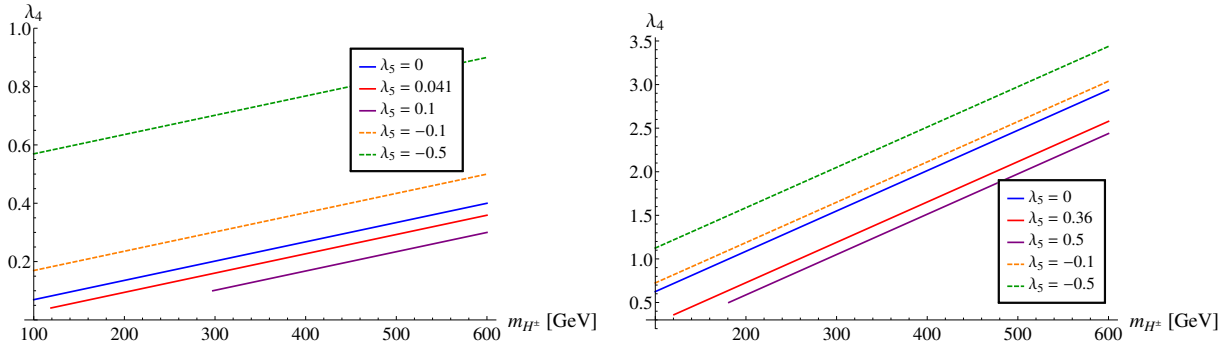

FIGURE 6.6: λ_4 as a function of $m_{H^\pm}$ for several fixed values of λ_5, as given by Equation 6.17. The curves are discontinued when m_{A^0} becomes smaller than $m_{H^\pm}$. *Left panel:* $\Delta m_{H^0 H^\pm}$ fixed to 10 GeV. *Right panel:* $\Delta m_{H^0 H^\pm}$ fixed to 70 GeV.

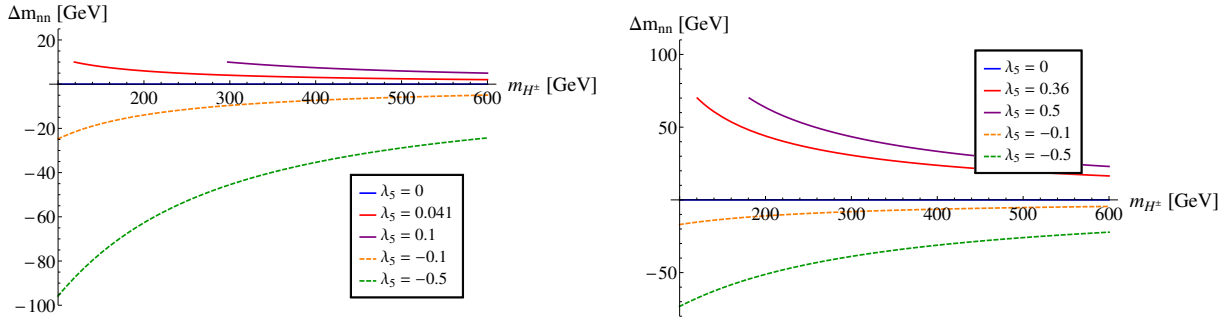

FIGURE 6.7: Mass splitting Δm_{nn} as a function of $m_{H^\pm}$ for several fixed values of λ_5, for $\Delta m_{H^0 H^\pm} = 10$ GeV (left panel) and 70 GeV (right panel). The curves are discontinued when m_{A^0} becomes smaller than $m_{H^\pm}$. Considering in particular the case $\lambda_5 > 0$, for $\lambda_5 = 0.041$ (0.36), we have $m_{A^0} > m_{H^\pm}$ for $m_{H^\pm} \gtrsim 120$ GeV. Increasing λ_5 increases this lower bound on $m_{H^\pm}$, as seen in Fig. 6.5.

$\lambda_4 = \lambda_5$) and grows linearly with the value of $m_{H^\pm}$. The maximum is

$$\lambda_5^{\max} = \frac{\Delta m_{H^0 H^\pm}}{v^2} \left(\Delta m_{H^0 H^\pm} + 2 m_{H^\pm}\right) \tag{6.25}$$

and is plotted in Figure 6.5 for the range $m_{H^\pm} \in [100\text{ GeV}, 600\text{ GeV}]$. Negative λ_5 values are found to be the most constrained by the unitarity bound F_+, which eliminates all viable parameter space at $\lambda_5 \lesssim -5$. However, such large $|\lambda_5|$ in the negative case imply neutral scalar mass splittings of several hundred GeV and therefore counteract the increase in production through ggF.

Finally, we plot λ_4 and Δm_{nn} for the considered $\Delta m_{H^0 H^\pm}$ values as a function of $m_{H^\pm}$ in Figures 6.6 and 6.7, respectively. The former, obtained with Equation 6.17, allows to infer whether a given (λ_3, λ_4, λ_5, $\Delta m_{H^0 H^\pm}$) combination is beneficial for H^0 or A^0 pair production via ggH. From the latter, one notices that already quite small $|\lambda_5|$ values can result in heavy neutral scalars relative to the charged scalars, as previously noted for the negative case. Small $|\lambda_5|$ do not contribute considerably to the combinations $\lambda_3 + \lambda_4 \pm \lambda_5$ relevant for production via the ggH process, yet large $|\lambda_5|$ values implying large neutral scalar masses lead to a considerable phase space suppression. Nevertheless, a λ_5 value that greatly differs from zero could potentially have the outcome of a non-negligible ggZ cross section for neutral scalar production, which is expected to be of the same order as the ggH cross section if $\lambda_5 \sim g \sim 0.65$ (see Analysis I). However, we opt to not investigate this possiblity, for simplicity of the analysis and a better viability of sizeable cross sections with a degenerate neutral scalar spectrum. Thus only the mass splitting Δm_{nc} defined in Equation 6.7 is from now on required.

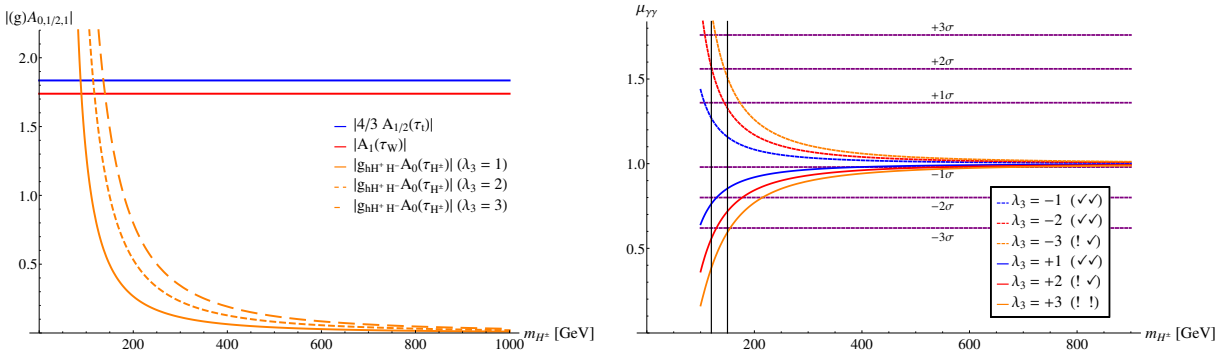

FIGURE 6.8: *Left panel:* Modulus of the loop functions $A_{1/2}$, A_1 and of $g_{hH^+H^-}A_0$, for three values of λ_3. The scalar contribution is very significant in the low-$m_{H^\pm}$ regime. *Right panel:* Signal strength $\mu_{\gamma\gamma}$ of the $h \to \gamma\gamma$ process, for the coupling strengths $\lambda_3 = -3$, -2, -1, +1, +2 and +3. If the mass splitting $\Delta m_{\rm nc}$ is not chosen too large, λ_4 remains perturbative throughout this range of $m_{H^\pm}$. The two black lines mark the masses 120 GeV and 150 GeV. With the check marks and exclamation marks, we indicate whether those values are allowed (*i.e.* within 3σ) or disallowed by ATLAS and CMS for $m_{H^\pm} = 120$ GeV (left) and 150 GeV (right).

□ Constraints on scalar couplings II: Phenomenological constraints

In this part we check for the fulfilment of two important constraints, namely those stemming from EWPO and the $h \to \gamma\gamma$ bound.

Starting with the EWPO, it is well-known that T in the IDM is by far the most restrictive oblique parameter [263]. Hence it suffices to compute the contribution ΔT because it coincides with the contribution to T in the scotogenic model. It reads

$$\begin{aligned}\Delta T &= \Delta T_{\rm IDM} \\ &= \frac{1}{32\pi^2 \alpha v^2}\left[F(m_{H^\pm}, m_{H^0}) + F(m_{H^\pm}, m_{A^0}) - F(m_{H^0}, m_{A^0})\right] ,\end{aligned} \tag{6.26}$$

where the loop function reads

$$F(m_1, m_2) = \frac{m_1^2 + m_2^2}{2} + \frac{m_1^2\, m_2^2}{m_1^2 - m_2^2} \ln \frac{m_1^2}{m_2^2} . \tag{6.27}$$

The Gfitter result [399] for T with U fixed to 0 and $m_{h,\rm ref} = 125$ GeV, $m_{t,\rm ref} = 173$ GeV is 0.05 ± 0.13, see Equation 5.31. We find that, for $\lambda_5 = 0$, ΔT is approximately constant over the whole $H^\pm$ mass range and equals ≈ 0.0009 (≈ 0.044) for $\Delta m_{\rm nc} = 10$ (70) GeV. These values lie well within the 1σ uncertainty of the fit. One may also test the effect of a non-vanishing λ_5 parameter. Varying it in the interval $[-0.3, 0.3]$ yields $\Delta T \in [0.0179, 0.0185]$ ($[0.015, 0.079]$), which still lies nicely within the allowed experimental region. It is not necessary to mind this bound any further.

We now compute the signal strength $\mu_{\gamma\gamma}$ of the $h \to \gamma\gamma$ process and compare it to the combined ATLAS and CMS result [402]. The combined 1σ range for the signal strength $\mu_{\gamma\gamma}$ amounts to $1.16^{+0.20}_{-0.18}$. Once again, $\mu_{\gamma\gamma}$ in the scotogenic model matches the prediction from the IDM, with the only deviation from unity being due to the presence of charged $H^\pm$ bosons in the triangle loop because Higgs production occurs as in the SM. Considering only the top quark contribution, the partial widths in the SM and the scotogenic model are

$$\Gamma(h \to \gamma\gamma)_{\rm SM} = \frac{G_{\rm F}\, \alpha_{\rm em}^2\, m_h^3}{128\sqrt{2}\pi^3} \left| N_{\rm c} Q_t^2 A_{1/2}(\tau_t) + A_1(\tau_W) \right|^2 , \tag{6.28a}$$

$$\Gamma(h \to \gamma\gamma)_{\rm scot.} = \frac{G_{\rm F}\, \alpha_{\rm em}^2\, m_h^3}{128\sqrt{2}\pi^3} \left| N_{\rm c} Q_t^2 A_{1/2}(\tau_t) + A_1(\tau_W) + g_{hH^+H^-} A_0(\tau_{H^\pm}) \right|^2 , \tag{6.28b}$$

where $g_{hH^+H^-} = \lambda_3 v^2/(2m_{H^\pm}^2)$ is the h-H^+-H^- coupling through which $\Gamma(h \to \gamma\gamma)_{\rm scot.}$ is sensitive to $m_{H^\pm}$ and λ_3 and the loop functions are given in Equations 5.9, 5.36a and 5.36b. The modulus of the loop functions is plotted in the right panel of Figure 6.8. Clearly, $\mu_{\gamma\gamma}$ is very sensitive to the size and sign of

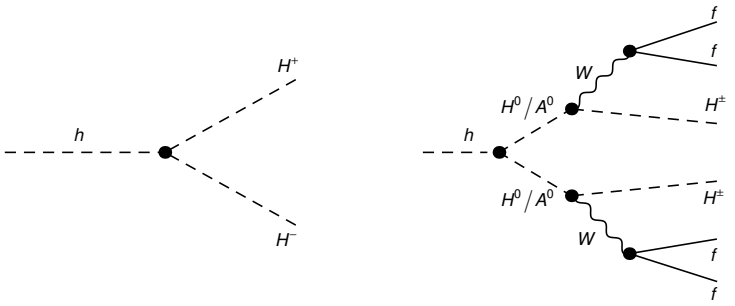

FIGURE 6.9: Main ggF production processes for $H^\pm$. *Left panel:* Subprocess 1 - Direct pair production. *Right panel:* Subprocesses 2 and 3 - H^0/A^0 production.

λ_3 for low $H^\pm$ masses.

For the full SM width, we take for $m_h = 125.1$ GeV [418]

$$\Gamma(h)_{\rm SM} = 4.08 \times 10^{-3}\,{\rm GeV}\,. \tag{6.29}$$

The same source also specifies a recommended $h \to \gamma\gamma$ branching ratio for the SM, giving $\Gamma(h \to \gamma\gamma)_{\rm SM} = 4.08\,{\rm MeV} \times 2.28 \times 10^{-3} = 9.30\,{\rm keV}$, but to be consistent with our LO calculation of the partial width, we compute the SM width at leading order and therefore rather take 10.58 keV, otherwise $\mu_{\gamma\gamma}$ does not approach unity as $H^\pm$ decouples. $\mu_{\gamma\gamma}$ is plotted in the right panel of Figure 6.8 for the quartic couplings $\lambda_3 = -3$ to $+3$, in steps of $\Delta\lambda_3 = 1$.

Selecting two low masses of interest, $m_{H^\pm} = 120$ and 150 GeV (black vertical lines), we note that the bound is not easily satisfied. For the lower mass, experimental constraints are violated when $|\lambda_3| \gtrsim 2$. For $\lambda_3 = -2$, the signal strength for 120 GeV lies exactly on the 2σ-3σ edge, however such a large negative value is forbidden by potential boundedness; the cases $\lambda_3 = -2$ and -3 are merely shown for illustration. Generally, when some λ_3 value is allowed for 120 GeV, it is viable for higher masses, but not vice versa. We thus find that $\mu_{\gamma\gamma}(\lambda_3 = +2)$ lies well within the 2σ range for $m_{H^\pm} = 150$ GeV set by the experiments, though for 120 GeV it is very incompatible with observations because it lies outside the 3σ region. One can conclude that a sizeable $H^\pm$ production cross section through ggH, which is mainly scaled by λ_3, acts against compliance with the current $h \to \gamma\gamma$ measurement. We shall return to this point at the end of the following part.

□ The ggF cross section

Since the ggZ channel plays no role, the terms ggF and ggH are from now on used interchangeably and the relevant subprocesses (SP1, SP2, SP3) are shown in the two diagrams in Figure 6.9. From Analysis I, the cross section formula in Equation 5.37 can be properly adapted. The interaction Lagrangian is

$$\mathcal{L}_{\rm int} = -\lambda_3\, v\, h\, H^+ H^- - \frac{1}{2}(\lambda_3 + \lambda_4 + \lambda_5)\, v\, h\, (H^0)^2 - \frac{1}{2}(\lambda_3 + \lambda_4 - \lambda_5)\, v\, h\, (A^0)^2\,, \tag{6.30}$$

giving

$$\hat\sigma(g\,g \to \phi\,\bar\phi) = \frac{1}{S}\frac{(n_{\rm id}!\,\Lambda_\phi)^2\, G_h^2\, \hat s\, \beta_\phi}{4096\,\pi\,(\hat s - m_h^2)^2} = \begin{cases} \frac{\Lambda_{H^\pm}^2\, G_h^2\, \hat s\, \beta_{H^\pm}}{4096\,\pi\,(\hat s - m_h^2)^2}\,, & \phi = H^\pm\,, \\ \frac{\Lambda_\phi^2\, G_h^2\, \hat s\, \beta_\phi}{2048\,\pi\,(\hat s - m_h^2)^2}\,, & \phi = H^0,\, A^0\,, \end{cases} \tag{6.31}$$

with the quartic couplings

$$\Lambda_{H^\pm} = 2\lambda_3\,, \qquad \Lambda_{H^0} = \lambda_3 + \lambda_4 + \lambda_5\,, \qquad \Lambda_{A^0} = \lambda_3 + \lambda_4 - \lambda_5 \tag{6.32}$$

and where S is the symmetry factor of the diagram and $n_{\rm id}$ the number of identical particles connecting to the triple scalar vertex vertex. Here, $n_{\rm id} = S = 1$ (2) when $\phi = H^\pm$ (H^0, A^0). The effective coupling G_h

	100 GeV	120 GeV	150 GeV	200 GeV	300 GeV	400 GeV	500 GeV	600 GeV
σ_1/λ_3^2	9.98258	4.20527	1.62722	0.35610	0.01777	0.00156	0.00020	0.00003
$\Delta m_{\rm nc} = 10$ GeV								
$\sigma_{2,3}/(\lambda_3+\lambda_4)^2$	3.12533	1.48695	0.61369	0.00681	0.00063	0.00018	0.00008	1×10^{-5}
r_1 [%]	2.165	1.786	1.600	1.083	0.305	0.107	0.045	0.022
r_{2+3} [%]	1.356	1.263	1.207	0.783	0.234	0.085	0.037	0.018
$\Delta m_{\rm nc} = 70$ GeV								
$\sigma_{2,3}/(\lambda_3+\lambda_4)^2$	0.46109	0.24659	0.09328	0.02045	0.00154	0.00018	0.00003	5×10^{-6}
r_1 [%]	4.604	3.508	2.882	1.773	0.449	0.148	0.060	0.029
r_{2+3} [%]	0.425	0.411	0.330	0.204	0.078	0.034	0.017	0.009

TABLE 6.3: Cross sections modulo coupling strengths of the three ggF subprocesses of spectrum A1 in fb for $\sqrt{s} = 8$ TeV pp CM energy, eight different $H^\pm$ masses and $\Delta m_{\rm nc} = 10$ and 70 GeV. The values have been obtained analytically in Mathematica using the CTEQ5L PDF set. As a crosscheck, the values were compared with CalcHep results and they were found to agree very well. Note that $\sigma_{2,3}$ is not the sum of subprocesses 2 and 3; each subprocess contributes individually with the same value which is listed. We also show the total $\sigma_{\rm ggF}/\sigma_{\rm DY}$ ratio modulo coupling strengths divided into the subprocess contributions r_1 and r_{2+3}, as defined in Equation 6.34, in percent. Here, r_{2+3} *does* correspond to the sum of subprocesses 2 and 3. The $\sigma_{\rm DY}$ values are given in Table 6.2.

is given by the expression in Equation 5.8. The full inclusive LO gg partonic cross section[3] is thus given by the sum

$$\hat{\sigma}(g\,g \to H^+H^- + X) \simeq \frac{G_h^2\,\hat{s}}{1024\,\pi\,(\hat{s}-m_h^2)^2}\left(\lambda_3^2\,\beta_{H^\pm} + (\lambda_3+\lambda_4)^2\,\beta_{H^0/A^0}\right)\,, \tag{6.33}$$

where the contributions to H^0 and A^0 pair production are approximately equal due to taking $\lambda_5 \simeq 0$. We can take the ratio of the ggF and the DY cross sections

$$\begin{aligned}\frac{\sigma(p\,p\to H^+H^-)_{\rm ggF}}{\sigma(p\,p\to H^+H^-)_{\rm DY}} &= \lambda_3^2\,\frac{\sigma_1(p\,p\to H^+H^-;\,\lambda_3=1)_{\rm ggF}}{\sigma(p\,p\to H^+H^-)_{\rm DY}} \\ &\quad + 2\,(\lambda_3+\lambda_4)^2\,\frac{\sigma_{2,3}(p\,p\to 2H^0/A^0;\,\lambda_3+\lambda_4=1)_{\rm ggF}}{\sigma(p\,p\to H^+H^-)_{\rm DY}} \\ &\equiv \lambda_3^2\,r_1 + (\lambda_3+\lambda_4)^2\,r_{2+3}\,,\end{aligned} \tag{6.34}$$

where the cross sections are also for inclusive H^+H^- pair production. For the same eight $H^\pm$ masses as in Table 6.2, we list the full proton-proton ggF cross sections and the $r_{1,2+3}$ contributions to the ratios $\sigma_{\rm ggF}/\sigma_{\rm DY}$, for $\sqrt{s} = 8$ TeV in Table 6.3, for the usual mass splittings. The cross sections are normalized to unit coupling strengths, for which all numbers are independent of the coupling constant values.

$\sigma_{\rm ggF}$ for $\lambda_3 = +1$ (dashed) and $\lambda_3 = +2$ (continuous) is plotted together with $\sigma_{\rm DY}$ in Figure 6.10 for $\sqrt{s} = 8$ TeV. Note that, at some point, $\sigma_{\rm ggF}(\Delta m_{\rm nc} = 70\,\text{GeV})$ (red) becomes larger than $\sigma_{\rm ggF}(\Delta m_{\rm nc} = 10\,\text{GeV})$ (orange) due to the higher values of λ_4, see Figure 6.6. Comparing the ggF cross section with the values obtained for DY, we infer that the ggF process could contribute sizeably to a given signal if the particles are light and the scalar couplings are large, *i.e.* $\gtrsim \mathcal{O}(1)$. For example, for $m_{H^\pm} = 100$ GeV, $\Delta m_{\rm nc} = 10$ GeV and $\lambda_3 \sim 1$, the ggF cross section corresponds roughly to 4% of the DY cross section, but for $\lambda_3 \sim 2$, it already amounts to 14%. For small charged scalar masses and small mass splittings around 10 GeV, a quartic coupling λ_3 of the order of 5 would render ggF as important as DY overall (exceedingly going against the $\mu_{\gamma\gamma}$ measurement). The larger the mass splitting, the smaller the λ_3 value for which this happens. The significance of the ggF process decreases with increasing charged scalar mass due to the higher phase space suppression. It turns out that the ggF contribution is too small to have an effect in Analysis IIA, whereas it will be found to be very significant for Analysis IIB because ggF preferably produces slow particles. We show this explicitly in Section 6.1.2.

[3]By inclusive, the decay products from the associated W bosons are meant, *cf.* Figure 6.9. QCD and electroweak corrections are not considered.

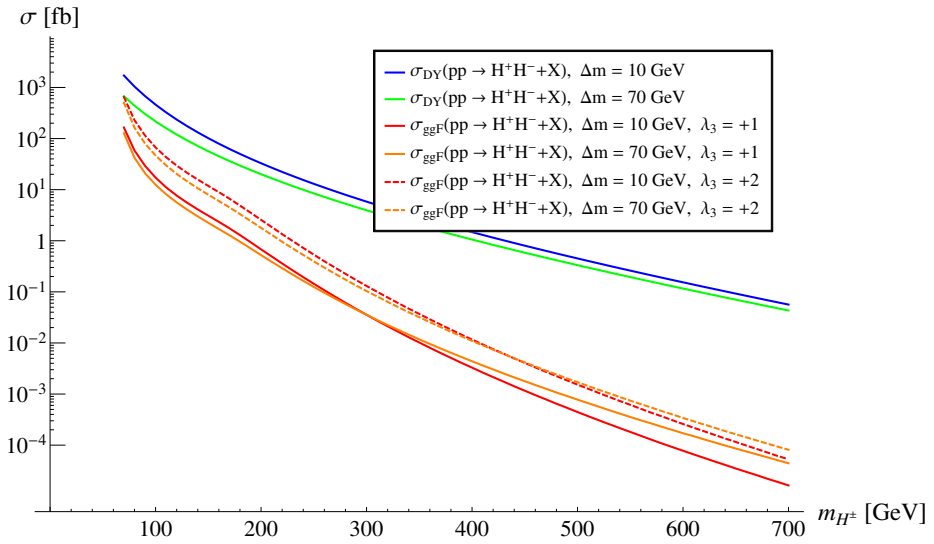

FIGURE 6.10: DY and ggF cross section curves with $\Delta m_{\rm nc} = 10$ and $\Delta m_{\rm nc} = 70$ GeV for scalar couplings $\lambda_3 = +1$ (continuous) and $+2$ (dashed) at $\sqrt{s} = 8$ TeV.

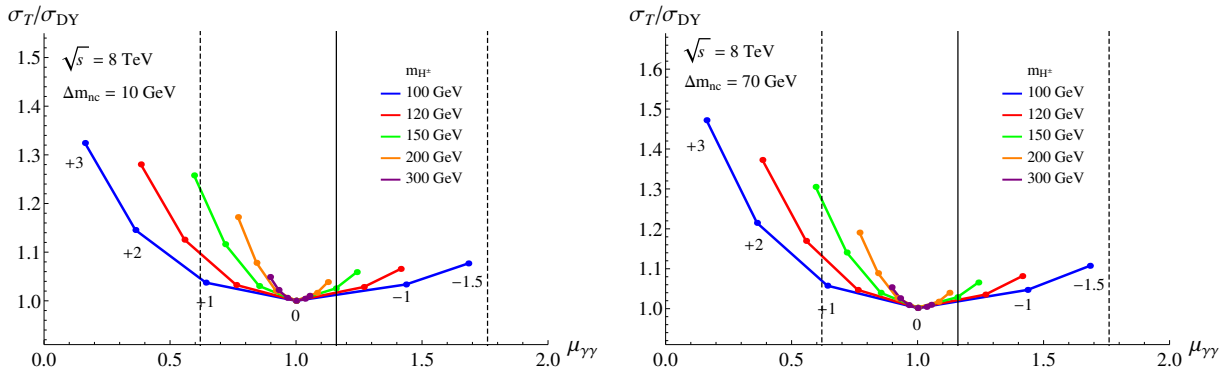

FIGURE 6.11: $h \to \gamma\gamma$ signal strength and the ratio of the total and the Drell-Yan $H^{\pm}$ production cross section for $\sqrt{s} = 8$ TeV. The considered masses are 100, 150, 200, 300 and 400 GeV, with quartic coupling $\lambda_3 = +3, +2, +1, 0, -1, -1.5$. The continuous vertical line marks the central experimental value of $\mu_{\gamma\gamma}$, the dashed lines correspond to the 3σ bounds [402]. *Left panel:* $\Delta m_{\rm nc} = 10$ GeV. *Right panel:* $\Delta m_{\rm nc} = 70$ GeV.

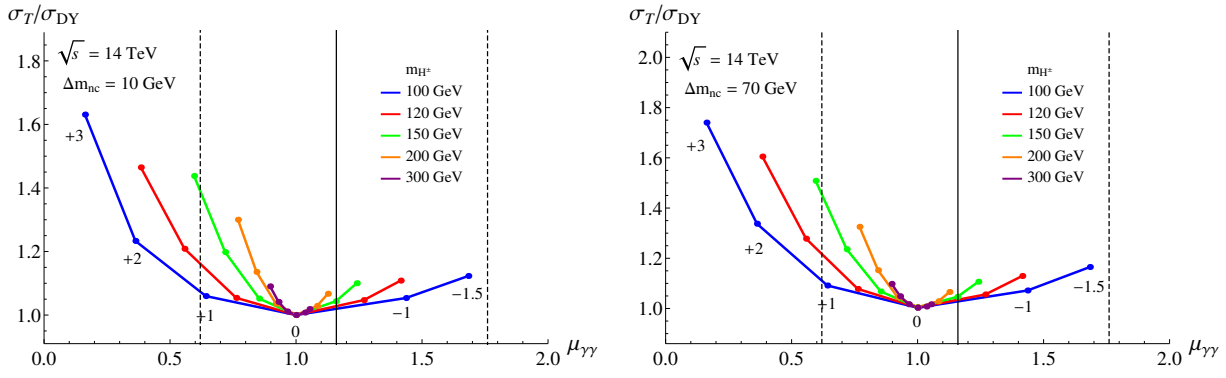

FIGURE 6.12: As above, for the case of a pp CM energy of $\sqrt{s} = 14$ TeV. *Left panel:* $\Delta m_{\rm nc} = 10$ GeV. *Right panel:* $\Delta m_{\rm nc} = 70$ GeV.

Lastly, we quantify how the production of charged scalar pairs and the $h \to \gamma\gamma$ rate in the scotogenic model are connected through the λ_3 coupling, given $\lambda_5 = 0$. In Figure 6.11, we show the ratio $\sigma_{\rm prod}/\sigma_{\rm DY} = (\sigma_{\rm DY} + \sigma_{\rm ggF})/\sigma_{\rm DY}$ as a function of $\mu_{\gamma\gamma}$, varied through λ_3, for $\sqrt{s} = 8$ TeV. Figure 6.12 depicts the same curves for the case of the nominal pp CM energy of 14 TeV. Again, the two quantities are compared for the usual mass splittings $\Delta m_{\rm nc} = 10$ GeV (left) and 70 GeV (right). Each curve corresponds to a specified $H^\pm$ mass and is drawn by connecting the points for $\lambda_3 = +3, +2, +1, 0, -1, -1.5$. The two dashed vertical lines mark the $\pm 3\sigma$ limits from the combined ATLAS and CMS measurements and the continuous black line is the central value of 1.16. These plots show that, if the excess in the measured rate should grow considerably larger with more data than it is at present, then (i) the model is ruled out if the scalars are not found to be produced through the Higgs portal and (ii) conversely, should these scalars be found at the LHC with a well measurable production cross section through some signature, the $h \to \gamma\gamma$ rate places strong constraints on the mass and the coupling.

6.1.2 Energy, momentum and pseudorapidity distribution of the $H^\pm$

The kinematics of a particle produced in a proton-proton collision are characterized by its energy $E = \gamma m$, or momentum $m\beta\gamma$, and its pseudorapidity $\eta = -\ln\tan\frac{\theta}{2}$ (*cf.* Section 3.1.2.1); both depend on the parton momentum distributions within the proton. Energy and pseudorapidity are not independent, so we are dealing with a bivariate distribution $f(\eta,\gamma) \neq f(\gamma) \times f(\eta)$. $f(\gamma)$ and $f(\eta)$ are the marginal distributions calculated by integrating over the other observable,

$$f(\gamma) = \int_{-\infty}^{\infty} d\eta\, f(\eta,\gamma)\,, \qquad f(\eta) = \int_{1}^{\infty} d\gamma\, f(\eta,\gamma)\,. \tag{6.35}$$

Note that $f(\eta,\gamma)$ is itself a marginal distribution, as we have integrated over the azimuth ϕ.

It is mandatory to have an idea of the energies the $H^\pm$ particles emerge with from the pp collisions in the detectors because the energy losses and the decay lengths depend on the initial momentum $\beta\gamma$ of the particles. We also require the information on pseudorapidity because (i) γ and η are not independent, as mentioned before, and (ii) the detectors are not spherical, meaning the path travelled through the detector layers depends on the angle with respect to the beam line, which has a large effect, as studied in Chapter 4.

We shall predominantly work with γ rather than employing $\beta\gamma$ or E. We use MadGraph/MadEvent [419] and CalcHEP [406] to generate samples of Monte Carlo events for each of the various subprocesses and create histograms from the binned counts within Mathematica for the full and marginal marginal distributions. From the histogram for subprocess x, the normalized marginal distributions are constructed through a fit to a polynomial, *i.e.* the distribution $f(\gamma)$ is given by the sum

$$f[\gamma(H^\pm)] = \sum_{\rm x} \frac{\sigma_{\rm x}}{\sigma_{\rm total}} f_{\rm x}[\gamma(H^\pm)]\,. \tag{6.36}$$

The marginal distributions are discussed first and afterwards we turn to the full distribution of the two dependent variables.

□ Drell-Yan

(i) γ, $\beta\gamma$ and η distributions

The first question we investigate is whether the γ distribution of a directly produced $H^\pm$ is significantly different from the case when it originates from the 3-body decay of a H^0/A^0. We are particularly curious about the effect of small and large mass splittings $\Delta m_{\rm nc}$.

For this check, we start by considering SP2, *i.e.* the on-shell production of the state $H^0/A^0\, H^\pm$, now for simplicity only for the case with H^0 without A^0, and regard all the scalar particles' boosts, including the boost of the charged scalar originating from the decay of the H^0. That is, we consider the two cases

$$pp \xrightarrow{W^*} H^0 + H^\pm\,, \qquad pp \xrightarrow{W^*} H^0 + H^\pm\,,\ H^0 \to H^\pm + 2f\,,$$

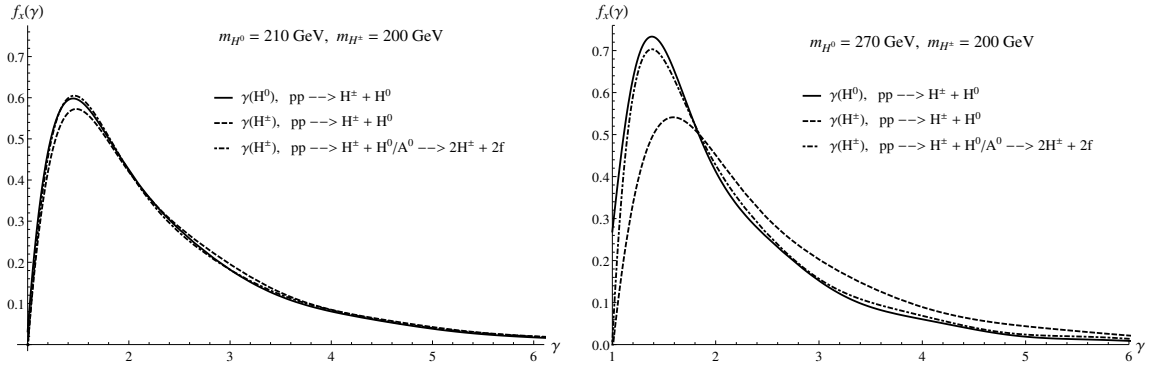

FIGURE 6.13: Boost factor distributions for subprocess 2. *Left panel:* Boost factor distribution for $m_{H^\pm} = 200$ GeV with $m_{H^0} = 210$ GeV. *Right panel:* Boost factor distribution for $m_{H^\pm} = 200$ GeV with $m_{H^0} = 270$ GeV.

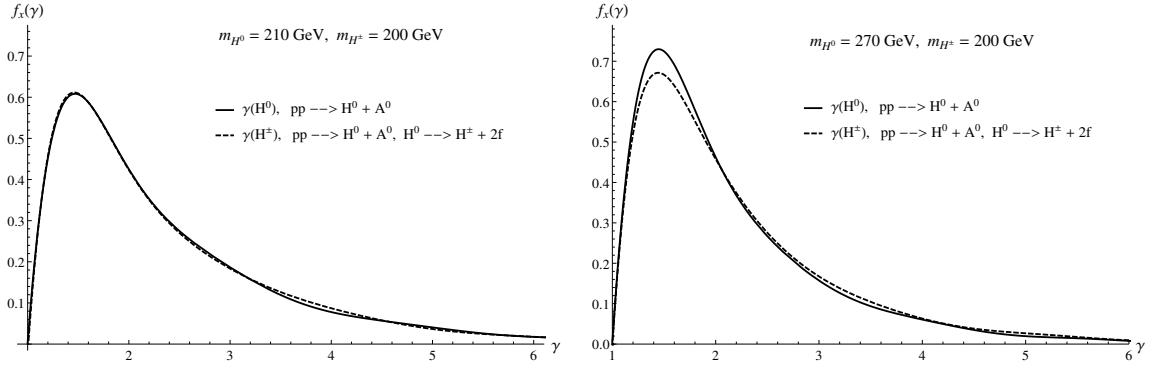

FIGURE 6.14: Boost factor distributions for subprocess 3. *Left panel:* Boost factor distribution for $m_{H^\pm} = 200$ GeV with $m_{H^0} = 210$ GeV. *Right panel:* Boost factor distribution for $m_{H^\pm} = 200$ GeV with $m_{H^0} = 270$ GeV.

and examine whether the differences between the energy distributions of the directly produced $H^\pm$, of the $H^\pm$ from the H^0 decay and of the H^0 itself depend strongly on the mass splitting for the exemplary mass $m_{H^\pm} = 200$ GeV and the cases $\Delta m_{\rm nc} = 10$ GeV and $\Delta m_{\rm nc} = 70$ GeV. In Figure 6.13, we compare for both of the spectra the boost distributions of the mother particle H^0 (continuous line), the associatively produced $H^\pm$ (dashed line) and the $H^\pm$ coming from the H^0 decay (dot-dashed line). For the compressed spectrum (left), all the curves peak at $\gamma \sim 1.45$-1.5. For the other spectrum (right), the distribution of the H^0 boost factor peaks at about $\gamma = 1.41$, the directly produced $H^\pm$ peaks at ~ 1.59 and if it stems from the neutral scalar decay, it peaks at 1.38. So for a large mass splitting $\Delta m_{\rm nc}$, there is a visible difference between the $\gamma(H^\pm)$ and $\gamma(H^0/A^0)$ distributions, whereas for a compressed spectrum there is not.

It is expected that the boost of the directly produced $H^\pm$ peaks at a higher value than it is the case with the H^0 because, since it is lighter, more of its energy can be kinetic. Note as well that, for large $\Delta m_{\rm nc}$, the peak of the boost of the $H^\pm$ originating from the H^0 decay is sharper than the peak for the curve of the directly produced $H^\pm$ and is located around the peak of the mother particle. The explanation lies in the lower available phase space volume, since a fraction of the energy is transferred to the two fermions. In the compressed case, there is not much energy available in the H^0 rest frame that can be delivered to the fermions, so that they can't be sufficiently boosted to produce a substantial recoil of the $H^\pm$. It will therefore propagate with most of the initial momentum and with almost the same boost as the mother particle due to its similar mass.

The analysis is repeated for the $H^\pm$ particles created in the two decays in SP3. We generate $pp \to H^0 + A^0$ events and let H^0 decay to $H^\pm + 2f$, plotting the obtained distributions for $\gamma(H^0)$ (continuous line) and $\gamma(H^\pm)$ (dashed line) in Figure 6.14. Again, part of the energy going to the two fermions causes

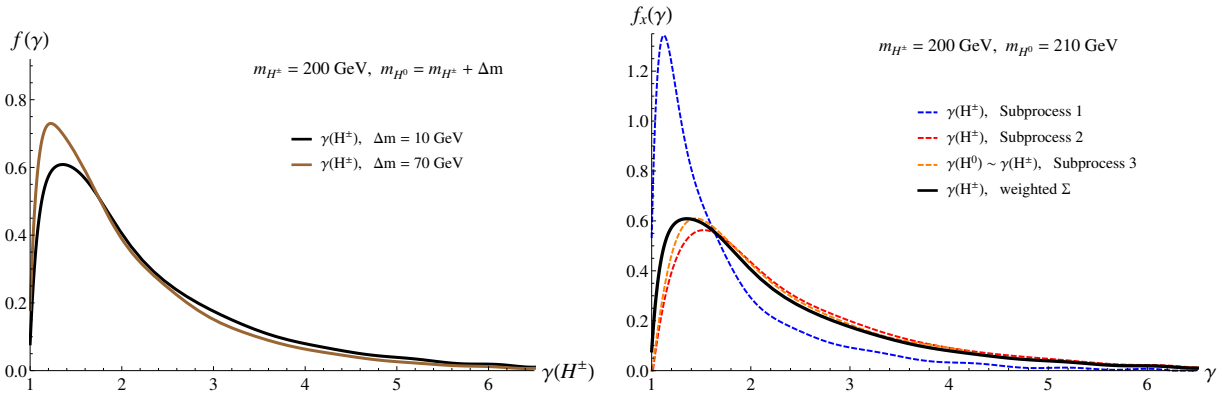

FIGURE 6.15: *Left panel:* $\gamma(H^\pm)$ distribution for all the subprocesses and for the sum given by Equation 6.37a, with $\Delta m_{\text{nc}} = 10$ GeV. *Right panel:* Comparison of $\gamma(H^\pm)$ distribution for $\Delta m_{\text{nc}} = 10$ GeV and $\Delta m_{\text{nc}} = 70$ GeV.

the distribution to resemble the distribution of the mother particle H^0.

Figure 6.15 contains the full weighted distribution of $\gamma(H^\pm)$ for $m_{H^\pm} = 200$ GeV in the left panel for $\Delta m_{\text{nc}} = 10$ GeV (black curve) and $\Delta m_{\text{nc}} = 70$ GeV (brown curve). In accordance with the previously gathered insights, the polynomials weigh the contributions for the respective mass splittings by the different subprocess distributions according to

$$f[\gamma(H^\pm)]_{10} = \frac{\sigma_1}{\sigma_{\text{total}}} f_1[\gamma(H^\pm)] + \frac{\sigma_2}{\sigma_{\text{total}}} f_2[\gamma(H^\pm{}_{\text{direct}})] + \frac{\sigma_3}{\sigma_{\text{total}}} f_3[\gamma(H^0)]\,, \tag{6.37a}$$

$$\begin{aligned} f[\gamma(H^\pm)]_{70} = {} & \frac{\sigma_1}{\sigma_{\text{total}}} f_1[\gamma(H^\pm)] + \frac{\sigma_2}{\sigma_{\text{total}}} \frac{1}{2} \left(f_2[\gamma(H^\pm{}_{(W1)})] + f_2[\gamma(H^\pm{}_{(W2)})] \right) \\ & + \frac{\sigma_3}{\sigma_{\text{total}}} f_3[\gamma(H^\pm)]\,, \end{aligned} \tag{6.37b}$$

where 'direct' stands for 'direct production', meaning the respective boost belongs to the directly produced charged scalar in SP2. Note that for SP3, we are considering the true $H^\pm$ boost factor instead of $\gamma(H^0/A^0)$ in Equation 6.37b. Through the factor of $1/2$ in $f[\gamma(H^\pm)]_{70}$, we account for the fact that detecting the directly produced $H^\pm$ (originating from the first W) is as probable as having it originate from the second W. By increasing Δm_{nc} from 10 to 70 GeV, the peak in γ decreases from ~ 1.35 to ~ 1.23.

In summary, a large mass splitting implies a larger number of slow particles, though this counteracts production through a smaller phase space for the final state. A smaller mass splitting results in almost equal momenta of the mother and daughter particles.

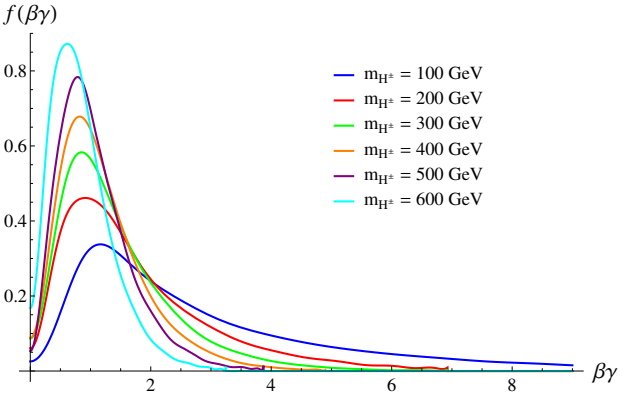

FIGURE 6.16: $\beta\gamma$ distribution for $\sqrt{s} = 8$ TeV and $\Delta m_{\text{nc}} = 10$ GeV, for six $H^\pm$ masses.

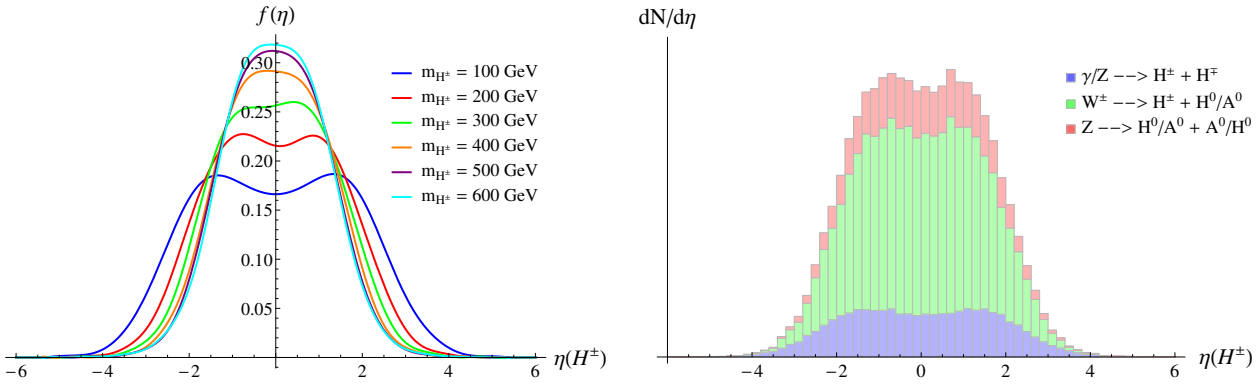

FIGURE 6.17: *Left panel:* η distribution for $\sqrt{s} = 8$ TeV and $\Delta m_{\rm nc} = 10$ GeV, for six $H^\pm$ masses. *Right panel:* Subprocess contributions to the case of $m_{H^\pm} = 200$ GeV and $\Delta m_{\rm nc} = 10$ GeV.

The $\beta\gamma$ distributions for the charged scalar masses of 100 to 600 GeV, in steps of 100 GeV, are shown in Figure 6.16 and the corresponding marginal pseudorapidity distributions are shown in the left panel of Figure 6.17. As a particular histographic example, the case of $m_{H^\pm} = 200$ GeV is depicted on the right, where the contributions of the three subprocesses are indicated by employing different colours in the histogram. SP2 is dominant due to the W field having twice the number of degrees of freedom of the photon and the Z and due to being slightly lighter than the latter. From Table 6.2, one infers that the proportions SP1 : SP2 : SP3 are about $1 : 3.2 : 08$.

(ii) $f(\eta, \gamma)$

Recall that γ ($\beta\gamma$) and η are not independent, one therefore requires the bivariate PDFs $f(\eta, \gamma)$. DY- and ggF-mediated $H^\pm$ pair production for the respective first subprocesses are compared in the event density plots in Figure 6.18 and one notices that they are similar, forming a U-shaped peak that is symmetric about the $\eta = 0$ axis. However, the gluon fusion distribution is far more concentrated at lower boosts. We will explore this behaviour below.

The explanation for the exhibited shape is as follows. According to the discussions in Sections 3.1.1 and 3.1.3, the CM frame of the colliding quarks within the protons is often not at rest with respect to the detector rest frame, but is moving with some net velocity along the $+z$ or $-z$ direction (with a negligibly small transversal component). The distribution of the quark momenta is contained in the quark PDFs, quantified as fractions of the proton momenta. The higher the partonic CM energy, the larger the probability of the center-of-mass of the colliding quark-antiquark pair to have a high net velocity $\beta_{q\bar{q}}$ in the forward or backward direction in the detector. Therefore the detector-frame z-components of the momenta of the $H^\pm$ particles, which are produced with a $\sin^3\theta$ distribution ($\sin\theta$ in the case of ggF) in the $q\bar{q}$ CM frame (*cf.* Section 5.3.3), experience the boost $\gamma(\beta_{q\bar{q}})$. This leads to more high-η collision products with increasing $\gamma(\beta_{q\bar{q}})$, as can be seen in the event density plots. The lower the charged scalar mass, the higher its forward or backward velocity increase due to the boost. For low $\gamma(\beta_{q\bar{q}})$, the distribution resembles the partonic CM frame $\sin^3\theta$ distribution characteristic of the DY process. The two bumps in the marginal pseudorapidity distribution follow from the integration over γ.

We remark that, although the two variables are dependent, they are not correlated due to this symmetry, as expected for an (assumed) absence of an experimental bias in η. This can be easily seen from the

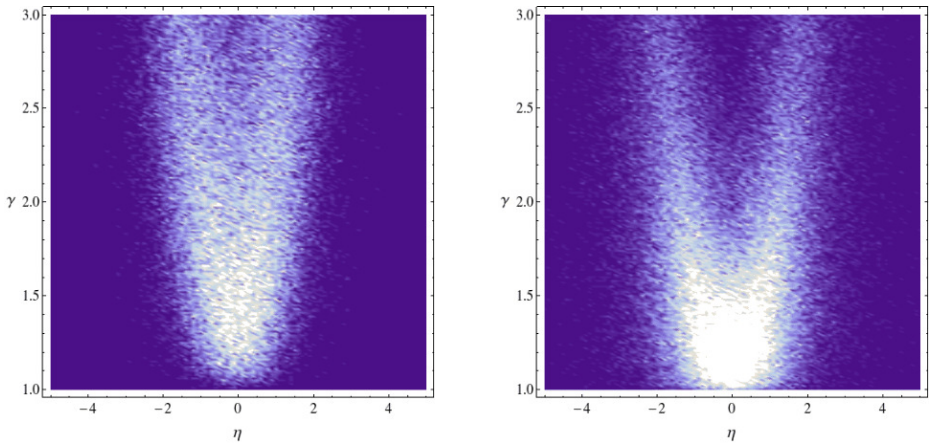

FIGURE 6.18: Event density plots for the first subprocesses of DY (left) and ggF (right) obtained by generating 25 000 events in MadGraph for each mechanism. We selected the mass $m_{H^\pm} = 150$ and the CM energy of the protons is 8 TeV. The distributions clearly differ from a factorized distribution and form a U-shaped peak.

expression for the covariance of γ and η,

$$\begin{aligned}\mathrm{cov}[\eta,\gamma] &= \int d\gamma \int d\eta\, f(\eta,\gamma)(\gamma - E[\gamma])(\eta - E[\eta]) \\ &= \int d\gamma\, (\gamma - E[\gamma]) \int d\eta\, f(\eta,\gamma)\, \eta \\ &= 0\,, \end{aligned} \tag{6.38}$$

using $E[\eta] = 0$ and the fact that f is a symmetric function of η.

□ Gluon fusion

For the gluon-gluon fusion process, the kinematics are in essence the same as for DY. Since the partonic cross sections depend on the scattering angle in the manner $\frac{d\sigma}{d\theta} \sim \sin\theta$, there is again a preference for small pseudorapidities, with $|\eta|$ increasing with the boost of the CM frame of the two colliding gluons.

The energy distribution is also comparable to DY, though with peaks at considerably lower boosts. Examining the impact of gluon fusion as an additional production mechanism to Drell-Yan is therefore important, because we are interested in the low-$\beta\gamma$ regime, where particles get stopped in the detector. Even if the couplings are too small to obtain a total cross section comparable to DY, the distribution in energy can still be sufficiently concentrated at low values such that its contribution to the number of stopped particles may turn out to be significant, the reason being the fact that low momentum values for gluons in the protons are always much more probable than for quarks, as can be seen in Figure 3.2. If we intend to compare the two mechanisms in a regime of low-energetic $H^\pm$ production, say, between $\tau = \tau_{\mathrm{thr}} = 4m_{H^\pm}^2/s$ (when the particle is at rest in the CM frame, $\gamma_{\mathrm{CM}}(H^\pm) = 1$) and $\tau = (1+f)\times\tau_{\mathrm{thr}}$ ($\gamma_{\mathrm{CM}}(H^\pm) = \sqrt{1+f}$),[4] for some small positive number $f \gtrsim 0$, we can quantify the relative contributions by considering the ratio

$$R_f \equiv \frac{\Delta_f \sigma_{\mathrm{ggF}}(p\,p \to H^+\,H^-;\, s)}{\Delta_f \sigma_{\mathrm{DY}}(p\,p \to H^+\,H^-;\, s)} = \frac{\int_{\tau_{\mathrm{thr}}}^{(1+f)\tau_{\mathrm{thr}}} d\tau\, \frac{d\mathcal{L}_{gg}}{d\tau}\, \hat{\sigma}(g\,g \to H^+\,H^-;\, \hat{s} = \tau\mathrm{thr})}{\sum_{q,\bar{q}} \int_{\tau_{\mathrm{thr}}}^{(1+f)\tau_{\mathrm{thr}}} d\tau\, \frac{d\mathcal{L}_{q\bar{q}}}{d\tau}\, \hat{\sigma}(q\,\bar{q} \to H^+\,H^-;\, \hat{s} = \tau s)}\,. \tag{6.39}$$

$R_f(\lambda_3 = +2)$ is plotted in Figure 6.19. All three leading subprocesses are considered and the pp CM energy is set at 8 TeV. It becomes smaller than 1 for $f \sim 0.13$ ($\gamma_{\mathrm{CM}} \sim 1.015$), for lower boosts, ggF is clearly dominant.

[4] The energy of a $H^\pm$ in the partonic CM frame is $\sqrt{\hat{s}}/2 = \sqrt{(1+f)\,\tau_{\mathrm{thr}}\,s}/2 = \sqrt{1+f}\,m_{H^\pm}$.

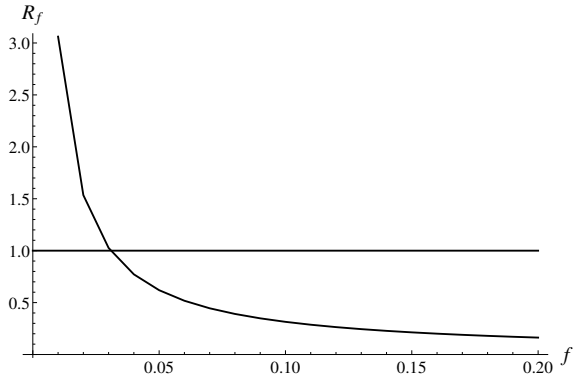

FIGURE 6.19: R_f as defined in Equation 6.39 for $\lambda_3 = +2$ in the range $f \in (0.01, 0.2)$.

To conclude this section, we compare the marginal $\beta\gamma$ distributions of a $H^\pm$ particle originating from Drell-Yan and gluon fusion production. The total normalized $\beta\gamma$ distribution is given by

$$\begin{aligned} f[\beta\gamma(H^\pm)] &= \tilde{f}_{\mathrm{DY}}[\beta\gamma(H^\pm)] + \tilde{f}_{\mathrm{ggF}}[\beta\gamma(H^\pm)] \\ &= \frac{\sigma_{\mathrm{DY}}}{\sigma_{\mathrm{T}}} f_{\mathrm{DY}}[\beta\gamma(H^\pm)] + \frac{\sigma_{\mathrm{ggF}}}{\sigma_{\mathrm{T}}} f_{\mathrm{ggF}}[\beta\gamma(H^\pm)]\,, \end{aligned} \tag{6.40}$$

with $\sigma_{\mathrm{T}} = \sigma_{\mathrm{DY}} + \sigma_{\mathrm{ggF}}$. $f_{\mathrm{DY,ggF}}$ are normalized to unity, resulting in

$$\int d\beta\gamma\, \tilde{f}_{\mathrm{DY}}(\beta\gamma) = \frac{\sigma_{\mathrm{DY}}}{\sigma_{\mathrm{T}}}\,, \tag{6.41}$$

$$\int d\beta\gamma\, \tilde{f}_{\mathrm{ggF}}(\beta\gamma) = \frac{\sigma_{\mathrm{ggF}}}{\sigma_{\mathrm{T}}}\,. \tag{6.42}$$

These distributions are depicted in Figures 6.20 - 6.22 for $m_{H^\pm} = 150$ GeV (left) and 300 GeV (right), for three quartic couplings $\lambda_3 = +1, +2, +3$ and a pp CM energy of $\sqrt{s} = 8$ TeV, again with the mass splitting chosen to be $\Delta m_{\mathrm{nc}} = 10$ GeV. Note that the last coupling is highly disfavoured by $h \to \gamma\gamma$ measurements and is herein considered as an academic example. These logarithmic plots close in on the region where the particles are slow. All three leading subprocesses for each production mechanism are incorporated in the Monte Carlo samples generated for this purpose. The functions shown correspond to $\tilde{f}_{\mathrm{DY}}$ (dashed), $\tilde{f}_{\mathrm{ggF}}$ (dot-dashed) and their sum (continuous).

We observe that, if the scalar quartic couplings are larger than ~ 2 and if the $\mathbb{Z}_2$-odd scalars are not much heavier than 100 GeV, gluon fusion leads to a significant number of slow particles and therefore needs to be taken into account in searches for HLLCPs in experiments where sensitivity to slow particles is enhanced. This is especially true in stopped particle searches. In Section 4.2, we investigated how electromagnetic interactions with the detector slow down the particles until they may eventually stop if they are sufficiently slow. Using the illustrated methods (*i.e.* the Bethe-Bloch equation), we worked out for each case the maximum value of $\beta\gamma$ until which $H^\pm$ particles are stopped in ATLAS, averaged over the η region of the ATLAS barrel. The stopping regions in the $\beta\gamma$ distributions are shaded in gray. In Analysis IIB, we shall show examples of stopping regions in the full two-dimensional (η, γ)-space.

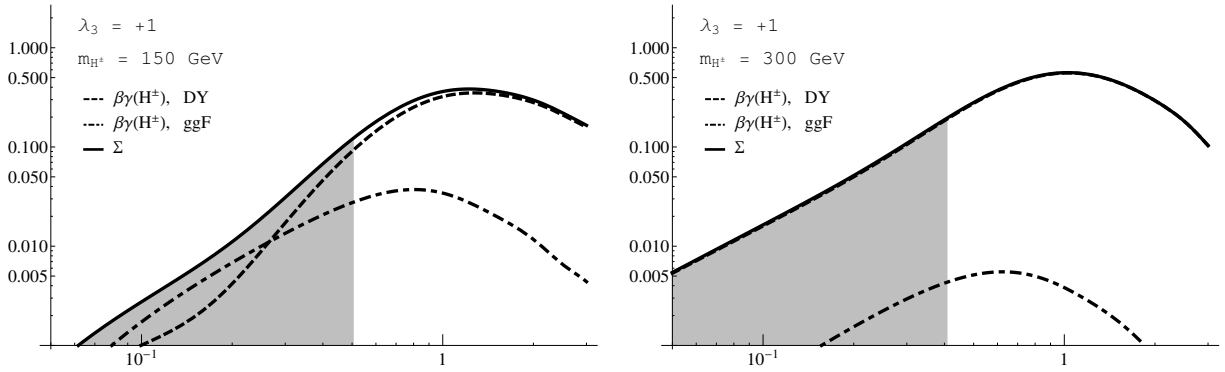

FIGURE 6.20: $\beta\gamma$ distributions of $H^{\pm}$ for $m_{H^{\pm}} = 150$ GeV (left panel) and $m_{H^{\pm}} = 300$ GeV (right panel) at $\sqrt{s} = 8$ TeV with $\Delta m_{\rm nc} = 10$ GeV via DY (dashed) and ggF (dot-dashed) mediation, given a quartic coupling $\lambda_3 = +1$. They are normalized such that integration over their sum (continuous) equals 1. The shaded region indicates the energies in which the particles stop in ATLAS, averaged over the detector geometry.

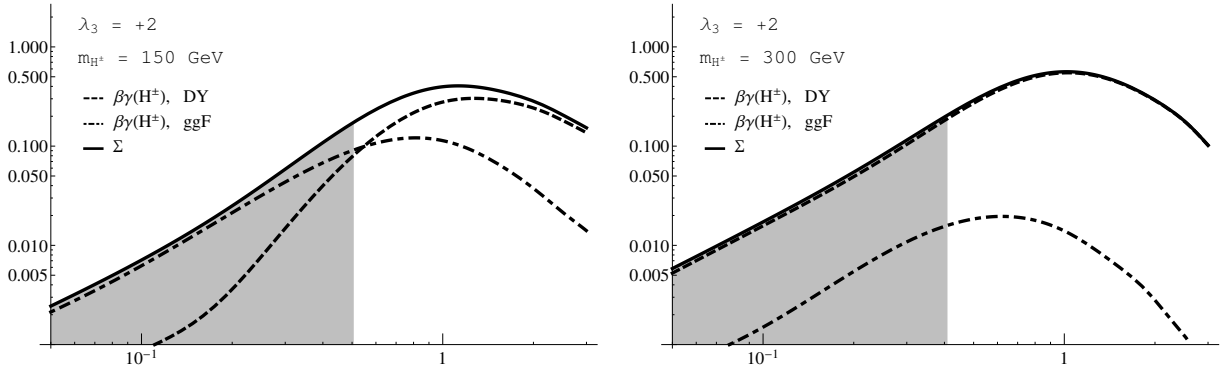

FIGURE 6.21: Case $\lambda_3 = +2$.

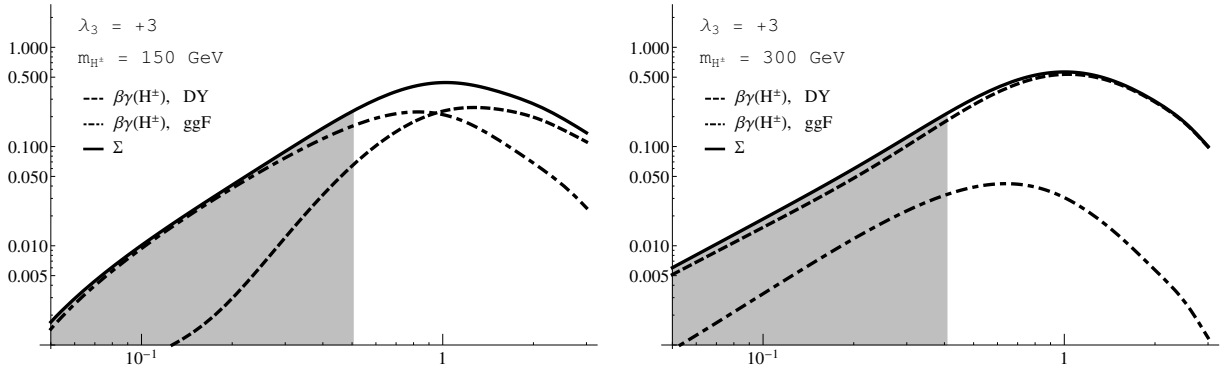

FIGURE 6.22: Case $\lambda_3 = +3$.

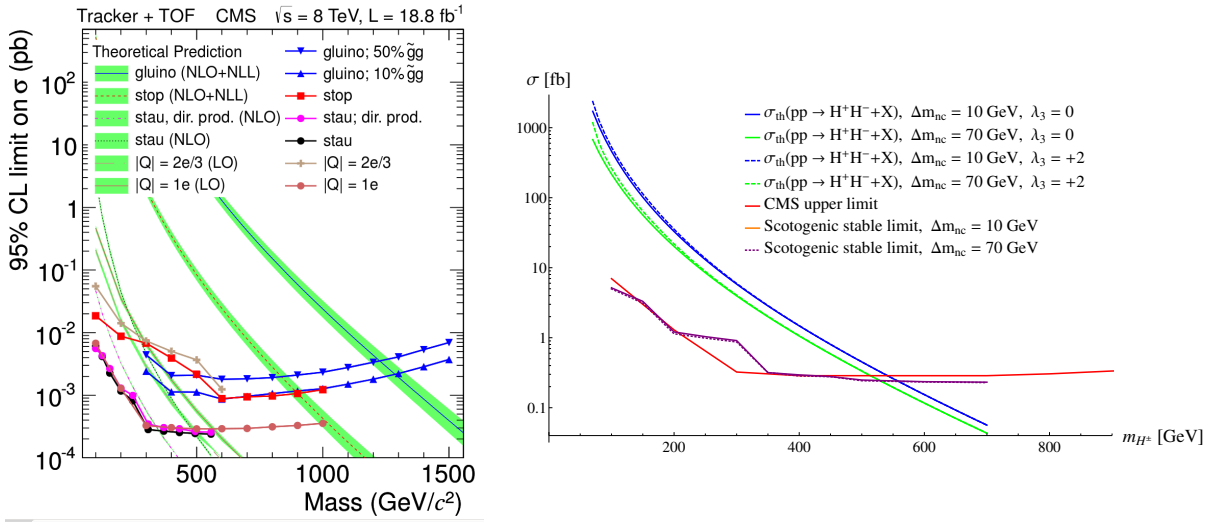

FIGURE 6.23: *Left panel:* Cross section limits obtained from the $\sqrt{s} = 8$ TeV sample with the tracker+TOF strategy. See the text for details. *Right panel:* $H^{\pm}$ pair production cross section with $\Delta m_{\rm nc} = 10$ GeV (blue) and $\Delta m_{\rm nc} = 70$ GeV (green) and the CMS upper bound for heavy singly-charged stable particles. We show the summed DY and ggF production cross sections with scalar couplings $\lambda_3 = 1$ (continuous) and 2 (dashed). If $H^{\pm}$ is stable on collider scales, then its mass is constrained to be $\gtrsim 541.1$ (513.9) GeV if $\Delta m_{\rm nc} = 10$ (70) GeV. The continuous orange and dotted purple lines are the limits we obtain in the limit of total metastablility of the scotogenic $H^{\pm}$ boson.

6.2 Analysis IIA: Long-lived $H^{\pm}$ particles producing stable charged tracks in the CMS detector

We calculate limits on the production of $H^{\pm}$ particles in the scotogenic model with the N_1 particle acting as a FIMP dark matter particle resulting in signatures with stable tracks. These signatures can be attributed to the signal region used for the determination of the upper limits on signal event numbers in the CMS analysis [45] searching for metastable particles that manage to escape the detector. From the inferred limits on event numbers, the search places limits on the HLLCP production cross section in various supersymmetric scenarios and on the production cross section of singly-, fractionally- and multiply-charged metastable heavy leptons. Through their results, we work out constraints on the parameter space of the considered scotogenic model.

CMS performed their analysis on data accumulated during the 2011 and 2012 operation of the LHC. Center-of-momentum energy and integrated luminosity in each set are, respectively, 7 TeV, 5.0 fb^{-1} and 8 TeV, 18.8 fb^{-1}. There are three search strategies. Our study is based on the 'tracker+TOF' sub-analysis, which is best suited to seek a signal of our target particle because it requires a high-quality track in the inner detector and in the muon system with an upper velocity bound set by the time-of-flight as described in Section 4.2.2. The other searches are in principle not applicable to a scenario such as ours because they are optimized for charge flipping as predicted for R-hadrons. Charge-flipping from charged to neutral might resemble the decay of a $H^{\pm}$ without the reconstructed lepton track, but a recast of a disappearing track analysis would be considerably more sensitive to such a signal [420]. Hence we exclusively focus on the measurements made with the tracker+TOF method. In the following we also never consider the CMS limits obtained from the $\sqrt{s} = 7$ TeV sample because they are much weaker.

The limits obtained from $\sqrt{s} = 8$ TeV data are shown in the left panel of Figure 6.23, taken from Figure 8 in the main reference. We can make the a priori observation that the stau or singly-charged lepton pair production targeted by CMS will exhibit kinematics that quite resemble the kinematics of the $H^{\pm}$ pair, because the production occurs through the Drell-Yan process either directly or via a cascade. For instance, taking the constraints on singly-charged pair-produced leptons at face value as a bound on the

$H^\pm$ pair production cross section in the limit of stability at collider scales, one would obtain a strongest lower bound of ~ 541 (~ 514) GeV on the mass, provided the presumed degenerate neutral scalars H^0 and A^0 are 10 (70) GeV heavier. This can be extracted from the intersection of the red curve in the plot in right panel of Figure 6.23 with the shown theoretical cross sections. In the plot, these are chosen with a vanishing and a sizeable quartic coupling λ_3. From the curves one infers that gluon fusion, at least at leading order, is an irrelevant production mechanism due to a high loop suppression. The actual upper limits on the cross section in the scotogenic model for a decay length that exceeds the detectors are included in the plot as red (almost superimposed) lines, each corresponding to one mass splitting. Their computation is outlined in Section 6.2.2.1. They differ a bit from the CMS limit because the kinematical distributions do, in fact, differ to some extent. Moreover, our computation is based on a poorer estimation of track selection efficiencies, as is explained next.

It must be remarked that the published analysis [45] is not sufficient for a recast; we rather need to combine the outcome of the tracker+TOF analysis with additional results by CMS given in Reference [421]. The latter is an application of the findings in [45] to supersymmetric frameworks containing heavy long-lived singly-charged 'lepton-like' (*i.e.* non-hadronic) particles, in particular long-lived charginos. Only the procedure of the estimation of the signal acceptance and the exemplary application to stau production are of interest here, not the results concerning chargino production. The reference provides as a supplement a tabulated list of online and offline charged track selection probabilities, P^{on} and P^{off}, depending on their true kinematics, which can be applied to any model containing such lepton-like long-lived particles that may escape the detector [422]. Acceptances are calculated by summing the factorized selection probabilities for each candidate track in the sample, $P^{\text{on}} \times P^{\text{off}}$. Since these probabilities are calculated from a very detailed simulation of the CMS detector, they account for effects that we cannot include in a simple Monte Carlo computation, so their exertion leads a very realistic CMS acceptance estimation. The utilization of this efficiency map is demonstrated through a repetition of the determination of direct and indirect stau production cross section limits at 95% C.L. in the context of GMSB. These limits are obtained by means of the CL_s technique [423], which depends on three nuisance parameters: the integrated luminosity, the signal acceptance and the expected background inside the signal region.

References [45] and [421] employ the same approach, however the computed acceptance for a given hypothesized HLLCP mass depends on a lower threshold m_{thr} imposed on the mass reconstructed from the charged track that is different in both analyses, resulting in somewhat different limits. Probabilities in the supplied efficiency map are only given for four values of m_{thr} set to *at most* 0.6 times the true mass of the hypothetical particle, varied in steps of 100 GeV, whereas the step in [45] is 10 GeV. A threshold of $\sim 0.6\,m$ is stated to contribute a factor of 95% to the selection efficiency. Clearly, a lower step leads to a more realistic background estimation. Thus the effect of the worse granularity in m_{thr} when using the tabulated efficiencies results in a background overestimation and yields a more conservative bound on the signal, as is especially visible in the mass range around $m_{H^\pm} = 300$ GeV in the right plot in Figure 6.23. Nevertheless, they are mostly found to agree with the limits in [45] within 15%. Besides applying the efficiency map, we also extract from [421] the number of excluded signal events for the given mass thresholds from the upper limits on the stau production cross sections, which are obtained with basis on the event count numbers underlying the results of [45]. These numbers can subsequently be converted into an upper limit on the inclusive production cross section of $H^\pm$ pairs in the scotogenic FIMP model and on the mass of the dark matter particle N_1, given the luminosity and the acceptance.

In the following section, the CMS search [45] is described in some qualitative and quantitative detail. Section 6.2.2 presents the analysis by first outlining the method and the showing the calculation in Section 6.2.2.1, followed by the results in Section 6.2.2.2.

6.2.1 The CMS search

The search uses data divided into three main subsets: The 'tracker-only' method requires tracks to be reconstructed in the tracker, ignoring activity in the rest of the detector, the 'muon-only' method requires tracks to be reconstructed in the muon system, ignoring the rest, and the 'tracker+TOF' strategy requires

reconstructed tracks in both systems that need to match. The strategies involving only one detector part intend to allow for the detection of charge-flipping R-hadrons, as these can at times be neutral and interact only via the nuclear force. Candidate masses are reconstructed as discussed in Section 4.1, *i.e.* through the energy deposited in the Si cells yielding $m_{\beta\gamma}$, *cf.* Equation 4.12. This energy is quite high if the particles are heavy, an essential property for triggering, as it sets the difference to known long-lived particles, such as muons and some mesons.

The experiment uses three technologies in the muon system, as explained in Appendix E. In the barrel, DT chambers are responsible for triggering, timing, bunch crossing identification and precise position measurement. In the EC, this task is fulfilled by CSCs. In both the barrel and EC layers, RPCs positioned between the DT/CSC and return yoke layers are used for redundant triggering and timing measurements to enhance the track reconstruction efficiency. For the tracker+TOF search, the L1 muon trigger is configured to accept tracks leaving hits in the RPCs in the 25 ns window containing the currently colliding pair of filled bunch slots and in the following 25 ns time window containing two unfilled slots (the bunch structure of the proton filling scheme used in 2011 and 2012 is described in Section 3.2.1.2). Allowing for HLLCPs to travel through the detector for up to 50 ns leads to the inclusion of low-β particles and allows for setting stringent upper bounds on accepted β values to discriminate against SM particles ($\beta \approx 1$). The velocity β is determined as the weighted average of at least eight independent TOF measurements from hits in the DTs and CSCs in the muon system, where the weight is set by the measurement resolution. Tracks traversing the barrel (EC) yield on average 16 (30) time measurements. There is no velocity determination within the tracker.

Background may stem from SM particles with mismeasured energy, timing or momentum or fluctuations in energy deposition. Before applying final criteria on the event candidate samples to estimate the background, a set of preselection cuts is established to accumulate the main sample, shown in Table 6.4. The first fundamental kinematic cut is the requirement that all tracks be within the pseudorapidity range $|\eta| < 2.1$. As we have seen in Section 6.1.2, this cut efficiently selects most events with heavy slow particles, as they will mostly be produced with a low pseudorapidity. Energies are limited to a region set by a lower p_{T} cut of 45 GeV and an upper limit on β by selecting $1/\beta > 1$. In the efficiency map, β is given in steps of 0.05, thus its application on a Monte Carlo sample implies the selection $\beta \leq 0.95$ or $\gamma \leq 3.203$. The offline trigger selects quite promptly produced HLLCPs by demanding sub-cm transverse impact parameters d_x and d_y. For track quality, the search demands a minimum of 8 tracker hits and a minimum of 2 hits in the pixel detector, with a track fit $\chi^2/n_{\mathrm{d.o.f.}}$ smaller than 5. To remove signals from clusters in the silicon strip detectors not consistent with depositions from single isolated charged particles, a narrowness cut is applied on the cluster shape. At least 6 dE/dx measurements are then required in the silicon strip detector modules. By demanding a high minimum number of dE/dx values, the analysis intends to minimize the uncertainty due to statistical fluctuations in energy depositions by SM particles. On average, a charged particle track will have 15 silicon-strip measurements of dE/dx. The total energy loss in the tracker is parametrized by the estimator I_{h} given in Equation 4.11. It is conditioned to be larger than 3.0 MeV/cm already in the candidate preselection step, in order to be above the typical energy loss of SM particles. On top of that, there are two track isolation requirements. The first is a cut on the sum of the transverse momenta of all tracks within a cone of size $\Delta R = 0.3$ around the candidate track, with a maximum of 50 GeV, the sum excluding the p_{T} of the candidate track itself. ΔR is the angular difference between the candidate under consideration and any other track in the event, $\Delta R = \sqrt{\Delta\eta^2 + \Delta\phi^2}$. The second cut acts on the ratio of deposited energy in the calorimeters and the candidate track momentum, with an upper limit of 0.3, also within a cone of $\Delta R = 0.3$ about the track.

Several final selection criteria dictated by the signature expected for the types of scenarios targeted by each of the three search strategies are defined for background prediction. Events counted as signal within the tracker+TOF sample are selected with three cuts. A cut of $1/\beta > 1.225$ is imposed to trigger for slow particles. A further condition for signal sensitivity enhancement is the requirement $I_{\mathrm{as}} > 0.125$, where I_{as} is a discriminator quantifying the probability for the observed energy loss in a particular way. Through this condition, energy depositions of the HLLCP candidate in the tracker are constrained to have a low probability to originate from a MIP, such as a muon. In addition, the transverse momentum is required

Preselection criteria	
$\lvert\eta\rvert$	< 2.1
p_{T} [GeV/c]	> 45
$1/\beta$	> 1
d_z and d_x [cm]	< 0.5
$\sigma_{p_{\mathrm{T}}}/p_{\mathrm{T}}$	< 0.25
Track χ^2/n_d	< 5
# Pixel hits	> 1
# Tracker hits	> 7
Frac. valid hits	> 0.8
$\sum p_{\mathrm{T}}^{\mathrm{trk}}(\Delta R < 0.3)$ [GeV]	< 50
$E_{\mathrm{cal}}(\Delta R < 0.3)/p$	< 0.3
# dE/dx measurements	> 5
dE/dx strip shape test	yes
I_{h} [MeV/cm]	> 3.0

TABLE 6.4: Preselection and final selection criteria used in the tracker+TOF analysis.

to be larger than 70 GeV. The three criteria define eight numbers, labelled A through H. A, F and G are, respectively, the numbers of events passing the condition on β, I_{as} and p_{T}. B, C and H are the numbers of events failing p_{T}, I_{as} and β. Finally, D (E) corresponds to the events passing (failing) all three criteria, hence D is the signal region as selected by the more stringent requirements. The background is estimated to be the quantity AFG/E^2, for introducing the smallest statistical uncertainty. In total, a systematic uncertainty of 20% is attributed to the background estimate. The resulting numbers of expected background and observed events is shown in Table 6.5. In the end, a limit is set on the number of events contributing to the signal region at 95% C.L. from the absence of an excess using the CL_s technique, yielding a number of excluded events N_{exc} and hence an upper limit on the production cross section through the computed acceptance within a given model.

6.2.2 Our recast

Recall that this analysis requires the track selection efficiency table supplementing Reference [421]. It is a probability map in $(\eta, \beta, p_{\mathrm{T}})$-space divided into four reconstructed mass thresholds[5] ($m_{\mathrm{thr}} > 0$ GeV, > 100 GeV, > 200 GeV, > 300 GeV) and by giving N_{exc} in these four regions in the form of exclusion limits on stau production, $\sigma_{\tilde{\tau},\mathrm{exc}}$, with the respective acceptances, $\mathcal{A}_{\tilde{\tau}}$. N_{exc} can be easily extracted by noticing that it is equal to $\sigma_{\tilde{\tau},\mathrm{exc}} \times L \times \mathcal{A}_{\tilde{\tau}}$. We calculated the averages of N_{exc} from the values listed in Table 2 from [421] for direct stau pair production and include them in Table 6.5 in the last column.

We simplify the analysis by ignoring three effects. First, the energy loss and possible stopping in the calorimeters is neglected. This is a very justified approximation because the fraction of particles affected by this effect is very small (see Analysis IIB) and the energies of the $H^{\pm}$ surviving the p_{T} cut contributing to the charged track signature are comparably high. Second, notice that a particle might decay before leaving hits in the outer MS layers and still produce eight good time measurements, thus contributing to the signal sample. For simplicity, we neglect this possibility and consider all particles that decay before exiting the detector to be discarded by the search. The fraction of these accepted 'bad' tracks is not specified in the CMS analysis and its determination is beyond our scope. Their possible occurrence is mentioned in [421], but, as is argued, derived limits for unstable particle production turn out to be conservative if one assumes that the particles survive the whole passage until they exit. Third, the efficiency map does not account for the effect of the two isolation cuts. However, we studied the effect of the $\sum p_{\mathrm{T}}^{\mathrm{trk}}$ requirement on leptonic tracks in our samples and found that the preselection cut on p_{T} renders it absolutely minimal, hence we shall ignore it. In addition, we also assume that the second isolation cut has a small effect on the shape of the distribution and don't consider it.

[5] For the ranges and granularities of $(\eta, \beta, p_{\mathrm{T}})$, see the appendix in [421].

m_{thr} [GeV]	True mass range [GeV]	# Events @ $\sqrt{s} = 8$ TeV		
		Predicted background	Observed	Excluded
0	< 166	44 ± 9	42	19.3
100	[166, 330]	5.6 ± 1.1	7	8.5
200	[330, 500]	0.56 ± 0.11	0	3.2
300	> 500	0.09 ± 0.02	0	3.0

TABLE 6.5: Predicted backgrounds for the considered mass regions, numbers of observed events in the tracker+TOF analysis and numbers of signal events excluded at 95% C.L. The uncertainties are statistical and systematic. N_{exc} is obtained from information in [421], as explained in the text.

6.2.2.1 Calculation

We are interested in the fraction of produced $H^{\pm}$ particles that survive inside the detector in the kinematical range $|\eta| \leq |\eta|_{\max}$, $\gamma \leq \gamma_{\max}$, $p_{\text{T}} \geq p_{\text{T}\min}$ and pass all other preselection criteria, for a given set of N_1 masses $\{M_1\}$. We showed in Section 4.5.2 that the experimental acceptance is equal to the observable survival fraction (OSF). In the continuous formulation, it reads

$$\mathcal{A} = \epsilon_{\text{sur}}(|\eta|_{\max}, p_{\text{T}\min}, \gamma_{\max}) = \int_{\text{SR}} d\eta\, d\gamma\, f(\eta,\gamma)\, P_{\text{sur}}(D(\eta),\gamma)\, \epsilon_{\text{eff}}(\eta,\gamma)\,, \tag{6.43}$$

where $f(\eta,\gamma)$ is the kinematical distribution and ϵ_{eff} is the efficiency function incorporating track selection probabilities. Summing over barrel and endcap regions is implied. $D(\eta)$ are the limits defined in Equation 4.53 and $\gamma_{\min}$ is calculated from the minimum allowed transverse momentum as

$$\gamma_{\min}(\eta) \equiv \gamma(p_{\text{T}\min}, \eta) = \sqrt{1 + \left(\frac{p_{\text{T}\min}}{m_{H^{\pm}} \sin\theta(\eta)}\right)^2}\,. \tag{6.44}$$

The search region (SR) integral is either defined to incorporate the cuts on η, p_{T} and β, or one includes them in ϵ_{eff}. The acceptance tends to increase with increasing $m_{H^{\pm}}$, since the kinematical distribution then concentrates at smaller boosts and pseudorapidities, leading to more particles passing the $\gamma_{\max}$ and $p_{\text{T}\min}$ thresholds. Equation 6.43 formally expresses that events are multiplied by reconstruction efficiencies on a one-by-one basis. More concretely, the integral is to be understood as a discrete sum over events, where the ingredient $\epsilon_{\text{eff}}(\eta,\gamma)$ is provided through the efficiency map from [421], which also includes the kinematical cuts on η, p_{T} and β. $\mathcal{A}$ is hence the sum of the probabilities of all charged tracks in the data sample to pass online and offline selection criteria. Usage of the efficiency map requires running through all N events, each containing M charged scalars and summing the online and offline passing probabilities,

$$\mathcal{A} = \frac{1}{N}\sum_{i=1}^{N} P^{\text{on}}(k_i^1, k_i^2, \ldots, k_i^M) \times P^{\text{off}}(m_{\text{thr}}, k_i^1, k_i^2, \ldots, k_2^M)\,. \tag{6.45}$$

k_i^a is representative of the kinematical variables (η, γ, p_{T}) of charged particle a comprised by event i and the probabilities are given by

$$P^{\text{on}}(k_i^1, k_i^2) = P^{\text{on}}(k_i^1) + P^{\text{on}}(k_i^2) - P^{\text{on}}(k_i^1)P^{\text{on}}(k_i^2)\,, \tag{6.46}$$

$$P^{\text{off}}(m_{\text{thr}}, k_i^1, k_i^2) = P^{\text{off}}(m_{\text{thr}}, k_i^1) + P^{\text{off}}(m_{\text{thr}}, k_i^2) - P^{\text{off}}(m_{\text{thr}}, k_i^1)P^{\text{off}}(m_{\text{thr}}, k_i^2)\,. \tag{6.47}$$

For the case of unstable particles in the scotogenic FIMP model, one needs to incorporate the survival probability as written in Equation 4.56 into P^{on}, *i.e.*

$$\mathcal{A} = \frac{1}{N}\sum_{i=1}^{N} P^{\text{on}}(k_i^1, k_i^2, \Gamma) \times P^{\text{off}}(m_{\text{thr}}, k_i^1, k_i^2)\,, \tag{6.48}$$

with

$$\begin{aligned} P^{\text{on}}(k_i^1, k_i^2, \Gamma) = {} & P^{\text{on}}(k_i^1)P_{\text{sur}}(k_i^1, \Gamma) + P^{\text{on}}(k_i^2)P_{\text{sur}}(k_i^2, \Gamma) \\ & - P^{\text{on}}(k_i^1)P^{\text{on}}(k_i^2)P_{\text{sur}}(k_i^1, \Gamma)P_{\text{sur}}(k_i^2, \Gamma)\,. \end{aligned} \tag{6.49}$$

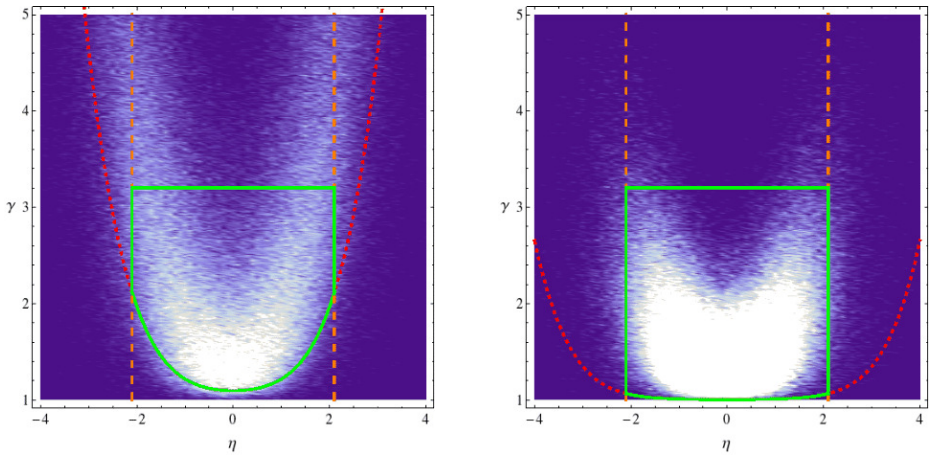

FIGURE 6.24: Density plots in (η, γ)-space of a sample of 100 000 pp collisions with $H^\pm$ pairs in the final state at $\sqrt{s} = 8$ TeV CM energy. We chose $m_{H^\pm} = 100$ GeV (left panel) and $m_{H^\pm} = 500$ GeV (right panel), with a mass splitting of $\Delta m_{\text{nc}} = 10$ GeV. The red dashed curve marks the lower bound set by $p_{\text{T,min}}$, Equation 6.44. The orange dashed line corresponds to the experimental cut in η and the green continuous contour encompasses the $H^\pm$ phase space region to which the search is sensitive. The upper limit on γ of 3.2 comes from the bound $\beta < 1$: Since the efficiency map lists β in steps of 0.05, the non-vanishing probabilities are all below $\beta = 0.95$. These samples have been produced for $\lambda_3 = 0$, minimizing the ggF contribution.

Notice that Equation 6.48 corresponds exactly to the acceptance found from the continuous quantities. The correctness of our implementation of the efficiency map has been verified with the reproduction of some of the acceptances for direct stau pair production listed in [421].

To find $\mathcal{A}$ for a considered mass spectrum, we generate a Monte Carlo sample of 100 000 pp collisions at $\sqrt{s} = 8$ TeV using CalcHep, with the decay chain having progressed to the presence of two charged scalar pairs and zero, two or four fermions among the final products, *cf.* Figures 6.2 and 6.9. The sample consists of DY and ggF subprocesses as weighted by the parton PDFs for the proton. In the main set of Monte Carlo samples, we reduce the ggF contribution to a minimum by setting λ_3 equal to zero. Mass splittings Δm_{nc} are selected to be equal to 10 and 70 GeV. Charged scalar masses are chosen between 100 and 600 GeV, with a 50 GeV step. In addition, we append the masses 60 and 70 GeV, plus 555 GeV for the case $\Delta m_{\text{nc}} = 10$ GeV. Even though we argued that ggF represents a negligible contribution, we verify this assumption by generating a second set of samples with $\lambda_3 = +2$, for the same charged scalar masses. A matrix of P_{sur} values fixed by M_1 and the relic density condition is computed, with the same granularity in $(\Delta\eta, \Delta\gamma)$ as the MC sample binning, *i.e.* (0.1, 0.01). Having then calculated the acceptances as instructed by the recipe in Equation 6.48, the limit on the total cross section can subsequently be obtained via

$$\boxed{\sigma_{\text{T}}(m_{H^\pm},\, M_1) \leq \sigma_{\text{u.l.}}(m_{H^\pm},\, m_{\text{thr}},\, M_1) = \frac{N_{\text{exc}}(m_{H^\pm},\, m_{\text{thr}})}{L\, \mathcal{A}(m_{H^\pm},\, m_{\text{thr}},\, M_1)}\,,} \tag{6.50}$$

where L is the integrated luminosity and $\sigma_{\text{u.l.}}$ is the upper limit on the total cross section calculated from the upper limit N_{exc} on signal events given by CMS in the corresponding mass threshold region. It is conservative because, as stated above, the background is somewhat overestimated due to the high step in m_{thr}. Note that it decreases monotonously with growing M_1 and tends asymptotically to a constant value because the acceptance eventually becomes saturated when M_1 increases. For a fixed value of $H^\pm$ and of Δm_{nc}, $\sigma_{\text{u.l.}}$ is interpolated as a function of M_1 with linear segments. If it coincides with σ_{T} for a given N_1 mass, this mass will be the maximally allowed value M_1^{max} for the given values of $m_{H^\pm}$ and Δm_{nc}. If it is above (below) σ_{T} in some range, then the value of $m_{H^\pm}$ is allowed (ruled out) for all N_1 masses in that range. As for the list of the latter for which we compute the limits, we first use the set in Equation 4.39 and after having obtained an intersection with σ_{T}, we repeat the computation for a smaller set with smaller separations around this preliminary value of M_1^{max}, to find a better estimate. This is necessary because the linear interpolation can lead to quite unprecise results, especially if the slope is very large.

6.2.2.2 Results

Picking the exemplary charged scalar masses $m_{H^\pm} = 100$, 200, 300, 400, 500 and 600 GeV, Tables 6.6 and 6.7 (6.8 and 6.9) list the $\sqrt{s} = 8$ TeV cross section limits for $\Delta m_{\rm nc} = 10$ (70) GeV. Choosing $\Delta m_{\rm nc} = 10$ GeV in particular, we plot the new limits in $(M_1, m_{H^\pm})$-space in Figures 6.25 - 6.27. The red continuous curves connecting the points correspond to the linearly interpolated values of $\sigma_{\rm u.l.}$, *i.e.* the bounds on the production cross section calculated with Equation 6.50, and the horizontal red dashed lines mark the upper limit $\sigma^{\rm metastable}_{\rm CMS\,u.l.}$ coming from the CMS search for metastable singly-charged particles produced via γ/Z (the red curve in the right plot in Figure 6.23). Since the acceptance increases with increasing M_1 and tends towards a final limiting value, the $\sigma_{\rm u.l.}$ curve always asymptotically approaches a horizontal line close to $\sigma^{\rm metastable}_{\rm CMS\,u.l.}$, as was anticipated in the beginning. The excluded region is specified in blue, where the cross section limit is located below the theoretical production cross section, meaning the search should be sensitive enough to observe an excess of events from the signal. As long as $\sigma_{\rm u.l.}$ intersects $\sigma_{\rm T}$, there exists an upper limit on M_1. For $\Delta m_{\rm nc} = 10$ (70) GeV, this ceases to happen at $m_{H^\pm}$ values close to the masses where $\sigma_{\rm T,10}$ ($\sigma_{\rm T,70}$) intersects the $\sigma^{\rm metastable}_{\rm CMS\,u.l.}$ curve, due to the similarity of the kinematics. These masses are, respectively, 541.1 and 513.9 GeV. Higher $m_{H^\pm}$ lead to production cross sections the CMS search cannot rule out for any $H^\pm$ mean lifetime.

Figure 6.28 summarizes this analysis. Each point corresponds to an obtained upper value of M_1 for a given charged scalar mass, selecting blue (green) for $\Delta m_{\rm nc} = 10$ (70) GeV. The set of points connected with continuous (dashed) segments was worked out for a quartic coupling of $\lambda_3 = 0$ (+2), the latter for the examination of the effect of ggF. As expected, there is no clearly noticeable impact. By comparing the $\Delta m_{\rm nc} = 10$ and 70 GeV curves, we observe that, the larger the $H^\pm$ production cross section, the larger the excluded parameter space, as is expected due to an enhanced experimental sensitivity. The intersections of the theoretical cross section with $\sigma^{\rm metastable}_{\rm CMS\,u.l.}$ are shown in the form of horizontal dot-dashed lines.

In dashed gray, we also draw the contours corresponding to the decay lengths $c\tau = 0.1$, 1, 10 and 100 meters, observing the expected behaviour that, the smaller the coupling, the more long-lived is the $H^\pm$, hence the more sensitive the search will be and the bounds to be set become stronger. The plot is useful to either pin down the dark matter mass or to exclude the spectrum, in case there will be a search for kinked tracks: If $m_{H^\pm}$ is measured with a reasonable precision and if $c\tau \sim \mathcal{O}(1\text{ m})$, then the plot should provide a fairly good determination of the realized spectrum if enough kink decay signals are found such that the decay length can be sufficiently well extracted from data, *i.e.* there might be a sensitivity to the dark matter mass. However, since the exclusion limits and the maximum decay lengths are very similar, it will be hard if not impossible to differentiate between small (~ 10 GeV) and medium-sized (~ 70 GeV) splittings between the neutral and charged bosons. On the other hand, if the scalars are found to be clearly lighter than ~ 500 GeV and to be stable at collider scales, then the model in this version is excluded.

Figure 6.29 superimposes the numbers of excluded signal events for the reconstructed mass thresholds 0, 100, 200 and 300 GeV as listed in Table 6.5, and the numerically calculated acceptances for $M_1 = M_1^{\rm max}$ through Equation 6.48. When stepping from $m_{H^\pm} = 300$ GeV to 350 GeV, the mass threshold switches from $m_{\rm thr} = 100$ GeV to 200 GeV, which very visibly reduces the calculated acceptance by a factor of about 0.75 for both spectra. The number of excluded signal events decreases by a factor of about 0.4. A downward kink in $\mathcal{A}$ should result in a sharper rise of $\sigma_{\rm u.l.} \sim N_{\rm exc}/\mathcal{A}$. However, the dominant effect is the decrease of $N_{\rm exc}$, thus $\sigma_{\rm u.l.}$ still increases, though it jumps to a lower value than predicted by the evolution with the previous mass threshold of 100 GeV. From then on, $\sigma_{\rm u.l.}$ evolves as before and the step from $m_{\rm thr} = 200$ GeV to 300 GeV produces no visible change in behaviour, as the values of $N_{\rm exc}$ and the selection probabilities are very similar. However, the decrease of $\sigma_{\rm u.l.}$ at the passage from 300 to 350 GeV results in a smaller increase of $M_1^{\rm max}$ than with the prior evolution, explaining the sharp kink in the curves in Figure 6.28.

	100 GeV		200 GeV		300 GeV	
σ_8 [fb]	217.20		20.13		3.96	
$\sigma^{\text{metastable}}_{\text{CMS u.l.},8}$ [fb]	6.98		1.29		0.32	
	$\sigma_{\text{u.l.}}$ [fb]	$\mathcal{A}$ [%]	$\sigma_{\text{u.l.}}$ [fb]	$\mathcal{A}$ [%]	$\sigma_{\text{u.l.}}$ [fb]	$\mathcal{A}$ [%]
1 keV	1570.00	0.07	$\gg 10^3$	$\ll 1$	$\gg 10^3$	$\ll 1$
5 keV	19.90	5.17	195.00	0.23	9540.00	$\ll 1$
10 keV	9.35	10.98	21.80	2.07	262.00	0.17
20 keV	6.59	15.58	5.23	8.65	24.20	1.874
50 keV	5.56	18.47	2.07	22.59	3.45	13.13
100 keV	5.33	19.27	1.49	30.35	1.65	27.52
200 keV	5.23	19.61	1.32	34.32	1.16	38.94
500 keV	5.19	19.79	1.24	36.39	0.98	46.16
1 MeV	5.17	19.84	1.22	36.96	0.94	48.20
2 MeV	5.17	19.87	1.22	37.22	0.92	49.06
5 MeV	5.16	19.88	1.21	37.37	0.91	49.51
10 MeV	5.16	19.89	1.21	37.42	0.91	49.65
20 MeV	5.16	19.89	1.21	37.44	0.91	49.72
50 MeV	5.16	19.89	1.21	37.45	0.91	49.76
100 MeV	5.16	19.89	1.21	37.46	0.91	49.77
200 MeV	5.16	19.89	1.21	37.46	0.91	49.78
500 MeV	5.16	19.89	1.21	37.46	0.91	49.78
1 GeV	5.16	19.89	1.21	37.46	0.91	49.78

TABLE 6.6: Upper limits on the H^+H^- production cross section and corresponding acceptances at $\sqrt{s} = 8$ TeV in the scotogenic model, Equation 6.50, for a mass splitting of $\Delta m_{\text{nc}} = 10$ GeV and a quartic scalar coupling $\lambda_3 = 0$, based on the limits on event numbers set by CMS on the production of metastable particles, for the masses $m_{H^\pm} = 100$, 200 300 GeV and the common subset of our chosen N_1 masses. On the top, we include the total theoretical cross section σ_8 for $\lambda_3 = 0$ and the limit set by CMS on the DY production cross section for metastable lepton-like particles, $\sigma^{\text{metastable}}_{\text{CMS u.l.},8}$. Cross section upper limits much above 1 pb and acceptances below 0.01% are not given explicitly.

	400 GeV		500 GeV		600 GeV	
σ_8 [fb]	1.06		0.33		0.12	
$\sigma^{\text{metastable}}_{\text{CMS u.l.},8}$ [fb]	0.29		0.29		0.29	
	$\sigma_{\text{u.l.}}$ [fb]	$\mathcal{A}$ [%]	$\sigma_{\text{u.l.}}$ [fb]	$\mathcal{A}$ [%]	$\sigma_{\text{u.l.}}$ [fb]	$\mathcal{A}$ [%]
1 keV	$\gg 10^3$	$\ll 1$	$\gg 10^3$	$\ll 1$	$\gg 10^3$	$\ll 1$
5 keV	$\gg 10^3$	$\ll 1$	$\gg 10^3$	$\ll 1$	$\gg 10^3$	$\ll 1$
10 keV	1990.00	$\ll 1$	$\gg 10^3$	$\ll 1$	$\gg 10^3$	$\ll 1$
20 keV	64.40	0.27	564.00	0.03	7020.00	$\ll 1$
50 keV	3.58	4.80	12.20	1.31	54.50	0.29
100 keV	0.992	17.30	1.940	8.27	5.05	3.17
200 keV	0.501	34.25	0.649	24.67	1.09	14.70
500 keV	0.347	49.52	0.337	47.44	0.395	40.52
1 MeV	0.315	54.51	0.281	56.92	0.291	55.07
2 MeV	0.303	56.61	0.262	61.18	0.256	62.43
5 MeV	0.298	57.66	0.253	63.27	0.242	66.15
10 MeV	0.296	57.97	0.251	63.84	0.238	67.15
20 MeV	0.295	58.11	0.250	64.10	0.237	67.59
50 MeV	0.295	58.19	0.249	64.25	0.236	67.83
100 MeV	0.295	58.22	0.249	64.30	0.236	67.91
200 MeV	0.295	58.23	0.249	64.32	0.236	67.95
500 MeV	0.295	58.24	0.249	64.34	0.235	67.97
1 GeV	0.295	58.24	0.249	64.34	0.235	67.98

TABLE 6.7: Cases $m_{H^\pm} = 400$, 500 and 600 GeV, with $\Delta m_{\text{nc}} = 10$ GeV.

	100 GeV		200 GeV		300 GeV	
σ_8 [fb]	461		33		5.83	
$\sigma^{\text{metastable}}_{\text{CMS u.l.,8}}$ [fb]	6.98		1.29		0.32	
	$\sigma_{\text{u.l.}}$ [fb]	$\mathcal{A}$ [%]	$\sigma_{\text{u.l.}}$ [fb]	$\mathcal{A}$ [%]	$\sigma_{\text{u.l.}}$ [fb]	$\mathcal{A}$ [%]
1 keV	1720.0	0.05975	$\gg 10^3$	$\ll 1$	$\gg 10^3$	$\ll 1$
5 keV	19.60	5.24	179.0	0.253	9750.00	$\ll 1$
10 keV	9.25	11.10	20.1	2.253	256.00	0.18
20 keV	6.49	15.81	4.88	9.279	23.10	1.96
50 keV	5.43	18.90	1.89	23.95	3.30	13.72
100 keV	5.18	19.83	1.41	32.10	1.58	28.71
200 keV	5.07	20.25	1.25	36.33	1.11	40.61
500 keV	5.01	20.48	1.17	38.58	0.94	48.20
1 MeV	4.99	20.55	1.15	39.23	0.90	50.37
2 MeV	4.99	20.59	1.15	39.53	0.88	51.30
5 MeV	4.98	20.61	1.14	39.70	0.87	51.80
10 MeV	4.98	20.62	1.14	39.75	0.87	51.95
20 MeV	4.98	20.62	1.14	39.78	0.87	52.02
50 MeV	4.98	20.62	1.14	39.80	0.87	52.07
100 MeV	4.98	20.63	1.14	39.80	0.87	52.08
200 MeV	4.98	20.63	1.14	39.80	0.87	52.09
500 MeV	4.98	20.63	1.14	39.81	0.87	52.09
1 GeV	4.98	20.63	1.14	39.81	0.87	52.10

TABLE 6.8: Cases $m_{H^\pm} = 100$, 200 and 300 GeV, with $\Delta m_{\text{nc}} = 70$ GeV.

	400 GeV		500 GeV		600 GeV	
σ_8 [fb]	1.48		0.45		0.15	
$\sigma^{\text{metastable}}_{\text{CMS u.l.,8}}$ [fb]	0.29		0.29		0.29	
	$\sigma_{\text{u.l.}}$ [fb]	$\mathcal{A}$ [%]	$\sigma_{\text{u.l.}}$ [fb]	$\mathcal{A}$ [%]	$\sigma_{\text{u.l.}}$ [fb]	$\mathcal{A}$ [%]
1 keV	$\gg 10^3$	$\ll 1$	$\gg 10^3$	$\ll 1$	$\gg 10^3$	$\ll 1$
5 keV	$\gg 10^3$	$\ll 1$	$\gg 10^3$	$\ll 1$	$\gg 10^3$	$\ll 1$
10 keV	2050.00	$\ll 1$	$\gg 10^3$	$\ll 1$	$\gg 10^3$	$\ll 1$
20 keV	64.20	0.26	569.00	0.03	7300.00	$\ll 1$
50 keV	3.49	4.92	12.00	1.34	55.60	0.29
100 keV	0.964	17.80	1.90	8.44	5.09	3.15
200 keV	0.486	35.31	0.636	25.18	1.09	14.72
500 keV	0.336	51.13	0.330	48.48	0.393	40.72
1 MeV	0.305	56.35	0.275	58.21	0.289	55.42
2 MeV	0.293	58.57	0.256	62.60	0.255	62.89
5 MeV	0.287	59.70	0.247	64.77	0.240	66.68
10 MeV	0.286	60.02	0.245	65.38	0.236	67.72
20 MeV	0.285	60.18	0.244	65.65	0.235	68.18
50 MeV	0.285	60.27	0.243	65.81	0.234	68.43
100 MeV	0.285	60.30	0.243	65.86	0.234	68.51
200 MeV	0.285	60.31	0.243	65.88	0.233	68.55
500 MeV	0.284	60.32	0.243	65.90	0.233	68.57
1 GeV	0.284	60.32	0.243	65.90	0.233	68.58

TABLE 6.9: Cases $m_{H^\pm} = 400$, 500 and 600 GeV, with $\Delta m_{\text{nc}} = 70$ GeV.

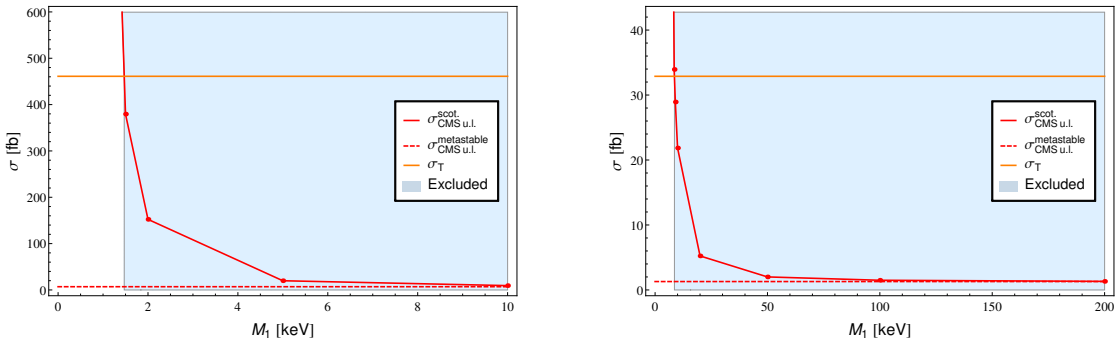

FIGURE 6.25: New scalar production cross section upper limits due to in-flight decay for $\sqrt{s} = 8$ TeV and $\Delta m_{\rm nc} = 10$ GeV. The red dashed line is the upper limit from the CMS metastable particle search and the orange continuous line is the theoretical cross section value. *Left panel:* $m_{H^\pm} = 100$ GeV, $M_1^{\rm max} = 1.45$ keV. *Right panel:* $m_{H^\pm} = 200$ GeV, $M_1^{\rm max} = 8.61$ keV.

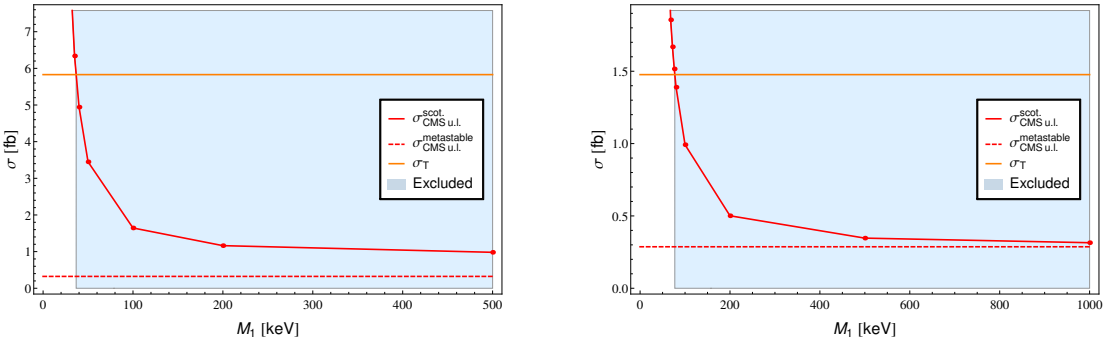

FIGURE 6.26: *Left panel:* $m_{H^\pm} = 300$ GeV, $M_1^{\rm max} = 36.82$ keV. *Right panel:* $m_{H^\pm} = 400$ GeV, $M_1^{\rm max} = 77.25$ keV.

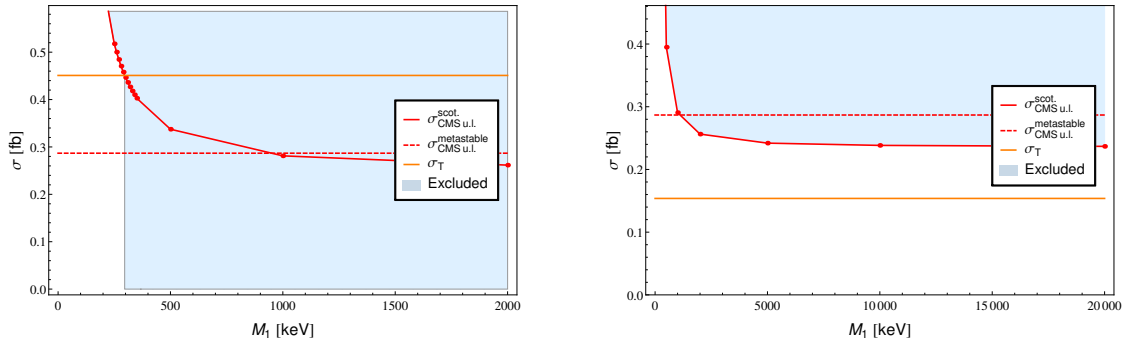

FIGURE 6.27: *Left panel:* $m_{H^\pm} = 500$ GeV, $M_1^{\rm max} = 296.26$ keV. *Right panel:* $m_{H^\pm} = 600$ GeV, the limit is always above $\sigma_{\rm T}$.

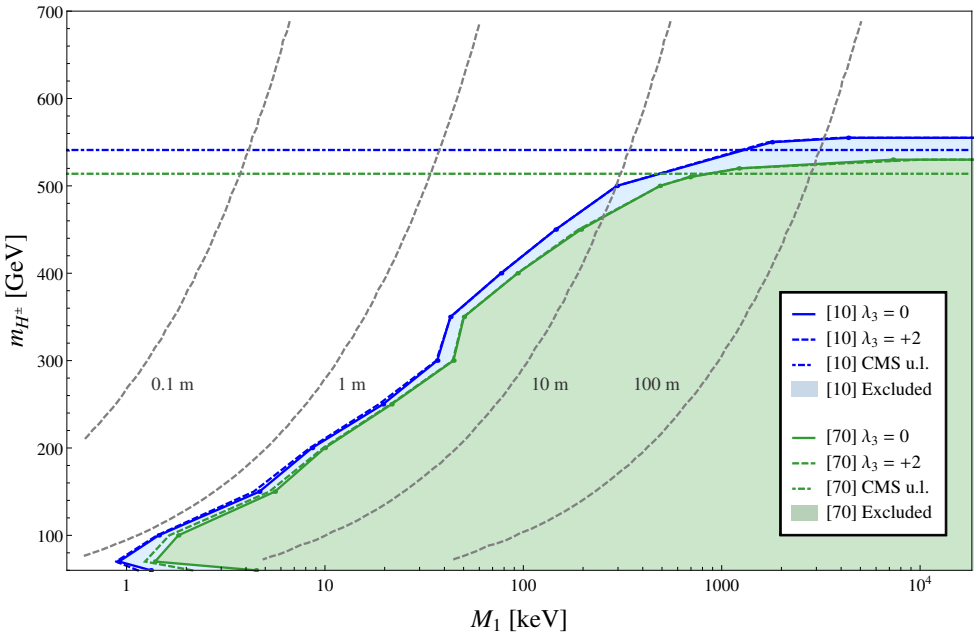

FIGURE 6.28: Excluded parameter space of the scotogenic model with a fermionic FIMP, obtained from CMS $\sqrt{s} = 8$ TeV data for $\Delta m_{\rm nc} = 10$ GeV (blue) and $\Delta m_{\rm nc} = 70$ GeV (green), with a λ_3 coupling of 0 (continuous) and +2 (dashed). Shown as horizontal dot-dashed lines are also the upper limits on $m_{H^\pm}$ extracted from the CMS search on metastable particles, which are 541.1 (513.9) for $\Delta m_{\rm nc} = 10$ (70) GeV. The gray dashed lines correspond to the contours $c\tau = 0.1$, 1, 10 and 100 meters.

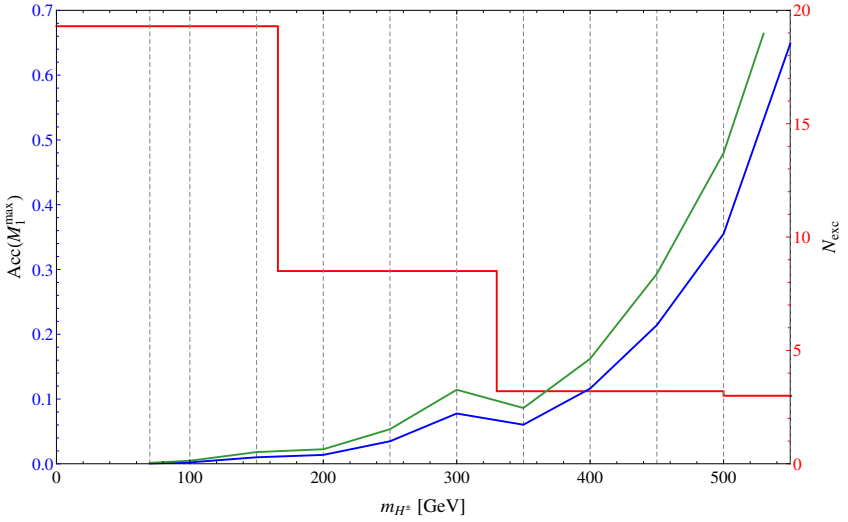

FIGURE 6.29: Blue and green curves: Acceptances obtained for $M_1 = M_1^{\rm max}$ through segmentwise linear interpolation of the acceptances calculated for the various considered N_1 masses. Blue (green) corresponds to $\Delta m_{\rm nc} = 10$ (70) GeV. Red curve: Number of excluded signal events at the thresholds $m_{\rm thr} = 0$, 100, 200 and 300 GeV.

6.3 Analysis IIB: Long-lived stopped $H^{\pm}$ particles decaying out-of-time in the ATLAS detector

Recall from observing Figure 4.13 that a $H^{\pm}$ may have a mean lifetime τ of the order of tens of nanoseconds or even larger, depending on the value of M_1. As has been discussed in Section 3.2.1.2, the pattern in the bunch structure at the LHC varies over a temporal scale of the same order, with several empty bunch slots placed at specific spots. Therefore, if a $H^{\pm}$ is sufficiently slow and sufficiently long-lived, it can be looked for with a search triggering for energy depositions in the calorimeters happening out-of-time with respect to filled bunch crossings in order to discriminate against QCD background events, as the latter happen within 10 ns after the crossing of two filled slots. This is done in the stopped R-hadron searches by ATLAS [46] and CMS [47]; both experiments do not report any excess of events. For reasons to be clarified shortly, the CMS search is not suited for a recast to our scenario.

This analysis intends to estimate the number of observable decays at ATLAS of long-lived scotogenic $H^{\pm}$ bosons stopped in the calorimetric modules, for the benchmark masses $m_{H^{\pm}} = 120$ and 150 GeV. The principal extracted quantity for the recast is the experimental timing efficiency computed for the first LHC run. Motivation is drawn from the large size and density of the ATLAS detector and the easily reducible non-collision background, *cf.* Section 3.2.1.2. While already for these two masses the results are not compelling, production of heavier charged scalars is far too suppressed to lead to a considerable number of particles in the relevant low-energy region of phase space described in Section 6.1.2. Expected numbers of observable events are computed for the set of N_1 masses listed in Equation 4.39, considering three different values of the quartic coupling λ_3, *i.e.* $\lambda_3 = +1, +2, +3$. Again, the larger value is taken for academic purposes.

Three sources of inefficiency work to our disadvantage: a small stopping efficiency (*cf.* Section 4.5.3), a small timing acceptance and the reconstruction efficiency. We remark that the collaborations trigger for energy depositions resembling hadronic jets. However, the $H^{\pm}$ decays to charged leptons, and a purely leptonic final state might have very different shower shapes in the calorimeters and this constitutes our major source of uncertainty in adapting the experimental results to the model. In fact, as muons are produced with an energy of $m_{H^{\pm}}/2$, they will be too energetic to transfer a significant amount of energy above threshold to the calorimeter. Consequently, the triggers would not fire. Electrons could prove more promising. However, the case that might resemble the expected R-hadron signature the most is the decay

$$H^{\pm} \to \tau^{\pm} + N_1 \tag{6.51}$$

followed by

$$\tau \to \text{hadrons}\,, \tag{6.52}$$

and this cascade is what we focus on. As was done in Analysis IIA, we begin by describing the search this analysis is based on, *i.e.* Reference [46].

6.3.1 The ATLAS search

An R-hadron search is complex on the theory side due to the unknown nature of the interaction of the R-hadrons with matter. There is the electromagnetic interaction, for which it is legitimate to employ the usual Bethe-Bloch stopping power. However, there may be 4-6 nuclear interactions taking place with the nuclei of the atoms in the detector material, the exact number and properties depending on the R-hadron model [46]. These scatterings introduce a very large amount of theoretical uncertainty. Such exchanges may alter the electric charge of the R-hadrons and, in particular, they can end up electrically neutral. The search takes several of these interaction hypotheses into account by computing different stopping efficiencies. On the experimental side, the backgrounds are of the non-collision type as described in Section 3.2.1.2. They are rather simple, though employing dedicated selection cuts is quite intricate. Next follows a brief summary of the relevant details of the search.

□ **Considered models:** Various supersymmetric scenarios containing long-lived sparticles are accounted for. After production, such a sparticle would outlive its hadronization time and form an R-hadron, that is, a colour-neutral bound state with quarks or gluons. A gluino can hadronize to an R-meson ($\tilde{g}q\bar{q}$), an R-baryon ($\tilde{g}qqq$) or an R-glueball ($\tilde{g}g$), whereas a squark can form the state $\tilde{q}q'$. Within R-parity conserving SUSY, a gluino decaying to a gluon and a gravitino in GMSB is suppressed through very small m_{P}-suppressed gravitino masses ($\tau \propto m_{\tilde{G}}^2$). The gluino is thus long-lived and has time to hadronize. In split-SUSY, the hierarchy and cosmological constant problems are solved by keeping the gauginos and higgsinos light while the sfermions are much heavier than the electroweak scale. Therefore a produced gluino would decay to a gluon and a neutralino. This decay contains a tree-level process with a squark in the t-channel and a loop process with a squark in one loop propagator, causing its decay to be suppressed through the high scalar mass scale m_{s}, $\tau \propto m_{\mathrm{s}}^4/m_{\tilde{g}}^5$, such as to allow for R-hadron formation. There is also the possibility to have R-parity violating (RPV) terms in the superpotential. The involved couplings are required to be small in order to stabilize the proton lifetime at a value far above the age of the Universe. It is possible to choose the RPV couplings in a way such that only baryon number is violated, allowing for RPV-suppressed squark and gluino decay while forbidding proton decay. The sparticles are finally taken to decay assuming specific benchmark branching fractions. For more theoretical details, see [424] and contained references.

□ **Data samples:** Two main samples of Run I data are analyzed in which an excess of events is looked for. The first contains pp collisions happening at a CM energy of $\sqrt{s} = 7$ TeV, the second contains all data of 2012 at $\sqrt{s} = 8$ TeV. The delivered integrated luminosities, in inverse femtobarns, are

$$5.0\,@\,7\,\mathrm{TeV} + 22.9\,@\,8\,\mathrm{TeV}\,.$$

□ **Backgrounds:** The main backgrounds for this search are NCBs (see Section 3.2.1.2) consisting of cosmic ray and beam-halo muons, instrumental noise is found to be negligible in comparison. Both types of muons can enter the detector at random times. Beam-halo muons that are produced close enough to the interaction point are seen as tracks or segments in the forward region of the muon system with an orientation nearly parallel to the beam line (the search triggers for segments with at least 4 hits). Cosmics mostly leave segments in the MS barrel region. Cosmic and beam-halo muons may deposit large enough randomly-timed amounts of energy in the calorimeters by emitting bremsstrahlung photons due to the magnetic field and need to be vetoed by checking for the characteristic muon system segments. The backgrounds are estimated by using small data control samples. The obtained number of cosmic muons in the cosmic control sample from early 2011 data is rescaled to the size of the search sample by the recorded livetime ratio for background estimation, a similar rescaling is done for the number of estimated beam-halo background muons with another control sample. After the relevant cuts, beam-halo muons turn out to be the dominant background, see Table 6.10. This is especially troublesome for analyses at higher energies and larger luminosities. Since the beginning of Run II, the instantaneous luminosity has doubled, so the beam-halo background has also at least doubled. Furthermore, the higher pp CM energies result in more energetic products from the collisions of the beam protons with the protons at rest within the pipe, as has been argued in Section 3.2.1.2. There is therefore not only an increase in the number of beam-halo muons, but also an increase in high-energy muons leading to calorimetric energy deposits passing threshold cuts.

□ **Event selection:** The search first triggers for low-threshold energy depositions (jets) in the calorimeters at L1 level happening at least six empty BX after the most recent filled BX, with the end of an efficient reduction of background from previous interactions. Out-of-time events are collected in a separate data stream governed by dedicated triggers targeting for jet-like objects with a minimum p_{T} of 30 GeV at the lowest level, see [424] for technical details. The trigger rate is only about 1-2 Hz, however final HLT selection needs to account for noise bursts, since these can increase the rate by a factor of up to 10. More stringent cuts are subsequently applied with the EF in order to further reduce backgrounds and to tighten quality requirements, such as rejection of events with simultaneous high instrumental noise, to cure the

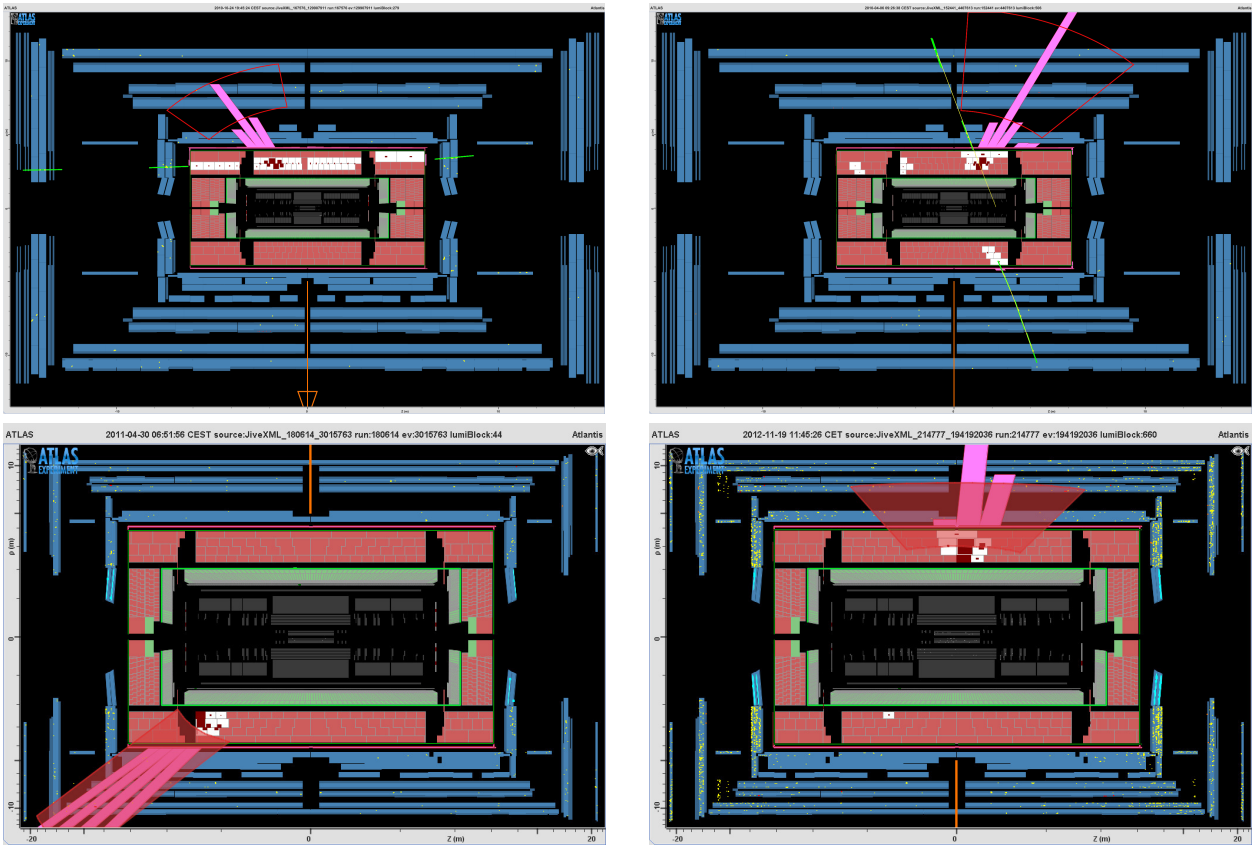

FIGURE 6.30: **Upper row:** Background events passing all criteria but the muon veto. White cells correspond to energy deposits in the TileCal, the size of the red squares indicates the amount of energy in the cell. Purple histograms show the deposited energy projected onto the barrel area and red curved semi-trapezoids mark jets. The orange arrow shows where the missing transverse energy vector is pointing. *Left panel:* Beam-halo muon event. *Right panel:* Cosmic ray muon event. **Bottom row:** Two candidate events passing all selection criteria.

problem of a potentially high L1 trigger firing rate. After jet reconstruction, a cut of 50 GeV is imposed on the leading jet energy, allowing for up to five additional jets. The leading jet is also required to carry more than 50% of the deposited energy. Furthermore, leading jets are only accepted within the barrel because R-hadrons are mainly produced with a small pseudorapidity (as is also the case with the $H^{\pm}$ bosons in the scotogenic model). For the leading jets, the search therefore requires $|\eta| < 1.2$. A few further minor selection criteria are applied which we do not discuss here. Figure 6.30 shows a beam-halo and a cosmic muon event in the upper panels, the lower panels show events passing all cuts and hence contributing to the signal.

□ **Experimental results:** The number of expected total background (cosmic + beam-halo muons) and observed events is shown in the cut-flow list in Table 6.10. Note that the cosmic muon background becomes very subleading compared to the beam-halo muons after applying the muon segment veto. As it will at least double with the luminosity, this background will also be a major obstacle in constraining the scotogenic model at higher pp CM energies.

Selection criteria	Cosmic BG	Beam-halo BG	Total BG	Observed
Trigger	not given	not given	not given	218076
Leading jet $\|\eta\| < 1.2$	not given	not given	not given	202015
$N_{\text{jets}} < 6$	not given	not given	not given	201628
Fractional $\not{E}_{\text{T}} > 0.5$	not given	not given	not given	201618
Leading jet n90 > 3	not given	not given	not given	85866
Leading jet width > 0.04	not given	not given	not given	34445
Leading jet TileCal $E_{\text{frac}} > 0.5$	not given	not given	not given	5396
Leading jet $E > 50$ GeV	4820 ± 570	900 ± 130	5720 ± 590	5396
Leading jet $E > 50$ GeV, MSV	2.1 ± 3.6	12 ± 3	14.2 ± 4.0	10
Leading jet $E > 100$ GeV	0.4 ± 2.7	6 ± 2	6.4 ± 2.9	5
Leading jet $E > 300$ GeV	2.4 ± 2.4	0.5 ± 0.4	2.9 ± 2.4	0

TABLE 6.10: Number of expected background and observed events after each selection constraint is applied. Table put together from tables III and V in the analysis. MSV stands for muon segment veto.

6.3.2 Our recast

Now follows the reinterpretation of the ATLAS analysis to the scotogenic FIMP scenario. Staying close to the notation and concepts used in the search, we start by discussing the involved efficiencies. In contrast to Analysis IIA, the procedure is to apply the continuous formulation based on kinematical Monte Carlo distributions as outlined in Section 4.5.1.

6.3.2.1 Stopping and reconstruction efficiencies

For a given set of $(m_{H^\pm}, M_1)$ values, the number of particles stopped by the detector can be written as the product of the scalar production cross section, the time-integrated luminosity and the stopping efficiency,

$$N_{\text{stop}}(\tau) = \sigma(S) \times L \times \epsilon_{\text{stop}}(\tau)\,, \tag{6.53}$$

where $\sigma(S)$ is the total scalar production cross section for any combination of scalar pairs, L is the integrated luminosity and ϵ_{stop} is the stopping efficiency introduced in Section 4.5.3, *i.e.* the fraction of stopped $H^\pm$ particles. Of course, all quantities in Equation 6.53 are evaluated at the same pp CM energy $\sqrt{s}$. Rather than considering the total stopping efficiency of the detector, we set the η integration range equal to the experimental interval, *i.e.* we work with the fiducial stopping efficiency. This stands in difference to the definition used by ATLAS, who include the cut on η in the jet reconstruction efficiency. Therefore we compute the stopping efficiency according to

$$\epsilon_{\text{stop}}(\tau) = \int_{|\eta|<1.2} d\eta \int_1^{\gamma_{0,\text{lim}}(\eta)} d\gamma_0\, f(\eta,\gamma_0)\, P_{\text{sur}}(\eta,\gamma_0)\,. \tag{6.54}$$

$\sigma(S)$ is the total production cross section for any combination of scalar pairs and $P_{\text{sur}}(\eta,\gamma_0)$ is the probability of a $H^\pm$ particle produced with a boost γ_0 in the direction η to survive until the time t_{stop} when it gets stopped, which introduces the dependence on τ, *cf.* Equation 4.58, and t_{stop} is calculated with the Bethe-Bloch equation. Finally, since the $H^\pm$ travel in approximately straight lines, they can be considered to maintain the pseudorapidity from production until stopping, justifying the use of the initial kinematic distribution f.

Now recall that we are experimentally tied to the decay $H^\pm \to \tau + N_1$, followed by $\tau \to$ hadrons. The number of observed signal events is therefore proportional to the two branching ratios and to the jet reconstruction efficiency,

$$N_{\text{sig}}(\tau) \propto \sigma(S) \times \mathcal{B}(H^\pm \to \tau\, N_1) \times \mathcal{B}(\tau \to \text{had}) \equiv \sigma\mathcal{B} \times \mathcal{B}(\tau \to \text{had}) \tag{6.55}$$

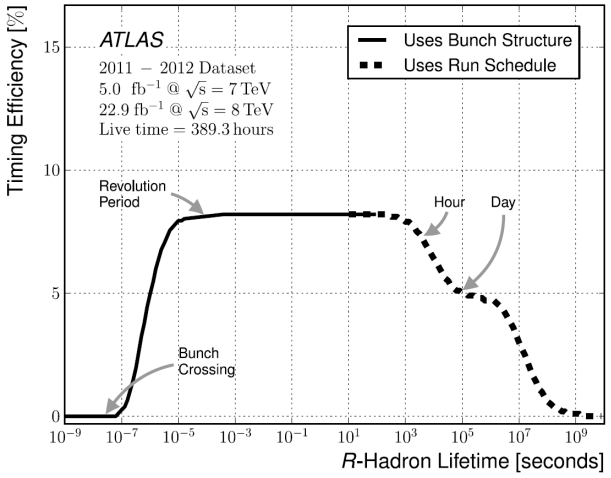

FIGURE 6.31: Timing acceptance function determined by ATLAS. It corresponds to Figure 7 in [46].

and

$$N_{\text{sig}}(\tau) \propto \epsilon_{\text{rec}} \,. \tag{6.56}$$

We opt to include $\mathcal{B}(\tau \to \text{had})$ in the reconstruction efficiency, so that ϵ_{rec} accounts for the probability of a tau event to successfully pass jet reconstruction. ϵ_{rec} is computed by passing simulated very low-energetic $H^{\pm}$ particles generated in CalcHEP decayed to τ leptons and showered in Pythia through the detector simulation software Delphes [425]; thus we have

$$N_{\text{sig}}(\tau) \propto \sigma\mathcal{B} \times \epsilon_{\text{stop}}(\tau) \times \epsilon_{\text{rec}} \,. \tag{6.57}$$

With Delphes, one finds

$$\begin{aligned} m_{H^{\pm}} = 120 \text{ GeV} \quad &\to \quad \epsilon_{\text{rec}} = 0.23 \\ m_{H^{\pm}} = 150 \text{ GeV} \quad &\to \quad \epsilon_{\text{rec}} = 0.39 \end{aligned}$$

For $m_{H^{\pm}} \gtrsim 300$ GeV, ϵ_{rec} approaches the limit imposed by the hadronic branching fraction of the τ [415].

6.3.2.2 Effective luminosity and timing efficiency

Inspired by the equivalent CMS analysis [47], we write the number of observed out-of-time decay events from signal at a given CM energy $\sqrt{s}$ in terms of an effective integrated luminosity,

$$N_{\text{sig}}(\tau) = \sigma\mathcal{B} \times L_{\text{eff}}(\tau) \times \epsilon_{\text{rec}} \,, \tag{6.58}$$

defining

$$L_{\text{eff}}(\tau) \equiv L \times \epsilon_{\text{stop}}(\tau) \times \epsilon_{\text{T}}(\tau) \,. \tag{6.59}$$

L_{eff} incorporates the *timing acceptance* or *timing efficiency* $\epsilon_{\text{T}}(\tau)$, a lifetime-dependent factor giving the fraction of stopped particle decays that are actually happening out-of-time. It is defined as the ratio of the number of stopped particles decaying during an empty BX and the total number of particles that stopped until that point. Ingredients for its determination are the delivered luminosity profile, the used LHC filling scheme (see Section 3.2.1.2), the particle's lifetime and the used trigger rules. The dependence on the filling scheme is due to the fact that out-of-time events are selected by using a dedicated trigger firing during the empty BX, which are temporally placed as depicted in Figure 3.4. The exact bunch structure is taken into account for $\tau < 1$ s; for larger lifetimes, it is averaged over. For short lifetimes (< 10 s), $\epsilon_{\text{T}}(\tau)$ is only based on the average bunch structure but not on luminosity block and run structure. For $\tau > 10$ s, the run schedule, *i.e.* the delivered luminosity block history, is taken into account. In the case of even larger

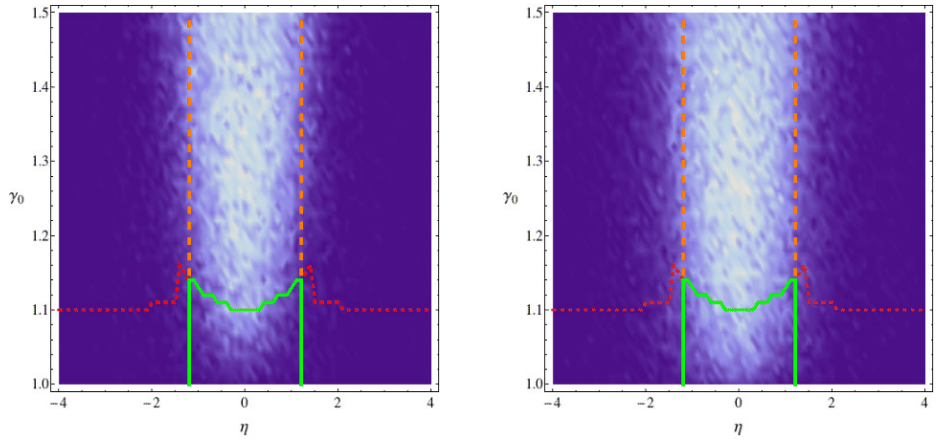

FIGURE 6.32: Density plots in (η, γ_0)-space of a sample of 100 000 pp collisions with $H^\pm$ pairs in the final state at $\sqrt{s} = 8$ TeV pp CM energy. The chosen parameters are $m_{H^\pm} = 120$ GeV, $\Delta m_{\text{nc}} = 10$ GeV, $\lambda_3 = +1$ (left panel) and $\lambda_3 = +3$ (right panel). The red dashed line delimits the phase space region in which $H^\pm$ particles stop as calculated with the Bethe-Bloch equation. The orange dashed line corresponds to the η cut imposed to restrict the events to the barrel region and the green continuous contour encompasses the $H^\pm$ phase space the search is sensitive to. Note that in the $\lambda_3 = +3$ case, the histogram is somewhat denser due to the presence of more slow particles produced through gluon fusion.

lifetimes (some minutes to hours), the timing acceptance depends only on the run schedule. For example, if the lifetime is very long, then a particle can stop in the calorimeter and only decay during the next day's run. Due to the temporal separation of five empty BX to the last filled BX, the timing efficiency vanishes for smaller lifetimes than 125 ns. To work out the timing efficiency, the authors developed a numerical algorithm working with data from the experiment conditions logging database used by ATLAS, where detailed luminosity history information is stored. $\epsilon_{\text{rec}}(\tau)$ is shown in Figure 6.31.

L_{eff} is computed using Monte Carlo simulations: R-hadron production is simulated in Pythia, their passage through the detector including energy loss is simulated in Geant4, yielding ϵ_{stop}, and finally Pythia is used again to simulate the decay. Ultimately, in combination with bunch structure and luminosity information, this allows for the computation of ϵ_{T} for a given hypothetical τ.

CMS reverts to the same notation, however instead of mentioning the timing acceptance, CMS directly presents the effective luminosities calculated for various hypotheses. Here lies the downside of the CMS analysis. The CMS study merely states the values of $L_{\text{eff}}(\tau)$, which contains ϵ_{stop}, but in their case the energy loss is also of nuclear nature — This stands in contrast to our model, where interactions of the $H^\pm$ bosons with the detector are purely electromagnetic. It is therefore impossible to disentangle ϵ_{T} and ϵ_{stop} from the given effective luminosities.

6.3.2.3 Calculation

We generally proceed like in Analysis IIA. That is, the number of observed signal events is obtained by means of a cut-free Monte Carlo sample of 100 000 decayed pp collisions with $H^\pm$ pairs in the final state, for a given charged and neutral scalar mass and a given pp CM energy. We exclusively consider a mass splitting of $\Delta m_{\text{nc}} = 10$ GeV, since the cross sections turn out to be far too small in the case of heavier neutral scalar masses. For production, all Drell-Yan and gluon fusion subprocesses contribute with a weight given by the parton distribution function at the respective value of $\sqrt{s}$. We sum the counts in the bins of the two-dimensional $(\Delta\eta, \Delta\gamma_0)$ histogram and multiply each bin by the efficiencies in that point of phase space. This number is then normalized to the total number of particles in the sample in order to end up with a distribution, as explained in Section 4.5.1. In fact, for each given $H^\pm$ mass, two MC samples are needed, since data at two different pp CM energies (7 and 8 TeV) have been combined in the experimental analysis. Moreover, three sets of λ_3 couplings will be considered in this study, so the number of samples needs to be further multiplied by 3. As we also estimate the sensitivity of ATLAS until the end of Run II,

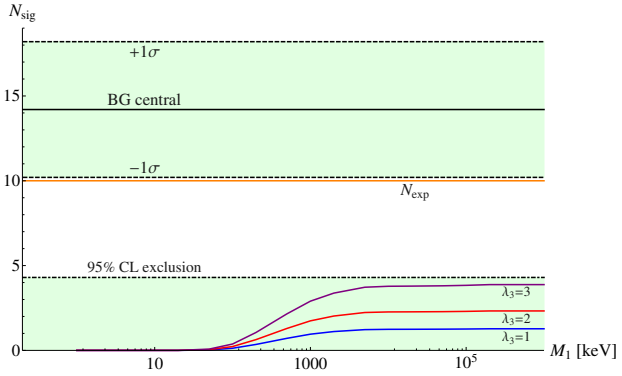

FIGURE 6.33: Results for $m_{H^\pm} = 120$ GeV and $\Delta m_{\rm nc} = 10$ GeV, combining $\sqrt{s} = 7$ and 8 TeV Motne Carlo data. The number of signal events for $\lambda_3 = 1$ and $\lambda_3 = 2$ are clearly below the 95% C.L. exclusion line, the unrealistic case of $\lambda_3 = 3$ being marginally close. All values lie within the 1σ uncertainty range of the expected number of background events.

samples with $\sqrt{s} = 13$ and 14 TeV are also added, amounting to a total number of 12 MC datasets. Figure 6.32 shows an exemplary density plot of MC events for the case $m_{H^\pm} = 100$ GeV, $\Delta m_{\rm nc} = 10$ GeV, $\sqrt{s} = 8$ TeV, $\lambda_3 = 1$ (left panel) and $\lambda_3 = 3$ (right panel). Particles produced within the green contour are in principle observable, provided they decay to reconstructed τ. We can therefore estimate the number of observed signal events for a given mass spectrum as

$$\begin{aligned} N_{\rm sig}(\tau) &= [\sigma\mathcal{B}_7 \times L_{\rm eff,7}(\tau) + \sigma\mathcal{B}_8 \times L_{\rm eff,8}(\tau)] \times \epsilon_{\rm rec} \\ &= [\sigma\mathcal{B}_7 \times L_7 \times \epsilon_{\rm stop,7}(\tau) + \sigma\mathcal{B}_8 \times L_8 \times \epsilon_{\rm stop,8}(\tau)] \times \epsilon_{\rm T}(\tau) \times \epsilon_{\rm rec}\,, \end{aligned} \tag{6.60}$$

where, according to Equation 6.54,

$$\epsilon_{{\rm stop},\sqrt{s_i}}(\tau) = \sum_{\text{bins }(\Delta\gamma_0,\Delta\eta)} \frac{N_{\rm counts}^{(\sqrt{s_i})}(\Delta\gamma_0,\Delta\eta)}{2N_{\rm events}^{(\sqrt{s_i})}} P_{\rm sur}(\Delta\gamma_0,\Delta\eta) \tag{6.61}$$

and $L_7 = 5.0$ fb^{-1}, $L_8 = 22.9$ fb^{-1}. $N_{\rm events}^{(\sqrt{s_i})}$ and $N_{\rm counts}^{(\sqrt{s_i})}(\Delta\gamma_0,\Delta\eta)$ denote the total number of events in the MC sample and the number of events in the bin $(\Delta\gamma_0,\Delta\eta)$, respectively.

In the following we assume $\mathcal{B}(H^\pm \to \tau + N_1) \approx 1$, resulting in an optimistic prediction for the number of observed signal events, which completely depends on the flavour structure inherent to the vector of small Yukawa couplings $Y_{\alpha 1}$. Different branching ratios can be accounted for by simply rescaling the resulting event numbers.

We present the results for $\Delta m_{\rm nc} = 10$ GeV in Tables 6.11 and 6.12, for the cases of $m_{H^\pm} = 120$ GeV and 150 GeV. As already mentioned, a higher mass splitting is not taken because the number of counts is already very low for 10 GeV. In conjunction with the counts, the average stopping fractions defined as the arithmetic mean

$$\langle\epsilon_{\rm stop}\rangle = \frac{L_7}{L_7+L_8}\,\epsilon_{\rm stop,7} + \frac{L_8}{L_7+L_8}\,\epsilon_{\rm stop,8}\,. \tag{6.62}$$

are also shown. We similarly define the average percentages of $H^\pm$ production events mediated by gluon fusion, for the full MC sample and for particles stopping in the search region (SR).

In 2015, ATLAS accumulated about 4.0 fb^{-1} of usable pp collision data and the LHC is projected to deliver about 90 fb^{-1} more until the end of Run II in 2018 [426]. For those luminosities, we additionally present the expected numbers of signal events combining 13 and 14 TeV data in Tables 6.13 and 6.14, in order to see what could be maximally gained for $m_{H^\pm} = 120$ and 150 GeV from all of Run II, assuming an equal timing efficiency.

6.3.2.4 Results

The numbers are not very compelling, taking into account the expected backgrounds listed in Table 6.10. As the decaying τ's deposit < 60 GeV of energy in the calorimeters, we need to consider the number of observed and expected background events after the muon segment veto cut of 50 GeV. Our calculated observable signal event numbers at $\sqrt{s} = 7$ & 8 TeV lie well within the 1σ uncertainty band of the background. With 10 observed events with a central expectation of 14 counts from beam-halo and cosmic muons, one can exclude 4.4 events at 95% C.L. using the Feldman-Cousins method [427]. This is illustrated in Figure 6.33 for the case $m_{H^\pm} = 120$ GeV. Although this downward fluctuation acts in favour of boosting the significance of our numbers, the signal exclusion is still too high for the outcome of a parameter space exclusion. That is, the low background rates are counteracted by a low (electroweak) production cross section, a poor timing efficiency of the ATLAS detector and low τ reconstruction efficiencies at low boosts. The numbers increase considerably for the $\sqrt{s} = 13$ & 14 TeV samples. We note that the cross sections roughly triple and another factor $\sim 3-4$ is provided by the larger integrated luminosity. Unfortunately, it is not to be expected that these numbers contribute a significant fraction of events when compared to the increasing background. The instantaneous luminosity is more than doubled due to the doubled number of filled bunch slots in the LHC beams during Run II. Moreover, beam-halo particles will be more highly boosted due to the increased pp CM energy, as outlined in Section 3.2.1.2, and a further factor of $\sim 3-4$ appears due to the larger integrated luminosity, as for the signal. One should thus not expect an analogous analysis at the end of Run II to serve to constrain the scotogenic model in its fermionic FIMP realization.

Nevertheless, one can state with confidence that this is an analysis which heavily benefits from the Higgs portal, in accordance with the idea of Analysis I. Already a quartic coupling λ_3 of order unity implies a contribution of about 20% to the signal. From Drell-Yan alone, one expects $N_{\text{sig}} = 1.03$ (0.67) on the plateau of a constant timing efficiency for $m_{H^\pm} = 120$ (150) GeV. ggF at leading order increases these to 1.27 and 2.33 (0.87 and 1.48) when λ_3 is taken to be 1 and 2. Furthermore, note that K-factors have been ignored completely. In Section 5.2, a point was made of the fact that Higgs-mediated gluon fusion benefits from K-factors up to 2 or even larger due to QCD corrections. While the calculation of such corrections to the production of scotogenic scalars is out of the scope of this work, it might well be the case that K-factors of equal sizes are obtained in this scenario. It could be worthwhile to verify the consequences of QCD corrections to the avail of the stopped particles signal, since the analysis does not only benefit from an increased total production cross section, but also takes advantage from the involved kinematics.

	$\lambda_3 = 1$		$\lambda_3 = 2$		$\lambda_3 = 3$	
σ_7 [fb]	193		208		233	
σ_8 [fb]	243		265		301	
$\langle\%\rangle_{\text{ggF,total}}$	2.98		10.99		21.59	
$\langle\%\rangle_{\text{ggF,SR}}$	18.68		48.08		67.63	
	N_{sig}	$\langle\epsilon_{\text{stop}}\rangle$ [%]	N_{sig}	$\langle\epsilon_{\text{stop}}\rangle$ [%]	N_{sig}	$\langle\epsilon_{\text{stop}}\rangle$ [%]
1 keV	~ 0	-	~ 0	-	~ 0	-
5 keV	~ 0	-	~ 0	-	~ 0	-
10 keV	~ 0	-	~ 0	0.235	~ 0	0.335
20 keV	~ 0	0.395	~ 0	0.618	~ 0	0.890
50 keV	~ 0	0.701	~ 0	1.136	~ 0	1.651
100 keV	~ 0	0.852	~ 0	1.401	~ 0	2.046
200 keV	~ 0	0.940	0.64	1.559	1.06	2.282
500 keV	0.71	0.998	1.29	1.663	2.16	2.439
1 MeV	0.96	1.018	1.74	1.700	2.90	2.493
2 MeV	1.11	1.028	2.03	1.719	3.38	2.521
5 MeV	1.22	1.034	2.23	1.730	3.72	2.538
10 MeV	1.24	1.036	2.27	1.734	3.78	2.544
20 MeV	1.24	1.037	2.27	1.736	3.79	2.547
50 MeV	1.25	1.038	2.28	1.737	3.81	2.549
100 MeV	1.26	1.038	2.30	1.737	3.83	2.549
200 MeV	1.27	1.038	2.33	1.737	3.88	2.549
500 MeV	1.27	1.038	2.33	1.737	3.88	2.550
1 GeV	1.27	1.038	2.33	1.737	3.88	2.550

TABLE 6.11: Number of observed decays of stopped $H^\pm$ particles in ATLAS $m_{H^\pm} = 120$ GeV, a mass splitting of $\Delta m_{\text{nc}} = 10$ GeV and a combination of $\sqrt{s} = 7$ and 8 TeV, including the average stopping fraction and the average percentage of ggF events in total and in the search region (SR). Count numbers less than 0.2 are taken to be ~ 0 and are not written explicitly. Furthermore, $\mathcal{B}(H^\pm \to \tau + N_1) = 1$ and $\epsilon_{\text{rec}} = 0.23$.

	$\lambda_3 = 1$		$\lambda_3 = 2$		$\lambda_3 = 3$	
σ_7 [fb]	82		88		97	
σ_8 [fb]	105		114		128	
$\langle\%\rangle_{\text{ggF,total}}$	2.91		10.34		20.20	
$\langle\%\rangle_{\text{ggF,SR}}$	22.60		49.64		67.88	
	N_{sig}	$\langle\epsilon_{\text{stop}}\rangle$ [%]	N_{sig}	$\langle\epsilon_{\text{stop}}\rangle$ [%]	N_{sig}	$\langle\epsilon_{\text{stop}}\rangle$ [%]
1 keV	~ 0	-	~ 0	-	~ 0	-
5 keV	~ 0	-	~ 0	-	~ 0	-
10 keV	~ 0	-	~ 0	-	~ 0	-
20 keV	~ 0	-	~ 0	0.290	~ 0	0.415
50 keV	0.003	0.499	0.005	0.767	0.009	1.111
100 keV	0.03	0.694	0.05	1.075	0.08	1.568
200 keV	0.13	0.821	0.22	1.277	0.36	1.871
500 keV	0.38	0.909	0.64	1.418	1.05	2.084
1 MeV	0.54	0.940	0.92	1.469	1.53	2.161
2 MeV	0.70	0.956	1.20	1.495	1.98	2.200
5 MeV	0.81	0.966	1.37	1.511	2.26	2.225
10 MeV	0.84	0.970	1.43	1.517	2.37	2.233
20 MeV	0.85	0.971	1.44	1.519	2.39	2.237
50 MeV	0.85	0.972	1.45	1.521	2.40	2.239
100 MeV	0.86	0.973	1.46	1.521	2.41	2.240
200 MeV	0.86	0.973	1.47	1.522	2.43	2.241
500 MeV	0.87	0.973	1.48	1.522	2.45	2.241
1 GeV	0.87	0.973	1.48	1.522	2.45	2.241

TABLE 6.12: $m_{H^\pm} = 150$ GeV, $\sqrt{s} = 7$ & 8 TeV, $\mathcal{B}(H^\pm \to \tau + N_1) = 1$, $\epsilon_{\text{rec}} = 0.39$.

	$\lambda_3 = 1$		$\lambda_3 = 2$		$\lambda_3 = 3$	
σ_{13} [fb]	528		602		722	
σ_{14} [fb]	591		678		821	
$\langle\%\rangle_{\text{ggF,total}}$	5.15		17.21		31.68	
$\langle\%\rangle_{\text{ggF,SR}}$	28.38		63.52		77.45	
	N_{sig}	$\langle\epsilon_{\text{stop}}\rangle$ [%]	N_{sig}	$\langle\epsilon_{\text{stop}}\rangle$ [%]	N_{sig}	$\langle\epsilon_{\text{stop}}\rangle$ [%]
1 keV	~ 0	-	~ 0	-	~ 0	-
5 keV	~ 0	-	~ 0	-	~ 0	-
10 keV	~ 0	-	~ 0	0.230	~ 0	0.334
20 keV	~ 0	0.386	~ 0	0.610	~ 0	0.889
50 keV	~ 0	0.703	~ 0	1.130	~ 0	1.653
100 keV	1.09	0.864	2.01	1.396	3.58	2.051
200 keV	3.04	0.959	5.66	1.557	10.10	2.290
500 keV	6.19	1.022	11.60	1.663	20.60	2.448
1 MeV	8.33	1.044	15.60	1.700	27.70	2.503
2 MeV	9.68	1.055	18.10	1.719	32.30	2.532
5 MeV	10.70	1.062	19.90	1.731	35.60	2.549
10 MeV	10.80	1.064	20.30	1.735	36.10	2.554
20 MeV	10.90	1.065	20.30	1.737	36.20	2.557
50 MeV	10.90	1.066	20.40	1.738	36.40	2.559
100 MeV	11.00	1.066	20.50	1.738	36.70	2.560
200 MeV	11.10	1.066	20.80	1.739	37.10	2.560
500 MeV	11.10	1.066	20.80	1.739	37.10	2.560
1 GeV	11.10	1.066	20.80	1.739	37.10	2.560

TABLE 6.13: $m_{H^\pm} = 120$ GeV, $\sqrt{s} = 13$ & 14 TeV, $\mathcal{B}(H^\pm \to \tau + N_1) = 1$, $\epsilon_{\text{rec}} = 0.23$.

	$\lambda_3 = 1$		$\lambda_3 = 2$		$\lambda_3 = 3$	
σ_{13} [fb]	240		271		323	
σ_{14} [fb]	270		307		369	
$\langle\%\rangle_{\text{ggF,total}}$	5.00		16.43		30.40	
$\langle\%\rangle_{\text{ggF,SR}}$	32.33		65.10		79.43	
	N_{sig}	$\langle\epsilon_{\text{stop}}\rangle$ [%]	N_{sig}	$\langle\epsilon_{\text{stop}}\rangle$ [%]	N_{sig}	$\langle\epsilon_{\text{stop}}\rangle$ [%]
1 keV	~ 0	-	~ 0	-	~ 0	-
5 keV	~ 0	-	~ 0	-	~ 0	-
10 keV	~ 0	-	~ 0	-	~ 0	-
20 keV	~ 0	-	~ 0	0.272	~ 0	0.429
50 keV	~ 0	0.433	~ 0	0.730	~ 0	1.150
100 keV	~ 0	0.602	~ 0	1.030	~ 0	1.623
200 keV	1.02	0.712	2.00	1.229	3.78	1.937
500 keV	2.93	0.788	5.80	1.368	11.00	2.158
1 MeV	4.25	0.815	8.42	1.418	16.00	2.238
2 MeV	5.50	0.829	10.90	1.444	20.70	2.279
5 MeV	6.29	0.837	12.50	1.460	23.70	2.304
10 MeV	6.58	0.840	13.10	1.465	24.70	2.313
20 MeV	6.64	0.842	13.20	1.468	25.00	2.317
50 MeV	6.66	0.843	13.20	1.470	25.10	2.319
100 MeV	6.69	0.843	13.30	1.470	25.20	2.320
200 MeV	6.75	0.843	13.40	1.470	25.40	2.321
500 MeV	6.80	0.843	13.50	1.471	25.60	2.321
1 GeV	6.80	0.843	13.50	1.471	25.60	2.321

TABLE 6.14: $m_{H^\pm} = 150$ GeV, $\sqrt{s} = 13$ & 14 TeV, $\mathcal{B}(H^\pm \to \tau + N_1) = 1$, $\epsilon_{\text{rec}} = 0.39$.

CHAPTER 7

Conclusion

Clarification of the origin of dark matter and of neutrino oscillations are two of the principal desiderata in the science of high-energy physics. With the absence of direct but a vast amount of indirect evidence for new physics at the fundamental level, model building is flourishing in every field and new theoretical scenarios intended to provide plausible solutions are continually added to the rich abundance of proposed SM extensions. Their common feature is the introduction of new (exotic) particles. Since one expects new physics to exist between the electroweak and TeV scales, there is good hope for these new particles to be detectable at colliders such as the LHC.

This thesis explored aspects of the detection of exotic new physics at the LHC in two different ways. A first analysis was dedicated exclusively to the production rates. The concrete goal was to systematically quantify the contribution of the Higgs portal to the number of produced uncoloured particles existing in new scalar or fermionic representations of the SM gauge group in a generic fashion. Motivation was drawn from the recent discovery of a boson with a mass of 125.09 GeV whose properties match the characteristics expected of the scalar boson predicted for the spontaneous breaking of the GWS symmetry intriguingly well. The boson is predicted to subdominantly accompany the Drell-Yan production of exotic particles in proton-proton collisions, mostly through the gluon fusion channel at LHC energies. We quantified this subdominant contribution, identifying the cases of relevance of the Higgs channel, also providing a glimpse on the possibilities achievable with a hypothetical 100 TeV proton-proton collider. In a second analysis, the LHC phenomenology of an as yet little studied but well-motivated variant of Ernest Ma's scotogenic model with a FIMP dark matter candidate has been investigated. The scotogenic model represents the simplest SM extension capable of explaining neutrino masses and providing a particle dark matter candidate that is rendered stable by imposing an odd parity symmetry onto the new particle sector. Until our study, no detailed analysis of the collider phenomenology in this version of the model has been undertaken. As is typical for FIMP scenarios, the model features long-lived particles, thus allowing for the possibility of very non-standard signatures. We investigated two imaginable cases by recasting existing LHC searches for long-lived particles. In the first, we derived bounds on the model's parameter space from a CMS search for singly-charged metastable particles leaving tracks in the tracker and muon systems. In a second analysis, we considered the ATLAS search for stopped R-hadrons decaying out-of-time in the calorimeters. Both searches have been re-interpreted in terms of signals created by long-lived charged scotogenic scalar bosons.

In the first study (Analysis I), it has been found that the Higgs portal to scalar production can be of the order of QCD corrections for quartic couplings of $\mathcal{O}(1)$. Couplings of this size are theoretically and phenomenologically viable in many scenarios and the Higgs portal should therefore not be neglected if the experimental precision requires inclusions of radiative effects. In particular, we have shown that the inert doublet and Higgs triplet models can be very sensitive to the Higgs channel, depending on the scalar masses and on the electric charge. The best situation was found for the singly-charged scalar triplet component, with an allowed Higgs portal contribution of up to 50% at $\sqrt{s} = 14$ TeV, depending on the mass. For the fermions, we chose the type I/III seesaw scenarios as benchmarks, for they are two of the best-motivated minimal fermionic SM extensions and quite representative of a wider class of models. It was found that the Higgs contribution is highly dominant on the resonance, confirming the known result that it is well suited to test the low-scale type I seesaw scenario. Moreover, gluon fusion is found to be highly significant in the regime $M_k \gtrsim 300$ GeV, which is still allowed by direct searches for type III fermions. Lastly, we have verified how the importance of gluon fusion evolves when $\sqrt{s}$ is increased to 100 TeV, as might be realized in a future hadron collider. For scalar and fermionic new particles, the relative importance of

gluon fusion is seen to increase by one order of magnitude. We also found that the scalar production cross section can increase by a factor of up to 100, depending on the quantum numbers. In the case of the seesaw mechanisms, the heavy fermions in the type III and low-scale type I scenarios are predominantly produced via the Higgs portal for masses $M_k \gtrsim 300$ GeV.

The second study was subdivided into two analyses (Analysis IIA and IIB). Analysis IIA examined the contribution of long-lived scotogenic $H^\pm$ bosons to the charged track signal searched for by CMS in $\sqrt{s} = 8$ TeV data. We found that their limits on singly-charged leptons produced via the Drell-Yan mechanism resemble the scotogenic signature in the case of metastability and similar constraints apply. However, by allowing for in-detector decays to charged leptons and missing energy in the form of the dark matter particle N_1, the bounds are significantly weakened and a large portion in the $(m_{H^\pm}, M_1)$ parameter space is opened, allowing charged scalar masses as low as $m_{H^\pm} \lesssim 70$ GeV. Analysis IIB focused on the interesting signature of out-of-time decays underwent by totally decelerated $H^\pm$ particles. Using a search by the ATLAS collaboration based on $\sqrt{s} = 7$ & 8 TeV data, we attempted to constrain the parameter space of the scotogenic FIMP scenario by means of incorporating the hugely significant Higgs portal contribution. The signal turns out to be too dominated by the expected non-collision background to result in significant event counts, which is caused by low production cross sections and a small timing efficiency of the ATLAS detector. Nevertheless, the results of this study strongly advocate the assertion of Analysis I: The portal to New Physics may well lie in the Higgs sector!

APPENDIX A

Basics of Friedmann-Lemaître-Robertson-Walker cosmology

Friedmann-Lemaître-Robertson-Walker (FLRW) cosmology is the commonly used framework to describe the dynamics of the Universe starting with the inflationary phase. In this appendix, we shall sum up the essential equations that are needed in several parts of Chapter 2, following standard textbooks.

The Friedmann-Lemaître equation

$$H^2(t) = \frac{8\pi G}{3}\rho(t) + \frac{1}{3}\Lambda + \frac{k}{R^2(t)}\,, \tag{A.1}$$

corresponds to the zeroth component of the Einstein field equations with a cosmological constant Λ, for the FLRW metric and the energy-momentum tensor of a cosmological perfect fluid. G is the gravitational constant and $H(t)$ is the Hubble rate defined in terms of the spatial scale factor $R(t)$,

$$H(t) = \frac{\dot{R}(t)}{R(t)} = \frac{\dot{R}(t)}{R_0}\frac{R_0}{R(t)} \equiv \frac{\dot{a}(t)}{a(t)} = 100\,h\ \text{km/s/Mpc}\,, \qquad h \equiv H_0/100\,. \tag{A.2}$$

A zero as a lower subscript always denotes $t = t_{\text{today}}$ and we defined the dimensionless scale factor $a(t) = R(t)/R_0$ and the reduced Hubble parameter h. The quantity k can take the values $+1$ (positive curvature, 'closed' universe), -1 (negative curvature, 'open' universe) or 0 (no curvature, 'flat' universe). An open universe will expand forever, whereas a closed universe eventually collapses. The most recent measurement of h is provided by the Planck collaboration [8], with the 68% C.L. being

$$h = 0.6774 \pm 0.0046\,, \tag{A.3}$$

coming from combining CMB power spectrum measurements, gravitational lensing and external data. In the absence of a cosmological constant, Equation A.1 is simply called Friedmann equation.

From covariant energy-momentum conservation, we can derive the continuity equation for a component i of the cosmological fluid. Assuming that its equation of state relates pressure and energy density in the form $p_i = w_i\rho_i$, for some number w_i, the continuity equation leads to the important relation

$$\rho_i(t) \propto a(t)^{-3(1+w_i)}\,. \tag{A.4}$$

For the three main components, *i.e.* dust (pressureless gas of non-interacting non-relativistic matter, short: matter), radiation and dark energy, the equations of state for these quantities read

$$\rho_{\text{m}}(t) = \rho_{\text{m},0}\,a^{-3}(t) \quad (w_{\text{m}} = 0)\,, \tag{A.5a}$$

$$\rho_{\text{r}}(t) = \rho_{\text{r},0}\,a^{-4}(t) \quad (w_{\text{r}} = 1/3)\,, \tag{A.5b}$$

$$\rho_\Lambda(t) = \rho_{\Lambda,0} = \frac{\Lambda}{8\pi G} \quad (w_\Lambda = -1)\,. \tag{A.5c}$$

Specifying $\rho_{i,0}$ and R_0 determines the full cosmological model at all cosmological times. It is more conventional to work instead with the dimensionless cosmological density parameters

$$\Omega_i(t) \equiv \frac{8\pi G}{3H^2(t)}\rho_i(t)\,. \tag{A.6}$$

The determination of the full ΛCDM model then consists of the specification of $\Omega_{i,0}$ and H_0, in terms of which the Friedmann-Lemaître equation can be written as

$$\Omega_{\text{m}}(t) + \Omega_{\text{r}}(t) + \Omega_\Lambda(t) + \Omega_k(t) = 1\,. \tag{A.7}$$

Note that we also introduced a density parameter for the curvature term, $\Omega_k(t) = -k/H^2(t)R^2(t)$. As stated above, knowing the present-day cosmological parameters lets us determine these parameters as well as the scale factor at all cosmic times. Integrating the cosmological field equation (neglecting curvature) in the form

$$\dot{a}^2 = H_0 \left(\Omega_{\mathrm{m},0}\, a^{-1} + \Omega_{\mathrm{r},0}\, a^{-2} + \Omega_{\Lambda,0}\, a^2 + 1 - \Omega_{\mathrm{m},0} - \Omega_{\mathrm{r},0} - \Omega_{\Lambda,0}\right) \tag{A.8}$$

leads to the time dependences of the scale factor $a(t)$. Ignoring integration constants, this yields

$$a_{\mathrm{RD}}(t) = (2H_0 t)^{1/2}\,, \qquad a_{\mathrm{MD}}(t) = \left(\frac{2}{3} H_0 t\right)^{2/3}\,, \qquad a_{\mathrm{VD}}(t) = \exp(\sqrt{\Lambda/3}t)\,, \tag{A.9}$$

for a radiation-dominated (RD), matter-dominated (MD) and vacuum-dominated (VD) expansion, respectively. For the present-day cosmological parameters, Planck [8] provides the values[1]

$$\Omega_{\mathrm{m},0} = 0.3089 \pm 0.0062\,, \tag{A.10}$$

$$\Omega_{\Lambda,0} = 0.6911 \pm 0.0062\,, \tag{A.11}$$

$$\Omega_{\mathrm{k},0} = 0.0008^{+0.0040}_{-0.0039}\,. \tag{A.12}$$

While the first two parameters are presented within the context of the strictly flat-space six-parameter ΛCDM model, $\Omega_{\mathrm{k},0}$ is to be seen as part of a one-parameter extension. Abundances of matter or energy types are usually specified in terms of Ωh^2. Baryonic and CDM abundances are separate densities contributing to $\Omega_{\mathrm{m},0}$, which are in fact taken as two base parameters for the cosmological standard model used by Planck, as mentioned in Section 2.2.1. They are determined to be

$$\Omega_{\mathrm{B},0}h^2 = 0.02230 \pm 0.00014\,, \tag{A.13}$$

$$\Omega_{\mathrm{c},0}h^2 = 0.1188 \pm 0.0010\,. \tag{A.14}$$

$\Omega_{\mathrm{r},0}$ can be calculated from the relic photon temperature. Neutrinos are massive and must therefore only be treated as radiation if they never became non-relativistic at some point. Neutrino oscillation measurements indicate that at least one neutrino is non-relativistic today. Assuming they all are, that leaves only the photons, *i.e.* $\Omega_{\mathrm{r},0} = \Omega_{\gamma,0}$. Using Equation 2.32 with the present-day CMB temperature $T_0 = 2.7255$ K [92] and $g_{*\rho} \to g_\gamma = 2$, we can obtain $\Omega_{\mathrm{r},0}$ through $\rho_{\gamma,0}$ (see also [78]),

$$\Omega_{\mathrm{r},0} = \frac{8\pi G}{3H_0^2}\,\rho_{\gamma,0} = 5.46(19) \times 10^{-5}\,. \tag{A.15}$$

The neutrino contribution would be a number of the same order if they were relativistic. Treating them all as non-relativistic particles, we have [78]

$$\Omega_{\nu,0} = \frac{\sum m_{\nu,i}}{93\,\mathrm{eV}}\,. \tag{A.16}$$

With three active light neutrinos, one obtains a lower bound on the sum of neutrino masses from assuming a mass hierarchy. In case of a normal hierarchy (NH) or an inverted hierarchy (IH), the mass scale of the heaviest neutrino is set by the $\Delta m^2_{\mathrm{atm}}$ measurement (see Section 2.3.2), yielding $\sum m_{\nu,i} \gtrsim 0.05$ eV or $\sum m_{\nu,i} \gtrsim 0.1$ eV, respectively. This gives the bound

$$\Omega_{\nu,0} > \left(1.193 \times 10^{-3}_{(\mathrm{NH})},\, 2.379 \times 10^{-3}_{(\mathrm{IH})}\right)\,, \tag{A.17}$$

Tritium decay experiments provide the upper bound $\sum m_{\nu,i} < 2$ eV, giving

$$\Omega_{\nu,0} < 0.04\,, \tag{A.18}$$

however the numbers shown here vary somewhat from reference to reference.

[1] These are 68% CL limits taking into account Planck measurements, aberration due to gravitational lensing and external data, like baryon acoustic oscillation measurements.

APPENDIX B

The Boltzmann equation

One describes the process of a quantity of a species in a thermodynamical system moving away from or towards thermal equilibrium by means of a differential equation, with the solution being the reaction yield of the species as a function of time or, equivalently in cosmology, of the photon bath temperature. This equation is the famous Boltzmann equation. It is generally used as a tool to quantify the fact that the number of particles in a volume that is comoving w.r.t. spatial change of the system is either constant or, in the presence of collisions and/or external forces and/or diffusion, changes according to the corresponding rates. The equation states that systems tend towards thermal equilibrium if left alone. Boltzmann proved this fact of Nature in 1872 by using his equation to prove his H-theorem, which can be regarded as the proof for entropy increase. As the Boltzmann equation is of central importance in cosmology and as we shall need it to explain dark matter freeze-in, we will in this part present and discuss the equation and, for completeness, explain how it is utilized in thermal freeze-out computations for cold relics. A recommendable read on the subject are Baumann's and Tong's notes [99, 428]. See also [429] for a mathematical treatment in relativistic quantum mechanics.

The phase space density $f_N(\vec{r}, \vec{p}, t)$ of a system of N indistinguishable particles ($N \sim 10^{23}$) obeys Liouville's equation describing phase space flow,

$$\mathrm{L}[f_N] = \mathrm{C}[f_N] + \mathrm{Dec}[f_N] + \mathrm{F}[f_N] + \mathrm{Dif}[f_N]\,, \tag{B.1}$$

where L is the Liouville operator $d/dt = \partial/\partial t + \{., H\}$, $\{., H\}$ being the Poisson bracket with the Hamiltonian H, and C, Dec, F and Dif are the collision, decay, external force and diffusion operators, respectively. In all that follows, we will ignore diffusion and external forces, since we will be interested in the universe as a whole. We will also be mainly focusing on two-particle interactions described by the collision term. Collisions are characterized by a collision rate and the final result will be readily applicable to decays if we exchange the collision rate by the decay rate, in addition to another very simple modification.

Using kinetic theory, one can show that the phase space densities for $n < N$ and for the other $n{+}1, \ldots, N$ particles of this system are related by

$$\frac{\partial f_n}{\partial t} + \{f_n, H_n\} = \sum_{i=1}^{n} \int d\Pi_{n+1} \frac{\partial U(\vec{r}_i - \vec{r}_{n+1})}{\partial \vec{r}_i} \frac{\partial f_{n+1}}{\partial \vec{p}_i}\,. \tag{B.2}$$

Here, H_n is an n-particle Hamiltonian including the two-particle interactions among all the n particles described by the distribution f_n, Π_{n+1} is the phase space measure of particle $n+1$ and $U(\vec{r}_i - \vec{r}_j)$ is the interaction potential between the particles at positions $\vec{r}_i$ and $\vec{r}_j$. Equation B.2 is known as the BBGKY (Bogoliubov, Born, Green, Kirkwood, Yuan) hierarchy: It states that in order to know the behaviour of a set of particles, one needs to know the behaviour of a set with the same number of particles, plus one. This is unsolvable and the Boltzmann equation corresponds to the truncation of this set of coupled integro-differential equations at $n = 1$, incorporating a few reasonable assumptions. First, it is assumed that collisions are practically instantaneous and particles are moving freely between collisions for very long times. Second, before collisions, all partaking particles are uncorrelated, which goes under the designation of molecular chaos: $f_2 \approx f_1 f_1$ (Note that this introduces an arrow of time, a crucial ingredient to the proof of the H-theorem). Third, energy and momentum are conserved in each collision, and fourth, interactions are invariant under parity and time reversal, leading to crossing symmetry of the interaction potential.[1]

[1] T or CP invariance conditions need to be relaxed when dealing with baryogenesis scenarios.

For definiteness, consider a $(1,2) \leftrightarrow (3,4)$ reaction and focus on particle 1. Suppressing the t dependence, the Boltzmann equation for f_1 has the form

$$\begin{aligned} \mathrm{L}[f_1(\vec{r}_1,\vec{p}_1)] = \int d\Pi_{i=2}^4 \, \Omega(1,2|3,4) \\ \times \left[f_1(\vec{r}_1,\vec{p}_3)\, f_1(\vec{r}_1,\vec{p}_4) \left\{1 + a_1\, f_1(\vec{r}_1,\vec{p}_1)\right\} \left\{1 + a_2\, f_1(\vec{r}_1,\vec{p}_2)\right\} \right. \\ \left. - \, f_1(\vec{r}_1,\vec{p}_1)\, f_1(\vec{r}_1,\vec{p}_2) \left\{1 + a_3\, f_1(\vec{r}_1,\vec{p}_3)\right\} \left\{1 + a_4\, f_1(\vec{r}_1,\vec{p}_4)\right\} \right] . \end{aligned} \tag{B.3}$$

We defined the phase space measure (*cf.* Equation 3.16)

$$d\Pi_i \equiv g_i \, \frac{đ^3 p_i}{2E_i} \, , \tag{B.4}$$

with $đ^3 p_i$ given in Equation 2.40, and[2]

$$a_i = \begin{cases} 0\,, & \text{Maxwell-Boltzmann} \quad \text{(MB)}\,, \\ +1\,, & \text{Bose-Einstein} \quad \text{(BE)}\,, \\ -1\,, & \text{Fermi-Dirac} \quad \text{(FD)}\,. \end{cases} \tag{B.5}$$

The non-negative measure $\Omega(1,2|3,4)$ is the interaction rate,

$$\Omega(1,2|3,4) = \omega(1,2|3,4)\, (2\pi)^4\, \delta^{(4)}(p_1 + p_2 - p_3 - p_4)\,, \tag{B.6}$$

which in quantum mechanics is to be identified with $|\, \langle 3,4|\, H_{\mathrm{int}}\, |1,2\rangle\, |^2$, where H_{int} is the 2-particle interaction Hamiltonian classically described by the potential U in Equation B.2. We have $\omega(1,2|3,4) = |\overline{\mathcal{M}}|^2_{12\leftrightarrow 34}$, where $\overline{\mathcal{M}}$ denotes the spin-averaged matrix element including possible symmetry factors, and the quantity $\Omega(1,2|3,4)\, d\Pi_{i=3}^4$ is the probability rate for the state $|1,2\rangle$ to be scattered into a state with 4-momenta in the ranges $[p_3, p_3 + dp_3]$ and $[p_4, p_4 + dp_4]$. It is a scattering rate, thus it will be proportional to the relative velocity of the colliding particles, which will be factored out later. The one-particle equilibrium distributions f_1^{eq} are obtained by taking the logarithm of the expression inside the square brackets in Equation B.3 and setting it equal to zero (what is called the 'detailed balance' condition). Furthermore, since we are ignoring external force fields like gravity, f_1 should be independent of the position in equilibrium. This leads to (see [428])

$$f_1^{\mathrm{eq}}(\vec{p}) = \frac{1}{\exp[\beta(E(\vec{p}) - \mu)] - a_1} \, . \tag{B.7}$$

f_1^{eq} corresponds to the known distributions if we identify β with the inverse temperature and μ with the chemical potential. Even if the Boltzmann equation is written in a covariant form, once a phase space distribution has been written explicitly, one has chosen a frame where it has that form and is from then on bound to it. Finally performing the integral $g_1 \int đ^3 p_1$ leads to the Boltzmann equation for the particle number density,

$$\begin{aligned} \frac{dn_1(\vec{r}_1,t)}{dt} = \int d\Pi_{i=1}^4 \, |\overline{\mathcal{M}}|^2_{12\leftrightarrow 34}\, (2\pi)^4\, \delta^{(4)}(p_1 + p_2 - p_3 - p_4) \\ \times \left[f_3\, f_4 \left\{1 + a_1\, f_1\right\} \left\{1 + a_2\, f_2\right\} \, - f_1\, f_2 \left\{1 + a_3\, f_3\right\} \left\{1 + a_4\, f_4\right\} \right] . \end{aligned} \tag{B.8}$$

Note that the lower index on n and f now denotes the particle it refers to, as does the index on a, and we suppressed the arguments. To write Equation B.8, we used that the relativistic Liouville operator can be written with an overall factor E_1 multiplying $\partial/\partial t$ and the streaming term given by the Poisson bracket. This E_1 can be brought to the r.h.s.; after integrating over $\vec{p}_1$, this results in the phase space integral $\int d\Pi_1$ (see [196]). In order to describe temporal variations of n_1 due to decays instead of collisions, we replace the collision rate by the decay and inverse decay rates responsible for depletion and production. Suppose that particle 2 decays to particles 1 and 3, $2 \to (1,3)$, and particles 1 and 3 can annihilate to particle 2 via

[2] Bosons feel an attractive potential, so the probability of scattering is enhanced if there is already a boson in the same final state, hence the $+$. Fermions will only scatter into that state if it is not already occupied, hence the $-$.

the inverse decay $(1,3) \to 2$. In that case, we have

$$\frac{dn_1(\vec{r}_1,t)}{dt} = \int d\Pi_{i=1}^4 \, (2\pi)^4 \, \delta^{(4)}(p_1 + p_3 - p_2) \\ \times \left[|\overline{\mathcal{M}}|^2_{2\to 13} \, f_2 \, \{1 + a_1 \, f_1\} \, \{1 + a_3 \, f_3\} \, - |\overline{\mathcal{M}}|^2_{13\to 2} \, f_1 \, f_3 \, \{1 + a_2 \, f_2\} \right] . \tag{B.9}$$

Such processes are relevant for freeze-in scenarios. Freeze-out scenarios, on the other hand, are described by $(1,2) \leftrightarrow (2,3)$ processes, however freeze-out may also constitute a necessary ingredient in models with freeze-in, as discussed in Section 2.2.3.3.

For the following derivation of the Boltzmann equation for WIMP dark matter freeze-out, we follow mostly Dodelson [197]. A system of particles is in kinetic equilibrium if its phase space distribution admits the Fermi-Dirac or Bose-Einstein form and it is in chemical equilibrium if the chemical potentials in reactions $\{a\} \leftrightarrow \{b\}$ add up to the same value, $\sum_a \{\mu_a\} = \sum_b \{\mu_b\}$. Scattering processes will enforce kinetic equilibrium, but in general not chemical equilibrium. However, energy conservation is guaranteed through the delta function, *i.e.* $\sum_a \{E_a\} = \sum_b \{E_b\}$. As a further simplification, we consider Maxwell-Boltzmann statistics for all particles, since we shall be working in a regime where $E_i - \mu_i \gg T$ (WIMP masses are larger than the temperatures at which they freeze out and their chemical potential is much smaller than their mass). Thus we write

$$f(E_i, \mu_i, T) = \mathrm{e}^{\beta \mu_i} \mathrm{e}^{-\beta E_i} \equiv \mathrm{e}^{\beta \mu_i} f(E_i, T) \, . \tag{B.10}$$

Let us return to $(1,2) \leftrightarrow (3,4)$ reactions. We reformulate the l.h.s. of Equation B.8 as $\dot{n}_1 + 3Hn_1$ using the FLRW metric, so the Boltzmann equation becomes

$$\dot{n}_1 + 3Hn_1 = \int d\Pi_{i=1}^4 \, |\overline{\mathcal{M}}|^2_{12\leftrightarrow 34} \, (2\pi)^4 \, \delta^{(4)}(p_1 + p_2 - p_3 - p_4) \\ \times \mathrm{e}^{-\beta(E_1+E_2)} \big[\mathrm{e}^{\beta(\mu_3+\mu_4)} - \mathrm{e}^{\beta(\mu_1+\mu_2)} \big] \, . \tag{B.11}$$

Next we use Equation B.10 to write the equilibrium number density as

$$\begin{aligned} n_i^{(\mathrm{eq})} &= g_i \int \mathrm{d}^3 p_i \, f_i(E_i, \mu_i, T) = \mathrm{e}^{\beta \mu_i} \, g_i \int \mathrm{d}^3 p_i \, \mathrm{e}^{-\beta E_i} \\ &= \mathrm{e}^{\beta \mu_i} \times \begin{cases} g_i \left(\frac{m_i T}{2\pi} \right)^{3/2} \mathrm{e}^{-m_i/T} \, , & m_i \gg T \\ g_i \frac{T^3}{\pi^2} \, , & m_i \ll T \end{cases} \\ &\equiv \mathrm{e}^{\beta \mu_i} \, \bar{n}_i \end{aligned} \tag{B.12}$$

where we defined $\bar{n}$ as the equilibrium number density with a vanishing chemical potential. Note that by neglecting the Bose enhancement and Pauli blocking terms ± 1 in $f(E_i, \mu_i, T)$, we approximate the factors $\zeta(3)$ and $\frac{3}{4}\zeta(3)$ in Equation 2.41 by 1. This amounts to accounting for the absence of Bose condensation and Fermi degeneracy. The Boltzmann equation now takes the very simple form

$$\dot{n}_1 + 3Hn_1 = - \langle \sigma v \rangle \left[n_1 n_2 - \frac{\bar{n}_1 \bar{n}_2}{\bar{n}_3 \bar{n}_4} n_3 n_4 \right] , \tag{B.13}$$

where we introduced the *thermally averaged annihilation cross section*,

$$\begin{aligned} \langle \sigma v \rangle &= \frac{1}{\bar{n}_1 \bar{n}_2} \int d\Pi_{i=1}^4 \, |\overline{\mathcal{M}}|^2 \, (2\pi)^4 \, \delta^{(4)}(p_1 + p_2 - p_3 - p_4) \, \mathrm{e}^{-\beta(E_1+E_2)} \\ &= \frac{\int \mathrm{d}^3 p_1 \int \mathrm{d}^3 p_2 \, \sigma_{12} \, v_{12} \, f(E_1, T) \, f(E_2, T)}{\int \mathrm{d}^3 p_1 \int \mathrm{d}^3 p_2 \, f(E_1, T) \, f(E_2, T)} \, . \end{aligned} \tag{B.14}$$

Here, v_{ij} is the relative velocity between particles i and j,

$$v_{ij} = \frac{\sqrt{(p_i \cdot p_j)^2 - m_i^2 \, m_j^2}}{E_i \, E_j} \, . \tag{B.15}$$

Clearly, the collision term vanishes in chemical equilibrium, because then the distributions are all in thermal

equilibrium and the production and annihilation terms cancel.

We see from Equation B.12 that in the NR limit, the number density (and also energy density and pressure) is suppressed by the mass. This is generally called Boltzmann suppression and does eventually lead to the decoupling of all massive species from the primordial plasma due to the temperature at some point ceasing to be high enough to provide the bath particles with enough energy for reactions for i-type particle creation. An exception may be the neutrinos, which decoupled when they were relativistic and, although being massive, still might be relativistic today.

APPENDIX C

The tree-level seesaw mechanisms of neutrino mass generation

The seesaw mechanisms of neutrino mass generation play an important role in several parts of this work. We qualitatively introduced the main types in Section 2.3, in particular the three tree-level seesaw realizations. As the calculational details leading to a Majorana mass lie somewhat out of the main scope and are very well known, we opt for presenting them separately in this appendix.

C.1 Type I

Of the three seesaw mechanisms at tree-level, the type I [13] is probably the most well known and constitutes the simplest of the canonical seesaw models, as it merely consists of adding $n \geq 2$ RH neutrino singlets ν_{Ri}, $i = 1, 2, \ldots, n$, to the SM particle spectrum. n is mostly taken to be 3 to regain the family symmetry between the lepton and quark sectors and to allow for generic light neutrino masses appearing due to fermion mixing after EWSB.

In addition to a kinetic term for the ν_{Ri}, the SM gauge group allows for a Yukawa interaction term with the ν_{Li} flavour fields and a Majorana mass term for the ν_{Ri},

$$\mathcal{L}_\nu = -(Y_N)_{ij}\, \bar{L}_i\, \tilde{H}\, \nu_{Rj} - \frac{1}{2}(M_R)_{ij}\, \overline{\nu_{Ri}^c}\, \nu_{Rj} + \text{h.c.}\,. \tag{C.1}$$

All fields are written in the weak eigenstate basis. $\nu_R^c = C\overline{\nu}_R^T$ is the (left-chiral) conjugate of ν_R, with the convention that the charge conjugation phase vanishes. $M_R = M_R^T$ is the $n \times n$-dimensional complex-valued Majorana mass matrix of the ν_R, containing values presumed to be very large, $|M_R| \gg v$. Y_N is $3 \times n$-dimensional. Note that these Yukawa and Majorana terms in conjunction violate lepton number by two units, which is allowed because lepton number is only an accidental symmetry in the SM. It is common to assign lepton number violation to the Majorana term. After EWSB, the Yukawa term becomes a Dirac mass term,

$$-(Y_N)_{ij}\, \bar{L}_i\, \tilde{H}\, \nu_{Rj} \;\longrightarrow\; -(m_\text{D})_{ij}\, \bar{\nu}_{Li}\, \nu_{Rj}\,, \quad m_\text{D} = \frac{Y_N}{\sqrt{2}} v\,. \tag{C.2}$$

Defining $\nu_R' \equiv \nu_L^c$ and using $\overline{\psi^c}\phi = \overline{\phi^c}\psi$, the neutrino mass Lagrangian can be compactly expressed in terms of a symmetric $(3+n) \times (3+n)$-dimensional mass matrix,

$$\mathcal{L}_{\nu N}^m = -\frac{1}{2}(\overline{\nu_R'^c}\;\; \overline{\nu_R^c})\, \mathcal{M}_{\nu N} \begin{bmatrix} \nu_R' \\ \nu_R \end{bmatrix} + \text{h.c.}\,, \qquad \mathcal{M}_{\nu N} = \begin{bmatrix} \mathbf{0} & m_\text{D} \\ m_\text{D}^T & M_R \end{bmatrix}. \tag{C.3}$$

Hence, all $3+n$ neutrino mass eigenstates are Majorana neutrinos. $\mathcal{M}_{\nu N}$ is diagonalized with a unitary matrix $U_{\nu N}$,

$$U_{\nu N}^T \mathcal{M}_{\nu N}\, U_{\nu N} = D_{\nu N} = \begin{bmatrix} \hat{m}_\nu & \mathbf{0} \\ \mathbf{0} & \hat{M}_N \end{bmatrix}, \tag{C.4}$$

with the diagonal physical mass matrices

$$\hat{m}_\nu = \text{diag}(m_1,\, m_2,\, m_3) = U^T\, m_\nu\, U\,, \tag{C.5a}$$

$$\hat{M}_N = \text{diag}(M_1,\, M_2, \ldots, M_n) = V^T M_N V\,. \tag{C.5b}$$

As done in Equation 2.92, it is common to write $U_{\nu N}$ in terms of submatrices [244],

$$U_{\nu N} = \begin{bmatrix} K & G \\ S & T \end{bmatrix}, \tag{C.6}$$

thus mixing in the charged gauge current interaction happens through the matrix $V_{\rm cc}^{\rm mix} = \left[U_L^{\ell\dagger} K,\, U_L^{\ell\dagger} G\right]$, as defined in Equation 2.95. Motivated by the presumption that rotating to physical states will not mix left- and right-handed neutrinos substantially, one can start to build $U_{\nu N}$ by a block diagonalization through the ansatz

$$\Omega = \begin{bmatrix} \mathbf{1}+\eta & R \\ -R^\dagger & \mathbf{1}+\eta' \end{bmatrix} + \mathcal{O}(R^3)\,, \qquad \text{with} \quad \eta = -\frac{1}{2} R R^\dagger\,, \quad \eta' = -\frac{1}{2} R^\dagger R\,, \tag{C.7}$$

where R is a complex $(3 \times n)$-dimensional matrix that turns out to be of order $v/|M_R|$, η is 3×3 and η' is $n \times n$. We have approximately $R^* \simeq m_{\rm D} M_R^{-1}$ [409] and block diagonalization yields

$$\Omega^T \mathcal{M}_{\nu N}\, \Omega \simeq \begin{bmatrix} m_\nu & \mathbf{0} \\ \mathbf{0} & M_N \end{bmatrix}, \tag{C.8}$$

with the well-known result [430]

$$m_\nu = -m_{\rm D}\, M_R^{-1}\, m_{\rm D}^T = -\frac{v^2}{2}\, Y_N\, M_R^{-1}\, Y_N^T\,, \tag{C.9a}$$

$$M_N = M_R + \frac{1}{2}\left(m_{\rm D}^\dagger\, m_{\rm D} (M_R^{-1})^* + (M_R^{-1})^*\, m_{\rm D}^T\, m_{\rm D}^*\right). \tag{C.9b}$$

Final diagonalization occurs through another unitary matrix which we term Γ. With the (3×3)- and $(n \times n)$-dimensional unitary matrices U and V, we define

$$\Gamma = \begin{bmatrix} U & \mathbf{0} \\ \mathbf{0} & V \end{bmatrix}, \tag{C.10}$$

giving

$$K \simeq (\mathbf{1}+\eta) U\,, \qquad G \simeq R V\,, \tag{C.11}$$

and

$$U_{\nu N} = \Omega \Gamma\,. \tag{C.12}$$

Hence the weak and mass eigenstates are related through the transformation

$$\begin{bmatrix} \nu_L \\ \nu_R \end{bmatrix} = \begin{bmatrix} P_L & \mathbf{0} \\ \mathbf{0} & P_R \end{bmatrix} U_{\nu N} \begin{bmatrix} \chi \\ N \end{bmatrix} = \begin{bmatrix} [(\mathbf{1}+\eta)U]\chi_L + [RV] N_L \\ -[R^\dagger U]\chi_R + [(\mathbf{1}+\eta')]\, V\, N_R \end{bmatrix}, \tag{C.13}$$

where χ are the 3 light and N the n heavy mass eigenstates satisfying the Majorana condition, $\chi = \chi^c$, $N = N^c$. Charged and neutral gauge interactions of the physical neutrinos after EWSB are

$$\begin{aligned} \mathcal{L}_{\rm cc} = -\frac{g}{\sqrt{2}}\, \overline{\ell'_L}\, \not{W}^-\, \nu_{L\ell} + \text{h.c.} \simeq & -\frac{g}{\sqrt{2}}\, \bar{\ell}_L\, \not{W}^-\, [U_L^\ell (\mathbf{1}+\eta) U]_{\ell i}\, \chi_{Li} + \text{h.c.} \\ & -\frac{g}{\sqrt{2}}\, \bar{\ell}_L\, \not{W}^-\, (RV)_{\ell i}\, N_{Li} + \text{h.c.}\,, \end{aligned} \tag{C.14}$$

$$\begin{aligned} \mathcal{L}_{\rm nc} = -\frac{g}{2 c_{\rm w}}\, \bar{\nu}_{L\ell}\, \not{Z}\, \nu_{L\ell} \simeq & -\frac{g}{2 c_{\rm w}}\, \bar{\chi}_{Li}\, \not{Z}\, [U^\dagger (\mathbf{1}+2\eta) U]_{ij}\, \chi_{Lj} \\ & -\frac{g}{2 c_{\rm w}}\, \bar{\chi}_{Li}\, \not{Z}\, [U^\dagger (\mathbf{1}+\eta) RV]_{ik}\, N_{Lk} + \text{h.c.} \\ & -\frac{g}{2 c_{\rm w}}\, \bar{N}_{Lk}\, \not{Z}\, [(RV)^\dagger (RV)]_{km}\, N_{Lm}\,, \end{aligned} \tag{C.15}$$

Note that K governs the mixing in the ℓ-χ interactions and therefore corresponds to the PMNS matrix.

In the type I seesaw, it is given by the non-unitary matrix

$$K = V_{\rm PMNS} \simeq U_L^{\ell\dagger}\,(\mathbf{1}+\eta)\,U + \mathcal{O}(R^3)\,, \tag{C.16}$$

hence $\eta \sim m_{\rm D}^2 M_R^{-2}$ represents the deviation of $V_{\rm PMNS}$ from unitarity. Besides gauge current terms, there are also interactions with the Higgs boson,

$$\mathcal{L}_h = -\frac{g}{2m_W}\bar{\nu}_L\, m_{\rm D}\,\nu_R\, h + \text{h.c.} \simeq -\frac{g}{2m_W}\bar{\chi}_L\,[U^\dagger(\mathbf{1}+\eta)\,m_{\rm D}\,(\mathbf{1}+\eta')V]\,N_R\,h + \text{h.c.}\,. \tag{C.17}$$

It is more common to work with the flavour eigenstates ν_{Li} rather than the three light fields χ_{Li}, because neutrinos are detected via their weak interactions, not through mass measurements. Moreover, we may work in a flavour basis where the charged lepton fields ℓ coincide with their mass eigenstates, *i.e.* $U_L^\ell = \mathbf{1}$, without loss of generality. Consequently, defining the $(3\times n)$-dimensional mixing matrix

$$\Theta \equiv RV\,, \tag{C.18}$$

we can write

$$\mathcal{L}_{\rm cc}^{\nu} = -\frac{g}{\sqrt{2}}\,\bar{\ell}_L\,\not{W}^-\,\nu_{L\ell} - \frac{g}{\sqrt{2}}\,\overline{\ell'_L}\,\not{W}^-\,\Theta_{\ell i}\,N_{Li} + \text{h.c.}\,, \tag{C.19a}$$

$$\mathcal{L}_{\rm nc}^{\nu} = -\frac{g}{2\mathrm{c_w}}\,\bar{\nu}_{Li}\,\not{Z}\,\nu_{Li} - \left(\frac{g}{2\mathrm{c_w}}\,\bar{\nu}_{Li}\,\not{Z}\,\Theta_{ik}\,N_{Lk} + \text{h.c.}\right)\,, \tag{C.19b}$$

$$\mathcal{L}_h = -\frac{gM_k}{2m_W}\,\bar{\nu}_{Li}\,\Theta^*_{ik}\,N_{Rk}\,h + \text{h.c.}\,. \tag{C.19c}$$

where in $\mathcal{L}_h$ we approximated $m_{\rm D}(\mathbf{1}+\eta')V \simeq m_{\rm D}V \simeq R^* M_R\,V = (RV)^*\hat{M}_N$. Thus, to a good degree, ν-N mixings in ν-N-Z and ν-N-h interactions are equal.

We note from Equation C.9a that $|m_\nu|$ is of order $|\Theta|^2|M_R|$. For sizeable Yukawa couplings of order ~ 1, neutrino masses of the order of an electronvolt require very heavy singlet neutrinos, $M_R \sim 10^{14}$ GeV. On the other hand, if the singlets have TeV-scale masses, production is suppressed due to the tininess of the mixing parameters, $\Theta_{ij} \sim 10^{-6}$, rendering detection at colliders impossible [431]. Motivation therefore exists to construct models with a low seesaw scale and naturally unsuppressed mixing.

The amount of literature available on the phenomenology associated with type I seesaw scenarios is vast and there is no intention to discuss the possible experimental signatures at this point. Instead, we limit ourselves to give some references. One has to note that existing experimental results do not suffice to significantly constrain the parameter space (Y_N^ν, M_R) in the simplest realizations, where the seesaw scale $\Lambda \sim M_R$ is large [410]. Further assumptions are henceforth usually made to render the theory more predictive, such as the presence of additional symmetries or a smaller seesaw scale, as previously noted. In the latter case, a particularly attractive scenario would be to have RHN masses of the order of the electroweak scale, which has received plenty of attention [372, 409, 410, 432]. For all three types, LHC phenomenology based on multi-lepton signatures is thoroughly discussed in [372] and aspects of indirectly probing the seesaw mechanisms through processes that violate lepton flavour and CP and change lepton electric dipole moments are reviewed in [433]. Constraints on $V_{\rm PMNS}$ (*i.e.* on the observable combination $|V_{\rm PMNS}V_{\rm PMNS}^\dagger|$) from universality tests and rare lepton decays calculated in [246] have been put to use in [434] to infer bounds within the type I parameter space.

C.2 Type II

A relativistically invariant Lagrangian allows for the existence of a Majorana mass term for the left-handed neutrinos contained in the electroweak doublets L, *i.e.*

$$\mathcal{L}_\nu^m = -\frac{1}{2}\overline{\nu_L^c}\,M_L\,\nu_L + \text{h.c.}\,, \tag{C.20}$$

provided one allows for lepton number violation. However, such a mass term violates gauge invariance because it has a weak isospin of -1 and a hypercharge of -2. Therefore it can only appear after the

breaking of $\mathcal{G}_{\rm SM}$ to $\mathrm{U}(1)_{\rm EM}$ through a Higgs field. The SM Higgs doublet H responsible for quark and charged lepton masses cannot play this role because there is no $\mathcal{G}_{\rm SM}$-invariant term of the form LLH, hence the mass term in Equation C.20 must be generated via at least one other Higgs field that is a complex triplet of $\mathrm{SU}(2)_L$. In fact, this corresponds to a simple extension of the leptonic Yukawa sector and scalar potential within the Higgs triplet model (HTM) [220] with a triplet of hypercharge +2 and is known as the seesaw mechanism of type II [14]. Lepton number is explicitly but softly broken by a dimension-3 term in the scalar potential. As in the HTM, when transforming to mass eigenstates, the scalar sector will consist of a doubly-charged, a singly-charged, a CP-even and a CP-odd neutral field, plus the usual three Goldstone bosons absorbed by the weak gauge bosons.

Writing the renormalizable Lagrangian is a pleasant exercise in representation theory, therefore we begin with a small detour to review some basic elements. A triplet $\vec{\Delta}$ of the adjoint of $\mathrm{SU}(2)_L$ has the form[1] $\vec{\Delta}_{\rm C} = (\Delta^1, \Delta^2, \Delta^3)^T$ in the Cartesian basis for the space of quantum states. This space corresponds to the vector space $V \sim \mathbb{C}^3$ spanned by the standard Cartesian basis vectors $\{\hat{e}_i\}$, with $(\hat{e}_i)_j = \delta_{ij}$, and state vectors $\vec{v} = v_i \hat{e}_i$ are acted upon by unitary matrices generated by three Hermitian matrices $\vec{T}_{\rm C}$ given by

$$T^1_{\rm C} = \begin{bmatrix} 0 & 0 & 0 \\ 0 & 0 & -i \\ 0 & i & 0 \end{bmatrix}, \quad T^2_{\rm C} = \begin{bmatrix} 0 & 0 & i \\ 0 & 0 & 0 \\ -i & 0 & 0 \end{bmatrix}, \quad T^3_{\rm C} = \begin{bmatrix} 0 & -i & 0 \\ i & 0 & 0 \\ 0 & 0 & 0 \end{bmatrix}. \tag{C.21}$$

These generators form the basis for the associative Lie algebra $\mathfrak{g} = \mathfrak{su}(2)$ (or $\mathfrak{so}(3)$) and satisfy the familiar commutation relations $[T^i_{\rm C}, T^j_{\rm C}] = i\epsilon^{ijk} T^k_{\rm C}$. It is more convenient to work in the one basis of V that leads to a set of basis matrices for $\mathfrak{g}$ in which the third generator is diagonal, so we may label the triplet components by their electric charges. This basis is the so-called spherical basis, where V is spanned by the complex unit vectors

$$\vec{e}_\pm = \mp \frac{1}{\sqrt{2}} (\hat{e}_1 \pm i\, \hat{e}_2), \qquad \vec{e}_0 = \hat{e}_3, \tag{C.22}$$

as is familiar from the spherical harmonic functions $Y_1^{1,0,-1}(\theta, \phi)$ [435]. The labels correspond to the eigenvalues $m = \{+1, 0, -1\}$ of $T^3_{\rm C}$. In this new basis, the generators are obtained by first performing a unitary similarity transformation

$$\vec{T}_{\rm C} \longrightarrow \vec{T}_{\tilde{\rm C}} = M^\dagger \vec{T}_{\rm C}\, M, \qquad \text{with} \qquad M = \begin{bmatrix} \frac{-1}{\sqrt{2}} & 0 & \frac{1}{\sqrt{2}} \\ \frac{-i}{\sqrt{2}} & 0 & \frac{-i}{\sqrt{2}} \\ 0 & 1 & 0 \end{bmatrix}, \tag{C.23}$$

giving

$$T^1_{\tilde{\rm C}} = \frac{1}{\sqrt{2}} \begin{bmatrix} 0 & 1 & 0 \\ 1 & 0 & 1 \\ 0 & 1 & 0 \end{bmatrix}, \quad T^2_{\tilde{\rm C}} = \frac{i}{\sqrt{2}} \begin{bmatrix} 0 & -1 & 0 \\ 1 & 0 & -1 \\ 0 & 1 & 0 \end{bmatrix}, \quad T^3_{\tilde{\rm C}} = \begin{bmatrix} 1 & 0 & 0 \\ 0 & 0 & 0 \\ 0 & 0 & -1 \end{bmatrix}. \tag{C.24}$$

These obey the same commutation relations as the generators $\vec{T}_{\rm C}$. Therefore they are still associated with the Cartesian coordinates $\{x, y, z\}$ and we require a combination of $T^1_{\tilde{\rm C}}$ and $T^2_{\tilde{\rm C}}$ that is associated with $\vec{e}_+$ and $\vec{e}_-$, *i.e.* two generators $T_\pm$. To begin, we work out the form of the adjoint triplet in this rotated representation. For that, we first observe that the transpose of M acts on the Cartesian basis vectors to transform to the spherical basis of $\mathbb{C}^3$ given in Equation C.22, *i.e.* $\vec{e}_m = M_{im}\, \hat{e}_i$, thus we find that components of vectors $\vec{v}$ are transformed using $M^\dagger$, since $(\vec{v}_{\rm sph})_m = \langle \vec{e}_m, \vec{v}_{\rm C} \rangle = M^*_{im} \langle \hat{e}_i, \vec{v}_{\rm C} \rangle = (M^\dagger)_{mi} v_{{\rm C},i}$.[2]

[1] In contrast to doublets, we write adjoint isovectors excplicitly as vectors, for notational clarity.

[2] This can also be inferred from inspecting the gauge-covariant derivative of a triplet field $\vec{\phi}$. Invariance of $|D_\mu \vec{\phi}|^2$ with $D_\mu \vec{\phi} = \partial_\mu \vec{\phi} - ig(\vec{A}_\mu \cdot \vec{T})\vec{\phi}$ under $\vec{T} \to M^\dagger \vec{T} M$ and $(\vec{A}_\mu, \vec{\phi}) \to (U\vec{A}_\mu, U\vec{\phi})$ demands the identification $U = M^\dagger$, such that $(\vec{\phi}, D_\mu \vec{\phi}) \to (M^\dagger \vec{\phi}, M^\dagger D_\mu \vec{\phi})$.

Hence the spherical form of the scalar triplet is reached through the transformation

$$\vec{\Delta}_{\rm sph} = \begin{bmatrix} |1,+1\rangle \\ |1,0\rangle \\ |1,-1\rangle \end{bmatrix} = M^\dagger \vec{\Delta}_{\rm C} = \begin{bmatrix} \frac{-1}{\sqrt{2}} & \frac{i}{\sqrt{2}} & 0 \\ 0 & 0 & 1 \\ \frac{1}{\sqrt{2}} & \frac{i}{\sqrt{2}} & 0 \end{bmatrix} \begin{bmatrix} \Delta^1 \\ \Delta^2 \\ \Delta^3 \end{bmatrix} . \tag{C.25}$$

Note that we haven't named the triplet states by their physical field content yet because of the subtle fact that their relative phases still need to be found. While the overall common phase is arbitrary, the relative phases between the states are essential for maintaining the correspondence between generators and basis quantum states as set by the commutation relations of the generators and their action on the basis states, which defines the construction of the adjoint representation. Cartesian states have the correspondence

$$T^i_{\rm C} \leftrightarrow \left|\Delta^i\right\rangle \implies [T^i_{\rm C}, T^j_{\rm C}] = i\varepsilon^{ijk} T^k_{\rm C} \leftrightarrow T^i_{\rm C}\left|\Delta^j\right\rangle = i\varepsilon^{ijk}\left|\Delta^k\right\rangle , \tag{C.26}$$

and one finds that

$$T^i_{\rm sph} \leftrightarrow \left|\Delta^i_{\rm sph}\right\rangle \implies [T^i_{\rm sph}, T^j_{\rm sph}] = iC^{ijk}_{\rm sph} T^k_{\rm sph} \leftrightarrow T^i_{\rm sph}|\Delta^j_{\rm sph}\rangle = iC^{ijk}_{\rm sph}\left|\Delta^k_{\rm sph}\right\rangle , \tag{C.27}$$

where $C^{ijk}_{\rm sph}$ are the spherical SU(2) structure constants, provided we select the set of generators

$$\{T^i_{\rm sph}\} = \left\{T_+ = T^1_{\tilde{\rm C}} + i\,T^2_{\tilde{\rm C}},\ T_0 = T^3_{\tilde{\rm C}},\ T_- = T^1_{\tilde{\rm C}} - i\,T^2_{\tilde{\rm C}}\right\} \tag{C.28}$$

and identify

$$T_+ \leftrightarrow \sqrt{2}\left|\Delta^{++}\right\rangle = \sqrt{2}(-\left|1,+1\right\rangle) , \quad T_0 \leftrightarrow \left|\Delta^+\right\rangle , \quad T_+ \leftrightarrow \sqrt{2}\left|\Delta^0\right\rangle = \sqrt{2}\left|1,-1\right\rangle . \tag{C.29}$$

We recognize $T_\pm$ as the usual raising and lowering matrices from angular momentum theory with the action $T_\pm\left|T,T_3\right\rangle = \sqrt{T(T+1) - T_3(T_3\pm 1)}\left|T,T_3\pm 1\right\rangle$ and T_0 gives $T_0\left|T,T_3\right\rangle = T_3\left|T,T_3\right\rangle$. Thus the scalar triplet in the spherical representation is found to be

$$\vec{\Delta}_{\rm sph} = \left(-\Delta^{++},\, \Delta^+,\, \Delta^0\right)^T \tag{C.30}$$

and the set of spherical generators of the adjoint representation is given by the matrices

$$\vec{T}_{\rm sph} = \left(\frac{1}{\sqrt{2}}T_+,\, T_0,\, \frac{1}{\sqrt{2}}T_-\right) = A\vec{T}_{\tilde{\rm C}} , \tag{C.31}$$

with the unitary matrix

$$A = \begin{bmatrix} \frac{1}{\sqrt{2}} & \frac{i}{\sqrt{2}} & 0 \\ 0 & 0 & 1 \\ \frac{1}{\sqrt{2}} & \frac{-i}{\sqrt{2}} & 0 \end{bmatrix} . \tag{C.32}$$

Notice that this matrix also rotates the vector $(\Delta^1, \Delta^2, \Delta^3)$ into $(\Delta^{++}, \Delta^+, \Delta^0)$. It is obvious that the transformation has to be the same as the transformation from $\vec{T}_{\tilde{\rm C}}$ to $\vec{T}_{\rm sph}$ because the commutator $[.\,,.]$ is linear in both of its arguments, therefore the generators need to be rotated exactly like the fields in order for the relations (C.26) to be altered to (C.29).

Equipped with the necessary group-theoretical background, we now intend to write the relevant Lagrangian terms in two commonly seen notations. The first uses the isovector $\vec{\Delta}$ explicity and the second features the field matrix

$$\Delta = \sqrt{2}\,\vec{\Delta}_{\rm C}\cdot\vec{\tau}_{\rm C} = \begin{bmatrix} \frac{\Delta^3}{\sqrt{2}} & \frac{\Delta^1 - i\Delta^2}{\sqrt{2}} \\ \frac{\Delta^1 + i\Delta^2}{\sqrt{2}} & -\frac{\Delta^3}{\sqrt{2}} \end{bmatrix} = \frac{1}{\sqrt{2}}\,\vec{\Delta}'_{\rm sph}\cdot\vec{\tau}_{\rm sph} = \begin{bmatrix} \frac{\Delta^+}{\sqrt{2}} & \Delta^{++} \\ \Delta^0 & -\frac{\Delta^+}{\sqrt{2}} \end{bmatrix} . \tag{C.33}$$

In the first form, $\vec{\Delta}$ is expanded in the Cartesian generators $\tau_{{\rm C},i} = \tau_i/2$ and in the second we defined

$$\vec{\Delta}'_{\rm sph} = \left(+\Delta^{++},\, \Delta^+,\, \Delta^0\right)^T , \tag{C.34}$$

and expand it in terms of the spherical generators

$$\vec{\tau}_{\rm sph} = (\tau_+\,,\tau_0\,,\tau_-) = \left(\begin{bmatrix} 0 & \sqrt{2} \\ 0 & 0 \end{bmatrix}, \begin{bmatrix} 1 & 0 \\ 0 & -1 \end{bmatrix}, \begin{bmatrix} 0 & 0 \\ \sqrt{2} & 0 \end{bmatrix}\right) = 2A\vec{\tau}_{\rm C}\,, \tag{C.35}$$

where $\tau_\pm = (\tau_1 \pm i\tau_2)/\sqrt{2}$ and $\tau_0 = \tau_3$, in analogy to (C.31). A is the matrix given in Equation C.32 and Δ transforms as $\Delta \to U\Delta U^\dagger$ under $\mathrm{SU}(2)_L$. To start with the vectorial form, a gauge-invariant Yukawa interaction with the neutrinos is formed with the symmetric triplet combination

$$\vec{\Psi}_{ij} = \frac{1}{\sqrt{2}}\,\overline{\tilde{L}_i}\,\vec{\tau}_{\rm sph}\,L_j = \left(\overline{\ell^c_{Li}}\ell_{Lj},\, \frac{1}{\sqrt{2}}\left(\overline{\nu^c_{Li}}\ell_{Lj} + \overline{\nu^c_{Lj}}\ell_{Li}\right),\, -\overline{\nu^c_{Li}}\nu_{Lj}\right)^T\,, \tag{C.36}$$

having the form

$$\mathcal{L}_{\rm Y}(\Delta, L) = -(Y_\Delta)_{ij}\,\vec{\Psi}_{ij}\cdot\vec{\Delta}'_{\rm sph} + \text{h.c.} = -(Y_\Delta)_{ij}\,\overline{\tilde{L}}_i\Delta L_j + \text{h.c.}\,, \qquad Y_\Delta = Y_\Delta^T\,. \tag{C.37}$$

The Clebsch-Gordan coefficient $1/\sqrt{3}$ has been absorbed in the Yukawa matrix Y_Δ.

When Δ^0 acquires its VEV v_Δ, the neutrinos gain a Majorana mass of order $Y_\Delta v_\Delta$ from the Yukawa term in Equation C.37. Notice that Y_Δ is the only source of flavour structure, therefore the type II seesaw is in a sense more 'economical' than the other types [436]. In particular, the Yukawa matrix elements can be extracted by knowing the light neutrino masses, v_Δ and the PMNS matrix,

$$(Y_\Delta)_{ij} = \frac{1}{v_\Delta}\left(V^*_{\rm PMNS}\,\hat{m}_\nu\,V^\dagger_{\rm PMNS}\right)_{ij}\,. \tag{C.38}$$

There are two reasons for why v_Δ is required to be small. First, if v_Δ were not small, Y_Δ would again have to be unnaturally tiny in order to explain the observed neutrino mass scale; for the same fact, Dirac neutrinos are commonly considered an unappealing option. Second and most important, v_Δ contributes to the weak gauge boson masses and hence to the ρ parameter [437]. Since the relation $\rho = m_W^2/(m_Z^2\mathrm{c}_\mathrm{w}^2) = 1$ is experimentally verified to be true within the existing uncertainty margins [78], v_Δ has to be quite small compared to v, the VEV of H, as the contribution to m_W^2 and m_Z^2 is, respectively, gv_Δ and $2g^2v_\Delta/\mathrm{c}_\mathrm{w}^2$. In fact, since at leading order

$$\rho = \frac{m_W^2}{m_Z^2\,\mathrm{c}_\mathrm{w}^2} = \frac{v^2}{v^2 + 2v_\Delta^2}\,, \tag{C.39}$$

the experimental 1σ result $\rho_{\rm exp} = 1.0004 \pm 0.00024$ [78] implies that $v_\Delta = \mathcal{O}(1\text{ GeV})$ at most.

The smallness of v_Δ is achieved via a seesaw mechanism that is quite different from what occurs in types I and III. One starts with the cubic scalar potential term allowed by the gauge symmetry,

$$\mathcal{V}_3(H,\Delta) = \mu_\Delta\left(H^\dagger\vec{\tau}_{\rm sph}\tilde{H}\right)\cdot\vec{\Delta}_{\rm sph} + \text{h.c.} = \mu_\Delta\sqrt{2}\,H^\dagger\Delta\tilde{H} + \text{h.c.}\,, \tag{C.40}$$

with a mass-valued parameter μ_Δ in which we again absorbed the Clebsch-Gordan coefficient $1/\sqrt{3}$. It can be taken to be real due to the possibility of CP phase redefinitions of H and Δ (though there exists the possibility for spontaneous CP violation [438]). Together with the Yukawa term, the μ_Δ term violates lepton number. Attributing LNV to the μ_Δ term, a lepton number of -2 is assigned to Δ and 0 to the Higgs doublet H, thus $\mathcal{V}_3$ violates lepton number by two units. There remains a quadratic term

$$\mathcal{V}_2(H,\Delta) = -\mu_H^2 H^\dagger H + M_\Delta^2\,\vec{\Delta}^\dagger\cdot\vec{\Delta} = -\mu_H^2 H^\dagger H + M_\Delta^2\,\mathrm{Tr}[\Delta^\dagger\Delta]\,, \tag{C.41}$$

where $\vec{\Delta}$ can be either $\vec{\Delta}_{\rm C}$ or $\vec{\Delta}_{\rm sph}$, and a quartic term

$$\begin{aligned}\mathcal{V}_4(H,\Delta) &= \lambda_1\,(H^\dagger H)^2 + \lambda_2\,(\vec{\Delta}^\dagger\cdot\vec{\Delta})^2 + \lambda_3\,(H^\dagger H)(\vec{\Delta}^\dagger\cdot\vec{\Delta}) + \lambda_4\,(H^\dagger\vec{\tau}H)\cdot(\vec{\Delta}^\dagger\,\vec{T}\,\vec{\Delta}) \\ &\quad + \lambda_5\,(\vec{\Delta}^\dagger\,\vec{T}\,\vec{\Delta})\cdot(\vec{\Delta}^\dagger\,\vec{T}\,\vec{\Delta}) \\ &= \lambda_1\,(H^\dagger H)^2 + \tilde{\lambda}_2\,(\mathrm{Tr}[\Delta^\dagger\Delta])^2 + \tilde{\lambda}_3\,(H^\dagger H)\,\mathrm{Tr}[\Delta^\dagger\Delta] + \tilde{\lambda}_4\,H^\dagger\Delta\Delta^\dagger H \\ &\quad + \tilde{\lambda}_5\,\mathrm{Tr}[(\Delta^\dagger\Delta)^2]\,.\end{aligned} \tag{C.42}$$

Here the combinations $H^\dagger\vec{\tau}H$ and $\vec{\Delta}^\dagger\vec{T}\vec{\Delta}$ are symbolic for the corresponding Cartesian and spherical

combinations. To be explicit, the λ_4 and λ_5 terms can be written as

$$\begin{aligned}(H^\dagger \vec{\tau} H)\cdot(\vec{\Delta}^\dagger \vec{T} \vec{\Delta}) &= (H^\dagger \vec{\tau}_{\rm C} H)\cdot(\vec{\Delta}^\dagger_{\rm C} \vec{T}_{\rm C} \vec{\Delta}_{\rm C}) = (H^\dagger \vec{\tau}_{\rm C} H)\cdot(\vec{\Delta}^\dagger_{\rm sph} \vec{T}_{\tilde{\rm C}} \vec{\Delta}_{\rm sph}) \\ &= \frac{1}{2}(H^\dagger \vec{\tau}_{\rm sph} H)\cdot P_{13}\cdot(\vec{\Delta}^\dagger_{\rm sph} \vec{T}_{\rm sph} \vec{\Delta}_{\rm sph}) \end{aligned} \tag{C.43}$$

and

$$\begin{aligned}(\vec{\Delta}^\dagger \vec{T} \vec{\Delta})\cdot(\vec{\Delta}^\dagger \vec{T} \vec{\Delta}) &= (\vec{\Delta}^\dagger_{\rm C} \vec{T}_{\rm C} \vec{\Delta}_{\rm C})\cdot(\vec{\Delta}^\dagger_{\rm C} \vec{T}_{\rm C} \vec{\Delta}_{\rm C}) = (\vec{\Delta}^\dagger_{\rm sph} \vec{T}_{\tilde{\rm C}} \vec{\Delta}_{\rm sph})\cdot(\vec{\Delta}^\dagger_{\rm sph} \vec{T}_{\tilde{\rm C}} \vec{\Delta}_{\rm sph}) \\ &= (\vec{\Delta}^\dagger_{\rm sph} \vec{T}_{\rm sph} \vec{\Delta}_{\rm sph})\cdot P_{13}\cdot(\vec{\Delta}^\dagger_{\rm sph} \vec{T}_{\rm sph} \vec{\Delta}_{\rm sph})\,. \end{aligned} \tag{C.44}$$

P_{13} is the $1 \leftrightarrow 3$ permutation matrix acting in the space of generators originating from the matrix A in Equation C.32,

$$P_{13} = A^* A^\dagger = \begin{bmatrix} 0 & 0 & 1 \\ 0 & 1 & 0 \\ 1 & 0 & 0 \end{bmatrix}. \tag{C.45}$$

The two sets of couplings are simply related via

$$\tilde{\lambda}_2 = \lambda_2 - \lambda_5\,, \qquad \tilde{\lambda}_5 = 2\lambda_5\,. \qquad \tilde{\lambda}_3 = \lambda_3 - \frac{\lambda_4}{2}\,, \qquad \tilde{\lambda}_4 = \lambda_4\,. \tag{C.46}$$

Extremization of the potential with respect to the neutral components of H and Δ in the approximation of small Δ^0 yields

$$\frac{\partial(\mathcal{V}_2+\mathcal{V}_3+\mathcal{V}_4)}{\partial\Delta^0} \approx \frac{\partial(\mathcal{V}_2+\mathcal{V}_3)}{\partial\Delta^0} = \mu_\Delta \Delta^{0*} + M_\Delta(\varphi^{0*})^2 = 0\,, \tag{C.47}$$

thus

$$v_\Delta \approx -\frac{\mu_\Delta v^2}{M_\Delta^2} \tag{C.48}$$

and neutrino masses will be of the order of $Y_\Delta \mu_\Delta v^2/M_\Delta^2$. v_Δ turns out to be small if $M_\Delta \gg v, \mu_\Delta$, which is the usual assumption in the type II seesaw mechanism. μ_Δ is expected to not become excessively large because it violates lepton number and is therefore self-renormalized.

Contrary to what happens in the other two types, the leptons don't mix with new heavy states, therefore no trilinear couplings between scalars, leptons and gauge bosons are generated. However, there will be interactions with the gauge bosons stemming from the covariant derivative $(D_\mu \vec{\Delta})^\dagger \cdot D^\mu \vec{\Delta}$. The $\Delta\Delta V_\mu$ interaction terms responsible for production at colliders can be found in [372], with the Feynman rules for three-point and four-point interactions involving the scalar mass eigenstates and the gauge bosons listed in Appendix C of the same reference.

The scalar sector of the type II seesaw model is thoroughly treated in [438] and its LHC signals are discussed in [372, 374, 434, 438, 439], for example. LFV processes and CP aspects are included in the review [433]. Further constraints from $h \to \gamma\gamma$ and electroweak precision observables are examined in [440].

C.3 Type III

The seesaw mechanism of type III [15, 16] introduces n fermionic Majorana triplets

$$\vec{\Sigma}_i = (\Sigma_i^1, \Sigma_i^2, \Sigma_i^3)\,, \qquad \vec{\Sigma}_i = P_R \vec{\Sigma}_i\,, \qquad i = 1, \ldots, n \tag{C.49}$$

of $\mathrm{SU}(2)_L$ with hypercharge $Y = 0$, which are usually chosen to be right-chiral. It is very similar to the type I seesaw model, in the sense that neutrinos gain their mass through the interplay of a Yukawa interaction with the SM Higgs doublet and a heavy Majorana mass of new neutral fermions, though its phenomenology is far richer. With the performed work in the discussion of the type II model, writing the Lagrangian with the fermionic triplet is easy. The triplet can be written in the Cartesian or in the spherical representation.

Suppressing the flavour index i, one has

$$\vec{\Sigma}_{\rm C} = \left(\Sigma^1,\, \Sigma^2,\, \Sigma^3\right)^T \;\stackrel{M^\dagger}{\longrightarrow}\; \vec{\Sigma}_{\rm sph} = \left(-\Sigma^+,\, \Sigma^0,\, \Sigma^-\right)^T \,, \tag{C.50}$$

M being the familiar transformation matrix from Equation C.23. As before, we can alternatively opt for the matrix notation with

$$\Sigma = \sqrt{2}\,\vec{\Sigma}_{\rm C}\cdot\vec{\tau}_{\rm C} = \begin{bmatrix} \frac{\Sigma^3}{\sqrt{2}} & \frac{\Sigma^1-i\Sigma^2}{\sqrt{2}} \\ \frac{\Sigma^1+i\Sigma^2}{\sqrt{2}} & -\frac{\Sigma^3}{\sqrt{2}} \end{bmatrix} = \frac{1}{\sqrt{2}}\,\Sigma'_{\rm sph}\cdot\vec{\tau}_{\rm sph} = \begin{bmatrix} \frac{\Sigma^0}{\sqrt{2}} & \Sigma^+ \\ \Sigma^- & -\frac{\Sigma^0}{\sqrt{2}} \end{bmatrix} . \tag{C.51}$$

where $\vec{\Sigma}'_{\rm sph}$ is defined with a positive sign for the first component, as was the case for the scalar triplet $\vec{\Delta}'_{\rm sph}$ in Equation C.34. Left-handed fields are introduced with the charge conjugate,

$$\Sigma^c = \begin{bmatrix} \frac{\Sigma^{3c}}{\sqrt{2}} & \frac{\Sigma^{1c}+i\Sigma^{2c}}{\sqrt{2}} \\ \frac{\Sigma^{1c}-i\Sigma^{2c}}{\sqrt{2}} & -\frac{\Sigma^{3c}}{\sqrt{2}} \end{bmatrix} = \begin{bmatrix} \frac{\Sigma^{0c}}{\sqrt{2}} & \Sigma^{+c} \\ \Sigma^{-c} & -\frac{\Sigma^{0c}}{\sqrt{2}} \end{bmatrix} , \tag{C.52}$$

We now write the type III seesaw Lagrangian employing the compact matrix notation. For this end, we define

$$\Psi_\Sigma \equiv \Sigma + \tilde{\Sigma}\,, \tag{C.53}$$

where the left-handed part is given by

$$\tilde{\Sigma} = \epsilon\,\Sigma^c\,\epsilon^{-1} = \begin{bmatrix} \frac{\Sigma^{0c}}{\sqrt{2}} & \Sigma^{-c} \\ \Sigma^{+c} & -\frac{\Sigma^{0c}}{\sqrt{2}} \end{bmatrix} , \qquad \epsilon = i\tau_2\,. \tag{C.54}$$

Apart from a gauge-kinetic term

$$\mathcal{L}_{\rm kin}(\Psi_\Sigma, W_\mu^{1,2,3}) = i{\rm Tr}[\bar{\Psi}_\Sigma \not{D}\Psi_\Sigma] = i{\rm Tr}[\bar{\Sigma}\not{D}\Sigma] + i{\rm Tr}[\overline{\tilde{\Sigma}}\not{D}\tilde{\Sigma}]\,, \tag{C.55}$$

one has a Yukawa interaction involving a $(3\times n)$-dimensional Yukawa matrix Y,

$$\mathcal{L}_{\rm Y}(L,\Psi_\Sigma,H) = -\sqrt{2}\,Y_{ij}\,\bar{L}_i\Psi_{\Sigma,j}\tilde{H} + {\rm h.c.} = -\sqrt{2}\,Y_{ij}\,\bar{L}_i\Sigma_j\tilde{H} + {\rm h.c.}\,, \tag{C.56}$$

(using $\bar{L}\tilde{\Sigma}=0$) and a Majorana mass term for the triplet,

$$\mathcal{L}_{\rm M}(\Psi_\Sigma) = -\frac{1}{2}{\rm Tr}[\overline{\Psi}_\Sigma M_\Sigma \Psi_\Sigma + {\rm h.c.}] = -\frac{1}{2}{\rm Tr}[\overline{\tilde{\Sigma}} M_\Sigma \Sigma + \overline{\Sigma} M_\Sigma^* \tilde{\Sigma}]\,, \tag{C.57}$$

the order of the symmetric mass matrix M_Σ being assumed to be much higher than Yv. We omitted the summation over flavours in $\mathcal{L}_{\rm kin}$ and $\mathcal{L}_{\rm M}$, the traces are over the SU(2) indices. M_Σ is a symmetric complex $(n\times n)$-dimensional matrix giving the same mass to all three members of the triplet Σ_i. Note also that the normalization of the Yukawa term in Equation C.56 is chosen such that, in the vectorial notation, $\vec{\Sigma}_{\rm C}$ is contracted with $\vec{\tau}$ rather than with $\vec{\tau}/2$, as seems to be the case in the overwhelming majority of the literature. From the notation with Ψ_Σ, it is obvious that the Lagrangian can be expressed in terms of the weak eigenstate combinations

$$E'_i = \Sigma_i^- + \Sigma_i^{+c}\,, \quad N'_i = \Sigma_i^0 + \Sigma_i^{0c}\,. \tag{C.58}$$

E'_i and N'_i are, respectively, Dirac and Majorana fermions and E'_i is negatively charged. Since the triplet $\vec{\Sigma}$ is right-handed, we have

$$E'_{Li} = \Sigma_i^{+c}\,, \quad E'_{Ri} = \Sigma_i^-\,, \quad N'_{Li} = \Sigma_i^{0c}\,, \quad N'_{Ri} = \Sigma_i^0\,. \tag{C.59}$$

We now work out the mass eigenstate Lagrangian, which for the neutrinos and the heavy Majorana fermions N'_i proceeds exactly like in the type I case,[3]

$$\mathcal{L}^m_{\nu N} = -\frac{1}{2}(\bar{\nu}'_L\;\; \bar{N}'_L)\,\mathcal{M}_{\nu N}\begin{bmatrix} \nu'^c_L \\ N'_R \end{bmatrix} + {\rm h.c.}\,, \qquad \mathcal{M}_{\nu N} = \begin{bmatrix} \mathbf{0} & m_{\rm D} \\ m_{\rm D}^T & M_\Sigma \end{bmatrix} , \tag{C.60}$$

[3]Contrary to the $\nu-\chi$ notation we employed for type I, light neutrino flavour and mass eigenstates are now denoted by ν' and ν, respectively.

with $m_{\rm D} = Yv/\sqrt{2}$. Like for type I, $\mathcal{M}_{\nu N}$ is $(3+n)\times(3+n)$-dimensional and the mass matrix expressions coincide (*cf.* Equation C.9a, C.9b). A mass matrix of equal dimension is responsible for the mixing of the heavy Dirac fermions and the charged leptons,

$$\mathcal{L}^m_{\ell E} = -(\bar{\ell}'_L \;\; \bar{E}'_L)\,\mathcal{M}_{\ell E}\begin{bmatrix}\ell'_R\\ E'_R\end{bmatrix} + \text{h.c.}\,, \qquad \mathcal{M}_{\ell E} = \begin{bmatrix} m_\ell & \sqrt{2}m_{\rm D}\\ 0 & M_\Sigma\end{bmatrix}, \tag{C.61}$$

where $m_\ell = Y^\ell v/\sqrt{2}$ is the (3×3)-dimensional charged lepton mass matrix. The relative factor of $\sqrt{2}$ between m_ℓ and $\sqrt{2}m_{\rm D}$ can be traced back to the normalization of the fields in the matrices Σ and $\tilde{\Sigma}$. Since $\mathcal{M}_{\ell E}$ is a Dirac mass matrix, it has to be diagonalized by means of a bi-unitary transformation,

$$U^\dagger_{\ell E,L}\,\mathcal{M}_{\ell E}\,V_{\ell E,R} = D_{\ell E} = \begin{bmatrix}\hat{m}_\ell & \mathbf{0}\\ \mathbf{0} & \hat{M}_E\end{bmatrix}, \tag{C.62}$$

with the diagonal mass matrices

$$\hat{m}_\ell = \text{diag}(m_e,\, m_\mu,\, m_\tau)\,, \qquad \hat{M}_E = \text{diag}(M_{E,1},\, M_{E,2},\ldots,\, M_{E,n})\,. \tag{C.63}$$

Finding $U_{\ell E,L}$ and $V_{\ell E,R}$ proceeds similarly as in the type I case, but is somewhat more cumbersome. One first notes that they diagonalize the Hermitian matrices $\mathcal{M}_{\ell E}\,\mathcal{M}^\dagger_{\ell E}$ and $\mathcal{M}^\dagger_{\ell E}\,\mathcal{M}_{\ell E}$, *i.e.*

$$U^\dagger_{\ell E,L}\,\mathcal{M}_{\ell E}\,\mathcal{M}^\dagger_{\ell E}\,U_{\ell E,L} = D^2_{\ell E}\,, \qquad V^\dagger_{\ell E,R}\,\mathcal{M}^\dagger_{\ell E}\,\mathcal{M}_{\ell E}\,V_{\ell E,R} = D^2_{\ell E}\,. \tag{C.64}$$

Including the neutrinos, we use the factorization ansatz

$$U_{\nu N} = \Omega_0\Gamma_0\,, \qquad U_{\ell E,L} = \Omega_L\Gamma_L\,, \qquad V_{\ell E,R} = \Omega_R\Gamma_R\,, \tag{C.65}$$

with $\Omega_{0,L,R}$ and $\Gamma_{0,L,R}$ having the same forms as in type I. Defining

$$\eta_0 = -\frac{1}{2}R_0R_0^\dagger\,, \qquad \eta'_0 = -\frac{1}{2}R_0^\dagger R_0\,, \qquad R_0 = m_{\rm D}^* M_\Sigma^{-1*}\,, \tag{C.66}$$

and

$$\eta_\Sigma = -\frac{1}{2}R_\Sigma R_\Sigma^\dagger\,, \qquad \eta'_\Sigma = -\frac{1}{2}R_\Sigma^\dagger R_\Sigma\,, \qquad R_\Sigma = \sqrt{2}m_{\rm D}^* M_\Sigma^{-1*}\,, \tag{C.67}$$

yields up to order M_Σ^{-2} the block-diagonalizing matrices [430, 434]

$$\Omega_0 = \begin{bmatrix}\mathbf{1}+\eta_0 & R_0\\ -R_0^\dagger & \mathbf{1}+\eta'_0\end{bmatrix}, \tag{C.68a}$$

$$\Omega_L = \begin{bmatrix}\mathbf{1}+\eta_\Sigma & R_\Sigma\\ -R_\Sigma^\dagger & \mathbf{1}+\eta'_\Sigma\end{bmatrix}, \tag{C.68b}$$

$$\Omega_R = \begin{bmatrix}\mathbf{1} & m_\ell^\dagger R_\Sigma M_\Sigma^{-1*}\\ -M_\Sigma^{-1}R_\Sigma^\dagger m_\ell & \mathbf{1}\end{bmatrix}. \tag{C.68c}$$

Final diagonalization is then achieved with

$$\Gamma_0 = \begin{bmatrix}U_0 & \mathbf{0}\\ \mathbf{0} & V_0\end{bmatrix}, \qquad \Gamma_L = \begin{bmatrix}U_L^\ell & \mathbf{0}\\ \mathbf{0} & V_L\end{bmatrix}, \qquad \Gamma_R = \begin{bmatrix}U_R^\ell & \mathbf{0}\\ \mathbf{0} & V_R\end{bmatrix}, \tag{C.69}$$

U_L^ℓ (U_R^ℓ) being the (3×3)-dimensional unitary matrices diagonalizing m_ℓ from the left (right) and U_0 diagonalizes m_ν. In analogy to Equation C.13, weak and mass eigenstates are related via

$$\begin{bmatrix}\nu'_L\\ N'_R\end{bmatrix} = U_{\nu N}\begin{bmatrix}\nu_L\\ N_R\end{bmatrix} = \begin{bmatrix}[(1+\eta_0)U_0]\,\nu_L + [R_0V_0]\,N_R\\ -[R_0^\dagger U_0]\,\nu_L + [(1+\eta'_0)V_0]\,N_R\end{bmatrix}, \tag{C.70a}$$

$$\begin{bmatrix}\ell'_L\\ E'_L\end{bmatrix} = U_{\ell E,L}\begin{bmatrix}\ell_L\\ E_L\end{bmatrix} = \begin{bmatrix}[(1+\eta_\Sigma)U_L^\ell]\,\ell_L + [R_\Sigma V_L]\,E_L\\ -[R_\Sigma^\dagger U_L^\ell]\,\ell_L + [(1+\eta'_\Sigma)V_L]\,E_L\end{bmatrix}, \tag{C.70b}$$

$$\begin{bmatrix} \ell'_R \\ E'_R \end{bmatrix} = U_{\ell E,R} \begin{bmatrix} \ell_R \\ E_R \end{bmatrix} = \begin{bmatrix} U_R\,\ell_R + [m_\ell^\dagger\, R_\Sigma M_\Sigma^{-1*} V_R]\, E_R \\ -[M_\Sigma^{-1} R_\Sigma^\dagger m_\ell U_R]\,\ell_R + V_R\, E_L \end{bmatrix} . \tag{C.70c}$$

The ℓ_L-ν_L charged current mixing matrix now receives a contribution from the mixing in the charged lepton sector,

$$V_{\rm PMNS} = U_L^{\ell\dagger}\,(\mathbf{1} + \eta_\Sigma^\dagger + \eta_0)\,U_0 + \mathcal{O}(R^3)\,, \tag{C.71}$$

meaning that here unitarity of $V_{\rm PMNS}$ is also violated at the order $m_{\rm D}^2 M_\Sigma^{-2}$. One can as well easily show that the difference in mass of the physical N and E fields at tree-level is of the order of the light neutrino mass and is therefore negligible [430]. We can therefore set

$$\hat{M}_N \simeq \hat{M}_E \equiv \hat{M} = {\rm diag}\,(M_1,\, M_2, \ldots,\, M_n)\ . \tag{C.72}$$

A more considerable difference than the splittings induced by the mixing is caused by quantum corrections [395]. Within the multiplet, one-loop effects generate a splitting of $\Delta M = M_{E^\pm} - M_N = 166$ MeV, which opens the decay channel to pions [373], a potentially interesting collider signature.

Turning finally to the interactions with the gauge and Higgs bosons, these are

$$\mathcal{L}_{\rm cc} = -\frac{g}{\sqrt{2}}\,[\bar\ell\ \bar E]\,\not{W}^-\ (g_L^{\rm cc} P_L + g_R^{\rm cc} P_R) \begin{bmatrix} \nu \\ N \end{bmatrix} + {\rm h.c.}\,, \tag{C.73a}$$

$$\mathcal{L}_{\rm nc}^{\ell EZ} = -\frac{g}{{\rm c_w}}\,[\bar\ell\ \bar E]\,\not{Z}\ (g_L^{\rm nc} P_L + g_R^{\rm nc} P_R) \begin{bmatrix} \ell \\ E \end{bmatrix}\,, \tag{C.73b}$$

$$\mathcal{L}_{\rm nc}^{\ell EA} = -e\,[\bar\ell\ \bar E]\,\not{A} \begin{bmatrix} \ell \\ E \end{bmatrix}\,, \tag{C.73c}$$

$$\mathcal{L}_{\rm nc}^{\nu N} = -\frac{g}{{\rm c_w}}\,[\bar\nu\ \bar N]\,\not{Z}\, g_\nu^{\rm nc} P_{\rm L} \begin{bmatrix} \nu \\ N \end{bmatrix}\,, \tag{C.73d}$$

$$\mathcal{L}_h^{\ell E} = -[\bar\ell\ \bar E]\ \left(g_L^{h\ell E} P_L + g_R^{h\ell E} P_R\right) \begin{bmatrix} \ell \\ E \end{bmatrix} h\,, \tag{C.73e}$$

$$\mathcal{L}_h^{\nu N} = -\frac{1}{\sqrt{2}}[\bar\nu\ \bar N]\ \left(g_L^{h\nu N} P_L + g_R^{h\nu N} P_R\right) \begin{bmatrix} \nu \\ N \end{bmatrix} h\,. \tag{C.73f}$$

The explicit forms of the coupling matrices g_i can be found in [441], though care should be taken due to some differences in the conventions applied here, most notably the exchange $Y \to Y^T$ and the fact that we are not working in a basis where M_Σ is diagonal. Staying at leading order, we find the particular terms

$$\mathcal{L}_{\rm nc}^{\nu N} = -\frac{g}{2{\rm c_w}}\,\bar\nu_L\,\not{Z}\,V_{\rm PMNS}^\dagger\, m_{\rm D}^*\, M_\Sigma^{-1*}\, V_0\, N_L + {\rm h.c.} = -\frac{g}{2{\rm c_w}}\bar\nu'_L\,\not{Z}\,\Theta_0\, N_L + {\rm h.c.}\,, \tag{C.74}$$

$$\mathcal{L}_h^{\nu N} = -\frac{1}{\sqrt{2}}\,\bar\nu_L\, V_{\rm PMNS}^\dagger\, \frac{m_{\rm D}^*\sqrt{2}}{v}\, V_0^*\, N_R\, h + {\rm h.c.} = -\frac{g}{2m_W}\bar\nu'_L\,\Theta_0\,\hat{M}\, N_R\, h + {\rm h.c.}\,, \tag{C.75}$$

where we defined

$$\Theta_0 \equiv R_0 V_0 \tag{C.76}$$

in analogy to the mixing matrix appearing in type I (*cf.* Equation C.18) and we used $m_{\rm D}^* M^{-1*} = R_0$ and $V_0^T M_\Sigma V_0 = \hat{M}_N = \hat{M}$. Similarly, we obtain in the charged sector

$$\mathcal{L}_{\rm nc}^{\ell EZ}(\ell_L, E_L) = -\frac{g}{{\rm c_w}}\,\bar\ell_L\,\not{Z}\, m_{\rm D}^*\, M_\Sigma^{-1*}\, V_L\, E_L + {\rm h.c.} = -\frac{g}{\sqrt{2}{\rm c_w}}\bar\ell'_L\,\not{Z}\,\Theta_L\, E_L + {\rm h.c.}\,, \tag{C.77}$$

$$\mathcal{L}_h^{\ell E}(\ell_L, E_R) = -\bar\ell_L\,\frac{m_{\rm D}^*\sqrt{2}}{v}\, V_L^*\, E_R\, h + {\rm h.c.} = -\frac{g}{\sqrt{2}m_W}\bar\ell_L\,\Theta_L\,\hat{M}\, E_R\, h + {\rm h.c.}\,, \tag{C.78}$$

with the mixing

$$\Theta_L \equiv R_\Sigma V_L\,. \tag{C.79}$$

Hence the mixing in ν-N-Z/h and ℓ-E-Z/h interactions in the type III seesaw mechanism is, to order $m_{\rm D}M_{\rm heavy}^{-1}$, exactly like the mixing in ν-N-Z/h interactions in type I, *cf.* Section C.1. This leads to flavour-violating neutral current interactions involving the SM leptons suppressed at the order $m_{\rm D}^2 M_{\rm heavy}^{-2}$. Moreover, rare decays such as $\mu \to 3e$ can occur at tree-level, while in type I these are only enabled at loop order due to the absence of tree-level charged lepton mixing. Notice that the model involves mixing in the interaction of ℓ and E with the Z boson (therefore leading to FCNC), but not with the photon. The mixing with the Z is traced to the fact that the Z couples to, say, E_L with $g_{E_L} = T^3 - {\rm s}_{\rm w}^2 Q = -{\rm c}_{\rm w}^2$, but to ℓ_L with $g_{\ell_L} = -\frac{1}{2} + {\rm s}_{\rm w}^2$. On the other hand, the electric charges of both fermions coupling to the photon are equal by means of the inherent $\mathrm{U}(1)_{\rm EM}$ gauge symmetry, therefore no mixing appears in the interaction with the photon field.

Collider search strategies for the type III seesaw model with the seesaw messenger masses at the electroweark scale are systematically discussed in [372], without counting the number of hard jets for signal discrimination. Reference [373] discusses the type III LHC phenomenology with treatment of events containing jets, events violating lepton or flavour number and events containing displaced decays of the heavy charged leptons. The latter signature is shown to be possible if the quantity $|\sum_j Y_{1j} v^2/M_1|$ is smaller than ~ 0.05 eV, leading to $E^\pm \to N\pi^\pm$ decays with decay lengths of the order of several cm, though the pions would presumably be too soft to be measured. Low-energy phenomenology consisting of universality breaking and lepton number and lepton flavour violating decays with the corresponding bounds on the mixing matrix $V_{\rm mix}$ is discussed in [434].

C.4 Inverse and linear seesaw mechanisms

For completeness, we finalize this appendix with a quick mention of the double or inverse (ISS) [213] and the linear (LS) [214] seesaw mechanism. These frameworks exploit the fact that lepton number is conserved in the SM. Hence one might propose the existence of new singlet fermions coupled in a lepton number violating manner, these couplings being very small, contrary to the type I/III case, where the Majorana mass is large. If one adds two types of singlet fermions, one set of RH neutrinos N_k and a vector-like singlet S, then the mass matrices are

$$\mathcal{M}_{\rm ISS}: \begin{array}{c} \\ \overline{\nu^c} \\ \overline{N} \\ \overline{S^c} \end{array} \begin{array}{c} \begin{array}{ccc} \nu & N^c & S \end{array} \\ \begin{bmatrix} 0 & Y\langle H\rangle_0 & 0 \\ Y^T\langle H\rangle_0 & 0 & M \\ 0 & M^T & \mu \end{bmatrix} \end{array}, \quad \mathcal{M}_{\rm LS}: \begin{array}{c} \\ \overline{\nu^c} \\ \overline{N} \\ \overline{S^c} \end{array} \begin{array}{c} \begin{array}{ccc} \nu & N^c & S \end{array} \\ \begin{bmatrix} 0 & Y\langle H\rangle_0 & \epsilon\, y\langle H\rangle_0 \\ Y^T\langle H\rangle_0 & 0 & M \\ \epsilon\, y^T\langle H\rangle_0 & M^T & 0 \end{bmatrix} \end{array}. \tag{C.80}$$

$Y\langle H\rangle_0$ is a Dirac mass matrix coupling ν_L to N, μ and ϵ are small LNV parameters and $y \sim 1$ is a further Yukawa matrix. The μ and ϵ terms guarantee non-vanishing entries for the $\overline{\nu^c}\nu$ term upon block diagonalization. One ends up with the small Majorana neutrino masses

$$m_\nu^{\rm ISS} \simeq -\mu\langle H\rangle_0^2\, Y^T M^{-2} Y\,, \qquad m_\nu^{\rm LS} \simeq \epsilon\langle H\rangle_0^2\, y^T M^{-1} Y\,. \tag{C.81}$$

It is natural to assume that μ and ϵ and hence the entries of m_ν remain small under renormalization group running. However, LFV processes are unaffected by these parameters and so they do not suffer from this suppression. Additionally, the new fermionic particles may be light enough to allow for production in colliders. In particular, the RHNs in the ISS scenario will form a pseudo-Dirac neutrino pair, possibly with a mass that is light enough for production at the LHC [409].

APPENDIX D

Decomposition of one-loop tensor integrals

D.1 Introduction

One-loop calculations are a standard occurrence in most perturbation theory computations of observables in particle physics today — either the processes occur only at the loop-level or the current or projected experimental sensitivity goes much beyond tree-level predictions. The technical challenge lies in evaluating complicated tensorial integrals over internal loop 4-momenta. Numerous techniques have been developed over the last few decades to evaluate such integrals, most notably dimensional regularization (DR) [367] for the treatment of eventually appearing UV and IR divergences. A compact overview on DR and related mathematical techniques can be found in [442], which is relied on for this appendix to a large extent. Our aim is to succinctly introduce the form used to present some of the one-loop expressions in this thesis, namely the Passarino-Veltman (PV) notation and the associated reduction scheme [443, 444]. This scheme is based on DR for treating the UV divergences, not the IR divergences due to mass and collinear singularities. The reader should however bear in mind that, although the PV procedure is still widely used for simple cases, more elaborate methods have been developed in recent years for calculating one-loop results needed for less trivial configurations, like multi-parton final states or special pathological configurations of external momenta leading to new unwanted divergences. We refer to [445] for a thorough modern treatment.

A rank-p one-loop tensor integral in $d = 4 - \epsilon$ dimensions with n connecting legs, each representing an external particle with mass m_i and 4-momentum p_i, has the form

$$T_n^{\mu_1 \cdots \mu_p} = \mu^\epsilon \int \frac{d^d \ell}{(2\pi)^d} \frac{\ell^{\mu_1} \dots \ell^{\mu_p}}{\mathfrak{D}_0 \mathfrak{D}_1 \dots \mathfrak{D}_{n-1}} , \tag{D.1}$$

where the dependence of the denominator factors on the loop particle momenta and masses can be assigned as[1]

$$\mathfrak{D}_i = (\ell + k_i)^2 - m_i^2 + i\epsilon , \qquad k_i = \sum_{j=1}^{i} p_j , \qquad k_0 = \sum_{j=1}^{n} p_j = 0 \tag{D.2}$$

and μ is the renormalization scale, formally introduced to isolate the dimensionality of the coupling constant. Note that we employ the common practice of defining the external momenta to be ingoing (see Figure D.1) and the momentum of the 0th propagator is simply the loop momentum without offset. By power counting, we also infer that the 4-dimensional integral will be UV divergent if the power of ℓ in the numerator of T_n is larger than or equal to $2n - 4$. If the theory is renormalizable, the highest such power that can be generated by a product of operators is n (when all internal particles are fermionic), hence only $n = 1, \dots,$ 4-point integrals can be UV divergent while higher-n integrals are UV finite. Due to Lorentz covariance, a tensor integral can always be written as a linear combination of scalar integrals with tensorial coefficients built from the tensors and vectors at disposal, *i.e.* the metric, the external momenta and the Levi-Civita tensor.[2] We shall first briefly showcase the tensor reduction process in a straightforward way,

[1] We write the denominator factors in a different font style in order to distinguish them from later appearing box form factors, also denoted by D.

[2] The Levi-Civita tensor will only appear (contracted with external momenta) if the numerator is a fermionic trace containing a γ^5 matrix, but then DR is subject to a dependence on how γ^5 is regularized. Generally, DR preserves all symmetries of the underlying theory unless a γ_5 matrix is involved.

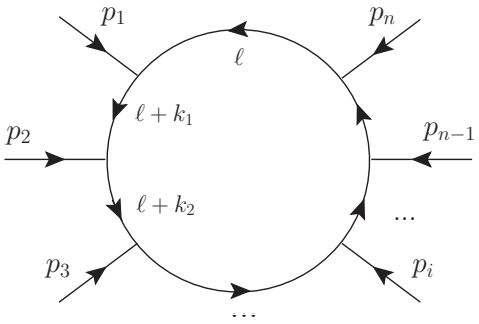

FIGURE D.1: Loop diagram with n external ingoing momenta.

following [442]. Here one needs to perform a Feynman parametrization before obtaining the expansion. It is illustrative to do so in order to compare this method to the PV scheme and see that they are equivalent, though the order of performed steps is different.

D.2 General tensor integral reduction

Using the Feynman parametrization, we first bring the denominator of T_n into the form

$$\mathfrak{D}_0\mathfrak{D}_1\dots\mathfrak{D}_{n-1} \xrightarrow{\text{F.P.}} [\ell^2 + 2\ell\cdot P_n - M_n^2 + i\epsilon]^n = [(\ell+P_n)^2 - C_n + i\epsilon]^n\,,$$

with

$$C_n \equiv P_n^2 + M_n^2\,, \qquad M_n^2 = \left(1 - \sum_{i=1}^{n-1} x_i\right) m_0^2 + \sum_{i=1}^{n-1} x_i(m_i^2 - k_i^2)\,, \qquad P_n^\mu = \sum_{i=1}^{n-1} x_i k_i^\mu\,. \tag{D.3}$$

The integral now reads

$$T_n^{\mu_1\cdots\mu_p} = \mu^\epsilon\,\Gamma(n)\int_0^1 dx_1\dots\int_0^{1-x_1-\dots-x_{n-2}} dx_{n-1}\, I_n^{\mu_1\cdots\mu_p}\,, \tag{D.4}$$

where we defined

$$\begin{aligned} I_n^{\mu_1\cdots\mu_p} &\equiv \int \frac{d^d\ell}{(2\pi)^d}\frac{\ell^{\mu_1}\dots\ell^{\mu_p}}{[(\ell+P_n)^2 - C_n + i\epsilon]^n} \\ &= \frac{i}{(4\pi)^2}\frac{(4\pi)^{\epsilon/2}}{\Gamma(n)}\int_0^\infty \frac{dt}{(2t)^p}\, t^{n-3+\epsilon/2}\frac{\partial}{\partial P_{\mu_1}}\cdots\frac{\partial}{\partial P_{\mu_p}}\cdots \mathrm{e}^{-t\,C_n}\,. \end{aligned} \tag{D.5}$$

These tensor integrals can be reduced to scalar integrals. We first perform a Wick rotation,

$$[(\ell+P_n)^2 - C_n + i\epsilon]^n \xrightarrow{\text{W.R.}} [(\bar\ell+P_n)^2 + C_n]^n\,, \tag{D.6}$$

introducing the Euclidean space 4-momentum

$$\bar\ell^\mu = (i\ell_{\mathrm{E}}^0, \vec\ell)\,, \qquad \bar\ell^2 = -\ell^2\,. \tag{D.7}$$

We accounted for the fact that the $i\epsilon$ can be dropped after the Wick rotation if $C_n > 0$ and the final result (D.9b) will also be valid for $C_n < 0$ via analytical continuation. Then we perform the shift $\bar\ell \to \bar\ell - P$ and find that I_n can be written as the sum

$$I_n^{\mu_1\cdots\mu_p} = \sum_m c_{(m)}^{\mu_1\cdots\mu_p}\, I_{m,n}\,, \tag{D.8}$$

where

$$I_{m,n} = \int \frac{d^d\bar{\ell}}{(2\pi)^d} \frac{(\bar{\ell}^2)^m}{[\bar{\ell}^2 + C_n]^n} \tag{D.9a}$$

$$= \frac{i}{(4\pi)^2}(-1)^{m-n}\left(\frac{4\pi}{C_n}\right)^{\frac{\epsilon}{2}} C_n^{2+m-n}\frac{\Gamma(2+m-\frac{\epsilon}{2})}{\Gamma(2-\frac{\epsilon}{2})}\frac{\Gamma(m-n-2+\frac{\epsilon}{2})}{\Gamma(n)}\,, \tag{D.9b}$$

with $m = 0, 1, \ldots$ and the tensorial expansion coefficients

$$c^{\mu_1\ldots\mu_p}_{(m)} = c^{\mu_1\ldots\mu_p}_{(m)}(g_{\mu\nu}, p_{i\mu})\,. \tag{D.10}$$

Note that the denominator in $I_{m,n}$ contains an even power of $\bar{\ell}$: The shift $\bar{\ell} \to \bar{\ell} - P$ rendered the power of $\bar{\ell}$ in the denominator in (D.6) even, therefore terms in I_n with an uneven number of free-index loop momenta in the denominator after the shift will vanish after integration. On the other hand, if there is an even number of loop momenta with free indices, then they reduce to factors of $g_{\mu\nu}$ and $p_{i\mu}$ multiplying integrals of the form (D.9a), *e.g.* through the identity $\int d^d\bar{\ell}\,\bar{\ell}_\mu\bar{\ell}_\nu = g_{\mu\nu}\int d^d\bar{\ell}\,\bar{\ell}^2/d$. Note further that the form (D.9a) is only valid for $d < 2(n-m)$, because otherwise one cannot undertake the Wick rotation. However, through analytical continuation we can calculate $I_{m,n}$ for all dimensions using Equation D.9b, except for values of d corresponding to the poles of $\Gamma(m-n-\frac{d}{2})$. If such poles are present, one deals with them with the usual renormalization procedure.

Analytical results for the integrals $I_n^{\mu_1\ldots\mu_p}$ in Equation D.5 are given in [442], expanded in the poles $1/\epsilon$. Let us list the cases $n = 1$ and $n = 2$. The tadpole ($n = 1$) integrals read

$$I_{0,1} = \frac{i}{(4\pi)^2}\,C_1\,(\Delta_\epsilon + 1 - \ln C_1)\,, \tag{D.11a}$$

$$I_1^\mu = 0\,, \tag{D.11b}$$

with $C_1 = m^2$ and for the self-energies ($n = 2$) we have

$$I_{0,2} = \frac{i}{(4\pi)^2}(\Delta_\epsilon - \ln C_2)\,, \tag{D.12a}$$

$$I_2^\mu = -I_{0,2}P^\mu\,, \tag{D.12b}$$

$$I_2^{\mu\nu} = \frac{i}{(4\pi)^2}\,\frac{1}{2}\,\left[C_2\,(1 + \Delta_\epsilon - \ln C_2)\,g^{\mu\nu} + 2\,(\Delta_\epsilon - \ln C_2)P^\mu P^\nu\right]\,. \tag{D.12c}$$

with $C_2 = x^2p^2 + (1-x)m_0^2 + x(m_1^2 - p^2)$. We defined the important quantity

$$\Delta_\epsilon = \frac{2}{\epsilon} - \gamma + \ln 4\pi\,, \tag{D.13}$$

containing the isolated one-loop divergence, and γ is the Euler-Mascheroni constant. Observe that there are logarithms of quantities with mass dimension 2. The arguments are made dimensionless by using that $\mu^\epsilon = (\mu^2)^{\frac{\epsilon}{2}} = 1 + \frac{\epsilon}{2}\ln\mu^2 + \ldots$ and neglecting $\mathcal{O}(\epsilon)$ terms because they don't contribute in the limit $\epsilon \to 0$. Hence, all expressions of the form $\mu^\epsilon(\Delta_\epsilon - \ln C)$ become $\Delta_\epsilon - \ln\frac{C}{\mu^2}$ in this limit. A similar expansion of $C^{-\frac{\epsilon}{2}}$ in Equation D.9b is responsible for the appearance of the $-\ln C$ terms in the $I_n^{\mu_1\ldots\mu_p}$ integrals.

D.3 The Passarino-Veltman scheme

Passarino and Veltman [443] worked out a scheme for the decomposition for $n = 1, 2, 3, 4$ (tadpoles, self-energies, triangles, boxes) because they were considering the $2 \to 2$ process $e^+e^- \to \mu^+\mu^-$, which was later completed to include $n > 4$ integrals (pentagons, hexagons, etc.) by Bern, Dixon and Kosower [444]. Since 4-dimensional Minkowski space is spanned by four independent 4-vectors, the $n > 4$ case reduces to the calculation of box diagrams, as they can be evaluated using the previous results by Passarino and Veltman. The appearing scalar coefficient functions can be further expanded in terms of only four basic scalar integrals, each containing no powers of the loop momentum in the numerator and without

recurring to Feynman parameters in the reduction process, hence this method is much more efficient than the previously discussed scheme, although the analytical expressions of the PV integrals can be obtained from the previously obtained ones. Feynman parameters still appear, however only *after* the reduction, for evaluation of the scalar integrals. Let us write the general rank-p tensor integral as

$$\begin{aligned} T_n^{\mu_1\dots\mu_p} &\equiv \mu^\epsilon \int \frac{d^d\ell}{(2\pi)^d} \frac{\ell^{\mu_1}\dots\ell^{\mu_p}}{\mathfrak{D}_0\mathfrak{D}_1\dots\mathfrak{D}_{n-1}} \times \left(\frac{i}{(4\pi)^2}\right)^{-1} \\ &= \frac{(2\pi\mu)^\epsilon}{i\pi^2} \int d^d\ell \frac{\ell^{\mu_1}\dots\ell^{\mu_p}}{\mathfrak{D}_0\mathfrak{D}_1\dots\mathfrak{D}_{n-1}} \end{aligned} \tag{D.14}$$

with the denominators defined as in (D.2). The prefactor is conventional, one must always include a factor of $i/(4\pi)^2$ in the end if one follows this convention. Another issue to consider is what mass scale μ to employ — some authors choose it beforehand to correspond to a specific renormalization scheme, like $\overline{\text{MS}}$, modifying the integration measure $\mu^{4-d}d^d\ell$ accordingly (see *e.g.* [446]). The rank-0 integral (denominator = 1) is what is commonly referred to as a scalar integral in the PV scheme. By power counting, we note that only one-point and two-point scalar integrals are UV-divergent. Generally, after the very final reduction step, a PV-expanded integral will be a linear combination of one- to four-point scalar integrals, the tensorial character being in the coefficients, which are evaluated in four dimensions. Schematically, the expansion of an n-point rank-p integral reads

$$T^{(n;p)} = \sum_i \sum_{j=1}^{\min\{4,n-1\}} c_{i;j}^{(p)} S_i^{(j)} \ [+\mathcal{O}(\epsilon) + \mathcal{R}_\epsilon\,] \tag{D.15}$$

in the limit $d \to 4$. $S_i^{(j)}$ are j-point scalar integrals of type i forming the expansion basis, where i specifies the combinations of external momenta and loop masses they depend on and the tensors, contained in $c_{i;j}^{(p)}$, they are proportional to. The $\mathcal{O}(\epsilon)$ terms vanish in the limit $\epsilon \to 0$ and $\mathcal{R}_\epsilon$ is called the rational part, which is a vestige of the dimensional regularization. It does not exist in the PV scheme, but occurs in reduction methods where the external momenta are taken to be $(4-\epsilon)$-dimensional and analytically continued to four dimensions in the end. The naming of $T^{(n)}$ is defined as starting from A for $n = 1$ and increasing in alphabetical order with increasing n. Due to energy-momentum conservation, only $n-1$ external momenta can be linearly independent. Furthermore, if $n \geq 5$, only four momenta are independent because spacetime is four-dimensional, hence the number of momenta appearing as expansion coefficients is generally given by $\min\{4, n-1\}$. Invoking Lorentz covariance, this leads to the following expansions in terms of so-called form factors (suppressing arguments for now):

$$B_\mu = p_{1\mu} B_1 \tag{D.16a}$$

$$B_{\mu\nu} = g_{\mu\nu} B_{00} + p_{1\mu} p_{1\nu} B_{11} \tag{D.16b}$$

$$C_\mu = \sum_{i=1}^{2} p_{i\mu} C_i \tag{D.17a}$$

$$C_{\mu\nu} = g_{\mu\nu} C_{00} + \sum_{i,j=1}^{2} p_{i\mu} p_{j\nu} C_{ij} \tag{D.17b}$$

$$C_{\mu\nu\rho} = \sum_{i=1}^{2} (g_{\mu\nu} p_{i\rho} + g_{\nu\rho} p_{i\mu} + g_{\mu\rho} p_{i\nu}) C_{00i} + \sum_{i,j,k=1}^{2} p_{i\mu} p_{j\nu} p_{k\rho} C_{ijk} \tag{D.17c}$$

For brevity, we only list the box tensor expansions schematically:

$$D_\mu = D_\mu(D_i) \tag{D.18a}$$

$$D_{\mu\nu} = D_{\mu\nu}(D_{00}, D_{ij}) \tag{D.18b}$$

$$D_{\mu\nu\rho} = D_{\mu\nu\rho}(D_{00i}, D_{ijk}) \tag{D.18c}$$

$$D_{\mu\nu\rho\sigma} = D_{\mu\nu\rho\sigma}(D_{0000}, D_{00ij}, D_{ijkl}) \tag{D.18d}$$

All form factors are totally symmetric in their indices. In the above expansions, we are following the convention in the original reference [445] and in [446, 447] of expanding in terms of the external momenta and use the same naming as in [445] for the form factors. Contrary to this, the convention in FeynCalc [386] and LoopTools [448] is to expand in terms of the loop momentum offsets, *i.e.* there one would replace $p_{i\mu} \to k_{i\mu}$.[3]

The form factors B_i, B_{ii}, C_i,... are the $S_i^{(j)}$ functions in Equation D.15. In the PV reduction step, they are expanded in terms of the four scalar integrals $S^{(j=1,2,3,4)} \equiv A_0, B_0, C_0, D_0$:

$$A_0(m_0^2) = \frac{(2\pi\mu)^\epsilon}{i\pi^2} \int \frac{d^d\ell}{\mathfrak{D}_0} \tag{D.19a}$$

$$B_0(p_1^2, m_0^2, m_1^2) = \frac{(2\pi\mu)^\epsilon}{i\pi^2} \int \frac{d^d\ell}{\mathfrak{D}_0\mathfrak{D}_1} \tag{D.19b}$$

$$C_0(p_1^2, p_2^2, p_{12}^2, m_0^2, m_1^2, m_2^2) = \frac{(2\pi\mu)^\epsilon}{i\pi^2} \int \frac{d^d\ell}{\mathfrak{D}_0\mathfrak{D}_1\mathfrak{D}_2} \tag{D.19c}$$

$$D_0(p_1^2, p_2^2, p_3^2, p_{123}^2, p_{12}^2, p_{23}^2, m_0^2, m_1^2, m_2^2, m_3^2) = \frac{(2\pi\mu)^\epsilon}{i\pi^2} \int \frac{d^d\ell}{\mathfrak{D}_0\mathfrak{D}_1\mathfrak{D}_2\mathfrak{D}_3}\,, \tag{D.19d}$$

where we defined $p_{i\ldots j}^2 = (p_i + \ldots + p_j)^2$ (the form factors have the same dependences, by definition). The determination of the form factors in terms of lower-rank form factors and finally only in terms of the basic scalar integrals relies on the contraction with external momenta and/or the metric, taking the limit $d \to 4$ in the end. If m functions are to be determined, one obtains a system of m independent linear equations in this way. In the case of contraction with a momentum, one applies the Passarino-Veltman reduction formula

$$\ell \cdot p_i = \frac{1}{2}\left(\mathfrak{D}_i - \mathfrak{D}_{i-1} - f_i\right)\,, \qquad f_i = k_1^2 - k_{i-1}^2 - m_i^2 + m_{i-1}^2\,, \tag{D.20}$$

the reduction to lower-rank form factors then happens through the cancellation of propagator denominators with the $\mathfrak{D}_i$ terms in (D.20). To have the fully reduced expression, previous results for the lower-rank form factors are to be inserted. The major drawback of the PV method is the occurrence of a division by the determinant of the Gram matrix

$$(G_{n-1})_{ij} = p_i \cdot p_j\,, \qquad i,j = 1,\ldots,n-1\,, \tag{D.21}$$

which for kinematic combinations at the edge of phase space may vanish, leading to instabilities in numerical evaluations of tensor integrals. For higher-point integrals, the Gram determinant even vanishes at other points in phase space. Another issue is the demonstration of gauge invariance of amplitudes containing on-shell scattering massless gauge bosons obtained with the PV scheme. As spacetime is four-dimensional, at most four incoming momenta of a higher-point amplitude can be linearly independent. The PV method does not a priori account for this constraint, hence proving the Ward identity of gauge invariance, *i.e.* replacing a polarization vector with the respective momentum vector and showing the vanishing of the expression, can be non-trivial. Newer methods seek to cure this shortcoming, see *e.g.* [445] for a discussion.

For the self-energy, triangle and box form factors, we obtain the reduction chains

$$\begin{aligned}
&B_{ii} \to B_{00}, B_i, B_0\,, \qquad B_{00} \to B_i, B_0, A_0\,, \qquad B_i \to B_0, A_0\,;\\
&C_{ijk} \to C_{00i}, C_{ij}, B_{ij}, B_i\,, \qquad C_{00i} \to C_{ii}, C_i, B_i, B_0\,, \qquad C_{ij} \to C_{00}, C_i, B_i, B_0\,,\\
&C_{00} \to C_i, C_0, B_0\,, \qquad C_i \to C_0, B_0\,;\\
&D_{ijkl} \to D_{00ij}, D_{ijk}, C_{ijk}, C_{ij}, C_i, C_0\,, \qquad D_{00ij} \to D_{ijk}, D_{ij}, C_{ij}, C_i\,,\\
&D_{0000} \to D_{00i}, D_{00}, C_{00}\,, \qquad D_{ijk} \to D_{00i}, D_{ij}, C_{ij}, C_i\,, \qquad D_{00i} \to D_{ij}, D_i, C_i, C_0\,,\\
&D_{ij} \to D_{00}, D_i, C_i, C_0\,, \qquad D_{00} \to D_i, D_0, C_0\,, \qquad D_i \to D_0, C_0\,.
\end{aligned}$$

[3] Reference [447] contains an appendix with the relations between our form factors and the LoopTools/FeynCalc form factors. Of course, the basic scalar integrals in both conventions coincide.

For example, contracting Equation D.16a with $p_1^\mu \equiv p^\mu$ and solving for B_1, we obtain

$$B_1(p^2, m_0^2, m_1^2) = \frac{1}{2p^2}\left(A_0(m_0^2) - A_0(m_1^2) - (p^2 - m_1^2 + m_0^2)\, B_0(p^2, m_0^2, m_1^2)\right) . \tag{D.22}$$

If we prefer to express the result only in terms of B_0 integrals, we can use that $A_0(m_0^2) - A_0(m_1^2) = (m_0^2 - m_1^2)B_0(0, m_0^2, m_1^2)$. As another example, to obtain the form factors in (D.17a), we contract both sides with p_1 and p_2 and use (D.20) to find

$$\begin{pmatrix} C_1 \\ C_2 \end{pmatrix} = \frac{1}{2} G_2^{-1} \begin{pmatrix} (m_1^2 - m_0^2 - p_1^2)\, C_0(0,1,2) + B_0(0,2) - B_0(1,2) \\ (m_2^2 - m_1^2 - p_2^2 - 2p_1\cdot p_2)\, C_0(0,1,2) + B_0(0,1) - B_0(0,2) \end{pmatrix} , \tag{D.23}$$

where we defined the argument of the scalar functions as the indices of the contained denominators, *i.e.*

$$\begin{aligned} C_0(0,1,2) &= C_0(p_1^2, p_2^2, p_{12}^2, m_0^2, m_1^2, m_2^2) = \frac{(2\pi\mu)^\epsilon}{i\pi^2}\int \frac{d^d\ell}{\mathfrak{D}_0\mathfrak{D}_1\mathfrak{D}_2} \\ &= \frac{(2\pi\mu)^\epsilon}{i\pi^2}\int \frac{d^d\ell}{(\ell^2 - m_0^2 + i\epsilon)((\ell+p_1)^2 - m_1^2 + i\epsilon)((\ell + p_1 + p_2)^2 - m_2^2 + i\epsilon)} . \end{aligned} \tag{D.24}$$

Consider further the calculation of the coefficient C_{00} in (D.17b). This time we contract with $p_{1\mu}$, $p_{2\mu}$ and the d-dimensional metric tensor, introducing a dependence on d. The system of equations leads to

$$\begin{aligned} C_{00}(0,1,2) = \frac{1}{2(d-2)}\big(&2m_0^2\, C_0(0,1,2) - (m_1^2 - m_2^2 - p_1^2)\, C_1(0,1,2) \\ &-(m_2^2 - m_1^2 - p_2^2 - 2p_1\cdot p_2)\, C_2(0,1,2)\big) \end{aligned} \tag{D.25}$$

and can be further decomposed using the result for C_1 and C_2.

Let us finalize this appendix by listing some explicit expressions of the scalar integrals and form factors in terms of Feynman parameters. They can be directly obtained from the $I_n^{\mu_1\cdots\mu_p}$ integrals through Equation D.4, since the expansions need to be equivalent. For $A_0(m)$, there is no Feynman parameter and we find

$$A_0(m) = \mu^\epsilon \left(\frac{i}{(4\pi)^2}\right)^{-1} I_{0,1} = m^2(\Delta_\epsilon + 1 - \ln\frac{m^2}{\mu^2}) . \tag{D.26}$$

The two-point scalar function reads

$$\begin{aligned} B_0(p^2, m_0^2, m_1^2) &= \mu^\epsilon \left(\frac{i}{(4\pi)^2}\right)^{-1} \int_0^1 dx\, I_{0,2} \\ &= \Delta_\epsilon - \int_0^1 dx\, \ln\left[\frac{-x(1-x)p^2 + xm_1^2 + (1-x)m_0^2}{\mu^2}\right] . \end{aligned} \tag{D.27}$$

Note that the expression is not symmetric under the exchange $m_0 \leftrightarrow m_1$. It simplifies in special cases, like $B_0(0, m_0^2, m_1^2)$ or $B_0(p^2, 0, m^2)$; these are given in [442], as well as the derivative dB_0/dp^2, an also frequently required quantity in renormalization. Here we give $B_0(0, m_0^2, m_1^2)$, because it is used in Chapter 2:

$$\begin{aligned} B_0(0, m_0^2, m_1^2) = B_0(0, m_1^2, m_0^2) &= \Delta_\epsilon + 1 + \frac{m_0^2}{m_0^2 - m_1^2}\ln\frac{m_0^2}{\mu^2} + \frac{m_1^2}{m_1^2 - m_0^2}\ln\frac{m_1^2}{\mu^2} \\ &= \Delta_\epsilon + 1 + \ln\frac{m_1^2}{\mu^2} + \frac{m_0^2}{m_1^2 - m_0^2}\ln\frac{m_1^2}{m_0^2} . \end{aligned} \tag{D.28}$$

For the form factor B_1, we have

$$\begin{aligned} B_1(p^2, m_0^2, m_1^2) &= \mu^\epsilon \left(\frac{i}{(4\pi)^2}\right)^{-1} \int_0^1 dx\, (I_2^\mu / p^\mu) \\ &= -\frac{1}{2}\Delta_\epsilon + \int_0^1 dx\, x \ln\left[\frac{-x(1-x)p^2 + xm_1^2 + (1-x)m_0^2}{\mu^2}\right] , \end{aligned} \tag{D.29}$$

since $P_2^\mu = xp^\mu$, so I_2^μ/p^μ means the coefficient in I_2^μ multiplying p^μ. Alternatively, we can use the Passarino-Veltman trick and contract Equation D.16a with p^μ to end up with (D.22) (notice the appearance

of the inverse Gram determinant — the case of $p^2 = 0$ has to be dealt with separately); then, Equation D.29 can be obtained by using the analytical results for A_0 and B_0. Expressions for the expansions of B_{00} and B_{11} are also given in [445]. We again point out that all that is initially needed to work out analytical expressions in our approach are the scalar integrals $I_{m,n}$.

We will consider the function C_0 as the last example, since it appears in the *g-g-h* vertex. $I_{0,3}$ is finite, therefore no Δ_ϵ or $-\ln C$ terms appear and we can take $\mu^\epsilon \to 1$. One finds

$$C_0(p_1^2, p_2^2, p_{12}^2, m_0^2, m_1^2, m_2^2) = \mu^\epsilon \left(\frac{i}{(4\pi)^2}\right)^{-1} \int_0^1 dx \int_0^{1-x} dy\, I_{0,3} = -\int_0^1 dx \int_0^{1-x} dy\, \frac{1}{2C_3}\,, \tag{D.30}$$

with

$$\begin{aligned} C_3 = {} & x^2 p_1^2 + y^2 (p_1 + p_2)^2 + 2xy(p_1^2 + p_1 \cdot p_2) + (1 - x - y) m_0^2 + x m_1^2 + y m_2^2 - x p_1^2 \\ & - y(p_1 + p_2)^2\,. \end{aligned} \tag{D.31}$$

The specific case of $p_1^2 = p_2^2 = 0$, $p_{1,2}^\mu = (\sqrt{s}/2, 0, 0, \pm\sqrt{s}/2)$ for Higgs mediation via gluon fusion with a fermion triangle requires the following C_0 function:

$$C_0(0, 0, s, m^2, m^2, m^2) = -\frac{\Gamma(3)}{2} \int_0^1 dx \int_0^{1-x} dy\, \frac{1}{sy(y + x - 1) + m^2}\,. \tag{D.32}$$

The integral is difficult to work out analytically, though very well-known in the literature. It is given by

$$C_0(0, 0, s, m^2, m^2, m^2) = -\frac{2}{s} f(\tau) \tag{D.33}$$

where (see for instance [291])

$$f(\tau) = \begin{cases} \arcsin^2 \dfrac{1}{\sqrt{\tau}} & \text{if } \tau \geq 1\,, \\ -\dfrac{1}{4} \left[\ln\left(\dfrac{1 + \sqrt{1 - \tau}}{1 - \sqrt{1 - \tau}}\right) - i\,\pi\right]^2 & \text{if } 0 \leq \tau < 1\,, \end{cases} \tag{D.34}$$

with $\tau = 4m^2/s$.

APPENDIX E

Detailed descriptions of ATLAS and CMS for the implementation of simplified detector models

Our collider phenomenology studies of HLLCP scenarios require detector simulations. One may opt for existing professional software like Geant4 [332], though it is simpler to focus on the relevant detector details and implement them as required. Analysis IIA necessitates nothing but the cylindrical volume of CMS, whereas Analysis IIB relies on the geometrical information of ATLAS up to the HCAL and the materials used for electromagnetic and hadronic calorimetry. Nevertheless, we shall treat ATLAS and CMS on an equal footing and work out a Mathematica code that contains the same amount of information on both detectors and is therefore applicable to both types of analyses. We first collect in Section E.1 all necessary technical information on the various detector modules after combing through the vast amount of technical design reports and other available documentation, performing some minor roundings all throughout.[1] The calorimeters in the very forward regions will be ignored, since we are not working with particles emitted with high pseudorapidities. Following that discussion, we calculate the material constants needed in the Bethe-Bloch equation for the stopping power of the electromagnetic and hadronic calorimeters in Section E.2. Since not all materials are pure but mixtures or sampled layers, we first present how to combine differing material properties into effective values to be used in the Bethe-Bloch equation in Section E.2.1. The outcome of this appendix is the list of toy detector specifications given in Table 3.2.

E.1 Detector descriptions including geometries and materials

E.1.1 ATLAS

□ **Inner detector**: At the core of ATLAS lies the inner detector [449], which consists of three modules. Going concentrically outwards, these are the pixel detector [450], the SemiConductor Tracker (SCT) [451] and the transition radiation tracker (TRT) [452]. The ID measures electrically charged particles' momenta and aids in particle identification. The use of different types of technologies with increasing radius is the decreasing particle flux. The pixel detector and the SCT both contain silicon cells for charged particles to deposit energy through ionization, whereas the TRT uses drift tubes filled with a gas mixture of Xe, CO_2 and O_2 to detect transition radiation X-ray photons created in the radiator material between the tube straws. While the pixel and SCT cells are planarly placed on their layers around the beam line in the barrel and perpendicularly in the EC disks, the TRT straws are spanned parallel to the beam line in the barrel and radially in the corresponding EC part (*cf.* Figures 4.2 and 4.3 in [303]). From the beam line, the radius of the cylindrical volume over which tracking occurs amounts to 102.8 cm and the distance from the center to the last TRT endcap layer is 272.0 cm. Maximum pseudorapidity coverage is reached at $|\eta| = 2.5$. On average, charged particles leave about 36 hits [303]. Track reconstruction followed by momentum determination happens offline by means of a χ^2 fitting procedure. The pixel and SCT are used for vertexing, b- and τ-tagging, while the TRT serves for electron-pion separation based on their expected dE/dx (this is complementary to the electron identification in the ECAL).

[1] In several instances, some sources provide slightly differing dimensional values given by others and some are not clear in their specifications. In those cases, we are forced to make decisions on what values to adopt and on how to interpret certain descriptions.

□ **Electromagnetic calorimeter**: The barrel and endcap electromagnetic calorimeters (EMB, EMEC) [336] consist of fine layers of liquid argon (LAr, active radiator) and lead (Pb, absorber) with kapton electrode layers placed in between to attract the drifting electrons. These LAr-Pb layers have an 'accordion' (zigzag) geometry to minimize the dead zones (*cf.* Figure 1.2 in [303]). Arrangement of the plates w.r.t. the beam line of these layers is radially outwards like bicycle wheel spokes and the accordion waves run parallel to the beam axis. The EMB module consists of two cylindrical half-modules summing up to 6.3 m in length and is 61.5 cm thick, covering a pseudorapidity range of $|\eta| < 1.475$. Out of these 61.5 cm, 50.5 cm correspond to the actual LAr-Pb layers used for absorption and energy measurement, the rest is electronics, cooling, presampling and various structural elements (*cf.* Fig. 3 in [453]). As seems suggestive from Figure 1.2 in [303], we take as the effective decelerating portion the segment formed by the wavy section of the absorber plates, corresponding to 47.5 cm or to 22.3 radiation lengths (*cf.* the two cited figures). The inner radius of the accordion sandwich structure, *i.e.* the distance from the beam line to the inner edge of the first absorber wave, is 150 cm, the outer radius is 197.5 cm. Each layer contains 14 folds forming the accordion geometry. In order to reach a sufficiently good energy resolution, the folding angle gradually decreases from 91.92° to 68.51° with increasing radius. Together with the chosen lead thicknesses of 1.5 mm (1.1 mm) for $|\eta| < 0.8$ ($0.8 < |\eta| < 1.475$) and the given lead-to-argon ratio of 0.36 (0.26), this geometry optimizes the energy resolution according to simulations.

Each EMEC wheel consists of two independent coaxial wheels covering complementing pseudorapidity ranges: the outer wheel covers $1.475 < |\eta| < 2.5$, the inner wheel covers $2.5 < |\eta| < 3.2$. The boundary at $|\eta| = 2.5$ coincides with the maximal rapidity covered by the tracker system. The wheels have an outer radius of 207.7 cm and a thickness of 63.2 cm at room temperature, with the total nominal active/absorber sampling layer thickness being 51 cm (6 wavelengths of 85 mm in the inner wheel and 9 wavelengths of 56.67 mm in the outer wheel) and the outer radius of the active/absorber volume being 203.4 cm. The distance from the plates to the plane perpedicular to the beam line going through the interaction point measures 370.4 cm. Since the wave lengths are kept constant in both wheels, the wave amplitudes (folding angles) need to increase (decrease) with the radius, which is necessary to achieve a uniform calorimeter response in ϕ. Together with the hadronic endcap and the forward calorimeters, the EMB and EMEC are grouped conceptually to compose the *LAr calorimeter*, based on the common radiator material.

□ **Hadronic calorimeter**: Contrary to the ECAL, the technologies employed in the hadronic barrel [454] and endcap [336] calorimeters are different. The tile calorimeter (TileCal) in the barrel region consists of stacks of radially placed modules containing laminated steel (absorber) and plastic scintillator tiles (active). The long barrel (HLB) part covering $|\eta| < 1$ is 5.8 m long and 1.97 m thick, its inner and outer radius extending to 2.28 m and 4.25 m, respectively. Higher pseudorapidities, *i.e.* $0.8 < |\eta| < 1.7$, are covered by the extended barrel (HEB) modules containing the same steel/scintillator tiles, each part with a length of 2.6 m and the same thickness as the barrel module.

On the other hand, the hadronic endcap (HEC) modules are part of the LAr system and consist of LAr-Cu layers. Materials were chosen for their radiation hardness and relatively low cost. There are two parallel wheels on each side of the interaction point, the thickness of the front wheel (HEC1) being 81.7 cm and the thickness of the rear wheel (HEC2) being 96.1 cm (*cf.* Figure 8.1 in [336]). The pseudorapidity coverage of the HEC system is $1.5 < |\eta| < 3.2$. Each wheel consists of 32 identical modules, each subtending an angle of 11.25°. HEC1 (HEC2) contains 25 (17) copper plates, the first plate having a thickness of 12.5 mm (25 mm) and the other 24 (16) plates being 25 mm (50 mm) thick. All inter-plate gaps are 8.5 mm wide. The first 9 plates of HEC1 are larger than all other plates: Their inner (outer) radius measures 37.2 cm (203.0 cm), while the other plates have the same outer radius but an inner radius of 47.5 cm, corresponding to a difference of 14.8 cm. For mechanical strength, the whole structure is reinforced by seven stainless-steel rods going through every plate, which we ignore.

□ **Muon spectrometer**: The outermost detector is the muon system or muon spectrometer (MS) [322, 455], which measures tracks, charges and momenta of charged particles exiting the calorimeters and in particular serves for muon identification. Measurements are made using monitored drift tube chambers

(DT or MDT), cathode strip chambers (CSC), resistive plate chambers (RPC) and thin gap chambers (TGC). The barrel part covers $|\eta| < 1.05$ and the endcap pseudorapidity coverage is $1.05 < |\eta| < 2.7$. By design, it measures muon p_{T} values in the range from 3 GeV to 1 TeV, with a resolution of less than 10%. This requires an extremely low uncertainty in resolving high-energy track sagittas (low-energy muon momenta can be directly measured knowing the deposited energy). A bias of 30 μm in the sagitta has been reported to correspond to a systematic bias in the transverse momentum of 60 GeV for a muon with a p_{T} of 1 TeV [322]. Three layers of chambers are concentrically layered in the barrel at radii of 5 m, 7.5 m and 10 m, while in each endcap region, the MS consists of wheels placed at 7.4 m, 10.8 m, 14 m and 21.5 m from the interaction point. Only MDT chambers are used for precision momentum and position measurements in all barrel layers and endcap wheels, except in the innermost wheels, where CSCs are used (*cf.* Figure 6.2 in [322]). RPC (TGC) layers are attached to the chambers in the barrel (endcaps) for L1-level triggering in the $|\eta| < 2.4$ range and for timing measurements, as they react faster, but have a worse spatial resolution than the MDTs and CSCs. For detailed information on the position and timing resolutions of the four detection devices, see Table 6.1 in [322].

E.1.2 CMS

□ **Inner detector**: The tracking system of CMS [456] is a pure silicon tracker, in fact, with about 200 m^2 of active silicon, the largest thus far built [316]. Like in ATLAS, pseudorapidity coverage is $|\eta| < 2.5$, with the innermost module being a pixel detector [457] and outside the pixel is a silicon microstrip detector. The latter is divided into four subsystems, namely the tracker inner barrel and disks (TIB, TID), the tracker outer barrel (TOB) and the tracker endcaps (TEC+, TEC-). The tracking volume is delimited by the latter two systems and extends to $|z| < 282$ cm and $|r| < 118$ cm (the radial coverage of 113.5 cm of the TECs actually being somewhat shorter). About 2-3 hits are to be expected in the pixel volume and up to 9 measurements can occur in the microstrip layers.

□ **Electromagnetic calorimeter**: The CMS ECAL [458] is, in contrast to the one of ATLAS, a homogeneous calorimeter consisting of 75 848 absorbing and scintillating lead tungstate ($PbWO_4$) crystals, 61 200 in the barrel part and 7 324 in each endcap part. These crystals have a high density and a small Molière radius, resulting in a high granularity and a short radiation length, $X_0 = 0.89$ cm. This allows the average distance between the inner and outer edge of the ECAL to be quite small, as required for the 'compact' design of the detector. Most of the energy (about 94%) of a single photon or electron will be contained in about 3×3 crystals.

Each crystal in the barrel part (EB) has a length of 230 mm ($25.8\,X_0$), the cross section is 22×22 mm^2 at the crystal front face and 26×26 mm^2 at the rear end. The crystals are arranged in a quasi-projective tapered manner, converging towards a point on the beam line with an inclination of 3° relative to the vector connecting the ends of the crystal axes with the interaction point in order to avoid empty spaces between crystals to be aligned with trajectories of particles. The crystals are grouped in 10-crystal submodules, which are grouped to 400- and 500-crystal modules. These in turn are joined in groups of four to 1700-crystal supermodules (*cf.* Figure 1 in [459]). The separation between the beam line and the front faces of the barrel crystals is 129 cm and the cylindrical surface formed by them extends from the interaction point out to 270.5 cm (estimated from Figure 1.6 of [458]).

In the forward pseudorapidity range $1.479 < |\eta| < 3.0$ lies the endcap ECAL (EE). Each endcap piece consists of two D-shaped halves, called 'Dees', positioned at a distance of 317 cm from the interaction point. Most crystals on Dees are grouped into 5×5-crystal arrays named supercrystals; each Dee contains 3662 crystals. Their front face and rear end cross sections are somewhat larger than the barrel crystal front faces, namely 28.62×28.62 mm^2 and 30×30 mm^2, while with a length of 220 mm ($24.7\,X_0$) they are a bit shorter. The EB pseudorapidity coverage is $|\eta| < 1.479$.

□ **Hadronic calorimeter**: The HCAL of CMS [460] is once again a sampling calorimeter. At a 0° polar angle, the hadronic barrel calorimeter (HB) thickness corresponds to $5.82\lambda_{\mathrm{I}}$ and increases like $1/\sin\theta$ to

an effective thickness of $10.6\lambda_I$ at $|\eta| = 1.3$. In addition, there are 1.1 interaction lengths provided by the EB crystals. The HB and hadronic endcap (HE) calorimeters are extended by an additional layer after the superconducting coil and the iron of the first muon system layer to absorb late forming showers (the 'tail catcher'). For this, the coil and the muon system iron then have the functionality of acting as additional absorbers. The pseudorapidity coverage of the HB is $|\eta| < 1.3$, while the hadronic endcap (HE) module covers $1.3 < |\eta| < 3.0$.

With a length of about 8.6 m, the HB is structured in terms of staggered wedges. Each wedge subtends an azimuthal angle portion of 20° with the beam line in the center and consists of 14 layers of brass absorbers with a stainless steel absorber at the top and bottom of each stack for mechanical strength. Brass layers 1-8 (counting radially outwards) have a thickness of 50.5 mm each and layers 9-14 are 56.5 mm thick. The front (back) steel plate has a thickness of 61 (75) mm. In total, this adds up to an absorber thickness of 879 mm. There are 17 slots at constant radial intervals providing space for trays of plastic scintillator material. The active material trays contain aligned Kuraray SCSN81 plastic scintillator tiles, except the innermost (layer 0), where a Bicron BC408 scintillator is placed. Choices of scintillator materials are guided by long-term stability and radiation hardness demands. The SCSN81 scintillator layers 1-15 have a thickness of 3.7 mm each, while layer 16 is 9 mm thick, as is layer 0. Layer 16 is placed onto the outermost steel plate, before the cryostat, layer 1 (15) is directly between brass plate 1 (14) and the inner (outer) steel plate. In total, this makes up 73.5 mm of active material. With the spaces occupied by these slots and the thickness of the material in the trays surrounding the scintillator material, the total sampling depth is about 96 cm.

Each HE module is an 18-sided polyhedron consisting of 36 trapezoidal segments corresponding to the shape formed by the HB wedges, each subtending an angle of 10° in ϕ. Two such elements are combined to form single segments subtending 20°. Absorber and active materials are the same as used in the HB, but the absorber thickness is now 79 mm. There are 18 absorber plates (layers 0-17) bolted together to a single monolithic element, with an additional ring (layer -1) covering $1.479 < |\eta| < 1.566$ to compensate for space in the outer back back part of the module, where the plate radii are shorter to accommodate front end electronics. The largest of the absorber plates have an outer radius of 270 cm. Gaps of 9 mm thickness for placing scintillator trays are placed in a staggered fashion with 35 mm inter-gap distance, defining a period (sampling layer thickness) of 88 mm. This adds up to a sampling depth of 158.4 cm, to which we can add the 10 cm of the stainless steel plate after the final brass layer used for attaching the HE modules to the muon system. 17 layers (1-17) with trays containing 3.7 mm of SCSN81 plastic scintillator material are positioned in the trapezoidal openings formed by the spacers between the sector plates. Again, an additional layer of 9 mm BC408 scintillator (layer 0) is placed in front of the first absorber to correct for particle type-dependent energy response and energy absorption in the mechanical structure.

□ **Muon spectrometer**: As in ATLAS, the CMS muon system [461] serves for muon identification, momentum measurement and triggering. Most relevant information can be gathered in [316], a document from 2008 that is more recent than the pre-construction TDR from 1997. Momentum measurement and identification in the barrel is done via DT chambers. 4 layer stations going concentrically around the beam line are interspersed with the plates of the steel flux return yoke, covering the pseudorapidity range $|\eta| < 1.2$. The barrel is segmented into 5 wheels containing the magnet yoke and MS chamber layers, where each wheel is divided into 12 sectors (*cf.* Figure 3.1.1 in [461]). In the endcap, CSCs are employed, also 4 stations alternating with the return yoke endcap disks. The endcap CSCs cover the range $0.9 < |\eta| < 2.4$. In the barrel and in the endcaps, fast reacting RPC plates are attached to the surfaces of the DT chambers and the CSCs for additional triggering and timing measurements over the nominal range of $|\eta| < 2.1$ (though during Run I, coverage was only until 1.6). They are also used to resolve ambiguities occurring in tracking from multiple hits within a DT chamber or a CSC. As can be seen in Figure 7.47 in [316], the barrel extends over a radius of about 7.38 m, the inner face of the last muon chamber being at a distance of about 7.1 m from the beam line; we take 7.38 m to be the radius of the CMS toy detector, such that we obtain a conservative result on the number of escaping particles passing the selection. From the same figure and accompanying text, we notice that the outer ring of CSC chambers on the outermost MS disk (ME station 4/2) covering pseudorapidities until $|\eta| \sim \pm 1.8$ was not in service during the first LHC run.

Since larger scattering angles are unprobable in our considered scenario, we limit the cylindric volume of the CMS toy detector to extend only to the outer faces of the third endcap muon stations, at $|z| = 9.75$ m (*cf.* Figure 4.1.1 in [461]).

E.2 Determination of the material constants

For evaluating the energy loss of a particle in the calorimeters by means of the Bethe-Bloch equation, we need a set of three properties for each of the materials: the average atomic number to atomic mass ratio $\langle Z/A \rangle$, the density ρ and the ionization energy I. For sampled materials, we take the sampling averages of these quantities, $\langle Q \rangle$ ($Q = \rho$, Z/A, I), by means of approximations that will suffice for our purposes. If X is a pure material, then $\langle Q \rangle_X = Q_X$. In the sampling case in which the calorimeter medium is a succession of layers consisting of a volume fraction f_X of an absorber X and a volume fraction $f_Y = 1 - f_X$ of an active material Y, then the sampling densities we take are

$$\langle \rho \rangle = f_X \langle \rho \rangle_X + (1 - f_X) \langle \rho \rangle_Y \,. \tag{E.1}$$

For mixtures and compounds (like alloys), we either use the tabulated values or, in case there is no information on Z/A_X or I_X ($\langle \rho \rangle_X$ is always given in the literature for the materials we require), we compute their sampling averages by making use of the Bragg additivity rule in terms of the weight fractions for the compound stopping power, as we will outline next. All material constants are either directly found in the TDRs or calculated from values found on PDG [78]. Note that these may vary with temperature and pressure; we assume these effects to be of negligible nature.

E.2.1 dE/dx for mixtures and compounds: The Bragg additivity rule

Bragg additivity [363] for the stopping power in mixtures and compounds states the following: Let n_j be the number of an atom species in the compound molecule[2] and w_j its weight fraction given by

$$w_j = \frac{n_j A_j}{\sum_k n_k A_k} \,, \qquad \sum_j w_j = 1 \,, \tag{E.2}$$

where A_k is the atomic weight of atom k and the sum over k runs over all kinds of atoms in the compound. Then the stopping power can be expressed as a sum over properly weighted layers of single-atom materials, which effectively results in a mean energy loss in a single kind of material,

$$\left\langle -\frac{dE}{dx} \right\rangle [\langle Z/A \rangle, \langle I \rangle] = \sum_j w_j \left\langle -\frac{dE}{dx} \right\rangle \Big|_j [(Z/A)_j, I_j] \,. \tag{E.3}$$

One uses the single-material Bethe-Bloch equation with the effective quantities $\langle Z/A \rangle$ and $\langle I \rangle$, which are calculated as

$$\langle Z/A \rangle = \frac{\sum_j n_j Z_j}{\sum_j n_j A_j} = \sum_j w_j (Z/A)_j \,, \tag{E.4}$$

$$\ln \langle I \rangle = \frac{\sum_j n_j Z_j}{\sum_k n_k Z_k} \ln I_j = \frac{\sum_j w_j (Z/A)_j}{\sum_k w_k (Z/A)_k} \ln I_j \,. \tag{E.5}$$

The second equation is equivalent to writing

$$\langle I \rangle = \prod_j I_j^{n_j Z_j / \sum_k n_k Z_k} = \prod_j I_j^{w_j (Z/A)_j / \langle Z/A \rangle} \,. \tag{E.6}$$

Molecular binding effects are neglected in this approximation, but the logarithmic dependence of the Bethe-Bloch equation on I attenuates this error. These effects can make up to a few percent in very tightly

[2] n_j need not be an integer if the material is a mixture of several kinds of molecules with arbitrary proportions.

bound materials [462].

E.2.2 ATLAS

□ Electromagnetic calorimeter

The absorber and radiator plates are described in Section 6 in [336]. Lead of 99.9% purity is used for the absorbers. As lead easily deforms, the accordion shape is reinforced by 0.2 mm thick stainless AISI-304 steel skin coat layers ($\sim$ 70% Fe, $\sim$ 20% Cr, $\sim$ 10% Ni) applied to both absorber faces using prepreg adhesive. In total, including presampling, the EMB thickness corresponds to about $25\,X_0$ and the EMEC thickness is about $26\,X_0$.

Since the path length travelled through the EMB increases with pseudorapidity, the thickness of the Pb absorber plates for high pseudorapidities is chosen to be thinner than for low pseudorapidities, in order to increase the energy resolution at high $|\eta|$ by keeping the LAr gap thickness constant. For $|\eta| < 0.8$, the absorber thickness is 1.5 mm, for $0.8 < |\eta| < 1.475$ it is 1.1 mm, while the LAr gap is kept at a nominal value of 2.1 mm through honeycomb spacers on each side of the readout electrode layer, which consists of copper sheets for conduction and kapton (polyimide) layers for insulation. Electrode and LAr layers define a constant gap of 4.5 mm between the absorber plates. We therefore obtain a Pb/LAr volume ratio of $1.5/(2 \times 2.1) \simeq 0.36$ for $|\eta| < 0.8$, as indeed specified in [336], and $1.1/(2 \times 2.1) \simeq 0.26$ for $0.8 < |\eta| < 1.475$. The materials and layer orderings in the EMEC are the same as in the EMB, though the absorber thicknesses are larger because high-η particles tend to be significantly more energetic. In the inner (outer) wheel, the absorber thickness is 2.2 (1.7) mm with increasing LAr gap thickness from 1.5 mm to 2.7 mm (0.9 mm to 2.7 mm) as the radius increases.

Rather than implementing all these details computationally,[3] we instead make an approximation and consider the particle going through the material with an effective sampling density calculated from the densities of all present materials and from the geometry. Relying on sources internal to ATLAS [464–466], we calculate the density as if the ECAL were made from a homogeneous material consisting of an 'equivalent molecule' with the chemical formula $\mathrm{Pb}_{30}\,\mathrm{Ar}_{56}\,\mathrm{Fe}_{24}\,\mathrm{C}_{21}\,\mathrm{H}_{41}$. The Fe-C-H portion parametrizes the steel and the electrode plates. The sampling density is then computed via

$$\langle\rho\rangle = \frac{\sum_k n_k \times \rho_k}{\sum_k n_k}\,, \tag{E.7}$$

where k denotes the atom type and n_k the number of k-type atoms in the molecule. For the ATLAS EMB in the first pseudorapidity range (R1: $|\eta| < 0.8$), the density is officially specified to be

$$\langle\rho\rangle = 4.01\ \mathrm{g\,cm^{-3}}\,. \tag{E.8}$$

In fact, with material constant numbers from PDG, one obtains $\langle\rho\rangle_\mathrm{s} \simeq 3.83\ \mathrm{g\,cm^{-3}}$, *i.e.* smaller by a factor of 1.057, but we will stick with the cited value, as it seems to be more 'official' and apparently describes well cosmic muon data [466].[4] But indeed, this hypothetical molecule leads to a Pb/LAr volume fraction close to 0.36. The weight fractions $w_\mathrm{Pb,LAr}$ of Pb and LAr as defined in Equation E.2 are 0.616 and 0.222, respectively. Thus, using

$$\frac{V_\mathrm{x}}{V_\mathrm{y}} = \frac{m_\mathrm{x}}{m_\mathrm{y}}\frac{\rho_\mathrm{y}}{\rho_\mathrm{x}} = \frac{w_\mathrm{x}}{w_\mathrm{y}}\frac{\rho_\mathrm{y}}{\rho_\mathrm{x}}\,, \tag{E.9}$$

where V_x is the volume occupied by component x and m_x is the sum of the masses of its atoms, we get

$$\frac{V_\mathrm{Pb}}{V_\mathrm{LAr}} = \frac{w_\mathrm{Pb}}{w_\mathrm{LAr}}\frac{\rho_\mathrm{LAr}}{\rho_\mathrm{Pb}} = 2.775 \times 0.123 \simeq 0.34\,. \tag{E.10}$$

[3] There is a computational tool called CaloSmpPidTool, developed for the internal ATLAS software package Athena, for this simulation [463].

[4] The motivation for the used chemical formula is not fully clear, as stainless steel of the 304 type contains significant amounts of Cr and Ni. We will however stick with the method of this equivalent molecule. The earliest source for the computation of this number for the effective density is an internal note and is therefore not publically available.

$[\lvert\eta\rvert_{\min}, \lvert\eta\rvert_{\max}]$		w_{Pb}	w_{LAr}	w_{Fe}	w_{C}	w_{H}
R1:	$[0, 0.8]$	0.616	0.222	0.133	0.025	0.004
R2:	$[0.8, 1.475]$	0.552	0.259	0.155	0.029	0.005
R3:	$[1.475, 2.5]$	0.753	0.098	0.122	0.023	0.004
R4:	$[2.5, 3.2]$	0.786	0.092	0.100	0.019	0.003

TABLE E.1: Weight fractions of the components of the 'effective molecule' used to characterize the ATLAS ECAL in terms of the Bragg additivity rule.

This number deviates a bit from the official value and the one obtained by considering the thickness ratios, but we are content with the overall level of agreement of this rather vaguely grounded procedure. Moreover, the ratio is sensitive to the used values for the material constants, which vary somewhat from reference to reference. Here we use numbers as given in PDG whenever possible, as stated above. We next calculate the sampling densities for the other pseudorapidity ranges, multiplying them by 1.057 to account for the before-mentioned difference regarding the official calculation, and compute $\langle Z/A\rangle_{\mathrm{s}}$ and $\langle I\rangle_{\mathrm{s}}$ by means of the Bragg additivity rule with help of the respective weight fractions.

The next goal is therefore to find the Pb (or Pb and LAr) content of the equivalent molecule for the second, third and fourth range, $0.8 < |\eta| < 1.475$ (outer barrel, R2), $1.475 < |\eta| < 2.5$ (outer EMEC wheel, R3) and $2.5 < |\eta| < 3.2$ (inner EMEC wheel, R4), leaving $n_{\mathrm{LAr,Fe,C,H}}$ ($n_{\mathrm{Fe,C,H}}$) untouched for the second (third and fourth) range. In the second range, the Pb/LAr volume ratio is 0.26. From Equation E.9, we infer that $w_{\mathrm{Pb}}/w_{\mathrm{LAr}}$ needs to be $\simeq 2.13$, as can only be obtained with $n_{\mathrm{Pb}} = 23$, leading to $\langle\rho\rangle = 3.67\ \mathrm{g/cm^3}$ after multiplying by 1.057. For the outer (inner) wheel, we approximate the LAr thickness by the average, which is 1.8 mm (2.1 mm), so the Pb/LAr volume ratio of $1.7/1.8 \simeq 0.94$ ($2.2/2.1 \simeq 1.05$) leads to a weight fraction ratio of $w_{\mathrm{Pb}}/w_{\mathrm{LAr}} \simeq 7.68$ (8.52). Another condition is needed to solve for $n_{\mathrm{Pb,LAr}}$. Considering the steel layer to be represented by the 24 Fe atoms in the molecule, the system formed with $w_{\mathrm{Fe}}/w_{\mathrm{Pb}} \simeq 0.16$ (0.13) is solved by taking $\mathrm{Pb}_{40}\,\mathrm{Ar}_{27}$ ($\mathrm{Pb}_{51}\,\mathrm{Ar}_{31}$), giving $\langle\rho\rangle = 5.01$ (5.39) $\mathrm{g/cm^3}$.

With the weight fractions listed in Table E.1, we can obtain the effective values of $\langle Z/A\rangle$ and $\langle I\rangle$, neglecting the C and H components. For example,

$$\left\langle\frac{Z}{A}\right\rangle(R1) = w_{\mathrm{Pb}}(R1)\left\langle\frac{Z}{A}\right\rangle_{\mathrm{Pb}} + w_{\mathrm{LAr}}(R1)\left\langle\frac{Z}{A}\right\rangle_{\mathrm{LAr}} + w_{\mathrm{Fe}}(R1)\left\langle\frac{Z}{A}\right\rangle_{\mathrm{Fe}} \simeq 0.406\,, \tag{E.11}$$

and

$$\langle I\rangle_{\mathrm{s}}(R1) = I_{\mathrm{Pb}}^{w_{\mathrm{Pb}}(R1)/\left\langle\frac{Z}{A}\right\rangle_{\mathrm{s}}(R1)} \times I_{\mathrm{LAr}}^{w_{\mathrm{LAr}}(R1)/\left\langle\frac{Z}{A}\right\rangle_{\mathrm{s}}(R1)} \times I_{\mathrm{Fe}}^{w_{\mathrm{Fe}}(R1)/\left\langle\frac{Z}{A}\right\rangle_{\mathrm{s}}(R1)} \simeq 487\ \mathrm{eV}\,, \tag{E.12}$$

ignoring the material of the electrode layers. The rest of the material constants are given in Table 3.2.

□ Hadronic calorimeter

The absorber/active materials are steel (Fe) and plastic scintillator (PS) tiles and the Fe/PS volume ratio is 4.67:1 [467]. Using again Equation E.9, one obtains $w_{\mathrm{Fe}}/w_{\mathrm{PS}} \simeq 36.8$, thus the PS component can be completely neglected when calculating the effective $\langle Z/A\rangle$ and $\langle I\rangle$ values by means of the Bragg additivity rule. So for those constants, we take

$$\left\langle\frac{Z}{A}\right\rangle = \left\langle\frac{Z}{A}\right\rangle_{\mathrm{Fe}} = 0.466\,, \qquad \langle I\rangle = I_{\mathrm{Fe}} = 286\ \mathrm{eV}\,. \tag{E.13}$$

The volume fraction can be used for the calculation of the sampling density via Equation E.1,

$$\langle\rho\rangle = \left(1 - \frac{1}{4.67}\right)\rho_{\mathrm{Fe}} + \frac{1}{4.67}\,\rho_{\mathrm{PS}} \simeq 6.40\ \mathrm{g\,cm^{-3}}\,, \tag{E.14}$$

as plastic scintillators typically have a density around $\gtrsim 1\ \mathrm{g\,cm^{-3}}$ [78].

The ATLAS HEC is a fairly simple sampling calorimeter with LAr active layers, like the ECAL, and with copper-plate absorbers. The density of the supplied copper is specified to lie between 8.89 and 8.94

g/cm^3 [336], so the average is 8.915 g/cm^3. The 8.5 mm gaps between the Cu plates are practically fully filled with LAr, since the volume occupied by the three layers of the readout system with a few 100 μm thickness is negligibly small (see Figures 8.7 - 7.10 in [336]). There are LAr gaps between each Cu plate with a thickness of 1.954 mm each, which we will simply round up to 8.5 mm. Ignoring the steel rods, the volume fractions of Cu/LAr in HEC1 (HEC2) are therefore 3.00 (6.07), leading to sampling densities of 7.04 (7.85) g/cm^3. Thus we get

$$\langle\rho\rangle = \frac{L_{\text{HEC1}}}{L_{\text{HEC1}} + L_{\text{HEC2}}} \langle\rho\rangle_{\text{s,HEC1}} + \frac{L_{\text{HEC2}}}{L_{\text{HEC1}} + L_{\text{HEC2}}} \langle\rho\rangle_{\text{s,HEC2}} \simeq 7.48 \,\text{g}\,\text{cm}^{-3} \,. \tag{E.15}$$

For $\langle Z/A\rangle$ and $\langle I\rangle$, we can use the values for copper and ignore the radiator, since $w_{\text{Cu}}/w_{\text{LAr}} \simeq 29.8$ by Equation E.9.

E.2.3 CMS

□ Electromagnetic calorimeter

The ECAL crystals are made of $PbWO_4$, having a density of $\rho = 8.28 \,\text{g}\,\text{cm}^{-3}$. Furthermore, PDG provides $\langle Z/A\rangle = 0.413$ and $I = 600.7$ eV.

□ Hadronic calorimeter

The HB absorbers are made of brass of type C26000 (cartridge brass), with a density of 8.53 g/cm^3 and amounting to about 70% Cu and 30% Zn in terms of volume [316]. By Equation E.9, this corresponds to $w_{\text{Cu}} \simeq 0.74$ and $w_{\text{Zn}} \simeq 0.26$. Using the Bragg additivity rule, we get $\langle Z/A\rangle = 0.457$ and $\langle I\rangle = 324$ eV for the brass. We have seen above that the total thickness of the EB is 96 cm, the brass plates adding up to 74.3 cm and the two steel plates to 13.6 cm. However, we will treat each steel plate as another brass plate, as their thicknesses were chosen such that they have an equal interaction length λ_{I} as the brass plates [460]. Thus we consider the wedges to be made of 9 and 7 layers of 50.5 mm and 56.5 mm thickness, respectively. For $\langle Z/A\rangle$ and $\langle I\rangle$, we choose the values of the brass, because the weight fraction of the plastic scintillator trays is volume- and density-suppressed according to Equation E.9. The sampling density is obtained from the brass/total sampling length ratio with the approximation that the PS tray modules have the same density as the PS itself of $\sim 1 \,\text{g}\,\text{cm}^{-3}$,

$$\langle\rho\rangle = \frac{79.35}{96} \rho_{\text{C26000}} + \left(1 - \frac{79.35}{96}\right) \rho_{\text{PS}} \simeq 7.224 \,\text{g}\,\text{cm}^{-3} \,. \tag{E.16}$$

For the HE, we also take the $\langle Z/A\rangle$ and $\langle I\rangle$ values of the brass and work out the sampling density in the same way. The 158.4 cm wide sequence of brass-PS layers has a period of 88 mm, 18 mm of which corresponding to the scintillator trays. Therefore the sampling density has the value

$$\langle\rho\rangle = \frac{70}{88} \rho_{\text{C26000}} + \left(1 - \frac{70}{88}\right) \rho_{\text{PS}} \simeq 6.990 \,\text{g}\,\text{cm}^{-3} \,. \tag{E.17}$$

For our toy detector implementation, we add to the 158.4 cm another 10 cm of brass, accounting for the 10 cm of stainless steel behind the last brass layer. As iron has similar properties, this is not a significant sacrifice of realism.

APPENDIX F

Understanding the effective ggZ vertex

The ggZ process was considered for the first time by D. A. Dicus and S. S. D. Willenbrock in [380] with basis on the explicit VVZ triangle calculation by J. S. Bell and R. Jackiw [72]. Bell and Jackiw intended to rescue the partially conserved axial current (PCAC) hypothesis by introducing auxiliary fields to obtain a vanishing $\pi^0 \to \gamma\gamma$ amplitude and to preserve gauge invariance, as it appeared clearly broken in the perturbative calculation. In this appendix, we verify that the Dicus-Willenbrock (DW) vertex is consistent with the Bell-Jackiw (BJ) calculation if gauge invariance is imposed and that this necessarily implies an anomalous axial Ward identity.

F.1 The Dicus-Willenbrock vertex

In [380], Dicus and Willenbrock use the VVA triangle vertex function obtained by Bell and Jackiw to compute the amplitude for the ggZ cross section in fourth generation lepton production. In explicit form, it was shown for the first time by Dicus and P. Roy in [390]. For a specific quark Q of mass m_Q propagating in the loop, the vertex has the form

$$F_{\mathrm{DW}}^{\alpha\mu\nu}(p,q,m_Q) = \text{couplings} \times I_{\mathrm{DW}}(\hat{s},m_Q)\cdot\epsilon^{\mu\nu\lambda\tau}p_\lambda q_\tau k^\alpha\,, \tag{F.1}$$

where the 4-momenta carried by the two gluons and the Z, are, respectively, denoted by

$$p,\quad q\quad (p^2=q^2=0),\qquad k=p+q\quad (\hat{s}=k^2)\,, \tag{F.2}$$

and the loop function reads explicitly

$$I_{\mathrm{DW}}(\hat{s},m_Q) = -\frac{1}{2\hat{s}}\left\{1+\frac{2m_Q^2}{\hat{s}}\int_0^1\frac{dx}{x}\,\ln\left[1-\frac{\hat{s}}{m_Q^2}\,x(1-x)\right]\right\}\,. \tag{F.3}$$

The amplitude for a $gg\to Z^*\to f\bar{f}$ process is then given by the expression

$$i\mathcal{M} = \sum_Q \epsilon_\mu(p)\,\epsilon_\nu(q)\,F_{\mathrm{DW}}^{\alpha\mu\nu}(p,q,m_Q)\,D^Z_{\alpha\beta}\,j^\beta\,, \tag{F.4}$$

D^Z being the Z propagator, $\epsilon_{\mu,\nu}$ the gluon polarization vectors and j^β the fermionic final state current. The vertex function in Equation F.1 is to be compared to the original expression for the triangle obtained by Bell and Jackiw in 1969 [72]. Since the amplitude is calculated from the Fourier transform

$$F^{\alpha\mu\nu}\sim\int d^4x\,d^4y\,e^{-ip\cdot x}e^{-iq\cdot y}\,\langle 0|\,T\left\{j^\mu(x)j^\nu(y)j^{5\alpha}(0)\right\}|0\rangle\,, \tag{F.5}$$

the vertex necessarily has pseudotensor character, is proportional to the ϵ tensor and has an odd number of momenta. Further necessary symmetries are Lorentz covariance and Bose symmetry (*i.e.* $(p,\mu)\leftrightarrow(q,\nu)$). Ignoring the couplings, Bell and Jackiw thus write the general form of the vertex as

$$\begin{aligned}F_{\mathrm{BJ}}^{\alpha\mu\nu}(p,q) = {}& F_1(\hat{s})\cdot\epsilon^{\mu\nu\lambda\tau}p_\lambda q_\tau k^\alpha\\ &+F_2(\hat{s})\cdot(\epsilon^{\alpha\mu\lambda\tau}q^\nu-\epsilon^{\alpha\nu\lambda\tau}p^\mu)\,p_\lambda q_\tau\\ &+F_3(\hat{s})\cdot(\epsilon^{\alpha\mu\lambda\tau}p^\nu-\epsilon^{\alpha\nu\lambda\tau}q^\mu)\,p_\lambda q_\tau\\ &+F_4(\hat{s})\cdot\epsilon^{\alpha\mu\nu\sigma}(p-q)_\sigma\,,\end{aligned} \tag{F.6}$$

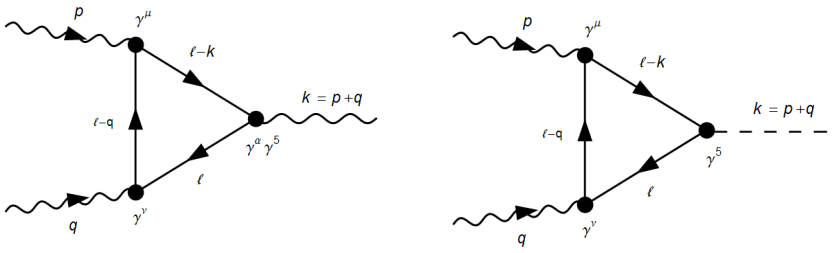

FIGURE F.1: Triangle diagrams corresponding to $F^{\alpha\mu\nu}$ (VVA, left) and $S^{\mu\nu}$ (VVP, right). We omitted the crossed diagrams, obtained through the interchange $(p,\mu) \leftrightarrow (q,\nu)$.

with the finite loop functions

$$F_1 = \int_0^1 dx \int_0^{1-x} dy \, \frac{(x+y)(1-x-y)+4xy}{m^2 - \hat{s}xy} \,, \tag{F.7}$$

$$-F_2 = F_3 = \int_0^1 dx \int_0^{1-x} dy \, \frac{(x+y)(1-x-y)}{m^2 - \hat{s}xy} \,, \tag{F.8}$$

$$F_4 = -1 + \frac{\hat{s}}{2} \int_0^1 dx \int_0^{1-x} dy \, \frac{(x+y)(1-x-y)}{m^2 - \hat{s}xy} = -1 + \frac{\hat{s}}{2} F_3 \,. \tag{F.9}$$

We remark that their function F_1 contains another term in the numerator inducing a pion mass pole, which we ignore. More importantly, note the -1 in F_4 — As we herein verify, this term violates gauge but *not* chiral symmetry.

F.2 Connection between the axial anomaly and the triangle amplitude

We notice that the DW vertex is of the form of the F_1 term, indicating that F_1 must be given by I_{DW} plus a multiple of F_3 (or equivalently F_2), since F_3 multiplies p, q and k as well. In fact, a direct comparison of Equation F.3 with experssions F.7 and F.8 reveals

$$I_{\mathrm{DW}} = F_1 - F_3 \tag{F.10}$$

and we intend to investigate how this comes about. For the anomaly discussion, we mostly follow [468] and [469].

It has first to be checked whether the triangle respects quantum versions of classical conservation laws (Ward identities), such that the theory remains renormalizable. Consider the Green function

$$\langle 0 | \, T \left\{ j^\mu(x) O^1(y_1) \dots O^n(y_n) \right\} | 0 \rangle \,, \tag{F.11}$$

O_i being local operators. The Ward identity reads

$$\begin{aligned} &\partial^x_\mu \, \langle 0 | \, T \left\{ j^\mu(x) \, O^1(y_1) \dots O^n(y_n) \right\} | 0 \rangle \\ &\quad = \langle 0 | \, T \left\{ \partial^x_\mu j^\mu(x) \, O^1(y_1) \dots O^n(y_n) \right\} | 0 \rangle \\ &\qquad + \sum_{i=1}^{n} \langle 0 | \, T \left\{ [j^0(x), O^i(y_i)] \, \delta(x_0 - y_{i0}) \, O^1 \dots O^{i-1} \, O^{i+1} \dots O^n \right\} | 0 \rangle \,, \end{aligned} \tag{F.12}$$

where the term $\partial^x_\mu j^\mu(x)$ is to be replaced by the classical conservation law. The classical vector and axial vector current conservation laws for the current densities[1] $j^\mu = \bar{\psi}\gamma^\mu\psi$ and $j^{5\mu} = \bar{\psi}\gamma^\mu\gamma^5\psi$ for fermions of mass m are directly obtained via the Dirac equation and read

[1] The generalization to Yang-Mills theories is straightforward and changes the results merely by group theory factors; see footnote 5 to see how this affects the anomaly.

$$\partial_\mu j^\mu = 0\,, \tag{F.13}$$
$$\partial_\alpha j^{5\alpha} = 2imP\,, \tag{F.14}$$

with the pseudoscalar density $P = \bar{\psi}\gamma^5\psi$. Now consider the following two Green functions in momentum space:

$$F^{\alpha\mu\nu}(p,q) = i\int d^4x d^4y d^4z\, e^{ip\cdot x+iq\cdot y+ik\cdot z}\,\langle 0|\,T\left\{j^\mu(x)j^\nu(y)j^{5\alpha}(z)\right\}|0\rangle\,, \tag{F.15}$$
$$S^{\mu\nu}(p,q) = i\int d^4x d^4y d^4z e^{ip\cdot x+iq\cdot y+ik\cdot z}\,\langle 0|\,T\left\{j^\mu(x)j^\nu(y)P(z)\right\}|0\rangle\,. \tag{F.16}$$

k is fixed by energy-momentum conservation. Using Equation F.12 on F.15 with the classical relation in Equation F.14, we obtain, after naïve[2] partial integration, the so-called *axial Ward identity*,

$$\begin{aligned} k_\alpha F^{\alpha\mu\nu} &= 2im\int d^4x d^4y d^4z\, e^{ip\cdot x+iq\cdot y+ik\cdot z}\,\langle 0|\,T\left\{j^\mu(x)j^\nu(y)P(z)\right\}|0\rangle \\ &= 2mS^{\mu\nu}\,. \end{aligned} \tag{F.17}$$

Its simple form stems from the vanishing of the commutators in Equation F.12 in this case, and we see that it connects $F^{\alpha\mu\nu}$ and $S^{\mu\nu}$ — these tensors express the amputated versions of the diagrams in Figure F.1. One obtains analogously momentum-space versions of the *vector Ward identitiy*, meaning gauge invariance, and altogether we have

$$(V1)\qquad p_\mu F^{\alpha\mu\nu} = 0\,, \tag{F.18}$$
$$(V2)\qquad q_\nu F^{\alpha\mu\nu} = 0\,, \tag{F.19}$$
$$(A)\qquad k_\alpha F^{\alpha\mu\nu} = 2mS_{\mu\nu}\,. \tag{F.20}$$

In lowest-order perturbation theory, $F^{\alpha\mu\nu}$ and $S^{\mu\nu}$ read

$$\begin{aligned} F^{\alpha\mu\nu}(p,q) = -\int\frac{d^4\ell}{(2\pi)^4}\,\mathrm{Tr}\Bigg[&\frac{i(\not\ell+m)}{\ell^2-m^2}\gamma^\alpha\gamma^5\frac{i(\not\ell-\not k+m)}{(\ell-k)^2-m^2}\gamma^\mu\frac{i(\not\ell-\not q+m)}{(\ell-q)^2-m^2}\gamma^\nu \\ &+(p,\mu\leftrightarrow q,\nu)\Bigg], \end{aligned} \tag{F.21}$$

$$\begin{aligned} S^{\mu\nu}(p,q) = -\int\frac{d^4\ell}{(2\pi)^4}\,\mathrm{Tr}\Bigg[&\frac{i(\not\ell+m)}{\ell^2-m^2}\gamma^5\frac{i(\not\ell-\not k+m)}{i(\ell-k)^2-m^2}\gamma^\mu\frac{i(\not\ell-\not q+m)}{(\ell-q)^2-m^2}\gamma^\nu \\ &+(p,\mu\leftrightarrow q,\nu)\Bigg]. \end{aligned} \tag{F.22}$$

$F^{\alpha\mu\nu}$ has been calculated by Bell and Jackiw (Equations F.6 - F.9).

The form in Equations F.7 - F.9 contains a choice due to an ambiguity in the calculation of F_4. To see this, first note that when k_α is contracted with $F^{\alpha\mu\nu}$, we *should* obtain expression F.20. But contrary to $S^{\mu\nu}$, the calculation of $F^{\alpha\mu\nu}$ features differences of integrals that are linearly divergent with the loop momentum ℓ, which results in calculational ambiguities that propagate into the part of the amplitude that is linear in the external momenta, *i.e.* F_4. The divergences cancel, but the finite remainder depends on how the integral is regularized and this will affect the Ward identities F.18-F.20. At present, there is no known regularization scheme preserving gauge invariance and chiral symmetry at the same time, so all results one can obtain for $j^{5\mu}$ and/or j^μ are anomalous. For example, if we choose to preserve gauge invariance with our regularization (as is most desirable), then we will necessarily end up with a modified version of Equation F.20, keeping Equations F.18 and F.19 unaltered, to wit

$$\partial_\mu j^\mu = 0,\quad \partial_\mu j^{5\mu} = 2imP + \mathcal{A} \tag{F.23}$$

[2]To see why this is uncareful, see [468]. In short, we are evaluating operators in operator products at equal spacetime points, leading to singularities whose regularization is ambiguous, hence the anomaly.

and

$$p_\mu S^{\mu\nu} = q_\nu S^{\mu\nu} = 0, \quad k_\alpha F^{\alpha\mu\nu} = 2mS^{\mu\nu} + \mathcal{A}^{\mu\nu} \,. \tag{F.24}$$

Alternatively, we can keep Equations F.14 and F.20 and modify Equations F.13, F.18 and F.19, or modify all of them. To check that $F^{\alpha\mu\nu}_{\mathrm{BJ}}$ is not gauge invariant, contract with a gluon momentum:

$$\begin{aligned} p_\mu F^{\alpha\mu\nu} = \; & 0 \cdot F_1 \\ & + (0-0) \cdot F_2 \\ & + [0 - \epsilon^{\alpha\nu\lambda\tau}(p\cdot q) p_\lambda q_\tau] \cdot F_3 \\ & + \epsilon^{\alpha\mu\nu\tau}(0 - p_\mu q_\tau) \cdot F_4 \,, \end{aligned} \tag{F.25}$$

by the antisymmetry of the ϵ tensor and $p^2 = 0$. Gauge invariance, $p_\mu F^{\alpha\mu\nu} = 0$, is therefore assured if

$$F_4 = \frac{\hat{s}}{2} F_3 \,, \tag{F.26}$$

since $p \cdot q = \hat{s}/2$. From Equation F.8 and F.9, we see that this is not the case: A term in F_4, namely

$$\Delta F_4 = -1 \,, \tag{F.27}$$

violates gauge invariance. Due to this term, Bell and Jackiw arrive at the identities

$$p_\mu F^{\alpha\mu\nu} = -\frac{1}{4\pi^2}\epsilon^{\alpha\nu\lambda\tau} p_\lambda q_\tau \,, \quad q_\nu F^{\alpha\mu\nu} = \frac{1}{4\pi^2}\epsilon^{\alpha\mu\lambda\tau} p_\lambda q_\tau \,. \tag{F.28}$$

F.3 Perturbative calculation of the anomaly

In this section, we investigate how the anomaly arises in perturbation theory. We apply the 'surface term' method, also originally used by Bell and Jackiw, however one can achieve the same results by other means. Using

$$\not{k}\gamma^5 = \gamma^5(\not{\ell} - \not{k} - m) + (\not{\ell} - m)\gamma^5 + 2m\gamma^5 \tag{F.29}$$

in the numerator of Equation F.21 gives

$$(p+q)_\alpha F^{\alpha\mu\nu} = 2mS^{\mu\nu} + R_1^{\mu\nu} + R_2^{\mu\nu} \,, \tag{F.30}$$

where

$$\begin{aligned} R_1^{\mu\nu}(p,q) = \int \frac{d^4\ell}{(2\pi)^4} \,\mathrm{Tr}\Bigg[& \frac{(\not{\ell} - \not{p} + m)}{(\ell-p)^2 - m^2}\gamma^5\gamma^\mu \frac{(\not{\ell} - \not{k} + m)}{(\ell-k)^2 - m^2}\gamma^\nu \\ & - \frac{(\not{\ell} + m)}{\ell^2 - m^2}\gamma^5\gamma^\mu \frac{(\not{\ell} - \not{q} + m)}{(\ell-q)^2 - m^2}\gamma^\nu \Bigg] \,, \end{aligned} \tag{F.31}$$

$$R_2^{\mu\nu}(p,q) = R_1^{\nu\mu}(q,p) \,. \tag{F.32}$$

A shift

$$\ell \to \ell + p \quad \text{and} \quad \ell \to \ell + q \tag{F.33}$$

in the first terms of R_1 and R_2 respectively seems to lead to $R_{1,2} = 0$ and therefore the Ward identities F.18 - F.20 are seemingly satisfied. But since the integrals are linearly divergent,[3] one has to be careful and the correct outcome is actually a finite and non-vanishing result. The expressions in Equations F.31

[3] There seems to be a quadratic divergence, but it disappears because the trace gives $\epsilon_{\mu\nu\alpha\beta}\ell^\alpha\ell^\beta = 0$.

and F.32 have the form of differences of linearly divergent integrals. In one dimension, we have

$$\Delta(a) = \int_{-\infty}^{\infty} dx\,[f(x+a) - f(x)] \;=\; \int_{-\infty}^{\infty} dx\left[af'(x) + \frac{a^2}{2!}f''(x) + \ldots\right]$$
$$= a\,[f(\infty) - f(-\infty)] + \frac{a^2}{2!}\,[f'(\infty) - f'(-\infty)] + \ldots \tag{F.34}$$

If $\int dx\, f(x)$ is at most logarithmically divergent, then $\partial_x^{(n)} f(\pm\infty) = 0$ for $n = 0, 1, \ldots$, and the shift can be done, so that $\Delta(a) = 0$. But if it is linearly divergent, then $f(\pm\infty) \neq 0$ and $< \infty$, $f^{(n)}(\pm\infty) = 0$ for $n = 1, \ldots$ and $\Delta(a) = a[f(\infty) - f(-\infty)]$, which may be non-vanishing.[4] This is called a surface term. In 4-dimensional Minkowski space, the analogue to Equation F.34 is [468, 469]

$$\Delta(a) = i2\pi^2 a^\mu \lim_{\ell\to\infty} \ell_\mu \ell^2 f(\ell)\,, \tag{F.35}$$

for some shift 4-vector a^μ. R_1 is of the form $\int d^4\ell[f(\ell-p)-f(\ell)]$ and R_2 is of the form $\int d^4\ell[f(\ell-q)-f(\ell)]$, so the use of Equation F.35 and of $\lim_{\ell\to\infty} \ell_\lambda \ell_\beta/\ell^2 = g_{\lambda\beta}/4$, with $a^\mu = -p^\mu$, yields

$$R_1^{\mu\nu} = \frac{1}{8\pi^2}\epsilon^{\mu\nu\lambda\sigma} p_\lambda q_\sigma\,, \tag{F.36}$$

and for R_2, with $p \leftrightarrow q$ and $\mu \leftrightarrow \nu$, we obtain the same result, leading to

$$(p+q)_\alpha F^{\mu\nu\alpha} = 2mS^{\mu\nu} + \frac{1}{4\pi^2}\epsilon^{\mu\nu\lambda\sigma} p_\lambda q_\sigma\,. \tag{F.37}$$

This clearly violates identity (A), but, in fact, we also 'chose' to violate (V1) and (V2).

F.4 Arbitrariness in the Ward identities and ambiguity in the triangle amplitude

Consider the difference

$$\Delta^{\alpha\mu\nu}(a) = F^{\alpha\mu\nu}(a) - F^{\alpha\mu\nu}(0) \tag{F.38}$$

with the loop momentum shift 4-vector

$$a = \alpha p + (\alpha - \beta)q\,, \tag{F.39}$$

where α and β are arbitrary real numbers. We easily obtain

$$F^{\alpha\mu\nu}(a) = F^{\alpha\mu\nu}(0) + \Delta^{\alpha\mu\nu}(a) = F^{\alpha\mu\nu}(0) + \frac{\beta}{8\pi^2}\epsilon^{\alpha\mu\nu\sigma}(p-q)_\sigma\,, \tag{F.40}$$

the α terms cancel. For the axial Ward identity, this means

$$k_\alpha F^{\alpha\mu\nu}(\beta) = 2mS^{\mu\nu} + \frac{1-\beta}{4\pi^2}\epsilon^{\mu\nu\lambda\tau} p_\lambda q_\tau\,. \tag{F.41}$$

In the same way one can calulate the vector Ward identities. In total, Equations F.18 - F.20 become

$$(V1) \qquad p_\mu F^{\alpha\mu\nu} = -\frac{1+\beta}{8\pi^2}\epsilon^{\alpha\nu\lambda\tau} p_\lambda q_\tau\,, \tag{F.42}$$

$$(V2) \qquad q_\nu F^{\alpha\mu\nu} = \frac{1+\beta}{8\pi^2}\epsilon^{\alpha\mu\lambda\tau} p_\lambda q_\tau\,, \tag{F.43}$$

$$(A) \qquad k_\alpha F^{\alpha\mu\nu} = 2mS_{\mu\nu} + \frac{1-\beta}{4\pi^2}\epsilon^{\mu\nu\lambda\tau} p_\lambda q_\tau\,. \tag{F.44}$$

Hence, the anomaly can be shifted from (V) to (A) and vice versa, however there is no value for β such that gauge and chiral symmetries are both maintained. The choice $\beta = -1$ then corresponds to choosing

[4] An example in one dimension would be $\tanh(x)$.

not to sacrifice gauge invariance and results in the axial anomaly term[5]

$$\mathcal{A}^{\mu\nu} = \frac{1}{2\pi^2}\epsilon^{\mu\nu\lambda\tau}p_\lambda q_\tau \,. \tag{F.45}$$

Note that the case of Bell and Jackiw, with the vector Ward identities as in Equation F.28, corresponds to choosing

$$\beta_{\mathrm{BJ}} = +1 \,. \tag{F.46}$$

This means that they are interested in preserving axial symmetry, what is also clear from the general context of their paper — the only breaking of axial symmetry should be due to a pseudoscalar field (the pion) coupling to the axial current, which in this context means Equation F.20.

It is hard to identify the source of the ambiguity in the original calculation of F_{BJ} in [72] due to few given details and the archaic context and notation. From Equation F.40, it is clear that it lies in the F_4 term, Equation F.9. The authors write the full amplitude as

$$\begin{aligned}
F^{\alpha\mu\nu} = &\int_0^1 dx \int_0^{1-x} dy \frac{1}{m^2 - \hat{s}xy} \\
&\times \left\{ \left[-m^2 - \hat{s}xy + \frac{\hat{s}}{2}(x+y)(1-x-y) \right] \epsilon^{\alpha\mu\nu\sigma}(p-q)_\sigma \right. && \text{(F.47a)} \\
&\quad + \left[(x+y)(1-x-y)((p-q)^\mu \epsilon^{\alpha\nu\lambda\tau} + (p-q)^\nu \epsilon^{\alpha\mu\lambda\tau}) \right. && \text{(F.47b)} \\
&\qquad \left. \left. + \; (x+y-(x-y)^2) k^\alpha \epsilon^{\mu\nu\lambda\tau} \right] p_\lambda q_\tau \right\} && \text{(F.47c)} \\
&+ \frac{2i}{\pi^2}\epsilon^{\alpha\mu\nu\sigma} \int d^4\ell \left\{ \frac{\ell_\sigma}{[(\ell+p)^2 - m^2][(\ell-q)^2 - m^2]} \right. && \text{(F.47d)} \\
&\qquad \left. + \int_0^1 dx \int_0^{1-x} dy \frac{(p-q)_\sigma}{[(\ell + px - qy)^2 - m^2 + \hat{s}xy]^2} \right\} \,. && \text{(F.47e)}
\end{aligned}$$

It is easy to verify that the line of F.47b coincides with the F_2 and F_3 terms and one readily sees that F.47c is the F_1 term. However, the treatment of the last two loop integrals is a bit imprecise. The first of these integrals is linearly divergent, therefore it is not uniquely defined when the integration variable is shifted. Bell and Jackiw calculate the (finite) value of the summed last two integrals to be

$$-\frac{1}{2}\epsilon^{\alpha\mu\nu\sigma}(p-q)_\sigma + 4\epsilon^{\alpha\mu\nu\sigma}(p-q)_\sigma \int_0^1 dx \int_0^{1-x} dy \frac{\hat{s}xy}{m^2 - \hat{s}xy} \,, \tag{F.48}$$

by performing an unspecified integration variable shift[6] and picking up the surface term

$$-\frac{1}{16}\epsilon^{\alpha\mu\nu\sigma}(p-q)_\sigma \,. \tag{F.49}$$

Note that Equation F.48 can be written as

$$\epsilon^{\alpha\mu\nu\sigma}(p-q)_\sigma \int_0^1 dx \int_0^{1-x} dy \frac{-(m^2 - \hat{s}xy) + 2\hat{s}xy}{m^2 - \hat{s}xy} \,. \tag{F.50}$$

When combining this expression with F.47a, one indeed obtains F_4 as written in (F.9), which violates gauge symmetry but respects axial symmetry. Equation F.50 combines with F.47a in such a way as to yield the -1 term (in modern terms, choosing $\beta = +1$), reasoning that the PCAC hypothesis for the pion necessarily breaks gauge invariance; as a cure, they introduce auxiliary fields.

[5] In the non-Abelian case, the gauge bosons coupling to the indices μ, ν and α each contribute with a generator of the gauge group's adjoint representation. Thus the amplitude gets multiplied by a group theory factor and so does the anomaly term,

$$\mathcal{A}^{\mu\nu}_{abc} = \frac{c_{abc}}{2\pi^2}\epsilon^{\mu\nu\lambda\tau}p_\lambda q_\tau \,, \qquad c_{abc} = \frac{1}{2}\mathrm{Tr}\left[\left\{T^a, T^b\right\}T^c\right] \overset{T^c \to 1}{\longrightarrow} c_{ab} = \mathrm{Tr}\left[T^a T^b\right] \,,$$

the limiting case of $T^c \to 1$ corresponding to our case of study.

[6] In other words, it is not clear how the authors rewrite the integral in the form $\int dx[f(x+a) - f(x)]$

F.5 Restoring gauge invariance and obtaining the Dicus-Willenbrock amplitude

Recall that one is allowed to change the triangle amplitude linearly in $\epsilon(p-q)$, *i.e.*

$$F^{\alpha\mu\nu} \to F^{\alpha\mu\nu} + C\epsilon^{\alpha\mu\nu\sigma}(p-q)_\sigma\,, \qquad C = \frac{\beta}{8\pi^2}\,. \tag{F.51}$$

We saw that choosing $\beta = -1$ renders $F^{\alpha\mu\nu}$ gauge invariant by setting $\Delta F_4 = 0$, but axial symmetry is broken by the anomaly term, Equation F.45. Dicus and Willenbrock clearly opted for sacrificing axial rather than gauge symmetry. An immediate consequence is the relation

$$F_4 = \frac{\hat{s}}{2}F_3\,, \tag{F.52}$$

hence we may write the DW matrix element F.4 as

$$\begin{aligned} i\mathcal{M} &= \sum_Q \epsilon_\mu(p)\,\epsilon_\nu(q)\,F^{\alpha\mu\nu}_{\rm DW}(p,q,m_Q)\,D^Z_{\alpha\beta}\,j^\beta \\ &\sim \epsilon_\mu(p)\,\epsilon_\nu(q)\,\left[F_1\cdot\epsilon^{\mu\nu\lambda\tau}p_\lambda q_\tau k^\alpha + F_4\cdot\epsilon^{\alpha\mu\nu\sigma}(p-q)_\sigma\right]D^Z_{\alpha\beta}\,j^\beta \\ &= \epsilon_\mu(p)\,\epsilon_\nu(q)\,\left[F_1\cdot\epsilon^{\mu\nu\lambda\tau}p_\lambda q_\tau k^\alpha + \frac{1}{2}F_3\cdot\epsilon^{\alpha\mu\nu\sigma}(p-q)_\sigma k^2\right]D^Z_{\alpha\beta}\,j^\beta\,, \end{aligned} \tag{F.53}$$

enforcing the transversality conditions

$$\epsilon(p)\cdot p = \epsilon(q)\cdot q = \epsilon(p)\cdot q = \epsilon(q)\cdot p = 0\,. \tag{F.54}$$

Using the four-dimensional Schouten identity for a 4-vector V^μ,

$$\epsilon^{\alpha\mu\nu\lambda}V^\tau + \epsilon^{\mu\nu\lambda\tau}V^\alpha + \epsilon^{\nu\lambda\tau\alpha}V^\mu + \epsilon^{\lambda\tau\alpha\mu}V^\nu + \epsilon^{\tau\alpha\mu\nu}V^\lambda = 0\,, \tag{F.55}$$

we can rewrite the F_3 term in $F^{\alpha\mu\nu}_{\rm DW}$ in the form

$$\begin{aligned} \epsilon^{\alpha\mu\nu\lambda}(p-q)_\lambda k^2 &= \epsilon^{\alpha\mu\nu\lambda}k^\tau(p-q)_\lambda k_\tau \\ &= \left[-\epsilon^{\mu\nu\lambda\tau}(p+q)^\alpha - \epsilon^{\nu\lambda\tau\alpha}(p+q)^\mu - \epsilon^{\lambda\tau\alpha\mu}(p+q)^\nu - \epsilon^{\tau\alpha\mu\nu}(p+q)^\lambda\right] \\ &\quad\times\,(p-q)_\lambda(p+q)_\tau\,. \end{aligned} \tag{F.56}$$

The second and third terms don't contribute because of the conditions (F.54). The first term yields

$$-\epsilon^{\mu\nu\lambda\tau}k^\alpha(p-q)_\lambda(p+q)_\tau = -\epsilon^{\mu\nu\lambda\tau}k^\alpha(p_\lambda p_\tau + p_\lambda q_\tau - p_\tau q_\lambda - q_\lambda q_\tau) = -2\epsilon^{\mu\nu\lambda\tau}p_\lambda q_\tau k^\alpha\,, \tag{F.57}$$

by the antisymmetry of the ϵ tensor. The fourth term is proportional to $(p+q)\cdot(p-q)$, which vanishes. Therefore we end up with

$$F^{\alpha\mu\nu}_{\rm DW}(p,q,m) \propto \epsilon^{\mu\nu\lambda\tau}p_\lambda q_\tau k^\alpha\,[F_1 - F_3]\,, \tag{F.58}$$

confirming Equation F.10. We now integrate over y in $F_1 - F_3$

$$\begin{aligned} F_1 - F_3 &= \int_0^1 dx \int_0^{1-x} dy\,\frac{4xy}{m^2 - \hat{s}xy} \\ &= -\frac{4}{\hat{s}}\int_0^1 dx\left\{1 - x + \frac{m^2}{\hat{s}x}\log\left[1 - \frac{\hat{s}}{m^2}\,x(1-x)\right]\right\} \\ &= -\frac{1}{2\hat{s}}\left\{1 + \frac{2m^2}{\hat{s}}\int_0^1 \frac{dx}{x}\log\left[1 - \frac{\hat{s}}{m^2}\,x(1-x)\right]\right\}\,, \end{aligned} \tag{F.59}$$

as written in Equation F.3, and arrive at the Dicus-Willenbrock vertex when including the loop factor $i/(4\pi)^2$ and all couplings (except the group theory factor),

$$F^{\alpha\mu\nu}_{\rm DW}(p,q) = (-)_Q\frac{\alpha_{\rm s}}{2\pi}\frac{e}{{\rm s_w c_w}}\frac{1}{\hat{s}}\epsilon^{\mu\nu\lambda\tau}p_\lambda q_\tau k^\alpha\left\{1 + \frac{2m_Q^2}{\hat{s}}\int_0^1\frac{dx}{x}\ln\left[1 - \frac{\hat{s}}{m_Q^2}\,x(1-x)\right]\right\}\,. \tag{F.60}$$

For a quark species Q, the axial coupling to the Z is given by $a_Q = \frac{1}{2}T^3_Q = \frac{1}{4}(-)_Q$, where $(-)_Q$ is $+1$ for up-type quarks and -1 for down-type quarks. The global $Zf\bar{f}$ coupling is $-ie/(\mathrm{s_w c_w})$ and we have two factors of $-ig_\mathrm{s} = -i\sqrt{4\pi\alpha_\mathrm{s}}$.

Bibliography

[1] A. G. Hessler, A. Ibarra, E. Molinaro, and S. Vogl, Phys. Rev., **D91**, 115004 (2015), arXiv:1408.0983 [hep-ph].

[2] A. G. Hessler, A. Ibarra, E. Molinaro, and S. Vogl, TUM-HEP-1058/16 (2016).

[3] S. L. Glashow, Nucl.Phys., **22**, 579 (1961); S. Weinberg, Phys.Rev.Lett., **19**, 1264 (1967); A. Salam, ed. N. Svartholm, Almqvist Wiksell Forlag AB; 8th Nobel Symposium, 367 (1968).

[4] M. Gell-Mann, Phys. Lett., **8**, 214 (1964); G. Zweig, (1964); H. Fritzsch, M. Gell-Mann, and H. Leutwyler, Phys. Lett., **B47**, 365 (1973).

[5] G. Aad *et al.* (ATLAS), Phys. Lett., **B716**, 1 (2012), arXiv:1207.7214 [hep-ex].

[6] S. Chatrchyan *et al.* (CMS), Phys. Lett., **B716**, 30 (2012), arXiv:1207.7235 [hep-ex].

[7] F. Englert and R. Brout, Phys.Rev.Lett., **13**, 321 (1964); P. W. Higgs, Phys.Rev.Lett., **13**, 508 (1964); G. S. Guralnik, C. R. Hagen, and T. W. B. Kibble, Phys.Rev.Lett., **13**, 585 (1964).

[8] P. A. R. Ade *et al.* (Planck), (2015), arXiv:1502.01589 [astro-ph.CO].

[9] R. Davis, Jr., D. S. Harmer, and K. C. Hoffman, Phys. Rev. Lett., **20**, 1205 (1968).

[10] N. Arkani-Hamed, S. Dimopoulos, G. R. Dvali, and J. March-Russell, *SUSY 98 Conference Oxford, England, July 11-17, 1998*, Phys. Rev., **D65**, 024032 (2002), arXiv:hep-ph/9811448 [hep-ph].

[11] Y. Grossman and M. Neubert, Phys. Lett., **B474**, 361 (2000), arXiv:hep-ph/9912408 [hep-ph].

[12] G. Perez and L. Randall, JHEP, **01**, 077 (2009), arXiv:0805.4652 [hep-ph].

[13] P. Minkowski, Phys. Lett., **B67**, 421 (1977); M. Gell-Mann, P. Ramond, and R. Slansky, *Supergravity Workshop Stony Brook, New York, September 27-28, 1979*, Conf. Proc., **C790927**, 315 (1979), arXiv:1306.4669 [hep-th]; T. Yanagida, *Proceedings: Workshop on the Unified Theories and the Baryon Number in the Universe, Tsukuba, Japan, 13-14 Feb 1979*, Conf. Proc., **C7902131**, 95 (1979), [Conf. Proc.C7902131,95(1979)]; R. N. Mohapatra and G. Senjanovic, Phys. Rev. Lett., **44**, 912 (1980).

[14] M. Magg and C. Wetterich, Phys. Lett., **B94**, 61 (1980); G. Lazarides, Q. Shafi, and C. Wetterich, Nucl. Phys., **B181**, 287 (1981); R. N. Mohapatra and G. Senjanovic, Phys. Rev., **D23**, 165 (1981); T. P. Cheng and L.-F. Li, Phys. Rev., **D22**, 2860 (1980).

[15] E. Ma, Phys. Rev. Lett., **81**, 1171 (1998), arXiv:hep-ph/9805219 [hep-ph].

[16] R. Foot, H. Lew, X. G. He, and G. C. Joshi, Z. Phys., **C44**, 441 (1989); E. Ma and D. P. Roy, Nucl. Phys., **B644**, 290 (2002), arXiv:hep-ph/0206150 [hep-ph]; T. Hambye, Y. Lin, A. Notari, M. Papucci, and A. Strumia, Nucl. Phys., **B695**, 169 (2004), arXiv:hep-ph/0312203 [hep-ph].

[17] L. Susskind, Phys. Rev., **D20**, 2619 (1979).

[18] P. Fayet, Phys. Lett., **B64**, 159 (1976); P. Fayet, Phys. Lett., **B69**, 489 (1977); G. R. Farrar and P. Fayet, Phys. Lett., **B76**, 575 (1978); P. Fayet, Phys. Lett., **B84**, 416 (1979).

[19] S. P. Martin, (1997), doi:10.1142/9789812839657_0001, [Adv. Ser. Direct. High Energy Phys.18,1(1998)], arXiv:hep-ph/9709356 [hep-ph].

[20] S. Weinberg, Phys. Rev. Lett., **29**, 1698 (1972); H. Georgi and A. Pais, Phys. Rev., **D10**, 539 (1974); H. Georgi and A. Pais, Phys. Rev., **D12**, 508 (1975); N. Arkani-Hamed, A. G. Cohen, T. Gregoire, and J. G. Wacker, JHEP, **08**, 020 (2002), arXiv:hep-ph/0202089 [hep-ph]; M. Schmaltz and D. Tucker-Smith, Ann. Rev. Nucl. Part. Sci., **55**, 229 (2005), arXiv:hep-ph/0502182 [hep-ph].

[21] N. Arkani-Hamed, S. Dimopoulos, and G. R. Dvali, Phys. Lett., **B429**, 263 (1998), arXiv:hep-ph/9803315 [hep-ph].

[22] L. Randall and R. Sundrum, Phys. Rev. Lett., **83**, 3370 (1999), arXiv:hep-ph/9905221 [hep-ph]; L. Randall and R. Sundrum, Phys. Rev. Lett., **83**, 4690 (1999), arXiv:hep-th/9906064 [hep-th].

[23] T. Appelquist, H.-C. Cheng, and B. A. Dobrescu, Phys. Rev., **D64**, 035002 (2001), arXiv:hep-ph/0012100 [hep-ph].

[24] T. Kaluza, Sitzungsber. Preuss. Akad. Wiss. Berlin (Math. Phys.), **1921**, 966 (1921); O. Klein, Z. Phys., **37**, 895 (1926), [Surveys High Energ. Phys.5,241(1986)].

[25] G. Belanger, M. Kakizaki, and A. Pukhov, JCAP, **1102**, 009 (2011), arXiv:1012.2577 [hep-ph].

[26] K. R. Dienes, E. Dudas, and T. Gherghetta, Phys. Lett., **B436**, 55 (1998), arXiv:hep-ph/9803466 [hep-ph].

[27] K. Agashe, G. Perez, and A. Soni, Phys. Rev., **D71**, 016002 (2005), arXiv:hep-ph/0408134 [hep-ph].

[28] R. D. Peccei and H. R. Quinn, Phys. Rev. Lett., **38**, 1440 (1977).

[29] S. Weinberg, Phys. Rev. Lett., **40**, 223 (1978); F. Wilczek, Phys. Rev. Lett., **40**, 279 (1978).

[30] L. D. Duffy and K. van Bibber, New J. Phys., **11**, 105008 (2009), arXiv:0904.3346 [hep-ph].

[31] L. Evans and P. Bryant, JINST, **3**, S08001 (2008).

[32] G. Aad *et al.* (ATLAS, CMS), *Proceedings, Meeting of the APS Division of Particles and Fields (DPF 2015)*, Phys. Rev. Lett., **114**, 191803 (2015), arXiv:1503.07589 [hep-ex].

[33] J. Alcaraz *et al.* (DELPHI, OPAL, ALEPH, LEP Electroweak Working Group, L3), (2007), arXiv:0712.0929 [hep-ex].

[34] M. Baak, M. Goebel, J. Haller, A. Hoecker, D. Ludwig, K. Moenig, M. Schott, and J. Stelzer (Gfitter), Eur. Phys. J., **C72**, 2003 (2012), arXiv:1107.0975 [hep-ph].

[35] B. W. Lee, C. Quigg, and H. B. Thacker, Phys. Rev., **D16**, 1519 (1977).

[36] G. Aad *et al.* (ATLAS), (2015), CERN-PH-EP-2015-125, arXiv:1507.04548 [hep-ex].

[37] V. Khachatryan *et al.* (CMS), Eur. Phys. J., **C75**, 212 (2015), arXiv:1412.8662 [hep-ex].

[38] G. Aad *et al.* (ATLAS), *Proceedings, Meeting of the APS Division of Particles and Fields (DPF 2015)*, Eur. Phys. J., **C75**, 476 (2015), [Erratum: Eur. Phys. J.C76,no.3,152(2016)], arXiv:1506.05669 [hep-ex].

[39] V. Khachatryan *et al.* (CMS), Phys. Rev., **D92**, 012004 (2015), arXiv:1411.3441 [hep-ex].

[40] E. Ma, Phys. Rev., **D73**, 077301 (2006), arXiv:hep-ph/0601225 [hep-ph].

[41] E. Ma, Phys. Rev. Lett., **86**, 2502 (2001), arXiv:hep-ph/0011121 [hep-ph].

[42] E. Molinaro, C. E. Yaguna, and O. Zapata, JCAP, **1407**, 015 (2014), arXiv:1405.1259 [hep-ph].

[43] L. J. Hall, K. Jedamzik, J. March-Russell, and S. M. West, JHEP, **03**, 080 (2010), arXiv:0911.1120 [hep-ph].

[44] G. Aad *et al.* (ATLAS), JHEP, **01**, 068 (2015), arXiv:1411.6795 [hep-ex].

[45] S. Chatrchyan *et al.* (CMS), JHEP, **07**, 122 (2013), arXiv:1305.0491 [hep-ex].

[46] G. Aad *et al.* (ATLAS), Phys. Rev., **D88**, 112003 (2013), arXiv:1310.6584 [hep-ex].

[47] V. Khachatryan *et al.* (CMS), Eur. Phys. J., **C75**, 151 (2015), arXiv:1501.05603 [hep-ex].

[48] W. Heisenberg and W. Pauli, Z. Phys., **56**, 1 (1929); S. Tomonaga, Prog. Theor. Phys., **1**, 27 (1946); J. S. Schwinger, Phys. Rev., **73**, 416 (1948); R. P. Feynman, Phys. Rev., **76**, 749 (1949).

[49] E. Fermi, Z. Phys., **88**, 161 (1934); E. Fermi, *Meeting of the Italian School of Physics and Weak Interactions Bologna, Italy, April 26-28, 1984*, Nuovo Cim., **11**, 1 (1934); R. P. Feynman and M. Gell-Mann, Phys. Rev., **109**, 193 (1958).

[50] D. Hanneke, S. Fogwell, and G. Gabrielse, Phys.Rev.Lett., **100**, 120801 (2008), arXiv:0801.1134 [physics.atom-ph]; T. Aoyama, M. Hayakawa, T. Kinoshita, and M. Nio, Phys.Rev.Lett., **99**, 110406 (2007), arXiv:0706.3496 [hep-ph]; T. Aoyama, M. Hayakawa, T. Kinoshita, and M. Nio, Phys.Rev.Lett., **109**, 111807 (2012), arXiv:1205.5368 [hep-ph]; F. Biraben, R. Bouchendira, P. Clade, S. Guellati-Khelifa, and F. Nez, Phys.Rev.Lett., **106**, 080801 (2011), arXiv:1012.3627 [physics.atom-ph].

[51] R. Barate *et al.* (OPAL, DELPHI, LEP Working Group for Higgs boson searches, ALEPH, L3), Phys. Lett., **B565**, 61 (2003), arXiv:hep-ex/0306033 [hep-ex].

[52] Tevatron New Physics Higgs Working Group, CDF collaboration, D0 collaboration, (2012), CERN-EP-2003-011, arXiv:hep-ex/1207.0449 [hep-ex].

[53] S. L. Glashow, J. Iliopoulos, and L. Maiani, *Meeting of the Italian School of Physics and Weak Interactions Bologna, Italy, April 26-28, 1984*, Phys. Rev., **D2**, 1285 (1970).

[54] A. J. Buras, Annalen Phys., **528**, 96 (2016).

[55] S. Troitsky, Phys. Usp., **55**, 72 (2012), [Usp. Fiz. Nauk182,77(2012)], arXiv:1112.4515 [hep-ph].

[56] A. Einstein, Sitzungsber. Preuss. Akad. Wiss., **1**, 844 (1915).

[57] K. A. Meissner and H. Nicolai, Phys. Lett., **B648**, 312 (2007), arXiv:hep-th/0612165 [hep-th].

[58] Y. B. Zeldovich, JETP Lett., **6**, 316 (1967), [Pisma Zh. Eksp. Teor. Fiz.6,883(1967)]; Ya. B. Zel'dovich, A. Krasinski, and Ya. B. Zeldovich, Sov. Phys. Usp., **11**, 381 (1968), [Usp. Fiz. Nauk95,209(1968)]; S. Weinberg, Rev. Mod. Phys., **61**, 1 (1989).

[59] A. Padilla, (2015), arXiv:1502.05296 [hep-th].

[60] A. D. Sakharov, Pisma Zh. Eksp. Teor. Fiz., **5**, 32 (1967), [Usp. Fiz. Nauk161,61(1991)].

[61] T. Gershon, in *Proceedings, 69th Scottish Universities Summer School in Physics : LHC Phenomenology (SUSSP69)* (2013) pp. 203–237, arXiv:1306.4588 [hep-ex].

[62] V. A. Kuzmin, V. A. Rubakov, and M. E. Shaposhnikov, Phys. Lett., **B155**, 36 (1985); M. E. Shaposhnikov, JETP Lett., **44**, 465 (1986), [Pisma Zh. Eksp. Teor. Fiz.44,364(1986)]; M. E. Shaposhnikov, Nucl. Phys., **B287**, 757 (1987).

[63] M. Fukugita and T. Yanagida, Phys. Lett., **B174**, 45 (1986).

[64] S. Weinberg, Phys. Rev., **D11**, 3583 (1975); G. 't Hooft, Phys. Rev., **D14**, 3432 (1976), [Erratum: Phys. Rev.D18,2199(1978)].

[65] G. C. Branco, L. Lavoura, and J. P. Silva, *CP Violation* (Clarendon Press, 1999).

[66] P. G. Harris *et al.*, Phys. Rev. Lett., **82**, 904 (1999).

[67] G. Gabadadze and M. Shifman, *Continuous advances in QCD. Proceedings, Conference, Minneapolis, USA, May 17-23, 2002*, Int. J. Mod. Phys., **A17**, 3689 (2002), [,521(2002)], arXiv:hep-ph/0206123 [hep-ph].

[68] E. Noether, Gott. Nachr., **1918**, 235 (1918), [Transp. Theory Statist. Phys.1,186(1971)], arXiv:physics/0503066 [physics].

[69] C.-N. Yang and R. L. Mills, Phys. Rev., **96**, 191 (1954).

[70] S. L. Adler, Phys. Rev., **177**, 2426 (1969).

[71] S. L. Adler and W. A. Bardeen, Phys. Rev., **182**, 1517 (1969).

[72] J. S. Bell and R. Jackiw, Nuovo Cim., **A60**, 47 (1969).

[73] C. Bouchiat, J. Iliopoulos, and P. Meyer, Phys. Lett., **B38**, 519 (1972); G. 't Hooft, Phys. Rev. Lett., **37**, 8 (1976).

[74] R. D. Peccei, *Axions: Theory, cosmology, and experimental searches. Proceedings, 1st Joint ILIAS-CERN-CAST axion training, Geneva, Switzerland, November 30-December 2, 2005*, Lect. Notes Phys., **741**, 3 (2008), [,3(2006)], arXiv:hep-ph/0607268 [hep-ph].

[75] L. D. Faddeev and V. N. Popov, Phys. Lett., **B25**, 29 (1967).

[76] Y. Nambu, Phys. Rev. Lett., **4**, 380 (1960); Y. Nambu and G. Jona-Lasinio, Phys. Rev., **122**, 345 (1961); Y. Nambu and G. Jona-Lasinio, Phys. Rev., **124**, 246 (1961); J. Goldstone, Nuovo Cim., **19**, 154 (1961).

[77] M. E. Peskin and D. V. Schroeder, *An Introduction to Quantum Field Theory* (Westview Press, 1995).

[78] K. A. Olive *et al.* (Particle Data Group), Chin. Phys., **C38**, 090001 (2014), Interactive material properties database: `http://pdg.lbl.gov/2015/AtomicNuclearProperties/index.html`.

[79] W. A. Bardeen, A. J. Buras, D. W. Duke, and T. Muta, Phys. Rev., **D18**, 3998 (1978).

[80] N. Cabibbo, *Meeting of the Italian School of Physics and Weak Interactions Bologna, Italy, April 26-28, 1984*, Phys. Rev. Lett., **10**, 531 (1963), [,648(1963)]; M. Kobayashi and T. Maskawa, Prog. Theor. Phys., **49**, 652 (1973).

[81] C. Jarlskog, Phys. Rev. Lett., **55**, 1039 (1985).

[82] G. C. Branco, H. R. C. Ferreira, A. G. Hessler, and J. I. Silva-Marcos, JHEP, **05**, 001 (2012), arXiv:1101.5808 [hep-ph].

[83] E. Hubble, PNAS, **15**, 168–173 (1929).

[84] M. J. Geller and J. P. Huchra (CfA Redshift Survey), Science, **246**, 897 (1989).

[85] J. A. Newman *et al.* (DEEP2 Galaxy Redshift Survey), Astrophys. J. Suppl., **208**, 5 (2013), arXiv:1203.3192 [astro-ph.CO].

[86] A. A. Friedmann, Z. Phys., **10**, 377–386 (1922).

[87] G. Lemaître, Ann. Soc. Sci. Bruxelles, Ser. A, **47**, 49–56 (1927), [Note: DOI is for English translation in MNRAS 91, p.483-490 (1931)].

[88] H. P. Robertson, Lond.Edinb.Dubl.Phil.Mag. Series 7, **5**, 835–848 (1928).

[89] A. A. Penzias and R. W. Wilson, Astrophys.J., **142**, 419 (1965).

[90] R. H. Dicke, P. J. E. Peebles, P. G. Roll, and D. T. Wilkinson, Astrophys. J., **142**, 414 (1965).

[91] G. A. Gamow, Phys. Rev., **74**, 505 (1948).

[92] D. J. Fixsen, Astrophys.J., **707**, 916 (2009), arXiv:0911.1955 [astro-ph.CO].

[93] P. J. E. Peebles, Astrophys. J., **153**, 1 (1968); Ya. B. Zeldovich, Astron. Astrophys., **5**, 84 (1970).

[94] R. K. Sachs and A. M. Wolfe, Astrophys. J., **147**, 73 (1967), [Gen. Rel. Grav.39,1929(2007)].

[95] B. A. Bassett and R. Hlozek, (2009), Extended version of chapter contributed to the book "Dark Energy", Ed. P. Ruiz-Lapuente, Cambridge University Press, arXiv:0910.5224 [astro-ph.CO].

[96] W. Hu and S. Dodelson, Ann. Rev. Astron. Astrophys., **40**, 171 (2002), arXiv:astro-ph/0110414 [astro-ph].

[97] S. Perlmutter *et al.* (Supernova Cosmology Project), Astrophys. J., **483**, 565 (1997), arXiv:astro-ph/9608192 [astro-ph]; S. Perlmutter *et al.* (Supernova Cosmology Project), Astrophys. J., **517**, 565 (1999), arXiv:astro-ph/9812133 [astro-ph]; A. G. Riess *et al.* (Supernova Search Team), Astron. J., **116**, 1009 (1998), arXiv:astro-ph/9805201 [astro-ph].

[98] P. A. R. Ade *et al.* (Planck), Astron.Astrophys., **571**, A16 (2014), arXiv:1303.5076 [astro-ph.CO].

[99] D. D. Baumann, "Cosmology," (2010), lecture notes for cosmology course at Cambridge University, [Link] `http://www.damtp.cam.ac.uk/user/db275/Cosmology/Lectures.pdf`.

[100] A. H. Guth, Phys. Rev., **D23**, 347 (1981).

[101] A. D. Linde, *In *Moscow 1981, Proceedings, Quantum Gravity*, 185-195 and Moscow Inst. Phys. Acad. Sci. - 81-229 (81,REC.DEC.) 15p*, Phys. Lett., **B108**, 389 (1982); A. D. Linde, Phys. Lett., **B114**, 431 (1982); A. Albrecht and P. J. Steinhardt, Phys. Rev. Lett., **48**, 1220 (1982).

[102] S. Weinberg, *Cosmology* (Oxford University Press, 2008).

[103] L. A. Kofman, A. D. Linde, and A. A. Starobinsky, Phys. Rev. Lett., **73**, 3195 (1994), arXiv:hep-th/9405187 [hep-th].

[104] L. A. Kofman (1996) arXiv:astro-ph/9605155 [astro-ph].

[105] D. Baumann, in *Physics of the large and the small, TASI 09, proceedings of the Theoretical Advanced Study Institute in Elementary Particle Physics, Boulder, Colorado, USA, 1-26 June 2009* (2011) pp. 523–686, arXiv:0907.5424 [hep-th].

[106] P. A. R. Ade *et al.* (BICEP2, Planck), Phys. Rev. Lett., **114**, 101301 (2015), arXiv:1502.00612 [astro-ph.CO].

[107] P. A. R. Ade *et al.* (BICEP2), Astrophys. J., **792**, 62 (2014), arXiv:1403.4302 [astro-ph.CO].

[108] P. A. R. Ade *et al.* (BICEP2), Phys. Rev. Lett., **112**, 241101 (2014), arXiv:1403.3985 [astro-ph.CO].

[109] R. Adam *et al.* (Planck), Astron. Astrophys., **586**, A133 (2016), arXiv:1409.5738 [astro-ph.CO].

[110] G. Luders, Annals Phys., **2**, 1 (1957), [Annals Phys.281,1004(2000)].

[111] P. S. Bhupal Dev, A. Mazumdar, and S. Qutub, Front. Phys., **2**, 26 (2014), arXiv:1311.5297 [hep-ph].

[112] R. A. Alpher, H. Bethe, and G. A. Gamow, Phys. Rev., **73**, 803 (1948).

[113] R. H. Cyburt, B. D. Fields, and K. A. Olive, Phys. Rev., **D69**, 123519 (2004), arXiv:astro-ph/0312629 [astro-ph].

[114] K. Jedamzik, in *Proceedings, fourth SFB-375 Ringberg workshop 'neutrino astrophysics' held Ringberg Castle, Tegernsee, Germany, 20-24 October 1997* (1998) arXiv:astro-ph/9805156 [astro-ph]; H. Kurki-Suonio, in *The Light elements and their evolution APS conference series, 1999, L. da Silva, M. Spite and J.R. de Medeiros, eds.* (2000) arXiv:astro-ph/0002071 [astro-ph].

[115] R. H. Cyburt, B. D. Fields, and K. A. Olive, JCAP, **0811**, 012 (2008), arXiv:0808.2818 [astro-ph].

[116] E. Aver, K. A. Olive, R. L. Porter, and E. D. Skillman, JCAP, **1311**, 017 (2013), arXiv:1309.0047 [astro-ph.CO].

[117] C. L. Bennett *et al.* (WMAP), Astrophys. J. Suppl., **208**, 20 (2013), arXiv:1212.5225 [astro-ph.CO].

[118] M. Kamionkowski and A. Benson, (2010), lecture notes for cosmology course at Caltech, [Link] `http://www.its.caltech.edu/~kamion/Ay127/`.

[119] K. Jedamzik and M. Pospelov, New J. Phys., **11**, 105028 (2009), arXiv:0906.2087 [hep-ph].

[120] D. Lindley, Astrophys. J., **294**, 1 (1985); J. R. Ellis, D. V. Nanopoulos, and S. Sarkar, Nucl. Phys., **B259**, 175 (1985); R. J. Scherrer and M. S. Turner, Phys. Rev., **D33**, 1585 (1986), [Erratum: Phys. Rev.D34,3263(1986)]; M. H. Reno and D. Seckel, Phys. Rev., **D37**, 3441 (1988); S. Dimopoulos, R. Esmailzadeh, L. J. Hall, and G. D. Starkman, Nucl. Phys., **B311**, 699 (1989).

[121] M. Pospelov, Phys. Rev. Lett., **98**, 231301 (2007), arXiv:hep-ph/0605215 [hep-ph].

[122] G. Bertone, D. Hooper, and J. Silk, Phys. Rept., **405**, 279 (2005), arXiv:hep-ph/0404175 [hep-ph].

[123] J. H. Oort, Bull. Astron. Inst. Neth., 249 (1932).

[124] V. C. Rubin and W. K. Ford, Jr., Astrophys. J., **159**, 379 (1970).

[125] M. S. Roberts and R. N. Whitehurst, Astrophys. J., **201**, 327 (1973).

[126] V. Rubin, Phys.Today, **59** (2006), doi:10.1063/1.2435662.

[127] V. C. Rubin, N. Thonnard, and W. K. Ford, Jr., Astrophys. J., **238**, 471 (1980).

[128] Y. Sofue and V. Rubin, Ann. Rev. Astron. Astrophys., **39**, 137 (2001), arXiv:astro-ph/0010594 [astro-ph].

[129] D. Zaritsky, R. Smith, C. Frenk, and S. D. M. White, Astrophys. J., **478**, 39 (1997), arXiv:astro-ph/9611199 [astro-ph].

[130] F. Zwicky, Helv. Phys. Acta, **6**, 110 (1933).

[131] W. Tucker, P. Blanco, S. Rappoport, L. David, D. Fabricant, E. E. Falco, W. Forman, A. Dressler, and M. Ramella, Astrophys. J., **496**, L5 (1998), arXiv:astro-ph/9801120 [astro-ph].

[132] M. Milgrom, Astrophys. J., **270**, 365 (1983).

[133] M. Milgrom, Statement concerning MOND and 1E0657-558; [Link] `http://www.astro.umd.edu/~ssm/mond/moti_bullet.html`.

[134] S. S. McGaugh, Can. J. Phys., **93**, 250 (2015), arXiv:1404.7525 [astro-ph.CO].

[135] D. Clowe, M. Bradac, A. H. Gonzalez, M. Markevitch, S. W. Randall, C. Jones, and D. Zaritsky, Astrophys. J., **648**, L109 (2006), arXiv:astro-ph/0608407 [astro-ph].

[136] M. Markevitch, A. H. Gonzalez, L. David, A. Vikhlinin, S. Murray, W. Forman, C. Jones, and W. Tucker, Astrophys. J., **567**, L27 (2002), arXiv:astro-ph/0110468 [astro-ph].

[137] D. Harvey, R. Massey, T. Kitching, A. Taylor, and E. Tittley, Science, **347**, 1462 (2015), arXiv:1503.07675 [astro-ph.CO].

[138] R. Massey *et al.*, Mon. Not. Roy. Astron. Soc., **449**, 3393 (2015), arXiv:1504.03388 [astro-ph.CO].

[139] F. Kahlhoefer, K. Schmidt-Hoberg, J. Kummer, and S. Sarkar, Mon. Not. Roy. Astron. Soc., **452**, 1 (2015), arXiv:1504.06576 [astro-ph.CO].

[140] C. Grupen, *Astroparticle Physics* (Springer Verlag, 2005).

[141] D. Scott and G. F. Smoot, Phys. Lett. B, **592**, 1 (2004), arXiv:astro-ph/0406567 [astro-ph].

[142] R. Adam *et al.* (Planck), (2015), arXiv:1502.01582 [astro-ph.CO].

[143] C. Alcock *et al.* (MACHO), Astrophys. J., **542**, 281 (2000), arXiv:astro-ph/0001272 [astro-ph]; P. Tisserand *et al.* (EROS-2), Astron. Astrophys., **469**, 387 (2007), arXiv:astro-ph/0607207 [astro-ph].

[144] E. Egami *et al.*, Astrophys. J., **618**, L5 (2004), arXiv:astro-ph/0411117 [astro-ph]; M. Iye, K. Ota, N. Kashikawa, H. Furusawa, T. Hashimoto, T. Hattori, Y. Matsuda, T. Morokuma, M. Ouchi, and K. Shimasaku, Nature, **443**, 186 (2006), arXiv:astro-ph/0609393 [astro-ph]; P. A. Oesch *et al.*, Astrophys. J., **804**, L30 (2015), arXiv:1502.05399 [astro-ph.GA].

[145] A. Zitrin, I. Labbe, S. Belli, R. Bouwens, R. S. Ellis, G. Roberts-Borsani, D. P. Stark, P. A. Oesch, and R. Smit, (2015), arXiv:1507.02679 [astro-ph.GA].

[146] C.-P. Ma, in *Neutrinos in physics and astrophysics from 10**(-33) to 10**28 CM. Proceedings, Conference, TASI'98, Boulder, USA, June 1-26, 1998* (1998) pp. 504–523, arXiv:astro-ph/9904001 [astro-ph].

[147] J. R. Bond, G. Efstathiou, and J. Silk, Phys. Rev. Lett., **45**, 1980 (1980).

[148] M. Viel, G. D. Becker, J. S. Bolton, and M. G. Haehnelt, Phys. Rev., **D88**, 043502 (2013), arXiv:1306.2314 [astro-ph.CO].

[149] S. Dodelson and L. M. Widrow, Phys. Rev. Lett., **72**, 17 (1994), arXiv:hep-ph/9303287 [hep-ph].

[150] M. Drewes, Int. J. Mod. Phys., **E22**, 1330019 (2013), arXiv:1303.6912 [hep-ph].

[151] T. Asaka, M. Shaposhnikov, and A. Kusenko, Phys. Lett., **B638**, 401 (2006), arXiv:hep-ph/0602150 [hep-ph].

[152] A. Boyarsky, J. Lesgourgues, O. Ruchayskiy, and M. Viel, JCAP, **0905**, 012 (2009), arXiv:0812.0010 [astro-ph].

[153] W. A. Bardeen, R. D. Peccei, and T. Yanagida, Nucl. Phys., **B279**, 401 (1987).

[154] L. J. Rosenberg and K. A. van Bibber, Phys. Rept., **325**, 1 (2000).

[155] J. E. Kim, Phys. Rev. Lett., **43**, 103 (1979); M. A. Shifman, A. I. Vainshtein, and V. I. Zakharov, Nucl. Phys., **B166**, 493 (1980).

[156] M. Dine, W. Fischler, and M. Srednicki, Phys. Lett., **B104**, 199 (1981); A. R. Zhitnitsky, Sov. J. Nucl. Phys., **31**, 260 (1980), [Yad. Fiz.31,497(1980)].

[157] M. Schumann, *Proceedings, Dark Matter, Hadron Physics and Fusion Physics (DHF2014)*, EPJ Web Conf., **96**, 01027 (2015), arXiv:1501.01200 [astro-ph.CO].

[158] T. Marrodán Undagoitia and L. Rauch, J. Phys., **G43**, 013001 (2016), arXiv:1509.08767 [physics.ins-det].

[159] E. Aprile *et al.* (XENON100), Phys. Rev. Lett., **109**, 181301 (2012), arXiv:1207.5988 [astro-ph.CO].

[160] D. S. Akerib *et al.* (LUX), Phys. Rev. Lett., **112**, 091303 (2014), arXiv:1310.8214 [astro-ph.CO].

[161] R. Bernabei *et al.*, Eur. Phys. J., **C73**, 2648 (2013), arXiv:1308.5109 [astro-ph.GA].

[162] R. Agnese *et al.* (CDMS), Phys. Rev. Lett., **111**, 251301 (2013), arXiv:1304.4279 [hep-ex].

[163] R. Agnese *et al.* (SuperCDMS), Phys. Rev. Lett., **112**, 241302 (2014), arXiv:1402.7137 [hep-ex].

[164] M. Cirelli, A. Strumia, and M. Tamburini, Nucl. Phys., **B787**, 152 (2007), arXiv:0706.4071 [hep-ph].

[165] E. Behnke *et al.* (COUPP), Phys. Rev., **D86**, 052001 (2012), [Erratum: Phys. Rev.D90,no.7,079902(2014)], arXiv:1204.3094 [astro-ph.CO].

[166] M. Felizardo *et al.*, Phys. Rev. Lett., **108**, 201302 (2012), arXiv:1106.3014 [astro-ph.CO].

[167] S. Archambault *et al.* (PICASSO), Phys. Lett., **B711**, 153 (2012), arXiv:1202.1240 [hep-ex].

[168] C. Amole *et al.* (PICO), Phys. Rev., **D93**, 052014 (2016), arXiv:1510.07754 [hep-ex].

[169] C. Amole *et al.* (PICO), Phys. Rev., **D93**, 061101 (2016), arXiv:1601.03729 [astro-ph.CO].

[170] M. G. Aartsen *et al.* (IceCube), Phys. Rev. Lett., **110**, 131302 (2013), arXiv:1212.4097 [astro-ph.HE].

[171] J. Silk, K. A. Olive, and M. Srednicki, Phys. Rev. Lett., **55**, 257 (1985).

[172] J. Conrad, in *Interplay between Particle and Astroparticle physics London, United Kingdom, August 18-22, 2014* (2014) arXiv:1411.1925 [hep-ph].

[173] W. B. Atwood *et al.* (Fermi-LAT), Astrophys. J., **697**, 1071 (2009), arXiv:0902.1089 [astro-ph.IM].

[174] F. Aharonian *et al.* (HESS), Astron. Astrophys., **457**, 899 (2006), arXiv:astro-ph/0607333 [astro-ph].

[175] C. Weniger, JCAP, **1208**, 007 (2012), arXiv:1204.2797 [hep-ph].

[176] L. Goodenough and D. Hooper, (2009), arXiv:0910.2998 [hep-ph].

[177] E. Bulbul, M. Markevitch, A. Foster, R. K. Smith, M. Loewenstein, and S. W. Randall, Astrophys. J., **789**, 13 (2014), arXiv:1402.2301 [astro-ph.CO].

[178] A. Albert (Fermi-LAT), *Proceedings, 13th International Conference on Topics in Astroparticle and Underground Physics (TAUP 2013)*, Phys. Procedia, **61**, 6 (2015).

[179] A. Merle and A. Schneider, Phys. Lett., **B749**, 283 (2015), arXiv:1409.6311 [hep-ph].

[180] R. Bartels, S. Krishnamurthy, and C. Weniger, Phys. Rev. Lett., **116**, 051102 (2016), arXiv:1506.05104 [astro-ph.HE]; S. K. Lee, M. Lisanti, B. R. Safdi, T. R. Slatyer, and W. Xue, Phys. Rev. Lett., **116**, 051103 (2016), arXiv:1506.05124 [astro-ph.HE].

[181] O. Adriani *et al.* (PAMELA), Nature, **458**, 607 (2009), arXiv:0810.4995 [astro-ph].

[182] L. Accardo *et al.* (AMS), Phys. Rev. Lett., **113**, 121101 (2014).

[183] (2015), Talks at the 'AMS Days at CERN', 15-17 april.

[184] B.-Q. Lu and H.-S. Zong, Phys. Rev., **D93**, 103517 (2016), arXiv:1510.04032 [astro-ph.HE].

[185] M. Ageron *et al.* (ANTARES), Nucl. Instrum. Meth., **A656**, 11 (2011), arXiv:1104.1607 [astro-ph.IM].

[186] A. Achterberg *et al.* (IceCube), Astropart. Phys., **26**, 155 (2006), arXiv:astro-ph/0604450 [astro-ph].

[187] S. Adrian-Martinez *et al.* (ANTARES), Phys. Lett., **B759**, 69 (2016), arXiv:1603.02228 [astro-ph.HE].

[188] V. Khachatryan *et al.* (CMS), Eur. Phys. J., **C75**, 235 (2015), arXiv:1408.3583 [hep-ex].

[189] E. Aprile *et al.* (XENON100), Phys. Rev. Lett., **111**, 021301 (2013), arXiv:1301.6620 [astro-ph.CO].

[190] D. S. Akerib *et al.* (LUX), Phys. Rev. Lett., **116**, 161302 (2016), arXiv:1602.03489 [hep-ex].

[191] M. Aaboud *et al.* (ATLAS), (2016), arXiv:1604.07773 [hep-ex].

[192] G. Aad *et al.* (ATLAS), Eur. Phys. J., **C75**, 299 (2015), [Erratum: Eur. Phys. J.C75,no.9,408(2015)], arXiv:1502.01518 [hep-ex].

[193] *Search for dark matter with jets and missing transverse energy at 13 TeV*, Tech. Rep. CMS-PAS-EXO-15-003 (CERN, Geneva, 2016).

[194] G. Busoni, A. De Simone, E. Morgante, and A. Riotto, Phys. Lett., **B728**, 412 (2014), arXiv:1307.2253 [hep-ph]; G. Busoni, A. De Simone, J. Gramling, E. Morgante, and A. Riotto, JCAP, **1406**, 060 (2014), arXiv:1402.1275 [hep-ph]; G. Busoni, A. De Simone, T. Jacques, E. Morgante, and A. Riotto, JCAP, **1409**, 022 (2014), arXiv:1405.3101 [hep-ph].

[195] D. Alves (LHC New Physics Working Group), J. Phys., **G39**, 105005 (2012), arXiv:1105.2838 [hep-ph].

[196] E. W. Kolb and M. S. Turner, *The Early Universe* (Westview Press, 1994).

[197] S. Dodelson, *Modern Cosmology* (Academic Press, 2003).

[198] G. Mangano, G. Miele, S. Pastor, T. Pinto, O. Pisanti, and P. D. Serpico, Nucl. Phys., **B729**, 221 (2005), arXiv:hep-ph/0506164 [hep-ph].

[199] G. Steigman, B. Dasgupta, and J. F. Beacom, Phys. Rev., **D86**, 023506 (2012), arXiv:1204.3622 [hep-ph].

[200] K. Griest and D. Seckel, Phys. Rev., **D43**, 3191 (1991).

[201] J. Edsjo and P. Gondolo, Phys. Rev., **D56**, 1879 (1997), arXiv:hep-ph/9704361 [hep-ph].

[202] J. L. Feng, A. Rajaraman, and F. Takayama, Phys. Rev. Lett., **91**, 011302 (2003), arXiv:hep-ph/0302215 [hep-ph].

[203] C. Kraus *et al.*, Eur. Phys. J., **C40**, 447 (2005), arXiv:hep-ex/0412056 [hep-ex]; V. N. Aseev *et al.* (Troitsk), Phys. Rev., **D84**, 112003 (2011), arXiv:1108.5034 [hep-ex].

[204] F. Fraenkle, *Proceedings, 2015 European Physical Society Conference on High Energy Physics (EPS-HEP 2015)*, PoS, **EPS-HEP2015**, 084 (2015).

[205] J. A. Formaggio, *Proceedings, 13th International Conference on Topics in Astroparticle and Underground Physics (TAUP 2013)*, Phys. Dark Univ., **4**, 75 (2014).

[206] J. Chadwick, Proc.Roy.Soc.Lond., **A136**, 692 (1932); J. Chadwick, Nature, **129**, 312 (1932).

[207] E. K. Akhmedov, JHEP, **09**, 116 (2007), arXiv:0706.1216 [hep-ph].

[208] A. Djouadi and A. Lenz, Phys. Lett., **B715**, 310 (2012), arXiv:1204.1252 [hep-ph].

[209] M. C. Gonzalez-Garcia and M. Maltoni, Phys. Rept., **460**, 1 (2008), arXiv:0704.1800 [hep-ph].

[210] S. Verma, Adv. High Energy Phys., **2015**, 385968 (2015).

[211] T. S. Kosmas, G. K. Leontaris, and J. D. Vergados, Prog. Part. Nucl. Phys., **33**, 397 (1994), arXiv:hep-ph/9312217 [hep-ph].

[212] G. 't Hooft, *Cargese Summer Institute: Recent Developments in Gauge Theories Cargese, France, August 26-September 8, 1979*, NATO Sci. Ser. B, **59**, 135 (1980).

[213] R. N. Mohapatra, Phys. Rev. Lett., **56**, 561 (1986); J. Bernabeu, A. Santamaria, J. Vidal, A. Mendez, and J. W. F. Valle, Phys. Lett., **B187**, 303 (1987).

[214] D. Wyler and L. Wolfenstein, Nucl. Phys., **B218**, 205 (1983); E. K. Akhmedov, M. Lindner, E. Schnapka, and J. W. F. Valle, Phys. Rev., **D53**, 2752 (1996), arXiv:hep-ph/9509255 [hep-ph]; S. M. Barr, Phys. Rev. Lett., **92**, 101601 (2004), arXiv:hep-ph/0309152 [hep-ph]; C. H. Albright and S. M. Barr, Phys. Rev., **D69**, 073010 (2004), arXiv:hep-ph/0312224 [hep-ph]; M. Malinsky, J. C. Romao, and J. W. F. Valle, Phys. Rev. Lett., **95**, 161801 (2005), arXiv:hep-ph/0506296 [hep-ph].

[215] J. Schechter and J. W. F. Valle, Phys. Rev., **D25**, 2951 (1982).

[216] H. V. Klapdor-Kleingrothaus, I. V. Krivosheina, A. Dietz, and O. Chkvorets, Phys. Lett., **B586**, 198 (2004), arXiv:hep-ph/0404088 [hep-ph]; C. E. Aalseth *et al.* (IGEX), Phys. Rev., **D65**, 092007 (2002), arXiv:hep-ex/0202026 [hep-ex]; J. Argyriades *et al.* (NEMO), Phys. Rev., **C80**, 032501 (2009), arXiv:0810.0248 [hep-ex]; M. Agostini *et al.* (GERDA), Phys. Rev. Lett., **111**, 122503 (2013), arXiv:1307.4720 [nucl-ex].

[217] S. Dell'Oro, S. Marcocci, M. Viel, and F. Vissani, Adv. High Energy Phys., **2016**, 2162659 (2016), arXiv:1601.07512 [hep-ph].

[218] S. Weinberg, Phys. Rev. Lett., **43**, 1566 (1979).

[219] F. Bonnet, D. Hernandez, T. Ota, and W. Winter, JHEP, **10**, 076 (2009), arXiv:0907.3143 [hep-ph].

[220] W. Konetschny and W. Kummer, Phys. Lett., **B70**, 433 (1977).

[221] W. Grimus and L. Lavoura, JHEP, **11**, 042 (2000), arXiv:hep-ph/0008179 [hep-ph].

[222] J. C. Pati and A. Salam, Phys. Rev., **D10**, 275 (1974), [Erratum: Phys. Rev.D11,703(1975)]; R. N. Mohapatra and J. C. Pati, Phys. Rev., **D11**, 2558 (1975); G. Senjanovic and R. N. Mohapatra, Phys. Rev., **D12**, 1502 (1975).

[223] A. Zee, Phys. Lett., **B93**, 389 (1980), [Erratum: Phys. Lett.B95,461(1980)].

[224] G. C. Branco, P. M. Ferreira, L. Lavoura, M. N. Rebelo, M. Sher, and J. P. Silva, Phys. Rept., **516**, 1 (2012), arXiv:1106.0034 [hep-ph].

[225] L. Wolfenstein, Nucl. Phys., **B175**, 93 (1980).

[226] X.-G. He, Eur. Phys. J., **C34**, 371 (2004), arXiv:hep-ph/0307172 [hep-ph].

[227] S. S. C. Law and K. L. McDonald, JHEP, **09**, 092 (2013), arXiv:1305.6467 [hep-ph].

[228] A. Zee, Nucl. Phys., **B264**, 99 (1986); K. S. Babu, Phys. Lett., **B203**, 132 (1988).

[229] D. Aristizabal Sierra, A. Degee, L. Dorame, and M. Hirsch, JHEP, **03**, 040 (2015), arXiv:1411.7038 [hep-ph].

[230] H. Sugiyama, in *2nd Toyama International Workshop on Higgs as a Probe of New Physics (HPNP2015) Toyama, Japan, February 11-15, 2015* (2015) arXiv:1505.01738 [hep-ph].

[231] D. Schmidt, T. Schwetz, and H. Zhang, Nucl. Phys., **B885**, 524 (2014), arXiv:1402.2251 [hep-ph].

[232] F. Bonnet, M. Hirsch, T. Ota, and W. Winter, JHEP, **07**, 153 (2012), arXiv:1204.5862 [hep-ph].

[233] D. Restrepo, O. Zapata, and C. E. Yaguna, JHEP, **11**, 011 (2013), arXiv:1308.3655 [hep-ph].

[234] S. Kanemura and H. Sugiyama, Phys. Rev., **D86**, 073006 (2012), arXiv:1202.5231 [hep-ph].

[235] E. Ma and D. Suematsu, Mod. Phys. Lett., **A24**, 583 (2009), arXiv:0809.0942 [hep-ph].

[236] K. I. Aoki, Z. Hioki, M. Konuma, R. Kawabe, and T. Muta, Prog. Theor. Phys. Suppl., **73**, 1 (1982).

[237] A. Denner and T. Sack, Nucl. Phys., **B347**, 203 (1990).

[238] B. A. Kniehl and A. Pilaftsis, Nucl. Phys., **B474**, 286 (1996), arXiv:hep-ph/9601390 [hep-ph].

[239] W. Grimus and L. Lavoura, Phys. Lett., **B546**, 86 (2002), arXiv:hep-ph/0207229 [hep-ph].

[240] Y. Fukuda *et al.* (Super-Kamiokande), Phys. Rev. Lett., **81**, 1562 (1998), arXiv:hep-ex/9807003 [hep-ex].

[241] Q. R. Ahmad *et al.* (SNO), Phys. Rev. Lett., **87**, 071301 (2001), arXiv:nucl-ex/0106015 [nucl-ex].

[242] L. Wolfenstein, Phys. Rev., **D17**, 2369 (1978); S. P. Mikheev and A. Yu. Smirnov, Sov. J. Nucl. Phys., **42**, 913 (1985), [Yad. Fiz.42,1441(1985)]; S. P. Mikheev and A. Yu. Smirnov, Nuovo Cim., **C9**, 17 (1986); S. P. Mikheev and A. Yu. Smirnov, Sov. Phys. JETP, **65**, 230 (1987), [Zh. Eksp. Teor. Fiz.92,404(1987)].

[243] E. K. Akhmedov and A. Yu. Smirnov, Phys. Atom. Nucl., **72**, 1363 (2009), arXiv:0905.1903 [hep-ph].

[244] G. C. Branco and M. N. Rebelo, New J. Phys., **7**, 86 (2005), arXiv:hep-ph/0411196 [hep-ph].

[245] B. Pontecorvo, Sov. Phys. JETP, **6**, 429 (1957), [Zh. Eksp. Teor. Fiz.33,549(1957)]; B. Pontecorvo, Sov. Phys. JETP, **7**, 172 (1958), [Zh. Eksp. Teor. Fiz.34,247(1957)]; B. Pontecorvo, Sov. Phys. JETP, **26**, 984 (1968), [Zh. Eksp. Teor. Fiz.53,1717(1967)]; Z. Maki, M. Nakagawa, and S. Sakata, Prog. Theor. Phys., **28**, 870 (1962).

[246] S. Antusch, C. Biggio, E. Fernandez-Martinez, M. B. Gavela, and J. Lopez-Pavon, JHEP, **10**, 084 (2006), arXiv:hep-ph/0607020 [hep-ph].

[247] S. Antusch and O. Fischer, JHEP, **10**, 094 (2014), arXiv:1407.6607 [hep-ph].

[248] L.-L. Chau and W.-Y. Keung, Phys. Rev. Lett., **53**, 1802 (1984).

[249] K. Zuber, Phys. Rept., **305**, 295 (1998), arXiv:hep-ph/9811267 [hep-ph].

[250] M. C. Gonzalez-Garcia, M. Maltoni, and T. Schwetz, JHEP, **11**, 052 (2014), arXiv:1409.5439 [hep-ph].

[251] D. G. Michael *et al.* (MINOS), Phys. Rev. Lett., **97**, 191801 (2006), arXiv:hep-ex/0607088 [hep-ex].

[252] P. F. Harrison, D. H. Perkins, and W. G. Scott, Phys. Lett., **B530**, 167 (2002), arXiv:hep-ph/0202074 [hep-ph].

[253] P. F. Harrison and W. G. Scott, in *Proceedings of the 2nd NO-VE International Workshop on Neutrino Oscillations* (2004) pp. 435–444, arXiv:hep-ph/0402006 [hep-ph].

[254] Z.-Z. Xing and Z.-H. Zhao, (2015), arXiv:1512.04207 [hep-ph].

[255] F. P. An *et al.* (Daya Bay), Phys. Rev. Lett., **108**, 171803 (2012), arXiv:1203.1669 [hep-ex].

[256] J. K. Ahn *et al.* (RENO), Phys. Rev. Lett., **108**, 191802 (2012), arXiv:1204.0626 [hep-ex].

[257] D. Suematsu, Eur. Phys. J., **C72**, 1951 (2012), arXiv:1103.0857 [hep-ph]; S. Kashiwase and D. Suematsu, Phys. Rev., **D86**, 053001 (2012), arXiv:1207.2594 [hep-ph].

[258] N. G. Deshpande and E. Ma, Phys. Rev., **D18**, 2574 (1978).

[259] A. Merle and M. Platscher, Phys. Rev., **D92**, 095002 (2015), arXiv:1502.03098 [hep-ph].

[260] J. A. Casas and A. Ibarra, Nucl. Phys., **B618**, 171 (2001), arXiv:hep-ph/0103065 [hep-ph].

[261] R. Bouchand and A. Merle, JHEP, **07**, 084 (2012), arXiv:1205.0008 [hep-ph].

[262] J. Kubo, E. Ma, and D. Suematsu, Phys. Lett., **B642**, 18 (2006), arXiv:hep-ph/0604114 [hep-ph].

[263] R. Barbieri, L. J. Hall, and V. S. Rychkov, Phys. Rev., **D74**, 015007 (2006), arXiv:hep-ph/0603188 [hep-ph].

[264] L. Lopez Honorez, E. Nezri, J. F. Oliver, and M. H. G. Tytgat, JCAP, **0702**, 028 (2007), arXiv:hep-ph/0612275 [hep-ph].

[265] D. Aristizabal Sierra, J. Kubo, D. Restrepo, D. Suematsu, and O. Zapata, Phys. Rev., **D79**, 013011 (2009), arXiv:0808.3340 [hep-ph].

[266] E. Ma, Phys. Lett., **B717**, 235 (2012), arXiv:1206.1812 [hep-ph].

[267] J. B. Rosenzweig, *Fundamentals of Beam Physics* (Oxford University Press, 2003).

[268] R. M. Godbole, (2010), arXiv:1007.0946 [physics.pop-ph].

[269] T. Han, in *Physics in $D \geq 4$. Proceedings, Theoretical Advanced Study Institute in elementary particle physics, TASI 2004, Boulder, USA, June 6-July 2, 2004* (2005) pp. 407–454, arXiv:hep-ph/0508097 [hep-ph].

[270] D. Zeppenfeld, in *Neutrinos in physics and astrophysics from 10^{-33} to 10^{28} cm. Proceedings, Conference, TASI'98, Boulder, USA, June 1-26, 1998* (1999) pp. 303–350, arXiv:hep-ph/9902307 [hep-ph].

[271] M. Perelstein, in *Physics of the large and the small, TASI 09, proceedings of the Theoretical Advanced Study Institute in Elementary Particle Physics, Boulder, Colorado, USA, 1-26 June 2009* (2011) pp. 421–486, arXiv:1002.0274 [hep-ph].

[272] *CERN Accelerator School: Synchrotron radiation and free electron lasers* (CERN, Geneva, 1998).

[273] W. A. Barletta, "Synchrotron radiation," Lecture held at US Particle Accelerator School 2009 (Unit 11 Lecture 18).

[274] H. Burkhardt, "Reminder of the edge effect in synchrotron radiation," Lecture held at US Particle Accelerator School 2009 (Unit 11 Lecture 18).

[275] R. Bruce *et al.*, Phys. Rev. ST Accel. Beams, **17**, 081004 (2014), arXiv:1409.3123 [physics.acc-ph].

[276] (2016), Delivered and recorded luminosities.
ATLAS Run I:
`https://twiki.cern.ch/twiki/bin/view/AtlasPublic/LuminosityPublicResults`;
ATLAS Run II:
`https://twiki.cern.ch/twiki/bin/view/AtlasPublic/LuminosityPublicResultsRun2`.
CMS:
`https://twiki.cern.ch/twiki/bin/view/CMSPublic/LumiPublicResults`. (accessed: 07/2016).

[277] R. P. Feynman, *3rd International Conference on High Energy Collisions Stony Brook, N.Y., September 5-6, 1969*, Conf. Proc., **C690905**, 237 (1969).

[278] J. M. Butterworth, G. Dissertori, and G. P. Salam, Ann. Rev. Nucl. Part. Sci., **62**, 387 (2012), arXiv:1202.0583 [hep-ex].

[279] T. Sjostrand, S. Mrenna, and P. Z. Skands, Comput. Phys. Commun., **178**, 852 (2008), arXiv:0710.3820 [hep-ph].

[280] M. Bahr *et al.*, Eur. Phys. J., **C58**, 639 (2008), arXiv:0803.0883 [hep-ph]; J. Bellm *et al.*, Eur. Phys. J., **C76**, 196 (2016), arXiv:1512.01178 [hep-ph].

[281] V. Khachatryan *et al.* (CMS), Eur. Phys. J., **C76**, 155 (2016), arXiv:1512.00815 [hep-ex].

[282] B. Ward, "A Tevatron Kinematics Primer," (2001).

[283] A. Korytov, in *Journeys Through the Precision Frontier: Amplitudes for Colliders (TASI 2014)*, edited by L. Dixon and et al. (2016) pp. 99–181.

[284] I. J. R. Aitchison and A. J. G. Hey, *Gauge Theories in Particle Physics, Vol. 1 (3rd rev. ed.)* (CRC Press, 2002); I. J. R. Aitchison and A. J. G. Hey, *Gauge Theories in Particle Physics, Vol. 2 (3rd rev. ed.)* (CRC Press, 2002).

[285] F. Halzen and A. D. Martin, *Quarks and Leptons: An Introductory Course in Modern Particle Physics* (Wiley & Sons, 1984).

[286] G. Fiore and G. Modanese, Nucl. Phys., **B477**, 623 (1996), arXiv:hep-th/9508018 [hep-th].

[287] S. Weinberg, *Quantum Theory of Fields, Vol. I: Foundations* (Cambridge University Press, 2005).

[288] D. Berdine, N. Kauer, and D. Rainwater, Phys. Rev. Lett., **99**, 111601 (2007), arXiv:hep-ph/0703058 [hep-ph].

[289] H. M. Pilkuhn, *The Interactions of Hadrons* (North-Holland, 1967).

[290] C. F. Uhlemann and N. Kauer, Nucl. Phys., **B814**, 195 (2009), arXiv:0807.4112 [hep-ph].

[291] A. Djouadi, Phys. Rept., **457**, 1 (2008), arXiv:hep-ph/0503172 [hep-ph]; A. Djouadi, Phys. Rept., **459**, 1 (2008), arXiv:hep-ph/0503173 [hep-ph].

[292] T. Kinoshita, J. Math. Phys., **3**, 650 (1962); T. D. Lee and M. Nauenberg, Phys. Rev., **133**, B1549 (1964), [,25(1964)].

[293] F. Bloch and A. Nordsieck, Phys. Rev., **52**, 54 (1937).

[294] V. N. Gribov and L. N. Lipatov, Sov. J. Nucl. Phys., **15**, 438 (1972), [Yad. Fiz.15,781(1972)]; Y. L. Dokshitzer, Sov. Phys. JETP, **46**, 641 (1977), [Zh. Eksp. Teor. Fiz.73,1216(1977)]; G. Altarelli and G. Parisi, Nucl. Phys., **B126**, 298 (1977).

[295] A. D. Martin, W. J. Stirling, R. S. Thorne, and G. Watt, Eur. Phys. J., **C63**, 189 (2009), arXiv:0901.0002 [hep-ph].

[296] J. Pumplin, D. R. Stump, J. Huston, H. L. Lai, P. M. Nadolsky, and W. K. Tung, JHEP, **07**, 012 (2002), arXiv:hep-ph/0201195 [hep-ph].

[297] R. D. Ball *et al.*, Nucl. Phys., **B867**, 244 (2013), arXiv:1207.1303 [hep-ph].

[298] R. D. Ball *et al.* (NNPDF), JHEP, **04**, 040 (2015), arXiv:1410.8849 [hep-ph].

[299] O. S. Bruning, P. Collier, P. Lebrun, S. Myers, R. Ostojic, J. Poole, and P. Proudlock, (2004), LHC Design Report Vol.1: The LHC Main Ring, [Link] `http://cds.cern.ch/record/782076`; O. Buning, P. Collier, P. Lebrun, S. Myers, R. Ostojic, J. Poole, and P. Proudlock, (2004), LHC Design Report Vol.2: The LHC infrastructure and general services, [Link] `http://cds.cern.ch/record/815187`; M. Benedikt, P. Collier, V. Mertens, J. Poole, and K. Schindl, (2004), LHC Design Report Vol.3: The LHC injector chain, [Link] `http://cds.cern.ch/record/823808`.

[300] LHC milestones [Link] `http://home.cern/topics/large-hadron-collider` (accessed: 07/2016).

[301] P. Giubellino, in *Hadron collider physics. Proceedings, 19th Symposium, HCP2008, Galena, USA, May 27-31, 2008* (2008) arXiv:0809.1062 [nucl-ex].

[302] M. Krämer (Editor) and F. J. P. Solver (Editor), *Large Hadron Collider Phenomenology*, Scottish Graduate Series (CRC Press, 2004).

[303] G. Aad *et al.* (ATLAS), *The ATLAS Experiment at the CERN Large Hadron Collider*, Tech. Rep. (2008).

[304] V. del Duca and E. Laenen, Int. J. Mod. Phys., **A30**, 1530063 (2015), arXiv:1510.06690 [hep-ph].

[305] A. A. Alves, Jr. *et al.* (LHCb), JINST, **3**, S08005 (2008).

[306] K. Aamodt *et al.* (ALICE), JINST, **3**, S08002 (2008).

[307] `http://home.cern/about/updates/2015/11/lhc-collides-ions-new-record-energy` (accessed: 07/2016).

[308] K. Aamodt *et al.* (ALICE), Eur. Phys. J., **C65**, 111 (2010), arXiv:0911.5430 [hep-ex].

[309] P. La Rocca and F. Riggi, *Proceedings, International Symposium on Entrance Channel Effect on the Reaction Mechanism in Heavy Ion Collisions (ECHIC 2013)*, J. Phys. Conf. Ser., **515**, 012012 (2014).

[310] K. Schindl, *The injector chain for the LHC*, Tech. Rep. CERN-OPEN-99-052 (1999); R. Bailey, in *Proceedings, CAS - CERN Accelerator School: Ion Sources* (2013) pp. 565–574, arXiv:1404.0966 [physics.acc-ph].

[311] R. Bailey and P. Collier, *Standard Filling Schemes for Various LHC Operation Modes*, Tech. Rep. LHC-PROJECT-NOTE-323 (CERN, Geneva, 2003).

[312] *Non-collision backgrounds as measured by the ATLAS detector during the 2010 proton-proton run*, Tech. Rep. ATLAS-CONF-2011-137 (CERN, Geneva, 2011).

[313] M. Boonekamp, F. Gianotti, R. A. McPherson, M. Nessi, and P. Nevksi, (2004).

[314] C. Lippmann, Nucl. Instrum. Meth., **A666**, 148 (2012), arXiv:1101.3276 [hep-ex].

[315] S. Cucciarelli, M. Konecki, D. Kotlinski, and T. Todorov, *Track reconstruction, primary vertex finding and seed generation with the pixel detector*, Tech. Rep. (2006).

[316] S. Chatrchyan *et al.* (CMS), JINST, **3**, S08004 (2008).

[317] N. M. Nikityuk and V. N. Samoilov, Phys. Part. Nucl., **38**, 659 (2007).

[318] J. Brooke (CMS), *Proceedings, 36th International Conference on High Energy Physics (ICHEP2012)*, PoS, **ICHEP2012**, 508 (2013), arXiv:1302.2469 [hep-ex].

[319] `http://scipp.ucsc.edu/personnel/atlas.html` (accessed: 07/2016).

[320] T. R. Holtz Jr., *Dinosaurs: The Most Complete, Up-to-Date Encyclopedia for Dinosaur Lovers of all Ages* (Random House Books for Young Readers, 2007) Appendix containing genus list available at `http://www.geol.umd.edu/~tholtz/dinoappendix/HoltzappendixWinter2011.pdf` (accessed: 07/2016).

[321] J. Goodson, *Search for Supersymmetry in States with Large Missing Transverse Momentum and Three Leptons including a Z-Boson*, Ph.D. thesis, Stony Brook University (2012), presented 17 Apr 2012.

[322] G. Aad *et al.* (ATLAS), *Expected Performance of the ATLAS Experiment - Detector, Trigger and Physics*, Tech. Rep. (2009) arXiv:0901.0512 [hep-ex].

[323] H. H. J. ten Kate, IEEE Trans. Appl. Supercond., **15**, 1267 (2005).

[324] T. Sakuma and T. McCauley, *Proceedings, 20th International Conference on Computing in High Energy and Nuclear Physics (CHEP 2013)*, J. Phys. Conf. Ser., **513**, 022032 (2014), arXiv:1311.4942 [physics.ins-det].

[325] H. Bertelsen *et al.*, *Proceedings, Topical Workshop on Electronics for Particle Physics (TWEPP14)*, JINST, **11**, C02020 (2016).

[326] A. Andreazza *et al.*, *The expected performance of the ATLAS inner detector*, Tech. Rep. (2009).

[327] S. Jung and H.-S. Lee, (2015), arXiv:1503.00414 [hep-ph].

[328] G. Aad *et al.* (ATLAS), JINST, **7**, P01013 (2012), arXiv:1110.6191 [hep-ex].

[329] S. Chatrchyan *et al.* (CMS), JINST, **5**, T03021 (2010), arXiv:0910.5530 [physics.ins-det].

[330] S. Dasu *et al.* (CMS), *CMS. The TriDAS project. Technical design report, vol. 1: The trigger systems*, Tech. Rep. (2000); P. Sphicas (CMS), *CMS: The TriDAS project. Technical design report, Vol. 2: Data acquisition and high-level trigger*, Tech. Rep. (2002); A. Tapper and D. Acosta (CMS), *CMS Technical Design Report for the Level-1 Trigger Upgrade*, Tech. Rep. (2013).

[331] S. Chatrchyan *et al.* (CMS), JINST, **9**, P10009 (2014), arXiv:1405.6569 [physics.ins-det].

[332] S. Agostinelli *et al.* (GEANT4), Nucl. Instrum. Meth., **A506**, 250 (2003).

[333] Wolfram Research, Inc., "Mathematica 9.0," (2012).

[334] K. Hamaguchi, Y. Kuno, T. Nakaya, and M. M. Nojiri, Phys. Rev., **D70**, 115007 (2004), arXiv:hep-ph/0409248 [hep-ph].

[335] A. Arvanitaki, S. Dimopoulos, A. Pierce, S. Rajendran, and J. G. Wacker, Phys. Rev., **D76**, 055007 (2007), arXiv:hep-ph/0506242 [hep-ph].

[336] *ATLAS liquid argon calorimeter: Technical design report*, Tech. Rep. (1996).

[337] N. Craig, in *Beyond the Standard Model after the first run of the LHC Arcetri, Florence, Italy, May 20-July 12, 2013* (2013) arXiv:1309.0528 [hep-ph].

[338] G. F. Giudice and R. Rattazzi, Phys. Rept., **322**, 419 (1999), arXiv:hep-ph/9801271 [hep-ph].

[339] R. Barbier *et al.*, Phys. Rept., **420**, 1 (2005), arXiv:hep-ph/0406039 [hep-ph].

[340] W. Buchmüller, L. Covi, K. Hamaguchi, A. Ibarra, and T. Yanagida, JHEP, **03**, 037 (2007), arXiv:hep-ph/0702184 [HEP-PH].

[341] A. Arvanitaki, N. Craig, S. Dimopoulos, and G. Villadoro, JHEP, **02**, 126 (2013), arXiv:1210.0555 [hep-ph].

[342] Z. Liu and B. Tweedie, JHEP, **06**, 042 (2015), arXiv:1503.05923 [hep-ph].

[343] F. Brechu (ATLAS), "Reconstruction of tracks with large impact parameter in the inner detector," (2012).

[344] C. W. Loh, *Search for Long-Lived Neutral Particles in Final States with a Muon and Multi-Track Displaced Vertex with the ATLAS Detector at the Large Hadron Collider*, Ph.D. thesis, British Columbia U. (2013-04-30).

[345] G. Aad *et al.* (ATLAS), JINST, **9**, P02001 (2014), arXiv:1311.7070 [physics.ins-det].

[346] W. Buchmüller, K. Hamaguchi, M. Ratz, and T. Yanagida, (2004), arXiv:hep-ph/0403203 [hep-ph].

[347] G. F. Giudice, M. A. Luty, H. Murayama, and R. Rattazzi, JHEP, **12**, 027 (1998), arXiv:hep-ph/9810442 [hep-ph]; L. Randall and R. Sundrum, Nucl. Phys., **B557**, 79 (1999), arXiv:hep-th/9810155 [hep-th].

[348] V. Khachatryan *et al.* (CMS), JHEP, **01**, 096 (2015), arXiv:1411.6006 [hep-ex].

[349] L. Calibbi, A. Mariotti, C. Petersson, and D. Redigolo, JHEP, **09**, 133 (2014), arXiv:1405.4859 [hep-ph]; C. Petersson, in *International Conference on High Energy Physics 2014 (ICHEP 2014) Valencia, Spain, July 2-9, 2014* (2014) arXiv:1411.0632 [hep-ph].

[350] N. Blinov, J. Kozaczuk, D. E. Morrissey, and A. de la Puente, Phys. Rev., **D93**, 035020 (2016), arXiv:1510.08069 [hep-ph].

[351] G. Aad *et al.* (ATLAS), Phys. Lett., **B707**, 478 (2012), arXiv:1109.2242 [hep-ex].

[352] V. M. Abazov *et al.* (D0), Phys. Rev. Lett., **97**, 161802 (2006), arXiv:hep-ex/0607028 [hep-ex].

[353] M. J. Strassler and K. M. Zurek, Phys. Lett., **B651**, 374 (2007), arXiv:hep-ph/0604261 [hep-ph].

[354] M. J. Strassler and K. M. Zurek, Phys. Lett., **B661**, 263 (2008), arXiv:hep-ph/0605193 [hep-ph].

[355] M. Verducci (ATLAS), *Proceedings, 2nd Symposium on Prospects in the Physics of Discrete Symmetries (DISCRETE 2010)*, J. Phys. Conf. Ser., **335**, 012068 (2011).

[356] V. Khachatryan *et al.* (CMS), Phys. Rev., **D91**, 052012 (2015), arXiv:1411.6977 [hep-ex].

[357] J. F. Ziegler, J. Appl. Phys. / Rev. Appl. Phys., **85**, 1249 (1999).

[358] H. Bethe, Ann. Phys., **5**, 325 (1930); H. Bethe, Z. Phys., **76**, 293 (1932).

[359] F. Bloch, Ann. Phys., **16**, 285 (1933); F. Bloch, Z. Phys., **81**, 363 (1933).

[360] J. Lindhard and A. H. Sorensen, Phys. Rev., **A53**, 2443 (2006).

[361] J. L. Feng and B. T. Smith, Phys. Rev., **D71**, 015004 (2005), [Erratum: Phys. Rev.D71,019904(2005)], arXiv:hep-ph/0409278 [hep-ph].

[362] E. Fermi and E. Teller, Phys. Rev., **72**, 399 (1947); J. Lindhard and M. Scharff, Phys. Rev., **124**, 128 (1961).

[363] W. H. Bragg and R. Kleeman, Philos. Mag., **10**, 318 (1905); D. E. Groom, N. V. Mokhov, and S. I. Striganov, Atom. Data Nucl. Data Tabl., **78**, 183 (2001).

[364] H. Bichsel, Nucl. Instrum. Meth., **A562**, 154 (2006).

[365] B. Schorr, Comput. Phys. Commun., **7**, 216 (1974).

[366] *dE/dx measurement in the ATLAS Pixel Detector and its use for particle identification*, Tech. Rep. ATLAS-CONF-2011-016 (CERN, Geneva, 2011).

[367] G. 't Hooft, Nucl. Phys., **B33**, 173 (1971); G. 't Hooft, Nucl. Phys., **B35**, 167 (1971); G. 't Hooft and M. J. G. Veltman, Nucl. Phys., **B44**, 189 (1972).

[368] W. A. Bardeen, C. T. Hill, and M. Lindner, Phys. Rev., **D41**, 1647 (1990).

[369] C. Csaki, C. Grojean, H. Murayama, L. Pilo, and J. Terning, Phys. Rev., **D69**, 055006 (2004), arXiv:hep-ph/0305237 [hep-ph].

[370] W. Meißner and R. Ochsenfeld, Die. Naturwiss., **21**, 787 (1933).

[371] L. D. Landau, Dokl. Akad. Nawk., USSR, **60**, 207 (1948); C.-N. Yang, Phys. Rev., **77**, 242 (1950).

[372] F. del Aguila and J. A. Aguilar-Saavedra, Nucl. Phys., **B813**, 22 (2009), arXiv:0808.2468 [hep-ph].

[373] R. Franceschini, T. Hambye, and A. Strumia, Phys. Rev., **D78**, 033002 (2008), arXiv:0805.1613 [hep-ph].

[374] A. Melfo, M. Nemevsek, F. Nesti, G. Senjanovic, and Y. Zhang, Phys. Rev., **D85**, 055018 (2012), arXiv:1108.4416 [hep-ph].

[375] F. Nuti, *Doubly-charged Higgs searches by ATLAS*, Tech. Rep. ATL-PHYS-PROC-2014-253 (CERN, Geneva, 2014).

[376] M. Muhlleitner and M. Spira, Phys. Rev., **D68**, 117701 (2003), arXiv:hep-ph/0305288 [hep-ph].

[377] S. D. Drell and T.-M. Yan, Phys. Rev. Lett., **25**, 316 (1970), [Erratum: Phys. Rev. Lett.25,902(1970)].

[378] (2016), LHC Higgs Cross Section Working Group: `https://twiki.cern.ch/twiki/bin/view/LHCPhysics/LHCHXSWG` (accessed: 07/2016).

[379] H. M. Georgi, S. L. Glashow, M. E. Machacek, and D. V. Nanopoulos, Phys. Rev. Lett., **40**, 692 (1978).

[380] S. S. D. Willenbrock and D. A. Dicus, Phys. Lett., **B156**, 429 (1985).

[381] R. N. Cahn and S. Dawson, Phys. Lett., **B136**, 196 (1984), [Erratum: Phys. Lett.B138,464(1984)]; G. Altarelli, B. Mele, and F. Pitolli, Nucl. Phys., **B287**, 205 (1987).

[382] (2016), Higgs cross sections for European Strategy studies in 2012: `https://twiki.cern.ch/twiki/bin/view/LHCPhysics/HiggsEuropeanStrategy2012` (accessed: 07/2016).

[383] S. L. Glashow, D. V. Nanopoulos, and A. Yildiz, Phys. Rev., **D18**, 1724 (1978).

[384] R. Raitio and W. W. Wada, Phys. Rev., **D19**, 941 (1979); Z. Kunszt, Nucl. Phys., **B247**, 339 (1984); A. S. Bagdasaryan, R. S. Egorian, S. G. Grigorian, and S. G. Matinyan, Sov. J. Nucl. Phys., **46**, 315 (1987), [Yad. Fiz.46,572(1987)].

[385] M. Spira, A. Djouadi, D. Graudenz, and P. M. Zerwas, Nucl. Phys., **B453**, 17 (1995), arXiv:hep-ph/9504378 [hep-ph].

[386] R. Mertig, M. Bohm, and A. Denner, Comput.Phys.Commun., **64**, 345 (1991).

[387] T. G. Rizzo, Phys. Rev., **D22**, 178 (1980), [Addendum: Phys. Rev.D22,1824(1980)].

[388] W. H. Furry, Phys. Rev., **51**, 125 (1937).

[389] F. del Aguila and L. Ametller, Phys. Lett., **B261**, 326 (1991).

[390] D. A. Dicus and P. Roy, Phys. Rev., **D44**, 1593 (1991).

[391] C. Liu and S. Yang, Phys. Rev., **D81**, 093009 (2010), arXiv:1005.1362 [hep-ph].

[392] D. B. Clark, in *Proceedings, Meeting of the APS Division of Particles and Fields (DPF 2015)* (2015) arXiv:1510.09200 [hep-ph].

[393] T. Hambye, F. S. Ling, L. Lopez Honorez, and J. Rocher, JHEP, **07**, 090 (2009), [Erratum: JHEP05,066(2010)], arXiv:0903.4010 [hep-ph].

[394] C.-H. Chen and T. Nomura, Phys. Rev., **D90**, 075008 (2014), arXiv:1406.6814 [hep-ph].

[395] M. Cirelli, N. Fornengo, and A. Strumia, Nucl. Phys., **B753**, 178 (2006), arXiv:hep-ph/0512090 [hep-ph].

[396] A. Pierce and J. Thaler, JHEP, **08**, 026 (2007), arXiv:hep-ph/0703056 [HEP-PH].

[397] M. B. Einhorn, D. R. T. Jones, and M. J. G. Veltman, Nucl. Phys., **B191**, 146 (1981); M. E. Peskin and T. Takeuchi, Phys. Rev. Lett., **65**, 964 (1990); M. E. Peskin and T. Takeuchi, Phys. Rev., **D46**, 381 (1992).

[398] L. Lavoura and L.-F. Li, Phys. Rev., **D49**, 1409 (1994), arXiv:hep-ph/9309262 [hep-ph].

[399] M. Baak, J. Cúth, J. Haller, A. Hoecker, R. Kogler, K. Mönig, M. Schott, and J. Stelzer (Gfitter Group), Eur. Phys. J., **C74**, 3046 (2014), arXiv:1407.3792 [hep-ph].

[400] K. Earl, K. Hartling, H. E. Logan, and T. Pilkington, Phys. Rev., **D88**, 015002 (2013), arXiv:1303.1244 [hep-ph].

[401] K. Hally, H. E. Logan, and T. Pilkington, Phys. Rev., **D85**, 095017 (2012), arXiv:1202.5073 [hep-ph].

[402] *Measurements of the Higgs boson production and decay rates and constraints on its couplings from a combined ATLAS and CMS analysis of the LHC pp collision data at $\sqrt{s}$ = 7 and 8 TeV*, Tech. Rep. ATLAS-CONF-2015-044 (CERN, Geneva, 2015).

[403] P. Posch, Phys. Lett., **B696**, 447 (2011), arXiv:1001.1759 [hep-ph]; B. Swiezewska and M. Krawczyk, Phys. Rev., **D88**, 035019 (2013), arXiv:1212.4100 [hep-ph]; M. Krawczyk, D. Sokolowska, P. Swaczyna, and B. Swiezewska, JHEP, **09**, 055 (2013), arXiv:1305.6266 [hep-ph].

[404] S. Y. Choi, K. Hagiwara, H. U. Martyn, K. Mawatari, and P. M. Zerwas, Eur. Phys. J., **C51**, 753 (2007), arXiv:hep-ph/0612301 [hep-ph].

[405] (2016), CTEQ Meta-Page: `http://users.phys.psu.edu/~cteq/`.

[406] A. Belyaev, N. D. Christensen, and A. Pukhov, Comput. Phys. Commun., **184**, 1729 (2013), arXiv:1207.6082 [hep-ph].

[407] CMS Collaboration (CMS), CMS-PAS-HIG-13-016 (2013).

[408] A. Delgado, C. Garcia Cely, T. Han, and Z. Wang, Phys. Rev., **D84**, 073007 (2011), arXiv:1105.5417 [hep-ph]; T. Ma, B. Zhang, and G. Cacciapaglia, Phys. Rev., **D89**, 093022 (2014), arXiv:1404.2375 [hep-ph].

[409] A. Ibarra, E. Molinaro, and S. T. Petcov, JHEP, **09**, 108 (2010), arXiv:1007.2378 [hep-ph]; A. Ibarra, E. Molinaro, and S. T. Petcov, Phys. Rev., **D84**, 013005 (2011), arXiv:1103.6217 [hep-ph]; D. N. Dinh, A. Ibarra, E. Molinaro, and S. T. Petcov, JHEP, **08**, 125 (2012), [Erratum: JHEP09,023(2013)], arXiv:1205.4671 [hep-ph].

[410] P. S. Bhupal Dev, R. Franceschini, and R. N. Mohapatra, Phys. Rev., **D86**, 093010 (2012), arXiv:1207.2756 [hep-ph]; C. G. Cely, A. Ibarra, E. Molinaro, and S. T. Petcov, Phys. Lett., **B718**, 957 (2013), arXiv:1208.3654 [hep-ph].

[411] G. Aad *et al.* (ATLAS), Phys. Rev., **D92**, 032001 (2015), arXiv:1506.01839 [hep-ex].

[412] *Search for heavy lepton partners of neutrinos in pp collisions at 8 TeV, in the context of type III seesaw mechanism*, Tech. Rep. CMS-PAS-EXO-14-001 (CERN, Geneva, 2016).

[413] E. Todesco and F. Zimmermann, eds., *Proceedings, EuCARD-AccNet-EuroLumi Workshop: The High-Energy Large Hadron Collider (HE-LHC10)*, CERN (CERN, Geneva, 2011) arXiv:1111.7188 [physics.acc-ph].

[414] (2014), BSM physics opportunities at 100 TeV: `http://indico.cern.ch/event/284800/overview`.

[415] M. Davier, A. Hocker, and Z. Zhang, Rev. Mod. Phys., **78**, 1043 (2006), arXiv:hep-ph/0507078 [hep-ph].

[416] R. H. Cyburt, J. R. Ellis, B. D. Fields, K. A. Olive, and V. C. Spanos, JCAP, **0611**, 014 (2006), arXiv:astro-ph/0608562 [astro-ph].

[417] I. F. Ginzburg and I. P. Ivanov, (2003), arXiv:hep-ph/0312374 [hep-ph].

[418] J. R. Andersen *et al.* (LHC Higgs Cross Section Working Group), (2013), doi:10.5170/CERN-2013-004, arXiv:1307.1347 [hep-ph].

[419] J. Alwall, R. Frederix, S. Frixione, V. Hirschi, F. Maltoni, O. Mattelaer, H. S. Shao, T. Stelzer, P. Torrielli, and M. Zaro, JHEP, **07**, 079 (2014), arXiv:1405.0301 [hep-ph].

[420] J. A. Evans and J. Shelton, JHEP, **04**, 056 (2016), arXiv:1601.01326 [hep-ph].

[421] V. Khachatryan *et al.* (CMS), Eur. Phys. J., **C75**, 325 (2015), arXiv:1502.02522 [hep-ex].

[422] Tabulated track selection probabilities: `http://hepdata.cedar.ac.uk/view/ins1343509` (accessed: 07/2016).

[423] A. L. Read, *Advanced Statistical Techniques in Particle Physics. Proceedings, Conference, Durham, UK, March 18-22, 2002*, J. Phys., **G28**, 2693 (2002), [,11(2002)].

[424] J. Cogan and D. Su, *Search for out-of-time decays of stopped particles at the ATLAS detector*, Ph.D. thesis, Stanford U. (2014), presented 09 Dec 2013.

[425] J. de Favereau, C. Delaere, P. Demin, A. Giammanco, V. Lemaître, A. Mertens, and M. Selvaggi (DELPHES 3), JHEP, **02**, 057 (2014), arXiv:1307.6346 [hep-ex].

[426] M. Lamont, "The LHC machine: Run 2 and beyond," (2015); M. Battaglia, "Status and expectations from LHC Run 2. CERN Winter School on Supergravity, Strings, and Gauge Theory 2015," (2015).

[427] G. J. Feldman and R. D. Cousins, Phys. Rev., **D57**, 3873 (1998), arXiv:physics/9711021 [physics.data-an].

[428] D. Tong, "Kinetic Theory," (2012), lecture notes on kinetic theory at Cambridge University, [Link] `http://www.damtp.cam.ac.uk/user/tong/kinetic.html`.

[429] M. Escobedo, S. Mischler, and P. D. Vall, Manuel A., Electron. J. Diff. Eqns, **Monograph 04**, 85 pages (2003).

[430] P. Bandyopadhyay, S. Choubey, and M. Mitra, JHEP, **10**, 012 (2009), arXiv:0906.5330 [hep-ph].

[431] F. del Aguila, J. A. Aguilar-Saavedra, J. de Blas, and M. Perez-Victoria, in *Proceedings, 43rd Rencontres de Moriond on Electroweak Interactions and Unified Theories* (2008) arXiv:0806.1023 [hep-ph].

[432] J. Chakrabortty, (2010), arXiv:1003.3154 [hep-ph]; W. Chao, Phys. Rev., **D82**, 016008 (2010), arXiv:1003.1468 [hep-ph]; F. M. L. de Almeida, Y. A. Coutinho, J. A. Martins Simoes, A. J. Ramalho, L. Ribeiro Pinto, S. Wulck, and M. A. B. do Vale, Phys. Rev., **D81**, 053005 (2010), arXiv:1001.2162 [hep-ph]; H. Zhang and S. Zhou, Phys. Lett., **B685**, 297 (2010), arXiv:0912.2661 [hep-ph]; P. S. B. Dev and R. N. Mohapatra, Phys. Rev., **D81**, 013001 (2010), arXiv:0910.3924 [hep-ph]; Z.-z. Xing and S. Zhou, Phys. Lett., **B679**, 249 (2009), arXiv:0906.1757 [hep-ph]; E. Molinaro, *Proceedings, 2013 European Physical Society Conference on High Energy Physics (EPS-HEP 2013)*, PoS, **EPS-HEP2013**, 303 (2013), arXiv:1312.5076 [hep-ph].

[433] R. N. Mohapatra *et al.*, Rept. Prog. Phys., **70**, 1757 (2007), arXiv:hep-ph/0510213 [hep-ph].

[434] A. Abada, C. Biggio, F. Bonnet, M. B. Gavela, and T. Hambye, JHEP, **12**, 061 (2007), arXiv:0707.4058 [hep-ph].

[435] W. Greiner, *Quantum Mechanics: Symmetries* (Springer, 1994).

[436] G. C. Branco, R. Gonzalez Felipe, F. R. Joaquim, and H. Serodio, Phys. Rev., **D86**, 076008 (2012), arXiv:1203.2646 [hep-ph].

[437] D. A. Ross and M. J. G. Veltman, Nucl. Phys., **B95**, 135 (1975).

[438] A. Arhrib, R. Benbrik, M. Chabab, G. Moultaka, M. C. Peyranere, L. Rahili, and J. Ramadan, Phys. Rev., **D84**, 095005 (2011), arXiv:1105.1925 [hep-ph].

[439] A. G. Akeroyd and S. Moretti, Phys. Rev., **D84**, 035028 (2011), arXiv:1106.3427 [hep-ph].

[440] E. J. Chun, H. M. Lee, and P. Sharma, in *1st Toyama International Workshop on Higgs as a Probe of New Physics 2013 (HPNP2013) Toyama, Japan, February 13-16, 2013* (2013) arXiv:1305.0329 [hep-ph].

[441] A. Abada, C. Biggio, F. Bonnet, M. B. Gavela, and T. Hambye, Phys. Rev., **D78**, 033007 (2008), arXiv:0803.0481 [hep-ph]; C. Biggio and F. Bonnet, Eur. Phys. J., **C72**, 1899 (2012), arXiv:1107.3463 [hep-ph].

[442] J. C. Romão, "Modern techniques for one-loop calculations," (2006), [Link] `http://porthos.ist.utl.pt/OneLoop/one-loop.pdf`.

[443] G. Passarino and M. J. G. Veltman, Nucl. Phys. B, **160**, 151 (1979).

[444] Z. Bern, L. J. Dixon, and D. A. Kosower, Phys. Lett. B, **302**, 299 (1993), [Erratum, ibid. B 318 (1993) 649].

[445] R. K. Ellis, Z. Kunszt, K. Melnikov, and G. Zanderighi, Phys.Rept., **518**, 141 (2012), [hep-ph/1105.4319], arXiv:1105.4319 [hep-ph].

[446] K. Hagiwara, S. Matsumoto, D. Haidt, and C. S. Kim, Z.Phys., **C64**, 559 (1994), arXiv:hep-ph/9409380 [hep-ph].

[447] M. Beccaria, G. J. Gounaris, J. Layssac, and F. M. Renard, Int.J.Mod.Phys., **A23**, 1839 (2008), arXiv:0711.1067 [hep-ph].

[448] T. Hahn and M. Perez-Victoria, Comput.Phys.Commun., **118**, 153 (1999), arXiv:hep-ph/9807565 [hep-ph].

[449] *ATLAS inner detector: Technical design report. Vol. 1*, Tech. Rep. (1997); *ATLAS inner detector: Technical design report. Vol. 2*, Tech. Rep. (1997).

[450] M. S. Alam *et al.* (ATLAS), Tech. Rep. (1998) ATLAS pixel detector: Technical design report.

[451] J. N. Jackson, *The ATLAS semiconductor tracker (SCT)*, Tech. Rep. (2005).

[452] E. Abat *et al.* (ATLAS TRT), *The ATLAS TRT barrel detector*, Tech. Rep. (2008); E. Abat *et al.*, *The ATLAS TRT end-cap detectors*, Tech. Rep. (2008).

[453] B. Aubert *et al.* (ATLAS Electromagnetic Barrel Liquid Argon Calorimeter Group), Nucl. Instrum. Meth., **A558**, 388 (2006).

[454] *ATLAS tile calorimeter: Technical design report*, Tech. Rep. (1996).

[455] *ATLAS muon spectrometer: Technical design report*, Tech. Rep. (1997).

[456] V. Karimäki, M. Mannelli, P. Siegrist, H. Breuker, A. Caner, R. Castaldi, K. Freudenreich, G. Hall, R. Horisberger, M. Huhtinen, and A. Cattai (CMS Collaboration), *The CMS tracker system project: Technical Design Report*, Technical Design Report CMS (CERN, Geneva, 1997).

[457] D. Kotlinski (CMS Pixel), *4th International Workshop on Semiconductor Pixel Detectors for Particles and Imaging (PIXEL 2008) Batavia, Illinois, September 23-26, 2008*, JINST, **4**, P03019 (2009).

[458] *The CMS electromagnetic calorimeter project: Technical Design Report*, Tech. Rep. (Geneva, 1997).

[459] S. Chatrchyan *et al.* (CMS), JINST, **8**, P09009 (2013), [JINST8,9009(2013)], arXiv:1306.2016 [hep-ex].

[460] *The CMS hadron calorimeter project: Technical Design Report*, Tech. Rep. (Geneva, 1997).

[461] *The CMS muon project: Technical Design Report*, Tech. Rep. (Geneva, 1997).

[462] G. J. Hine and G. L. E. Brownell, *Radiation Dosimetry* (Academic Press, 1956).

[463] M. D. Joergensen, *Search for long lived massive particles with the ATLAS detector at the LHC*, Master's thesis, Bohr Inst. (2011).

[464] M. Aurousseau, *Mesure in situ de l'uniformité du calorimètre électromagnétique et recherche des premiers événements di-photons dans ATLAS.*, Ph.D. thesis, LAPP (2010).

[465] A. A. Abdelalim and A. Blondel, *Study on the Impact of Cross-Talk in the ATLAS Electromagnetic Calorimeter on the Signal Prediction in the Strip Layer*, Master's thesis, Geneva U. (2008), presented Sept 2008.

[466] S. Laplace and P. Iengo, (2010), [Link]: `https://indico.in2p3.fr/event/2475/material/slides/0.pdf`.

[467] K. Anderson, T. Del Prete, E. Fullana, J. Huston, C. Roda, and R. Stanek, Int. J. Mod. Phys., **A25**, 1981 (2010).

[468] R. A. Bertlmann, *Anomalies in Quantum Field Theories* (Clarendon Press, 2000).

[469] L. H. Ryder, *Quantum Field Theory (2nd Ed.)* (Cambridge University Press, 1996).

Acknowledgements

I am deeply indebted to my advisor, Alejandro Ibarra, for welcoming me in his group, for letting me be active in the research field of my highest interest and for his continuous support.

Furthermore, I am grateful to Emiliano Molinaro and Stefan Vogl for being excellent collaborators. It has been a pleasure to write articles together.

I also thank my colleagues of the groups T30d and T30e and Karin Ramm for making the environment so enjoyable.

I furthermore need to thank João Seixas, who often took his time to discuss physics with me.

I would like to express my gratitude to Kristina, my family and close friends, for their moral backup and encouragement.

In particular, I very much thank my parents, Rudolf and Fátima, for their never-ending love and support. I dedicate this thesis to them.

Last but not least, I am grateful for the financial support by the Fundação para a Ciência e a Tecnologia, who serve science so significantly.